

Honda R&D

Technical Review

October 2010

Vol.22 No.2



Comment on the Cover

Our present circumstances—our environmental problems, our economic situation—pose a stiff challenge to us. But difficult times like these are exactly the right time to rejoice and take pride in the fact that we are in a position to realize our dreams.

[Cover design]
The boy on the cover, distracted from his toys, is completely absorbed in drawing pictures, which then spring to life.
Centuries ago, Sesshu used his own tears to draw a mouse that seemed to jump into life. Like Sesshu, our emerging ideas bring our fantasies to life. The cover expresses just such a scene.



Automobile R&D Center
Ryo NAKAYAMA

Technical Review

October 2010

Honda R&D

CONTENTS

Introduction of new technologies

Styling Design of CR-Z . . . . . Takashi NAGURA, Takafumi OZAKI
. . . . . Yoshihisa YANAGIMOTO, Eiko HASHIMOTO 1

Styling Design of 2011 Model Year Odyssey . . . . . Eric SCHUMAKER, Catalin MATEI, Devon FUJIOKA
. . . . . Lori ISHIDA, Nathan BROWN 9

Styling Design of VFR1200F . . . . . Toshiaki KISHI 15

Development of ENEPO Gas Canister-powered Generator
. . . . . Michihiro IIDA, Joji MAEDA, Takeshi SASAJIMA
Masanori FUJINUMA, Jun FUKANO 20

Introduction of High Differential Pressure Water Electrolysis-type Solar Hydrogen Station (SHS2)
. . . . . Koji NAKAZAWA, Hisashi NAGAOKA, Jun TAKEUCHI
Frank MOBURG, Ikuya YAMASHITA, Masanori OKABE 28

Piston Temperature Measurement Technology for Actual HSDI Diesel Engines
. . . . . Koji KATSUMATA, Kenji SHIMIZU
Tadanobu AOKI, Hidemi ARAI 36

Development of V10 500-HP Engine
– Technologies for High-performance and Low-emission Clean Powertrain –
. . . . . Takahiro OKUYAMA, Takeshi FUKUZAWA, Akira HASHIMOTO 41

Development of V10 500-HP Engine – Technologies for High Performance and Reliability –
. . . . . Takahiro OKUYAMA, Makoto NAKADA 50

Development of New Structural Optimization Methodology for Vehicle Crashworthiness
. . . . . Sanjaya FONSEKA 59

Development of Low-profile Fuel Tank System and Zero Leak Valve for North American Market
. . . . . Tetsuhiro ITO, Hisayuki GOMA, Jason GRAHAM 66

Automated Tool for Brake Squeal Analysis . . . . . Sanjib NATH, Scott PAUL 74

Development of Idling Stop System for PCX. . . . . Takeshi YANAGISAWA, Teruhide YAMANISHI
. . . . . Katsuhiro UTSUGI, Toshiya NAGATSUYU 80

Development of Bicycle Simulator for Safety Riding Education. . . . . Kenji SUZUKI, Yukio MIYAMARU 87

Brain Machine Interface Technology Enabling Control of Machine by Human Thought Alone
. . . . . Tatsuya OKABE, Kentaro YAMADA, Masahiro KIMURA, Akihiro TODA
Masaaki SATO, Okito YAMASHITA, Yusuke TAKEDA, Mitsuo KAWATO 93

System Modeling Technology for Powerplant Control Systems
. . . . . Makoto MURAKAMI, Kazunori NOMURA
Takashi HISAKI, Yasuhiko KASAHARA 101

Development of Large-scale PIV Measurement Technique. . . . . Gensuke HOSHINO, Takashi YOSHINO
. . . . . Yuichi FUKUCHI, Minoru TERAMURA 109

Rapid Trial-Production Technique for Aluminum Alloy Engine Components with Hollow Construction
using Block Buildup-Brazing
. . . . . Takeshi WADA, Tatsuo JIKIMOTO, Hidenori OKAJIMA 118

Technical papers

Research on Expansion of Premixed Charge Compression Ignition (PCCI) Diesel Combustion Operation Range
. . . . . Junichi HATANO, Takeya HARADA, Kazuhiro MATSUI
Hiroki KOBAYASHI, Ryuta MATSUI 123

Enhancement of Low-temperature Combustion in Flexible Fuel Vehicle (FFV) Engine
. . . . . Susumu NAKAJIMA 131

Verification of Equivalent Indicated Mean Effective Pressure Measurement Method
. . . . . Keiichi NAGASHIMA, Keiji MIURA, Masahiko MATSUMOTO
Naoki HANADA, Yoshito TSUKAMOTO, Kazuo TSUCHIYA 139

Prediction Method of Low-cycle Fatigue Breakdown in HSDI Diesel Cylinder Head
. . . . . Shohei MIKAMI, Koichi OGINO, Mitsumasa SORAZAWA 147

Effects of Low-viscosity Engine Oil on Fuel Economy and Wear
. . . . . Yosuke OKUYAMA, Daichi SHIMOKOJI, Syouji KAWAUCHI
Takeshi HATTA, Masashi MARUYAMA 158

Prediction Technology of Output Power and Intake-Exhaust Noise Using 1D-Simulation for Small-Displacement Motorcycles
. . . . . Hiroshi HORIKAWA, Hideki KIDO
Satoshi IIJIMA, Yasuo MURAKAMI 166

Study of Upshift Control Method by Estimation of Acceleration Waveform
. . . . . Shintaro KAMEDA, Yasushi INAGAWA 176

Fuel-Efficient and Low-Noise Steering Systems in Large and Heavy Vehicles using Variable Displacement Pump Technology
. . . . . Jinghong YU, Jon HASKELL 182

Study of Low-temperature CO Oxidation Cycle on Precious Metal-supported CeO_2
. . . . . Yoshiyuki NAKANISHI, Hiroki TAKEORI
Masanori HASHIMOTO, Takayuki WATANABE 189

Microstructure and Mechanical Properties of Heat-resistant Mg-Zn-Y Cast Alloys with Addition of Fourth Elements
. . . . . Yuichi IENAGA, Kenshi INOUE, Mitsumoto KAWAI 196

Galvanic Corrosion Prediction Technology for Aluminum Parts of Chassis . . . . . Takahiro MIZUKAMI 205

Establishment of Prediction Technology of Fatigue Strength in Roots of Internal Thread for Crankcase Assembly and Application in Product Development
. . . . . Hiroshi KURIBARA, Junya SAITO
Hideki SAITO, Daisuke SEKIYA 215

Study of Mechanism of Silencer Drainage Noise . . . . . Osamu MATSUDA, Michihiro TOKUNAGA 222

Styling Design of CR-Z

Takashi NAGURA* Takafumi OZAKI*
Yoshihisa YANAGIMOTO* Eiko HASHIMOTO*

ABSTRACT

Using hybrid technology, the CR-Z realized a balance between addressing the environmental issues associated with fossil fuel consumption and offering the natural "joy of driving" an automobile. It was developed as a new-generation compact sports car based on the ground concept of a "Hybrid Café Racer."

The exterior design with a theme of "Advanced Sensual Bullet" expresses compactness, strength and an advanced feel. The interior design with a theme of "Smart Cockpit" expresses an advanced feel and sportiness that lets the driver concentrate on driving.

1. Introduction

Since Honda entered the automobile market full-scale in 1963, it has always sold passenger vehicles developed with the concepts of "joy of driving" and "joy of using." A core goal of Honda's automobile development is enhancing fuel efficiency and low emissions performance to address the global environmental issues that stem from the consumption of fossil fuels.

In the category of sports cars, however, the increasing weight and emissions that come with higher functionality are likely to have an opposite impact on such environmental issues. In addition, the compact sports car market in particular is declining steadily.

Faced with these environmental issues and the desire to offer vehicles that are fun in ways that suit the times, Honda designers started development that would give more customers of a new generation access to the 'fun of operating' experience of the sports category.

2. Design Goals

Honda began by defining a sports car as a vehicle the driver can operate as he or she pleases, while making driving more fun. Also, an important part of the sports car was the form expression which enables the customer to imagine and feel uplifted by the sense of fun that comes with owning and using the vehicle.

Honda developed the CR-Z as a new-generation hybrid sports car on the ground concept of a "Hybrid Café Racer," meaning a sports car just the right size for many customers to operate as they please, with a style that proclaims at a glance that this is a new-generation sports car, with an interior that lets the driver concentrate on driving, and a design that lets the driver enjoy all these features with everyday comfort (Fig. 1).

The expression "Café Racer" comes from England's "Ace Cafe London," a popular spot for motorcycle aficionados. The concept expresses the desire for a sports car that is grounded in everyday life but which is fun and satisfying to drive and makes one proud to show it off to one's companions.



Fig. 1 Ground concept

* Automobile R&D Center

3. Package Layout

The package layout was based on a sports package concept to achieve the low vehicle height essential for a sports car. The short body enables the driver to operate the car as he or she pleases, and the wide stance enhances cornering performance and expresses the bearing of a sports car – all leading to selection of the keywords "Low, Short and Wide."

A package was chosen offering excellent everyday user friendliness while providing conditions expected of a sports car, such as a low, short and wide form, a driving position offering accurate operation, and a wide field of vision.

The low, short and wide form was based on the platform of the 2009 model year INSIGHT. The layout was refined to optimize the engine height, arrangement of supplementary equipment and layout of the suspension, and a full range of fine adjustments to the forward field of vision and comfort factors resulting in a low overall height of just 1350 mm (exclusive of antenna) and a short overall length of 4080 mm (Fig. 2).

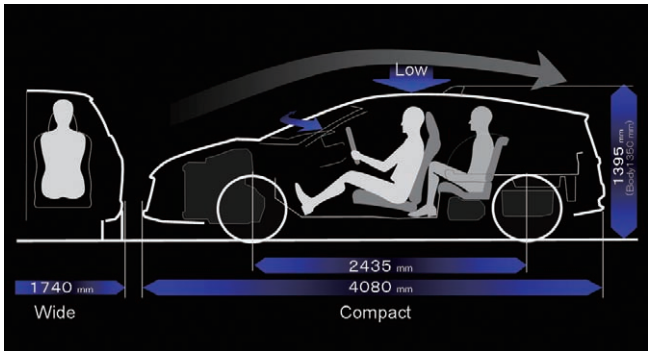


Fig. 2 Package design

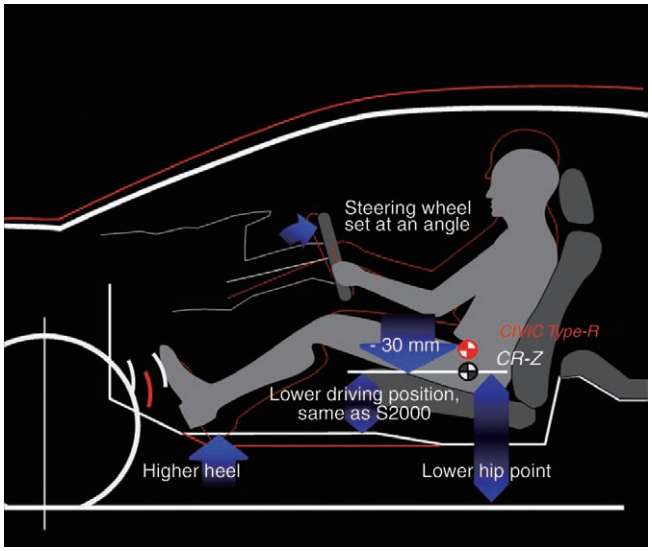


Fig. 3 Driver's position

A low driving position was chosen to suit sports cruising. The driver's hips are held firmly in the seat and the driver can accurately perceive the car's behavior. In addition, the steering wheel is set at an angle and arranged so that even at high cornering G force the driver's shoulder is unlikely to lift off the seat and the driver can operate the car correctly (Fig. 3).

The advanced one-motion silhouette and traditional long nose were successfully fused to each other with a deeply curving front glass by press working. As a result, the lower end of the front pillar is pulled back and its cross-section is more slender, enabling wide horizontal visibility (Fig. 4).

The broadly rounded front window contributes to a sense of the glass area being a single piece with the side windows.

For Europe and Japan, seating is 2+2 style, with the front two seats for main use and the rear two seats for supplementary use. The rear seats are designed to accommodate an ISOFIX universal child seat (Fig. 5). For

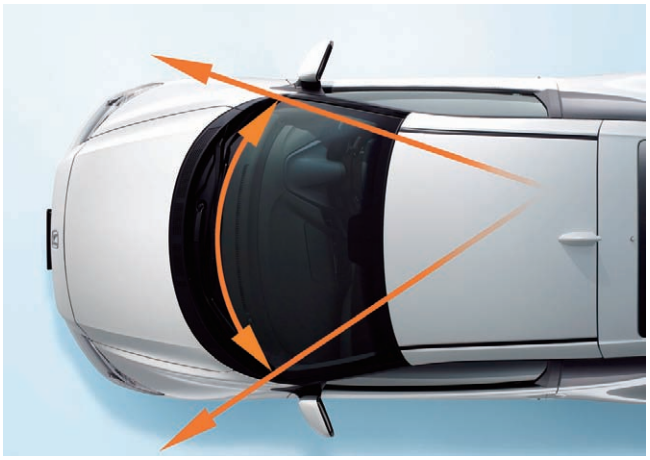


Fig. 4 Front window



Fig. 5 Child seat





Fig. 6 Luggage compartment

the North American market, only the two front seats are provided, with the rear space being used as a "mid-ship console."

To enhance everyday ease of use the trunk room aims to offer the volume necessary for day-to-day use. With the rear seat in use position it can hold two small B suitcases (655 x 480 x 255 mm), and when the rear seat back is folded to make a large flat area it can also hold two popular 9.5-inch golf bags, and depending on size and shape, one mountain bike with the front wheel removed, or four tires (Fig. 6).

4. Exterior Design

The exterior, built on a concept of an "Advanced Sensual Bullet," aims to express the unique bearing of a sports car that makes the owner feel an uplifting sense of joy (Fig. 7).

Starting with a strong, compact mass that projects a sense of presence, the exterior expresses the advanced feel of a hybrid and liveliness of a sports car.

The one-motion silhouette extending from the engine hood to the cabin, the front window with its dynamic curvature, and the low offset black front pillar increase the sense of continuity with the side windows so that the body looks strong and dense while remaining compact.

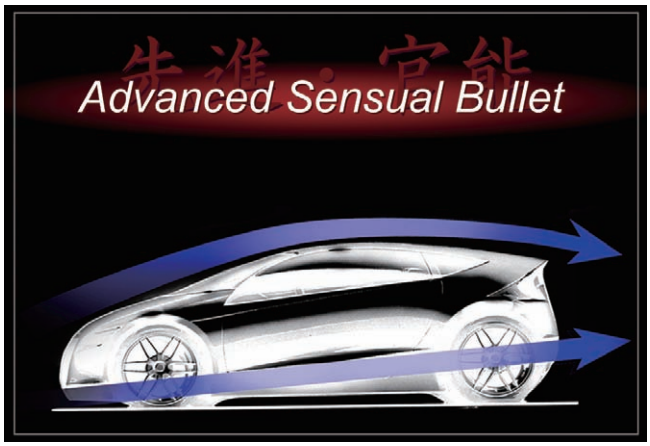


Fig. 7 Exterior design concept

In addition, pulling the lower end of the front pillar rearward fuses the advanced look of the one-motion silhouette with the traditional sports car expression of a long nose (Fig. 8).

The fender area features a low-lying protruding front grill and tires that transmit power to the ground, wrapped in dynamic surfaces that make abundant use of curves giving CR-Z a sports car's bearing and lively expression (Fig. 9).

The lower side of the front bumper is wing-shaped to create a nimble and speedy expression (Fig. 10), while the main motif of the rear bumper is a diffuser form that contributes to aerodynamic performance (Fig. 11). These features are symbolic of a sports car for a new generation,



Fig. 8 Side view of 2010 model year CR-Z



Fig. 9 Overhead view of 2010 model year CR-Z



Fig. 10 Front bumper



Fig. 11 Rear bumper





Fig. 12 “Cubic crystal” image

namely one that takes a sporty approach while also addressing environmental concerns.

The lighting, including the headlights and rear combination lamps, were designed with a “cubic crystal” theme to project an image of the car’s advanced qualities contained in a body full of liveliness much like a living organism. The lights are unified in their design with geometric forms, including rectangular projectors, hexagonal LED unit forms and layered turn signals, expressing the subtleness and clean feel of a hybrid (Fig. 12).

The door mirrors were made smaller, their projected area as seen from the front was reduced, and their form was optimized aerodynamically, thereby enhancing aerodynamic performance without compromising visibility (Fig. 13).

The outer door handle has a bullet motif to maintain the theme of the exterior. Taking aerodynamic performance and ease of use into account, the handle was given a concave hollow for the fingers to enter on the outer panel side, and a vertical flap-type handle was used to limit protrusion and keep the handle compact (Fig. 14).

The “Advanced Dynamic” themed 16-inch aluminum wheels express an energetic spoke form while reducing overall weight by 5 kg compared to the wheels used on the INSIGHT thus help enhance fuel efficiency (Fig. 15).

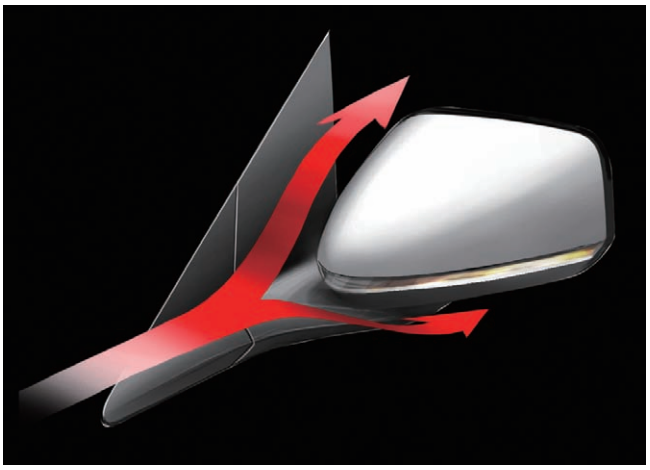


Fig. 13 Door mirror



Fig. 14 Door handle



Fig. 15 Aluminum alloy wheel

5. Interior Design

The interior design features styling based on the concept of a “Smart Cockpit.”

As a hybrid sports car, the CR-Z offers an interior space with a sporty cockpit that allows the driver to concentrate on driving, along with the advanced look of a hybrid car and a design for everyday ease of use.

The instrument panel is based on a form spreading out from side to side, and positions the information display and meters needed for driving in front of the driver as a meter cluster panel. There is just the right amount of snugness in the driver space so that the driver can concentrate on accurate driving. The passenger seat side, in contrast, has a simple structure that gives it a refreshing look (Fig. 16).

The upper part of the instrument panel is called a “floating upper pad.” The audio components are formed to integrate with the motif of spreading wings, and the light gray color of the lower part makes the upper part appear to float giving it a nimble expression.

The upper part has a center upper box while the lower part has, among other features, a glove box that connects to the air conditioner for warm or cold storage and a center lower box, together providing utility that considers everyday ease of use (Fig. 17).



Fig. 16 Interior design concept

To further enable the driver to concentrate on driving through enhanced visibility and operability, the meter cluster panel layout positions the steering wheel in the center surrounded by frequently used switches and information displays essential to cruising.

The climate control is compactly arranged on the left side of the panel. The activation of each switch was unified so that all operations could be easily controlled with the fingertips. The dial to adjust cabin temperature is thin with a wide diameter.

On the right side of the panel, a three-mode drive switch controls one of the major characteristics of the CR-Z. The three modes from the top, are “SPORT,” “NORMAL” and “ECON.” Changing the mode changes the cruising characteristics as well as the color of the interior lighting of the tachometer, making the driver instantly aware of the driving mode (Fig. 18).

The crystal-like scales and blue illumination of the meters express a “futuristic” look at a glance. The centrally placed speedometer and tachometer provide essential information for cruising. The speedometer uses a tele-focus digital display to enhance visibility so that the eyes’ focal



Fig. 17 Floating upper pad



Fig. 18 Meter cluster panel

length does not have to change very much when changing between views of the speedometer and exterior. Because the readings of the tachometer change frequently, an analog display was chosen so that rather than reading it the driver senses it directly. Additionally, to the left and right of the meter are horizontal displays of the fuel gauge, battery level, etc. Thus the meters have been clearly zoned to enhance visibility (Fig. 19).

An MID (multi-information display) shows an "eco-drive bar," advising the driver about accelerator and brake pedal operation when driving in ECON mode. Cars with a manual transmission come with a shift indicator which tells the driver the optimum time to shift to further enhance fuel economy.

On the door lining the armrest was formed so that, like the instrument panel, it appears to float, and its light gray color gives it an airy look. Soft material was used to form the black upper part of the interior door panel giving it a high-quality feel since the shoulder and hand often touch it.

The sense of confidence and quality are further enhanced by the solid metallic look of the ornamental panel and center console, and the look and feel of the door grip, which also offers the passenger added support during sports cruising (Fig. 20).

Based on the concept of a "smart sport seat," the front seat combines cruising performance with safety functions at a high level. The bucket's silhouette is integrated with a garnish that connects the headrest and seat back. It provides two levels of side support to accommodate different body types and holds the driver and passenger in place during sports cruising. The seat is also deeply contoured so that it does not touch the elbow or interfere with shifting, and the headrest functions to help mitigate neck injuries in a rear collision, further enhancing safety.

The seat sides use cloth with high elasticity to accommodate deeply contoured shaping so that driver and passenger are enveloped, while the seat cushions use cloth woven in a checked pattern, which helps keep the hips from slipping on the seat. The cloth is glossy silver, which gives a futuristic, high-quality look (Fig. 21).

The rear seats and trunk were made into a compact space packed with functionality to meet the needs for a compact sports car and a car for everyday ease of use.

The rear seats provide sufficient space for a child or other person of small stature, while the seat backs can be folded forward with just a touch from a front seat to form a soft box with soft cushioning to protect cameras, laptop computers and other precision devices. This also helps prevent theft, because items can be hidden from view from the outside (Fig. 22).

For the North American market, the car has only two seats and the rear space is used as a mid-ship console. The rear surface is a tray with a bulkhead separating the cabin from the trunk. The tray has increased space enabling the area to accommodate more of the goods needed for daily life.

The bulkhead folds forward with just a touch, but also can be used to help prevent cargo from intruding into the front area in the event of a collision. A damper has also been incorporated to reduce the noise of impact with the tray adding to the high-grade operating experience (Fig. 23).



Fig. 19 Meter



Fig. 20 Center console and door ornament panel



Fig. 21 Smart sport seat

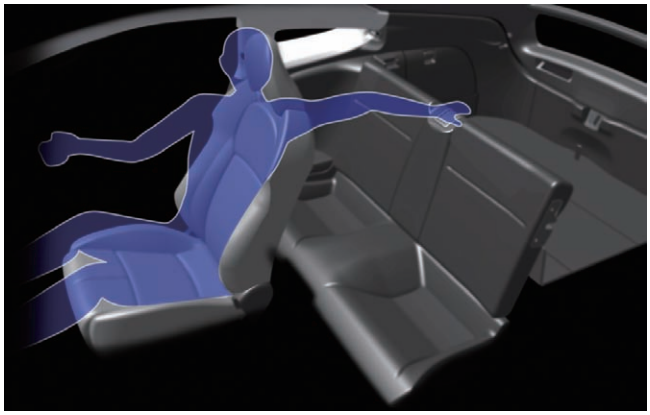


Fig. 22 Rear seat



Fig. 23 Mid-ship console

6. Color Design

Following a theme of "advanced sporty color" (Fig. 24), a lineup of refined, dignified sporty colors was chosen for the exterior to appeal to adult sensibilities.

Of these, new colors exclusive to the CR-Z strongly announce the futurism and high quality of this hybrid.

The two exclusive colors are "Dark Pewter Metallic" and "Horizon Turquoise Pearl."

Dark Pewter Metallic refers to a gray that is metallic with a touch of color. It mixes an astringent green with gun-metal color for a color with presence and chic style, while eliciting feelings of the strength of sports.

Horizon Turquoise Pearl gives the viewer an elegant, premium impression. While a calm color, blue lends it freshness and agility and elicits a sporty feel; a flip-flop visual effect is used to bring out the richness of form.

The rest of the lineup includes the clean and fresh Premium White Pearl; Milano Red - a standard choice for a sports car; the lively looking Brilliant Orange Metallic; Deep Sapphire Blue - bright without being too showy; Crystal Black Pearl for a high-class, high-quality look, and the widely popular Storm Silver Metallic.

Close attention was also paid to the original coloration of the rear diffuser in which fine aluminum flakes are mixed into dark gray resin to give metallic sparkle to emphasize the three-dimensional character of the form and elicit a sense of high quality.

The interior color theme is "Exciting & Tense" (Fig. 25) as the interior creates an image of a "sports space brimming with excitement and tension." Instead of using a combination of black and primary colors as conventionally seen in sports cars, the CR-Z has a bold, high-contrast interior combining black and light gray. With its tension-filled modern and futuristic space, one feels the interior's expression of the elation of sports along with a sense of futurism the very moment they open the door.

The interior lining consists of monotone colors throughout based on the two bold tones of black and gray. The "Gloss on Gloss" combination of different glossy materials elicits a fresh expression, while the "Tone on Tone" combination of similar colors evokes a cool and solid image of the near future.

Image not displayed for copyright reasons.

Fig. 24 Exterior color design

Image not displayed for copyright reasons.

Fig. 25 Interior color design

Much attention was given to providing a high-quality, premium expression in the upper part of the instrument panel. For the first time, Honda used a RIM (reaction injection molding) process to create a texture pleasing to the touch. Newly designed leather-like material reproduces even very fine pores to create an authentic-looking material and to appeal to Europeans with their traditional appreciation of material feel.

For seat fabric, checkered textile was used as the main material for the area where the occupant sits. The silver gray portion brings out a thorough gloss, and the seat, while comfortable, holds the hips firmly in place because the weave pattern suppresses slip. The side material is a glossy gray mesh jersey. By using elastic jersey material, the fabric can easily adapt to the shape of the seat and properly support the body. The shiny white stitching evokes an even more premium and sporty look, and the highest-gloss jersey material was used as support material. Visually, the seat itself projects a three-dimensional form, which is a major accent.

High-luster aluminum film was used for the first time to give the door grips, ornamental panel, and center console a futuristic, high-class look. The mirror-like metallic luster jumps out at the eye the moment the door is opened making a huge impact.

7. Conclusion

High performance and high output - two important elements of the “joy of driving” a sports car - have an impact on the global environment. Therefore, in times like these, to develop sports cars, manufacturers will have to address these environmental issues to maintain the very existence of the sports car category or it could be in jeopardy.

With its name “CR-Z” standing for “Compact Renaissance Zero,” this car definitely suggests a new direction for sports cars, and is certainly a major step forward in bringing the “joy of driving” an automobile to the next era.

■ Author ■


Takashi NAGURA


Takafumi OZAKI


Yoshihisa YANAGIMOTO


Eiko HASHIMOTO

Styling Design of 2011 Model Year Odyssey

Eric SCHUMAKER* Catalin MATEI* Devon FUJIOKA*
Lori ISHIDA* Nathan BROWN*

ABSTRACT

The 2001 Honda Odyssey redefines the American minivan market by more completely fulfilling a family's rational needs and their emotional desires. Previous generations of the Odyssey led the competition in adaptable utility and spirited driving dynamics. The fourth generation Odyssey, guided by the concept of "Cool Family Dream," completely satisfies the minivan user's need for flexibility, utility, and comfort, while completely delighting the customer with exciting interior and exterior styling. It breaks free from the traditional image that a minivan works for a family, but is not something to desire.

For the 2011 Odyssey, the Interior Design Team's goal was to create an experience balancing emotional and rational needs. As a minivan, Odyssey's paramount mission is to satisfy a wide range of user expectations. Versatility and functionality are the cornerstones of the minivan's existence, and this new generation of Odyssey set forth to enhance Odyssey's already class-leading functionality and flexibility. The challenge came with adding an emotional aspect to that formula. Words such as "athletic" and "stylish" describe some traits the development team added as a new dimension to this pragmatic segment by way of a fresh interior layout and design.

The exterior design, based on the concept "Dynamic Monovolume," wraps the increased functionality of the interior with athletic forms and lines. The result is a new-generation Odyssey not just pleasant to look at, but truly stylish and desirable. No longer will the Odyssey be considered a "Mommy Mobile" or a necessary family household tool needing to be excused. The 2011 Odyssey is a stylish and smart expression desired by positive young families.

1. Introduction

The Honda Odyssey debuted in the North American market in 1995 as a smaller minivan with a more world market size and drive train. The second generation, introduced in 1999, targeted the mainstream North American minivan market in size, seating capacity, drive train, and features. It set the standard for minivan family utility and comfort with innovative automatic doors on both sides and a rear seat folding into the floor. Starting in 2005, the third generation extended its market segment leadership with improvements in comfort, performance, and convenience in package layout and solidified its position as the most spirited minivan in North America. It was enjoyed by customers as the minivan that fulfilled the family's needs yet supplied some style and driving pleasure. However, in the overall marketplace, minivans still carried the stigma of a vehicle that a family succumbed to buy—not one they truly wanted. Minivans were purchased by growing American families to support their wide range of activities, and by Empty Nester couples who needed a vehicle to support their traveling and activity with their grown children's families. Understanding this foundation, the 2011 Odyssey design team set out to create a vehicle that worked even better for these two main groups and added the style and emotion that made them want to buy a minivan and display it with pride as an expression of their positive, active lifestyle. In particular, the design team imaged the younger Generation Y family.

The team came up with the grand concept of "Cool Family Dream" as the theme of the overall development for the new Odyssey with the goal to "delight the kids and the parents." The team learned that for today's growing families, enjoying family time is a priority. They are proud to be a family and want to project a positive image of their life stage (Fig. 1).

* HONDA R&D AMERICAS, INC.



Fig. 1 Development concept

2. Package Layout

The package layout is the foundation of the family minivan. Odyssey has led the market with the most user-friendly flexible seating, and the 2011 Odyssey team desired to enhance this practical leadership and add more emotional exterior styling. One might consider these two goals to be contradictory. To deal with this challenge, the team honored the foundational characteristic of a minivan—its package layout. The new Odyssey provides three rows that will seat eight adults comfortably or adapts to a wide variety of seating for any family situation (Fig. 2).

The primary target area for improvement was the center row seating for three. These three seats were given equal status, which required widening the middle row by 100 mm, moving the left and right seats outboard by 50 mm, and making the doors more vertical by 45 mm at the top of the windows. This allows three adults to sit side-by-side or three child seats to be harnessed, or combinations of both. Adding further adaptability to the seating, the middle row center seat can be moved forward, which allows closer access to the front row (Fig. 3). This feature gives a parent in the front row closer access to a child in the center seat of the middle row. Finally, the two outboard seats of the middle row can be moved inboard closer to the center seat or the center seat can be removed completely and the outboard seats moved next to each other. This allows very clear access to the third row of seats from the widened side sliding doors. An additional 25 mm of leg room was added to the third row to improve comfort.

Odyssey's third row "magic seat" system revolutionized the minivan segment and spawned many variations from competitors. The new Odyssey aims to re-establish itself as the "king of packaging" by making this feature simpler. Now, the customer can make either side of the 60/40 split third row "disappear" with a simple pull of a one seat strap versus two straps in the previous Odyssey.

The wider center row increased width and height in the center of the vehicle. The roof tapers and drops from the center to the front and rear, and narrows in width fore and aft from the center row. Overall, Odyssey gained a 35 mm wider stance and width, and 45 mm length on an unchanged wheelbase of 3000 mm. The driver position was made more car-like by lowering the hip point by 12 mm, and forward side visibility improved by moving the touchdown of the A-pillar forward by 127 mm. The windshield became more raked and flowing into the rounder side view roof line.

This layout would ultimately support the exterior designers' goal of creating a more fluid and stylish exterior shape (Fig. 4) and better aerodynamics with a 3% Cd reduction compared to the previous Odyssey's more conventional, rectangular form.



Fig. 2 Sample seating arrangement options

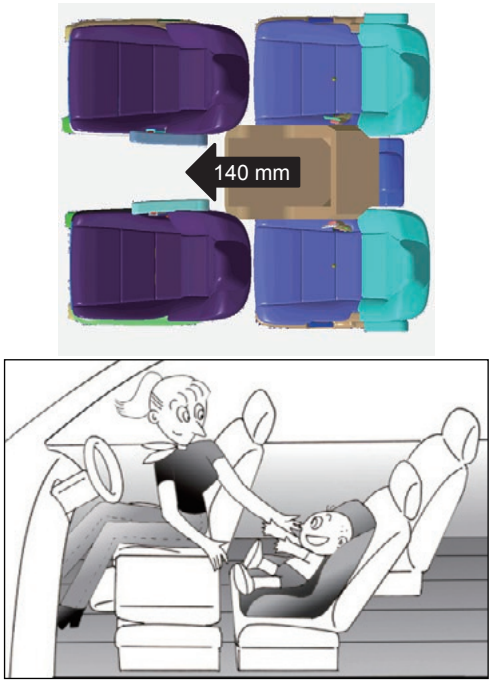


Fig. 3 Center seat function and adaptability

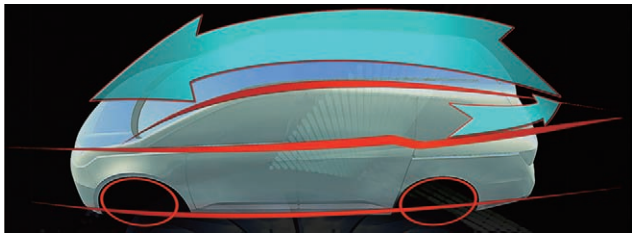


Fig. 4 2011 Odyssey body volume description

3. Exterior Design

To achieve the vehicle concept, the team wanted a vehicle that looked progressive and athletic while maintaining the classy, up-market look of the current Odyssey. Further, the designers wanted the styling to express the Odyssey's class-leading sporty driving traits. They desired to break free from the traditional minivan image of an emotionless box used to do the family hauling chores. In effect, redefine the minivan as something positive. The team envisioned a minivan that fathers wanted to buy and mothers felt younger while driving. Again, this was to be done without ever compromising the Odyssey's exceptional utility, comfort, and adaptability.

The team wanted to create a side view that will make the Odyssey unique in appearance from 100 m away. The side profile was styled to flow with the new package layout: a lower nose, low-angled windshield, raised roof in the center of the passenger area, and a tapered and lower tail. These characteristics changed the overall profile of the Odyssey away from the standard rectangle of a typical minivan. To complement the new profile, the window design introduced a rearward tapering upper edge and a belt line with a lightning bolt shape interacting with the body side forms as shown in Fig. 5. The body side is dominated by a spear form extending from the rear side panel between the rear side window and the C-line. It sets the overall forward dynamic stance of the body. It also works with the side door slide groove to both improve interior packaging and styling. The side door slide groove is lower and thus more outboard than the previous Odyssey and competitors. This allows for wider seats and a lower side window in the rear seat area, both of which provide better visibility for the passengers.

The overall mass and center line shape; the strong, dynamic window graphic and body forms; and smart functional engineering combine to achieve a vehicle that looks fluid, athletic, modern and confident, and functions better for the Cool Family.

3.1. Detail Design

The front end theme of the new Odyssey maintains Honda's family heritage from the FCX. It incorporates jewel-like projector headlights and adds HID in the Touring package. The grille and headlights form one wrapping front mask with secondary detail design using a mix of bright chrome, satin chrome, and dark metallic finished grille bars. The front end components are positioned lower than the previous Odyssey to give a more car-like, air-penetrating appearance. The impression is classy and athletic.

The horizontally-oriented rear design theme leans the new Odyssey in a more automotive direction than previous minivans. The taillights extend from the side spear form wrapping around into a European proportioned license opening. The upper area of the tailgate integrates side and upper spoilers that extend smoothly from the tapered cabin. These spoilers were designed integrally with the Aerodynamic Engineers to achieve exceptional performance while enhancing the fluid styling. The Touring model has additionally rich detailing with gloss black finish on the cabin spoilers and center window pillar garnishes, and body color finish on the side sill garnishes. The expressive side window graphic is traced with bright trim just as the previous Odyssey. This maintains the upscale look while introducing the sportiness of the new window graphic shape. Finally, the door handles are designed to integrate with the body side spear shape while adding a jewel-like detail with a modern watch inspired shape and bright finish.



Fig. 5 Unique beltline shape



Fig. 6 Styling rendering showing lower, more car-like wrapping front end theme



Fig. 7 Styling sketch of rear shows car-like wide tail lamp design

Overall, the initial impression of the new Odyssey is more personal in size and more emotional than functional. Upon interaction, the customer realizes that the interior size, comfort and adaptability is better than the previous class-leading Odyssey. It looks emotional, but is actually more functional. The exterior styling achieves the concept of the "Cool Family Dream."

4. Interior Design

The Interior Design team's goal was to create an experience that balanced emotional and rational needs. Versatility and functionality are the cornerstones of the minivan owner's wide range of expectations. The challenge came with adding athletic and stylish emotion to the new Odyssey (Fig. 8).

From a styling standpoint, the team created leaner, more athletic shapes, surfaces, and lines. Radii were minimized and surfaces simplified through minimal breaks. By doing this, the appearance lends itself to a more thoughtful concise statement: more youthful, modern, and dynamic in appearance. The design unifies the overall interior design theme by minimizing changes in patterns, textures and gloss between different materials and finishes. The final outcome is a product with depth and sophistication that can be appreciated, not only from the first impression, but also over time. The team aimed to create or improve on the instrument layout, passenger amenities, and seating to enhance the user experience.

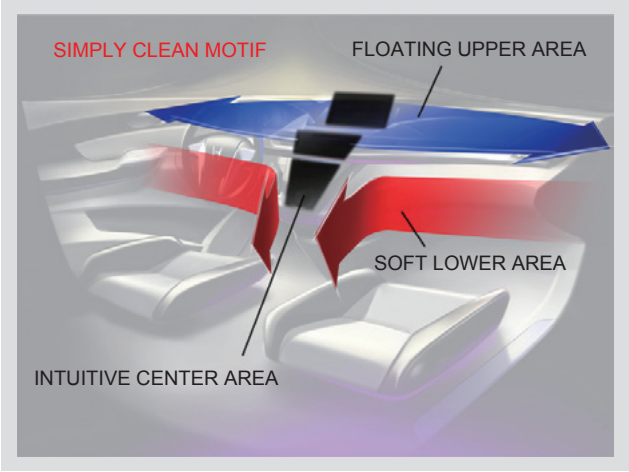


Fig. 8 Interior styling concept



Fig. 9 Key interior styling sketch

Instrumentation. The team recognized that as technology becomes more of a presence in peoples' lives, it creates a more complex experience for the customer. Therefore, a major objective was to simplify the instrumentation, especially the heater and audio controls, to create an easy-to-use and easy-to-understand interaction. Several different design techniques were used, such as color indication, surface treatment, and "zoning" logic, to achieve good ergonomics and clean appearance.

Cool Box. Minivans are the ultimate road-trip vehicles. So it seemed only natural to add a cooler box to the Instrument Panel to refrigerate and store cold beverages for the family. This feature is also practical to keep market or pharmacy items cold.

Split Screen. Another amenity new to the Odyssey is the Split Screen Rear Entertainment System, which is offered on the Touring Tech trim level, that allows second and third row passengers to watch two programs simultaneously. One video feed comes from the DVD player on the instrument panel; a second feed can be added through the HDMI input in the rear seat.

5. Color Design

A "Distinctive Living" concept guided the color and materials design for the 2011 Odyssey. The overall design of the vehicle was targeted for a stylish family wanting a vehicle that expressed their distinctive living and design sense. The interior and exterior materials and colors needed to express a carefree, relaxed, yet fresh and modern stylishness of owners who are embracing their family image—not held back by it.

The color and material design, much like the interior and exterior design, started from the customer's usage of the inside of the vehicle and then radiated out. The foundation was the fabric. A double Rochelle knit with a flowing line graphic pattern was created. It expresses a carefree, relaxed, stylish feeling of a flat surface with a fresh, slight sheen and warmth to the touch. Practically speaking, the material is very durable and cleanable.

5.1. Interior

The 2011 Odyssey offers a choice of three new interior colors, one of which is exclusive (Fig. 10). The "New Beige" color is greyer, darker, and more natural than the beige on the previous generation, and together with the new fabric complements the modern, stylish family. "New Grey" is a lighter mid-tone hue with a redder earth tone, again

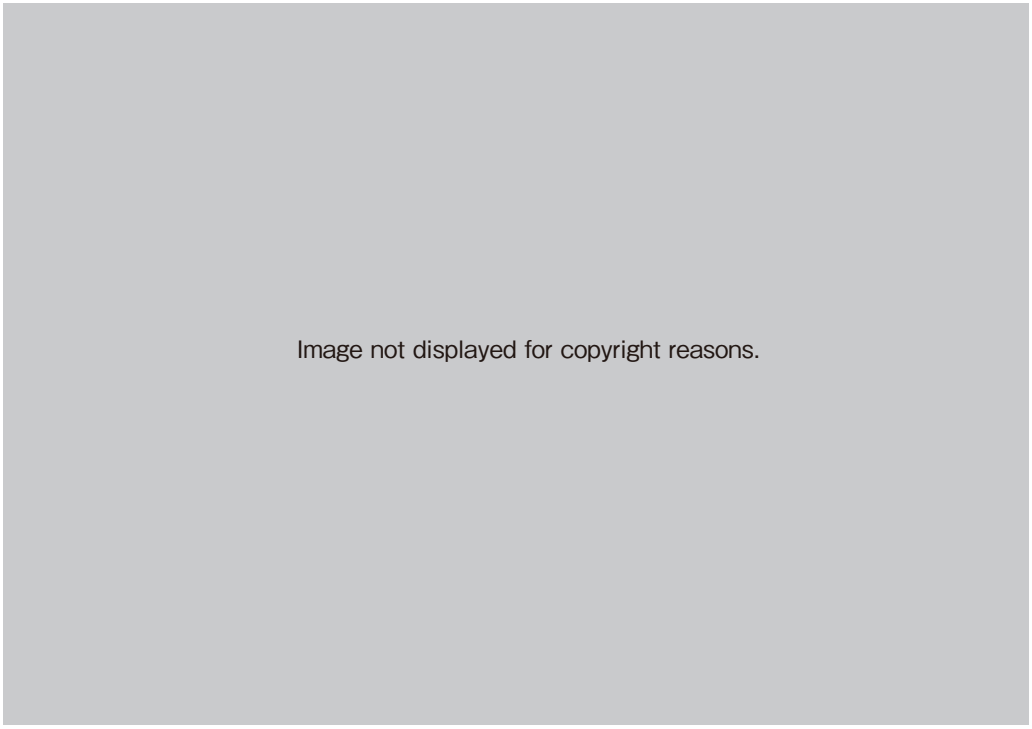


Fig. 10 Interior color and material coordination

projecting a softer, more natural and friendlier feel. The new "Truffle" color, exclusive to the Odyssey, is a dark warm grey that exemplifies the Odyssey family who are proud of their life stage and their sense of modern style. It carries the undertone of luxury and style, without the formality of black, while projecting sportiness and modernity with just a hint of warm, natural hue. It is a medium tone that can be dressed up or down with different exterior colors to meet any occasion, much like the stylish family's home and fashion design.

5.2. Exterior

Complementing the interior colors is a pallet of eight exterior colors including two new colors designed specifically for Odyssey; one exclusive. Smokey Topaz was designed along with the exclusive Truffle interior color. It is a dark metallic color with rich, warm, almost red-brown side hue and bright, clean direct highlights. It accentuates the long, flowing exterior forms and crisp lines. It is similar in value to the window areas thus shows the entire vehicle as one interrupted form. Together with the new sporty, modern interior and exterior forms and designs, Smokey Topaz and Truffle present the carefree, relaxed, stylishness of the Odyssey family. They are a color set which is very upscale, confident, yet inviting. New Celestial Blue was designed for Odyssey and sedans. It is a light value cold color with just enough warmth to keep from being unfriendly. It complements the modern, crisp, machine surfacing of Odyssey's exterior, and because of its light value, allows the unique exterior window graphic shapes be expressed. Celestial Blue enhances and complements the different materials of the exterior's bright chrome window trim, door handle details, grille and lamps, and gloss black pillars and rear air valance. The exterior pallet will soon offer a new Pearl White with the simplicity and cleanliness of straight shade white and the added luxury and richness of pearl. Rounding-out the color offerings are Alabaster silver, Polished Metal metallic, Crystal Black pearl, Dark Cherry red metallic, and Mocha metallic. All together, the 2011 Odyssey color and materials design expresses the carefree and stylish family who are proud of their family lifestyle.

6. Conclusion

The Honda Odyssey has established itself as the minivan with spirit. With each generation of design, Honda has delighted the American family with a vehicle combining clever utility and convenience and fun-to-drive character. The fourth generation Odyssey establishes an almost new category of vehicle: a sporty family minivan. By focusing deeply on the theme "Cool Family Dream," the design team has created a vehicle that exceeds the young family's functional needs with flexible, easy to use seating, unprecedented features, and exceptional visibility. Trend-setting young families will be excited to show off their life stage through the styling expression of the new Odyssey. It embraces and celebrates the joys of family and parenting. The package layout design establishes a solid foundation of equal comfort and seating flexibility for all passengers. The clean, athletic interior design styling seamlessly

blends an unprecedented amount of features. The exterior design wraps the new layout and interior design in a fluid yet crisp athletic and dynamic form with modern, elegant graphics and details. And the colors and materials complete the expression by providing different sets of exterior and interior finishes to fit the individuality of these vibrant families. All together, the 2011 Odyssey is a minivan to proud of.

■ Author ■


Eric SCHUMAKER


Catalin MATEI


Devon FUJIOKA


Lori ISHIDA


Nathan BROWN

Styling Design of VFR1200F

Toshiaki KISHI*

ABSTRACT

Honda has undertaken the challenge of a new styling design in the development of a new model in the VFR series, the only product in the sports tourer category to use a V-4 engine and one which has captured a unique position in the European market. Based on the design concept of a sports tourer with refined styling for mature riders, the design effort sought to achieve a form for mass concentration that fused, to a higher degree, the dynamism of a sports motorcycle with the high functionality of a tourer. Honda sought to create a new kind of attractiveness in achieving such a design by realizing four external appearance elements as a single form. The result was a styling design that retained the refined expression built up in successive generations of the VFR, while boasting an advanced and premium look suitable to the flagship of Honda motorcycles.

1. Introduction

Since the debut of the first-generation VFR750F (Fig. 1) in 1986, users have consistently supported successive generations of the VFR, which is the only product in the sports tourer category to use a V-4 engine. By introducing Honda's leading-edge technology at the time, the succeeding generations have realized the concept of blending a unique hard package with high performance and functionality and refined styling for adults. Many users, especially loyal Honda customers, have referred to this uniqueness as "the showcase of the latest Honda technology," "intelligent sports" and so on over the years. The VFR has had continuously stable sales in the European middle sports class, where it is a strong brand and has no competitors.

No major model change had occurred since the fifth-generation VFR800 of 2002 and sales had continued with only minor alterations, but as the novelty of the model declined, the VFR brand value, which had been built up over such a long period, was starting to seem less special.

The sixth-generation VFR, the VFR1200F (Fig. 2), had the mission of rebuilding the Honda brand image in Europe, making the leap in terms of engine displacement and vehicle status from middle-class sports tourer to the European premium sports category, where competition was growing year by year, and serving as the flagship for Honda's sports motorcycles. As a brand-leading model incorporating Honda's unique leading technology and enviable styling, it would be sold mainly in industrialized countries starting with Europe, the key market for the vehicle, and also including North America and Japan.



Fig. 1 1986 model year VFR750F



Fig. 2 2010 model year VFR1200F

* Motorcycle R&D Center

2. Concept

The VFR originally came with the V-4 engine and body directly descended from Honda works racing machines like the RVF and had a technical package rivaling even super sports, while being characterized by elegant styling that departs from a racing image. Its ability to combine high-mobility performance with its capabilities as a tourer that even two could ride for long distances gained it support from highly experienced adult users who were dissatisfied with the racer replica style. During the development process, Honda understood the need to constantly protect the high-performance image indicative of the VFR's historical racing machine lineage as the backbone of its concept, and also protect this appeal to users.

However, with the rise nowadays of a group of super sports motorcycles with racer replica styling and the trend to radical performance, the position of the VFR in the market has changed gradually from a "sports bike that can also be used for touring" to a "touring bike that is also available for sports use." Market needs for the VFR have also changed: many users were looking for the roominess and status of a large premium sports tourer instead of the latest racing machine technology and a reflection of such an image. The VFR was additionally tasked with serving as the Honda motorcycle brand leader, which greatly transformed its concept.

Specifically, the VFR1200F aimed to bring new value to restructure attractiveness in response to user needs while retaining its basic structure as a sports tourer with Honda's latest technology without depending on racing elements.

During development of the VFR1200F, Honda believed that the value that would appeal to users would be a product that could give them greater individuality and let them build a new motorcycle lifestyle, instead of projecting an image of quantified performance and high functionality. Three concept keywords were chosen: "Unique," "Intelligent Technology" and "Riding Fun," along with the styling development keywords, "The Gentleman Challenger."

In the technical domains composing the VFR1200F, releasing the developers from having to continue using the racing image as the concept backbone expanded their freedom with technical options in one stroke. The newly designed 1200 cm^3 V-4 engine (Fig. 3) has a lightweight, compact unicam (SOHC with both direct lift and rocker arm)[1] head such as is used in motocross racer engines instead of a twin cam head with a strong high-performance image. It has unique technologies such as a rear wheel drive system that replaces the chain drive used in successive generations of the VFR with an offset pivot shaft drive that is clean and has outstanding maintenance performance. This was a new undertaking for the VFR, pushing it into the premium domain. While keeping the advantages of the existing manual transmission, the new motorcycle became the world's first to use a dual clutch transmission and highly automated electronically controlled automatic transmission,

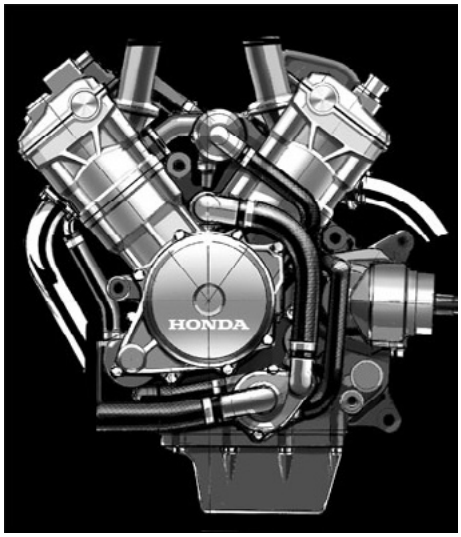


Fig. 3 Initial sketch of V4 engine's appearance

creating for users a strong impression of the new VFR value proposed by Honda.

3. Styling

3.1. Basic Direction of Styling

The styling of successive generations of the VFR visually brought out the VFR concept of performance and uniqueness, not by directly communicating its high performance with expressions like "speed" and "superiority," but by styling with a refined technical expression of the technical "forwardness" with a racing lineage that generates that performance.

Additionally, rather than styling that lets the viewer directly sense the motorcycle's speed and performance, as seen in super sports styling, the VFR expresses its high-quality nature by simplifying design elements including stripes as much as possible and designing the essence of each function simply.

This restrained expression of performance extends to the styling expression of touring performance, which is part of the VFR's capabilities, and the nature of the motorcycle as a distinguished long-distance runner, such as its comfort for both rider and passenger, is expressed as understated performance without drawing attention strongly to the external appearance.

If super sports design consists of "styling by addition," or using performance for decoration and show, the styling of the VFR can be described as using none of its many capabilities as lavish decoration, and this deep, restrained expression resembling the Japanese aesthetic sense has resonated with many adult users.

3.2. Styling Issues with the VFR1200F

The styling of the VFR1200F required a major transformation to bring out strong individuality and novelty and to express innovation sufficient to pull the Honda sports

lineup ahead as its flagship model.

Because the product image appealing to users does not require backup by racing technology, in terms of styling, a new styling expression was needed that does not depend on the "refined racing technology expression" that was naturally continued by successive generations of the VFR. A concept sketch is shown in Fig. 4.

The basis of the VFR1200F styling concept has much to do with a transformation of the basic framework of the body. A motorcycle's proportions are greatly influenced by the form and placement of the engine and the layout of the drive system. Regardless of the more compact engine size, made possible by the VFR1200F's use of a unicam head, changes such as extending the swing arm and enlarging the frame to take advantage of the shaft drive characteristics — used for the first time in the successive generations of the VFR— allowed the wheel base to increase to 1545 mm as compared to the 1460 mm of the chain-driven predecessor model, the VFR800. Thus, the frame was transformed into something grander, a large sports tourer instead of the previous sports bike-like compact proportions. One issue of concern with the styling of the VFR1200F was that the combination of a shaft drive, which has an imperfect sports image as compared to a chain drive, and the large body size would create a strong image as a touring motorcycle model. Strongly believing that "the VFR should always have the appearance of a sports bike," the design development team set out to develop a styling with new ideas about the issues they were assigned to tackle.

3.3. Evoking Lightness by Dividing Volume into Parts

The styling of an ordinary sports motorcycle is based on a single-piece shell construction in which the form of the cowling has a smooth, continuous surface (the so-called speed shape). With the VFR1200F, however, the designers wanted to avoid any increase in visual mass as a result of external components made larger in response to the greater body size. They divided the volume of the cowling into three elements and gave each one a different expression, creating a visual lightness and achieving both the demanded cruising performance and rider wind protection.

Also, strongly concentrating the styling center of gravity in the center element part helped to realize a "form for mass concentration," which is the basic theme of Honda sports design that has been continued since the HRC racer RC211V (Fig. 5), which debuted in 2002.

The first element is the so-called external appearance part, which is painted the body color and connects from the shelter part that covers the fuel tank (and which acts as the styling center of gravity) to the middle cowl. The second is the part with strongly functional elements, such as the blacked-out under cowl, the headlight with large surface area and the screen that connects to it. And the third is the silver-painted layer part that cuts across the two and functions as an aero part.

By giving each of these parts a completely different visual expression suited to its function, artificially dividing the absolute volume necessary as a cowling, and bringing out compactness, the designers avoided changing the VFR1200F into the styling of a touring motorcycle with a thick and heavy image (Fig. 6).



Fig. 5 2002 model year RC211V



Fig. 4 Concept sketch



Fig. 6 Final rendering

3.3.1. Expression of external appearance elements

To begin, the first part ("external appearance") contains elements that most determine the characteristics of the VFR1200F's styling as the styling center of gravity. The designers enhanced the comfort and aerodynamic performance such as the wind protection with the cowling, and at the same time completely eliminated technical elements such as the air outlet that would be included in the layout to cool the engine if this were an ordinary cowling. The result was a thoroughly "seductive" surface. With the elegantly continuous surface from the fuel tank part to the middle cowl, and with the side surface construction, which has a simple look and gives the appearance of volume, there were possibilities of creating visual heaviness for sports bike styling, but a thorough job was done of creating the expression in clay models. By paying careful attention to changes in surface tension and changes in corner radii of the character lines, which occur at surface switches, the designers were able to create a seductive form with a sense of rhythm and some tension suitable for the appearance of a sports bike (Fig. 7).

3.3.2. Expression of functional elements

The second part, "function," was given an expression common to important functional components such as the engine and suspension parts, and its styling emphasized contrast with the "external appearance" part. The hard expression of the under cowl, which has an air management function and looks as if it might be part of the engine, and the design of the screen that allows the structure supporting the meters to be seen from the front, are among parts carrying on some of the VFR's traditional "refined technical expression" (Fig. 8).

3.3.3. Aerodynamic layer expression

The third part (the "layer") has important functions such as a radiator cooling exhaust effect, along with a technical expression of tension such as that created by the molding of metal plates. This is the pivotal styling point, threading between the two design elements of "external appearance" and "function," and holding the various parts together in a single form that would otherwise be separate because of their division. This threading furthermore is continuous with the expression from the front cowl to the rear cowl, giving the entire body a unified look. This is an important part, the cool expression of which may seem to stand in contrast to the elegance of the "external appearance" part to create a sense of tension in the styling as a whole (Fig. 9).

3.3.4. Gap design

The VFR1200F also has a fourth element that lightens the visual volume of its styling, that being the gaps between the three parts above. Because the three parts of the cowling would never be brought together, the goal was instead to design the gaps as expressive "spaces," thereby reducing the sense of absolute volume of the cowling and letting the different parts emphasize each other's individuality. Also, the use of inner air management enables these gaps to have important functions substituting for the independent air intake ducts, air outlet ducts, etc., as would be found in an ordinary sports model's cowling design, and this change results in greatly expanded possibilities for changing overall styling (Fig. 10).



Fig. 8 Styling of under cowl composed of functional elements



Fig. 7 Graceful surfacing and character lines



Fig. 9 Layer panel with technical expression

3.4. Other Styling Characteristics

Many new things were tried with other parts of the VFR1200F that related to overall proportions.

One of these was the front face. The existing "Line Beam System" was further developed, and the internal structure with a wider light source made the new headlight shape create a strong impression of the face's overall expression. Furthermore, the headlight shape couples with the space beyond the screen, and the air intake duct (i.e., a space with a dynamic expression with effective inflection between layer and cowl) divides the absolute sense of volume in the front view similarly to the side view and presents a compact and individualistic expression.

Also, as a "form for mass concentration," in designing the seat, which creates the impression one gets of the rear with its sharp expression (as opposed to the front, which has more volume), the designers sought a seat form with sure performance that would create a sharp impression in side view yet not be lacking in comfort even on long rides. To do this, Honda used composite manufacturing of the seat skin and the cushion urethane for the first time, making it possible to get a sharp seat design in three dimensions that ensured a seating area with uniform surface pressure (Fig. 11).



Fig. 10 Emotional and functional space between each part



Fig. 11 Sharp and three-dimensional seat profile

The VFR1200F has technologies and ideas in the details as well, such as the rear fender design with its one-touch function for easily attaching hard pannier cases without any inelegant-looking stays, providing a smart response for long touring trips when the rider has a lot of baggage. These technologies and ideas cleverly enhance the motorcycle's functionality with styling.

4. Conclusion

Despite being a step up to the upper class of motorcycles, the styling concept of the VFR1200F, like the successive generations of VFR before it, does not directly or strongly appeal to the viewer with its exceptional innovative technologies and high-mobility performance, and instead passes on its unique value to a new generation with its refined appearance.

However, there were major changes in design: just as new technologies have been used, the designers actively took on a new frontier of styling design for the functional expression rather than getting stuck in existing ways of thinking. By carefully building each necessary function as a new functional expression bringing out the essence of the motorcycle, the designers achieved a new styling as the benchmark for the next generation of sports tourers while appealing to many experienced adult users' sense of beauty.

Reference

(1) Hoshi, N., Shimura, Y., Okuma, T., Nomura, A., Gogo, K.: Introduction of CRF450R Equipped with 4-Stroke Engine, Honda R&D Technical Review, Vol. 14, No. 1, p. 21-30

■ Author ■



Toshiaki KISHI

Development of ENEPO Gas Canister-powered Generator

Michihiro IIDA* Joji MAEDA* Takeshi SASAJIMA*
Masanori FUJINUMA* Jun FUKANO*

ABSTRACT

A generator was developed that uses a gas canister for fuel in order to make it easy to handle and store, as well as to use for people who are not accustomed to generators. Development was aimed at opening up new market opportunities focused on residential usage.

In outward appearance, the generator was given a tall, slim form in order to enhance its maneuverability and to make it more flexibly storable by minimizing its footprint. The handle was also optimized for enhanced transport, and the generator design was made functional and easy for residential user.

The generator was given a dual gas canister specification to assure continuous operation time of one hour or more, and this structure was also configured to prevent backflow of fuel between the gas canisters. A mechanism to prevent the gas canisters from being installed incorrectly, a system to stop the engine when the generator is excessively leaned, and an external breather structure to prevent the emission of white smoke when starting the generator after it has been lying on its side were also adopted.

As techniques for enhancing marketability that take handling quality into account, a wheel and handle were included as standard equipment to make the generator easier to carry. The traditional choke system was also eliminated and an engine switch interlinked with the fuel valve was adopted to simplify the starting procedure.

1. Introduction

The generator market in Japan is largely a market for industrial use generators, and the home use market is still relatively undeveloped. Factors in this situation include the difficulties of storing and handling the fuel, namely gasoline.

There has been an increase in fully electrified residences, however, and lifestyles are growing more thoroughly dependent on electrical products. In this context, people can be expected to use electricity in a variety of different situations as part of residential use, and the heightening awareness of disaster preparedness is likely to be accompanied by a growing need for backup power sources.

There is also thought to be a potential market for power sources to support camping, gardening, and other "second life" leisure activities by members of the baby boom generation who have been retiring in recent years.

The aim of this development was to provide customers with easy-to-handle generators fueled by gas canisters that are readily available and storable. The purpose in doing so was to stimulate the latent needs among general consumers who had never used a generator before, and to create a new personal market for this product.

2. Development Concept

2.1. Concept

The concept of this development was to aim for placement as a gas-canister generator for residential users, with the slogan, "One for Every Household." Under ordinary conditions, it could easily be used for family leisure, special activities and events, hobbies, and so on. Moreover, when the need arose, it could also serve as a household portable generator for backup power supply. The specific requirements for these purposes were as follows:

(1) The generator should be easy to use and simple to operate, even for people who are unaccustomed to such equipment.

* Power Products R&D Center

(2) The generator should be easily portable and quickly usable for family leisure and hobby activities.
(3) The generator should be in a format that allows easy storage in small spaces, in consideration of housing conditions in the Tokyo area.
(4) The generator should allow worry-free use.
(5) The generator should be a product that provides the pleasure of ownership.

This generator was named by combining the words "Energy," "Portable," and "Epoch" to form ENEPO, embodying the meaning of "portable energy that inaugurates a new era for generators." Figure 1 shows an external view of the ENEPO.

2.2. Target Users

Given the product concept of "One for Every Household," the target user was broadened from the two-generation family living in a detached house in the suburbs of Japan to also include the nuclear family living in an apartment in the Tokyo metropolitan area. This target was envisioned as also including the older generation that has no particular familiarity with generators. The use of the product was also envisioned as providing a power source for barbecues, auto camping, cherry blossom viewing, and other such family activities, as well as for do-it-yourself work, gardening, fishing, and other such individual pastimes.

2.3. Conceptual Approach to the Exterior Design

The ENEPO styling was based on the key words "Smart Slim Design" (Fig. 2). The image was derived from a slim longitudinal form suggesting ease of storage even in the cramped dwelling spaces of metropolitan Tokyo. The image was also designed to convey, rather than a working machine, something smart and slender like a household appliance or item of furniture with inherent cleanliness (although the generator must not be used in the home). The aspect of portability was envisioned with the widely popular caster bag in mind, in order to suggest a smartly transportable style.



Fig. 1 External view of ENEPO



Fig. 2 Conceptual image of exterior design

3. Longitudinal Design

3.1. Advantages of Longitudinal Design

3.1.1. Enhance ease of operation

In order to enable more effective ease-of-use of the longitudinal slim design, the controls were placed higher up. This was done to minimize the sequence of operations that requires users to bend over at the waist. The generator was also configured with a total height (a) (as shown in Figs. 3 and 5) that would not require users to bend as much at the waist or knees when picking up the generator by the upper grip.

The gas canister loading mechanism (b) was located at the top of the generator to allow a closer view and encourage positive loading of the canisters.

The engine switch (c) was then placed below that, and the Stop switch position was placed at the top to make it more conspicuous (as shown in Figs. 4 and 5).

Considering the length the grip would be pulled, the position of the recoil grip was set at the appropriate height (d), where users could start the generator with a sense of security, bending the waist as little as possible (Fig. 5).

The layout has the AC socket location (e) low down on the right side of the generator. As this position makes it less likely that users walking by might trip on plugged-in AC cords, this configuration was determined with usability in mind. The 250-mm above-ground height of (e) (above the ground) is about the usual height of AC sockets in ordinary houses, and the height that home users will be most accustomed to (as shown in Figs. 5 and 6).

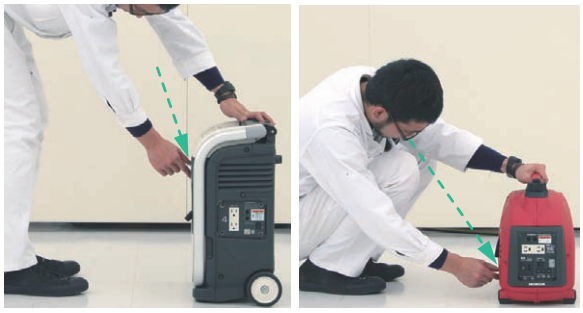
3.1.2. Increase freedom of placement

The functionality for "One for Every Household," especially for users in dwellings in the Tokyo metropolitan area, includes storage of the generator when not in use (the generator must not be used in the home). This matter of the storage location can also be an important motivation for purchase. The envisioned storage locations consist mainly of store rooms, storage shelves, and other such places, with a storage size about 450 mm in width at the narrowest, about 270 mm in depth, and varying heights. These locations were taken into consideration in deciding the generator footprint. The longitudinal design of the generator also contributed greatly to reduction of its footprint, yielding superior storage performance (Fig. 7).



ENEPO EU9i

Fig. 3 Comparison of postures when lifting



ENEPO EU9i

Fig. 4 Comparison of postures when using controls

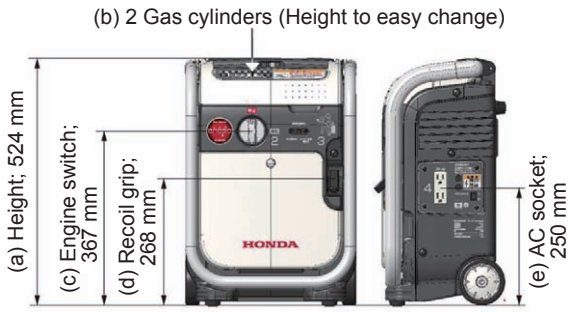


Fig. 5 Height of ENEPO controls



Fig. 6 Height of EU9i controls

3.1.3. Enhanced mobility

When pulling the generator along like a caster bag, a sense of comfortable movement can be achieved by optimizing the generator's load toward the operator as well as the distance between the user and the wheels.

In the case of the ENEPO, the user grip point (A) was therefore set at 750 mm. Next, the center of gravity when the generator is tipped over was displaced from the vertical toward the user and the tipping angle for pulling was set at 26° (B), and the clearance (C) between the generator and the user when walking was established. The required length of the handle (D) when extended from the generator was then determined (Fig. 8).

The configuration takes ideal advantage of the generator's longitudinal design by placing the hinge point (E) of the handle on the diagonal line across the side face of the generator. This method of folding the handle maximizes the

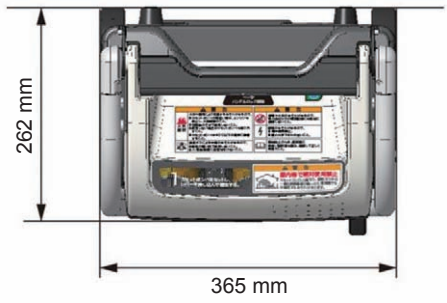


Fig. 7 ENEPO footprint

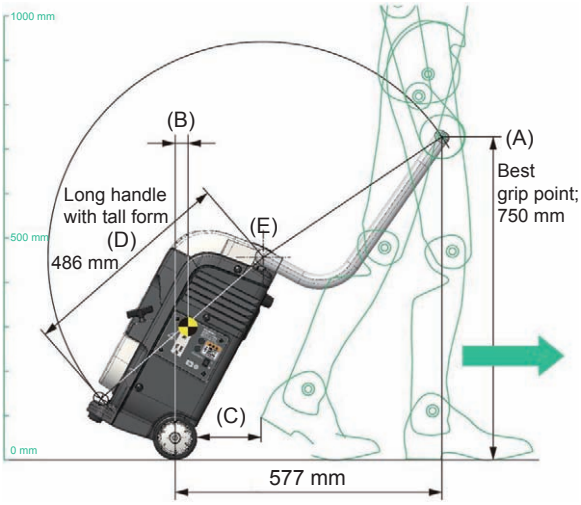


Fig. 8 Side view (generator being pulled)

distance of extension when the handle is extended to point (A) and does so with simplicity and durability.

3.1.4. Functional, clean-looking exterior design

The longitudinal design is offered with a functional layout that locates the controls high up for ease of use, has a small footprint for ease of storage, and is well suited to the use of a folding handle. This layout was then given a simple, clean-looking exterior design in order to further refine the generator's functional beauty. The purpose, which was also the development concept, was to give the product a market appeal in its external appearance that would match the tastes of home users in the Tokyo metropolitan area.

The following techniques were used:

(1) The folding handle was formed from extruded silver-colored aluminum parts. When stored, the handle is recessed into the generator body to provide a unified appearance.

(2) The exterior cover was given two-tone coloring that combines whites and blacks. Complex louver shapes and the controls were made all black to enhance the generator's simplicity and longitudinal slimness, and this realized a clean-looking external appearance with market appeal.

As a result, the generator design was more like a household appliance than a working machine for outdoor use, achieving differentiation from conventional products (Fig. 9).

3.2. Design of Control Indicators

3.2.1. Numerical indicators in line with operating procedures

Envisioning first-time generator users and blackouts or other such occasions when power is needed quickly, a system of indicators was devised to ensure error-free operation with a sense of security. The numbers from 1 to 4 were marked on the front surface of the generator with a height of 17 mm to indicate the order of operations from loading the gas canisters to starting the engine and plugging in to the power socket. This indicates what needs to be done first to start operating the generator. The words in the explanations accompanying those numbers were also made large and easy to read with a height of 4.5 - 7.5 mm. Further consideration was given to ease of sensory comprehension by adding large illustrations (Fig. 10).

3.2.2. Designing warning marks for gas canister use

ENEPO and other engine generators are like motorcycles and automobiles in that they emit carbon monoxide. Therefore, it is an iron-bound rule that they be operated outdoors, as carbon monoxide poisoning will typically occur during indoor operations. Gas cooking stoves, however, which are the most widely used products employing gas canisters for home use, are products for indoor use. In order to make certain that home users who are accustomed to handling these products do not operate the ENEPO indoors in the same way they do gas canister stoves, a warning mark (a) strictly prohibiting indoor operation and a general warning mark (b) about engine generators are displayed on the generator. The warning mark (a), in particular, includes the statement, "The exhaust contains a higher concentration of carbon monoxide than is found with gas canister stoves, so there is a risk of carbon monoxide poisoning from use even for a short time." In order to make users recognize these warnings before operating the generator, a design was adopted that prominently displays the (a) and (b) warnings together with illustrations at the most visible position close



Fig. 10 Numbers indicating operating procedure sequence



Fig. 9 ENEPO coloring

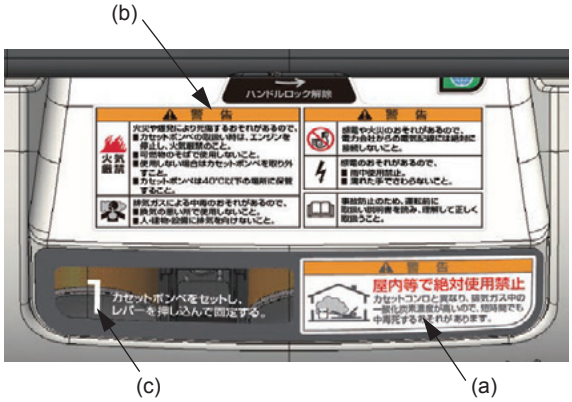


Fig. 11 Warning marks

to the number 1 marking the first operating procedure (c) as described above. This ensures that the warnings will easily be in view (Fig. 11).

4. Technology Employed in ENEPO

4.1. The ENEPO Gas Canister System

The gas canister connector on the generator differs from the Pianta compact domestic-use cultivator[1], which was Honda's first such gas-powered product, in that the generator is capable of loading two gas canisters. This enables the generator to provide 1.1 hours of continuous operation at the rated load of 900 VA (Fig. 12).

Figure 13 shows a structural drawing of the gas canister adaptor that is the fuel connector for the two gas canisters.

This gas canister adaptor has the following three functions:

(1) Manual cock to open and close the path for fuel removed from the gas canisters in liquid phase
(2) Fuel cut valve that is operated by fuel pressure
(3) Backflow prevention valve that prevents fuel from charging the gas canisters

The following selects the backflow prevention valve (3) out of these three functions and describes the history of its development, its function, and its structure.

4.1.1. History of backflow prevention valve development

The gas canisters are non-refillable, and their refueling is forbidden under the High Pressure Gas Safety Act. However, the pressure inside the gas canisters will change with the ratio of components in the gas canisters (ratio of isobutane to normal butane) and the temperature of the canisters themselves. Consequently, the two canisters will not necessarily be under identical pressure. When the gas canisters are connected in parallel with the adaptor between them, therefore, the fuel that flows together into the gas canister adaptor will flow from the canister with the higher pressure to the canister with the lower pressure. This can result in phenomena similar to refueling and overcharging. For the ENEPO, therefore, a structure was devised and adopted to prevent fuel flowing from one gas canister to the other when two canisters are loaded.



Fig. 12 Comparison of gas canister connectors

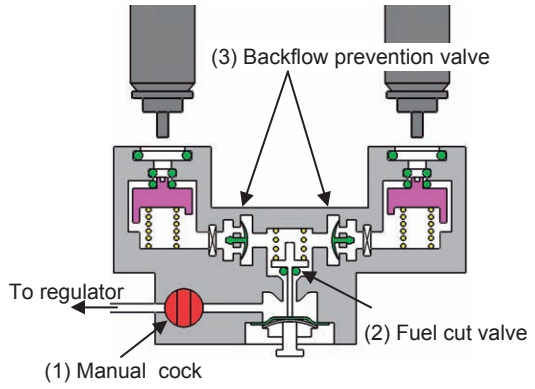


Fig. 13 Structural drawing of gas canisters and adaptor

4.1.2. Function and structure of the backflow prevention valve

Figure 14 shows a conceptual image of the backflow prevention valve mechanism in operation. For example, when the internal pressure of gas canister A is greater than that of gas canister B, then the backflow prevention valve on the A side opens and the backflow prevention valve on the B side closes, preventing the backflow of fuel to gas canister B. As a result, charging of gas canister B does not occur.

4.1.3. Gas canister loading system

The gas canister loading system on the ENEPO was structured to yield the force necessary to fix the gas canister against a spring by moving a control lever that has a linking mechanism. This allowed the use of a single control lever to hold two gas canisters securely in place (as shown in Figs. 15 and 16).

The ENEPO is like the Pianta in that it takes fuel from the gas canister in liquid phase. Since the gas canisters need to be fixed in place with the notch down, users will be required to insert the gas canisters with the notch down[1].

Consequently, in the developed configuration, when the notch on the flange of a gas canister is not facing down, the

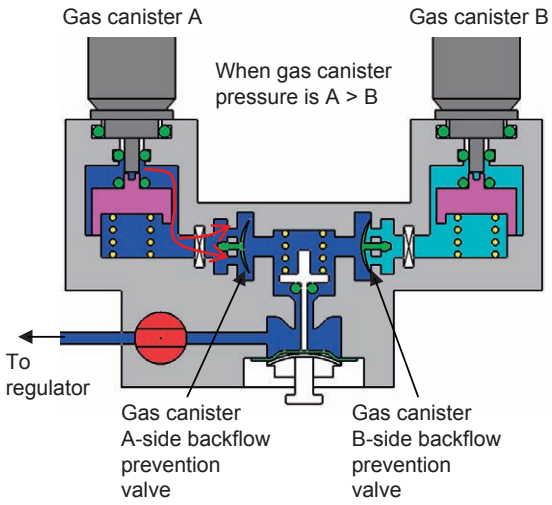


Fig. 14 Conceptual image of operation of backflow prevention valve

sensor arm that is usually held up by the force of the return spring will be depressed by the flange. If the user starts to move the control lever with the canister in that state, the sensor arm and the top cover will come into contact, and the mechanism is designed to lock up the control lever when that happens (Fig. 17).

The specifications also call for the parts to be configured so that the gas canisters are fixed in place tilted at an angle of 25°. This forces the fuel in the gas canisters to be consumed to the fullest extent (Fig. 15).

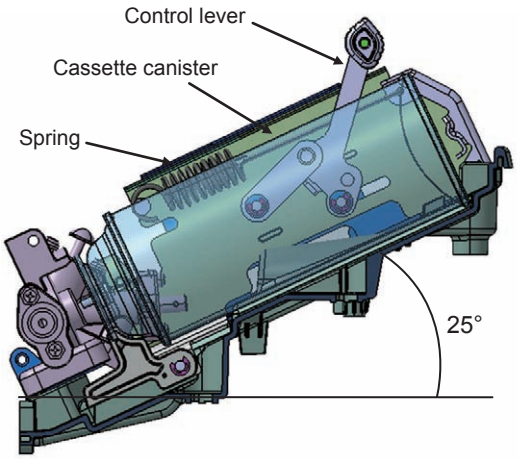


Fig. 15 Before setting

The gas canister loading system yields the force against a spring by moving a control lever.

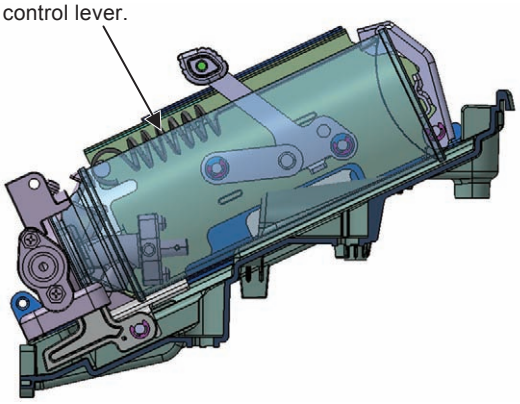


Fig. 16 After setting

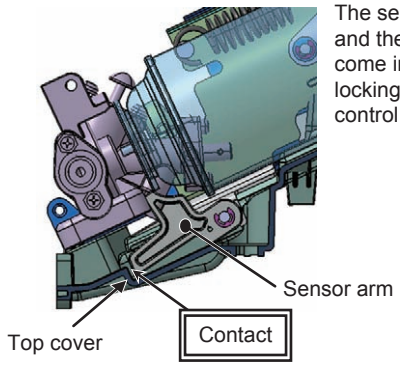


Fig. 17 Incorrect setting

4.2. Engine Stop System

When operation of the engine is continued while tilted over at too sharp an angle, the lubricating oil flows into the combustion chamber or passes through the breather and the air cleaner to infiltrate the combustion chamber. This causes the oil to ignite inside the combustion chamber, and white smoke is generated as a result. A system was therefore devised to detect tilting in the generator's operating attitude and automatically stop the engine.

The detection and control of the generator's angle is handled using an acceleration sensor in an inverter unit and an electronic controller to process its output. The system detects the tilt of the generator from the direction of acceleration relative to the earth's axis. The system is thus designed to allow stopping of the generator engine and power generation at the desired amount of tilt and after the desired amount of time by configuring a freely selectable threshold angle value that will stop the generator when tilted to the extent that it cannot remain standing on its own.

The quantity G_{xyz}, which is the combination of accelerations on the X, Y, and Z axes of the acceleration sensor, comes to 1 g, as shown by the equation below:

$$G_{xyz} = \sqrt{G_x^{\,2} + G_y^{\,2} + G_z^{\,2}} = 1g \qquad (1)$$

By determining the angle of the Z axis, the angles in all directions can be detected.

$$\theta_z = \sin^{-1}\frac{G_z}{G_{xyz}} \qquad (2)$$

The actual tilt angle is $\Delta\theta = 90° - \theta_z$.

The direction of the Z axis, however, is subject to the influence of acceleration from engine vibration and other such factors, and this influence is observed in actual angle detection. It was determined from test results that, as a result, use of this quantity in detection becomes complicated.

Rather than using the Z axis component in the acceleration sensor, therefore, the quantities G_{xyz} and G_{xy}, which are the combined accelerations on the X and Y axes, are used instead to calculate the $\Delta\theta$ that is the tilt of the generator. G_{xy} is calculated as follows:

$$G_{xy} = \sqrt{G_x^{\,2} + G_y^{\,2}} \qquad (3)$$

G_x: Acceleration in the X-axis direction
G_y: Acceleration in the Y-axis direction
G_{xy}: Combined acceleration from the X and Y axes

G_{xyz} and G_{xy} can be used to calculate the $\Delta\theta$ in Fig. 18.

$$\triangle\theta = \sin^{-1}\frac{G_{xy}}{G_{xyz}} \qquad (4)$$

It is apparent from the fact that the $\Delta\theta$ angle can be calculated using just the X axis and Y axis that the angle in all directions can be detected using the X axis and Y axis. However, the quantity G_{xy} cannot distinguish the state in which the generator has top and bottom reversed (is upside down). It was decided, therefore, to use the Z axis to distinguish this state for detection purposes. In this development project, the judgment angle has been configured as $\Delta\theta = 53°$, in order to ensure reliable detection for the excessively leaned state without compromising usability.

Figure 19 shows the total detection range of this generator, including angle detection by the above combined XY-axis acceleration for 360° around the generator and top-bottom reversal detection from the Z axis. This system allows for detection within this entire range.

4.3. External Breather Structure

The ENEPO is constructed to allow the generator to be placed on its side, for convenience when transporting it by car. When the generator is started after having been held on its side, however, oil that has pooled within the breathing channel may enter the engine combustion chamber and cause white smoke to be produced. For this reason, the check valve has been located in the external breather tank, as shown in Fig. 20, in a structure that prevents oil from pooling inside the breathing channel when the generator is placed on its side, and even in the unlikely event that it falls over forward or backward (as shown in Figs. 21 and 22).

4.4. Carrying Handle Locking Mechanism

A structure was devised to keep the locking pin on the handle constantly pushed out by the force of the return spring. Thus, when the handle arrives at a specified position, the handle locking pin slides into a hole in the handle and automatically locks it in place.

Turning the handle knob in the handle unlocking direction simultaneously draws the left and right handle locking pins inward, unlocking the handle (Fig. 23).

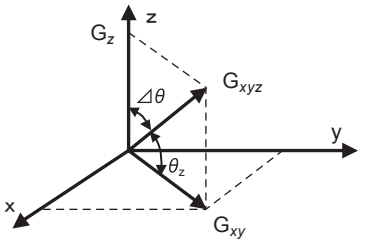


Fig. 18 Relationship of $\Delta\theta$ and coordinate axes

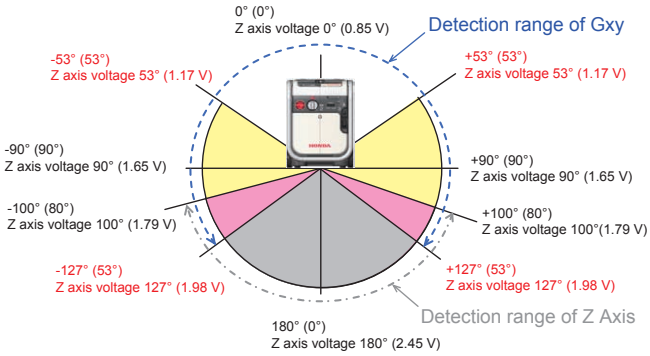


Fig. 19 Generator tilt-angle detection range

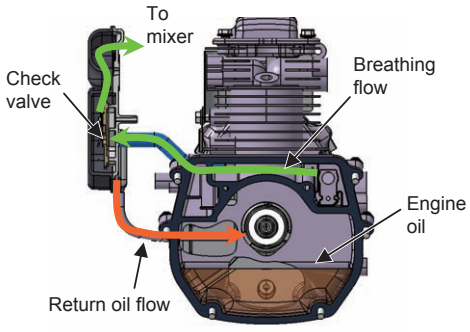


Fig. 20 External breather structure

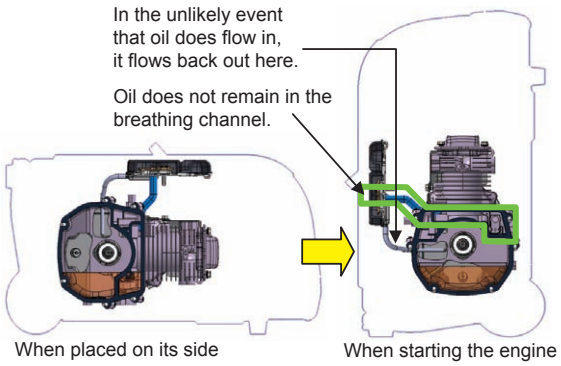


Fig. 21 When generator is placed on its side

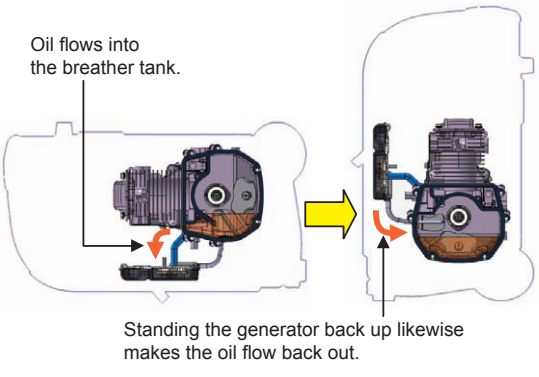


Fig. 22 When generator falls over forward

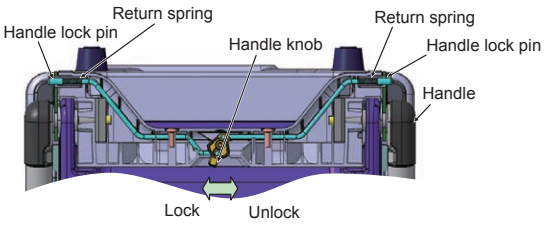


Fig. 23 Handle lock (unlock)

This structure allows automatic locking of the handle and simultaneous unlocking for both sides with a single knob.

4.5. Structure Enabling Simple Engine Starting

The ENEPO features an engine starting procedure comprising the simple actions of (1) loading the gas canisters, (2) operating the engine switch, and (3) pulling the recoil starter.

4.5.1. Chokeless structure

A shutoff valve that automatically closes the gas flow when the engine is stopped is required to use gas fuel. The shutoff valve features a variety of electric-type (such as the solenoid valve) or mechanical-type (such as the vacuum cock) mechanisms.

Power products unequipped with a battery generally employ the shutoff valve with a vacuum cock. However, even if intake manifold vacuum were to be used for the vacuum cock, sufficient vacuum might not be obtained due to the throttle opening at the engine start and limitation in recoil pulling speed. To avoid this, a choke system such as used in a gasoline fuel generator has been installed, and operated at the engine start. This being the case, the ENEPO is designed to use the crankcase pressure to open and close the shutoff valve, eliminating the need for a choke.

Figure 24 shows the shutoff valve drive system.

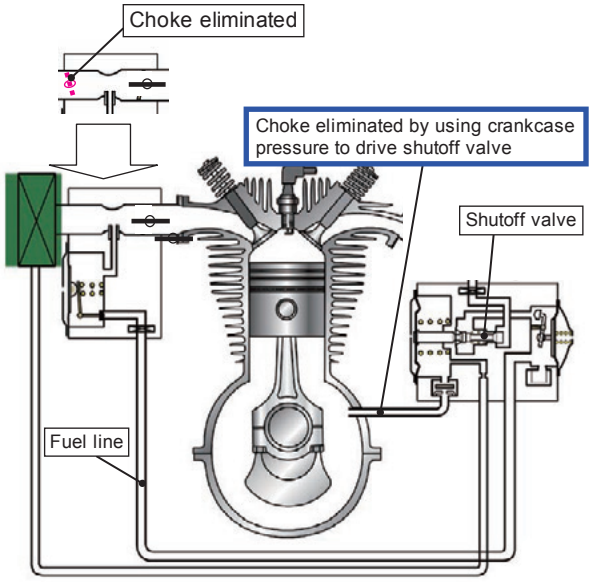


Fig. 24 Shutoff valve drive system

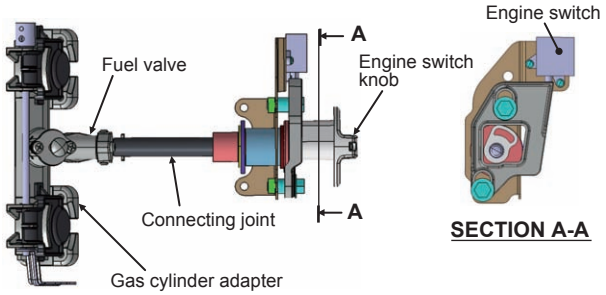


Fig. 25 Engine switch interlinked with fuel valve

4.5.2. Engine switch interlinked with fuel valve

Since the engine switch and fuel valve are linked by a connecting joint, turning a single knob simultaneously operates the engine switch and the fuel valve.

This reduced the number of steps in starting the engine, simplifying the operation of the generator (Fig. 25).

5. Conclusions

This development project resulted in commercialization of an easy-to-handle generator. At the same time, applying a slim, functional design lowered the barrier for users who have no previous experience with generators, raising expectations that this generator could open up a new market.

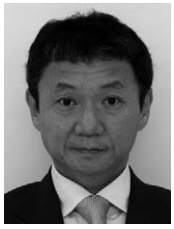
Future goals include studying the potential for the product not only in Japan but in international markets as well, and to develop the generator as a worldwide product.

Reference

(1) Kojima, H., Ito, T., Sato, T., Fujinuma, M.: Development of Pianta Gas Canister-fueled Compact Cultivator for Kitchen Garden, Honda R&D Technical Review, October, 2009, p. 27-37

■ Author ■


Michihiro IIDA


Joji MAEDA


Takeshi SASAJIMA


Masanori FUJINUMA


Jun FUKANO

Introduction of High Differential Pressure Water Electrolysis-type Solar Hydrogen Station (SHS2)

Koji NAKAZAWA* Hisashi NAGAOKA* Jun TAKEUCHI*
Frank MOBURG** Ikuya YAMASHITA** Masanori OKABE*

ABSTRACT

A high differential pressure water electrolysis-type solar hydrogen station (SHS2) was built with installation in ordinary households in mind. This SHS2 was equipped with a newly developed high differential pressure electrolyzer, which is an innovative technology. The stack differs from the ordinary high-pressure electrolyzer that keeps both the anode side and the cathode side in a high-pressure state. Here, instead, the anode side is under normal pressure and only the cathode side is maintained under the high pressure of 35 MPa. Compared to the ordinary high-pressure electrolyzer, therefore, this one has a simpler structure and can be made compact. Furthermore, the stack here has the functions of both generating and compressing hydrogen, so that the SHS2 with this stack mounted was made into a compact, highly efficient and low-noise, home-sized hydrogen refueling appliance.

Compared to the previous solar hydrogen station (SHS1), the SHS2 is 60% more compact and realizes an increase of 25% in system efficiency.

1. Introduction

Honda has engaged in the development of fuel cell electric vehicles based on its understanding that fuel cells utilizing hydrogen are the ultimate next-generation powerplant in terms of providing an alternative to fossil fuels, reducing emissions, and minimizing the impact on global warming.

It is desirable to use sustainable energy sources in the process of manufacturing the hydrogen that is the fuel for fuel cell electric vehicles, in order to minimize the use of fossil fuels and reduce CO_2 emissions. For reasons like these, we are also conducting research and development of a solar hydrogen station that uses solar cells for the source of input power. This should contribute to the formation of a hydrogen society in the future. Testing began in July 2001 at the Los Angeles Center campus of Honda R&D Americas in Torrance, California, USA, using a combination of commercially available equipment. The SHS1 entered operation in October 2003, with a water electrolyzer, which was our proprietary technology, and a prototype CIGS (copper, indium, gallium, and selenium compounds) thin film solar cell[(1), (2)].

The results[(3)] from proving tests of the SHS1 conducted to date suggest that a renewable hydrogen station of a size suitable for household use would require still greater compactness and higher efficiency. It became clear, as a point of approach for this, that it would be important to reduce the dehumidification energy and the compression energy of hydrogen.

The SHS2 is an evolved form of the SHS1 for ordinary household use. It involved updating the SHS1 and installing it at the Los Angeles Center campus of Honda R&D Americas, where it entered operation in January 2010. This article will introduce the SHS2 design, the performance of the station, and the technology of the high differential pressure electrolyzer.

2. Concept and Design of the High Differential Pressure Water Electrolysis-type Hydrogen Station (SHS2)

2.1. Concept

Figure 1 shows an exterior view of the SHS2 that is discussed here.

The concept for the SHS2 was defined as “Intuitive and Integrated.” Therefore, the dispenser unit, which requires the user to perform hydrogen filling operations, was designed to allow superior operability with an intuitive quality. With the electrolysis unit, the aim was to achieve

* Automobile R&D Center
** HONDA R&D AMERICAS, INC.



Fig. 1 External view of high differential pressure water electrolysis-type Solar Hydrogen Station (SHS2)

greater compactness by integrating the hydrogen generating and compressing functions.

2.2. Steps Toward Installation in Households

In order to install the SHS2 in households, it is necessary to make it seem approachable and non-intimidating to users. Since it should not give the user an overpowering impression, the shape of the station as a whole, as well as of the component units, was designed deliberately not to have any sharp angular lines. By giving them rounded curves, they were made to convey a sense of security and accessibility. The component units were also made compact so as to fit the human sensibility and to be of a size not to intimidate users or give them an impression of being overpowered.

If the SHS2 is envisioned as installed in the garage of a domestic dwelling, then the dispenser unit that is accessed by users will be located inside the garage. Here, therefore, the SHS2 was configured with a scoop-shaped structure, intended to seem as though wall-mounted in the garage, with a dispenser unit placed in front of it and the electrolysis unit located behind it.

Previously, there had been seven round concrete columns 150 mm in diameter and 900 mm in height, called bollards, placed in front of the units at approximately 1600 mm intervals to protect them from being hit by a car. Instead of using bollards this time, however, curving sidewalls were built on either side of the units and the unit bases were raised approximately 150 mm (6 inches) above the roadway level as measures to protect against collision. This enabled the external appearance of the SHS2 to be given a simple, non-intimidating appearance that would not give the user an impression of being overpowered.

2.3. Packaging

Figure 2 shows the external appearance of the electrolysis unit. The electrolysis unit was built on the assumption of outdoor installation, so environmental factors such as rain and wind have been taken into consideration. In terms of shape, it was made simple with curved surfaces, for a styling that does not make it seem intimidating.



Fig. 2 Electrolysis unit

Figure 3 shows the external appearance of the dispenser unit and scoop. The height of the units was determined by the placement of the user interface (UI), and their width by the allowable bending radius of the fueling hose. Operability and usability were taken into consideration by fabricating actual-size mockups and checking the method of housing the fueling nozzle and the length of the hose in advance.

2.4. User Interface (UI)

Figure 4 shows the UI screen display. The screen display has been simplified and conveys an adequate amount of necessary information in order to make it acceptable to ordinary users. The display is organized by layered menus, and the operational diagrams are designed to be intuitive and easy to understand.

The user connects the hydrogen fueling nozzle in the dispenser unit to the fuel cell electric vehicle, then presses the start button (Start Filling) on the display. This causes hydrogen filling to begin. Then the user can press the stop button (Stop Filling), or hydrogen filling ends automatically when the tank on the fuel cell electric vehicle reaches the full state (35 MPa).

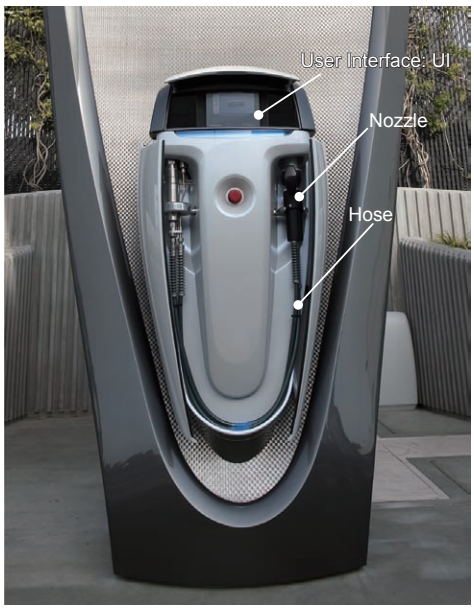


Fig. 3 Dispenser unit with User Interface

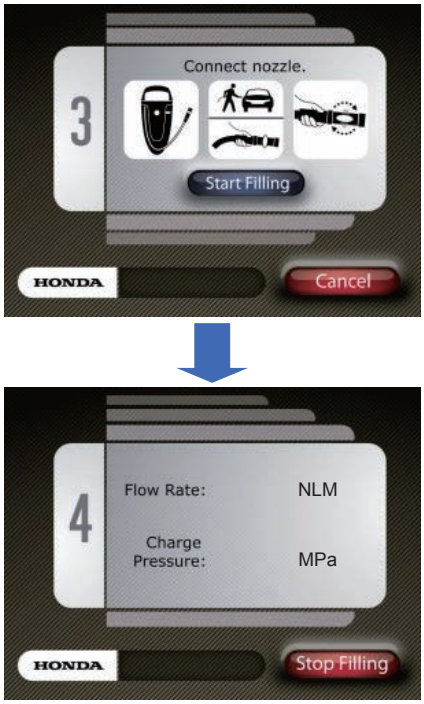


Fig. 4 UI screen

3. System Overview of the High Differential Pressure Water Electrolysis-type Hydrogen Station (SHS2)

3.1. System Configuration

Figure 5 shows a comparison of the system configuration in the SHS1 and SHS2 hydrogen stations.

In the SHS1, hydrogen was generated at normal pressure (max. 0.12 MPa) in the water electrolyzer, and hydrogen compression was carried out in the mechanical compressor. The SHS2, on the other hand, is equipped with a high differential pressure electrolyzer that integrates the hydrogen compression function into the water electrolyzer. The high differential pressure electrolyzer is unlike the mechanical compressor in that there are no sounds of vibration or motor operation when hydrogen compression is taking place, so it is very quiet. Furthermore, it uses an electrochemical method of hydrogen compression, so it is highly efficient and not subject to the kind of friction loss or motor loss found in a mechanical compressor. Furthermore, the elimination of the mechanical compressor and update of the system configuration enabled greater compactness, with an approximately 60% reduction in volume of the electrolysis unit compared to the SHS1. Consequently, the SHS2 equipped with a high differential pressure electrolyzer is an effective choice for installation in ordinary households.

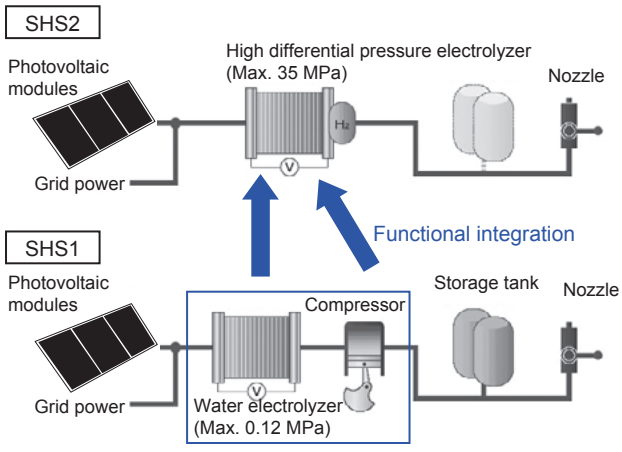


Fig. 5 Comparison of solar hydrogen stations

Table 1 Specifications of SHS2

Hydrogen production	Flow rate	0.7 Nm^3/h (0.5kg/8h)
	Filling pressure	35 MPa (max.) (approx. 5000 psi)
	Purity	> 99.99%
Component	Photovoltaic modules	CIGS thin film solar cell 6 kW system (approx. 53 m^2)
	Electrolysis unit	High differential pressure electrolyzer
Utility	Electricity	240 VAC
	Water	Tap water
Unit volume		Approx. 0.33 m^3 (approx. 12 cf)

3.2. Specifications

Table 1 shows the SHS2 specifications.

The SHS2 is like the SHS1 in being equipped with a 6-kW capacity CIGS thin film solar cell manufactured by Honda Soltec Co., Ltd. The system was designed to use 240 VAC, which is already available in most average households in the USA, as its input power. The electric power generated by the solar cells during daylight is exported over the grid, and the electric power to operate the system at night is imported from the grid. The system only needs to be supplied with tap water and electricity to operate, and it is able to fill the fuel cell electric vehicle with high-purity hydrogen under maximum pressure of 35 MPa. The hydrogen production volume is approximately 0.7 Nm^3 per hour. If a Honda FCX Clarity is filled up with hydrogen generated over an eight-hour period at night, when electricity rates are lower, it will be able to drive approximately 30 miles[4] (50 km) the next day. The present system does not have a fixed emplacement of high-pressure storage tanks, but installation of such tanks would enable fast filling of a fuel cell electric vehicle. Furthermore, the system is capable of manufacturing hydrogen with electric power from its solar cells during the day, so it could be operated for 24 hours and store the hydrogen in the tanks, in which case it could manufacture enough hydrogen to drive the car approximately 90 miles (150 km) in a day.

One purpose of proving tests is to evaluate the durability and reliability of component parts over a long period of time. For that reason, the hydrogen pressure inside the high differential pressure water electrolyzer system is not linked with the tank pressure in the fuel cell electric vehicle. Instead, it is designed to maintain a pressure of 35 MPa, and evaluation of its durability and reliability can therefore be conducted under very demanding pressure conditions.

4. Initial Performance Evaluation of the High Differential Pressure Water Electrolysis-type Hydrogen Station (SHS2)

4.1. Fueling Test of Fuel Cell Electric Vehicle

Figure 6 shows the results of hydrogen filling tests carried out with the fueling nozzle connected to a fuel cell electric vehicle.

Figure 6(a) shows changes in the data over a 20-minute system start-up period after the start button on the UI screen has been pressed. As preparation for start-up, the interiors of the electrolysis unit and dispenser unit are first ventilated, and the equipment, piping, and so on are checked to make certain there are no hydrogen leaks. Then an initial check of sensors is carried out to determine whether the system is in a state capable of coming on line. If the check results are normal, then the pure water generator is started up, the water circulation pump is started up, completing the preparations for operation. The time taken to complete preparations for operation is largely determined by the pure water generator start-up time. Figure 6(a) shows the preparations for operation were complete after approximately 6 minutes. Once the preparations for operation have been completed, then voltage is supplied to the high differential pressure electrolyzer and electrolysis of water begins. The hydrogen pressure in the high differential pressure electrolyzer starts at normal pressure, and when it reaches 35 MPa, the hydrogen starts flowing outside the system, the fuel cell electric vehicle starts filling, and the vehicle tank pressure gradually starts rising. In the present tests, hydrogen filling

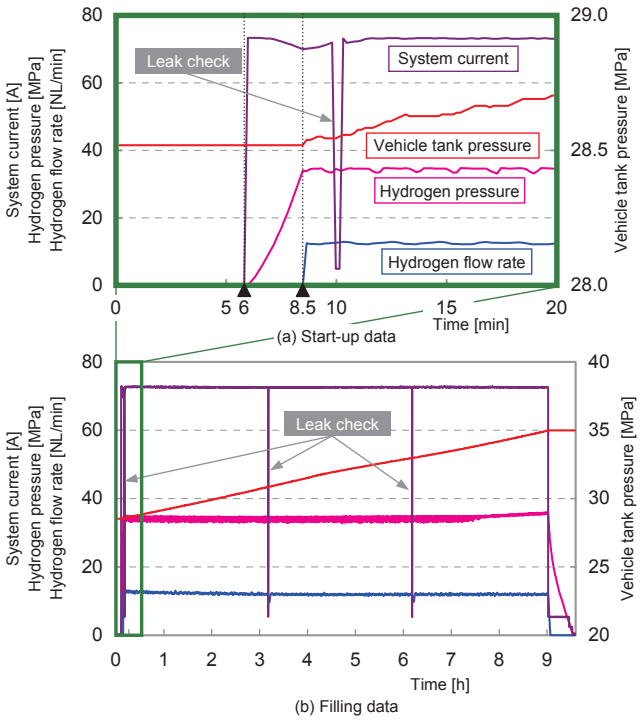


Fig. 6 System operating result for one day in January 2010

of the fuel cell electric vehicle started approximately 8.5 minutes after the start button was pressed, indicating that the differential pressure electrolyzer had finished starting up after only 2.5 minutes.

Consideration has also been given to the safety of ordinary users. In order to check that the fueling nozzle is securely connected to the fuel cell electric vehicle, hydrogen production is temporarily stopped immediately after hydrogen filling of the fuel cell electric vehicle begins, and a leak check is conducted for approximately 20 seconds to determine whether there is any drop in pressure due to a hydrogen leak in the nozzle connector.

Figure 6(b) shows the results of the series of filling tests conducted this time. In addition to the initial leak check shown in Fig. 6(a), checks are also conducted every three hours during hydrogen filling to make certain there are no leaks from the nozzle connector and hose. When the hydrogen filling is to be stopped, either the user presses the stop button on the UI screen or the tank pressure in the fuel cell electric vehicle reaches the full state of 35 MPa, at which time the system automatically stops operating. These tests confirmed that the system stopped when the tank became full approximately nine hours after the start button was pressed, when the tank pressure in the fuel cell electric vehicle had risen from about 28.5 MPa to about 35 MPa.

4.2. Hydrogen Quality

The quality of the hydrogen supplied to fuel cell electric vehicles is prescribed in ISO 14687 (Hydrogen fuel – Product specification)[5]. The quality of hydrogen obtained through operation of the SHS2 is shown in Table 2.

The SHS2 electrolyzes purified water to obtain hydrogen. As a result, the only contaminants contained in the hydrogen are oxygen and moisture. It is characteristic of the high differential pressure electrolysis cell that the cathode side is maintained at high pressure, with a solid polymer membrane (proton exchange membrane: PEM) separating it, while the anode side, where oxygen is generated, is at atmospheric pressure. Consequently, the amount of oxygen that diffuses to the high-pressure cathode side is very small, reaching a level of 5 ppm or less, even though no process is carried out to lower the concentration of oxygen in the hydrogen. As for moisture, it is removed by an adsorbent placed in a later stage of the high differential pressure electrolyzer.

The hydrogen quality measurement results show that the hydrogen produced by the SHS2 clears the ISO 14687-2 standards and is of a quality adequate for use in fuel cell electric vehicles.

4.3. System Efficiency

Figure 7 shows the energy expended in compression and dehumidification at a hydrogen pressure of 35 MPa in the SHS2 and SHS1.

The energy consumption of the low flow rate mechanical compressor intended for use in small stations

Table 2 Hydrogen quality of SHS2

	ISO14687-2	SHS2
H_2	>99.99%	>99.99%
H_2O	<5 ppm	<1 ppm
Hydrocarbon	<2 ppm	<0.1 ppm
O_2	<5 ppm	1 ppm
He, Ar, N_2	<100 ppm	<16 ppm
CO_2	<1 ppm	<0.1 ppm
CO	<0.2 ppm	<0.001 ppm
Sulfur	<0.004 ppm	<0.0008 ppm
HCHO	<0.01 ppm	<0.001 ppm
HCOOH	<0.2 ppm	<0.001 ppm
NH_3	<0.1 ppm	<0.02 ppm
Halogenates	<0.05 ppm	<0.004 ppm

and installed in the SHS1 shows a greater influence from friction loss than a high flow rate compressor, and the hydrogen compression energy is greater. Meanwhile, the high differential pressure electrolyzer installed in the SHS2 uses electrochemical compression by means of a PEM, so there is no friction loss or motor loss. As a result, the hydrogen compression energy is lower, making this a more efficient method of hydrogen compression. According to ISO 14687-2, the allowable amount of moisture in the hydrogen for use in fuel cell electric vehicles is under 5 ppm. It is therefore necessary to conduct dehumidification of the hydrogen produced.

The hydrogen produced by the water electrolyzer in the SHS1 reached a pressure of approximately 0.1 MPa, so the water content of the hydrogen was high, at approximately 35800 ppm. At a later stage in the water electrolyzer, a Peltier cooling-type condenser was installed in order to reduce this water content by cooling the hydrogen and lowering the amount of saturated vapor. Most of the cooling energy was used in condensation of the water vapor. A thermal swing adsorption (TSA)-type adsorber was also

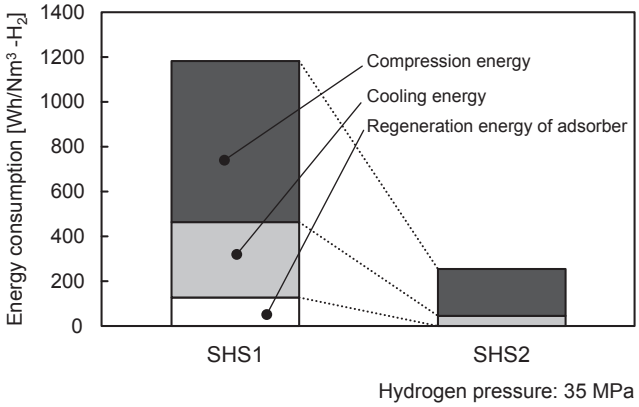


Fig. 7 Comparison of power consumption

placed at an earlier stage of the compressor, and this imposed a regeneration energy requirement on the adsorber for the electric heater.

Meanwhile, the hydrogen produced by the high differential pressure electrolyzer in the SHS2 was at a higher pressure of 35 MPa, so that the water content of the hydrogen was approximately 100 ppm. This was approximately one 350th or less of the amount in the SHS1. This means that the energy for Peltier cooling (cooling energy) is notably lower. The adsorber placed in a later stage of the Peltier cooling-type condenser also had an internal capacity of approximately 700 cm^3, and the adsorbent placed there would thereby maintain its adsorbent performance for half a year or more. This time, therefore, a replacement adsorber was adopted in place of a regenerative adsorber, making a system that had no need for regeneration energy. As a result of these differences, the energy required for compression and dehumidification came to approximately one-fourth that in the SHS1.

Mounting a high differential pressure electrolyzer not only enabled a reduction in the energy required for compression and dehumidification, it also allowed the system to be simplified so that the power for solenoid valves and other auxiliary devices could be reduced. As a result, the SHS2 has achieved a 25% boost in system efficiency relative to the SHS1.

5. High Differential Pressure Electrolyzer

5.1. Principle of High Differential Pressure Electrolysis

Figure 8 shows the schematic of a high differential pressure electrolysis cell.

In electrolysis cells that use PEMs when purified water is supplied and a voltage is continuously applied to the PEM, the cells will continue to generate oxygen and hydrogen. Therefore, if a high-pressure tank is placed at the hydrogen exit side, the pressure inside the tank will gradually continue rising and high pressure hydrogen will eventually be obtained. The oxygen, on the other hand, is at atmospheric pressure, which is why a pressure difference is created in a high differential pressure electrolysis cell with a PEM separating the different pressure areas.

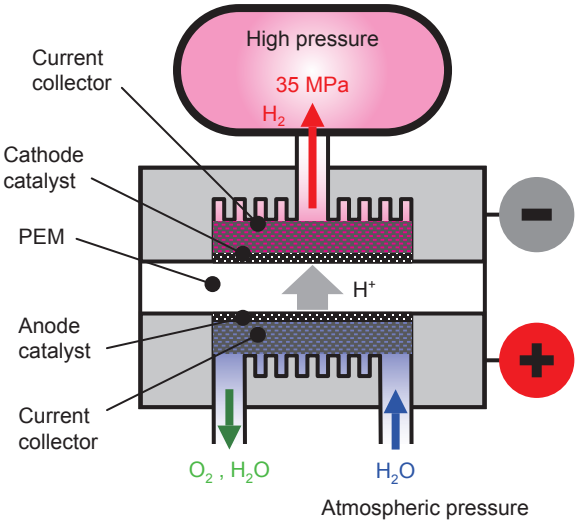


Fig. 8 Schematic of high differential pressure electrolysis cell

Equations (1) and (2) show the reactions that occur in high differential pressure electrolysis.

$$H_2O \rightarrow 2H^+ + \frac{1}{2}O_2 + 2e^- \quad (1)$$

$$2H^+ + 2e^- \rightarrow H_2 \quad (2)$$

When a voltage is applied across the PEM, the purified water on the anode side becomes oxygen and protons H^+. The protons travel to the counter electrode and form hydrogen. This phenomenon is the same as in ordinary water electrolysis, but when the protons travel to the counter electrode, an electromotive force should be applied because of the partial pressure difference in the hydrogen.

Equation (3) shows the electrolysis voltage E_{WE} required in high differential pressure electrolysis.

$$E_{WE} = E_1 + \frac{RT}{2F} \ln \frac{P_1}{P_2} + ir \quad (3)$$

R: Gas constant
T: Absolute temperature
F: Faraday constant
P_1: Hydrogen partial pressure of high pressure side
P_2: Hydrogen partial pressure of low pressure side

In addition to the theoretical electrolysis voltage E_1 of water electrolysis and the cell resistance ir, high differential pressure electrolysis occurs through application of the potential difference in hydrogen concentration required in a gas concentration cell[6]. The second term on the right side of Eq. (3) will be the Nernst electromotive force needed from the Nernst equation hydrogen concentration difference.

5.2. Results of High Differential Pressure Electrolyzer Performance Evaluation

Figure 9 shows two sets of values for the energy consumption when the high differential pressure electrolyzer is used to electrolyze water and the generated hydrogen is compressed from normal pressure to 35 MPa. One is the actual measured value for energy consumption and the other is the calculated value derived from Eq. (3).

With the hydrogen at normal pressure, the total energy consumption was approximately 4000 Wh/Nm^3, of which 3544 Wh/Nm^3 was the theoretical electrolysis energy (hydrogen conversion energy), and the remainder was the cell resistance. The cell resistance includes contact resistances and membrane resistance between the

membrane and the electrode and between the electrode and the collector, as well as anodic and cathodic overvoltages and ohmic dissipation.

With the hydrogen pressure at 35 MPa, the compression energy is approximately 200 Wh/Nm^3. Compared to the compression energy of 700 Wh/Nm^3 for the SHS1 mechanical compressor shown in Fig. 7, the compression energy required for the high differential pressure electrolyzer is small, and it also coincided with the calculated value. In the low-pressure range, however, the actual measured values for energy consumption were lower than the calculated value, and this is thought to be because of a decrease in cell resistance components – primarily a decrease in contact resistances between the membrane and the electrode and a decrease in membrane resistance due to changes in membrane thickness – that occurred as the pressure increased.

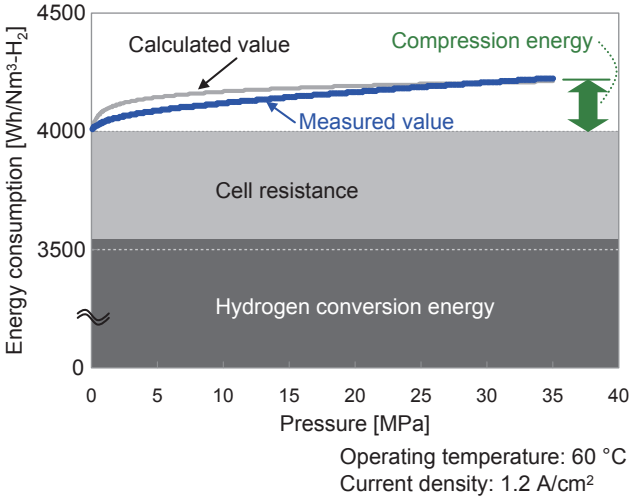


Fig. 9 Hydrogen compression curve of high differential pressure electrolyzer

The total energy consumption by the high differential pressure electrolyzer with the hydrogen pressure at 35 MPa was 4200 Wh/Nm^3, showing an efficiency of approximately 84% relative to the theoretical electrolysis energy (3544 Wh/Nm^3). The SHS2 can be considered an energy conserver as a high-pressure hydrogen generator.

5.3. Durability of the High Differential Pressure Electrolyzer

A unit durability test of the high differential pressure electrolyzer was carried out at a hydrogen pressure of 35 MPa. Since the SHS2 was envisioned as operating for

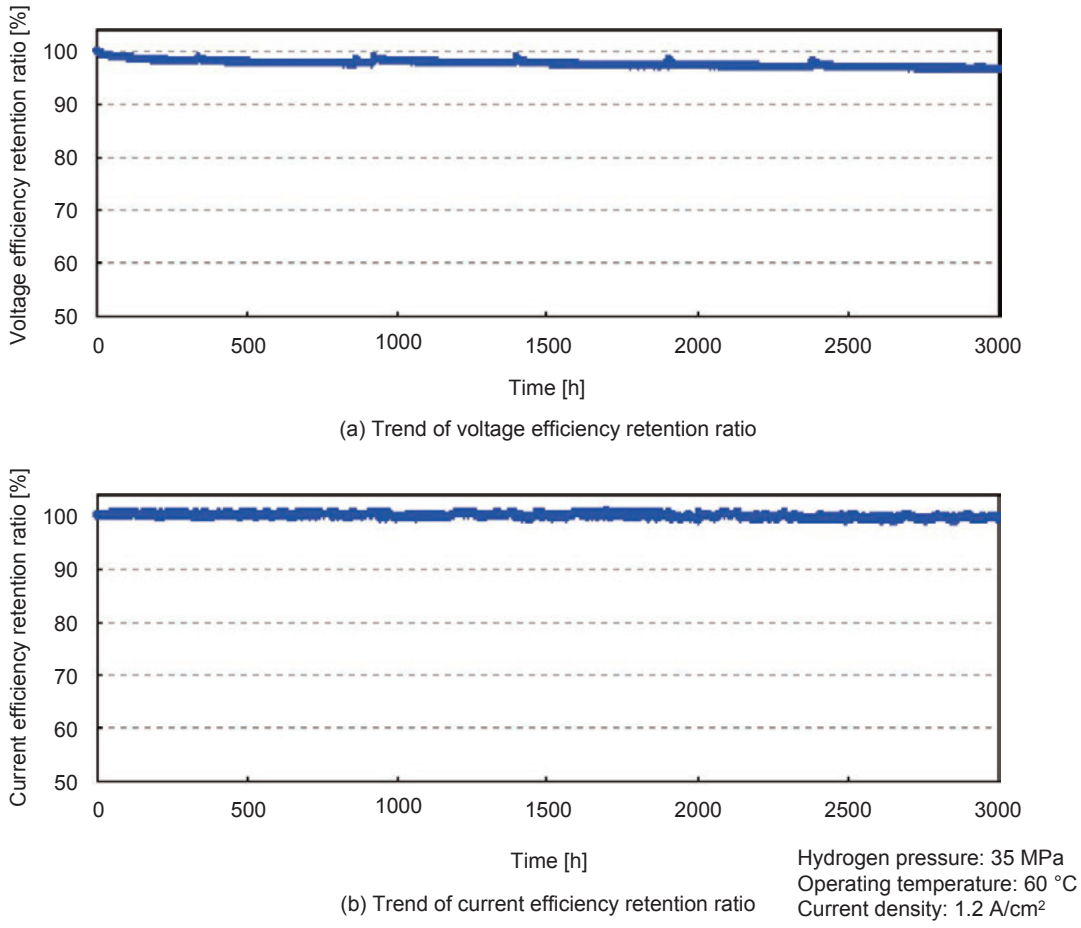


Fig. 10 Durability performance of high differential pressure electrolyzer

eight hours per day, 3000 hours amounts to approximately one year of operation. Figure 10 shows (a) the voltage efficiency retention rate and (b) the current efficiency retention rate of the high differential pressure electrolyzer.

The high differential pressure electrolyzer shows no sharp declines in voltage efficiency. After 3000 hours, there was a change of approximately 4%. This decrease in performance coincided closely with the decrease in performance of the water electrolyzer. It appears likely, therefore, that no increase over time took place in membrane resistance due to high-pressure hydrogen, nor any degradation in catalytic performance, nor any increase in contact resistances due to deformation of current collectors or other such stack components.

The current efficiency retention rate remained constant from the beginning through 3000 hours. The performance in high-pressure hydrogen production remained stable. No hydrogen leak to the outside of the stack was observed throughout the durability test.

Given the above, and given that the high differential pressure electrolysis displayed no particular change in durability, but retained its efficiency at a rate equivalent to a water electrolyzer, the prospective outcome of long-term durability proving tests of the SHS2 using this stack became apparent.

6. Conclusions

The installation of the high differential pressure water electrolysis-type solar hydrogen station (SHS2), which has the purpose of reducing CO_2 emissions, and initial performance evaluations of the SHS2 yielded the following results:

(1) The SHS2 was developed with installation in ordinary households in mind, and consideration was given accordingly to its safety and operability. Compared with the SHS1, the SHS2 was made approximately 60% more compact, realizing a size that allows installation in average households.
(2) The development of a highly efficient, high differential pressure electrolyzer system meant that the SHS2 achieved a system efficiency 25% higher than that of the SHS1.
(3) The efficiency of hydrogen production at 35 MPa using a high differential pressure electrolyzer is approximately 84%. This showed that the SHS2 is a high-pressure hydrogen generator that operates with greater energy-saving than the SHS1, which used a water electrolyzer with a mechanical compressor.
(4) The high differential pressure electrolyzer unit was subjected to durability testing equivalent to one year of operation. The results showed that the change in power efficiency it underwent was the same as the change in efficiency undergone by a water electrolyzer.

The high differential pressure water electrolysis-type solar hydrogen station (SHS2) will be subjected to proving tests, and the feasibility of its function and performance in actual environmental conditions will be confirmed.

References

(1) Ueyama, M., Kita, M., Taguchi, S., Nakazawa, K., Nagaoka, H., Arakawa, S.: Introduction of Hydrogen Refueling Station with Photovoltaic Modules, Honda R&D Technical Review, Vol. 15, No. 2, p. 31-38
(2) Taguchi, S., Handa, K.: Study of Hydrogen Refueling Station with Photovoltaic Modules, EVS-22 proceedings, p. 350-357 (2006)
(3) Okabe, M., Nakazawa, K., Taruya, K., Handa, K.: Verification Test of Solar-powered Hydrogen Refueling Station (SHS) with Photovoltaic Modules, Honda R&D Technical Review, April, 2008, p. 72-79
(4) U.S. Department of Energy (DOE), Office of Energy Efficiency and Renewable Energy (EERE), U.S. Environmental Protection Agency (EPA): Model year 2010 Fuel Economy Guide, p. 22 (2010)
(5) ISO 14687-2: Hydrogen fuel – Product specification – Part 2, Type 1, Grade D
(6) The Electrochemical Society of Japan: Electrochemical handbook, Vol. 5, p. 155 (2000)

■ Author ■


Koji NAKAZAWA


Hisashi NAGAOKA


Jun TAKEUCHI


Frank MOBURG


Ikuya YAMASHITA


Masanori OKABE

Piston Temperature Measurement Technology for Actual HSDI Diesel Engines

Koji KATSUMATA* Kenji SHIMIZU*
Tadanobu AOKI* Hidemi ARAI*

ABSTRACT

A new telemetry-based method for measuring piston temperatures in real time was introduced that is suited to the development of diesel engines, which are becoming higher output and using various types of combustion control in recent years. This method was used to measure temperature characteristics in engine bench tests and while cruising in an actual vehicle.

The new method uses a compact telemeter, and the amplifier and antenna can be mounted on the piston, facilitating both layout and work. This method was confirmed to provide measurement accuracy equivalent to that of the conventional linkage system and to have durability of 15 hours or more in diesel engines with an average piston speed of 14 m/s or more.

The new method was used to understand the effects of the diesel engine operation parameters on piston temperature. In addition, a piston temperature map was created that covers all operating conditions, and the contribution to fuel economy and emissions reduction was also investigated.

1. Introduction

Diesel engines for passenger cars are an effective means of reducing CO_2 emissions, but support for strict exhaust gas regulations is also demanded. For this reason, various types of combustion control are performed in recent diesel engines[1), 2)]. Increasing the power output density by turbo-charging and downsizing should also be considered. Against this background, piston temperature measurement becomes an important technology for understanding combustion states and investigating the effects on durability.

Various temperature measurement methods have been proposed to date, but none are currently able to completely support recent development needs. Indirect methods that convert the reduction in material hardness to temperature require operation at a constant speed, which imposes time restrictions if various temperature measurements are to be taken. In the widely used linkage system, the parts of the sensing elements that bend experience fatigue failure in long-stroke engines and high-speed engines, so lifespan is limited, making it is unsuited to measurement over long periods.

Compact methods using thermistors have also been developed as applications for high-speed engines such as those used in motorcycles and race cars[3)-5)]. However, due to the characteristics of the NTC thermistors mainly used in these methods, the resistance values do not change sufficiently in the diesel piston temperature range that can reach as high as 400°C, so temperature accuracy cannot be obtained.

The new measurement system uses a compact telemeter, and sheathed-type thermocouples as the temperature sensing elements. An additional feature is that the telemetry system is compact enough to fit inside the piston. This facilitates application to V-type engines and actual vehicles in which wired methods using a linkage system made layout a challenge.

The new measurement system enables measurement of piston temperatures both in engine bench tests and during actual vehicle operation. This paper reports the results of investigating durability compared to conventional methods, and the potential for enhanced fuel economy.

* Automobile R&D Center

2. Overview of Measurement System

Figure 1 shows the overall measurement system. The digital signal transmitted from the piston at the bottom dead center is D/A-converted inside the receiver, and output as an analog signal. This enables piston temperatures during actual operation to be understood in real time by converting the output analog signal to the temperature using a measuring device and a PC.

Figure 2 shows the signal transmission conditions. A sensor amplifier and a coil-shaped rotor antenna are mounted on the piston. Electric power and the measurement signal are transmitted and received when this rotor antenna and a rod-shaped antenna mounted on the cylinder block side approach each other near the bottom dead center. Electric power is supplied to the piston side by inductive coupling, and the sensor amplifier uses this supplied electric power to amplify the electromotive force of the thermocouple. Then, after A/D conversion the data is superposed onto a carrier wave and the measurement signal is transmitted to the rod antenna. The signal is transmitted by digital transmission, so it is highly resistant to noise.

The sensor amplifier mounted on the piston can measure up to six channels. Division into multiple channels by a multiplexer is supported, so ungrounded sheathed-type thermocouples need to be used for the temperature sensing elements.

Figure 3 shows the sensor amplifier and rotor antenna actually mounted on the piston.

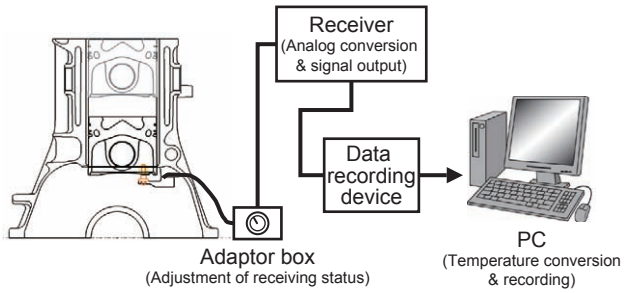


Fig. 1 Configuration of measurement system

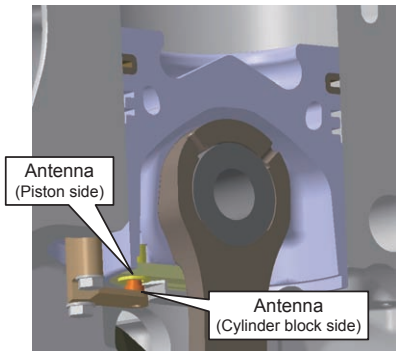


Fig. 2 Temperature measurement system

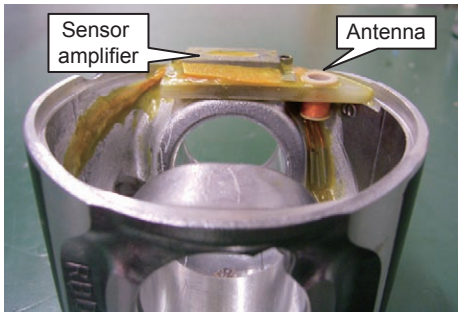


Fig. 3 Measurement piston mounted with new telemetry system

3. Measurement Performance

The measurement accuracy and durability of this measurement system were confirmed. Table 1 shows the specifications of the diesel engine used in this study. Basic performance was confirmed using a 2004 year model i-CTDI engine, and the measurement points were selected as shown in Fig. 4. The tips of the thermocouples at the points facing the combustion bowl were located 0.5 mm to the inside from the surface.

Accuracy was confirmed by locating a conventional exposed-type thermocouple and an ungrounded sheathed-type thermocouple next to each other on the pin boss area of the same piston, simultaneously measuring the former with the linkage system and the latter with the telemeter system, and comparing the results.

Figure 5 shows the results of verifying the temperature accuracy. The difference between the two methods was approximately 2°C regardless of the engine output power, which confirmed that the new measurement system using a telemeter has sufficient accuracy compared to the conventional method. The measurement values used the average values during steady-state operation one minute after the temperature stabilized at each operating condition.

Figure 6 compares the temperature transient characteristics. These results show that the new method exhibits good response, with the temperature rising and falling together with the torque in the same manner as the conventional linkage system.

Figure 7 shows the results of evaluating the measuring instrument durability during continuous operation. This test was conducted while confirming the effects of different operation parameters at high loads, and the lifespan exceeded 15 hours. This is sufficient durability in consideration of the fact that the high-speed test results for the linkage system were approximately 2 hours.

These results indicate that the new system has sufficient accuracy and durability performance as a measuring instrument.

Table 1 Specifications of test engine

Specification	04M/Y i-CTDI diesel engine	08M/Y i-DTEC diesel engine
Bore x Stroke (mm)	85 x 97.1	85 x 96.9
Displacement (cm^3)	2204	2197
Compression ratio	16.7	16.7
Max engine power (kW/rpm)	103/4000	110/4000
Max engine torque (Nm/rpm)	340/2000	350/2000
Max piston speed (m/s)	14.6	14.5

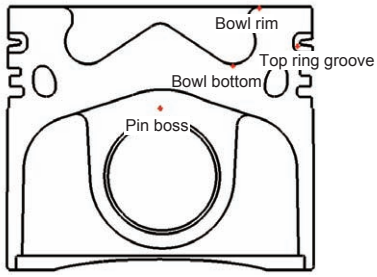


Fig. 4 Measurement points in thrust cross-section

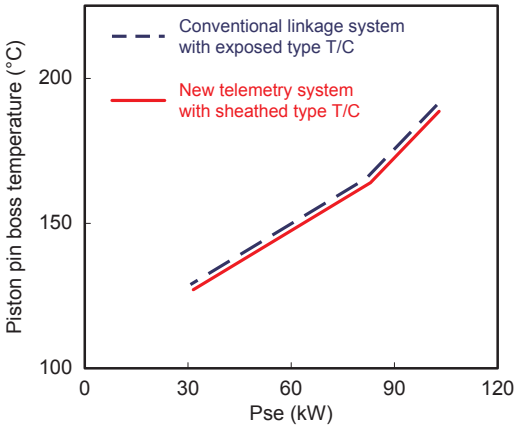


Fig. 5 Temperature correlation of both measurement systems

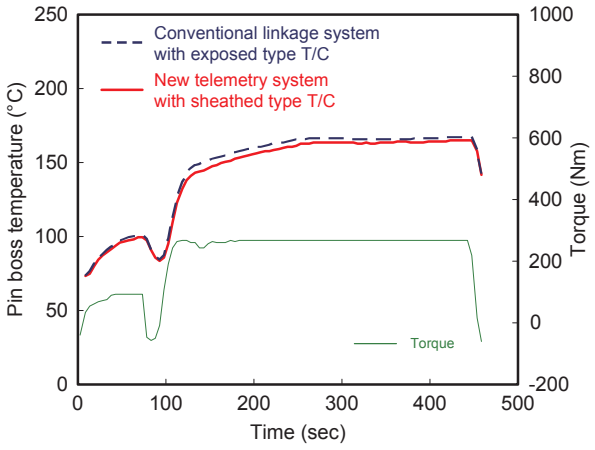


Fig. 6 Comparison of transient reaction of both systems

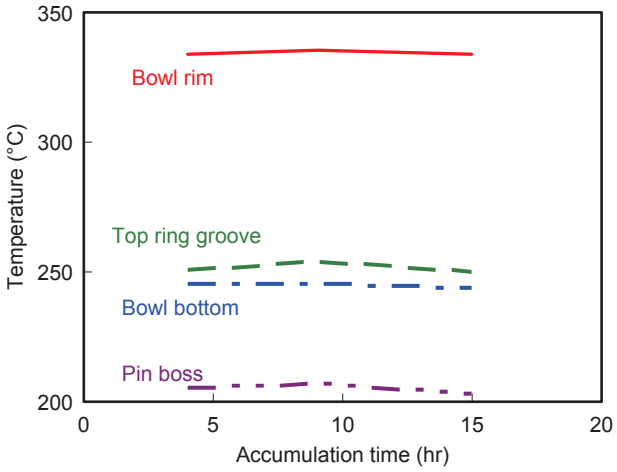


Fig. 7 Durability of telemetry system

4. Engine Bench Test Results

The new measurement system was used to confirm the effects of the diesel engine operation parameters on piston temperature. The results are as follows.

Figure 8 verifies the effects of water temperature and oil temperature on piston temperature. The operating conditions for all cases were 4000 rpm at full load, and the same indicated mean effective pressure and intake air temperature were also used from the standpoint of comparing temperatures. The horizontal axis shows the temperature of the oil discharged from the oil jets and the water temperature at the engine inlet, and the vertical axis shows the temperature at each piston location. The results showed that the piston temperature rose linearly in conjunction with the rise in oil and water temperatures, at all locations from near the combustion bowl to around the pin boss. In addition, arranging the slope by water temperature showed that the piston temperature rises by

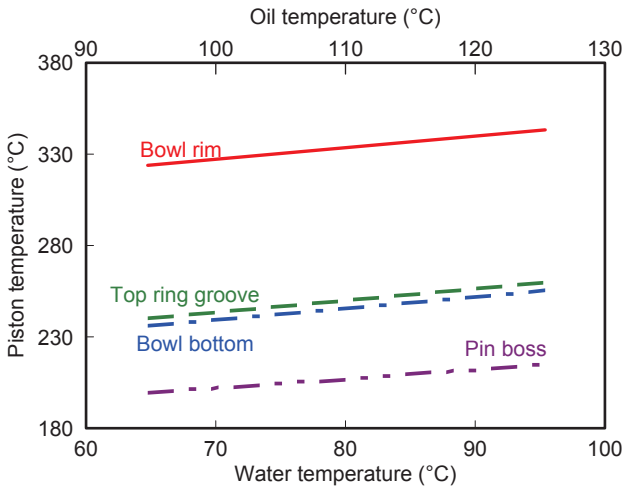


Fig. 8 Piston temperature against water and oil temperature

0.5°C to 0.6°C per 1°C of water temperature, with little difference between positions.

In turbocharged diesel engines, the heat resistance limit temperature of the turbocharger should also be taken into account, so the effects on exhaust gas temperature were also investigated. Figure 9 shows the relationship between exhaust gas temperature and piston temperature. In addition, the effects of cylinder pressure due to fluctuations in the turbocharged pressure are also shown. The operating conditions were the same 4000 rpm at full load as noted above, and the indicated mean effective pressure and intake air temperature were also the same.

Increasing the turbocharged pressure by 30 kPa produced a drop in the exhaust gas temperature of 100°C or more. The effect on the pistons was such that the temperature rise was limited to 4°C, but the cylinder pressure rose by 1.5 MPa.

These results indicate that the size and weight of each part can be further reduced by controlling the thermal and mechanical loads.

Figure 10 shows a temperature map created by measuring the piston temperature at the combustion bowl rim over the entire operation conditions range using a 2008 year model i-DTEC engine[1]. Conventional piston temperature measurement mainly aimed to evaluate durability, so measurement of the high load side was given priority. In addition to the conventional data, this study also obtained data for the low to medium load ranges, which is useful for future development.

The effects of piston temperature on fuel economy and emissions were also investigated using the i-DTEC engine. The piston temperature was controlled by varying the flow rate of the oil jet used to cool the piston. Figure 11 shows the results of confirming the correlation with the indicated specific fuel consumption (ISFC) when the piston temperature rises due to the load in the cruising mode range. Fuel consumption was confirmed to decrease as the piston temperature rises. This is because the thermal loss decreases as the piston wall surface temperature rises. Note that there was no change in NOx, soot and pumping loss due to different piston temperatures at this time. Further investigation is needed to enhance fuel economy, but these results indicated the possibility that piston temperature control can contribute to enhancing fuel economy.

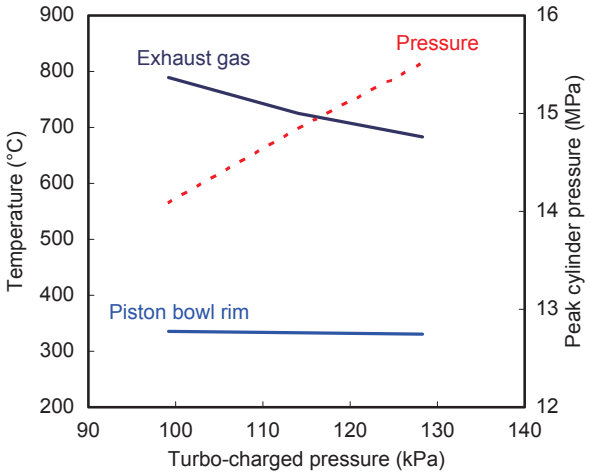


Fig. 9 Relation between piston temperature, exhaust temperature, cylinder pressure and turbo-charged pressure

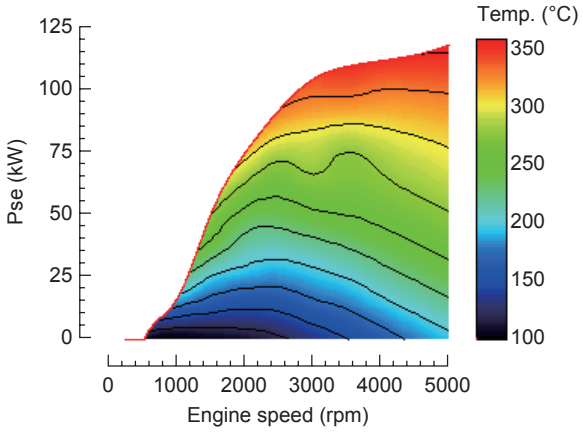


Fig. 10 Piston temperature map

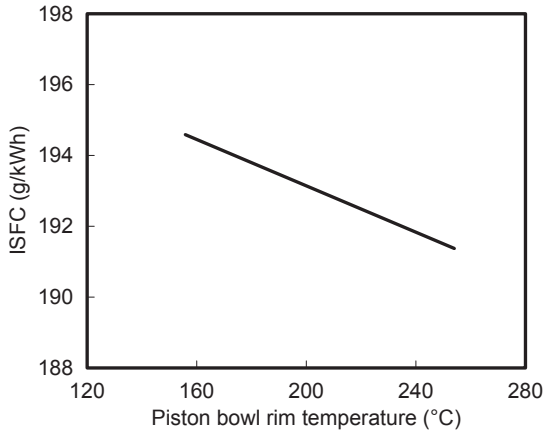


Fig. 11 Relation between fuel consumption and piston temperature

5. Results of Temperature Measurement in an Actual Vehicle

An engine incorporating the new measurement system was mounted in a vehicle, and temperature measurement was performed to confirm the transient states in an actual vehicle and changes in temperature occurring in the actual operating condition. The cruising mode was the NEDC mode used to measure fuel economy and emissions in the EU region. In addition, a CR-V equipped with the i-CTDI engine was used in the tests. The test vehicle was equipped with both a diesel particulate filter (DPF) that captures the particulate matter (PM) generated by combustion, and a DPF regeneration function that combusts the collected PM

to help prevent filter plugging. This function generally sends non-combusted hydrocarbons to the DPF by post-injection within the cylinder, and then combusts the PM[(2)]. The effects of this regeneration function on piston temperature were confirmed.

Figure 12 compares the piston temperature in the normal NEDC cruising mode (without DPF regeneration control) and when DPF regeneration control, that is to say, post-injection, is performed while cruising. In both cases the temperature tended to rise sharply in response to vehicle acceleration, and then fall quickly at the approximate load ranges for maintaining the speed. In addition, the piston temperature rose during post-injection control compared to normal operation. The post-injected fuel should normally be input to the DPF as fuel used to combust the PM, but the piston temperature indicates that it is atomized and partially used for combustion inside the cylinder.

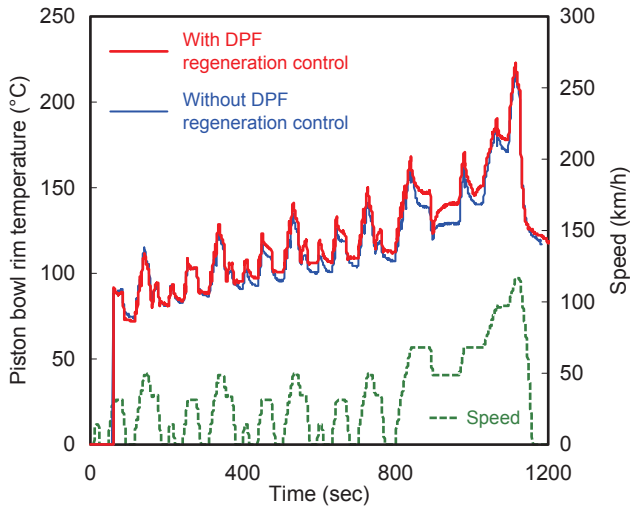


Fig. 12 Effect of regeneration control in NEDC mode on piston temperature

6. Conclusion

A telemetry-based temperature measurement system was introduced that is suited to measuring piston temperatures in a turbo-charged diesel engine. This compact measurement system was shown to have accuracy equivalent to that of the conventional linkage system, and durability that enables measurement over long periods in the high-speed range.

The new measurement system was used to measure piston temperatures in engine bench tests, and the effects of different operation parameters on piston temperature were quantitatively understood. In addition, a piston temperature map was created for engine operating conditions from low to high loads, and the results indicated the potential for piston temperature control to enhance fuel economy.

The new measurement system was mounted in an actual vehicle and used to measure and compare the fluctuation in piston temperatures in NEDC mode, and temperatures during DPF regeneration.

The new measurement system features durability and ease of mounting, and use in the future is expected to increase overall vehicle efficiency including engine heat management.

References

(1) Matsui, R., Shimoyama, K., Chiba, I., Hidaka, S., Nonaka, S.: Development of High-performance Diesel Engine Compliant with Euro-V, Honda R&D Technical Review, April, 2008, p. 19-24
(2) Chiba, I., Kaneko, I., Matsui, R., Ishihara, Y., Matsukado, R.: Development of DPF System for the EURO-IV-compliant Diesel Engine, 2005 JSAE Annual Congress Proceedings, No. 103-05, p. 15-18 (2005)
(3) Inami, N., Takeuchi, K., Kato, T., Osaki, R.: Piston temperature measurement for a CART High Speed Race Engine, 2002 JSAE Annual Congress Proceedings, No. 89-02, p. 1-4 (2002)
(4) Suzuki, M., Ueda, S.: Real-time Piston Temperature Measurement Using Electromagnetic Induction Telemetry, Honda R&D Technical Review, Vol. 18, No. 1, p. 77-80
(5) Isarai, R., Sugino, M., Iwade, K., Otsubo, M., Serai, T., Moritsugu, M., Nakamura, M.: New Telemeter to Measure Engine Parts during Operation, 2007 JSAE Annual Congress Proceedings, No. 62-07, p. 17-20 (2007)

Author


Koji KATSUMATA


Kenji SHIMIZU


Tadanobu AOKI


Hidemi ARAI

Development of V10 500-HP Engine – Technologies for High-performance and Low-emission Clean Powertrain –

Takahiro OKUYAMA* Takeshi FUKUZAWA* Akira HASHIMOTO*

ABSTRACT

This article introduces environmental support technologies for the V10 500-HP engine that was developed for use in super sports cars. A new valve assembly was developed that adds a cylinder deactivation function to the high engine performance DOHC i-VTEC mechanism in order to achieve a balance between high engine performance and fuel economy. In order to achieve a balance between high engine performance and low emissions, the exhaust manifold was made a long type, a two-bed closed couple (CC) catalyst (CAT) and an under-floor (UF) catalyst were configured as the exhaust emissions control system, and a secondary air system was adopted. Misfire detection was supported by the adoption of a cylinder pressure sensor system. These various technologies enabled achievement of a balance between high output performance at the top of its class among competing cars and high environmental performance that responds to the demands of the times.

1. Introduction

The V10 500-HP engine was developed starting in late 2004, and was slated to be mounted in the successor to the NSX. Under the impact of the worldwide economic downturn that followed upon the Lehman Brothers Shock, however, development was canceled at the end of 2008. Principle technologies in this engine, for which development had largely been completed, are now being introduced in two parts[(1)]. This article presents an overview of the engine and describes the technology that addresses the era's demand for environmental performance.

2. Development Goals and Objectives

2.1. Development Goals

The first goal of this engine was to serve as the core of commercial product appeal for the super sports car that would be the successor to the NSX, satisfying the user with its overwhelming engine performance. On the other hand, it was also considered necessary for this to serve as the flagship engine that is situated at the very peak of Honda's engine lineup, and as such, it would have to fulfill Honda's corporate responsibility to provide the environmental support demanded by the times. Given this perspective, it was decided to pursue development of this engine under the aim of achieving a balance between power performance that creates acceleration reaching into a whole different dimension, and environmental performance that addresses the demands of the times.

2.2. Development Objectives

The objectives first defined for development are shown below. Figure 1 shows their placement.

(1) Power: 500 HP or more
(2) Fuel economy: Clear the US Gas Guzzler Tax regulations
(3) Emissions: Comply with California State LEV2-ULEV regulations

* Automobile R&D Center

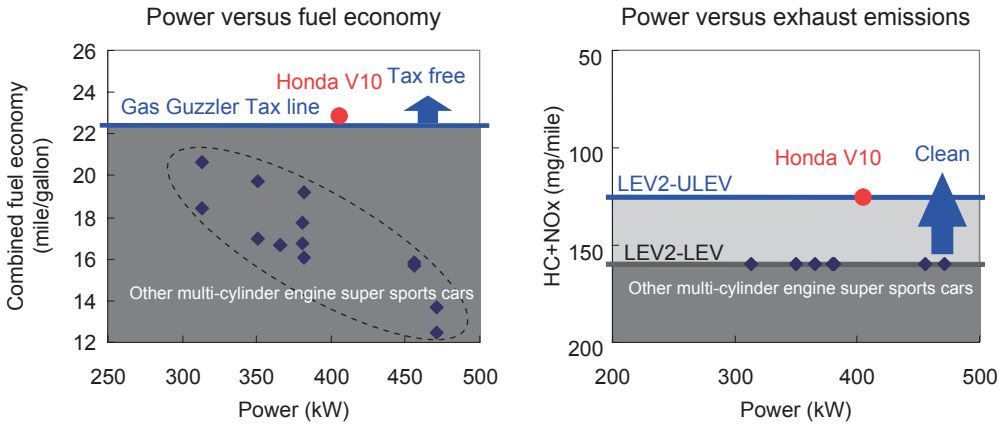


Fig. 1 Competitiveness of power, fuel economy and exhaust emissions

Table 1 Engine specifications

Cylinder configuration	V10
Bank angle	90°
Firing interval	90°-54°(uneven firing)
Bore pitch / offset	102 / 20
Bore × Stroke (mm)	90 × 78.5
Displacement (cm^3)	4993
Compression ratio	12.3 : 1
Valve train	DOHC i-VTEC VCM
Number of valves	4 per cylinder
Valve diameter IN / EX (mm)	37 / 31.5
Gasoline	Premium (RON95)
Max. power (kW/rpm)	405 / 8200
Max. torque (Nm/rpm)	513 / 7000
Idle / Fuel cut (rpm)	850 / 8500
Fuel economy City / Hwy label (mpg)	16 / 21
Unadjusted Combined (mpg)	22.8
Emissions	LEV2-ULEV

3. Overview of Engine Frame

The number of cylinders and the air intake system were determined so as to be appropriate to the engine's position as a flagship model for Honda. It was therefore given the 10-cylinder V configuration (V10) typical in the lineage of Honda F1 engines, and natural air (NA) intake. The displacement per cylinder was set at 500 cm^3 for a superior balance between horsepower and torque in a high-performance NA engine, with a total engine displacement of 5.0 L. The maximum displacement for the engine frame was set at 5.5 L, in consideration of future development possibilities. The bank angle was determined in light of engine balance, the feeling of a step in noise and vibration (NV) when switching back and forth between all-cylinder operation and cylinder-deactivated operation, the engine room package, common points with the V8 in terms of a production machine, and so on. For superior performance in all these factors, a 90° angle with unequal interval ignition (no crank pin offset) was adopted.

Table 1 shows the main specifications of this engine.

4. Technology for Balancing High Engine Performance with Fuel Economy

Various steps were taken to achieve a balance between high power performance and enhanced fuel economy. Change to a higher compression ratio for enhanced combustion efficiency was combined with the use of lighter-weight component parts, typified by the adoption of titanium conrods, for reduction of mechanical loss. A variable cylinder management system (VCM) was also adopted, and a three-stage VTEC valve assembly mechanism that incorporates cylinder deactivated operation (three-stage VTEC VCM mechanism) was newly developed. This achieved a level of fuel economy that rises as high as 22.8 mpg, above the line defined by the US Gas Guzzler Tax regulations.

4.1. Three-stage VTEC VCM Mechanism

A new DOHC four-valve mechanism that switches valve timing and lift between three stages of low speed, high speed, and cylinder deactivation was developed. Table 2 shows the major specifications in comparison with production models.

(1) Basic structure

Figure 2 shows the rocker arm structure. Bank 1, which operates with normal combustion without performing cylinder deactivation, is a two-stage mechanism similar to previously existing high-performance DOHC VTEC implementations. Bank 2 adds two rocker arms and synchronized pistons for cylinder deactivation switching to the VTEC mechanism found in Bank 1, making it a mechanism capable of cylinder deactivation. A two-loop hydraulic switching system that performs coupling and decoupling hydraulically was adopted to implement valve operation and deactivation switching so as to place an emphasis on switching responsiveness at low speeds.

Figure 3 shows the configuration of components in the three-stage VTEC VCM mechanism. To the conventional VTEC mechanism, Bank 2 has added two hydraulic passages for low speed and deactivation and a three-way

Table 2 Valve train specifications

Engine code		–	J35Z2	F20C	LDA-MF5
Cylinder configuration		V10	V6	L4	L4
Valve train		DOHC	SOHC	DOHC	SOHC
		3-stage VTEC VCM	VCM	VTEC	3-stage VTEC VCM
Number of valves per cylinder		4	4	4	4
VCM	Running	○	○	–	–
	Deceleration	○	○	–	○
	Idle	○	–	–	–
VTEC	In	○	–	○	○
	Ex	○	–	○	–
VTC		○	–	○	–
Max. engine speed (rpm)		8500	6900	9000	6500

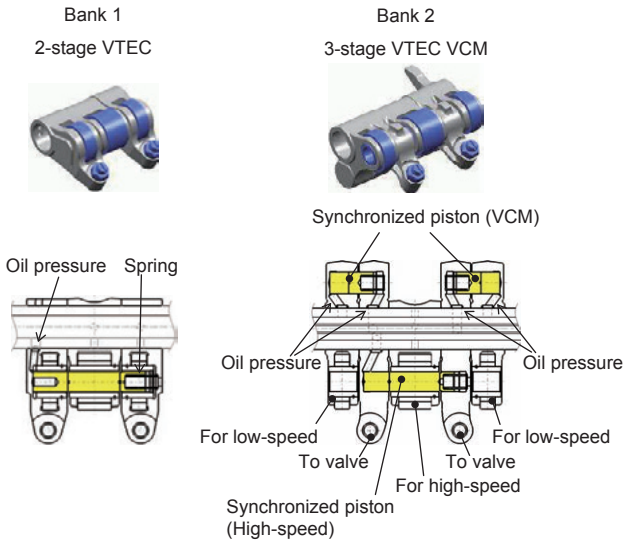


Fig. 2 Components of rocker arm

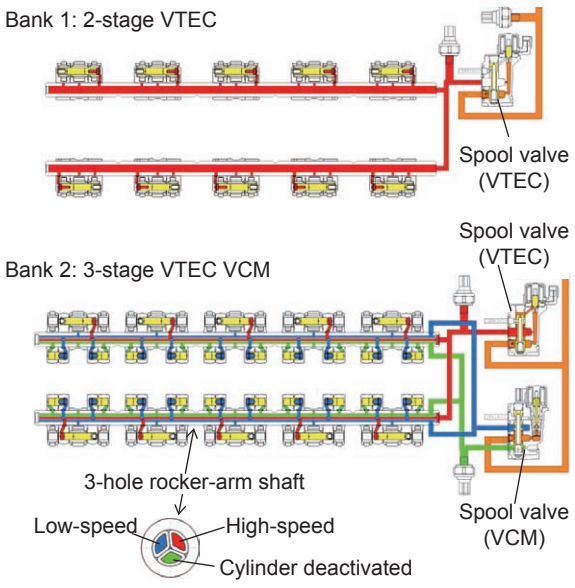


Fig. 3 Components of 3-stage VTEC VCM

spool valve to carry out the hydraulic switching.

(2) Operating mechanism

Figure 4(a) shows the operational state of the hydraulics and synchronized pistons when starting and at low speeds. The hydraulic state shown in blue causes the deactivation switching synchronized pistons to move so that the rocker arm on the valve stem is coupled with a rocker arm that is driven by a low-speed cam, and the valve is driven by the low-speed cam.

When the hydraulics shown in red are added to this state, the high-speed synchronized piston is made to move, as shown in Fig. 4(b). The rocker arm on the valve stem is coupled with a rocker arm that is driven by a high-speed cam, and the valve is driven by the high-speed cam, which has a higher lift.

When the hydraulic state shown in blue in Fig. 4(a) switches over to the hydraulic state shown in green, the deactivation switching synchronized piston moves so that the rocker arm on the valve stem and the rocker arm driven by a low-speed cam are decoupled. This results in the state of cylinder deactivation shown in Fig. 4(c).

4.2. VCM Operating Conditions

The engine's VCM operates primarily on the basis of throttle opening information to determine whether the vehicle is in a cruise, deceleration, or idle state from the vehicle speed, engine speed, engine oil temperature, gear

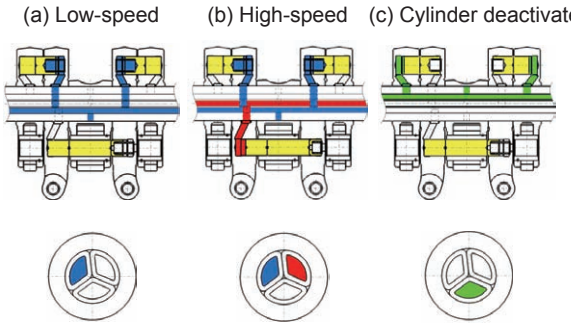


Fig. 4 Operating principle of 3-stage VTEC VCM

speed, and the like. Then, as shown in Fig. 5, it deactivates one bank of cylinders and switches over to five-cylinder operation. At the same time, out of environmental concern, it also determines whether the catalyzer temperature and other such factors in the exhaust emissions reduction system are in a state appropriate for switching over.

Measures have also been taken to ameliorate the reduction in drivability resulting from torque level differences when switching occurs. The accuracy of switch-over response in the VTEC mechanism has already been increased, as in the V6 VCM, and ignition control[2), 3)] has already been applied. Moreover, intake air volume control by cylinder bank was applied this time so that switching over can take place smoothly and without torque level differences.

4.3. Fuel Economy Enhancement Effect of VCM

When this engine is running under cylinder deactivation, all the valves on the deactivated side are stopped in their seated state. This reduces pumping loss and valve drive loss. On the operating cylinder bank side, the throttle opening is larger, and this also reduces pumping loss.

Taking advantage of the characteristics of the multiple-cylinder engine, the idle speed can also be configured for cylinder deactivation. Since the displacement is so large, the engine power can be maintained to a high level even when running with cylinders deactivated, and this allows operation with cylinder deactivation across a wide range of speeds from idle to approximately 100 mph (160 km/h).

The pink area in Fig. 6 shows the operating range of the engine with cylinders deactivated in EPA LA-4 and highway modes. The frequency of cylinder deactivation in LA-4 mode was 68% and in highway mode it was 91%. The enhancement effect on combined mode fuel economy was 13% (relative to having all cylinders active).

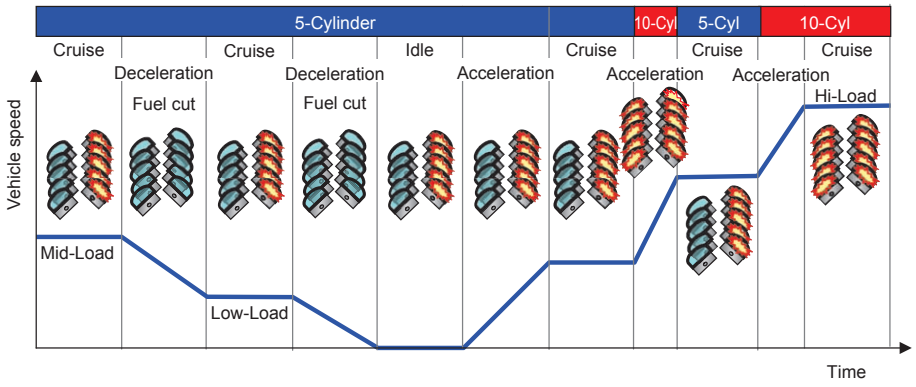


Fig. 5 Operation of VCM

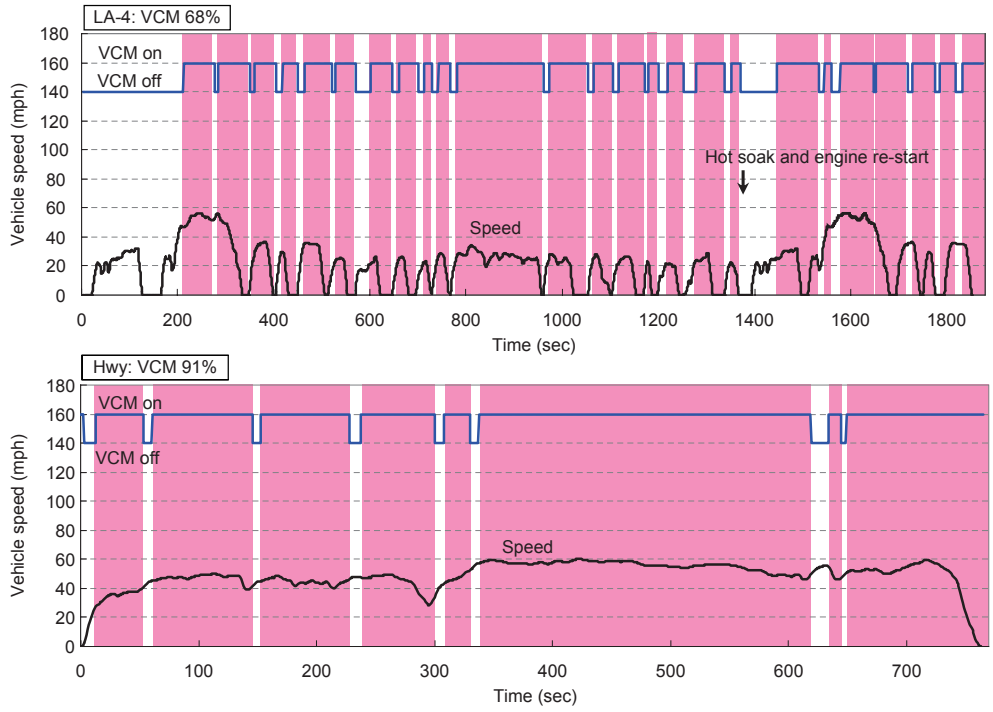


Fig. 6 Operation of VCM in LA-4/Hwy mode

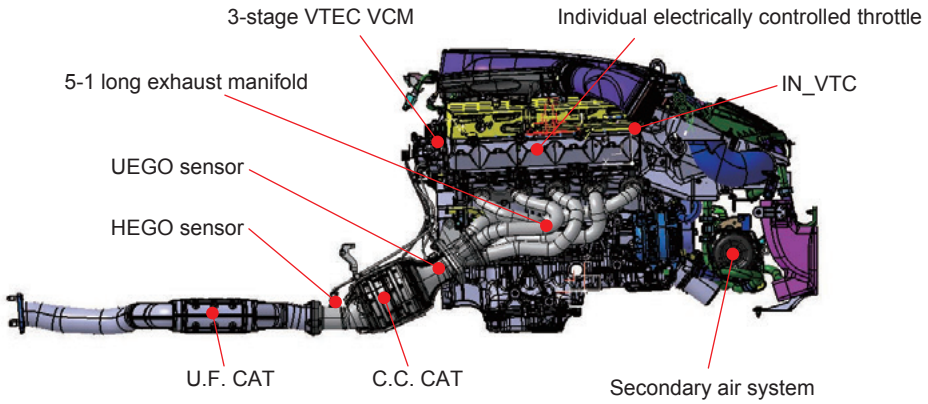


Fig. 7 Configuration of emissions control system

5. Technology for Achieving a Balance of High Power Performance and Low Emissions

Seeking to achieve a balance of high power performance and low emissions first involved work on the engine alone. The combustion chamber shape was optimized to reduce unburned gases, and retard control at startup using valve timing control (VTC) together with optimization of the fuel injection method were used to reduce feed emissions.

In order to enhance purification performance of feed emissions using the catalyzer, it is important that the catalyst be made to heat up quickly during cold starts. When the objective is low emissions, the heat mass of the exhaust manifold located upstream from the catalyzer needs to be minimized by designing the manifold to be as small and light as possible. Since the emphasis with this engine is on power performance, however, it needs to have a large, long exhaust manifold of the 5-1 type. The exhaust emissions control system, as shown in Fig. 7, consists of a closed couple (CC) catalyzer placed at the exhaust manifold using a three-way catalyst of the two-bed type (Fig. 8), and an under-floor (UF) catalyzer using a three-way catalyst of the one-bed type, as well as a secondary air system adopted to raise the catalyst temperature.

5.1. Feed Emissions Purification Technology

In order to reduce the heat mass of the exhaust manifold, the fabrication method was changed from welding together a number of curved pipes to hydroforming by bending thin-sheet pipe. The number of parts and the weight were reduced.

For the front bed of the closed couple (CC) catalyzer, a metal catalyst support that heats up quickly was adopted.

These measures yielded the results shown in Figs. 9 and 10. The catalyst temperature at the initial stage of LA-4 mode had risen to 250°C within 20 seconds after engine startup. This is on a par with LEV2-ULEV vehicles with V6 engines.

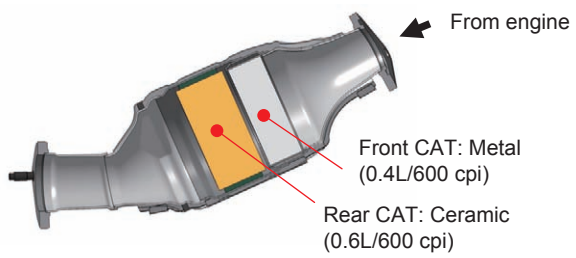


Fig. 8 Layout of C.C. CAT

5.2. Technology to Achieve Balance with Fuel Economy Enhancement

When the engine is operated with cylinders deactivated for a long period in order to enhance fuel economy, the temperature of the catalyst on the deactivated bank side will decline. Achieving emissions purification performance equal to that when operating with all cylinders requires that the catalyst on the deactivated bank side maintain its light-off condition. When the catalyst temperature declines rapidly, the time to deactivation of the catalyst will be reduced, the time spent with cylinders deactivated will be limited, and the rate of fuel economy enhancement will decline.

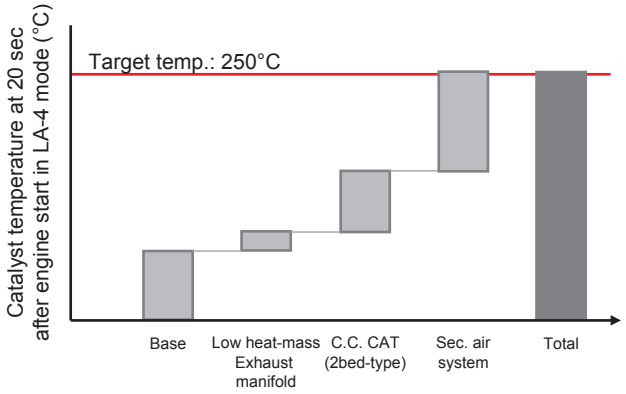


Fig. 9 Catalyst temperature after engine start

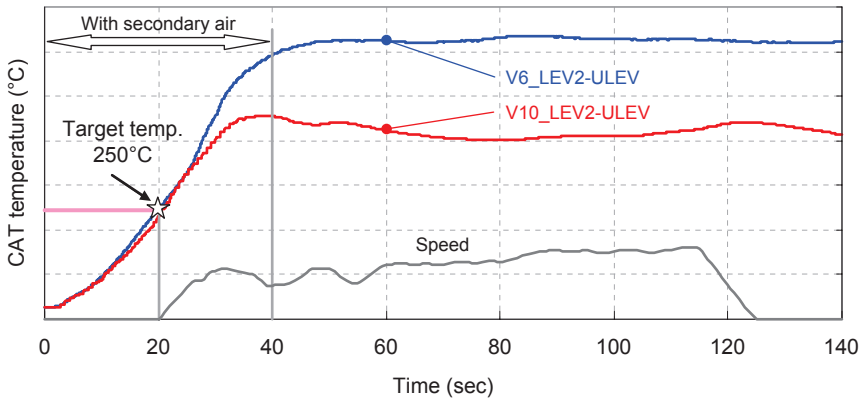


Fig. 10 Catalyst temperature after engine start in LA-4 mode

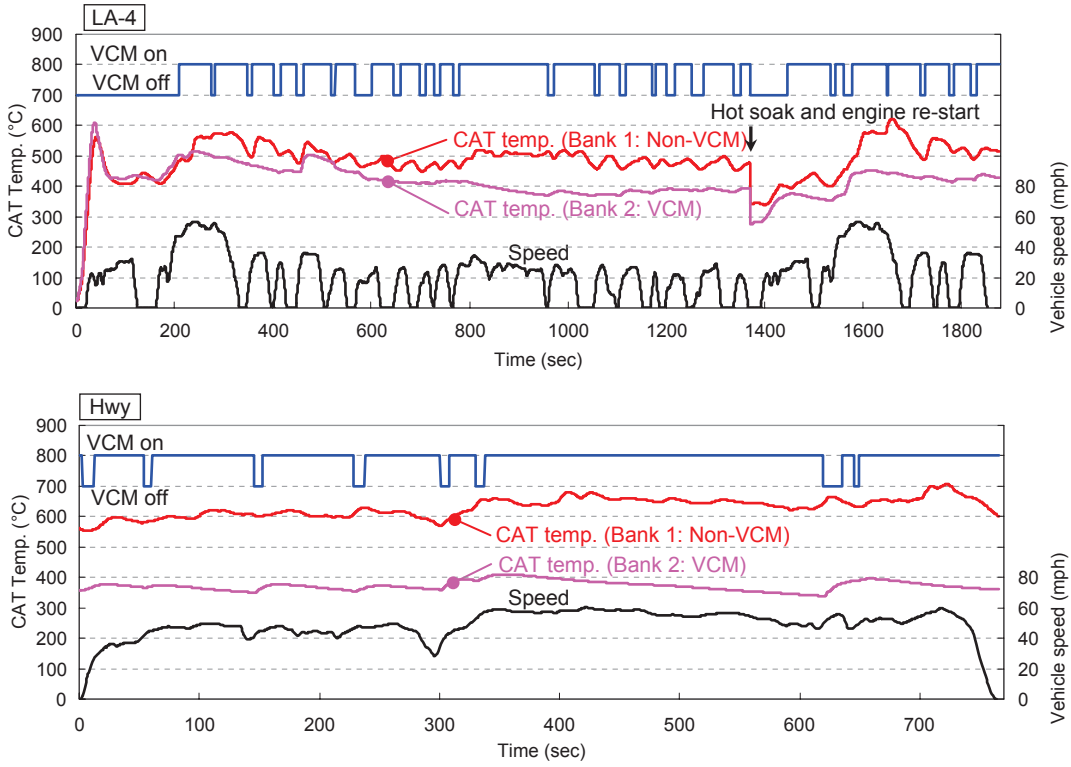


Fig. 11 Relationship between VCM and catalyst temperature

Therefore, a ceramic catalyst support with superior heat retention was adopted for the rear bed of the closed couple (CC) catalyzer. This limits the drop in catalyst temperature and enables maintaining the light-off temperature of approximately 320°C over a long time. This served to achieve a balance with fuel economy enhancement.

Figure 11 shows how the catalyst temperature on the deactivated bank side maintains the light-off state in LA-4 and highway modes.

6. Misfire Detection Technology

Support for misfire detection is a prerequisite to taking environmental measures for all destinations. However, to deal with determination of multiple misfires in 10 cylinders by means of the total pattern using the conventional method of detecting fluctuations in crank angle speed would require enormous software development. For this engine, therefore, the characteristics of a cylinder pressure sensor system[4] employing adaptive calculation were used to advantage in a system capable of knocking detection as well as misfire detection.

6.1. System Configuration

As shown in Fig. 12, the system is configured with cylinder pressure sensors and a cylinder pressure unit. The system is set up to transfer data to the engine control unit (ECU) by means of the controller area network (CAN).

Inside the cylinder pressure unit, signals from the sensors are converted into voltages and then into digital signals by an AD converter, and fed into the central processing unit (CPU). Inside the CPU, the cylinder pressure for each crank angle is also computed using crank pulses and cylinder pulses. One 100-MHz CPU is used for each five cylinders (one per bank), and the AD converters are configured for sampling at 50 kHz. The result is that cylinder pressure can be measured for each degree of crank angle at speeds up to 8000 rpm or more.

Misfire detection and knocking detection require different frequency filtering for their respective waveform acquisition. Digital filtering is therefore performed within the CPU and the optimal pressure waveforms are subjected to computation.

6.2. Structure of Cylinder Pressure Sensors

The cylinder pressure sensors are placed to minimize their effect on the valve assembly and valve layout. As shown in Fig. 13, therefore, they were installed between the spark plugs and cylinder heads, sharing the fitting with the plugs.

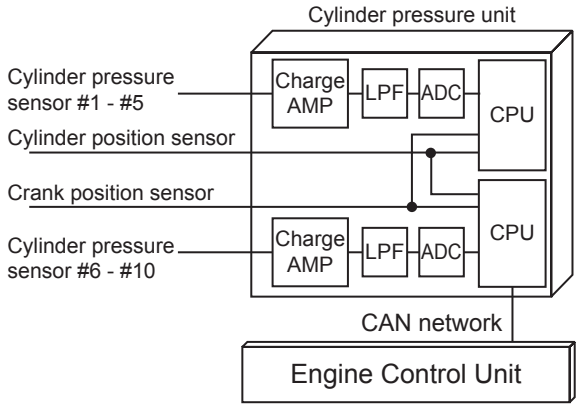


Fig. 12 Cylinder pressure unit configuration

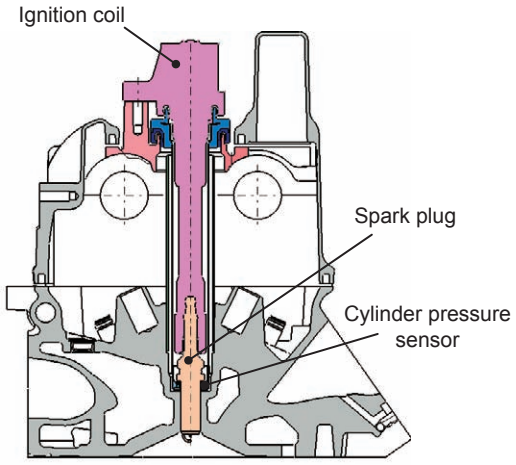


Fig. 13 Installation of cylinder pressure sensor

Figure 14 shows the structure of the sensors. They are basically configured with a piezoelectric element fitted inside a cylindrical housing in a simple washer-like structure that senses strain between the cylinder head and the spark plug. Lead titanate ($PbTi0_3$) was used for the piezoelectric elements.

6.3. Sensor Output Compensation by Adaptive Calculation

It is widely known that one of the basic properties of lead titanate ($PbTi0_3$) is that its piezoelectric constant changes greatly with the temperature. In order to use this substance as a cylinder pressure sensor in an automobile engine, that and various other property changes should be addressed.

The varying rate of sensor properties under the environmental conditions in which this engine is used is large, ranging from 120% to -80%. The sensor output cannot be used just as it is, so output compensation is performed by adaptive calculation within the cylinder pressure unit. The method used is outlined below.

(1) The motoring pressure is estimated by calculation from the operational state.
(2) The motoring pressure obtained by calculation and the actual measured motoring pressure are made to agree by mapping, and that value is stored in the ECU as the standard pressure.
(3) The cylinder pressure during the compression cycle is largely determined by the intake air volume, and is not influenced by subsequent misfiring or combustion. The sensor signal is therefore corrected at each cycle so as to agree with the standard motoring pressure obtained in (2), and a stable estimated cylinder pressure is thus obtained for each crank angle.

6.4. Misfire Detection

The cylinder pressure waveform following correction shows the pressure rising with combustion when normal combustion occurs, but when misfiring occurs, it will agree with the motoring pressure computed within the

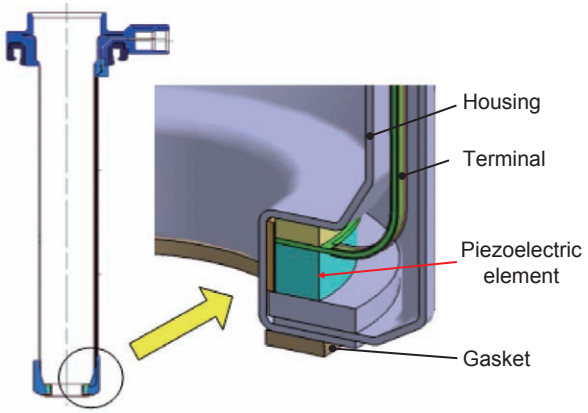


Fig. 14 Cylinder pressure sensor structure

unit. Making use of this characteristic, the ratio between the cylinder pressure waveform during combustion and the motoring pressure waveform is determined, which allows determination of whether or not energy was generated by combustion, or, in other words, determination of a misfire state.

Figure 15 shows the waveforms for combustion and misfire in the identical operational state. As a result of these innovations, 100% misfire detection performance can be achieved in a V10 engine over the entire range of speeds and under all conditions of the environment of use.

Figure 16 shows an example of detection performance when misfires occur continuously in a single cylinder of an actual engine. The red portion shows normal combustion, and the blue shows continuous misfiring in a single cylinder, indicating how the determination of misfiring can be made.

6.5. Knocking Detection

Sensors to measure cylinder pressure are placed in every cylinder. These can therefore also be used to advantage to detect knocking. Figure 17 shows a comparison of the layout of conventional knocking sensors and of cylinder pressure sensors.

Figure 18 shows waveform processing being carried out. When knocking occurs, a pressure fluctuation wave caused by the knocking is added to the cylinder pressure waveform. A bandpass filter can then be used to isolate just the frequencies of the pressure fluctuation wave caused by the knocking. This constitutes knocking detection. The sensor placement and waveform processing described above have enabled stable knocking detection.

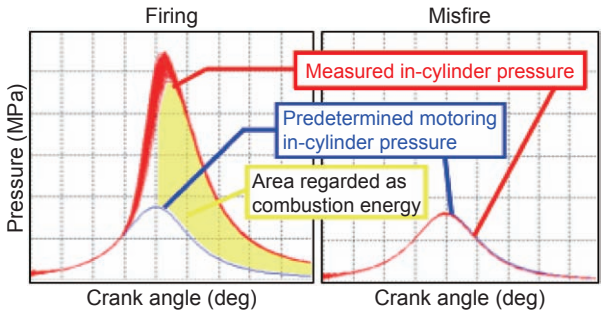


Fig. 15 Difference between firing pressure and misfire pressure

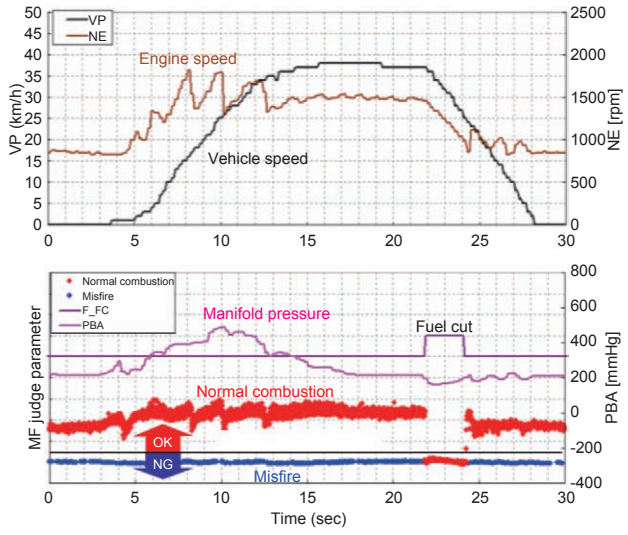


Fig. 16 Single continuous misfire on actual driving pattern

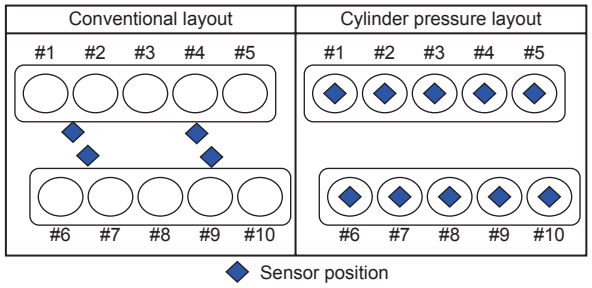


Fig. 17 Sensor layout

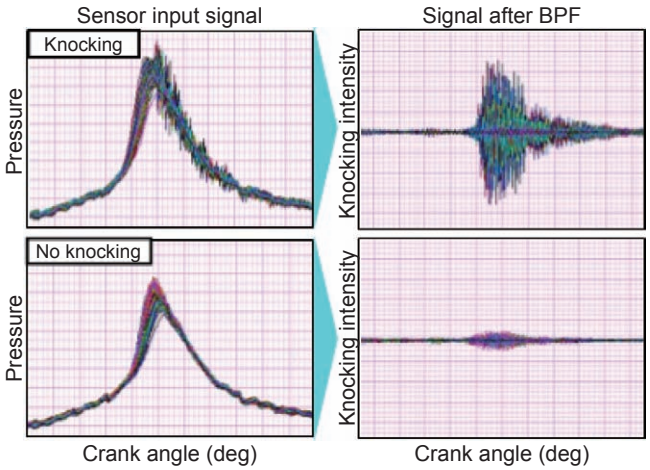


Fig. 18 Knocking signal processing

7. Conclusions

This engine has achieved the below environmental performance objectives in a way that has no precedent among 500-HP class multiple-cylinder engines mounted in super sports cars.

(1) Fuel economy: Cleared the US Gas Guzzler Tax regulations

(2) Emissions: Complied with California State LEV2-ULEV regulations

For people who love engines, the NA, high-RPM, multiple-cylinder engine is an endless object of attraction, and it was a joy for the authors to be involved in this development project. The environmental performance

objectives for this engine were set at unprecedentedly high levels out of the strong desire to build an engine that would meet the demands of a new era. The authors hope that this article may serve to advance the future development of such engines.

References

(1) Okuyama, T., Nakada, M.: Development of V10 500-HP Engine –Technologies for High Performance and Reliability–, Honda R&D Technical Review, October, 2010, p. 50-58
(2) Noguchi, K., Fujiwara, M., Segawa, M., Sawamura, K., Suzuki, S.: Development of V6 i-VTEC Engine with Variable Cylinder Management, Honda R&D Technical Review, Vol. 16, No. 1, p. 85-92
(3) Segawa, M., Kumagai, K., Sato, R., Tamura, Y., Fujiwara, M.: Development of V6 Engine with New Variable Cylinder Management, Honda R&D Technical Review, April, 2008, p. 35-42
(4) Yamamoto, Y., Akazaki, S., Ohara, M., Mizuno, T.: Development of Cylinder Pressure Measurement System Using Adaptive Calculation, Honda R&D Technical Review, October, 2007, p. 93-99

Author


Takahiro OKUYAMA


Takeshi FUKUZAWA


Akira HASHIMOTO

Development of V10 500-HP Engine – Technologies for High Performance and Reliability –

Takahiro OKUYAMA* Makoto NAKADA*

ABSTRACT

This article introduces technology related to the power output and reliability of the V10 500-HP engine developed for use in super sports cars. In order to achieve high power exceeding 500 HP, thoroughgoing measures were taken to reduce interference of intake air and exhaust air between cylinders, and laser clad welded valve seats were adopted. Individual throttles were adopted for the purpose of high response, which is of similar importance to power output for sports cars, and comprehensive weight reductions were made in major moving parts. As to reliability assurances, an examination was made of how the successor vehicle to the NSX, which was slated to have this engine mounted in it, would be used. Test criteria were formulated on the basis of actual running data to enable issuance of a guarantee in all areas, including running on the circuit, and testing was carried out. The above measures produced an engine that would allow enjoyment of running with the high degree of attractiveness set as an objective and with a sense of security in all situations.

1. Introduction

The principal technologies in the V10 500-HP engine are being introduced in two parts[1]. This article will describe the technologies for high performance and reliability.

A super sports car realizes its true value when it runs on the circuit at speeds so high that it is in a different dimension from ordinary automobiles. This engine, which had been slated for mounting in the NSX successor car, had to have both the high power output and the high response of a racing engine in order to provide that kind of pleasure in running. As a high-performance sports car engine, this engine also required a conceptual approach and technologies different from an ordinary car for its reliability guarantee. The following will introduce those technologies.

2. Power Performance

2.1. Overview of High-performance Technology

Figure 1 shows the engine performance characteristics. Table 1 shows the major specifications.

Enhancing intake and exhaust efficiency, enhancing thermal efficiency, and reducing friction are important in achieving high performance. The technologies adopted with this engine for these purposes will be introduced, in that order, below.

Figure 2 shows the overall layout of this engine's intake and exhaust system. The intake system was divided into independent left and right banks in order to reduce interference between cylinders. The intake chamber volume was increased to obtain fully adequate capacity that would not cause diminished power output, because the adoption of individual throttles helped resolve the issue of a reduction

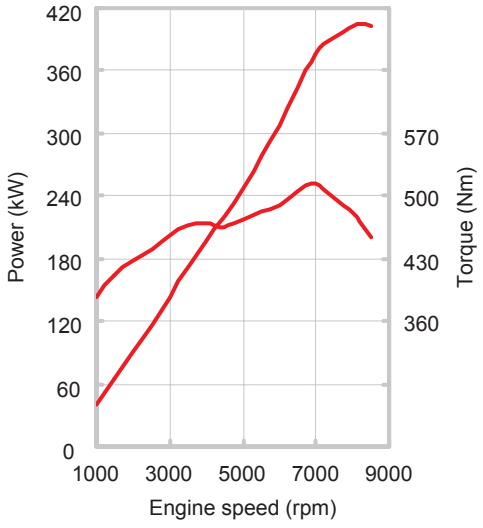


Fig. 1 Engine performance

* Automobile R&D Center

Table 1 Engine performance specifications

Max. power (kW/rpm)		405 / 8200
Max. torque (Nm/rpm)		513 / 7000
Displacement (cm^3)		4993
Bore × stroke (mm)		90 × 78.5
Compression ratio		12.3:1
Main part	Valve (mm)	Inlet: ϕ37 × 2 Exhaust: ϕ31.5 × 2
	Piston & Ring	Forged & 3 Ring
	Connecting rod	Titanium
	VTC	Operation angle: 50 degrees
Air intake system	Surge tank	Product made of resin (vol: 9.4 L × 2) Each bank independent
	TH/B : Pri	ϕ38 × 2
	TH/B : Sec	ϕ50 × 10
Exhaust system	Exhaust manifold	ϕ38.1 × 440 Thickness: 1.0-1.5
	C.C.	2BED (0.4+0.6 L) 600/1.2 metal +600/3.5 ceramic
	Exhaust pipe-A	ϕ60.5 Thickness: 1.2
	U.F.	ϕ118 race track 1.4L 300/1.2 metal
	Exhaust pipe-B	ϕ65 - Exhaust chamber ϕ115 Each bank independent

in response when the capacity was increased. The exhaust system was also divided into independent left and right banks in order to reduce interference between cylinders. An exhaust manifold of the long 5-1 type was adopted, and where the five pipes come together, a stainless steel chamber made by lost-wax casting was installed to reduce interference between cylinders due to the exhaust. This is the GT chamber shown in Fig. 3. In addition to these means used to reduce interference between cylinders in the intake and exhaust system, laser clad welded valve seats were adopted and the shape of the area around the intake port valve seats was refined, further enhancing intake and exhaust efficiency.

Thermal efficiency was enhanced by the use of spark plugs with fine center electrodes and aluminum sleeves, and shape optimization of the combustion chambers and water jackets achieved a compression ratio of 12.3:1.

Measures taken to reduce friction include extensive reduction in the weight of major moving parts together with refinement of passages between the cylinders in the cylinder block and of the layout of oil return passages from the cylinder heads to the crankcase.

2.2. Laser Clad Welded Valve Seat (LCVS)

One of the main technologies for enhancement of engine performance is the laser clad welded valve seat (LCVS), and this technology will be explained here. The valve seats were formed by welding powder metal, and for this reason, the LCVS[(2)] used in Honda F1 engines were able to have the seat material occupy a smaller area around the valve seat location than in conventional press-fit seats, allowing increase of the valve diameter. In this engine, a 0.7 mm increase in the diameter was realized.

With press-fit seats, it is most common that the connection between the rotary processed shape of the valve seating area of the valve seat and the cast port shape was performed by rotary processing. With the Honda F1 engine using the LCVS, on the other hand, the entire assembly from the valve seating area of the valve seat to the port could be continuously worked for optimization in three dimensions, providing a stable port with a high flow coefficient. In the present engine, the processing that connects the rotary processed shape of the valve seating area of the valve seat on the intake side and the cast port shape is the three-dimensional funnel shape shown in Fig. 4, which was intended to provide stable enhancement of the flow coefficient.

Funnel-shaped processing together with expansion of the valve diameter by the adoption of LCVS yielded a confirmed 18-kW enhancement in power output.

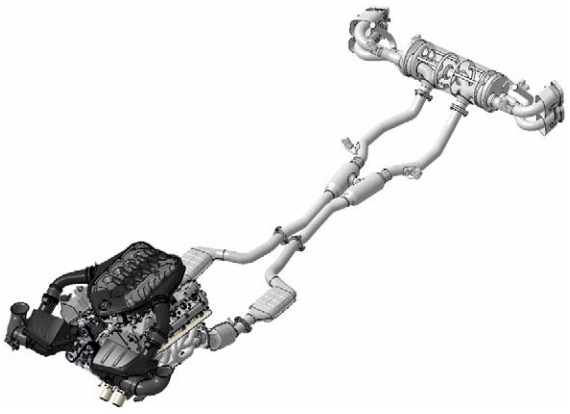


Fig. 2 Engine inlet and exhaust L/O

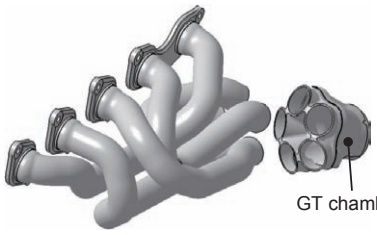


Fig. 3 Exhaust manifold and GT chamber

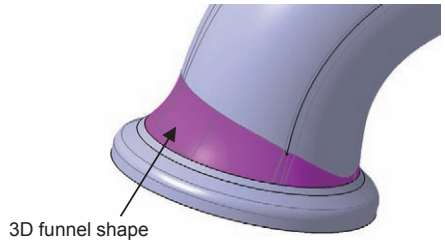


Fig. 4 Funnel shape of LCVS

3. Technology to Enhance Response

Although one of the conditions for running with greater speed on the circuit is to have high performance, it is also important to have positive response whereby engine speed increases and decreases according to the opening or closing of the throttle (TH). It has been conventional in racing engines, therefore, to employ an individual TH in order to enhance response by having a small air intake volume downstream from the TH valve. This engine also employs such a mechanism. Figure 5 shows the results for response performance measured under snap acceleration with no load.

Having individual TH can enhance response, as described above. However, this can also make it more challenging to control small volumes of intake air in the low-flow region, and differences in valve openings at individual TH can tend to result in differences in the air fuel ratio between those cylinders. Differences in air fuel ratio can make it more complicated to conform to exhaust emissions controls. The type of configuration shown in the diagram in Fig. 6 was therefore employed to limit those differences, and this system will be described below.

(1) The individual TH is used primarily to control air intake volume in the high-flow region, and it was designated the secondary TH.
(2) Control of air intake volume in the low-flow region, including idling, is performed by a single TH placed on each bank of five cylinders in order to reduce air fuel ratio differences between cylinders. This was designated the primary TH, and there is one installed on each bank.
(3) Purge and PCV circuit are installed only on Bank 1, where cylinder deactivation does not occur[1].

Figure 7(a) shows a model of parts on the Bank 1 side as actually designed for the above configuration. Similar

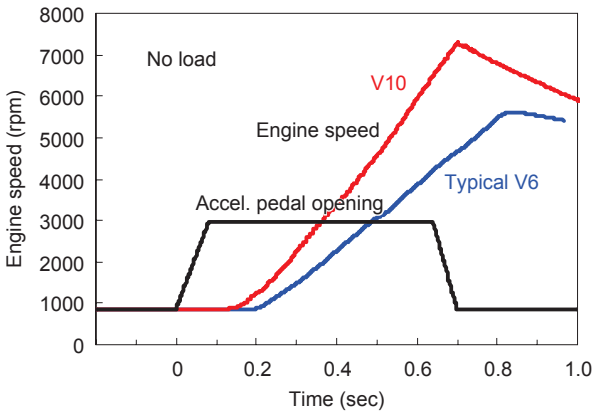


Fig. 5 Engine response

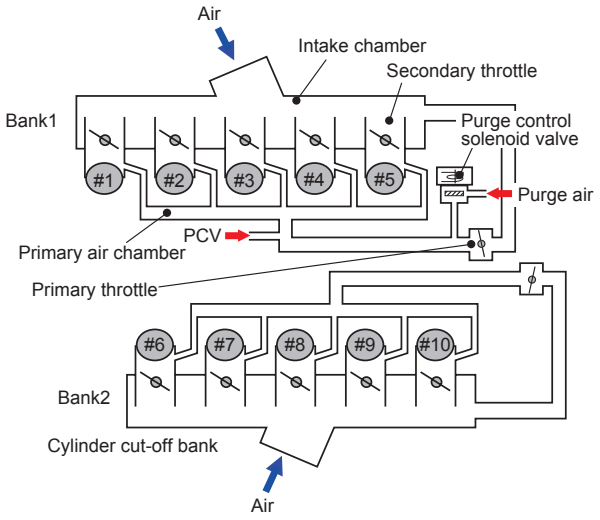


Fig. 6 Schematic diagram of throttle system

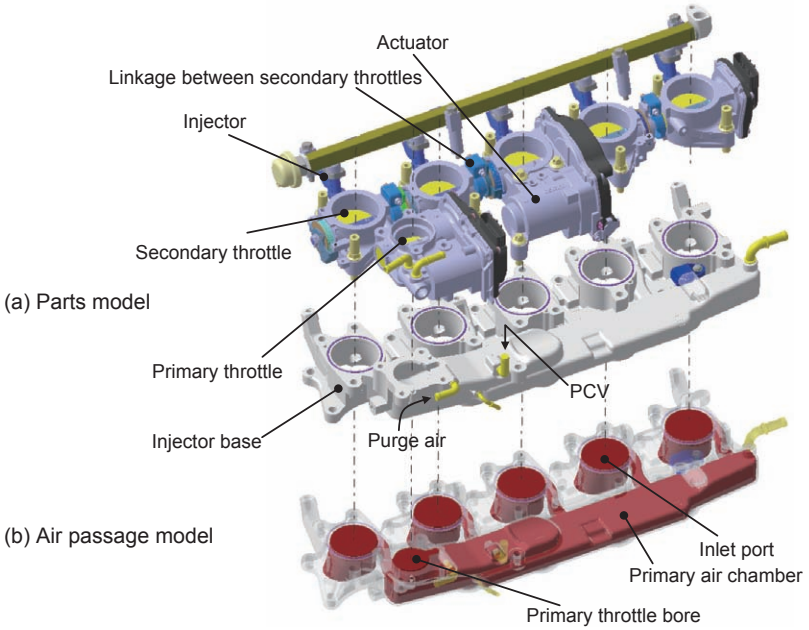


Fig. 7 3D model of throttle system

parts were installed symmetrically to these on the Bank 2 side. Details of this design are explained in the following.

(1) Primary TH

With a bore diameter of 38 mm, this was designed for a maximum flow of 1450 L/min, which should largely cover general driving in the US. As shown in Fig. 8, the system is configured so that the secondary TH does not open until the primary TH is fully open. This greatly limited air fuel ratio differences between cylinders during ordinary driving.

(2) Secondary TH

The independent TH body is bolted to the injector base (INJ base). The actuator that operates the TH is located in the center bore. A TH and its adjoining TH are joined by links.

The TH in each cylinder is fitted with a return spring. This is designed so that if the return mechanism malfunctions, the TH will return to the fully closed position.

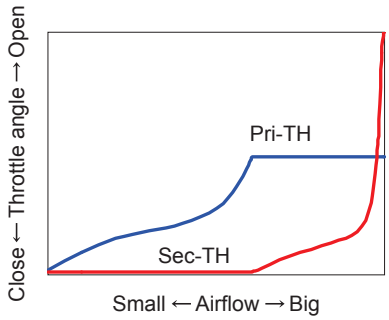


Fig. 8 Throttle open pattern

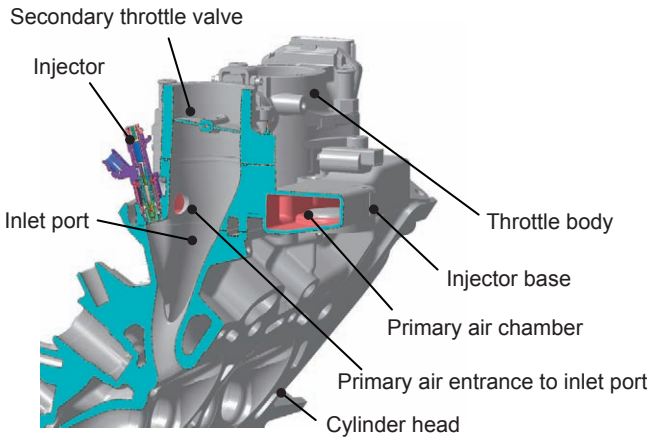


Fig. 9 Primary air passage and inlet port

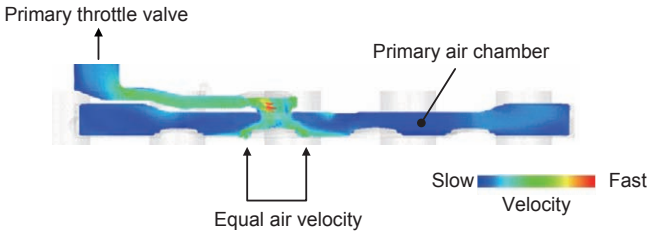


Fig. 10 Air flow analysis of primary air passage

(3) INJ base

As shown in Fig. 7(b), the air passage from the primary TH passes through the primary air chamber inside the INJ base and connects to each cylinder port.

The primary air entrance to the inlet port was placed upstream from the INJ in the location shown in Fig. 9 so as not to affect the fuel injection form.

Important considerations in determining the shape of the passage from the primary TH to the chamber are making the flow of air into each cylinder equal in order to reduce air fuel ratio difference, and mixing purge gas and air to make the mixtures homogeneous. Figure 10 shows an example of CAE performed to make the flow of air to each cylinder equal. It shows that the air flow from the merge location to either side of it was made equal by determining the appropriate location for merging the air passage into the chamber.

4. Weight Reduction in Major Moving Parts

Reducing the weight of major moving parts is an effective means of reducing inertial force so as to enhance power output and response. This approach also reduces the diameters of the crankpin and the main journal, resulting in reduced friction and enhanced fuel economy. The following will describe weight reduction measures taken with the present engine.

4.1. Pistons

Measures taken to reduce weight were, employing forged pistons, application of CAE for thermal stress to optimize the thickness of each part and application of piston behavior CAE to minimize the area of the piston skirt. Figure 11 shows the results of piston behavior CAE to configure the piston skirt with the appropriate stiffness and form. The result, as seen here, was a favorable surface pressure distribution with a maximum surface pressure area at the center sloping gently outwards to reduced pressures around it.

4.2. Connecting Rods (Conrods)

A weight reduction of 18% relative to steel was sought by the adoption of titanium conrods (Fig. 12) connected by bolts that do not employ nuts. The thrust-receiving surface on the large end of the conrod was given a diamond-

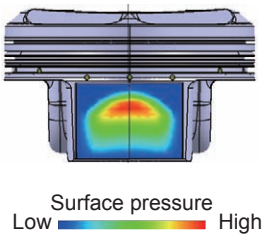


Fig. 11 Piston skirt surface pressure distribution analysis

like carbon (DLC) coating as a measure against seizing. A molybdenum disulfide surface treatment with a stable torque coefficient was also applied to the conrod bolt so that even repeated tightening would not cause scoring.

4.3. Crankshaft

As shown in Fig. 13, the stress relief groove that had been adopted in the Honda F1 engine was situated on the weakest crankshaft web. Carving out a groove reduces the stiffness of the area around crankpin fillet R, where stress figures rise high. This also mitigates the tendency for deformation to be concentrated on that fillet R and reduces the stress. This approach yielded a 7% reduction in stress, allowing the crankpin diameter to be reduced by 3 mm.



Fig. 12 Titanium connecting rod

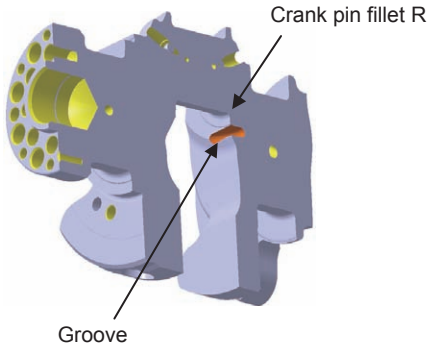


Fig. 13 Stress relief groove of crankshaft

5. Reliability Assurance Technology

5.1. Conceptual Approach for Reliability Assurance

The basic purpose of reliability assurance is to provide the full necessary assurance covering a wide range of operating conditions, from driving at the limit, as done in racing cars on the circuit, to everyday driving on city streets.

The race circuit is an operating environment that cannot be envisioned for ordinary engines, and in order to assure reliability for driving at the limit in that environment, frequency of use in terms of engine speed, engine load, engine oil temperature, and the like when driving on the circuit were determined. This was done by actual driving and by simulation on major world circuits such as Suzuka in Japan and Nürburgring in Germany. Figure 14 shows one example of engine speed frequency when driving at the limit on the Nürburgring Circuit. It is apparent here that the engine is constantly being operated close to its upper speed limit. Figure 15 shows one example of a dynamometer durability testing mode used to assure reliability when driving under extreme circuit conditions like these. This durability test models continuous operation for 48 hours over the fastest lap on the Nürburgring Circuit.

The goal for service life was to satisfy the standards of the US ACURA for the wide range of use extending from driving on the circuit to driving for everyday transportation, and development was pursued accordingly. On the other hand, excessive quality for durability can sacrifice performance, and the durability testing standards were therefore considered carefully in light of data from actual driving on public roads, and the test was configured differently than for ordinary engines.

First of all, Fig. 16 shows the frequency of power output and engine speed when driving on the Autobahn in Germany as organized by the engine's highest performance. The vertical axis on the left shows the engine working ratio, which is the amount of engine work for driving a certain distance on the Autobahn, normalized by the amount of

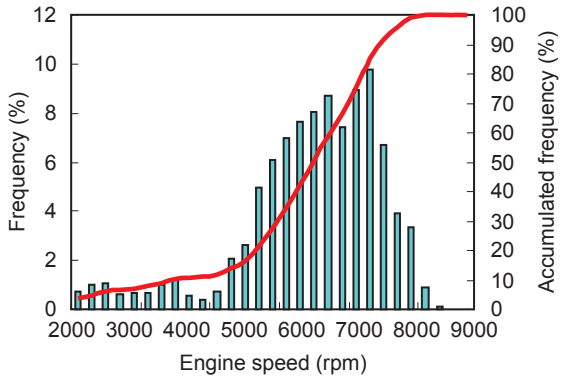


Fig. 14 Engine speed frequency of circuit driving

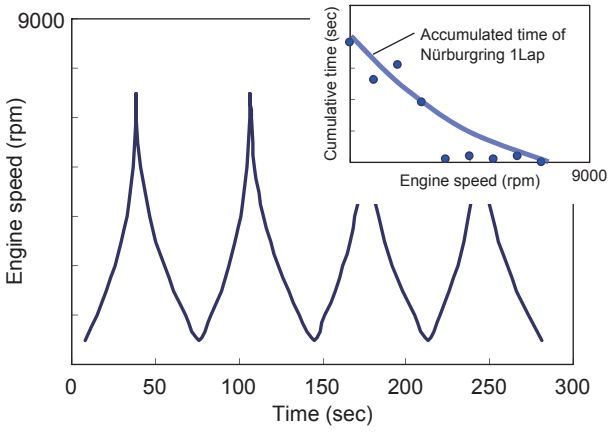


Fig. 15 Simulated circuit driving test mode of durability on dynamometer

work done when driven for a certain period of time with the engine at maximum power output. The vertical axis on the right is the frequency of use of high engine speed when driving on the Autobahn. The horizontal axis is the maximum power output of the engine in the test vehicle. It is apparent that in cars with higher maximum engine power, both the work ratio and the high engine speed frequency are lower.

Next, driving simulation was used to calculate the high engine speed frequency in ordinary driving on city streets and on highways in North America. The results show that 99% of use is at 3000 rpm or under, and the average engine speed came out to about 1800 rpm.

In addition to the above results, the circuit driving frequency discussed above was also taken into consideration. The reliability assurance test standards were therefore determined from the following three perspectives.

(1) Determination of durability conditions using engine work as a standard

It is apparent from the work ratio trend for driving on the German Autobahn, as shown in Fig. 16, that the frequency of use in the engine's high-performance region will be lower in cars that have higher maximum power output. It is therefore necessary to reflect this point in the durability conditions. As a result, the power output conditions for dynamometer durability testing, which is ordinarily conducted at maximum power output, were set lower to match the work ratio described above.

(2) Determination of high-speed durability conditions

As is apparent from Fig. 16, the frequency of use in the high engine speed region is also lower in cars that have higher maximum power output. The time of continuous dynamometer durability testing at high engine speed was therefore made shorter than usual. As discussed above, however, as circuit driving makes more use of high engine speeds, an additional, special durability test was set up for the limit engine speeds shown in Fig. 15.

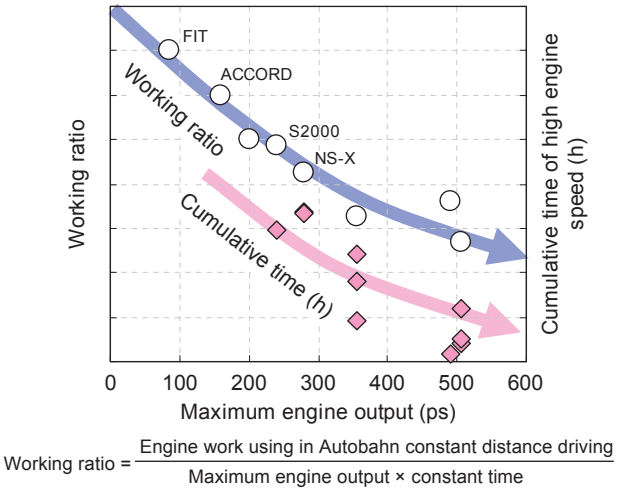


Fig. 16 Working ratio and high engine speed characteristic of high-power vehicles

(3) Determination of durability conditions to guarantee driving on ordinary public roads

Ordinary driving in North America involves a higher frequency of use at low engine speed. This characteristic is common to ordinary roads and expressways in all the countries of the world, with the exception of the Autobahn in Germany. This was addressed by using a longer than usual durability time in the evaluation mode for friction in moving parts, as represented by the valve assembly.

Figure 17 shows the concept of reliability assurance shown above as expressed in terms of engine speed and load frequency. As discussed above, the reliability assurance test standards were set up for the conditions of driving on the circuit, driving on the Autobahn in Germany, and ordinary driving in North America. These standards are considered to have enabled the full reliability assurance necessary for all operating regions in which this engine will be used.

5.2. Crank Lubrication Specifications

The topic here is determination of specifications for crankshaft lubrication, which is of particular importance in assuring reliability when driving on the circuit.

The first step was to show how this engine is situated in terms of load by comparing the PV value of the crankpin bearing in the vicinity of the red zone for this engine with those of mass-production engines, as shown in Fig. 18. This engine has the highest PV value, indicating the necessity for

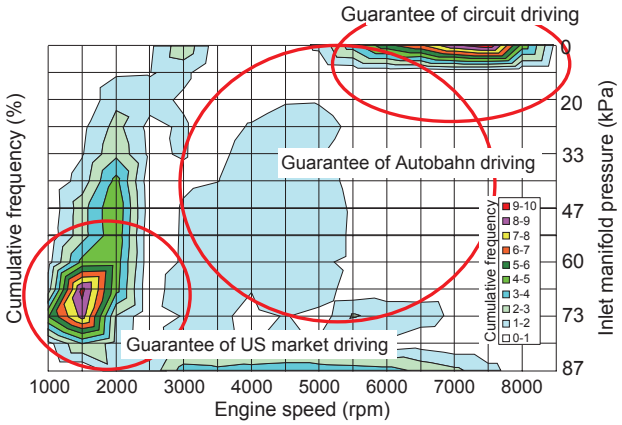


Fig. 17 Concept of reliability guarantee

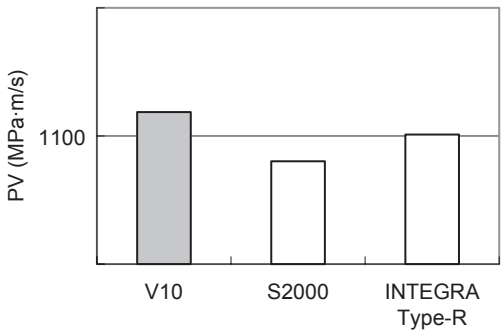


Fig. 18 PV value of crankpin bearing

new technology for reliability assurance.

Ordinary lubrication from the main journal was used for the crankpin lubrication layout in the present engine. During initial development, the engine started out with a center lubrication system of the kind commonly used in racing. As shown in Fig. 21 (to be discussed below), however, this did not have sufficient aeration toughness, and this approach was abandoned as inappropriate for mass-production vehicles, which did not provide the stringent degree of oil volume control it required. Figure 19(a) shows that a characteristic of the lubrication layout is that pressure loss due to centrifugal force can be reduced by placing the branching point between the lubrication port in the main journal of the crank and the lubrication port in the crankshaft web as far out toward the periphery as possible. Figure 19(b) further shows how steps were taken to enhance oil volume and oil pressure due to the "scraping in" effect by refining the shape of the area where oil flows in from the crank bearing through the lubrication port placed in the main journal and making the opening wider in the direction of rotation.

These measures caused the oil pressure immediately before the crank pin bearing to increase 1.2 times in the average value and 2.0 times in the minimum value, as shown in Fig. 20. The temperature in the crank pin bearing was reduced by approximately 10°C.

Figure 21 shows how it was confirmed that this crank specification was advantageous even when aeration occurred. These data represent measurements made of changes in the oil pressure in the main gallery and the oil pressure immediately before the crankpin bearing, as well as of the aeration rate, when air was blown into the main gallery before oil entered the crank. This can be explained in terms of the blue line, which represents the oil pressure in the present engine. Point A represents the oil pressure in the main gallery (horizontal axis) and the oil pressure immediately before the crankpin bearing (vertical axis) when aeration is zero. When aeration is increased, the oil pressure shifts the blue line to the left. With the present crank specifications, there is only a slight decline in the oil pressure immediately before the crankpin bearing when aeration increases, and it is apparent that reliability is high under limit conditions.

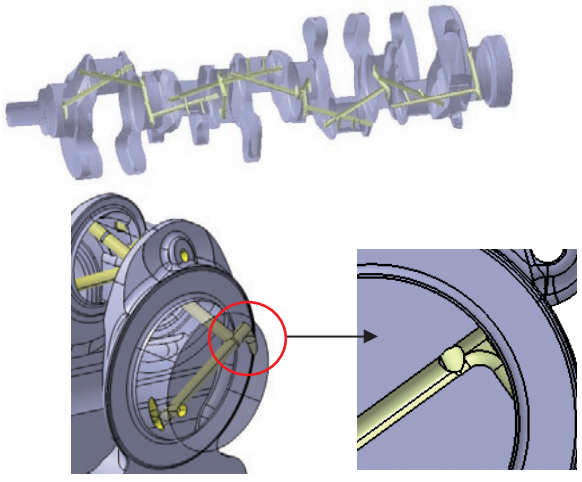


Fig. 19 Layout of crankshaft oil circuit

5.3. Measures to Counter Spark Plug Ground Electrode Damage

Finally, the measures taken to counter damage to the spark plug ground electrode will be described. This damage became an issue during the high engine speed durability testing performed for the purpose of providing a guarantee for driving at the limit on the circuit, as mentioned in the foregoing section. It had long been recognized that one of the reasons for damage to the spark plug ground electrode was that vibrations generated by the impact force of the intake and exhaust valves seating when the engine was running in the high-speed range were transmitted to the spark plug. Only rarely, however, had this been expressed in quantitative terms. For this engine, it was considered necessary to obtain a quantitative grasp in order to take

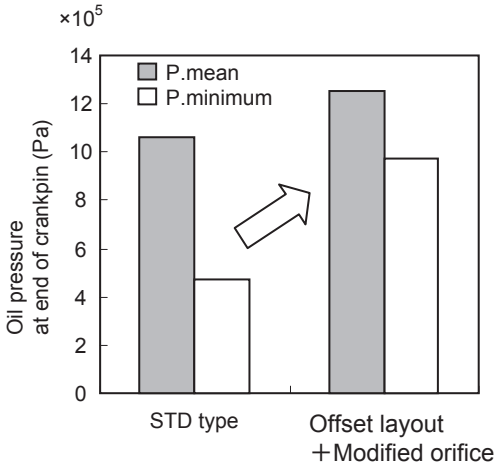


Fig. 20 Oil pressure at end of crankpin

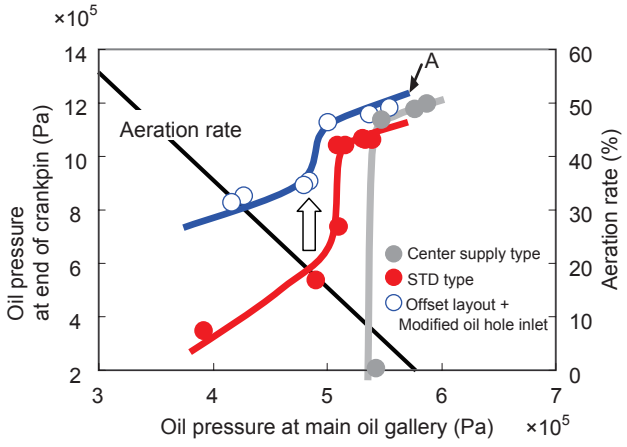
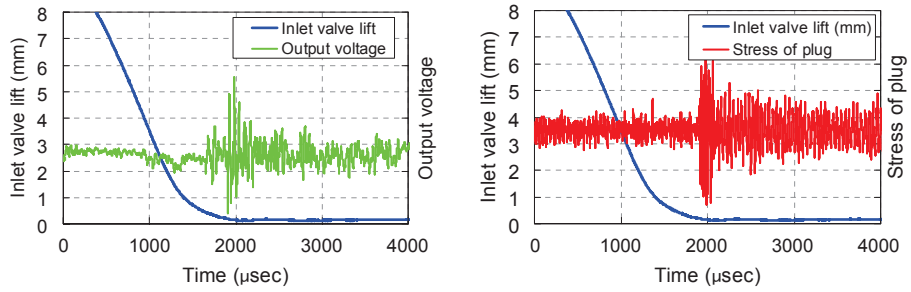


Fig. 21 Toughness of aeration



(a) Output voltage of cylinder pressure sensor and inlet valve lift

(b) Stress wave of spark plug ground electrode and inlet valve lift

Fig. 22 Analysis result of spark plug ground electrode

proper measures against that phenomenon. Measurements were therefore made of the vibration generated in the spark plug seating surface due to the impact force arising when valves seated. Measurements were also made of stress in the spark plug ground electrode, for higher frequencies up to 200 kHz.

Figure 22(a) shows valve lift characteristics at high engine speeds and the output value from a cylinder pressure detection system[(1)], which represents spark plug seating-face vibration during motoring. Figure 22(b) shows valve lift characteristics and stress at the location of spark plug ground electrode damage. From this it could be confirmed that vibration was generated by the impact of valve seating, and synchronously with that, stress was generated in the ground electrode of the spark plug. Figure 23 shows the results from frequency (PWR) analysis of the stress waveform in Fig. 22(b). It was ascertained from Fig. 23 that the frequency components from 20 kHz to the vicinity of 60 kHz were the determining stress components. When CAE was used to find the resonance frequencies in the spark plug ground electrode, the first resonance frequency was found to be approximately 20 kHz and the second resonance frequency approximately 60 kHz. It was confirmed from the preceding that the excitation force from the valve seating caused sympathetic vibrations on the outside of the spark plug that tended to result in damage. Alteration of the cam profile was considered as a countermeasure, but this resulted in diminished power output. It was decided, therefore, to change the shape of the spark plug ground electrode to raise the resonance frequency. This change was confirmed to have raised the first resonance frequency by approximately 3 kHz and the second resonance frequency by approximately 12 kHz.

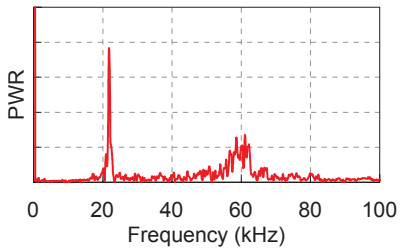
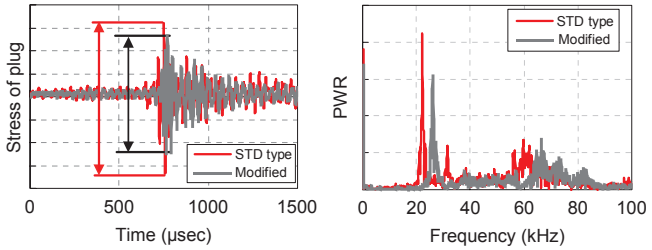


Fig. 23 Frequency analysis of spark plug ground electrode stress



(a) Stress wave

(b) Frequency analysis

Fig. 24 Analysis result of before and after shape change

Figure 24(a) shows the results from stress measurement before and after the shape change. Figure 24(b) shows the results from frequency analysis of the waveform in (a). It could be confirmed that the stress frequencies had shifted toward higher frequencies after the shape change, and that the amplitude of the stress had diminished as well. Durability testing was conducted with items incorporating the countermeasure, and no damage occurred.

6. Conclusions

The following achievements were realized regarding power output and reliability.

(1) High performance: Power of 405 kW (550 PS) achieved
(2) High response: Developed an individual throttle that complies with California State LEV2-ULEV
(3) Weight reduction: Change of material and optimization of shape by means of CAE resulted in comprehensive weight reductions of major moving parts
(4) High reliability: Durability tests were conducted based on actual operating data from both driving on the circuit and ordinary driving, and fully adequate reliability was established.

Given the above results, it can be concluded that an

engine was developed that achieves a balance of high performance and high reliability, such that it can provide the pleasure of driving on the circuit as in a race car with performance in an entirely different dimension from that of an ordinary car, and on the other hand can be used like an ordinary automobile for everyday transportation on expressways and city streets.

References

(1) Okuyama, T., Fukuzawa, T., Hashimoto, A.: Development of V10 500-HP Engine –Technologies for High-performance and Low-emission Clean Powertrain–, Honda R&D Technical Review, October, 2010, p. 41-49
(2) Imai, N., Hishida, H.: Development of Laser Clad Welded Valve Seat, Honda R&D Technical Review, 2009 F1 Special, p. 263-265

■ Author ■


Takahiro OKUYAMA


Makoto NAKADA

Development of New Structural Optimization Methodology for Vehicle Crashworthiness

Sanjaya FONSEKA*

ABSTRACT

The automotive industry continues to face the challenge of developing efficient side body structures that help to reduce the risk of injury to occupants in collisions. The B-pillar, Roof, and Side Sill are key structural members that help reduce the risk of injury to the occupants during a side impact crash event. This study used a simulation-based global optimization method to find optimum thickness for the B-pillar, Roof, and Side Sill components considering baseline material specification and vehicle performance in the IIHS SICE (Side Impact Crashworthiness Evaluation) and FMVSS 216 (Roof Crush Resistance) safety tests.

Fifteen design variables were defined by selecting structural members from a unibody vehicle design. The objective of the optimization was to find the most efficient distribution of mass for the structural members that are vital for the occupant safety. Automated simultaneous simulations were conducted using a global optimization method called Self-Adaptive Evolution. This methodology resulted in a 11% increase in occupants survival space (or decrease in occupant compartment intrusion), and 1.7% reduction in total mass compared to the baseline structure. Also this optimization result met the FMVSS 216 roof crush resistance requirement.

1. Introduction

Government and insurance institutions have introduced many safety standards with the intent to help reduce the risk of serious and fatal injuries to occupants during side impact crashes. To achieve a desired crashworthiness, the auto industry focuses on developing better vehicle side body structures that help reduce the risk of injury to occupants in collisions. When considering safety standards in development, available design and test technologies only allows the engineer to design and tune the vehicle side structure to each test mode separately. However, this can be inefficient and somewhat imprecise since it requires a lot of design time and experience to find an appropriate strength and balance for the side structure. Still the engineer may not find the optimum structure respect to weight and strength.

A new simulation-based structural optimization method was developed to help design the structure more efficiently considering the crash modes simultaneously. This method was validated during the initial phase of side structure development for 2011 Odyssey. The objective was to find the optimum thickness for the side structural members that would help to reduce the risk of injury to occupants in collisions and meet the requirements of the Side Impact Crashworthiness Evaluation (SICE) and Federal Motor Vehicle Safety Standard (FMVSS) No. 216, Roof crush resistance modes. These modes were selected since they are the most dominant for side impact crashes.

The numerical optimization method used was Self Adaptive Evolution (SAE). This is a global optimization algorithm[(1)] in which the results are not dependent on a starting point, such as it is in the gradient-based methods.

Furthermore, iterations are calculated in parallel and tend to converge to a global optimum.

Generally, global optimization methods require a large number of simulations and dedicated computer resources. To facilitate this, computer resources at the Ohio Supercomputing Center (OSC) were used.

2. Side Impact Crash Modes

Roof crush resistance and SICE simulation models were used simultaneously to find the optimum gauges for the side structure (Fig. 1).

Total mass of these parts, shown in Fig. 2, was 36.93 kg. These parts were selected primarily based on their direct contribution to withstand the side crash modes. Part size was a secondary factor since more mass can be taken out

* HONDA R&D AMERICAS, INC.

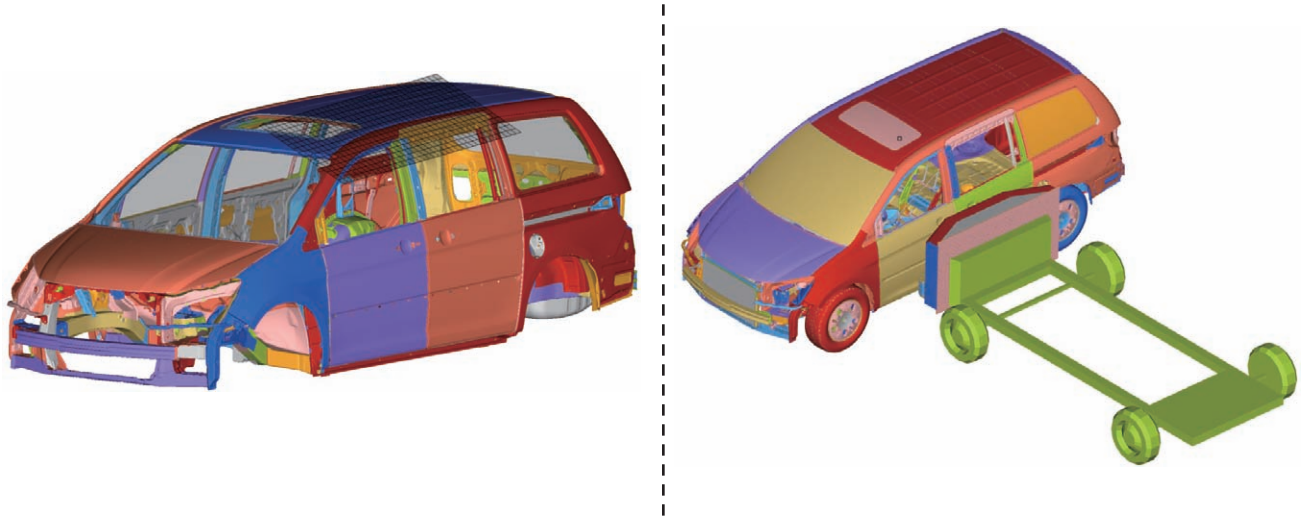


Fig. 1 Simulation models

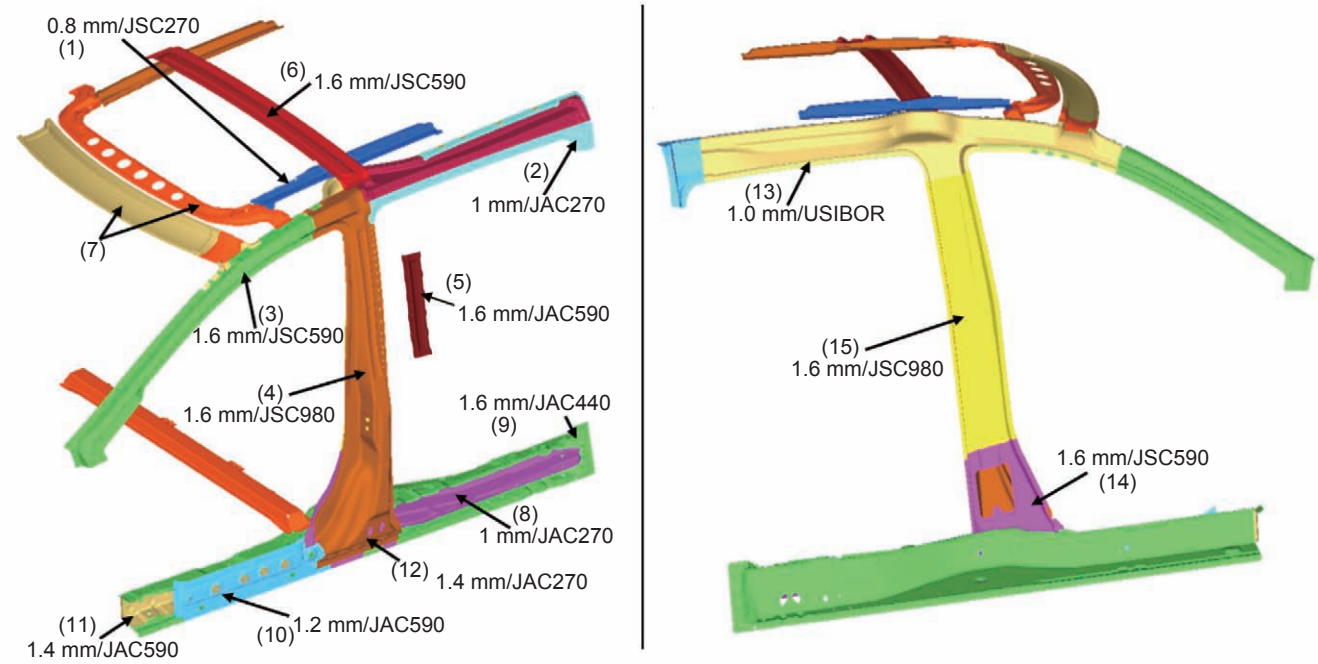


Fig. 2 Side structural members selected for optimization

from larger structural members. The objective of this study was to find the optimum thickness to the structural members that would meet the target force level and occupant survival space for roof crush resistance and SICE crash modes respectively.

3. System Workflow

Figure 3 shows the optimization workflow[2] that was developed using OPTIMUS software. This is a fully automated workflow that varies the thickness of the side structure, simulates the two crash modes, and extracts the roof crush resistance force and survival space.

Using this workflow, many simulations were run successfully. OPTIMUS easily interacts with other software that control the simulation submission process and can incorporate user scripts, which is essential since some of the simulations required extracting complex results. For this study, a separate script was written to extract the occupant survival space from the SICE simulation. All the simulations were done using LS-DYNA[3] software. The OSC was used to process the 200-plus simulations that were needed to complete this optimization.

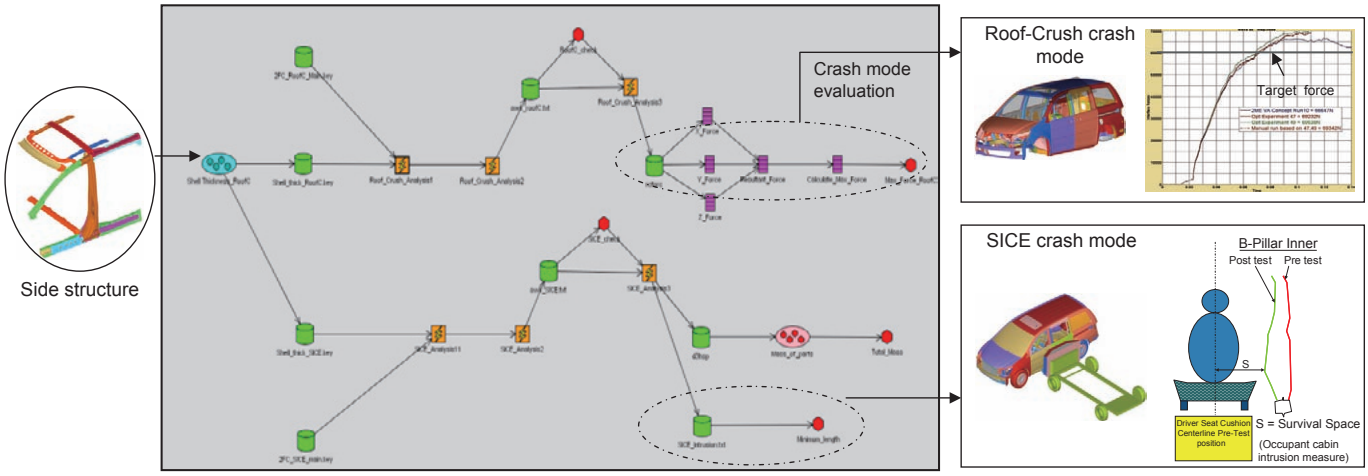


Fig. 3 Optimization workflow

Table 1 Baseline (first design milestone) simulation results

	Roof-crush force (N)	Survival space (mm)	Total mass (kg) [Comps for optimization]	Total mass (kg) [Comparing the both sides of the car]
Target	66400	116	Reduce mass	Reduce mass
Baseline run	73414	117	36.9	69.5

4. Optimization

The noisy, non-linear nature of crash analysis reduces the use of gradient-based optimization methods; therefore, a global optimization method called SAE was selected to drive the optimization. The SAE strategy is directly based on absolute valued vectors when dealing with continuous parameter optimization studies. The algorithm is a multi-recombinant scheme based on a population of designs and its strategy is to imitate biological mutation and selection[4]. Designs with the best fit from the current total population will be selected as the parents for the next generation. The multi-recombinant method used here selects multiple parents to generate one offspring, and mutation is independently applied to each design so the old generation produces a new generation. The new generation's fitness is then calculated and new offspring are made. The algorithm has convergence criteria and, for certain ranges, algorithm parameter values have been determined for improved performance.

Objective: Minimize total mass of the selected parts.

Constraint 1: Roof crush resistance force has to be greater than 66400 N

Constraint 2: Distance from center of the vehicle to B-Pillar Inner has to be greater than 551 mm for SICE.

Occupant survival space is calculated as 551 - 435 = 116 mm

Where 435 mm is the distance from center of the vehicle to the center of driver seat cushion, which is a constant.

Thickness of the parts varies between 0.7 and 2.3 mm.

Number of Simulations required is calculated as

Number of Load Cases (Roof-Crush and SICE)
× *Population Size* (number of simulations for each generation)
× *Number of generations*,

Therefore total number is 2 × 15 × 8 = 240 simulations.

Table 1 shows the baseline results compared to the target.

5. Optimization Results

Table 2 shows the results of the first 22 simulations. In the OPTIMUS workflow, Max_Force_RoofC refers to Constraint 1 and Minimum_length refers to Constraint 2. It is observed that when going from one generation to the next, the optimization algorithm finds more feasible solutions in allocating less mass to the structural members.

Figures 4 and 5 show the behavior of total mass respect to the two constraints. It is clear from Fig. 5 that the efficient mass distribution among the structural members can give better roof crush resistance force and survival space. It is also evident that SICE or Minimum_length is the driving constraint for the optimization.

Table 3 shows the best mass distribution among the structural members found through this optimization study.

As shown in Table 4, simulations 76 and 114 show better roof crush resistance force and better survival space with same or less mass compared to the baseline.

Table 2 Optimization results

Ex...	Sill_Stf_11	Sill_Mid_Gusset_12	Roof_Rail_Midl_13	B_Plr_Innr_Lower_14	B_Plr_Innr_15	Max_Force_RoofC	RoofC_check	SICE_check	Minimum_length	Mass	Mass_Roof_Pnl_stfa_1	Mass_Roo...
1	1.4	1.4	1	1.6	1.6	73414.05988	1	1	551.80119	0.03693	0.00067	0.00142
2	2.17527	1.07986	0.9259	1.8068	0.82217	74098.89675	1	1	480.71187	0.04024	0.0015	0.00149
3	2.26034	1.45738	1.13839	1.58647	1.26983	83555.64269	1	1	522.36654	0.04132	0.00096	0.00298
4	0.73922	1.02046	1.26649	2.14818	1.03945	72408.99837	1	1	487.86479	0.0398	0.00079	0.00189
5	0.9197	1.72167	0.73424	1.63261	1.99598	81279.00918	1	1	553.16775	0.04573	0.00167	0.00236
6	1.23412	1.75231	2.21306	1.08029	1.35413	81371.44184	1	1	562.77054	0.04604	0.0011	0.00143
7	1.52989	2.08538	1.44351	1.01872	1.44085	79934.56033	1	1	562.73009	0.04241	0.00128	0.00318
8	2.01739	1.27882	2.18121	1.34293	2.22882	86990.55015	1	1	539.72879	0.04652	0.0016	0.0018
9	1.08419	1.92358	1.83202	1.23219	1.75651	74629.93174	1	1	483.58532	0.0339	0.00183	0.0029
10	1.81663	0.91657	1.94495	1.84493	1.52692	82692.24098	1	1	526.78253	0.04378	0.00193	0.00224
11	1.32462	2.28692	1.586	0.73092	0.7034	76685.33638	1	0	0	0	0	0
12	1.62001	2.05898	1.7118	0.88489	1.87067	74045.01601	1	1	497.4169	0.04211	0.00064	0.00254
13	1.00175	1.16911	0.97682	2.05075	1.63053	80076.50215	1	1	506.12295	0.03863	0.00139	0.0021
14	1.89399	1.53783	1.36992	1.42941	2.16825	68574.24987	1	1	544.5277	0.03591	0.00101	0.00104
15	1.43257	0.75562	2.06329	2.2798	1.15273	83475.05342	1	1	478.04627	0.04159	0.00077	0.0027
16	1.52574	1.46687	2.15844	1.32224	2.23749	87324.91362	1	1	575.81261	0.04727	0.00157	0.00108
17	1.91985	1.46763	0.78527	1.50638	1.98987	76008.33082	1	1	550.23227	0.04088	0.00131	0.00247
18	0.8661	1.38715	2.00255	1.54866	2.1108	85255.95634	1	1	566.1369	0.04411	0.00087	0.0028
19	1.22032	0.88859	1.55661	1.13431	1.46839	79604.92029	1	1	535.50341	0.04416	0.00098	0.00207
20	1.47562	2.01973	0.98894	1.4871	1.38109	77435.46488	1	0	0	0	0	0
21	2.28307	1.35723	1.30305	1.04271	2.1189	72373.9723	1	1	546.67652	0.04379	0.00101	0.00134
22	1.91869	1.77888	0.72418	1.45207	2.00793	77139.49329	1	1	546.38456	0.04377	0.00166	0.00239

Move towards a feasible region (s)

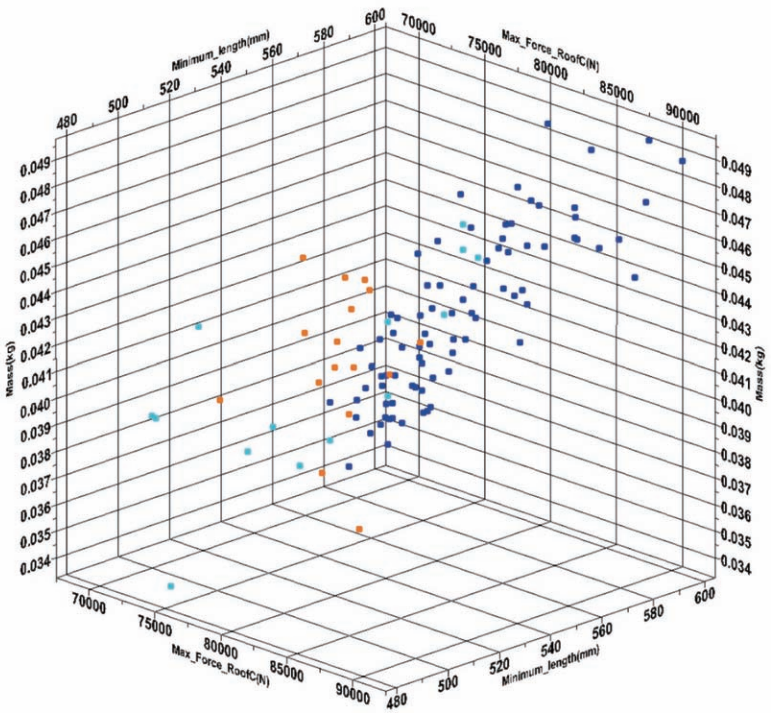


Fig. 4 Mass versus Roof crush force, Minimum_length

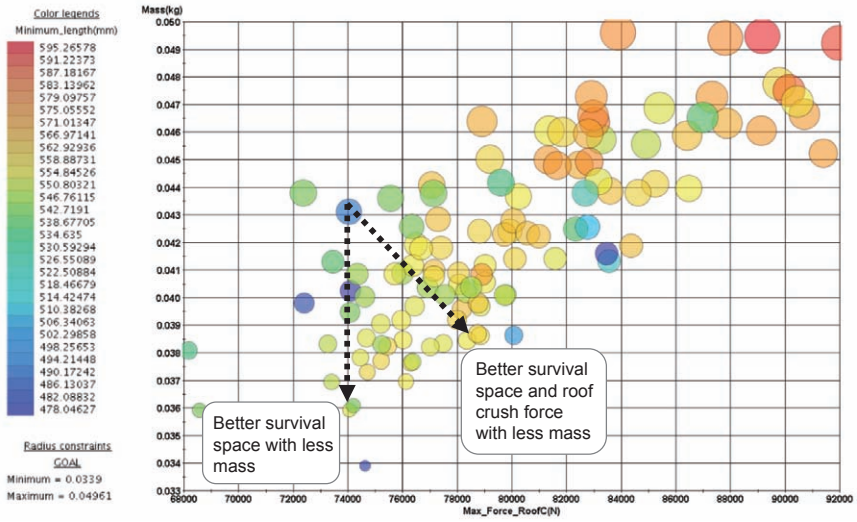


Fig. 5 Mass versus roof crush resistance force

Table 3 Optimization results with efficient mass distribution

Exp. Num.	Iter	B_Plr_Innr_15	Max_Force_RoofC	RoofC_check	SICE_check	Minimum_length	Mass
1	0	1.6	73414.05988	1	1	551.80119	0.03693
61	4	2.06459	76316.01867	1	1	565.17467	0.03762
76	5	2.10386	74064.04847	1	1	555.82743	0.03591
110	7	2.09286	76131.41799	1	1	560.37781	0.03695
114	7	2.19667	74716.40748	1	1	564.97335	0.0373

Table 4 Simulations 76 and 114 compared with baseline

	Roof-crush force (N)	Survival space (mm)	Total mass (kg) [Comps for optimization]	Total mass (kg) [Comparing the both sides of the car]
Target	66400	116	Reduce mass	Reduce mass
Baseline run	73414	117	36.9	69.5
Run 076	74064	121	35.9	-
Run 114	74716	130	37.3	-

6. Refinement of the Optimization Results

It is essential that optimization results should be analyzed further as global optimization methods will require many more number of simulations to converge to an optimized single solution. Because of the limitation on the computer resource availability this many simulations were not feasible. As already large numbers of simulations were completed and a good scatter was available for the responses (mass, constraints), these results were analyzed based on the Design of Experiments (DOE) principle.

Based on correlation values in Fig. 6, optimization results were further refined.

Correlation value table gives information about the level of correlation between the design variables (thickness of structural members) and the responses. The correlation value is always between +1 and -1. A correlation value closer to +1 or -1 signifies that responses and corresponding

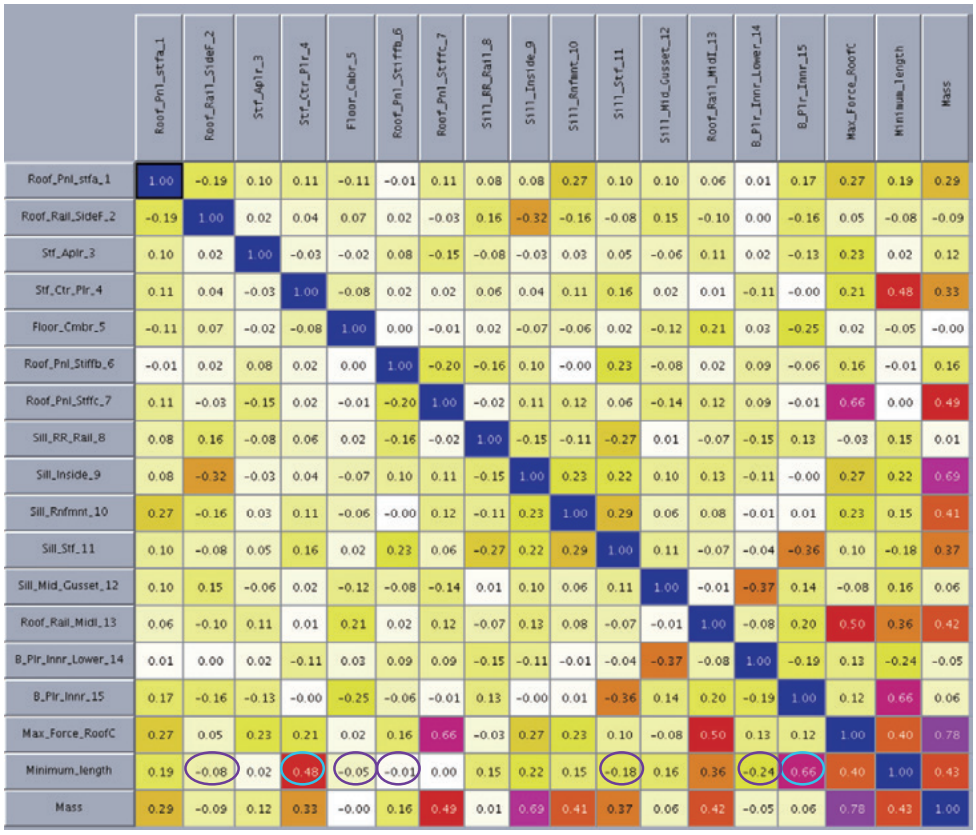


Fig. 6 Correlation value table

Table 5 Thickness values for simulations 76a, 114a were based on 76,114

	Roof_Rail_SideF_2	Floor_Cmbr_5	Roof_Pnl_Stiffb_6	Sill_Stf_11	B_Plr_Innr_Lower_14	B_Plr_Innr_15
1	1.00	1.60	1.60	1.40	1.60	1.60
76	0.82	0.77	1.00	0.91	1.66	2.10
114	1.91	1.77	1.01	0.73	1.40	2.20
76a	0.82	0.67	0.80	0.81	1.50	2.10
114a	1.01	1.60	1.01	0.73	1.40	2.20

Table 6 Manual Simulations 76a and 114a compared with baseline

	Roof-crush force (N)	Survival space (mm)	Total mass (kg) [Comps for optimization]	Total mass (kg) [Comparing both sides of the car]
Target	66400	116	Reduce mass	Reduce mass
Baseline run	73414	117	36.9	69.5
Run 076	74064	121	35.9	-
Run 076a	68760	120	35.0	66.5 (3.0) ↓
Run 114	74716	130	37.3	-
Run 114a	71692	130	36.0	68.3 (1.2) ↓

design variables are mostly linearly-related, while a value closer to zero indicates that they are fairly independent.

The high correlation value of 0.66 indicates that the B-pillar inner (part 15) is the most important for SICE. This is very much in line with the design experience.

Negative correlation values for parts 2, 5, 6, 11, and 14 indicate that they are not significant for SICE. Therefore, thickness for these can be reduced and still provide the same occupant survival space. To further reduce mass, the thickness of these parts was reduced and new simulations, called 76a and 114a, were run manually. Thickness comparison is shown in Table 5.

Table 6 shows the results for simulations 76a and 114a compared with optimization results.

Simulation 76a shows that mass can be reduced by about 3 kg per vehicle and still provide more occupant survival space and roof crush resistance force compared to the baseline. Simulation 114a shows a survival space improvement of 13 mm over the baseline condition and with a reduction in mass of about 1.2 kg less per vehicle. Figures 7 and 8 show comparison of the baseline to the simulations 76a and 114a with respect to roof crush resistance force and SICE.

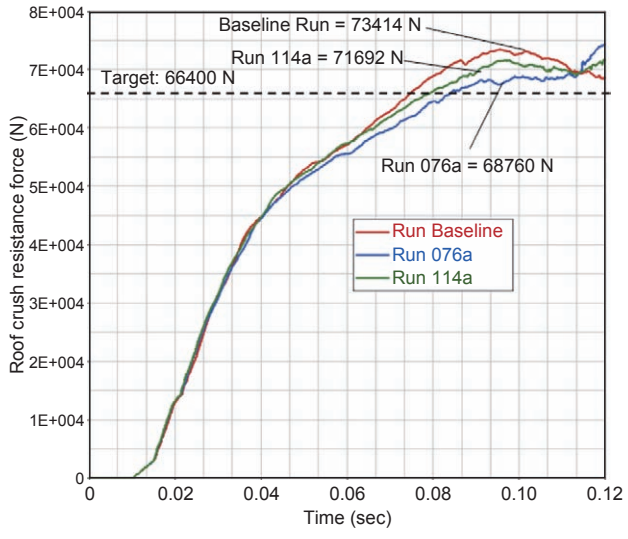


Fig. 7 Roof Crush force

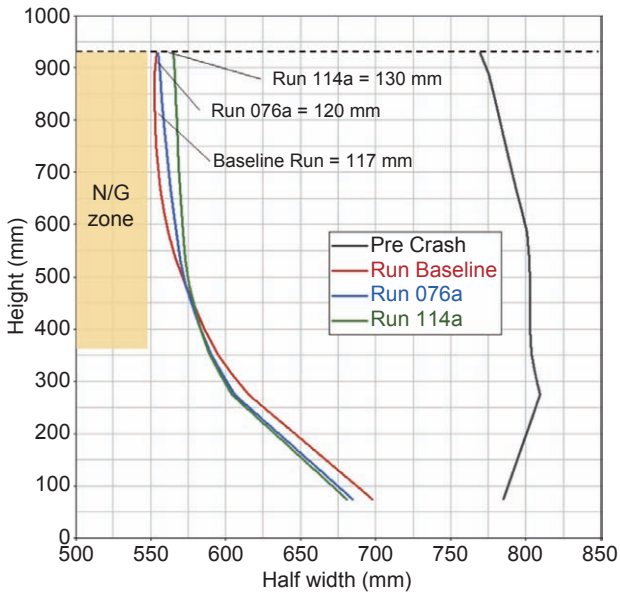


Fig. 8 Occupant survival space for SICE

7. Conclusion

(1) The global optimization simulation method used in this study can be applied to similar situations where a structure is designed using several test modes. In this study, the number of simulations required was a major challenge since each one required approximately 20 hours to complete. This required a parallel processing environment with many available CPUs. To use these computer resources efficiently, only the most dominant test modes were considered for the optimization workflow.

(2) During optimization, 7 out of 240 simulations did not complete correctly due to numerical instabilities caused by the unbalanced structure. When the optimization process assigned thickness, in extreme situations the structure became severely unbalanced and led to numerical instabilities in the simulation. This was an unavoidable situation that was considered in the planning stages of the study by having few additional simulations than required and aslo designing the optimization workflow to ignore such results.

(3) The optimization results in Table 5 show thickness of the B-pillar inner to be 2.1 mm. This may be infeasible to manufacture as a single part. Therefore, consideration is made to apply reinforcement to the B-pillar inner so that the combined thickness gives a similar strength as 2.1 mm B-pillar inner.

References

(1) Schwefel, Hans-Paul. Numerical Optimization of Computer Models. New York: John Wiley & Sons, 1981.

(2) Fonseka, Sanjaya, and Gaetan Van Den Bergh. “Development of a DOE/Optimization CAE Method to Simultaneously Improve Side Impact Occupant Restraint System Performance for Multiple Test Modes.” 20th International Technical Conference on the Enhanced Safety of Vehicles, Lyon, France, June 18-21, 2007. http://www-nrd.nhtsa.dot.gov/departments/esv/20th/ (Accessed April 20, 2010).

(3) Livermore Software Technology Corporation (LSTC). LS-DYNA® Keyword User’s Manual, Version 971. Vol. 1. Livermore, CA: LSTC, 2007.

(4) Noesis Solutions NV, OPTIMUS Documentation

■ Author ■



Sanjaya FONSEKA

Development of Low-profile Fuel Tank System and Zero Leak Valve for North American Market

Tetsuhiro ITO* Hisayuki GOMA* Jason GRAHAM*

ABSTRACT

In the North American market, the US Honda Odyssey is commonly regarded as the "King of Minivans" because of the great value it provides to customers. Among other things, its low-flat floor packaging offers significant value, and the fuel tank system packaged under the floor greatly contributes to securing sufficient cabin space and making the low floor possible.

For the development of the fourth generation Odyssey, which applies an exclusive platform for the North American market, the underfloor platform was carried over from the previous model. However, the overall fuel tank system design was changed to further improve its reliability and reduce cost.

Specifically, fuel leakage was successfully eliminated by using a 2-vent system located on the top of the tank that consists of a Vent Shut Float (VSF), which detects when the fuel tank is full, and a Rollover Valve (ROV), which allows the tank to vent when the VSF is closed. As a result, the liquid-vapor separation device that was applied to the previous model to address this issue could be removed, thereby simplifying the low-profile tank vent system.

1. Introduction

The fuel line connected to the fuel tank normally consists of two lines: a feed line, which supplies fuel to the engine, and a vent line, which adjusts the tank's internal pressure by releasing fuel vapor from the tank to a canister. An important function of the fuel tank system is "liquid-vapor separation performance," which measures the system's ability to prevent a fuel leak during refueling and maintain an open ventilation passage during various conditions.

To achieve adequate liquid-vapor separation performance, multiple vents may be necessary depending on the fuel tank's shape. However, based on the vehicle' s inclination, the vents can be submerged in fuel, which can cause fuel to flow out the vent line. Preventing this has traditionally complicated the system. The proposed system and valves discussed in this paper achieve the required performance and simplify the system.

2. Challenges with Prior Design

Generally, fuel tank systems used in Japan and Europe have a rollover valve (ROV) positioned at the top of the tank (Fig. 1) at the location where fuel vapor remains at all times. The ROV position prevents fuel from escaping out the vent line, even when the vehicle is inclined.

During refueling, fuel vapor is released to the atmosphere through a breather tube that is connected to the fuel inlet pipe. When the tank is filled, the breather is submerged, which cuts off the vapor flow to stop refueling.

However, vehicles sold in North America must comply with government regulations that prohibit the release of fuel vapor to the atmosphere during refueling. To comply with this regulation, an On-board Refueling Vapor Recovery (ORVR) system guides the fuel vapor to a canister that adsorbs it during refueling and, when the engine is running, desorbs and releases it to the engine for burning. A vent shut float (VSF), which detects when the fuel tank becomes full, is used to cut off the flow of fuel vapor to automatically stop refueling and to prevent liquid fuel from reaching the canister. Since the VSF also affects the aforementioned

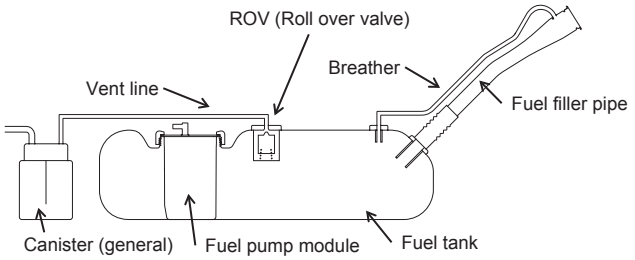


Fig. 1 General fuel system diagram

* HONDA R&D AMERICAS, INC.

liquid-vapor separation performance, just like the ROV, normally the VSF is positioned in an area at the top of the fuel tank where only fuel vapor is present.

Other North American regulations that pertain to gases evaporating from a vehicle include the California Air Resource Board's (CARB) Low Emission Vehicle 2 (LEV2) regulation and the Environmental Protection Agency's (EPA) Tier 2 regulation. Both regulations set different conditions, but the LEV2 requirements are stricter and also cover ORVR. Figure 2 shows the conventional LEV2 fuel system.

The "low-flat floor package" in the minivan category makes it difficult to ensure a sufficient fuel tank capacity and an efficient liquid-vapor separation at the same time. A fuel tank with a low-profile (flat) shape must be made larger to accommodate a fuel vapor area where a ROV and a VSF can be installed. However, a larger tank requires more package space, increases weight, adds volume to the vapor area, and ultimately requires a larger canister and higher purge flow rate for the engine to burn the increased amount of vapor. These factors are considerable disadvantages with regards to treating vapors in the fuel tank and improving fuel economy.

To solve these technical challenges, the 2005 model year Odyssey adopted a "2-vent system" (Fig. 3) and a liquid-vapor separation device called a "vent tower" (Fig. 4). The VSF, which is normally positioned at the top of the tank, was moved to a higher location within the vehicle's wheel housing, and the two ROVs were connected to the vent tower by separate lines. This LEV2 system achieved the required liquid-vapor separation performance, enhanced the tank's capacity filling efficiency, and contributed to a low-floor package.

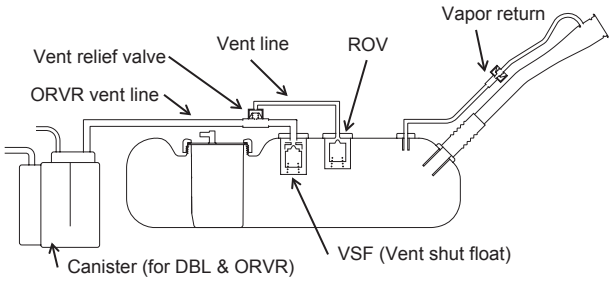


Fig. 2 LEV2 fuel system diagram

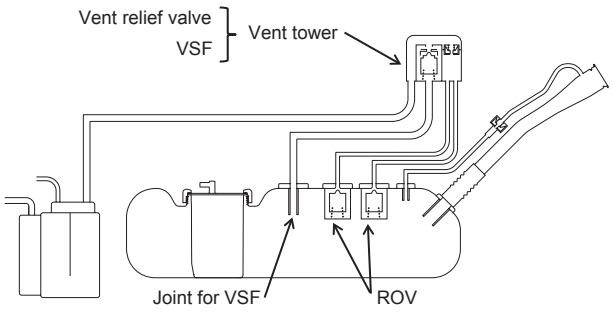


Fig. 3 2005 model year Odyssey fuel system diagram

Despite the advantages of the 2-vent system to marketability, compared to a conventional LEV2 system, the positioning of the vent tower still required the following:

- Increased part cost
- Increased package space inside the wheel housing
- Additional tube connections with lines extending from the tank
- Increased fuel permeation amount
- Additional assembly tasks in the manufacturing process
- Protection for the vent tower in the event of a vehicle crash or other dangerous situation

For the 2011 model year Odyssey, the fuel system was redesigned to eliminate the vent tower while maintaining marketability in terms of low floor packaging, fuel tank capacity, and filling efficiency; reduce cost; and enhance reliability.

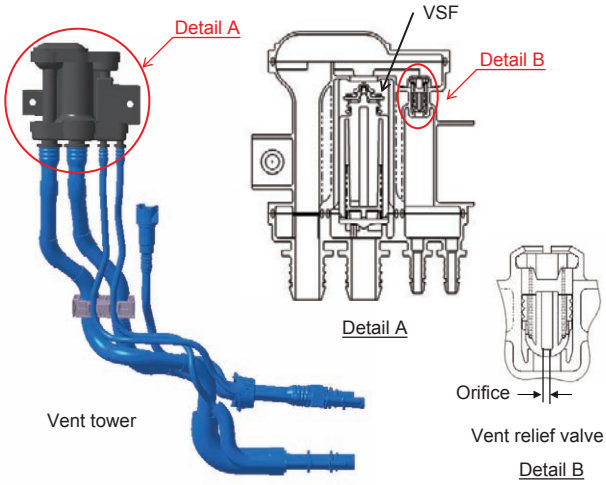


Fig. 4 Vent tower on 2005 model year Odyssey

3. System Concept and Technical Requirements for Components

3.1. System Concept

To achieve the development target, the overall concept of the fuel system had to be clearly defined. This design began with positioning the VSF and ROV on top of the tank, just as a conventional LEV2 tank system.

To ensure the same capacity and filling efficiency of a low-profile tank, a multi-vent system (that is, a system where two or more ROVs are applied) would be adopted as the 2005 model year Odyssey did. However, with the multi-vent system, one of the valves will be submerged when the vehicle is inclined in a certain direction. To meet the required liquid-vapor separation performance, the multi-vent design needs to reliably prevent fuel from leaking out the vent line via the submerged valve.

In other traditional multi-vent systems, a liquid trap is provided in the form of a separator to achieve the required

liquid-vapor separation performance. However, such systems require an additional joint between the vent line and separator as well as measurers to prevent permeation of fuel from the separator itself. This specification could not be adopted since it would be incompatible with the LEV2 regulation. Consequently, a new zero-leak VSF and ROV technology was needed to keep the amount of fuel leak to zero without adding a separator.

Generally, in multi-vent systems, the greater the number of vents, the smaller the required vapor volume, hence a 3-vent system is better than a 2-vent system. However, additional vents require more ROV welding locations on the tank and longer tubes for the vent line, both of which are negative factors since they affect cost, fuel permeation amount, and reliability. To minimize these factors, the "2-vent system with zero-leak valves" concept has only two valves, one ROV and a VSF that also provides the ROV function. Furthermore, a relief valve with an orifice was set at the joint between the vent line on the VSF side and the vent line on the ROV side. As shown in Fig. 5, all of these parts are installed to the fuel tank as one assembly.

3.2. Technical Requirements for Components

After defining the system concept, the specific performance requirements for each system component had to be clearly defined.

3.2.1. VSF

(1) General performance of the VSF shall be ensured, while keeping the level of leak to zero, using a traditional, anti-stick type multi-stage float.
(2) One valve shall provide both the "full-tank detection" function and "ROV" function to create a 2-vent system.
(3) An orifice shall be provided to control the pressure inside the tank when the vehicle is inclined, which actuates the ROV near full-tank capacity.
(4) The orifice shall control vapor inside the tank in such a way that sufficient auto-refueling stop performance is ensured and the amount of fuel that can be added after auto-stop is kept low. In doing so, the required total P-Q (pressure versus flow rate) characteristics of the entire system shall be satisfied by a combination of this orifice and the orifice in the vent relief valve, which is explained later.

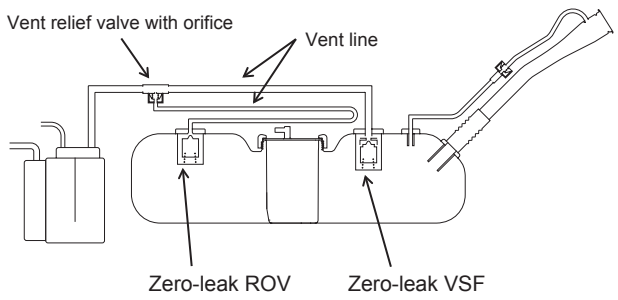


Fig. 5 Concept for 2-vent system with zero-leak valves

3.2.2. ROV

General performance of the ROV shall be ensured, while keeping the level of leak to zero.

3.2.3. Vent relief valve

(1) The pressure inside the fuel tank shall be adjusted properly through the vent line on the ROV side when the VSF is submerged and flow of vapor is cut off due to inclination of the vehicle.
(2) The amount of vapor flow shall be adjusted so that when the specified fuel level is reached during refueling, the VSF will actuate to cut off the vapor passage and thereby cause refueling to stop automatically.
(3) When combined with the VSF orifice, the valve must keep the amount of fuel that can be added after auto-stop low and to a level at which the full-tank level can be maintained.
(4) When combined with the VSF orifice, the valve shall achieve an appropriate flow of vapor to prevent spit-back of fuel upon auto refueling stop.

3.2.4. Fuel tank

(1) The structure shall be such that the above valves are retained on the fuel tank.
(2) The nominal capacity shall be ensured and equivalent filling efficiency achieved based on the same package space as on the previous model.

As listed above, the system concept and technical requirements for each component were clarified before the start of development.

4. Key Technologies

4.1. Zero-leak VSF Construction

Honda's traditional VSF adopts a 2-stage float and its valve re-opening pressure is designed to prevent the valve from sticking when a high volume of vapor is generated in the tank. Traditionally, a large diameter seal is achieved by contact between plastic and rubber, whereas a small diameter seal is achieved between plastic and plastic. However, the small diameter seal design has been associated with a small leak due to either fuel sloshing inside the tank or the seal remaining submerged in fuel for a long period. Therefore, the new design had to eliminate this leak.

If the sealing effect is lost, a leak will occur if the vehicle is inclined and the valve is submerged in fuel. Although this does not pose a concern in a normal system where the VSF is positioned in a vapor area, it did pose a significant challenge in designing the new system. For the new system, the zero-level leak requirement must be 1 ml or less over 1000 hours when the sealed area of the valve is submerged in fuel. Figure 6 shows a structural diagram of the zero-leak VSF.

Furthermore, actuation of the float to provide sealing is based on the reactive force of a spring and buoyancy of fuel, so sealing performance may be lost due to fuel sloshing.

During development, it was discovered that the conditions most susceptible to leak occurred from vehicle vibration input. Accordingly, an allowable amount of leak was set for each vehicle vibration condition that could occur with the vehicle traveling while the float is submerged. The hardware specifications were set to meet these target values.

The new adopted structure incorporates the following setting to prevent fuel leak, achieve an appropriate seal compression margin, and to ensure sufficient seal performance in a low-temperature environment:

- Seal structure based on plastic and rubber in the small-diameter area
- FKM Sifel material used for the seal rubber
- Adoption of a 3-stage float structure and setting of an auto-pivoting adjustment mechanism capable of absorbing angle variation
- Addition of a float stroke stopper for the small-diameter area

Furthermore, the following changes were made to suppress the effect of an external force to buoyancy behavior and to ensure sufficient sealing performance under vibration and in a submerged state:

- Setting of a core float to reduce the influence of the air volume trapped inside the lower float
- Adoption of POM for the lower float and lightweight PA12 for the core float to reduce the effect of the float's weight
- Increase of the stroke margin in each of the three float stages compared to the traditional structure to improve the valve's ability to remain closed when the lower float drops due to vibration

These design measures allowed us to achieve the zero-leak target value.

4.2. Zero-leak VSF Auto-stop Function

The VSF automatically stops refueling in one of two ways.

4.2.1. Float buoyancy method

As shown in Fig. 7, as the fuel level rises, the float rises and cuts off the flow of vapor and refueling stops.

4.2.2. Breather-type method

As shown in Fig. 8, as the fuel level rises, the vent holes in the VSF case are submerged, the vapor route is cut off, and refueling stops. This cutoff of vapor flow by the actuation of the float occurs secondarily.

The VSF of this system adopted the breather-type level detection method to achieve "full-tank detection" and "ROV" functions with a single valve.

In this system, vapor flow must be shut off in the tank when the full-tank level is detected. However, with the 2-vent system, vapor flow must be permitted when the ROV is inclined and submerged in fuel.

Accordingly, an orifice was integrated in the VSF case

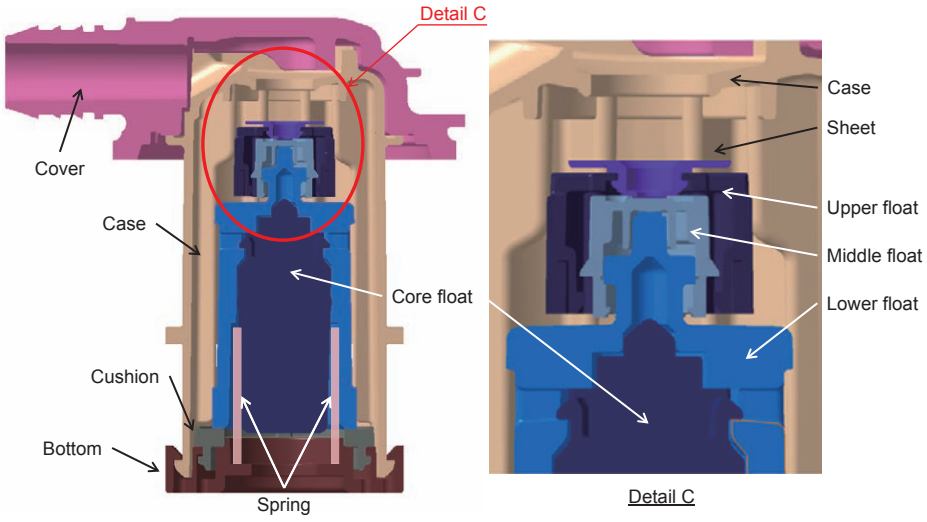


Fig. 6 Zero-leak VSF construction

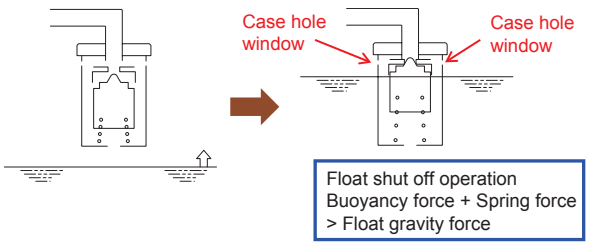


Fig. 7 Float buoyancy type VSF operation mechanism

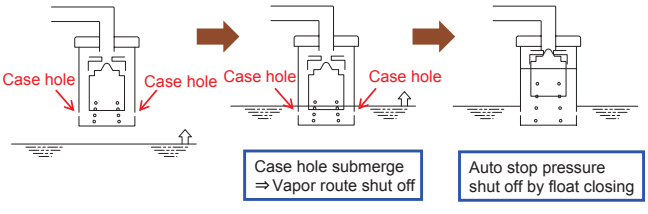


Fig. 8 Breather-type VSF operation mechanism

to permit vapor to flow to the vapor line even when the vehicle is inclined near its full-tank capacity. When setting the orifice diameter, the "total P-Q characteristics" of the entire system must be investigated, the details of which are explained later.

4.3. VSF Marketability Requirement

When the VSF was installed on the redesigned tank, actuation noise from the plastic of the float contacting the plastic of the bottom plate permeated into the cabin. This had not occurred on the previous model or any other model that used the traditional VSF design. To resolve this issue, an impact-absorbing rubber cushion was added to the bottom plate of the VSF.

4.4. Zero-leak ROV

The traditional seal structure of the ROV was based on contact of "plastic" and "plastic." As a result, a small amount of fuel leak occurred due to sloshing of fuel inside the fuel tank or the seal remaining submerged in fuel for a long period, just as the small-diameter seal area of the VSF. Accordingly, the new design had to eliminate this leak.

To achieve sealing, the ROV, like the VSF, is structured so that the float is actuated by a force resulting from the reactive force of a spring and buoyancy of fuel. However, the ROV does not have a full-tank detection function, so a one-stage float is applied. The same leak requirement value applied to the VSF was adopted and hardware specifications were investigated to satisfy these requirements.

Figure 9 shows a structural diagram of the zero-leak ROV. This ROV is adopts the float buoyancy method.

The newly adopted structure incorporates the following setting to prevent fuel leak, achieve an appropriate seal compression margin, and ensure sufficient seal performance in a low-temperature environment:

- Seal structure based on "plastic" and "rubber" in the seal area
- FKM Sifel material used for the seal rubber
- Ensuring sufficient seal compression margin through a structure that holds the outer periphery of the rubber all round and causes the rubber to deflect toward the inner periphery side
- Addition of a float stroke stopper

Furthermore, the following changes were made to suppress the effect of an external force to buoyancy behavior and to ensure sufficient sealing performance under vibration and in a submerged state:

- Setting of a core float to reduce the influence of the air volume trapped inside the float
- Adoption of POM for the float and lightweight PA12 for the core float to reduce the effect of the float's weight

These design measures allowed us to achieve the zero-leak target value.

4.5. Vent Relief Valve

A relief valve with orifice was set at the joint between the vent line on the VSF side and the vent line on the ROV side. This valve controls the flow rate on the ROV side. A structural diagram is shown in Fig. 10.

The valve seal diameter was increased from the conventional structure to ensure the required P-Q characteristics. Furthermore, to stabilize the accuracy of parts, a laser welding method was adopted instead of conventional vibration welding, and the valve was welded after the assembly.

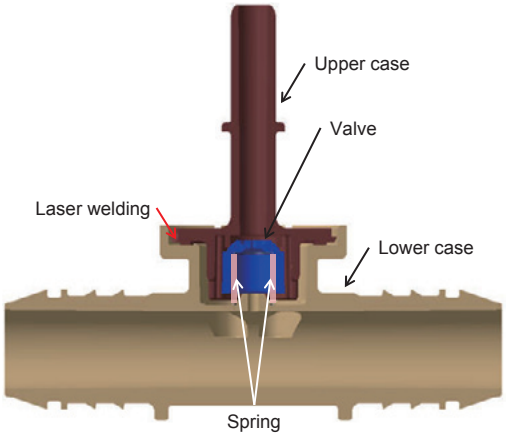


Fig. 10 Vent relief valve for zero-leak 2-vent system

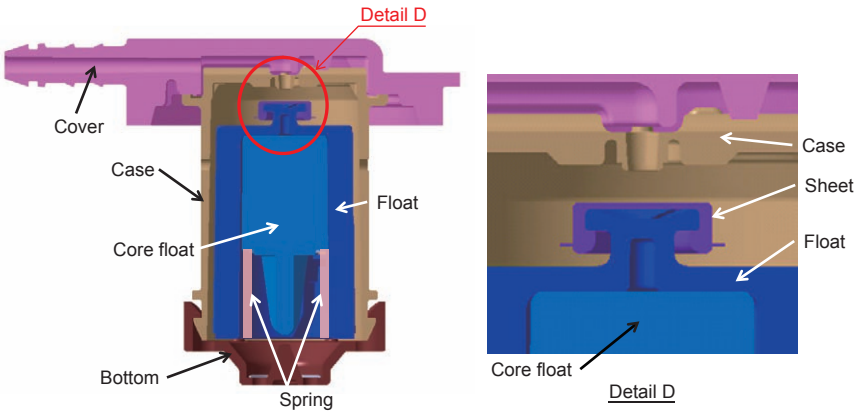


Fig. 9 Zero-leak ROV construction

4.6. Fuel Tank

For the 2011 model year Odyssey, a new low-profile plastic fuel tank that allows for a low-floor package was designed. The tank capacity is 21 gal. (79.5 L) that achieves an 84% capacity filling efficiency.

Figure 11 shows the tank's liquid-vapor separation performance.

As shown in Fig. 12, the valves constituting the vent system are positioned on top of the tank along with their respective vent lines.

Although the general outline of the fuel tank has a profile similar to that of the previous model, the upper and lower halves are welded at three Stand Off locations to ensure sufficient unit strength against the internal pressure of the tank. To most effectively suppress the deforming impact of vacuum on the plastic fuel tank, the welds are located near the three tank bands that hold the tank to the vehicle body. This design minimizes tank vibration bounce that occurs upon deflection by vacuum during engine purge and is effective in minimizing the inputs received by the valves on the tank.

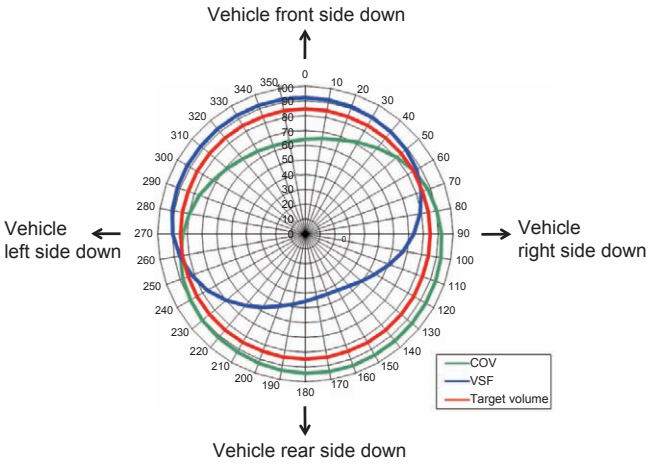


Fig. 11 Vapor-liquid separation performance

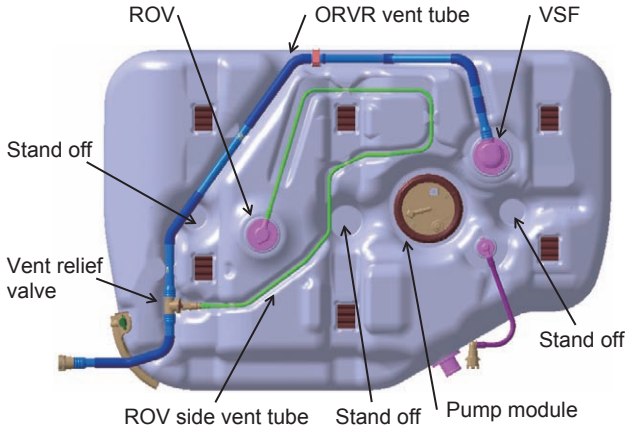


Fig. 12 Fuel tank assembly for 2011 model year Odyssey

5. Evaluation of System Soundness

5.1. 2-vent System – Total P-Q Characteristics

Vapor control is significantly different between a conventional system and the new 2-vent system.

In the conventional system, an optimal vapor flow setting for a refueling period can be achieved only by controlling and adjusting the P-Q characteristics of the vent relief valve.

In the proposed 2-vent system, the P-Q characteristics of the relief valve and of the VSF orifice must be considered at the same time. In other words, "total P-Q" control and adjustment is required.

First, the total P-Q characteristic of the entire system for the refueling period was verified to set the overall ventilation orifice size to Ø1.4 or equivalent. As shown in Fig. 13, this was attained through a VSF orifice diameter of Ø0.8 at two locations and a vent relief valve orifice diameter of Ø0.8 at one location.

These separate orifices were positioned to maintain vapor flow. Although the specific situation can vary based on the vehicle's inclination angle, vapor flow depends only on the VSF's P-Q characteristics when the ROV is submerged in fuel; thus the vapor flow passage is cut off when the main vent hole in the VSF is submerged. For this reason, a fairly large orifice size was set on the VSF side to maintain vapor flow.

Figure 14 shows the total P-Q characteristics of the 2-vent system, as well as the individual P-Q characteristics of the VSF orifice and relief valve.

The area requiring control during refueling and the area

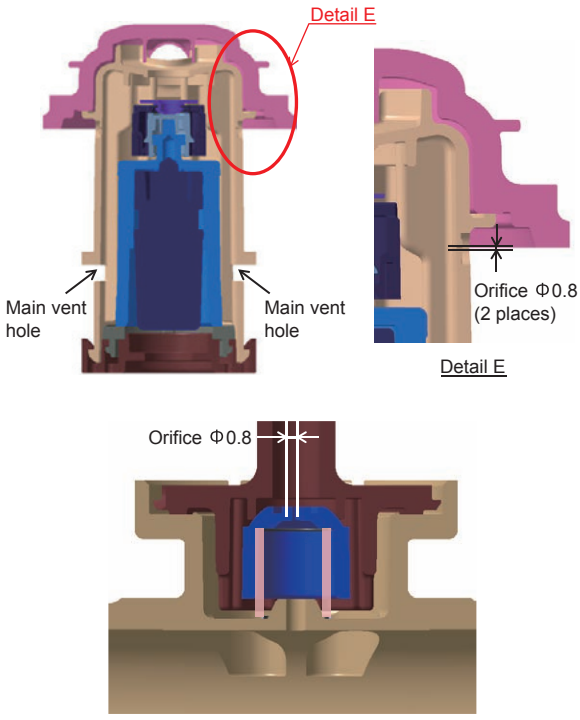


Fig. 13 Orifices for VSF and vent relief valve

where the flow rate should be increased to prevent excessive pressure in the fuel tank were addressed by combining the VSF orifice characteristics with the characteristics due to opening of the relief valve. However, when vapor is passed through the main vent hole of the VSF, the pressure becomes low relative to the flow rate, at which time the P-Q characteristics do not apply.

5.2. Vapor Flow Characteristics at Diurnal Breathing Loss (DBL)

Although both the VSF and ROV achieve zero-level leak through their respective seals, the volume of fuel vapor generated was checked to confirm that the vent system met the required vapor flow performance and to evaluate any effect caused by a valve seal failure.

The condition where vapor flows only through the VSF orifices due to the vehicle's inclination occurs only near the full capacity of the fuel tank. Vapor flow needs to be maintained regardless of the pressure inside the tank. If vapor is generated by a change in outside air temperature while the vehicle is parked on a slope, no fuel leaks should occur. To confirm system performance, the temperature shift specified by CARB's Diurnal Breathing Loss (DBL) requirement was measured and vapor generation was checked under the condition of a leaking ROV seal.

Vapor generation was also checked in the condition where vapor was flowing only through the ROV and the VSF seal was leaking. The vapor flow was maintained and no fuel leaked to the canister. As shown in Fig. 12, a line connects each valve on the tank and prevents any fuel leakage.

Figure 15 shows how the fuel temperature and gasoline vapor generation in the fuel tank change due to a DBL temperature shift.

Given this data and the P-Q characteristics of the individual orifices shown in Fig. 14, it is clear that there is little pressure in the fuel tank as long as vapor is flowing.

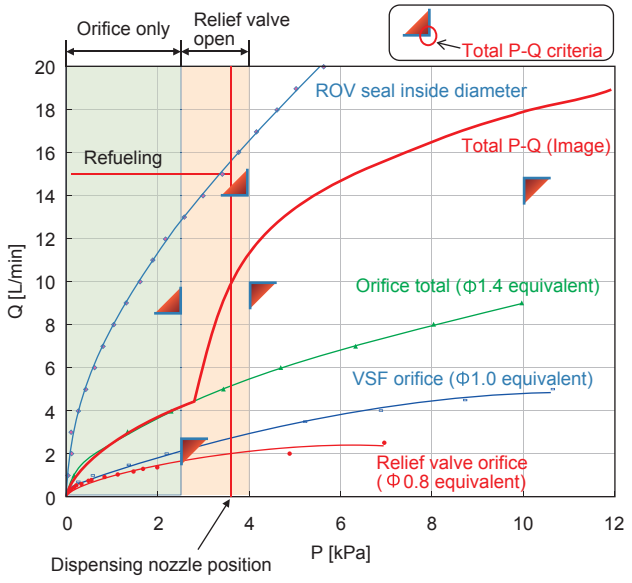


Fig. 14 Vent system P-Q characteristic

5.3. Refueling Performance

The operating pattern of the newly-adopted VSF and refueling based on the P-Q characteristics of the vent system were checked. Smooth refueling was possible until automatic refueling stop, and the volume of initial and subsequent refueling were confirmed to be at levels where the full-tank volume could be achieved. In addition, there was no spit-back of fuel after automatic refueling stopped and all targets set as initial technical requirements were met.

5.4. Evaporative Emission Performance

Evaporative emissions from the new system were evaluated according to the conditions under the LEV2 regulation. While the regulation specifies the full test based on 3 days of DBL from the entire system, and the short test based on 2 days of DBL, the development adopted a permeation target value of 200 mg or less per day from the system only. Figure 16 shows the evaluation results of 2 days of DBL from the fuel system components only. As shown, the new system meets the development target.

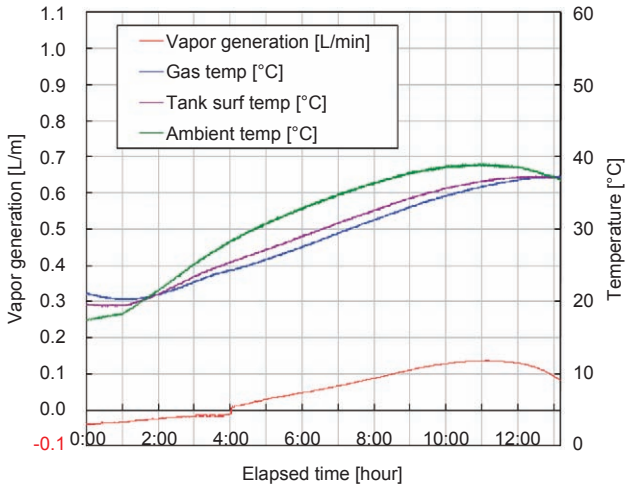


Fig. 15 DBL temperature and vapor generation

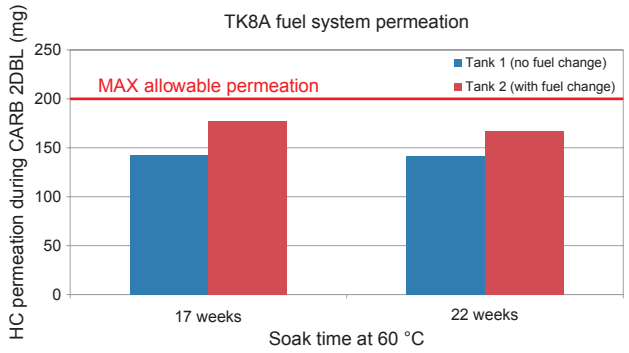


Fig. 16 Fuel system permeation (CARB 2DBL mode)

6. Summary

The outcomes of this development are summarized below.

(1) The “2-vent system with zero-leak valves” technology was established.
(2) Zero fuel leak level was achieved based on sealing between “plastic” and “rubber” materials in each seal area for both the VSF and ROV.
(3) Zero fuel leak level was achieved, even in a fuel-submerged environment, by adopting a lightweight, external-force adsorbing design for each float.
(4) Appropriate levels of marketability in terms of refueling, and vapor flow in an inclined state, were achieved by implementing total P-Q control of the vapor generating in the 2-vent system.
(5) The fuel system development target for the 2011 model year Odyssey eliminated the vent tower while maintaining marketability in terms of low floor packaging, fuel tank capacity, and filling efficiency; reduced cost; and enhanced reliability.

7. Acknowledgment

The authors would like to thank the group members of Toyoda-gosei Co. Ltd. and the group members of Yachiyo industries Co. Ltd. for their cooperation in the development.

■ Author ■


Tetsuhiro ITO


Hisayuki GOMA


Jason GRAHAM

Automated Tool for Brake Squeal Analysis

Sanjib NATH* Scott PAUL*

ABSTRACT

Brake squeal analysis is a difficult process to set-up because selecting proper solver parameters and boundary conditions is complex. For that reason, an automation tool has been developed to mesh, set contacts, set constraints, define the non-linear and complex eigenvalue analysis parameters, and apply a gradual pressure load. The key benefit of this tool is that it helps a non-specialist quickly find unstable modes in the brake system design without prior knowledge of complicated CAE tools.

1. Introduction

Brake squeal is a high-frequency vibration that can be caused by vibrations between the brake pads and rotor, pads and the caliper, or caliper and its mounts. Brake squeal occurs in a high frequency range greater than a 1000 Hz vibration of the brake system during a braking event. Brake noise is annoying to passengers and can lead to customer dissatisfaction.

2. Contributing Factors to Brake Squeal

Figure 1 shows the brake components that can cause brake squeal. Applying the brake increases brake line pressure, which causes a caliper piston to push brake pads against a spinning rotor. An unstable mode occurs when a combination of piston pressure, friction, and damping effects cause two stable modes to merge.

Different brake noise phenomena exist in different frequencies. Figure 2 shows the different noise phenomena that exist in the human hearing range[3]. This study focused on low and high squeal frequencies in the 1-20 kHz range.

Figure 3 shows a tree of how different simulations are used to predict brake squeal.

Complex eigenvalue analysis (CEA) is one of the critical simulations for predicting unstable modes for brake squeal. The simulation is very difficult to properly setup. There was no easy tool capable of performing CEA confirmation prior to engine running testing. The main objective is to introduce new NVH techniques in order to improve marketability. CEA runs could be completed to find the best way to optimize the brake corner.

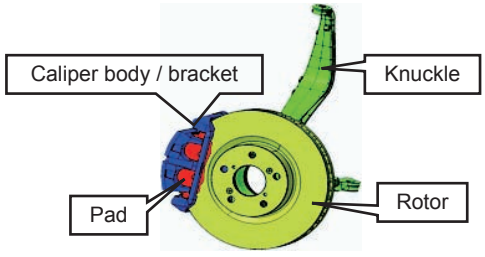


Fig. 1 Components that can cause brake squeal

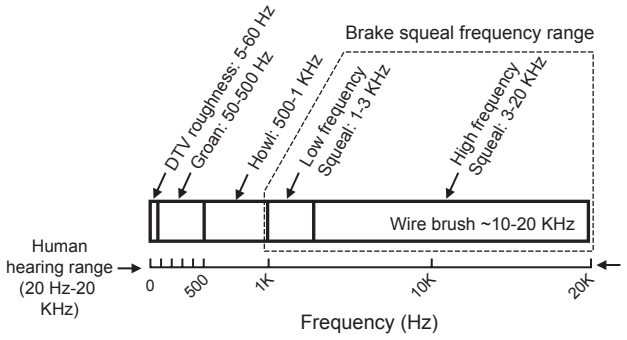


Fig. 2 Frequency range for brake noise phenomena

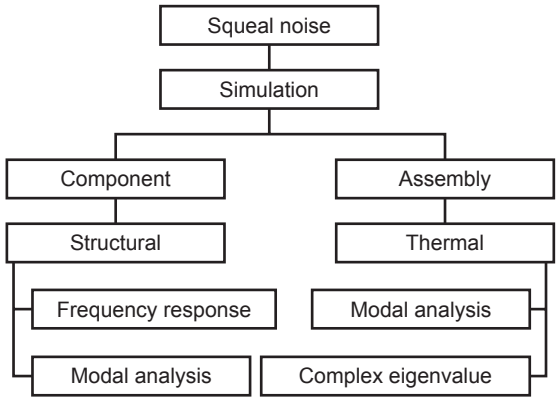


Fig. 3 Simulation dependencies for squeal noise

* HONDA R&D AMERICAS, INC.

3. Modeling Techniques

The rear brake assembly model was considered to illustrate the modeling technique and analysis. Altair HyperMesh software was used to setup the model and complex eigenvalue analysis carried out using MD Nastran solver.

3.1. Brake Components

The rear brake assembly includes rotor, caliper body, caliper bracket, piston, inner pad lining, outer pad, retainer, back plates, and shim. The brake assembly with all the components is shown in the Fig. 4.

3.2. Material Property

Anisotropic material property was used for the lining material and isotropic material property was used for the rest of the components.

3.3. Contact Definition

Touch and glue types of contacts (in MD Nastran solution) were used between the mating parts. Touch contact was used where friction is involved and movement is allowed between components. The glue contact was used where no friction is involved and a rigid connector between components is allowed. Three different friction values of 0.1, 0.3 and 0.5 were applied between the rotor and pad and default values (blank) were used for the rest of the contact pairs. Contact pair for different mating parts is shown in Fig. 14 in section 4.4.

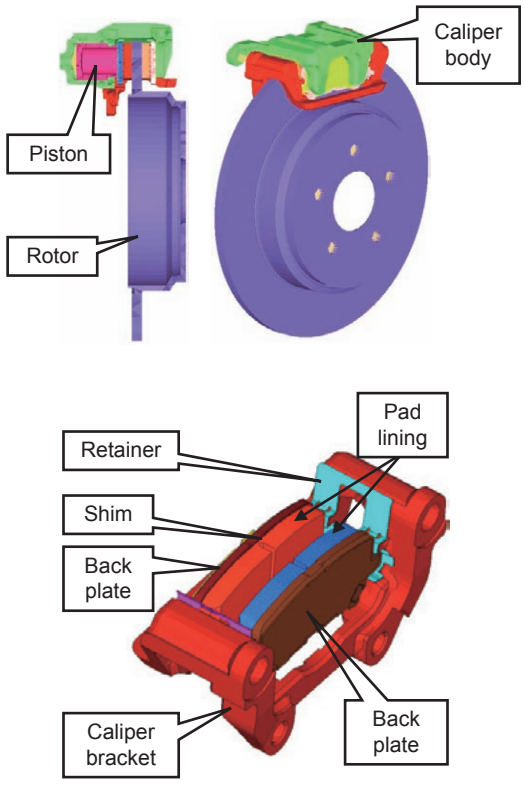


Fig. 4 Brake assembly

Table 1 MD Nastran parameters

Parameters	Definition
SOL 400	Nonlinear static and transient analysis
NLPARAM	Nonlinear static analysis parameter selection
NLIC	Defines nonlinear initial condition
METHOD	Selects real eigenvalue extraction parameters
CMETHOD	Selects complex eigenvalue extraction parameters
EIGRL	Defines data needed to real eigenvalue analysis
EIGC	Defines data needed to perform complex eigenvalue analysis
MAT1	Defines material properties for linear isotropic materials
MAT9	Defines material properties for linear anisotropic materials
BSQUEAL	Specifies data for brake squeal analysis
BSURF	Defines a contact body or surface defined by elements IDs
BCONTACT	Initiates and controls 3D contact
BCTABLE	Defines contact table
BCBODY	Defines flexible or rigid contact body

3.4. Constraining the Model

The rotor and caliper bracket bolt holes were fix-constrained. Rigid body elements were used instead of modeling pin and caliper contacts (virtual pin). The pin between the caliper body and bracket was only allowed to move in the Z axis (axial). The constraints details are shown in Fig. 10 and Fig. 11.

3.5. Loading Condition

The same and opposite pressure was applied to piston (bottom) and caliper body (bore bottom) which is shown in Fig. 12 in section 4.3.

3.6. Analysis Solver

MD Natran Solution 400 was used to solve the complex eigenvalue analysis. Some of the important brake squeals and contact parameters used in the analysis are listed in Table 1[1].

4. Developing Brake Squeal Analysis Tool

CEA is one of the established methods to predict squeal noise; however, it is a difficult analysis to set-up because selecting the proper solver parameters and boundary conditions are complex. For that reason, a wizard based GUI was developed for a non-expert to set-up a CEA step-by-step. The wizard is accessed in the Altair HyperMesh workbench, which is used for setting-up and viewing the results of the analysis. It uses the MD Nastran advanced non-linear solution sequence to solve the CEA. The overall process is shown in Fig. 5.

4.1. Brake Squeal Simulation GUI

The tool (as shown in Fig. 6) enables the designer to go through the following steps, with meshed parts as the starting point:

1. Update parts to represent correct material properties and orientation
2. Define the right boundary conditions
3. User defined contact pairs and contact properties
4. Export the input data to solve in MD Nastran

4.2. Part Update Function

After the user imports a mesh model, the Part Update function (as shown in Fig. 7) is used to adjust the materials and properties and create coordinate systems of the model. The process involves the following steps:

(a) Select a part from the Components list box.
(b) Select a material from the Materials list box.
(c) Display the part in the graphics window.
(d) Update the component properties.
(e) Specify a rectangular coordinate system (for pads) or cylindrical system (for rotors).
(f) Assign new references to parts.

The imported mesh model is shown in Fig. 8.

4.3. Load and Boundary Conditions Function

The Load and Boundary Conditions function (as shown in Fig. 9) constrains and applies load to the model. The process involves the following steps:

a. Specify directions for nodal constraints. Since solid tetra

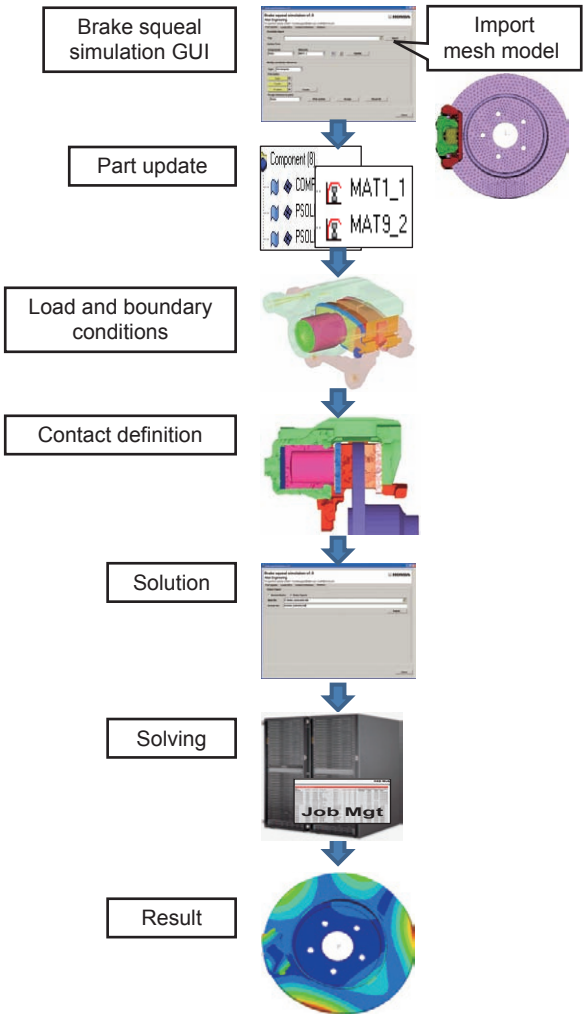


Fig. 5 Overall analysis process

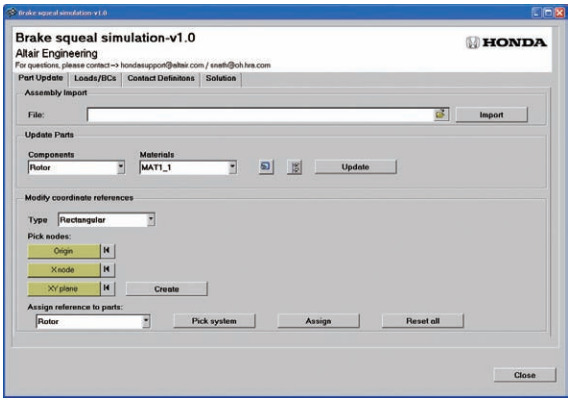


Fig. 6 Brake squeal simulation GUI

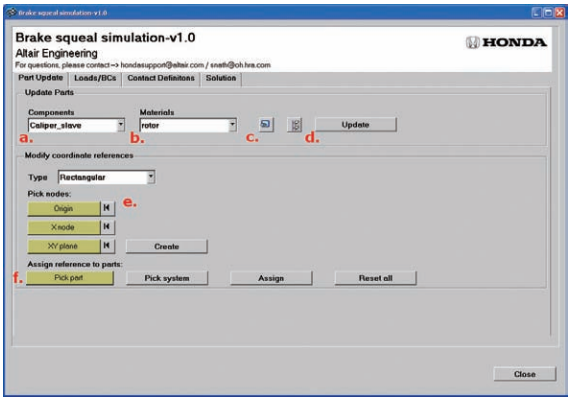


Fig. 7 Part update function

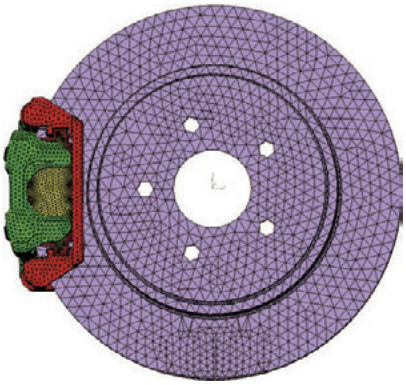


Fig. 8 Imported mesh model

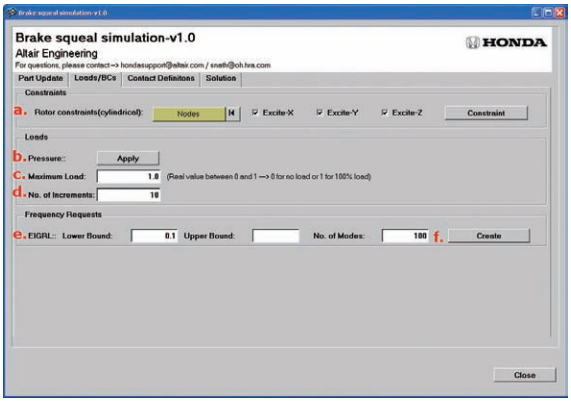


Fig. 9 Load and boundary conditions

elements are being used, only 3 degrees of freedom is necessary.

b. Specify pressure loads to be applied to the piston or the caliper, usually in equal and opposite pressure values (5 to 10 bars).
c. Indicate the maximum fraction of total load to be applied.
d. Enter the number of load increments for the non-linear static case.
e. Specify the lower and upper frequency bounds. The squeal mode usually occurs between 3-20 kHz. User also can define number of modes to be extracted.
f. Create the request for real and complex Eigenvalues.

Rotor and caliper were constrained shown in Fig. 10.

Virtual pin is allowed to move along the pin axis which is shown in Fig. 11.

Same and opposite pressure load were applied to piston and caliper body which is shown in Fig. 12.

4.4. Contact Definitions Function

Glue and touch contacts were defined between the mating parts using the GUI (as shown in Fig. 13). There is no user input required to select specific elements of the rotor and pad, which will potentially participate in contact surfaces. MD Nastran parameters automatically calculate the contact between deformable bodies by selecting rotor and pad components. The process involves the following:

a. Select a contact pair name.
b. Graphically pick master and slave parts.
c. Select Touch or Glue type of contacts.
d. Create a contact pair.
e. Select a coordinate system for the rotor.
f. Apply a friction coefficient between rotor and pad at different steps.
g. Review/modify/delete contact pairs.
h. Assign contact stiffness.

Glue and touch contacts were defined in the following contact pairs shown in Fig. 14.

4.5. Solution Function

Two simulation cases can be created: Normal Modes and Brake Squeal simulation. The analysis was solved in MD Nastran SOL 400 and the input file was exported from the GUI (as shown in Fig. 15).

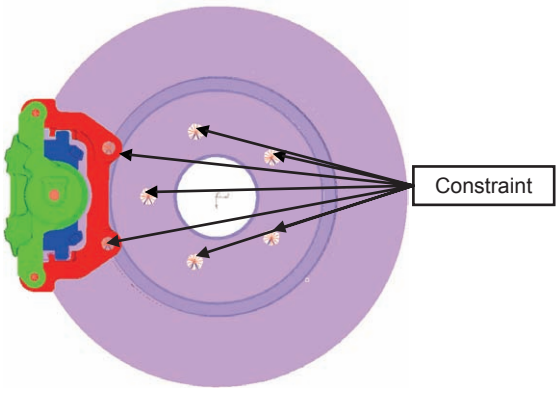


Fig. 10 Constraining model

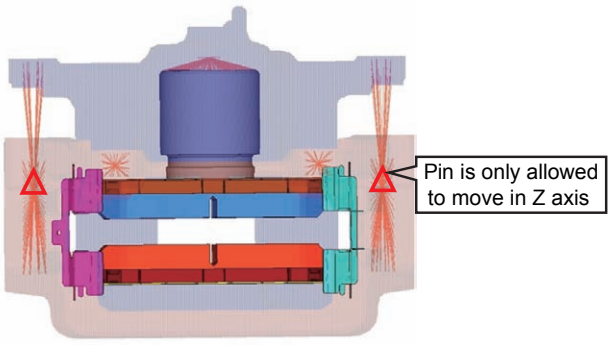
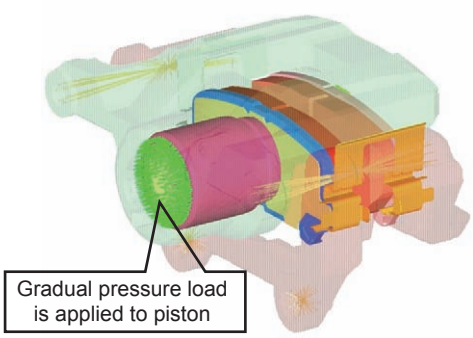


Fig. 11 Constraining virtual pin



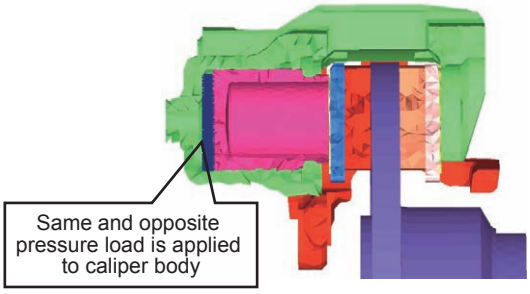


Fig. 12 Pressure load applied to piston and caliper

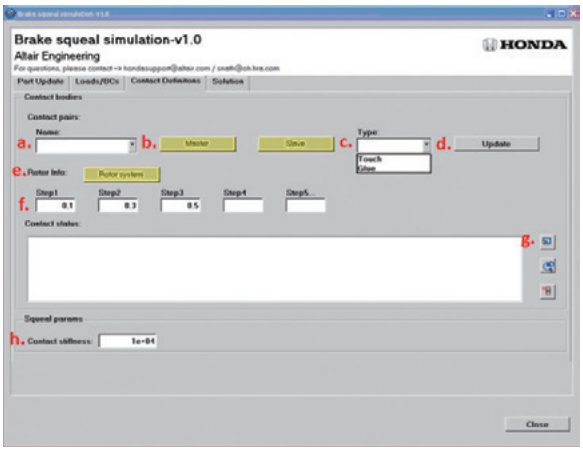


Fig. 13 Contact settings

4.6. Solving the Analysis

The MD Nastran model was submitted to a remote Cluster through a web-based job submission process.

4.7. The Result

After the analysis was solved, MD Nastran extracted the number of modes (based on frequency range) in different frequencies. If the mode contains a positive damping coefficient in a particular frequency called a stable mode and with a negative damping coefficient called an unstable mode. In addition, wherever an unstable damping mode exists there will also be an unstable positive real part (eigenvalue). These unstable real parts have a higher propensity for brake squeal.

All the unstable modes at different friction values are listed which is shown in Table 2. The highest Real Part values at that particular frequency and friction the more potential for brake squeal. The highest values were considered in each friction value.

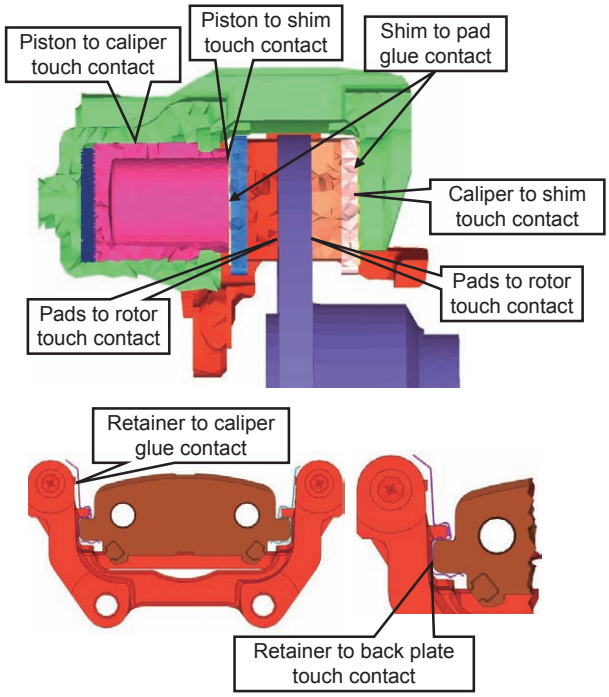


Fig. 14 Contact pair between mating parts

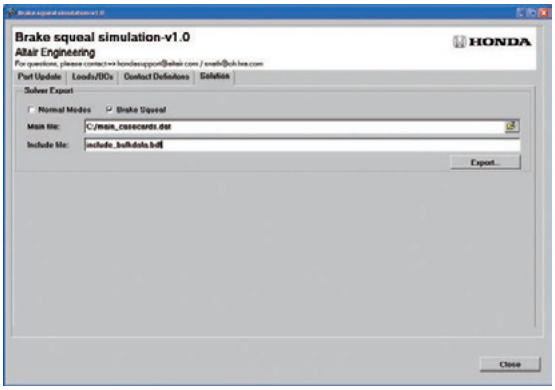


Fig. 15 Exporting Nastran input file

Table 2 List of unstable modes

Friction Coefficient					
0.1		0.3		0.5	
Frequency	Damping coefficient	Frequency	Damping coefficient	Frequency	Damping coefficient
1436.1	-1.0879E-02	765.9	-1.6644E-01	334.2	-3.9757E+00
1581.8	-7.3663E-02	1089.2	-2.1251E-01	1205.1	-9.1807E-02
2329.9	-1.2960E-02	1389.2	-2.6517E-02	2327.9	-5.0113E-02
2218.8	-1.3124E-01	2528.0	-1.6859E-01	2552.6	-1.1247E-01
1661.3	**-9.5757E-01**	2268.2	-5.0868E-01	3090.9	-2.6059E-01
2563.3	-9.3130E-03	3852.6	-4.4087E-02	3463.1	-2.7524E-02
4468.5	-2.5986E-03	4505.9	-1.8205E-02	3740.3	-4.6142E-02
5722.9	-3.4972E-02	4926.9	-9.4900E-02	4478.7	-8.0819E-02
5877.6	-2.2904E-02	5712.1	-5.0749E-02	3933.4	-5.2205E-02
7175.0	-4.5128E-03	5827.2	-1.2575E-02	5100.6	-5.8908E-02
7056.3	-4.9961E-02	7089.4	-6.6410E-01	6018.7	-5.2367E-02
		12719.1	-2.5516E-01	5644.7	-1.0792E+00
		11472.6	-1.0793E+00	11392.2	-8.9748E-01
		12897.3	**-1.8317E+00**	15360.0	-2.2695E-01
				10462.0	**-2.6509E+00**

The following plot (as shown in Fig. 16) was created to see the most unstable modes in different way. Real and imaginary parts of eigenvalues were plotted (shown in the left image in Fig. 16) and positive and negative values of damping coefficient were plotted (shown in the right image) with corresponding frequencies at a particular friction values of 0.3. The real part of eigenvalue and negative values of damping coefficient are the unstable regions. The farthest point from the axis center in unstable regions in both plots is the most unstable mode shown below.

Displacement contour of one of the unstable modes is shown in Fig. 17.

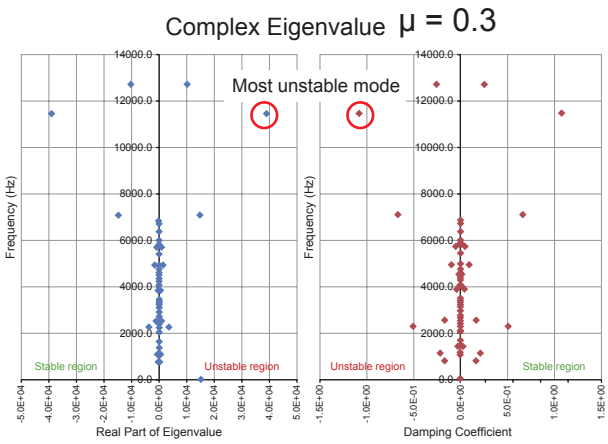


Fig. 16 Most unstable mode

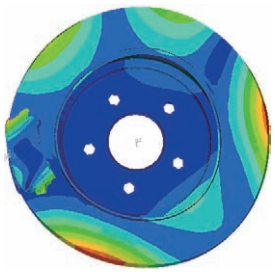


Fig. 17 Displacement contour of unstable mode

The most unstable mode listed above may not necessarily guarantee squeal on vehicle. Depending on the concerned frequencies, friction values, and applied pressure, a number of unstable modes could be considered. In verification with the test result will also be required to judge the simulation result.

5. Conclusion

Developing and implementing a brake squeal analysis tool have contributed to vehicle development in the following ways:

(1) The tool makes it easy to quickly set-up and run a Complex Eigenvalue Analysis.
(2) The wizard-based GUI helps the user quickly set-up and execute a simulation.
(3) A design engineer can use the tool without prior knowledge of complicated CAE tools, such as Hypermesh and Nastran.

References

(1) MSC Nastran R3 User Guide
(2) Kinkaid, NM O'Reilly, and P. Papadopounds. "Automotive disk brake squeal." Journal of Sound and Vibration 267 (2003): 105-166
(3) Liu, W. and J.L. Pfeifer. Introduction to Brake Noise & Vibration. Honeywell Friction Materials.

Author


Sanjib NATH


Scott PAUL

Development of Idling Stop System for PCX

Takeshi YANAGISAWA* Teruhide YAMANISHI*
Katsuhiro UTSUGI* Toshiya NAGATSUYU*

ABSTRACT

An idling-stop system that can be mounted on the 125-cm^3 engine of the PCX scooter was developed in order to enhance the environmental performance of the PCX. The system was made to use an ACG starter, which does not have a reduction mechanism for use in starting, in order to realize quiet starts with an impression of high quality. Cranking this engine requires a large ACG starter, and mounting this starter within the space given for attaching the ACG in the 125-cm^3 engine became an issue. This issue was addressed by reducing the engine cranking torque by means of a decompression device and by adopting a cranking method that makes use of inertial force. This approach realized an ACG starter of a size that allows mounting in the space for mounting the ACG in a 125-cm^3 engine.

1. Introduction

Heightened concern for environmental issues in recent years has led to demand for reduction of CO_2 emissions, or in other words, further measures to enhance fuel economy, with the motorcycle field being no exception. One technology to address this issue is the idling-stop system utilizing an ACG starter, but practical application of such systems has stopped at the 50-cm^3 engine. There is demand for application to vehicles of the 125-cm^3 class, which make up a large proportion of unit sales worldwide. A system capable of application to 125-cm^3 engines was therefore developed and mounted on the PCX, which is a model for global deployment, and this article describes the technical points involved.

2. Overview of the PCX Model

The PCX is a model that was developed to address diversifying customer needs through the key phrases "High-quality feel and advanced styling exceeding its class,""Balance of high engine performance and environmental performance," and "Comfort and good drivability demanded of a scooter." The intention was to deploy this product globally as a next-generation 125-cm^3 scooter raised one rank higher. Figure 1 shows the appearance of the PCX, and Table 1 lists its major specifications.

The engine is a newly developed 4-stroke, single-cylinder, liquid-cooled type with integrated radiator[(1)], made light and compact with 125-cm^3 displacement



Fig. 1 Appearance of PCX

Table 1 Major specifications of PCX

Items		Specifications
Overall length	(mm)	1915
Overall width	(mm)	740
Overall height	(mm)	1090
Wheelbase	(mm)	1305
Vehicle mass	(kg)	126 (Wet)
Engine type		Liquid-cooled, 4-stroke OHC, single cylinder
Engine displacement	(cm^3)	124.9
Bore x Stroke	(mm)	52.4 x 57.9
Compression ratio		11
Fuel supply system		PGM-FI
Maximum power	(kW/rpm)	8.33/8000
Fuel economy	(km/L)	45.9 *
Front tire size		90/90-14M/C 46P
Rear tire size		100/90-14M/C 57P

*In-house test value: EURO-3 control mode, with idling-stop system

* Motorcycle R&D Center

to produce a high-quality drive. It was designed with installation of the ACG starter in mind, so it does not have the starter motor, reduction gear, one-way clutch, driven gear, and other starter system parts found in conventional specifications. This enhances the scooter's quietness when starting while simplifying the construction. The weight is reduced by approximately 1.4 kg and the engine width is reduced by 15 mm relative to scooters with conventional starter systems. Figure 2 shows a comparison of starter system parts.

The adoption of a fuel injection system that provides optimal fuel supply for a variety of operating conditions achieved a balance of environmental performance and engine output with plenty of power to spare. It was also equipped with an idling-stop system (ACG-starter type) that automatically stops the engine at traffic signals, in congestion, and other temporary stops. This is a first in a 125-cm^3 class scooter. This reduces the wasteful consumption of fuel and emission of exhaust gases during idling, realizing higher environmental performance.

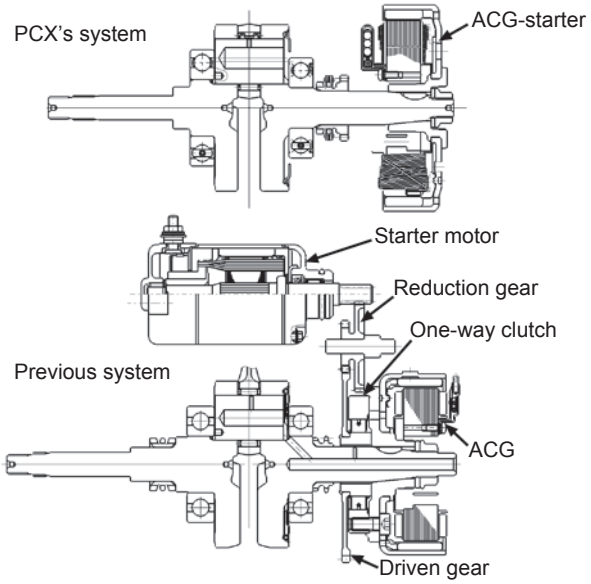


Fig. 2 Comparison of starter system parts

3. Overview of System

Figure 3 shows an overview of the idling-stop system for the PCX. This system is made up of the ACG starter that combines the AC generator and starter motor functions, a decompression device to reduce cranking torque when restarting the engine, an electronic control unit (ECU) that controls ignition, fuel injection, and idling-stop as well as electric power generation and motor drive control, and various sensors and indicators.

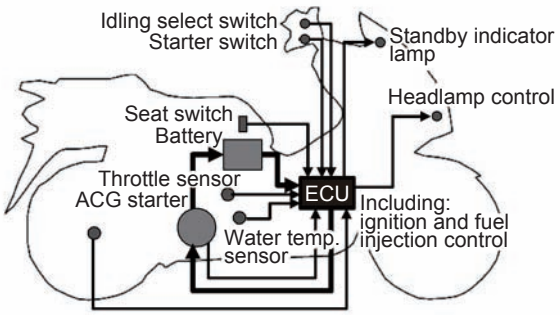


Fig. 3 Configuration of idling-stop system for PCX

4. Idling-stop System Operation

The method used to first start up is to press the starter button in the same way as when starting an ordinary scooter. Under these conditions, the engine will idle even when the scooter is stopped, and this state will continue until the scooter shifts to the idling-stop execution mode, which will be described next.

After the engine has started and the scooter is detected to be running at 10 km/h or faster and the water temperature is 60°C or higher, the system shifts to the mode that executes idling-stop. From that point, the engine will stop automatically and enter the idling-stop state when the system detects that the throttle is fully closed, the driver is seated, and the scooter is continuously stopped for three seconds or more. When the system detects that the driver is seated and the throttle is opened, the engine is restarted by the ACG starter and the scooter will be able to start moving[(2)].

5. Features of the Idling-stop System for the PCX

5.1. ACG Starter

5.1.1. Structure and performance

As shown in Fig. 4, the starter device has the newly developed ACG starter located on the engine crankshaft

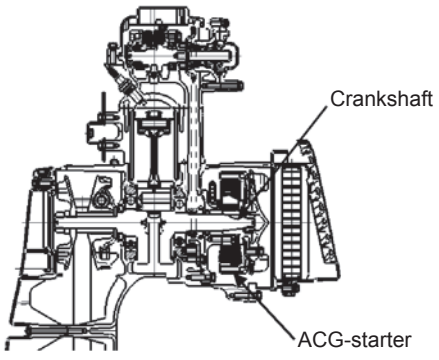


Fig. 4 Layout and configuration of ACG-starter and transmission

so that it drives the crankshaft directly. This ACG starter is an outer-rotor type, three-phase DC brushless motor. The flywheel is of the surface permanent magnet (SPM) type that is easy to manufacture. Figure 5 shows the configuration of the ACG starter.

Conventional ACG starters used dedicated sensor magnets. These were eliminated by inserting an angle sensor between the stator coil poles, as shown in Fig. 6, to detect the crankshaft phase from the position of the magnet for power generation. The effect on the angle sensor's crank angle detection accuracy from the magnetic field generated when power to the motor was on was at the level shown in Fig. 7, which does not affect the motor torque characteristic.

The ACG starter was also made more compact in size for this system by a starting system that makes use of inertial force. When cranking, therefore, it is important to raise the engine cranking speed higher just before the compression start. Figure 8 shows the engine cranking speed just before the compression start that this system is capable of. When the engine starts, as shown in Fig. 9, the system turns the crankshaft back from its current position to immediately after compression top dead center one stroke before, and then starts the crankshaft moving in the normal manner (swingback movement). This can provide an adequate cranking angle up to just before the compression start, and can make maximum use of the inertial force.

The above measures enabled the ACG starter to be made in a size that would fit in the space allotted for mounting the ACG. Figure 10 shows the motor torque characteristics of this ACG starter.

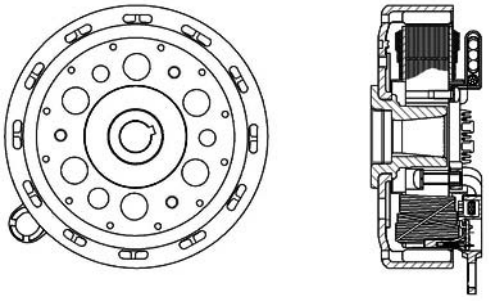


Fig. 5 Design of ACG-starter

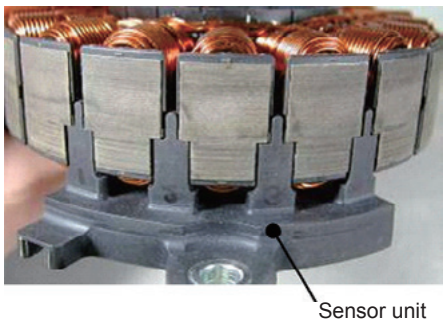


Fig. 6 Layout of angle sensor

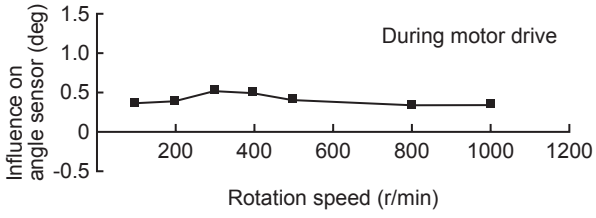


Fig. 7 Influence on angle sensor (at motor drive)

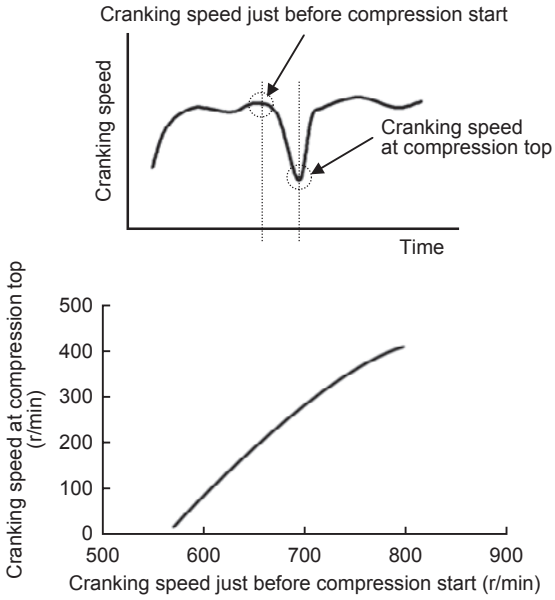


Fig. 8 Relation of cranking speed just before compression start and the compression top

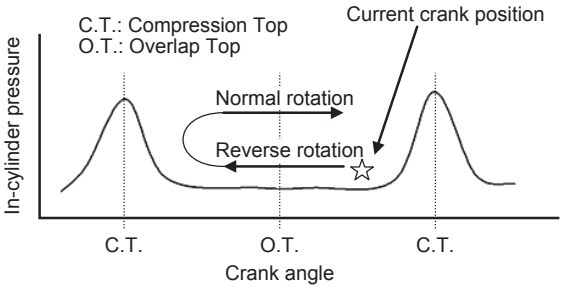


Fig. 9 Explanation of swing-back movement

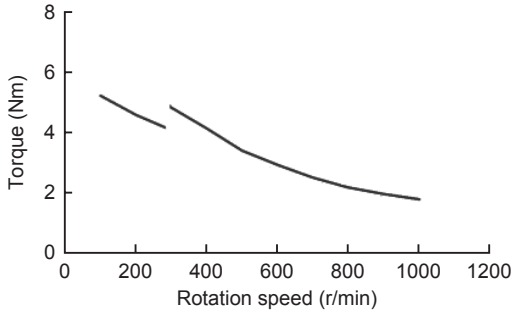


Fig. 10 Motor characteristics of ACG-starter

5.1.2. Electric generation control

In this system, the power generated by the ACG is controlled by advancing or retarding the electricity phase of the three-phase bridge for driving the ACG starter, as shown in Fig. 11. Figure 12 shows the relationship between the electricity phase and the power generated by this ACG starter. Adoption of this method enabled a reduction of electrical friction loss relative to the ordinary short-circuit type of regulator as shown in Fig. 13. Figure 14 shows the difference in electrical friction loss between the electricity phase angle control method and short circuit method.

5.2. Decompression Device

5.2.1. Structure and configuration

This system makes use of a decompression device to reduce cranking torque. At the cranking speed obtained with the ACG starter, the rocker arm is temporarily pushed up by the decompression cam during the engine compression stroke. This lifts the exhaust valve and reduces the pressure in the cylinder, allowing reduction of the cranking torque when the engine restarts.

On the other hand, centrifugal force on the decompression arm when the speed rises above idling will cause the decompression cam to turn, deactuating the decompression function. Figure 15 explains the operation of the decompression device. When the decompression device is actuated during idling, noise may be generated due to the repeated operation of the decompression arm and the engine might stop due to reduced compression. Therefore, the decompression release rotation speed was set at 1100 r/min, allowing some extra margin from the lower idling limit. Furthermore, it is necessary to set the upper limit on ACG starter speed at or below the decompression release rotation speed in order to avoid cranking faults due to deactuation of decompression. In order to satisfy these conditions, the decompression release rotation speed was set at 850-1100 r/min and the upper limit on ACG starter speed was set at 850 r/min (Fig. 16).

Moreover, in order to assure the necessary combustion force to start the engine, it is necessary to assure a minimum level of compression. Given the results of the limit test on startability, the compression lower limit was set at 720 kPa.

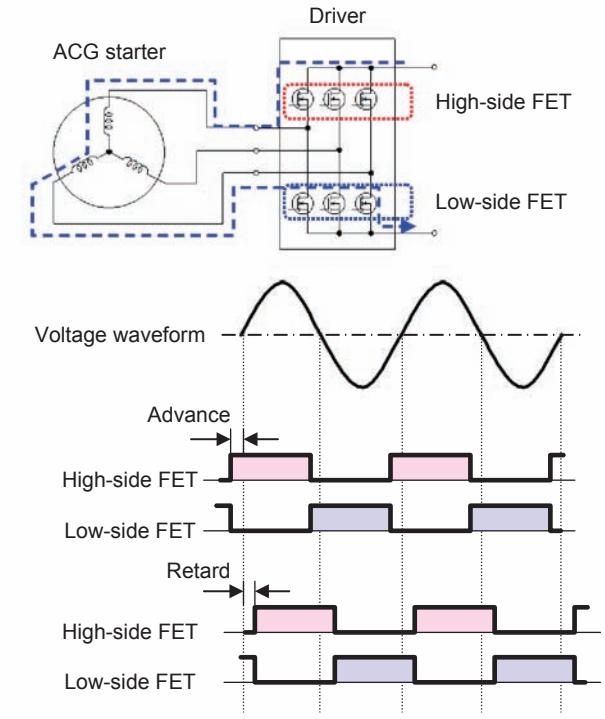


Fig. 11 Output electric current control by phase control

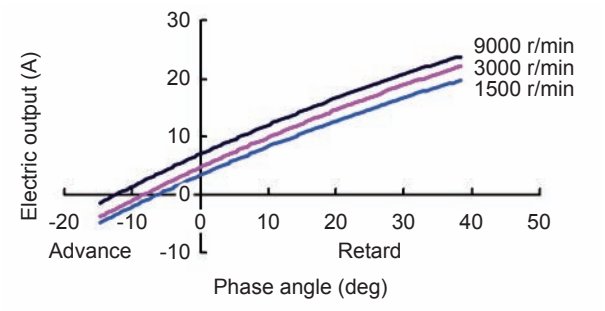


Fig. 12 Relation of phase angle and output current

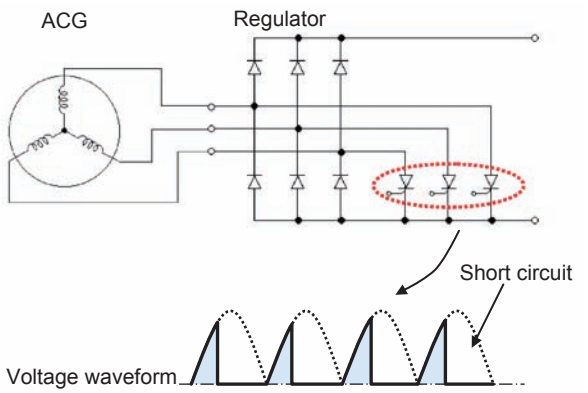


Fig. 13 Short circuit type regulator

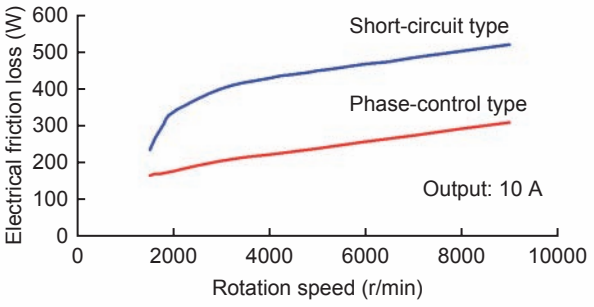


Fig. 14 Difference of electrical friction loss during electric generation by difference of control method

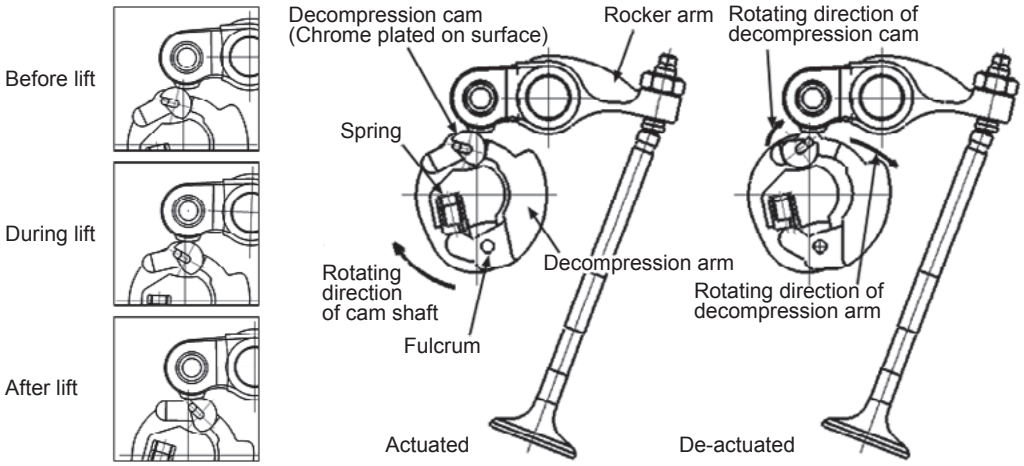


Fig. 15 Actuation of decompression device

5.2.2. Decompression device issues and responses

Previous engines in the same category had the decompression cam part and the weight part in a single integrated structure. The angle of rotation of the decompression arm was large, so that when the decompression arm hit the stopper it would generate an impact sound. In the case of the idling-stop system, the frequency of operation increased, raising concerns about the effect on product appeal. Therefore, the decompression cam part and the decompression arm part were made separate parts employing a linking structure that reduced the angle of rotation of the decompression arm and reduced the impact noise. Figure 17 shows a comparison of the specifications of the newly developed decompression device and the previous decompression device. The new development contributes to realization of the PCX aim for "High-quality feel exceeding its class." This new device also allowed reduction of the space situated so as to avoid interference by the decompression arm with other parts, thus contributing to making the cylinder head part more compact.

The decompression cam in previous engines not equipped with idling-stop system was made from carburized SCM420H steel. However, taking into consideration the frequency of starting involved on the assumption that idling-stop system is installed, there is concern that the decompression cam may undergo unusual wear. Therefore, the decompression cam surface was chromium plated to enhance its wear resistance. This reduced the wear on the decompression cam to a level that would not become an issue.

The fulcrum point for the decompression arm was placed ahead of the weight part relative to the direction of rotation so that the inertial force generated when reverse rotation switches to forward rotation during swingback operation would not deactuate decompression.

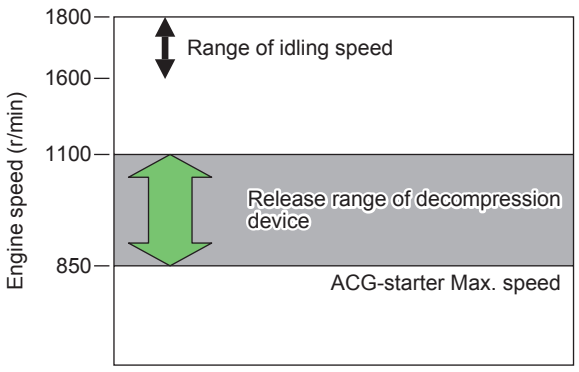


Fig. 16 Release rotation speed range of decompression device

5.2.3. Effects of decompression

The installation of a decompression device, as shown in Fig. 18, enabled reduction of the compression torque (peak value) from 18 Nm to 12 Nm. This enabled cranking the 125-cm^3 engine while holding the ACG starter size down to a minimum, contributing to making the engine more compact.

5.3. Control of Engine Stopping and Restarting

Stopping the engine when idling-stop occurs is done by stopping the injection of fuel in order to reduce the outflow of non-burned gasoline. When the engine is automatically stopped by the idling-stop system, the swingback movement is performed immediately after the engine stops so that cranking can take place promptly in the normal direction the next time the engine is started.

On the other hand, it may become necessary to restart the engine immediately after it has been automatically stopped and while it is still turning under its momentum. In such cases, it may be that the engine can be started more smoothly if the swingback movement is not performed. It is necessary, therefore, to judge whether or not to implement

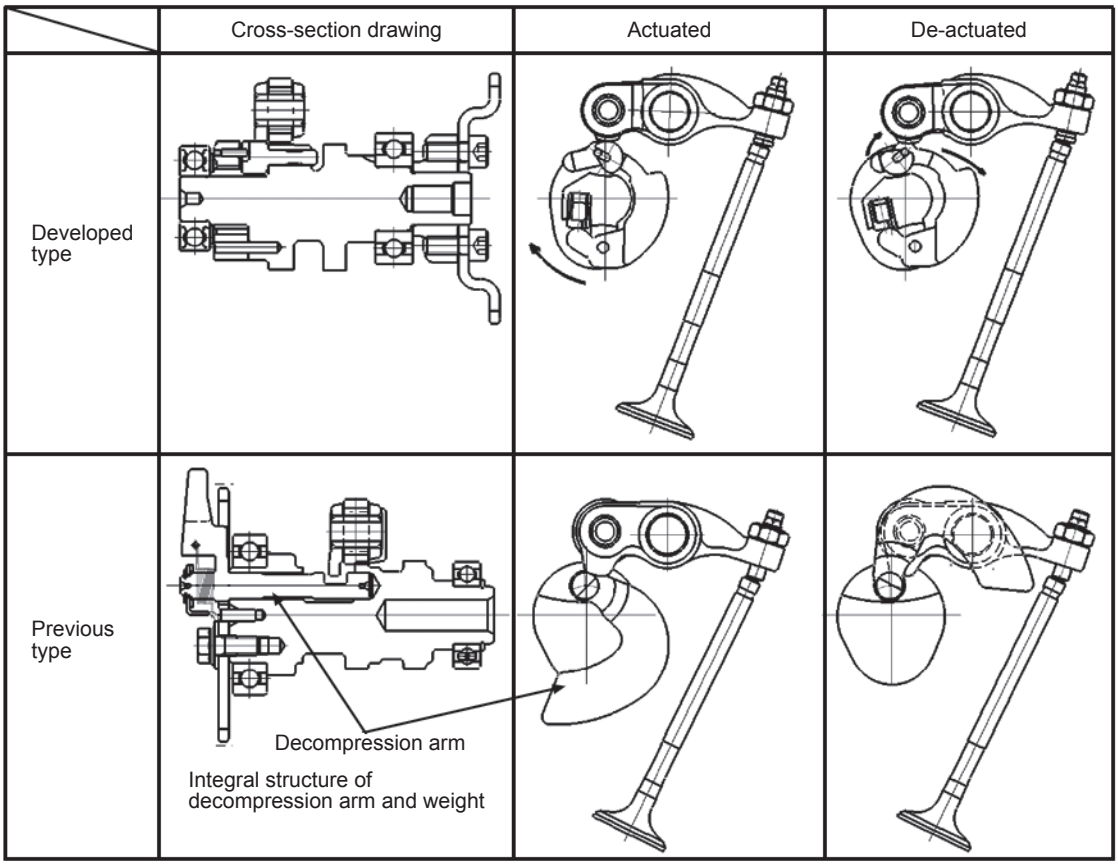


Fig. 17 Comparison between developed and previous decompression devices

the swingback movement. This is decided by the crankshaft position and speed. Figure 19 shows the swingback decision table.

Electric power consumption during idling-stop is reduced by dimming the headlamp and stopping the fuel pump. Therefore, a fuel pump with the increasing characteristic of the fuel pressure required for restarting was used. Figure 20 shows the increasing characteristic of the fuel pressure in the fuel pump.

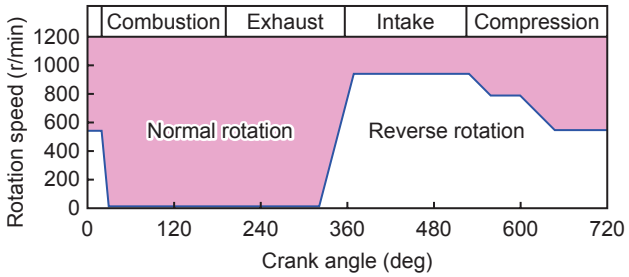


Fig. 19 Transition of swing-back operation during idling-stop

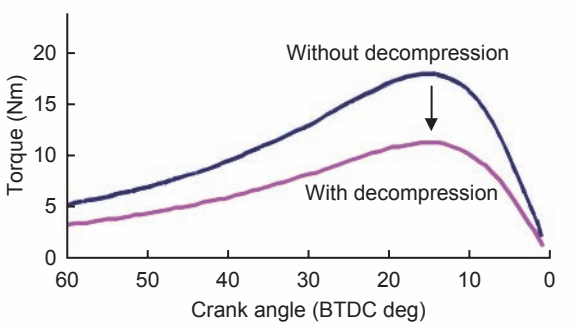


Fig. 18 Effect of reduction of demand torque by decompression device

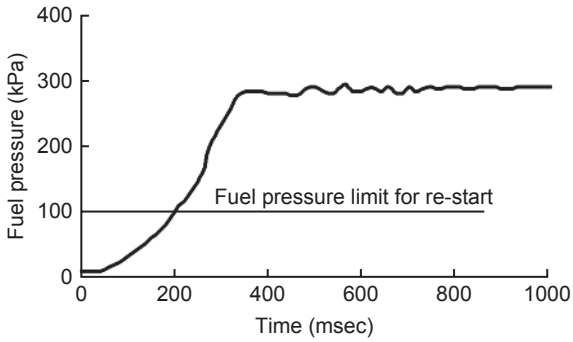


Fig. 20 Increasing characteristic of the fuel pressure in pump

6. Effects Obtained by Idling-stop

Making use of idling-stop yielded a 7.5% increase in fuel economy and a 7.0% reduction in CO_2 emissions (Table 2). The EURO3 control mode was used as the measurement mode (Fig. 21).

Table 2 Effects of Idling-stop

	Fuel economy (km/L)	CO_2 (g/km)
Without idling-stop system	42.7	53.0
With idling-stop system	45.9	49.3
Effect	7.5%	- 7.0%

In-house test value: EURO-3 control mode

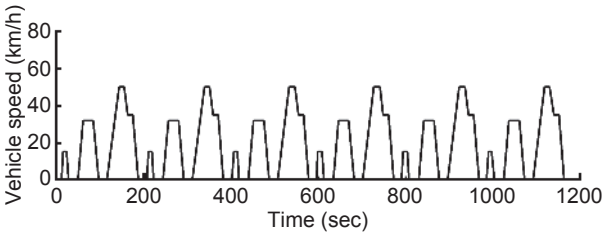


Fig. 21 Measurement mode of EURO 3 control

7. Conclusion

An idling-stop system that can be mounted on a 125-cm^3 scooter was developed. The ACG starter drives the crankshaft by a direct link to realize quiet starts and enhance the impression of PCX quality.

The following are the technical points involved.

- An ACG starter capable of starting a 125-cm^3 engine with low electrical friction loss was developed.
- A decompression device was adopted in order to reduce cranking torque.
- A cranking system that makes use of inertial force was adopted in order to keep the size of the ACG starter down to a minimum. The effects of this system were a 7.5% increase in fuel economy and a 7.0% decrease in CO_2 emissions (in EURO3 control mode).

8. References

(1) Sugioka, K., Sekiya, Y., Hayashi, H., Keiji, K., Nakajima, H., Toriyama, M.: Development of Scooter with 4-Stroke Engine “GIORNO Crea”, HONDA R&D Technical Review, Vol. 11, No. 2, p. 9-14 (in Japanese)

(2) Toriyama, M., Iwadate, T., Yuhara, T., Shinmura, H.: Development of Idling Stop System for Scooter, JSAE Review, Vol. 22, No. 1, p. 92-94 (2001)

■ Author ■


Takeshi YANAGISAWA


Teruhide YAMANISHI


Katsuhiro UTSUGI


Toshiya NAGATSUYU

Development of Bicycle Simulator for Safety Riding Education

Kenji SUZUKI* Yukio MIYAMARU*

ABSTRACT

Lifelong Education of Traffic Safety necessitates educating not only motorcycle and automobile drivers but also giving traffic safety education to bicycle users who may not have driving licenses. A "Bicycle Simulator" was developed for teaching safe riding to a wide age range, with effective functions to teach traffic rules and manners and enhance the student's ability to predict risks.

1. Introduction

People of a wide age range use bicycles in Japan for all types of reasons, including everyday transportation and leisure. According to the Japan Bicycle Promotion Institute (JBPI), the number of bicycles owned increases year by year[1] (Fig. 1). In addition, the fact that bicycles create little environmental burden as a means of transportation is expected to further promote their use.

However, a look at accident statistics from the Institute for Traffic Accident Research and Data Analysis (ITARDA) shows that accidents increase proportionately with increases in bicycle users, and there has been a rapid increase in accidents involving pedestrians in particular[2] (Fig. 2). Moreover, because no license is required to operate a bicycle, there is little sense of the bicycle as a light vehicle under traffic law, with the accompanying obligation of bicycle riders to obey traffic laws as they ride. For that reason, the fact that some riders violate rules and manners is widely seen as a social issue. Under the circumstances, creating a healthy transportation society necessitates preparing a road infrastructure, offering administrative guidance and providing further traffic safety education for bicycle operators.

The Bicycle Simulator gives users a way to safely experience the risks involved in mixed traffic situations, which would be difficult in actual transportation settings. By this means, the user can objectively review, understand and grasp his or her own operations. Honda has developed motorcycle and automobile simulators that can be used as part of the curriculum at driving schools, as well as a "Riding Trainer"[3] that lets users learn safe bicycle operation at nearby motorcycle shops. To take advantage of that experience, and to help achieve lifelong education of traffic safety as part of its obligation as a mobility enterprise, Honda has developed the "Bicycle Simulator," which can be used effectively by a wide age range of users.

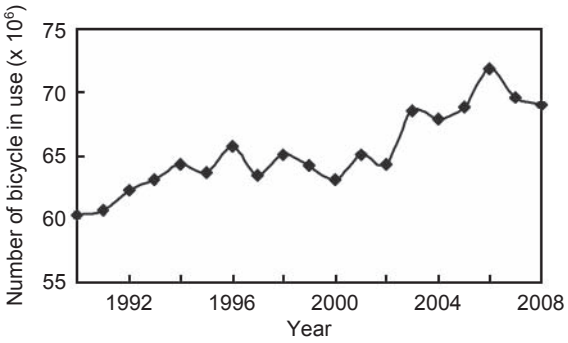


Fig. 1 Number of bicycles in Japan

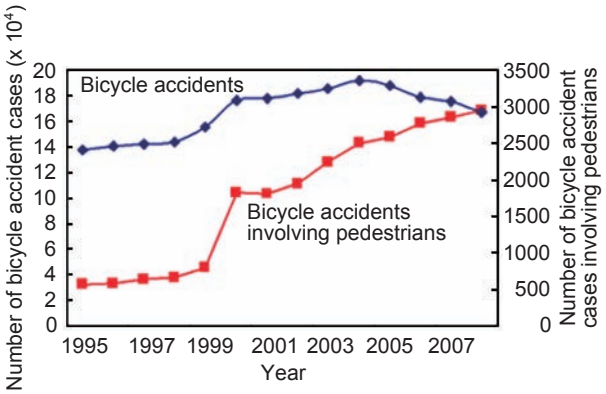


Fig. 2 Number of bicycle accidents and those involving pedestrians

* Motorcycle R&D Center

2. Traffic Accident Situation and the Current State of Bicycle Training

As the bicycle accident factors in ITARDA's accident statistics indicate, violations of safe driving obligation, violations of intersection safety traffic obligation, stop sign violations, etc., have a rather high percentage, and about 70% of bicycle operators commit some kind of legal violation[4] (Fig. 3). Additionally, a look at bicycle-related traffic accidents by age group indicates that, while those involved comprise a wide age range, from children to senior citizens, the highest percentage is among operators aged 19 and younger, who account for about 30% of accidents[4] (Fig. 4). This suggests that an effective way to help reduce bicycle accidents is to provide traffic rules education and risk prediction training starting in childhood, when bicycle operators are just beginning to experience road traffic[5].

There already are many examples of bicycle safety education, including bicycle clinics given by police departments, general learning time at schools, club activities, and as part of the local activities provided by driving schools and automobile dealers. According to documents of the National Police Agency[6], bicycle clinics are being given more frequently. In 2005, 2.53 million people attended about 22,000 such events. Typical educational techniques include classroom learning, simulations of road conditions in open-air spaces, and checking safety when passing through intersections, during takeoff and in places with poor visibility. Increasingly, traffic safety education is being given not only to young children and students, but also in bicycle clinics for senior citizens and events that mix three generations (children, parents and senior citizens). However, it has been said that bicycle safety training is not yet sufficient for all ages, and that in general "there is no sign of the participating children and students being self-directed"[7]. It is desirable that new initiatives be taken that provide highly effective training and create interest among the participants.

3. Configuration of Simulator

The Bicycle Simulator developed by Honda is shown in Fig. 5. The simulator consists of a front monitor, monitor stand, controlling PC, main body and rear view monitor. It is designed for easy mobility, dismantling and reassembly for transportation, in order to conform to the circumstances in which bicycle clinics are given. The main body, just like an actual bicycle, has an operating system with a handlebar, brake levers and pedals.

Because both children and adults use them, the handlebar and seat can be moved up and down, and the adjustment direction of the handlebar has also been taken

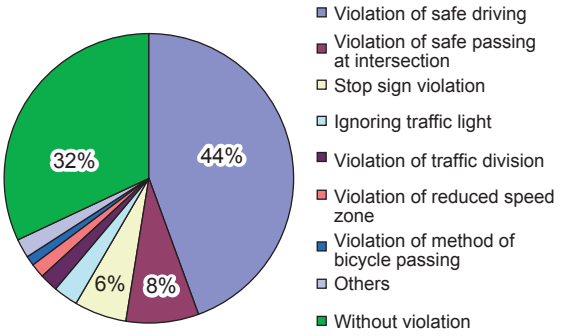


Fig. 3 Bicycle accident factors (2008)

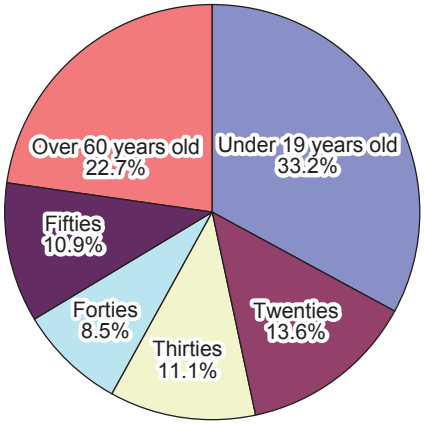


Fig. 4 Ratio of traffic accidents related to bicycles according to age group

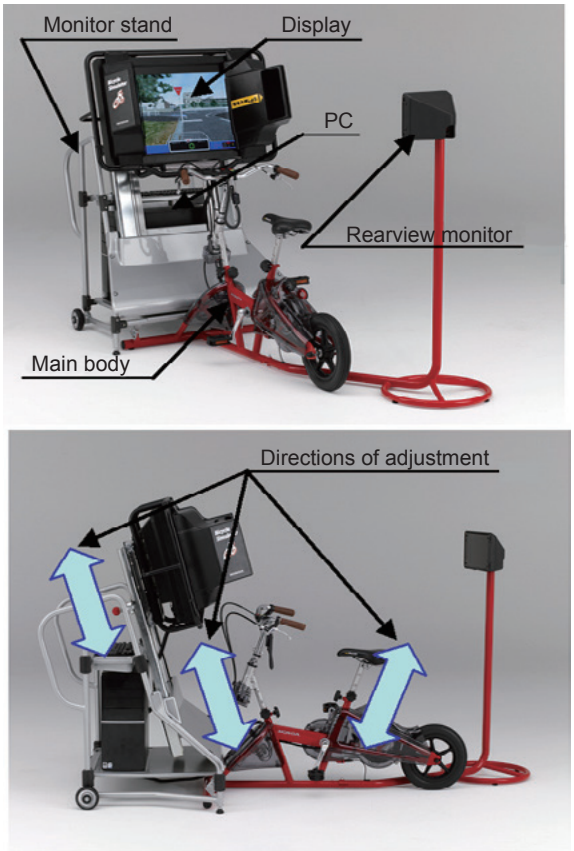


Fig. 5 Bicycle Simulator

into account. The front monitor height adjuster uses a mechanism that combines a gas damper and slide rail so the monitor can be moved up and down without too much force, making it easy to adjust to a height suitable to the user's line of vision. Handlebar operation and pedals put an appropriate burden on users so that their experience is true to that of actual road riding.

The Bicycle Simulator is designed for riders as young as five-year-old children, about the age when people start riding bicycles. To confirm whether children can actually have safe experiences with the simulator, Honda did field tests at kindergartens. The tests looked at whether any part of the simulator could cause injury or whether mischief could lead to concerns, and Honda incorporated these issues into the specifications.

To keep the simulator affordable and save space, a single PC was used to operate the controller, including video and audio. The part ridden by the user and the PC were designed to interface by USB.

The simulator was also equipped with "Mirror Boxes" for checking safety to the sides, a "Rear View Monitor" for the same check to the rear, and a "Step Sensor" so that the user could act as if walking and pushing the bicycle. Together, these mechanisms let the rider master the vital act of checking for safety as a function conforming to the content of bicycle clinics. Device details are given in the next chapter.

4. Characteristics and Functions of the Simulator

4.1. Side Safety Check Function

To help the user develop a habit of checking for safety to the sides at intersections with poor visibility and in alleys, it is necessary that the simulator have a function that makes the user perform side safety checks. This function has been realized in the simulator by a combination of screen partitions and Mirror Boxes. The monitor screen is partitioned into four parts: a central field that displays the front view, left and right fields that give smaller displays of the left and right views, and a rear field that displays the rear view (Fig. 6). The smaller views displayed by the left and right fields are magnified by Fresnel lenses, and there is a mechanism built into the Mirror Box to change the angle of view by 90° using mirrors (Fig. 7). As a result, in order to check safety to the side, the user has to move his or her upper body forward to look into the Mirror Box, encouraging the user to develop the habit of using his or her body when checking side safety. This also helps reduce cost and space, since a single monitor can provide the same functionality as if monitors had also been placed on the left and right.

Because the central, left, right and rear fields are all displayed on the front monitor, a projector can be connected to show the same video on a screen, allowing observers other than the user to see the same riding status as the user. This makes the simulator easy to use in group teaching.

4.2. Rear Safety Check Function

Just as in the case of checking side safety, it is necessary to have repeated actual practice in checking rear safety to make this a habit during takeoff or when changing line of travel, so a Rear View Monitor (8" screen with USB connectivity) is provided. The video of the rear field as shown on the front monitor is cut out by software and shown on the Rear View Monitor, where the rear traffic situation is shown (Fig. 8). When the simulated bicycle is stopped, this monitor shows a number superimposed on

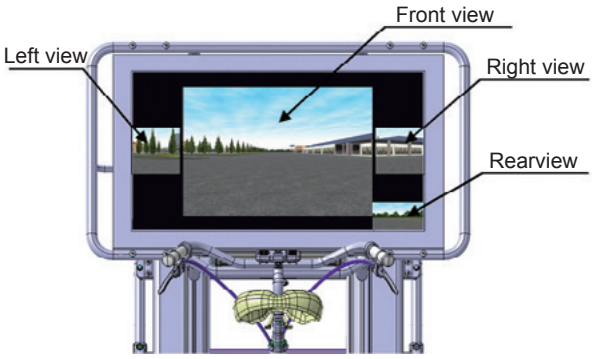


Fig. 6 Screen image

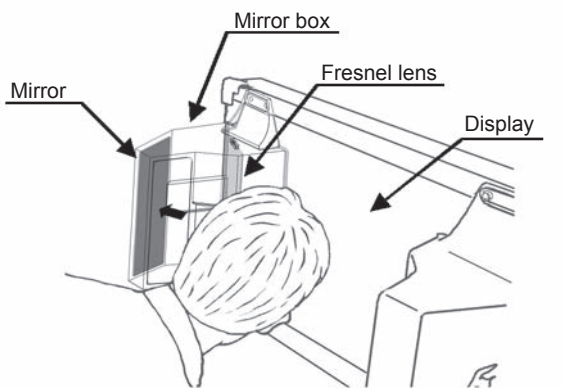


Fig. 7 Structure of "Mirror Box"



Fig. 8 Photo of "Rearview Monitor"

the rear video. The user looks back to check the number, then presses the number button of the "Handle Switch" that is on the handle (Fig. 9). If the number of the button pressed matches the number displayed on the screen, the simulator makes an affirming sound that indicates the user made the rear check correctly. If the numbers do not match, a buzzer sounds, or if the user takes off without checking and pressing a button, the simulator gives a warning encouraging him or her to check, thereby developing the habit of checking to the rear during takeoff.

During the early stages of development, developers did the same thing using only a three-color LED display device[8]; with this mechanism, however, evaluations of field tests indicated that the user could not make decisions in keeping with circumstances because he or she did not understand the rear traffic conditions when turning to the rear. Based on these results, the current monitor specifications were adopted allowing display of rear traffic conditions.

4.3. Walking and Pushing Function

Articles 17 and 63 of the Road Traffic Law (Japan) state that when operating a bicycle, the rider must dismount and walk and push the bicycle on pedestrian-only walkways and in crowds of people, or any time that the bicycle would be an obstacle to pedestrians, such as in pedestrian crossings, but in general these rules are not well known. In order to teach these points, a function was added to simulate walking and pushing the bicycle. A specially designed Step Sensor is used to detect this walking and pushing action (Fig. 10). Inside the Step Sensor is a semiconductor-type three-axis acceleration sensor. The user dismounts from the bicycle, puts the Step Sensor on his or her waist and walks in place, which allows the sensor to detect hip acceleration.



Fig. 9 Photo of "Handle Switch"

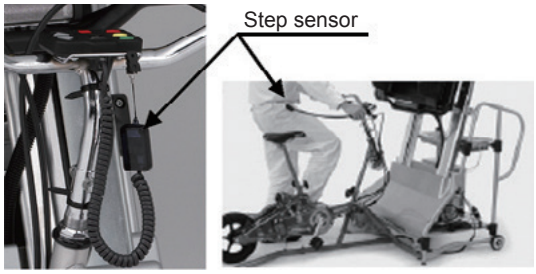


Fig. 10 Photo of "Step Sensor"

The simulator calculates walking speed based on this acceleration, and is set up so that the video moves forward in the direction the handlebar is being held.

4.4. Acceleration/Deceleration Calculation

A typical technique (in exercise machines, for example) for calculating cruising speed is to detect the rotating speed of the bicycle's rear wheel driven by the pedals and taking the result, as is, as the cruising speed[9]. However, unless a load and inertial mass equivalent to actual situations is attributed to the rear wheel, it is difficult to reproduce realistic acceleration/deceleration operation, necessitating a large, heavy flywheel and making the entire Bicycle Simulator larger and heavier. The simulator uses a small flywheel rotated and driven by pedals and chain, as well as a pickup that detects rotating speed (Fig. 11). It uses a newly devised speed calculation algorithm to reproduce cruising speed with a compact, lightweight system. The rotating speed signal detected by the pickup is multiplied by a coefficient described below, and this is considered the acceleration expected by the operator. Deceleration, found from the amount of brake application, the grade of the road and rolling resistance, is reflected in this acceleration to determine the total acceleration/deceleration. This acceleration/deceleration is integrated to calculate cruising speed. The coefficient that is multiplied by the rotating speed signal is larger when starting to pedal and smaller after starting to cruise. The video's movement, as a result, shows that speed rises directly in relation to the user's stepping on the pedals when first pedaling, but after starting to cruise, the motion accelerates rather moderately, thus creating a sense of acceleration/deceleration closer to that of an actual bicycle (Fig. 12).

4.5. Teaching Function

In addition to the experiential function that simulates the unique motions of bicycles, the simulator has a function as a teaching device, as described below.

The courses provided include the "Practice Course" (to learn the basic actions of cruising, turning and stopping), the "Easy Course" (to learn about the law while experiencing road cruising), the "Difficult Course" (to experience road

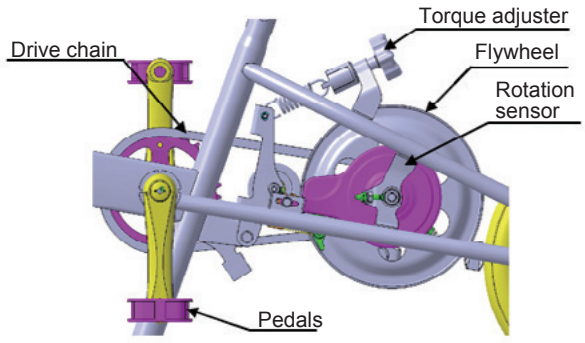


Fig. 11 Structure of drive parts

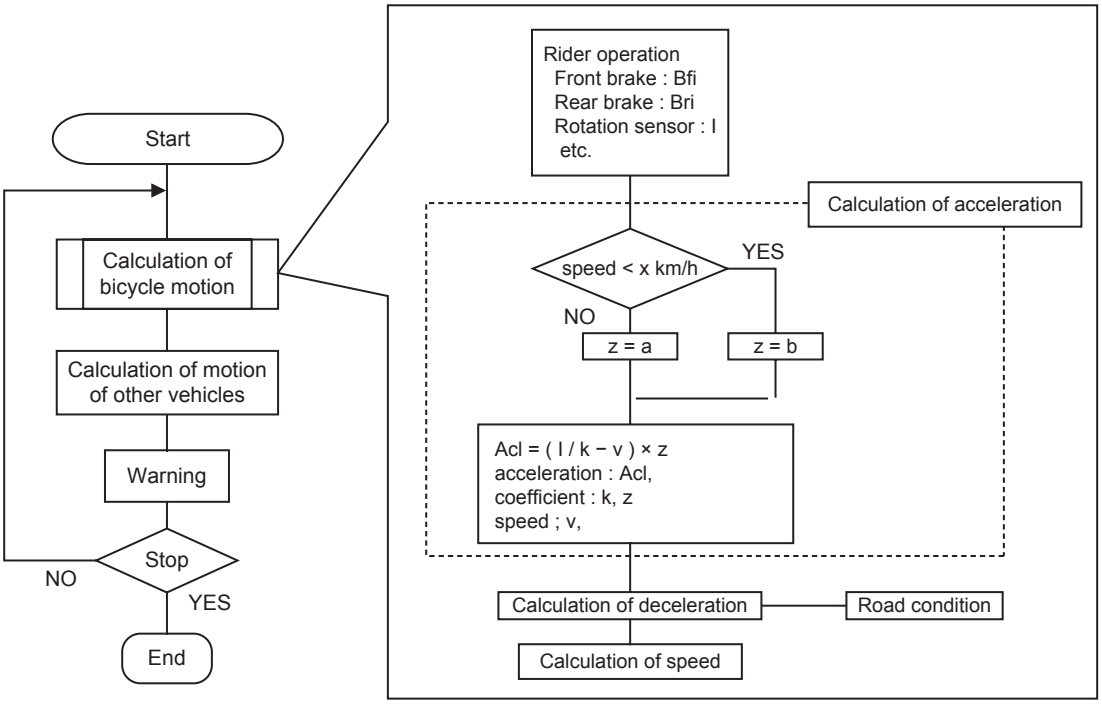


Fig. 12 Control flow of bicycle motion

risks and to learn to predict them), the "Quiz Course" (to learn about traffic signs and markings, rules and manners in a question format), and the "Case Study Course" (to help the user experience, in a short period of time, certain points anticipated about road cruising, such as cautions when crossing pedestrian crossings and the importance of stopping and checking for safety when going through intersections).

Riding simulators used at driving schools[10] assume that the rider is old enough to get a driving license, and consist of systems that let them function as teaching tools. The Bicycle Simulator, however, is also targeted at children who do not yet know the traffic rules, so effort was put into making learning fun and interesting. "ASIMO" is used as a character to explain points and give advice, by animation and voice. While earlier simulators compiled and evaluated results after cruising was finished, the new simulator considers the wide age range of learners, especially how lesson effectiveness diminishes as a young person's memory of how he or she operated the bicycle fades. So in addition to the general evaluation after cruising, the simulator reads riding position, collision type and the setting of encountered risks in real time and gives appropriate spoken explanations and advice instantly as the user operates the simulator.

The user is asked to select his or her age before starting to cruise, which enables changing what is in the field of vision (according to appropriate eye level for his or her physique) as well as cruising performance (maximum speed, acceleration/deceleration, etc.), the explanations and expressions used for the level of understanding of the age group, and traffic scene settings reflecting differences in applicable laws. This lets the simulator provide education in safe bicycle usage for a wide range of ages.

Aside from giving advice each time at the moment an unsafe situation occurs, if an accident happens while cruising on a course, immediately afterwards it is automatically replayed with a bird's eye view, so that the user can reflect on what happened and why, as soon as it happens. On the accident playback screen, the speed is shown numerically, and the amount of braking applied in front and back is displayed by bar graph. Because the simulator knows how the user was operating the left and right brakes, the system can provide instruction on brake operation (Fig. 13).

Finally, Fig. 14 shows the simulator in use in an actual traffic safety clinic.

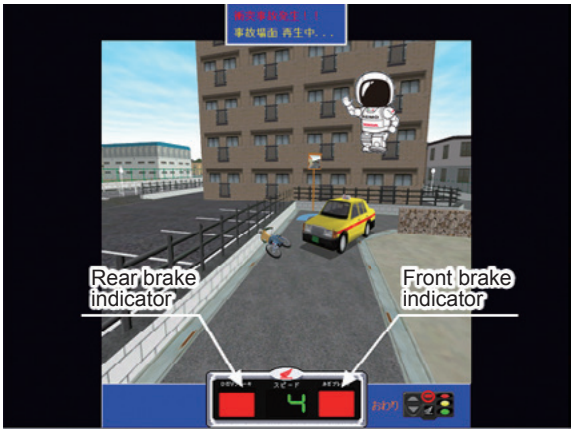


Fig. 13 Screen image of replay after riding



Fig. 14 Bicycle simulator in actual training

5. Conclusion

Honda has developed a Bicycle Simulator that is fun and interesting for everyone from children to senior citizens to learn traffic rules and manners and enhance their ability to predict risks. The Bicycle Simulator has the following functions.

- A function to learn the action of checking for side and rear safety
- A function that corresponds to walking and pushing the bicycle to learn the correct way to ride in conformity with the Road Traffic Law (Japan)
- A function to give training content and advice appropriate for each age group
- A function to experience risky situations that can be encountered in mixed traffic situations

6. Afterword

After trials with a prototype at numerous elementary, middle and high schools, senior citizen bicycle clinics, events and exhibitions, Honda received many comments saying that even children not yet able to ride a bicycle were able to learn safe operation and found it fun and interesting. The simulator was released as a product in October 2009 and went into mass production in February 2010. Honda hopes that as the Bicycle Simulator becomes widely disseminated and used, it will help to achieve a healthy traffic society.

References

(1) Japan Bicycle Promotion Institute (JBPI): Bicycle statistics in Japan, Vol. 42 (2008) (in Japanese)
(2) Institute for Traffic Accident Research and Data Analysis (ITARDA): The annual traffic accident statistical database, Edition 2008 (2009) (in Japanese)
(3) Ichimi, S., Miyamaru, Y., Aoki, K., Suzuki, K.: Development of Riding Trainer for Safety Riding Education and Its Features, Journal of Society of Automotive Engineers of Japan, No. 121-06, p. 15-18 (2006) (in Japanese)
(4) Institute for Traffic Accident Research and Data Analysis (ITARDA): The annual traffic accident statistical database, Edition 2006 (2007) (in Japanese)
(5) Ogawa, K.: Evaluation of a Road Safety Educational Program "Production of Hazard Maps" for Schoolchildren, International Association of Traffic and Safety Science Review, Vol. 32 No. 04, p. 31-40 (2007) (in Japanese)
(6) http://www.npa.go.jp/bicycle/pdf/0611teigen.pdf, 2010/4/22
(7) http://www.npa.go.jp/bicycle/pdf/0705menkyo.pdf, 2010/04/22
(8) Suzuki, K., Miyamaru, Y., Ichimi, S., Aoki, K.: Development of Bicycle Simulator and Its Features, Journal of Society of Automotive Engineers of Japan, No. 71-07, p. 15-18 (2007) (in Japanese)
(9) JP, 07-21391, A(2007)
(10) Miyamaru, Y., Yamasaki, G., Aoki, K.: Development of a Riding Simulator and Its Prehistory, Journal of Society of Automotive Engineers of Japan, No. 59-00, p. 1-4 (2000) (in Japanese)

■ Author ■



Kenji SUZUKI



Yukio MIYAMARU

Brain Machine Interface Technology Enabling Control of Machine by Human Thought Alone

Tatsuya OKABE* Kentaro YAMADA* Masahiro KIMURA* Akihiro TODA*
Masaaki SATO** Okito YAMASHITA** Yusuke TAKEDA** Mitsuo KAWATO**

ABSTRACT

Recently, brain machine interface (BMI) technology has gathered a lot of attention in regard to controlling a machine without any physical devices. Although this interface is often seen in science fiction, it is becoming realistic due to dramatic progress in brain and computer science. By directly connecting a human's brain with a machine, a machine can be controlled by human thought alone.

Honda has challenged the development of this BMI in collaboration with ATR and Shimadzu. By developing a new brain measurement using electroencephalography (EEG) and near-infrared spectroscopy (NIRS) and applying sparse logistic regression into BMI to detect a human's intention correctly, we successfully developed a highly accurate interface of BMI.

To validate our BMI system, we used 4-motor imagery task often used in BMI research. The performance of our BMI is more than 90% accuracy. This result is competitive against other BMI research groups.

1. Introduction

Because of the dramatic progress in brain science and the rapid development of computer science, the possibility of controlling a robot or a computer by thought alone is becoming more realistic. This technology is called brain machine interface (BMI) or brain computer interface (BCI). By connecting a brain with a machine directly, a machine can be controlled by human thought without any physical devices[(1)-(3)].

Honda began to research brain machine interface technology in 2005 with collaboration of the Advanced Telecommunication Research Institute International (ATR) in Kyoto. In 2006, Honda and ATR succeeded to control a robot hand by BMI using functional Magnetic Resonance Imaging (fMRI) in real time and showed the potential of BMI[(4), (5)]. In this experiment, a user lay in fMRI and really performed the game of scissors-paper-rock. The fMRI measured the brain activity in the user's primary motor area that controls the muscle of hand. Then, the data obtained were analyzed to detect a human's task, i.e., scissors, paper or rock. We achieved more than 85% accuracy of detecting a task to control a robot hand. However, there were several issues to be solved, i.e., the real movement that contradicts the merit of BMI, the huge size of a brain scanner that cannot be used in daily life and the difficulty to show the future possibility with BMI due to the simple machine.

Therefore, we tried to replace a rather big fMRI by electroencephalograpy (EEG)[(6)] and near-infrared spectroscopy (NIRS)[(7)] to create a brain-activity scanner which can be used in daily life. In addition, we challenged to realize a BMI system that can control a machine or a robot by a human's thought alone and used a real robot that can more clearly show the future possibility with BMI.

Although both EEG and NIRS can be used in daily life, the noise-signal ratio is worse than fMRI. Therefore, the key-topic of BMI with EEG and NIRS are how to enhance the performance of BMI. Furthermore, the replacement of really performing actions by imagining actions results in weak and unclear signals. To tackle these issues, we developed a new algorithm and simultaneous and real-time brain-activity scanner of EEG and NIRS.

* Fundamental Technology Research Center

** Advanced Telecommunications Research Institute International Computational Neuroscience Laboratories

To validate our BMI system, we performed 4-motor imagery tasks explained later and achieved 91.6% accuracy of BMI. Using this BMI system, we also succeeded to control a robot by human thought alone with high accuracy.

In this paper, we introduce this new BMI which was released to the world on 31st, March, 2009.

2. Future Possibilities with BMI

Figure 1 shows future possibilities if the BMI technology is fully developed. As examples, we show four possibilities. Since BMI has huge possibilities, however, these are only a few examples.

A robot or robots can help perform housework when you are busy like washing dishes (a). A trunk of a car can be opened only by thought when you have a lot of packages (b). The room temperature can be adjusted by controlling the air-conditioner according to a user's own desire (c). One can communicate with other people without any utterance and/or can gather information by imaging an object. If we look around our lives, we can easily find possibilities which BMI can support us and make our lives more fruitful. We strongly believe that the realization of BMI can lead to a more enjoyable life.

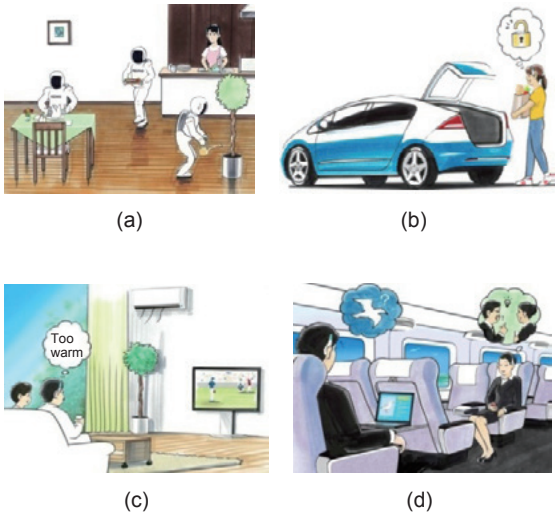


Fig. 1 Images of our future lives using BMI

3. Brain Machine Interface

As the term of BMI explicitly indicates, BMI is a direct interface between a brain and a machine. Following the dramatic progress of brain science and the revelation of brain functionalities, the research for BMI has been encouraged since 1980s and many research outputs have been reported since 2000s[2]. In the beginning of BMI research, a so-called invasive BMI, which needs surgery to install sensors on/in a cortex, was popular due to clear brain signals. Although invasive BMI has much attention, in particular, in the USA, non-invasive BMI, which needs no surgery and no damage of a cortex, a skull and a scalp, has started to be researched recently.

We can also classify BMIs reported in the literature into two areas, an input-type BMI and an output-type BMI. An input-type BMI inputs electric signals of a machine into a human's brain. A famous example of this BMI is a cochlear implant which is already used by millions of persons in the world[3]. Oppositely, an output-type BMI detects brain-activity signals by a brain scanner, understands the meaning of these signals and sends a human's intention to a machine to control it. According to the direction of signals toward a brain or a machine, we can classify BMI as an input-type or output-type BMI.

Our BMI reported here is a non-invasive and output-type BMI since we use scanners which need no damage against human's body. As our BMI is non-invasive, it has the possibility to become an innovative interface for not only disabled people but also healthy people.

The basic flow of a non-invasive and output-type BMI is shown in Fig. 2.

First, scanners measure brain signals generated by the brain activity of the subject, i.e., a user of BMI (a) and obtain the data (b). Although we will explain the details of scanners later, we use both electroencephalograpy (EEG) whose data is shown in the upper images of (b) and near-infrared spectroscopy (NIRS) whose data is shown in the lower images of (b). Thereafter, a certain signal processing is carried out for the obtained data and the human's intention is determined by a "classifier," which learns the pattern of data and classifies new data to understand the human's intention (c). Finally, this analyzed intention is sent to a machine to do a pre-programmed action (d). From Fig. 2, it is easy to understand the importance of measuring brain signals correctly and detecting a human's intention accurately from the data obtained. These two topics are key issues of BMI.

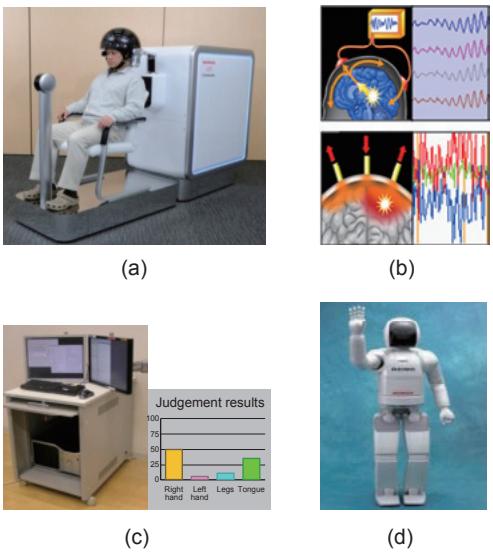


Fig. 2 Basic flow of our BMI

4. Newly Developed Brain-Activity Scanner

We developed a new brain-activity scanner which can simultaneously measure EEG and NIRS and process these data in real time. This scanner is named the "Simultaneous and real-time brain-activity scanner of EEG and NIRS" (hereafter EEG-NIRS scanner). Before our development, the simultaneous EEG-NIRS scanner has been already developed by Shimadzu Corporation[7]. However, this system is an off-line system where the system stores the EEG and NIRS data and the data obtained can be analyzed after an experiment. Therefore, a real-time BMI could not be realized only using this EEG-NIRS scanner. In addition, the EEG and NIRS are controlled independently. This results in the difficulty to synchronize both data and to exploit them to enhance the performance of BMI. Hence, we tried to develop a new EEG-NIRS scanner which can solve the above issues. By developing a new EEG-NIRS scanner, a real-time and highly accurate BMI system can be realized.

In this section, we first explain the basic principles of EEG and NIRS and thereafter we introduce our EEG-NIRS scanner.

4.1. Electroencephalograpy (EEG)

When a certain region of a cortex works, tiny electric flow exists in the region. Although a skull is nearly an insulator, a small amount of electricity leaks from a skull and flows on a scalp. An EEG measures this flow as electric potential.

Note that cerebrospinal fluid (CSF) which is a conductor, fills up between a cortex and a skull and EEG cannot measure the brain-activity strongly even with the sensor on the working regions. The conductivity of CSF and the insulation of a skull result in the difficulty of determining the working area in a cortex by EEG sensors. Due to this difficulty, the performance of BMI by EEG is dramatically reduced.

4.2. Near-Infrared Spectroscopy (NIRS)

The activated region of a cortex consumes oxygen. To provide new oxygen to this area, blood with oxygenated hemoglobin gathers and brings oxygen. By using near-infrared light, the NIRS watches this blood to determine the activated area. NIRS uses three lights, i.e., 780 nm, 805 nm and 830 nm of wave length, and introduces these lights at the scalp. According to the difference of absorption of these lights passing oxygenated or deoxygenated hemoglobin, NIRS measures brain activity. Since a few seconds are necessary to gather blood in an activated area, NIRS needs a few seconds to measure brain activity. Therefore, as explained later, our experiment is forced to continue a motor imagery for about 10 seconds due to this phenomenon.

4.3. EEG-NIRS Scanner

Figure 3 shows our developed EEG-NIRS scanner. Using a commercial off-line system of simultaneous measurement by EEG and NIRS (Shimadzu Corporation)[7], our on-line system of an EEG-NIRS scanner was developed. To realize this system, we developed a synchronization system of EEG and NIRS and a framework of a real time system which can calculate in real time. The former is necessary for measuring brain activity correctly since a gap of a few milliseconds results in the difficulty of understanding brain activity. The latter sends measured signals of EEG and NIRS via local area network (LAN) to another computer that can process signals in real time.

The right-bottom figure in Fig. 3 shows the EEG and NIRS sensors that are installed on a human's scalp. The sensors with black cables are the NIRS and the white cables are the EEG. In the NIRS sensors, the sensors with red labels are transmitters which generate near-infrared light and the ones with blue labels are receivers which receive near-infrared lights passing through the cortex. There are 16 red NIRS transmitters and 16 blue receivers. Since the combination of a transmitter and a receiver consists of one logical channel, our system can measure 48 areas. Each logical channel measures oxygenated hemoglobin and deoxygenated hemoglobin simultaneously. The number of EEG sensors is 66. Since 2 of 66 sensors are used as reference sensors, the EEG can measure 64 areas.

Figure 4 shows the details of the synchronization system and the on-line system. The personal computer with the role of controlling time sends 8-bit TTL signals (0 V or 5 V) to the EEG and NIRS via the BNC cables. Both EEG and NIRS record brain-activity data and the TTL signals. Then, these data are sent to the personal computer with role of synchronization via LAN. Thereafter, the synchronization is carried out using TTL signals in the EEG and NIRS data.

The real-time system mainly consists of sharing files and ring buffers. In a computer where signal processing is performed, several sharing files where ring buffers are installed are made. Using these files, a computer can receive the data of the EEG and NIRS in the real time. Furthermore,

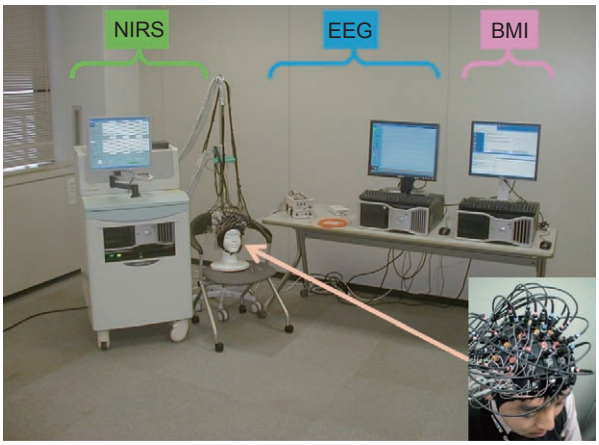


Fig. 3 Brain activity real-time measurement system using EEG and NIRS

the system has the functionality called “broadcasting” to quickly send the data to several computers.

The apparatus shown in Fig. 5 incorporates all the components shown in Fig. 3. Although this collection seems to be easy, an issue appears, e.g., electric-magnetic interference, and results in the worsening of the signal-noise ratio of EEG. Therefore, to minimize the effect of the electric-magnetic interference, we divided the apparatus seen in Fig. 5 so they are independent from others in regard to electric-magnetic interference. Furthermore, the arrangements of each apparatus are optimized to reduce noises. To more easily use this scanner as a BMI system, we added a display that identifies the tasks toward a subject, a chair for the subject, a LED that shows the status of the BMI system and casters that let us easily bring this system. To avoid unnecessary burden for a subject caused by sensors, an arm is located between the big white box and the sensors to help reduce the weight of the sensors.

The approximate size of this apparatus is 2000 (mm) length, 700 (mm) width and 1400 (mm) height and the approximate weight is 300 (kg). Although this apparatus is rather large, it can be used in many places and we believe it is the first step of BMI being used as an innovative interface in daily life.

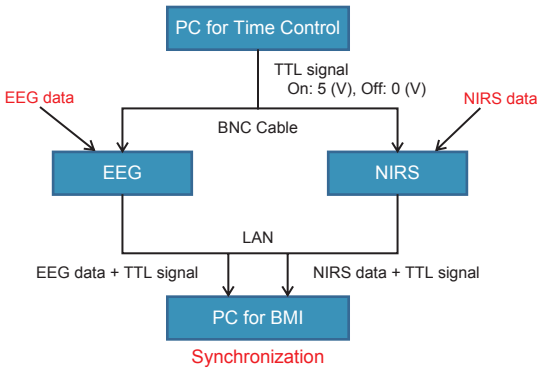


Fig. 4 EEG-NIRS synchronization system



Fig. 5 Brain activity measurement system for BMI

5. Algorithm for the Detection of a Human’s Intention

5.1. Extraction of Features

By using our EEG-NIRS scanner, we can obtain 96 data (oxygenated and deoxygenated hemoglobin) from NIRS and 64 data from EEG per one sampling. In this paper, the sampling rate of NIRS is 7.69 Hz and of EEG is 256 Hz. Since a subject images for 10 seconds, about 170 million data can be collected even if we record brain activity during the task of image. Furthermore, as several signal processing can be used, the number of total data becomes too huge.

However, most of the data are not important for detecting a human’s intention. Therefore, it is significant to detect the important data correctly. For tackling this issue, we applied Sparse Logistic Regression (SLR) proposed by Yamashita[8] into our BMI system. By using SLR, we tried to extract the important features from the huge amount of data. The main target of SLR is the calculation of the boundary by automatically eliminating unimportant data from stochastic point of view. In Fig. 6, each point shows the data from a task. Generally, the dimension of the data is very high. To avoid the difficulty of visualization for high dimensional data, we simplify Fig. 6 as 2 dimensional data.

In SLR, the boundary for classifying data is first calculated using the labeled data obtained in the learning session. Thereafter, a test session is started. In the test session, a human’s intention will be determined according to whether new data are located in the right side of the boundary or the left side. For example, if new data are the left side of the boundary, these data are considered as ones from the image of A.

5.2. Combination of EEG and NIRS Data

As explained in the latest chapter, we can measure brain activity by EEG and NIRS simultaneously. To exploit this capability, we stochastically combine the results of EEG and NIRS to correctly detect a human’s intention. From each data of EEG and NIRS, two results of a human’s intention are obtained. At the same time, we can easily calculate the correctness of the resultant class which relates to the distance between considered data and the boundary. In addition, the output of SLR is two of a resultant class

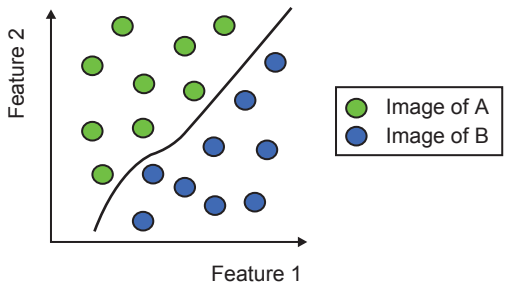


Fig. 6 Image of classification (binary classification shown as example)

and the correctness that can be calculated from the distance between calculated boundary and new data; the correctness is calculated using the distance and the sigmoid function. Since two correctness are calculated from EEG and NIRS, we simply multiply both of them, normalize them and pick up the larger correctness as a final result (Fig. 7).

Let denote P_i^E, P_i^N, I, and T as the probability of the task i by EEG, the one by NIRS, the set of all possible tasks, and the expected task, respectively. The above procedure can be shown in mathematical forms as follows:

$$T = \arg\max_{i \in I} P_i^{Total}$$

Here, P_i^{Total} can be calculated as follows:

$$P_i^{Total} = \frac{P_i^E \cdot P_i^N}{\sum_{i \in I} P_i^E \cdot P_i^N}$$

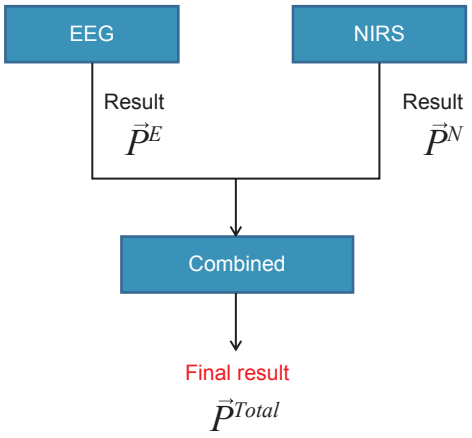


Fig. 7 Combination of EEG / NIRS results

6. Experiments

6.1. Tasks

To validate our BMI system, we use four-motor imagery task which is famous in the community of BMI. In this task, a user's right hand, left hand, tongue or foot is selected and the user imagines the movement of the selected part of body. We did not indicate how to the user should imagine but strictly ordered no body movement while imaging. In this four-motor imagery task, we can easily expect 25% of correctness even if we determine a human's intention randomly. This percentage is called "chance rate" which indicate the expected percentage if you determine randomly. In BMI, the performance of system should be considered comparing this chance rate. It is not necessary to say that we should talk BMI after showing the number of selections and the performance of BMI.

6.2. Experimental Protocol

In this paper, we examine a test consisting of 10 runs (learning sessions) where learning data are obtained and 1 run (test session) where an obtained boundary is tested using test data accordingly. Since the total time of learning sessions is rather long, voluntary intervals are added during sessions.

One run consists of 28 images by combination of each 7 imagery of right hand, left hand, tongue and foot. Here, the order of imagery is random. One image is often called one trial in the BMI community. To indicate which part of the body should be considered, we use a small display in front of a user to order a task. One trial is carried out with a 3-second rest, a beep sound 1 second before task indication, a 1-second task indication, a 10-second imagery and a 6-second rest. To use signal processing easily, we add a 5-second rest and a 10-second rest before an experiment and after an experiment. See Fig. 8 for details.

To learn SLR, we use 280 data (each 70 images of the right hand, left hand, tongue and foot) obtained as learning data in the experimental day and past day (if necessary). After learning SLR, we validate our BMI system using 28 data obtained as test data.

Principally, we do not have to indicate tasks during a test session because the user can freely control a machine or a robot using BMI. However, we indicate the task using the frontal display to evaluate the performance of our BMI since we cannot see a user's intention, that is necessary to check whether the result of BMI is correct or not.

Figure 9 shows examples that identify tasks to a user. To correctly carry out an experiment, we remove EOG signals caused by the movement of eyes and EMG signals generated by the movement of muscles. Furthermore, we

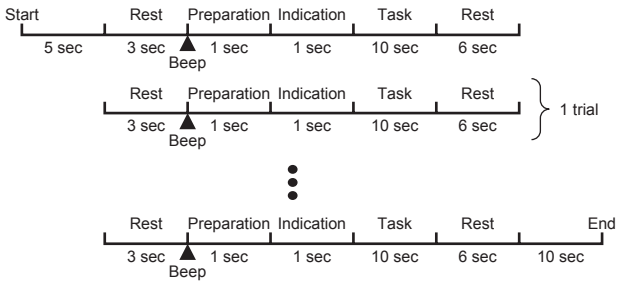
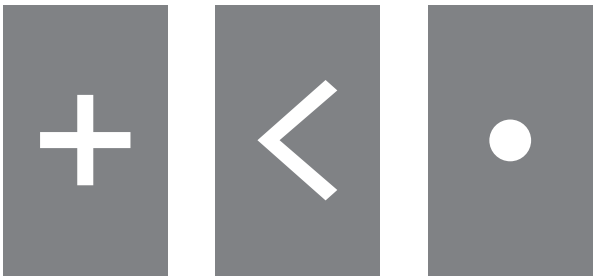


Fig. 8 Experimental protocol. 'One run' includes 28 trials.



(a) Rest (b) Task indication (Left hand) (c) Task (Image)

Fig. 9 Indications for subjects

sufficiently avoid big visual stimuli by controlling the brightness of the display.

6.3. Experimental Environment

As explained before, our final target is the usage of BMI in daily life, so we did not use a special environment instead we performed our experiment in a normal meeting room with several windows.

6.4. Sensor Position

The positions of the NIRS sensors on a scalp are shown in Fig. 10. Although EEG can cover a whole head, NIRS cannot because of the restricted number of sensors. Therefore, we install NIRS sensors around the C3 and C4 areas noted in Fig. 10 which are defined by 10-20 method[6]. To cover the C3 area and C4 areas, 4×4 sensors cover one of two. The interval of each sensor is 3 cm.

6.5. Subjects and Informed Consent

Three healthy men (20-40 years old, right handed) participated in this experiment. Based on the ethics provision defined by our company, we explained the details of our experiment and obtained their agreement before carrying out our experiment.

6.6. Performance Evaluation

To evaluate the performance, the correctness in 28 trials in the test session is calculated. Using the latest data in the latest 115 sessions including 10 learning sessions in an experimental day, SLR is learned. Thereafter, 28 trials were tested.

6.7. Data Processing

The data processing used here for EEG and NIRS are as follows. First 9-second data are picked up from original EEG data and adjusted to remove biases. Then, the important sensors are selected and band-pass filtering is done. Finally, we calculate the square of the data and averaged them by moving averaging. These data called as "features" are used for learning SLR. Regarding NIRS, we use on-line band-pass filtering, select the important sensors and times. Finally, we carry out moving average to obtain features.

In this flow, several parameters should be fixed, e.g., cut-off frequency, time window, etc. To determine the parameters, we obtained the data for tuning parameters. Using several parameter set, we determined the one of them that shows the best performance of the BMI on the data for tuning parameters. Note that the data for tuning parameters are never used in the validation to avoid overestimation.

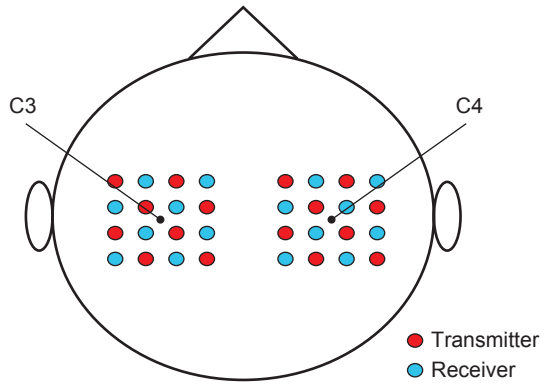


Fig. 10 Positions of NIRS sensors. The red points show transmitters and the blue ones are receivers.

7. Results

7.1. Obtained Data

Examples of data obtained are shown in Fig. 11. In Fig. 11, (a) was obtained by EEG and (b) by NIRS. Due to the space limitation, only a part of the data is shown. Each row indicates a task, i.e., left hand, right hand, tongue and foot, respectively, from top to bottom. Using these data and the explained signal processing, we can obtain features which are used as features for the classifier.

7.2. Effects of Newly Developed Methods

The resultant performance of our BMI is shown in Fig. 12. In Fig. 12, 18-day results are shown.

Although a certain variance can be observed, the averaged performance is 91.6% which is world-wide level of 4 motor-imagery tasks in BMI. Note that the performance of 91.6% is little bit different from the one which was introduced on 31st, March, 2009. The main reason of this difference is a change in signal processing.

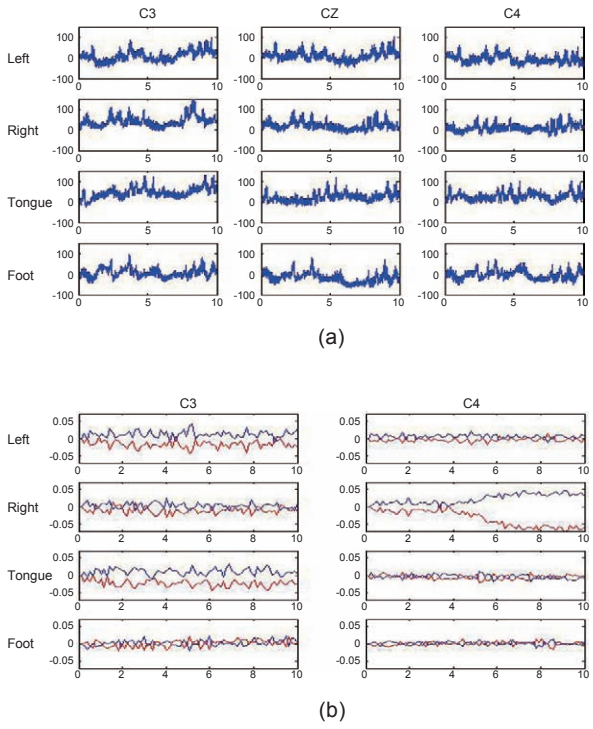


Fig. 11 Raw data of EEG (a) and NIRS (b)

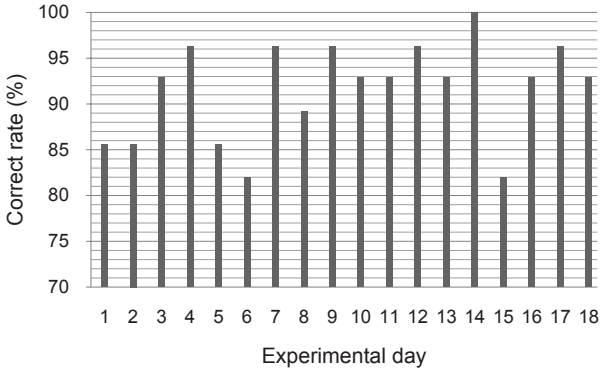


Fig. 12 Performance of our BMI system under 4 motor imagery tasks

8. Demonstration using a Robot

In a test session, we really move a machine. For this experiment, we used a humanoid robot, ASIMO. The intention (right hand / left hand / tongue / foot) determined by our BMI is sent to ASIMO as a command by a wireless LAN, and then ASIMO acts the predefined action shown in Table 1 and Table 2. By this, we can control a robot using a human's intention alone. Note that the tables are one of examples of motions.

When ASIMO receives a result as a command from the BMI system, ASIMO first speaks the sentences defined in Table 1 according to P_T^{Total}. As explained before, P_T^{Total} is the probability of the task T. Then, ASIMO acts and speaks according to T (the expected task) shown in Table 2.

9. Summary and Future Works

This paper introduces a new technology called brain machine interface (BMI) that enables the control of a robot / a machine by a human's thoughts. By developing an information extraction scheme and an EEG-NIRS scanner, we achieved 91.6% accuracy in the 4-motor imagery task. Furthermore, we succeeded in the combination of our BMI and a humanoid robot ASIMO to be controlled by a human's thought alone. In the future, we would like to develop a smaller scanner which can easily be used in our daily life and to improve the performance of our BMI system.

Acknowledgment

This research was done with strong collaboration of the Honda Research Institute Japan, Honda R&D, Advanced Telecommunications Research Institute International and Shimadzu. We appreciate the many staffs for their devoted support. In particular, we would like to express our gratitude to Mr. Takao Sako, Mr. Takahito Tamagawa and Mr. Ryosuke Hayashi. Without their contribution, we could not have finished this work.

Table 1 First actions of ASIMO in BMI experiment

Range of P_T^{Total}	Action and speech of ASIMO
$P_T^{Total} \geqq 0.90$	Speaks "Hai, kekka wo uketorimashita. Machigai nai to omoimasu". (Yes, I received the result. I strongly believe that the result is correct.)
$0.90 > P_T^{Total} \geqq 0.70$	Speaks "Hai, kekka wo uketorimashita. Tabun, atteiru to omoimasu". (Yes, I received the results. Maybe, the result is correct.)
$0.70 > P_T^{Total}$	Speaks "Hai, kekka wo uketorimashita. Chotto jishinga arimasenga". (Yes, I received the results. I am not sure that the result is correct.)

Table 2 Second actions of ASIMO in BMI experiments

Image by subject	Action and speech of ASIMO
Right hand	Raises a right hand. Speaks "Migi-desu" (right hand)
Left hand	Raises a left hand. Speaks "Hidari-desu" (left hand)
Tongue	Imitates eating. Speaks "Shita-desu" (tongue)
Foot	Steps. Speaks "Ashi-desu" (foot)

References

(1) Dornhege, G., Millán, J. R., Hinterberger, T., McFarland, D. J., Müller, K.: Toward Brain-Computer Interfacing, The MIT Press (2007)
(2) Wessberg, J., Stambaugh, C. R., Kralik, J. D., Beck, P. D., Laubach, M., Chapin, J. K., Kim, J., Biggs, S. J., Srinivasan, M. A., Nicolelis, M. A.: Real-time prediction of hand trajectory by ensembles of cortical neurons in primates, Nature, 408, p. 361-365 (2000)
(3) Kawato, M.: Brain Network Interface, Journal of the institute of electronics, Information and communication engineers, 91[2], p. 123-130 (2008) (in Japanese)
(4) Kamitani, Y., Tong, F.: Decoding the visual and subjective contents of the human brain, Nat Neurosci, 8(5), p. 679-685 (2005)
(5) http://www.honda.co.jp/news/2006/c060524a.html
(6) Ichijo, S. Takahashi, K.: The 101 chapters for reading electroencephalography, Igaku-Shoin (2003) (in Japanese)
(7) http://www.an.shimadzu.co.jp/prt/nirs/nirs_top.html
(8) Yamashita, O., Sato, M., Yoshioka, T., Tong, F., Kami-

tani, Y.: Sparse estimation automatically selects voxels relevant for the decoding of fMRI activity patterns, Neuroimage, 42, p. 1414-1429 (2008)

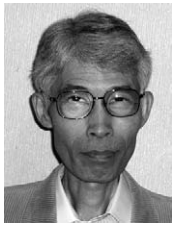
■ Author ■


Tatsuya OKABE


Kentaro YAMADA


Masahiro KIMURA


Akihiro TODA


Masaaki SATO


Okito YAMASHITA


Yusuke TAKEDA


Mitsuo KAWATO

System Modeling Technology for Powerplant Control Systems

Makoto MURAKAMI* Kazunori NOMURA*
Takashi HISAKI* Yasuhiko KASAHARA*

ABSTRACT

Developing automobile control systems requires shortened development times even as it becomes more complex each year to enhance fuel efficiency, take environmental measures and meet high safety standards. The more complex and large-scale a system becomes, the greater the impact that upstream design precision during V-process development has on subsequent processes, and the greater the issue becomes of shortening development time. To resolve this issue, this research devised a technique that uses a use-case scenario and a Quality Function Deployment sheet (QFD sheet) to elicit requirements. In addition, it uses a total trial sheet (TTS) incorporating elements of Model Driven System Engineering (MDSE), a requirements analysis and system model design technique, to analyze requirements and design a system model, thereby increasing specification completeness at the start of development.

1. Introduction

A development style called a V-process, as shown in Fig. 1, is frequently used to develop control systems. This process lays out the series of actions, from examination of specifications to completion of product, in the form of a V. A product is designed and then verified; if there are failures, the specifications are amended and the product verified again, and as this cycle is repeated, development goes forward. Recently, techniques have been used in which the developer uses simulation tools like Matlab or Simulink to design specifications up to the point of verification and do software development[1), 2)]. This lets the developer detect design errors in advance, such as logical errors in the specifications or inconsistencies in specifications and implement codes, which reduces the burden during actual equipment verification and lets software development proceed efficiently. In power plant development heretofore, consistencies between specifications and implement code enabled a high degree of development efficiency. On the other hand, like the electronics field in which the enhancement of microcomputer performance has enabled a rapid increase in the number of software applications, it is said that the greater the scale of the system under development, the greater the share of development that goes into eliciting and analyzing requirements and designing the system model[3)]. This makes it important to increase not only consistency between specifications and implement code, but also between pre-implementing requirements and specifications.

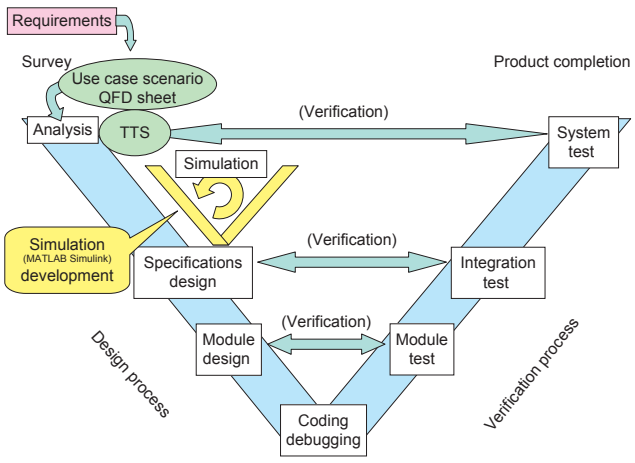


Fig. 1 V-process development

* Automobile R&D Center

Automobile control system development is expected to become more complex in the future, and a variety of initiatives have been tested[4), 5)]; increasing specification completeness at the start of development requires examining procedures that make requirement elicitation and analysis and system model design more efficient.

2. Development Goal

During power plant control system development, control specifications are written out to a point close to implement code in order to enhance development efficiency and quality. This has achieved shorter software development times and enhanced quality. On the other hand, it has become apparent that the grounds and particulars of such control specifications are hardly understood by anyone other than the designer, making it a challenge to convey the designer's technical intention to others.

To solve the above issues relating to the growing scale of systems hereafter and enhance development efficiency, it is important to elicit and analyze requirements and design system models efficiently at the design stage upstream in the V-process development and to document the process in a form understandable to those who are not directly involved in it, so this was set as the development goal.

The following techniques were devised as means for achieving the above aim.

(1) A technique for eliciting requirements with a use-case scenario and QFD sheet

(2) A requirements analysis and system model design technique using a TTS incorporating elements of MDSE

The relationship between techniques (1) and (2) is shown in Fig. 2.

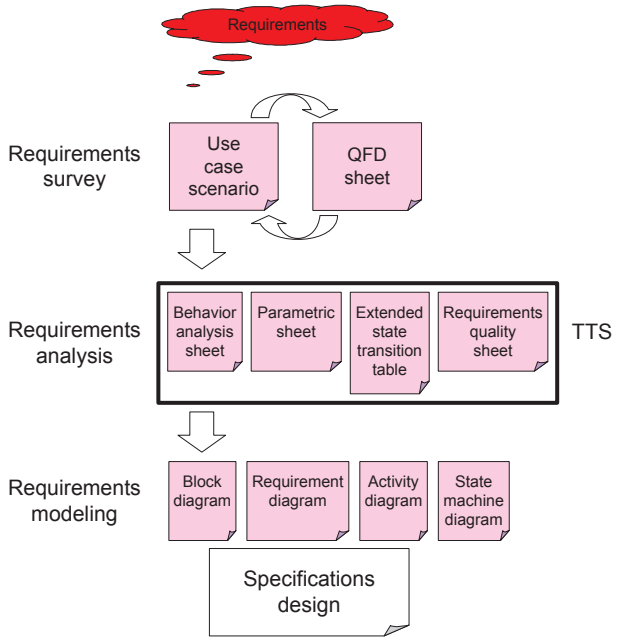


Fig. 2 Development flow

3. Requirements Elicitation Technique

To elicit the requirements at the upstream design stage, a use-case scenario is used, and a QFD sheet is drawn up to clarify the system configuration, constraints and requirement quality for those requirements.

3.1. Eliciting Requirements with Use-case Scenario

A use-case scenario[6)] sets up a scene to make it easy to elicit requirements and help the designer find requirements based on that scene. At this stage, a list is made of typical scenes in which the control is used, focusing on the when, where, what, who, why and how. A scenario is created that basically describes the listed scenes in text format, and first a main scenario is drawn up, that is, a scenario in which the system works normally. Figure 3 gives an example of such a description used for a power plant ECU control specification. Cases in which the condition of normal operation in the main scenario did not materialize are drawn up as extension scenarios. Additionally, exception scenarios are brought to light based on past troubles and designers' knowledge to find exceptional requirements. Figure 4 gives an example of an extension scenario and exception scenario used for a power plant ECU control specification. Thus, the scenario descriptions describe the system's functions as behaviors.

Inquiry work of scenario according to scene

Main actor: Compatibility check

Actors: Compatibility information, MIL, meter, ECM, TCM

Case 1: Cycle of usual drive

Case1-1: A compatibility check transmits compatibility information to other units, when it becomes Ignition-ON.

Case1-2: A compatibility check will perform a compatibility check if compatibility information about other units is received.

Case1-3: The compatibility check compares the compatibility information on other units with compatibility information on the subject unit, and judges a compatibility error.

MIL; Malfunction indicator lamp
ECM; Engine control module
TCM; Transmission control module

Fig. 3 Use case scenario

Case1: Cycle of usual drive

<Extended scenario>

Case1-1: **********

Case1-e1: **********

Case1-2: A compatibility check will perform a compatibility check if compatibility information about other units is received.

Case1-e2: When compatibility information about other units cannot be acquired, a compatibility check judges a compatibility error, and ends the compatibility check of this driving cycle.

Case1-3: **********

Case1-e3: **********

<Exception scenario>

Case1-ex1: After Ignition-ON, when compatibility check judged that the power supply was shut off, And compatibility check will perform a compatibility check again.

Fig. 4 Extension scenario and exception scenario

3.2. Clarifying System Configuration, Constraints and Requirement Quality with QFD Sheet

A QFD sheet clarifies the system configuration, constraints and requirement quality by examining the requirements, methods and technologies for each scene. The QFD sheet is prepared as a template as shown in Fig. 5, which increases the inclusiveness of the sheet so more requirements can be elicited. During product development, interviews alone are not sufficient to determine techniques for meeting requirements if the party that is the origin of the requirements does not grasp the system as a whole. QFD helps to clarify vaguely stated requirements in terms of quality characteristics and constraints, making these requirements more concrete.

Based on the scene for which the main scenario of the use-case scenario has been found, the technical requirements are determined with the following procedure to elicit who is the stakeholder and how this party relates to the system.

(1) Scene selection

The stakeholder is selected, and a scene brought to light for how that stakeholder relates to the system. Scene details are written in the scenario space. An example is shown in Fig. 6.

(2) Requirements selection

System requirements are brought to light for each scene. This clarifies who is the party that is the origin of that requirement.

(3) Clarification of technology for meeting requirements

This brings solutions to light for meeting requirements and clarifies constraints for meeting them with ECU. An example is shown in Fig. 7.

| (1) | | (2) | | (3) | | | | (4) | | | | | | | | | | (5) | | | | | | | | | |

(4) Technical requirements selection

The requirement quality is elicited by checking to what quality characteristics the solutions to the chosen issues relate. An example is shown in Fig. 8.

(5) Categorization according to quality characteristics

A check is made of what quality characteristics the solutions to the elicited issues relate to. Also, the comprising components from the QFD sheet are checked to clarify the system configuration. An example is shown in Fig. 9.

As above, the system configuration, constraints and requirement quality are clarified by QFD sheet. The clarified system configuration, constraints and requirement quality as well as the new scenario are reflected in the use-case scenario and managed as requirements documentation.

(4)								
Technical requirements								
	Relation post							
Technical requirements	Driver	Car	Engine	Service	ECM	TCM	Meter	Regulations
Add compatibility communicative function					○	○	○	○

Fig. 8 Relation post

| (5) | | | | | | | |

(Fig. 12). States are placed in rows and triggers in columns, and actions and transition results are written in for each combination. The extended state transition table includes the information necessary to create a state machine diagram.

Creating a state machine diagram makes it possible to discover transitions that would not be easy to discern in requirements documentation written in natural language (Fig. 13).

Serial	Requirement	
	ID	
1	1	A compatibility check transmits compatibility information to other units, when it becomes IG-ON.

Prior state				Trigger				Relationship (Prior state and trigger)	Action							
State ID	Block	Property	Condition	Trigger ID	Block	Property	Action		Action ID	Block	Object1		Object2		Action or state	
											Block	Property	Block	Property	Operation mode	Verb
C0101	System		IG-OFF	T0101			IG-ON	C0101&T0101	A0101	Compatibility check		Compatibility information	Other units			Transmits

Fig. 10 Total trial sheet (behavioral constructs study)

Serial	Prior state			
	State ID	Block	Property	Condition
14	C0901	System	State	Compatibility judge
15	C2801	System	State	Compatibility check
16	C3001	System	State	Compatibility analysis

Serial	Prior state			
	State ID	Block	Property	Condition
14	~~C0901~~			
15	C2801	System	State	Compatibility check
16	~~C3001~~			

Fig. 11 Example of term unification

State ID			S10	S100	S200	S210	S220
State name			Sleep	Initialization	Compatibility check		
					Data not received	Compatibility judging	Complete
Trigger							
ID	Block	Property	Action				
T0401	IG	State	ON	S100 TX0401				
T0402	ECM	State	Initialization process is completed		S200 TX0402			
T0501	ECM	State	Received compatibility information			S210 TX0501		
T0601	ECM	State	Judged compatibility (Pass)				S220 TX0601	
T0602	ECM	State	Judged compatibility (Fault)				S220 TX0602	
T3101	IG		OFF		S10 TX3101	S10 TX3101	S10 TX3101	S10 TX3101
Action ->					AC0401 AC0402	AC2801		

Trigger
State
Transition
Action

Fig. 12 Extended state transition table

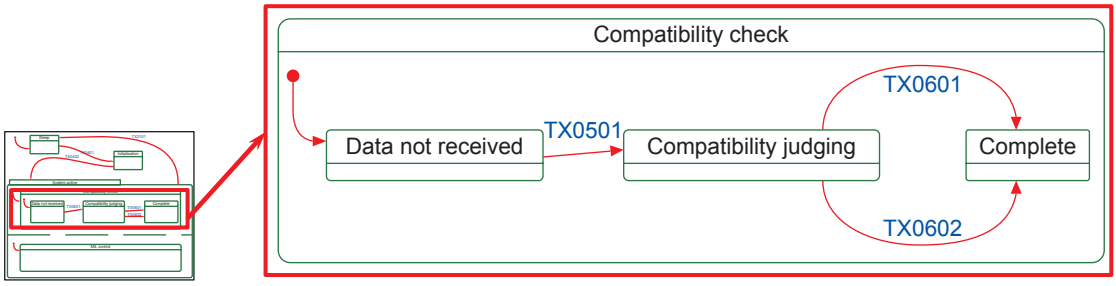


Fig. 13 State machine diagram

4.2. Model Design by Configuration Analysis

"Configuration analysis" refers to eliciting and analyzing lines of text from the requirements documentation that describe the configuration and relationships of components comprising the system and functions of those components.

"Components" refers to systems, parts and physical devices, and these have to be extracted both from a control system perspective and hardware perspective. In Section 4.1, components were picked out from a document expressing behavior. In this section, components are extracted from documents other than behavior documents (i.e., from "explanatory documents") and term unification is performed. Based on term unification results, one checks whether each element depends on existing systems or techniques, creates a hierarchy based on level of dependence to existing systems (those with a low dependence level are ranked higher) and summarizes the results on a block diagram (Fig. 14).

4.3. Model Design by Constraints Analysis

"Constraints analysis" refers to eliciting and analyzing lines of text from the requirements documentation that describe specifications and constraints as determined numerically, such as various factors or elements and target performance.

A constraints formula is examined from the parts of the requirements documentation in which specifications such as performance and limit values are expressed, where they are expressed numerically, and a parametric diagram is created by selecting the variables used in the constraints formula. As an example, Fig. 15 shows a parametric diagram that concerns ECM compatibility control. In this diagram, ECM and TCM have respective compatibility data within certain control values, and the diagram indicates that a compatibility judgment is made based on the relative size relationship.

4.4. Model Design by Requirement Quality Analysis

"Requirement quality analysis" refers to eliciting and analyzing sentences from the requirements documentation that describe quality requirements that cannot be expressed numerically.

Based on words that express degree, adverbs and adjectives in the sentences, as well as qualitative requirements of degree, state, etc. such as "optimal" or "automatically," are identified and written on a requirement diagram (Fig. 16). In upstream design stages, work is done only up to the point of summarizing requirement quality

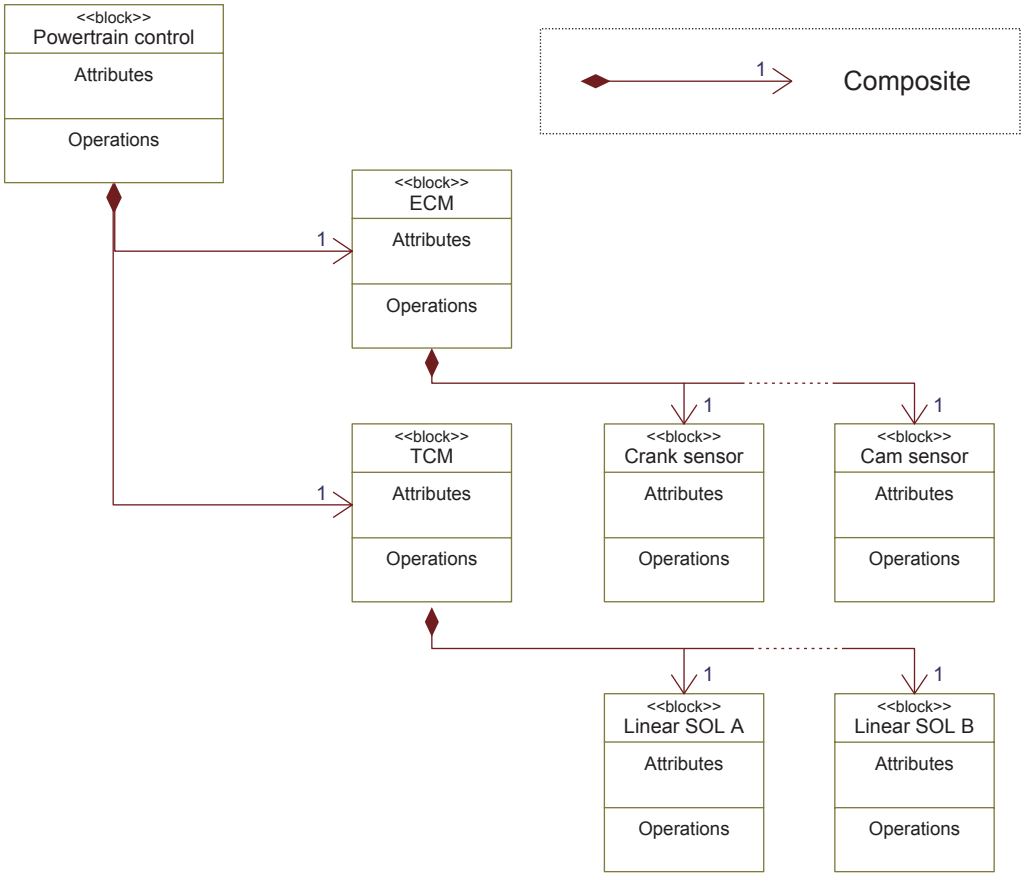


Fig. 14 Block diagram

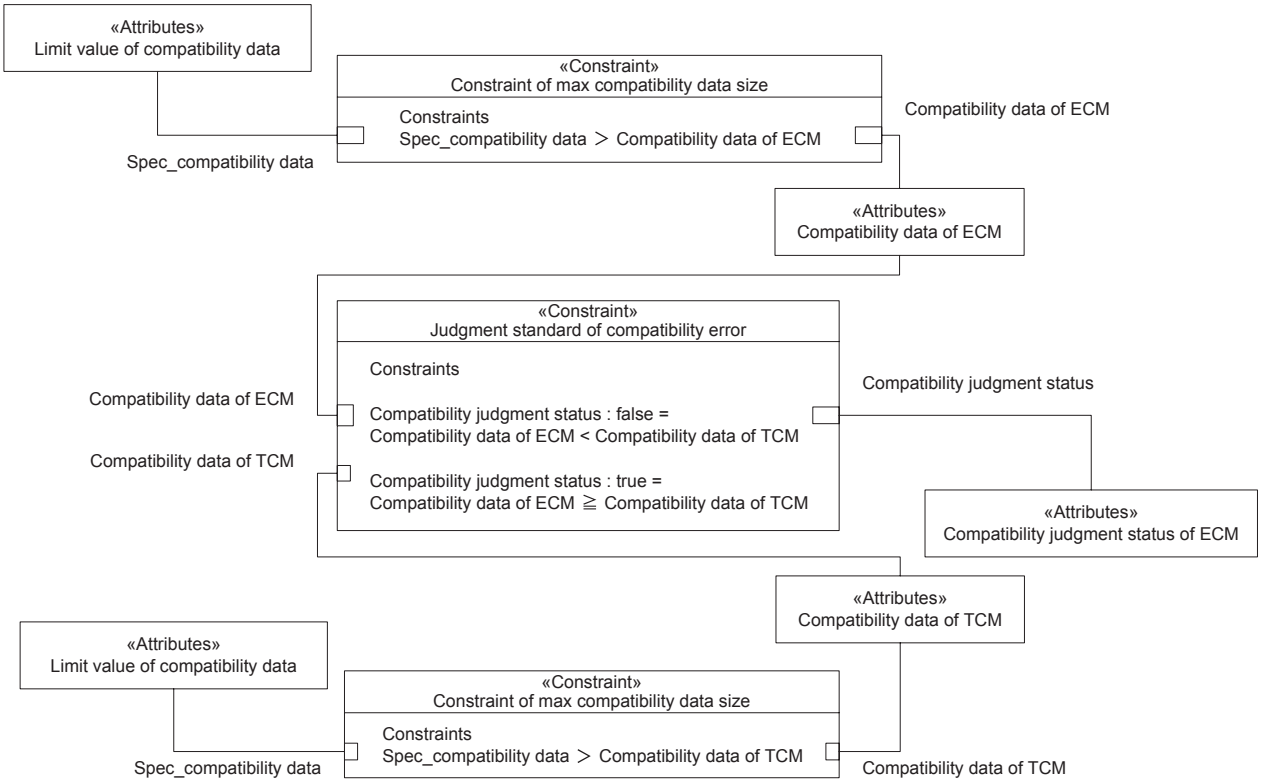


Fig. 15 Parametric diagram

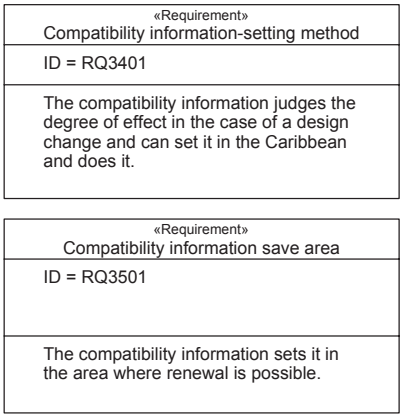


Fig. 16 Requirement diagram

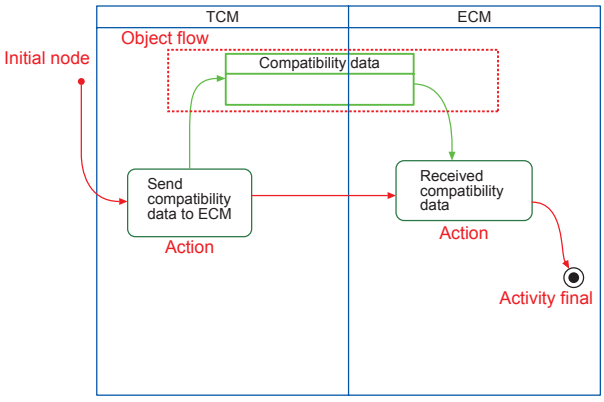


Fig. 17 Activity diagram

in a requirement diagram, and this is then developed into behaviors and constraints at the stage of examining specific ways of achieving it.

4.5. Behavior Detailing and Model Design

The state machine diagram created in Section 4.1. does not express the actions included in states. In order to clarify behavior, this section expands on functions using an activity diagram. Actions in each state are expressed using an activity diagram. In the activity diagram, information flowing out of the content of each action is anticipated and an object flow is added. Figure 17 gives an example of information sharing between components. Using an activity diagram to detail behavior can clarify data shared between components and help discover insufficiencies of data shared between components for the sake of continuity.

5. Conclusion

This paper has proposed a technique that can increase specification completeness at the start of development, help ensure a simple transition to downstream development with V-process development and keep work from being sent back upstream by using a use-case scenario and QFD sheet to pick out requirements and by using TTS incorporating elements of MDSE, a requirements analysis and system model design technique, to analyze requirements and conduct system model design.

References

(1) Minowa, S., Hirota, T., Yokoyama, H., Ishiguro, T., Ohtsuka, S.: Autocoding of Power Plant Control Software, Honda R&D Technical Review, Vol. 16, No. 1, p. 243-248
(2) Matsuyama, Y., Hagiwara, K., Seino, S.: Approach to Application of Executable Specifications in Development of Automatic Transmission Control Software, Honda R&D Technical Review, October, 2009, p. 120-129
(3) http://www.stevemcconnell.com/articles/art06.htm
(4) http://www.autosar.org/
(5) Katai, M.: Denshi seigyo software kaihatsu no youkyu kanri prosess no jirei shoukai, IBM, AT International 2008 (in Japanese)
(6) Cockbum, A., trans. by Yamagishi, K., Yazaki, H., Mizutani, M., Shinohara, A.: Writing Effective Use Cases, Shoueisha, p. 331 (2001) (in Japanese)

■ Author ■


Makoto MURAKAMI


Kazunori NOMURA


Takashi HISAKI


Yasuhiko KASAHARA

Development of Large-scale PIV Measurement Technique

Gensuke HOSHINO* Takashi YOSHINO*
Yuichi FUKUCHI* Minoru TERAMURA*

ABSTRACT

Particle Image Velocimetry (PIV) is one of the techniques used to experimentally clarify fluid flow phenomena. The advantage of PIV is the ability to non-intrusively measure the instantaneous velocity vectors of a flow field at multiple points. The flow field around an actual vehicle has large-scale flow structures, and requires a wide measurement area. A large-scale PIV measurement technique was developed that can measure this type of large-scale flow field.

An index capable of quantitatively evaluating the quality of the measurement was introduced, and the relationship between this index and the measurement accuracy was clarified. In addition, a seeding device that enables temporally and spatially uniform seeding of particles to the flow field, and a method to decrease laser light reflection were developed. Application of these technologies realized PIV measurement capable of evaluating an instantaneous velocity field over the large scale of 1.7 m x 1 m. A scanning system and integrated measurement software were also constructed, enabling multi-section measurement in a short time.

1. Introduction

Honda products center on mobility, and have a strong relation to fluid flow. It is thought that the need to examine and control various fluid flow phenomena will further increase in the future, from the viewpoint of enhancing fuel economy and comfort. Hot-wire anemometers, pitot tubes and other methods that insert probes for measurement are widely used as flow field measurement techniques to experimentally clarify flow field phenomena. However, there is the issue that probe insertion affects the flow field, making it a challenge to measure the original flow field. Laser Doppler Velocimetry (LDV) is a non-intrusive measurement method that does not use probes, but as measurement is performed at single points, a large number of measurement points is required to understand the entire flow field.

Particle Image Velocimetry (PIV) measures the velocity of a flow field by irradiating laser light into a seeded flow field, using cameras to image the scattered light reflected from the particles, and analyzing the particle images. By using this type of measurement method, PIV can non-intrusively and simultaneously measure the instantaneous velocity vectors of a flow field at multiple points. This makes it easier to understand the entire flow field, so PIV has come to be widely used in recent years.

However, PIV requires much measurement know-how, and trial and error is needed before accurate measurement is possible, so PIV can hardly be called an established measurement technology.

In addition, when measuring the flow field around an actual vehicle, the flow structure has a large scale, so wide-area measurement is desired. One example of this type of measurement is measurement over a 0.3 m x 0.3 m area by Pininfarina S.p.A.[1] However, when measuring an even wider area, the seeding method and the method for acquisition of clear particle images are issues. Therefore, this study organized and addressed these and other issues to establish a large-scale PIV measurement technique that can measure wide areas. This paper reports these technical contents.

2. Overview of PIV Measurement

PIV measurement seeds a flow field with micro particles that sufficiently track the flow, and irradiates the flow field with sheet-shaped laser light (light sheet) two times at a small time difference. This light sheet is reflected by the seeding particles, producing scattered light that is captured by imaging equipment such as a CCD camera. The particles move together with the flow, so the particle positions change in the two particle images shot at a small time

* Fundamental Technology Research Center

difference. This particle movement amount is obtained from the two particle images, and the velocity is calculated from the movement amount and the imaging time difference. Figure 1 shows a typical PIV measurement system configuration. Figure 2 shows an example of the obtained particle images.

The method used to calculate the velocity from the pair of particle images shot at a small time difference is as follows. First, the paired particle images are each divided into lattice-shaped interrogation windows. Correlation values are obtained as the movement amount parameter, from the distribution of brightness values (light intensity) within the interrogation windows that correspond to the same positions in both particle images. These correlation values are calculated using convolution operations and FFT. Figure 3 shows an example of an obtained correlation value distribution map. The movement amount that results in the maximum correlation value (first peak value) is used as the average movement value of the particle group within that interrogation window. Next, a velocity vector is calculated from that movement value and the time difference. The two-component velocity field within a two-dimensional plane can be visualized quantitatively by applying this method to all of the divided interrogation windows. In addition, a three-component velocity field can be measured (stereoscopic PIV) by acquisition of particle images using stereoscopic photography with two cameras, and performing the appropriate camera calibration.

This is the PIV measurement principle, so it is important to acquire clear particle images. This requires much measurement know-how, including seeding methods, laser power, and imaging conditions.

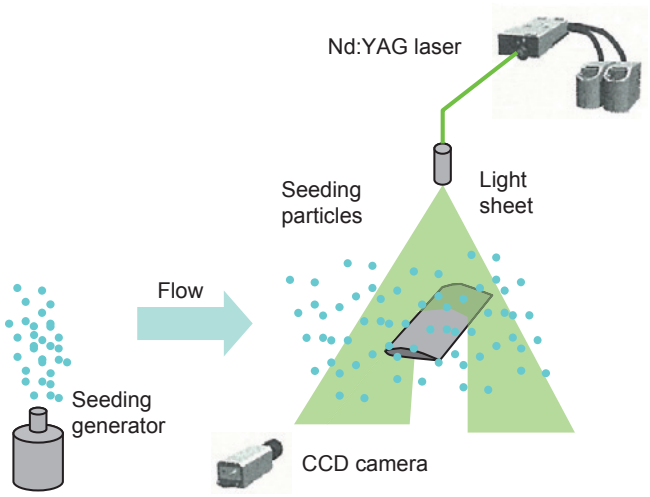


Fig. 1 PIV system

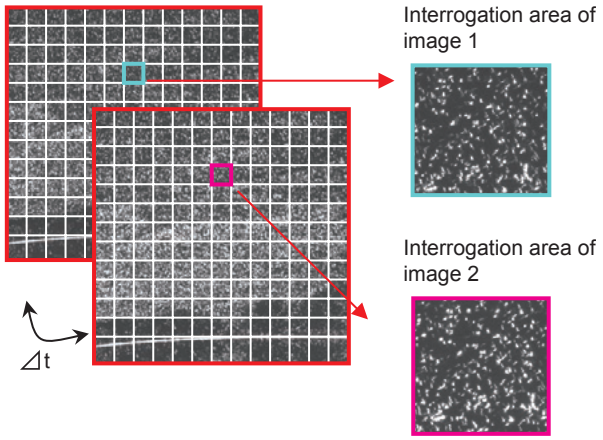
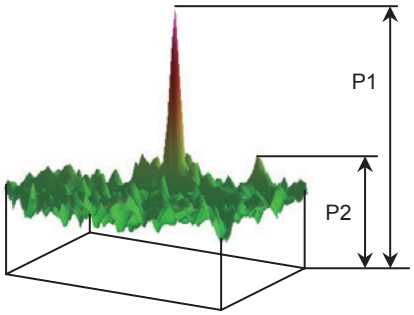


Fig. 2 Example of particle images



P1: First peak value
P2: Second peak value

Fig. 3 Correlation map

3. Target Values for Large-scale PIV Measurement

Technical development of large-scale PIV measurement was initially promoted by application to the downstream flow after the front tire of an F1 racing car[2]. Examination of the flow phenomena required a measurement area scale of 1 m x 1 m, so this is set as the measurement area target value.

In addition, the ratio of the number of vectors obtained, excluding error vectors, to the total number of vectors that can be obtained within the subject measurement area was defined as the vector acquisition ratio. This vector acquisition ratio target value was set at 90% or more. Here, error vectors refer to vectors for which the correct movement amount could not be calculated from the particle images. The basis for setting a vector acquisition ratio of 90% or more as the target value is that even when a single error vector point occurs, as long as the vectors for the surrounding eight vector points can be obtained, that error vector can be eliminated and interpolation performed as appropriate using the surrounding vectors.

The PIV measurement procedure consists of acquisition of particle images, transferring the shot images to a PC for analysis, and performing post-processing on the analyzed velocity field. When performing PIV measurement in a wind tunnel, shortening the time required for the series of measurement and analysis operations at the test site is also desired.

Measurement of the downstream flow after the front

tire of an F1 racing car had a low vector acquisition ratio of approximately 20%. In addition, many particle images had to be shot and analyzed to evaluate the average flow field, which took much time.

The measurement and analysis time target value for two-component measurement was set at 20 minutes (excluding the setup time) per measurement section.

In addition, detailed three-component measurement of a flow field requires multi-section measurement. When performing multi-section three-component velocity measurement, wind tunnel operation has to be stopped each time there is work to change the measurement section. Therefore, a system was constructed that can measure ten sections without the need to stop wind tunnel operation during three-component measurement, and the measurement time target value was set at 30 minutes.

4. Technical Issues for Large-scale PIV Measurement

4.1. Quantization of Evaluation Method and Applicable Limits of Measurement Conditions

Particle image quality is important in PIV measurement. Factors thought to determine particle image quality include seeding, laser power, spatial distribution of the light sheet intensity, camera sensitivity, imaging magnification, and the noise level, that is to say the background light and light reflected from the test object. Thus far there was no index to quantitatively evaluate the quality of PIV measurement, so clear guidelines could not be set for the various measurement parameters mentioned above. For this reason, trial and error was needed before measurement could be performed each time the measurement subject or measurement location changed. This made it important to clarify the application limits of the measurement parameters before measurement.

4.2. Reduction of Reflected Light

During PIV measurement, in addition to scattered light reflected from the seeding particles, light sheet reflected from the surface of the test object is also included in the shot images as noise, and may result in a drop in particle image quality. The effects of this reflected light can be reduced by image processing, but when the reflection intensity is high, this may hinder detection of the scattered light reflected from the particles, which is an issue. Figure 4 shows the conventional technique for reducing reflected light. The wall surface is coated with a fluorescent paint that, when irradiated by light, emits light (fluorescence) with a different wavelength than the incident light. This fluorescence is then reduced using a band-pass filter installed in front of the camera (wavelength shift method).

However, even when using this method, some test objects have surfaces that are a challenge to treat directly, so a more general-purpose method to reduce reflected light was needed.

4.3. Seeding

Seeding is an important technique that affects PIV measurement quality, and involves many items that need to be investigated such as the material and diameter of the particles to be used, and the method of seeding the particles to the flow field. Laskin nozzle generators that can atomize fluids such as olive oil, and fog generators that can vaporize glycol-based solvents into particles are commercially available and widely used. Laskin nozzle generators can produce uniform particles with a diameter of approximately 1 μm. In addition, fog generators are able to generate large volumes of particles.

Achieving a uniform temporal and spatial distribution of seeding particles over a wide area is an issue for large-scale PIV measurement. When the particle distribution is temporally or spatially uneven, velocity vectors cannot be obtained in areas that lack sufficient particles, and the vector acquisition ratio drops. A major advantage of PIV measurement is the ability to quantitatively visualize an instantaneous two-dimensional flow field. However, full use cannot be made of this advantage when there is particle unevenness. The commercially available seeding devices mentioned above were unable to address this issue, so efforts were made to develop a new seeding device.

4.4. Acquisition of Clear Images of Particles

To image a wide area, the light sheet should be irradiated over a wide area. Assuming that the same laser device is used, this means that the laser power per unit area drops, and the images of the particles in the shot particle image become unclear. In these cases the error vectors increase and sufficient velocity vectors cannot be calculated. Therefore, acquisition of clearer particle images even at a low laser power per unit area is an issue.

4.5. Shortening Measurement and Analysis Times

The average flow field obtained by the PIV measurement procedure described in Chapter 3 is obtained by averaging multiple instantaneous velocities acquired from a pair of particle images. When these instantaneous velocities have many missing vectors due to error vectors or other factors,

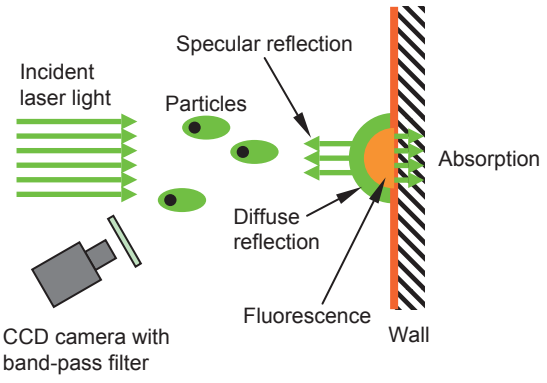


Fig. 4 Schematic view of laser light reflection from fluorescent coated wall

the average number of measurement times, that is to say the number of shot particle images, has to be increased, which increases the measurement and analysis time.

In addition, when the particle image quality is low, image processing is needed before analyzing the particle images, which is also a factor increasing the analysis time.

For these reasons, a method that enables evaluation with a small average number of measurement times without processing images in advance is needed to shorten the measurement and analysis times. Obtaining better quality particle images and increasing the vector acquisition ratio can lead to shorter measurement and analysis times.

When measuring and examining a complex flow field, it is better to understand the three-dimensional flow field, and the results using only a single section are insufficient. In these cases, multiple sections should be measured as described in Chapter 3. Changing the measurement section involves tasks such as setting up the laser optics system and camera and calibrating the camera, and performing these tasks efficiently is an issue.

5. Methods for Addressing Each Issue

5.1. Quantization of Evaluation Method Using the Peak Ratio

Investigations were carried out to address the various issues described in Chapter 4. First, an index capable of quantitatively evaluating the quality of PIV measurement was introduced. Basic tests were performed, and it was found that using the peak ratio as this index enabled quantitative evaluation of the measurement quality. As described in Chapter 2, the velocity vector is calculated from the movement amount, which is the peak correlation value of the light intensity distribution in a pair of interrogation windows. The peak ratio is expressed by the ratio between the first peak value and second peak value of these correlation values (Fig. 3).

PIV measurement was performed using a flow of a known velocity with different measurement conditions, such as the laser power and imaging magnification, to obtain the relationship between the peak ratio and measurement error. The difference between the measured movement amount and the movement amount obtained from the actual velocity was used as the error. Figure 5 shows the relationship between the peak ratio and measurement error. The figure shows the error as the number of pixels.

This figure shows that measurement error increases when the peak ratio is less than 1.2. Therefore, peak ratio is used as an index to evaluate measurement, and velocity vectors with a peak ratio value of 1.2 or less are judged as error vectors.

Use of the peak ratio as an evaluation index enabled clarification of the measurement conditions such as the laser power, imaging magnification, camera lens aperture, and particle density.

5.2. Reduction of Reflected Light by Application of a Fluorescent Sticker

The new technique addressed the issue of reducing reflected light described in Section 4.2, by using fluorescent film with adhesive (fluorescent sticker). This increased the general applicability and effectively reduced reflected light. The basic tests performed to realize this method are described below.

Figure 6 shows a schematic diagram of the test apparatus.

The test apparatus irradiated the test piece with a Nd:YAG laser that emitted light sheet using a cylindrical lens, imaged the reflected light with a CCD camera, and evaluated the light intensity. Three types of coverings were applied to the test piece surface based on the wavelength shift method described in Section 4.2. These were a fluorescent spray (Asahipen Corporation), a fluorescent sticker (Sumitomo 3M Limited), and a matte-coated fluorescent sticker. Material that emitted fluorescent light with a wavelength of 532 nm, which is the second harmonic wave of the Nd:YAG laser, was selected as the fluorescent material. The fluorescent film had a glossy surface, so evaluation was also performed in the matte condition to evaluate the effects of the surface condition on the reflection characteristics.

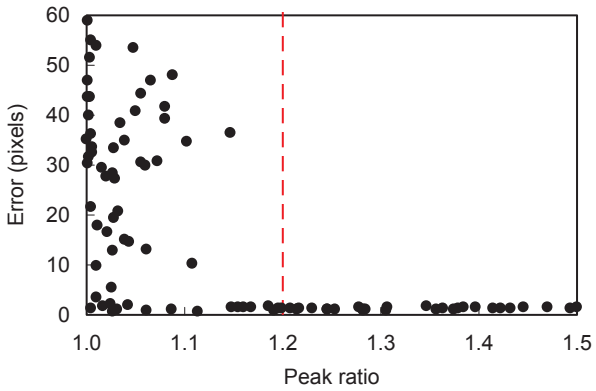


Fig. 5 Relationship between peak ratio and measurement error

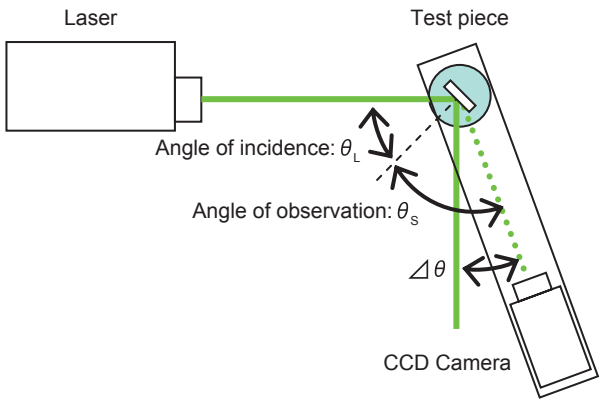


Fig. 6 Schematic diagram of experimental setup for reflection intensity

In actual PIV measurement, the angles at which reflected light is imaged differ according to the shape of the test object and the measurement layout such as the camera position. Therefore, the reflection intensity was evaluated at different imaging angles. Figure 7 shows these results. The figure shows the relationship between the intensity of the reflected light from the imaged test piece and the imaging angle $\Delta\theta$. $\Delta\theta$ is defined as the angle calculated from the difference between θ_S and θ_L in Fig. 6. The reflection intensity of the fluorescent sticker was the maximum at an imaging angle of 0° (mirror reflection), and decreased as the angle increased (diffuse reflection). The figure also shows that the fluorescent sticker had a smaller reflection intensity than the fluorescent spray at angles greater than 0°.

In addition, the matte-coated fluorescent sticker exhibited approximately the same reflection intensity as the fluorescent spray, indicating that the glossy condition of the surface affects the reflection characteristics. The reflection that affects the particle images in PIV measurement is mainly diffuse reflection, so the fluorescent sticker with a glossy surface is the most effective at reducing reflected light. Use of this fluorescent sticker enabled reduction of light reflection from the wall surface to 1/10 compared to the conventional fluorescent spray.

5.3. Development of an Original Seeding Device

A seeding device was developed to address the issues described in Sections 4.3 and 4.4. Development aimed for global seeding that fills the entire wind path area with particles to realize a temporally and spatially uniform particle distribution. This required long-lived particles to help prevent particle extinction during the measurement time. Basic tests were performed on particle life, and the results showed that Dioctyl sebacate (DOS) was suitable as a particle material.

An additional aim was to increase the particle diameter to acquire clearer particle images during large-scale measurement. This is because the intensity of the scattered light reflected from the particles is thought to be proportional to the square of the particle diameter. The AKI D impinging-type pneumatic spray nozzle [H.IKEUCHI Co., Ltd.] can increase the particle diameter, so this AKI D nozzle was investigated as a device component by comparison with a Laskin nozzle using DOS. A Laskin nozzle and an AKI D nozzle were used to seed DOS inside a compact circular wind tunnel to simulate the particle status in a wind tunnel. The diameter of the particles inside the circular flow was measured by the phase Doppler anemometer. Figure 8 shows the particle diameter distribution for a sample size of 50000 particles. The horizontal axis of the graph shows the particle diameter, and the vertical axis shows the number of particles measured. Note that the vertical axis does not show numbers of particles greater than 150.

This comparison showed that the AKI D nozzle distribution included larger diameter particles than that of the Laskin nozzle. These results indicate that the maximum particle diameter in the circular flow was approximately 4 μm. In addition, Fig. 9 compares the peak ratios when PIV measurement is performed using AKI D nozzle particles and Laskin nozzle particles.

This figure shows that the AKI D nozzle particles result in a higher peak ratio. This is thought to indicate that percentage of large-diameter particles increased, which increased the peak ratio.

In addition, PIV measurement measures the movement amount of seeding particles mixed into the flow, so having the particles sufficiently track the flow is important

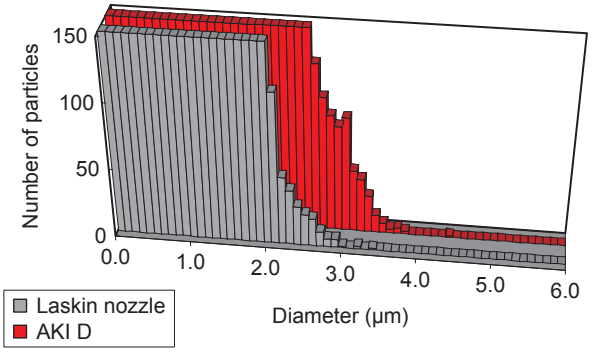


Fig. 8 Histogram of particle diameter

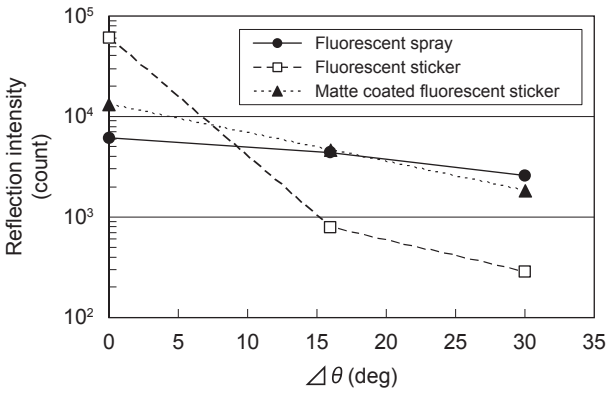


Fig. 7 Comparison of reflection intensity

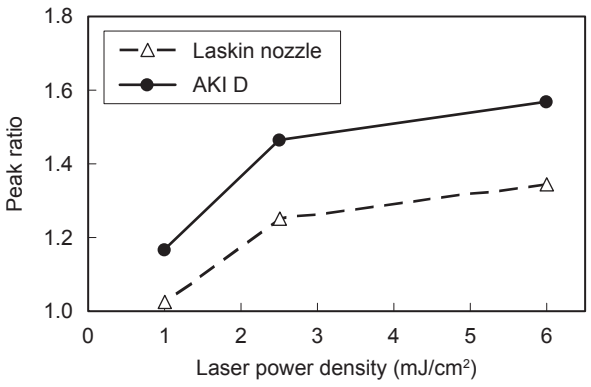


Fig. 9 Comparison of peak ratio

from the viewpoint of accurate flow measurement. Flow tracking performance generally tends to decrease as the particle diameter increases. As mentioned above, the particles sprayed by the AKI D nozzle have a maximum particle diameter of 4 μm. Therefore, the flow tracking performance[3] of particles of this diameter was confirmed. Figure 10 shows the frequency at which the flow fluctuates and the tracking performance of the particles, using the particle diameter as the variable parameter. The vertical axis of the graph shows the ratio of the particle velocity to the flow velocity. In this figure, for example when the area around a door mirror (typical length 0.2 m) is measured at a flow velocity of 100 km/h, the typical frequency at which the flow fluctuates is thought to be approximately 140 Hz. At this frequency, the tracking error of particles with a particle diameter of 5 μm is approximately 0.2%. This indicates that particles seeded by the constructed device adequately track the flow.

Based on the above results, an original seeding device was constructed using AKI D nozzles. This enabled temporally and spatially uniform seeding, which in turn enabled acquisition of clear particle images with a low laser output per unit area. Figure 11 shows a photograph of the device. The device used four AKI D nozzles with the aim of reaching the particle density required for measurement in a short time. Pressurized air and DOS are supplied to each of the nozzles. The DOS is supplied to the nozzles from a pressurized tank.

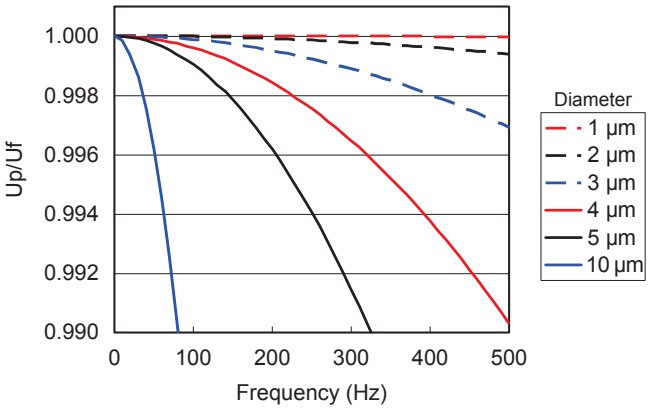


Fig. 10 Velocity lag in periodic air flow

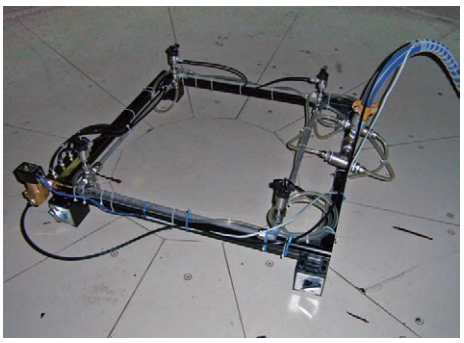


Fig. 11 Seeding system

5.4. Development of an Original Scanning System and Integrated Control Software

When performing stereoscopic PIV measurement as described in Chapter 2, it is important to calibrate the cameras to calculate the three-component velocity using the parallax between the two cameras. This camera calibration is performed using an imaging object (calibration target) with calibration points arranged in a lattice shape. The calibration method consists of setting the calibration target at the measurement position parallel to the light sheet, imaging the calibration target with each camera, and analyzing the images. When performing multi-section measurement, calibration should be performed for each measurement section, which increases the task process time and the measurement time. Therefore, for this technique, a scanning system was constructed to reduce the task process and measurement times. Figure 12 shows this scanning system.

This system places two cameras and a light sheet optical system on a coaxial traverse system, enabling movement to an arbitrary position while maintaining the relative distances between the two cameras and the light sheet. Use of this scanning system enabled multi-section measurement with a single camera calibration. In addition, the scanning system needs to control various devices such as the traverse device, cameras, laser device, and timing controller. Therefore, integrated control software was compiled that controls these devices and enables automated multi-section measurement.

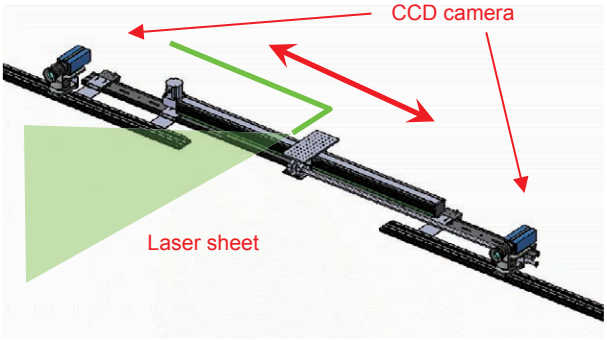


Fig. 12 Scanning system

6. Technical Verification Tests

6.1. Wind Tunnel Tests Using an Actual Vehicle

PIV measurement was performed around an actual vehicle in a vehicle wind tunnel to verify the various technologies described thus far in actual wind tunnel tests. The subject flow was the downstream flow after the door mirror. This flow was measured by irradiating light sheet in a horizontal section from the side and measuring the two-component velocity in the two-dimensional plane imaged from above by the camera.

Light sheet was also irradiated in a vertical section from the side, and stereoscopic PIV measurement was

performed using two cameras positioned on both sides of that light sheet. In addition, scanning stereoscopic PIV measurement was performed by traversing this stereoscopic PIV measurement section in the direction of the flow, and the obtained particle images were analyzed for streamline tracing and to extract the vortical structure and other information.

The light source used for PIV measurement in this vehicle wind tunnel had a wavelength of 532 nm, which is the second harmonic wave of a double-pulse Nd:YAG laser [New Wave Research] with output power of 200 mJ/pulse. The particle images were shot using PCO4000 CCD cameras [PCO AG] with 4008 x 2672 pixels. The laser irradiation and CCD camera exposure timing were controlled by a LC880 timing controller [Labsmith]. The fluorescent sticker described in Section 5.2 was attached to the vehicle body as shown in Fig. 13, as a light reflection countermeasure. The seeding device described in Section 5.3 was installed on the floor sufficiently downstream from the vehicle. When seeding was performed using this seeding device, the particle density required for measurement was reached in approximately 30 seconds. The particle images were analyzed using the PIV analysis software Koncerto [Seika Corporation], and analysis was performed by parallel processing using a PC cluster to shorten the analysis time.

6.2. Measurement Results

Figure 14 shows the measurement results for the instantaneous two-component velocity at the door mirror position.

The measured area was 0.7 m x 0.5 m. Error vectors were eliminated, and the eliminated vectors were interpolated using the surrounding vectors.

The vector acquisition ratio here was 95%, which achieved the initial target. Figure 14 shows that the door mirror wake is quantitatively visualized, and a flow structure of approximately the same scale as the door mirror can be seen.

Figure 15 shows the average instantaneous velocity vectors. These averages were calculated from the results of measuring the instantaneous velocity vectors obtained in Fig. 14 100 times at a frequency of 0.5 Hz. The figure shows that reversing flow occurs in the area immediately after the mirror. The reversing flow structure seen in the instantaneous velocity field did not appear in the averaged flow field, indicating that this structure is an unsteady flow phenomenon.

In this manner, PIV measurement can be used to evaluate steady flow fields, and also unsteady flow phenomena.

Figure 16 shows the average three-component velocity measurement results obtained by scanning stereoscopic PIV.

The measured area was approximately 1.7 m x 1 m, and ten sections were scanned at a pitch of 60 mm in the flow direction. The measurement frequency and the post-processing of the obtained vectors were the same as those noted previously. The measurement time for each measurement section was 200 s. When the flow velocity was 100 km/h and a door mirror dimension of 0.2 m was set as the typical length, the characteristic time of the flow field was approximately 1/140 s. The measurement time at each section was sufficiently long compared to the characteristic time of the flow field, so the obtained measurement results are thought to be a steady flow three-dimensional three-



Fig. 13 Car with fluorescent sticker

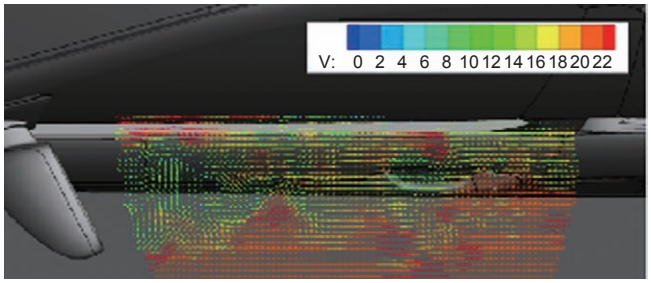


Fig. 14 Measurement result (instantaneous velocity field)

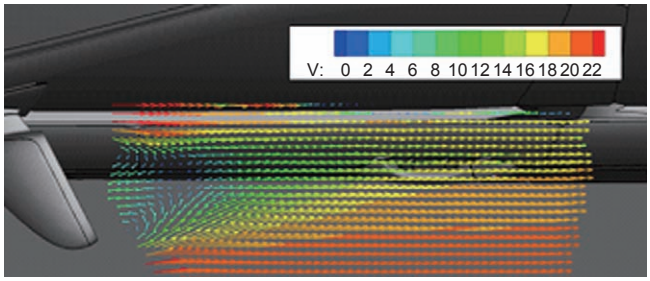


Fig. 15 Measurement result (time averaged velocity field)

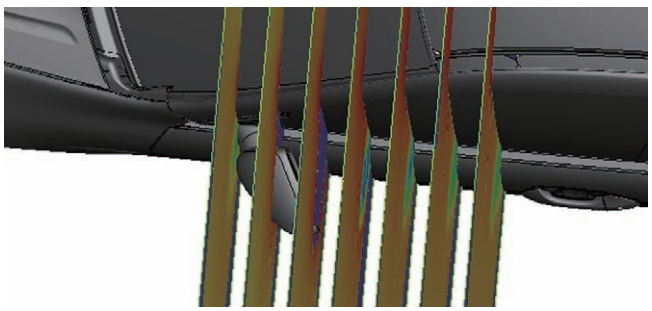


Fig. 16 Measurement result (scanned planes)

component velocity field, and three-dimensional streamline tracing is possible.

Figure 17 shows the streamline tracing results at typical points. This figure shows that the velocity loss area to the rear of the door mirror recovers while swirling in a three-dimensional vortex. Applying the scanning system to this type of complex flow field enables experimentally clarifying actual phenomena, and further deepening understanding of flow phenomena.

6.3. Shortening Measurement and Analysis Times

The PIV measurement of the downstream flow after the front tire of an F1 racing car first performed as described in Chapter 3 had a low vector acquisition ratio of approximately 20%. This meant that 400 instantaneous velocity field measurements needed to be averaged to evaluate the average flow field, so the analysis time was 175 minutes per measurement section.

In contrast, application of the technique described thus far to measurement around the door mirror of an actual vehicle increased the vector acquisition ratio to 95%, which enabled evaluation of the instantaneous velocity fields, and also reduced the number of particle images required for evaluation of the average flow field. The average flow field could be evaluated by averaging 100 instantaneous velocity field measurements as described in Section 6.2. This resulted in a measurement and analysis time of 15 minutes per measurement section, which was less than the initial target of 20 minutes. Realizing temporally and spatially uniform seeding and acquiring clear particle images reduced the number of particle images required, and reducing the reflection intensity reduced the need for image processing before analysis, resulting in a shorter time.

In addition, construction of a scanning system and integrated control software enabled three-component measurement of multiple sections with a single wind tunnel operation. Specifically, the measurement time for ten sections was 24 minutes, which was less than the target of 30 minutes. This was achieved by enhancing the vector acquisition ratio, which reduced the number of particle images required, and by enhancing operability and enabling automated measurement with the integrated control software.

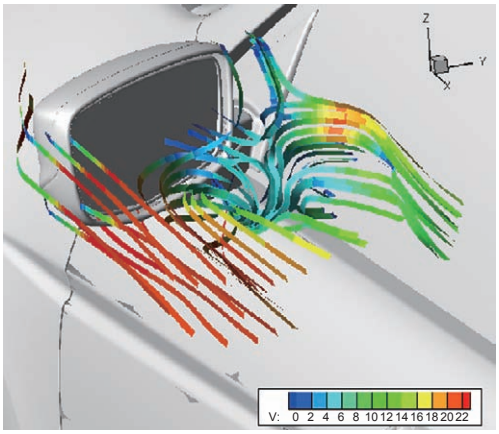


Fig. 17 Streamline around mirror

7. Conclusions

A large-scale PIV measurement technique was developed that can measure large-scale flow fields such as those around an actual vehicle. This technique was verified by measuring the downstream flow after a vehicle door mirror. This technique was able to measure a 1.7 m x 1 m area with a vector acquisition ratio of 95%, thus confirming it as a method for experimentally clarifying the flow field around an actual vehicle.

(1) The peak ratio was introduced as an index that can quantitatively evaluate the measurement quality. This enabled judgment of error vectors as well as quantitative evaluation of the effects of various measurement parameters on measurement, which helped to ascertain the measurement limits.

(2) Use of a fluorescent sticker increased general applicability, and realized a method for reducing the light reflected from the test object to 1/10 that of the conventional method.

(3) A new seeding device was developed that is suited to large-scale PIV measurement. This device realized temporally and spatially uniform seeding and enabled the acquisition of clear particle images at low laser output per unit area, which increased the vector acquisition ratio.

(4) Increasing the vector acquisition ratio enabled reducing the number of particle images required, and achieved a measurement and analysis time of 15 minutes per measurement section during two-component measurement.

(5) Construction of a scanning system and integrated control software enabled measurement of multiple sections with a single wind tunnel operation, and achieved a measurement time for ten sections of 24 minutes.

8. Afterword

PIV measurement can be applied to various flow fields, from micro-scale flows to large-scale flows such as reported in this study. The effective use of this PIV technology can help verify CFD and experimentally clarify various fluid flow phenomena. This is expected to enhance performance of machines that are affected by fluid flow, and lead to further development of fluid flow dynamics.

References

(1) Cogotti, A.: Upgrade of the Pininfarina Wind Tunnel-the New “13-Fan” Drive System, SAE Paper, 2006-01-0569 (2006)

(2) Ogawa, A., Mashio, S., Nakamura, D., Masumitsu, Y.,

Minagawa, M., Nakai, Y.: Aerodynamics Analysis of Formula One Vehicles, Honda R&D Technical Review, F1 Special (The Third Era Activities), p. 152-162
(3) Prestridge, K., Vorobieff, P., Rightley, P., Benjamin, R.: Flow visualizations and measurements of the mixing evolution of a shock-accelerated gas curtain, International Symposium on Shock Waves (ISSW22) (1999)

■ Author ■


Gensuke HOSHINO


Takashi YOSHINO


Yuichi FUKUCHI


Minoru TERAMURA

Rapid Trial-Production Technique for Aluminum Alloy Engine Components with Hollow Construction using Block Buildup-Brazing

Takeshi WADA* Tatsuo JIKIMOTO* Hidenori OKAJIMA*

ABSTRACT

A process was developed for manufacturing cylinder heads and other such aluminum alloy engine components with hollow construction by means of block-buildup brazing and a high-speed machining technique. This approach does not use a mold as the conventional sand-mold casting technique does, so it was able to manufacture a high-precision cylinder head for preliminary test purposes in a short period of time, and so allow a rapid determination of specifications.

1. Introduction

In the initial stages of engine development, there is demand for manufacture of test engines in a short time for the purpose of performance verification and other such activities for the early determination of specifications. However, the trial production of water-cooled cylinder heads and other such integral components with hollow construction ordinarily involves sand-mold casting using a core, and the mold building and casting require considerable time. The establishment of buildup-brazing technology and high-speed machining from solid material with dividing of the hollow construction made mold-building unnecessary and enabled trial production in a short time.

2. Block-Buildup Brazing and High-Speed Machining Technique

Figure 1 shows the fabricating process. Working from a 3D model that is a manufacturing drawing, a 3D

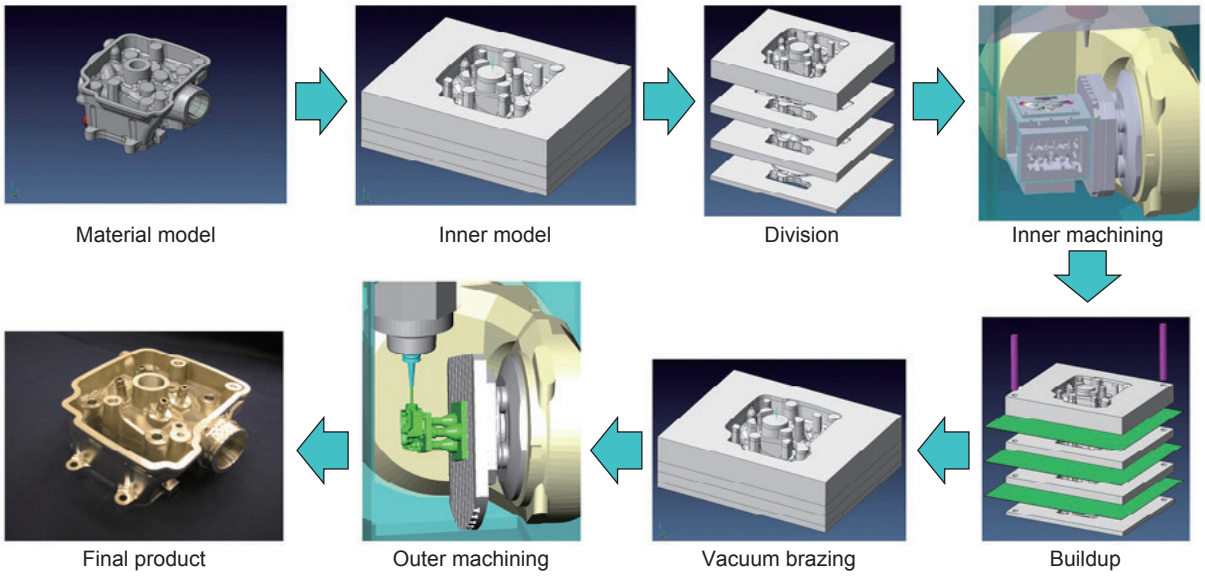


Fig. 1 Rapid trial-production process for engine components with hollow construction

* Motorcycle R&D Center

model that is an extract just of the portion with hollow construction is created. The slice locations are decided as described below in section 4.1. Blocks that are machined to the determined thickness are then subjected to dowel hole drilling. The dowel hole is taken as a machining datum, and the upper and lower surfaces of the portion with hollow construction are subjected to machining using a 3- and 5-axis high-speed machine. Using the dowel hole as a datum, buildup is carried out by placing brazing sheets that are like pieces of aluminum foil 0.04 mm thick in between the individual blocks, then subjecting them to brazing by heating them while pressing them in a vacuum furnace. The block subjected to brazing is then given T6 treatment (JIS H0001-1998), following which it undergoes external surface machining and drilling, the valve seat and valve guide are press-fit, and finish machining is carried out. The component is then complete.

3. Buildup-Brazing Technology

3.1. Forming the Hollow Construction Part

There is a method of forming the hollow construction part that uses powder rapid prototyping, but it involved issues of strength and precision. Buildup-brazing technology was therefore considered as a technique for manufacturing high-strength, high-precision components more quickly. Methods for joining aluminum materials include pulse electric current bonding[(1)] and diffusion bonding[(2)], but these have issues with joining strength because of the oxide film residue on the joining surface[(3)], and this is why the buildup-brazing method, which readily provides joining strength, was chosen (Fig. 2). The buildup brazing-method involves buildup by sandwiching brazing sheet with a lower melting point than the block parent material between the individual blocks. All this is then pressed in a vacuum furnace while subjecting it to preheating to a temperature at which the parent material will not melt. After that, it is subjected to brazing by heating it to a temperature at which only the brazing metal melts.

3.2. Brazing Quality Verification

The block that is subjected to dividing into parts with thickness that allows machining will have a complex joining surface, and variations in surface area and surface contact pressure will occur. As shown in Fig. 2, the application of a load during brazing causes the brazing metal to adhere to the joining surface and stabilizes quality. Brazing quality verification was conducted under the following three headings.

- Surface contact pressure distribution analysis of the joining surface by means of CAE
- Strength analysis of the joining surface
- Accuracy verification of hollow parts by means of x-ray CT

3.2.1. Surface contact pressure distribution analysis of joining surface

Brazing is performed by applying a certain amount of load. Due to the complexity of the joining surface, however, there are concerns about variation in surface contact pressure and instability in brazing quality. CAE was therefore used to conduct surface contact pressure distribution analysis. As shown in the diagrams on the left side of Fig. 3, the surface contact pressure is low (shown in blue) in the vicinity of the valve guide area inside the inlet and exhaust port, which do not have support in their upper parts. Therefore, reinforcement was added in the form of support in their upper parts as a means of equalizing the surface contact pressure distribution. The results are shown in the diagrams on the right side of Fig. 3. An increase in surface contact pressure (shown in green) was confirmed in the reinforcement area.

3.2.2. Joining surface strength analysis

Surface contact pressure analysis can be performed by CAE using a 3D model of the product shape. In strength verification, however, the issue is the adhesive strength of the joining surface. Because of this, test pieces that have undergone brazing with different surface contact

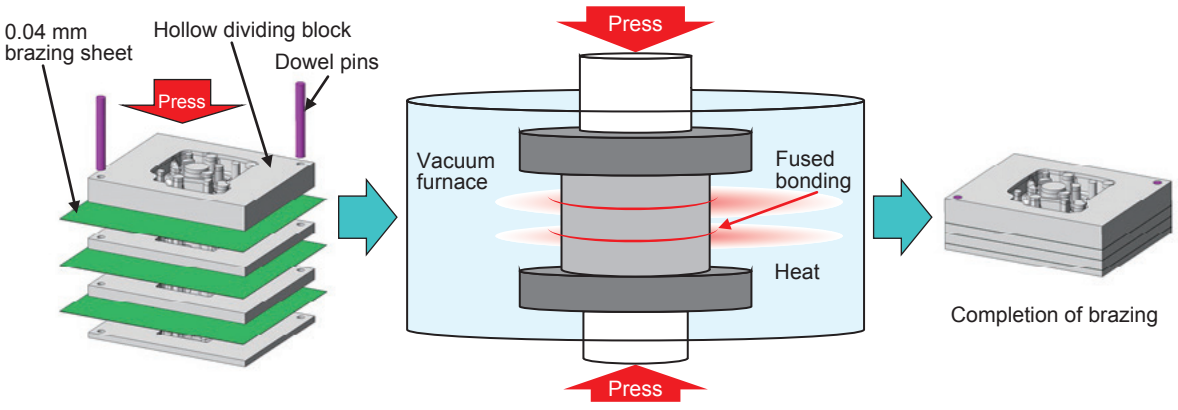


Fig. 2 Block buildup brazing process

pressures and loads are subjected to a tensile test. A logic was established that estimates strength from the combined results of the surface contact pressure analysis and the tensile test. Figure 4 shows the results from the tensile tests at different surface contact pressures. The dotted lines in the graph show the tensile strength of materials A6061-T6 and AC2B-T6. This approach could provide tensile strength approximately 20% higher than the sand-mold casting material.

3.2.3. Accuracy verification of hollow parts by means of x-ray CT

Figure 5 shows the deformation that occurs from the press when brazing the water jacket and inlet and exhaust port hollow parts. Deformation within ±0.2 mm is shown in gray, and deformation of greater than plus or minus 0.2 mm is shown in other colors. The green portions have deformation of approximately 0.3 mm, and this could be confirmed as being within the allowance shown in the drawing for the 3D model shape.

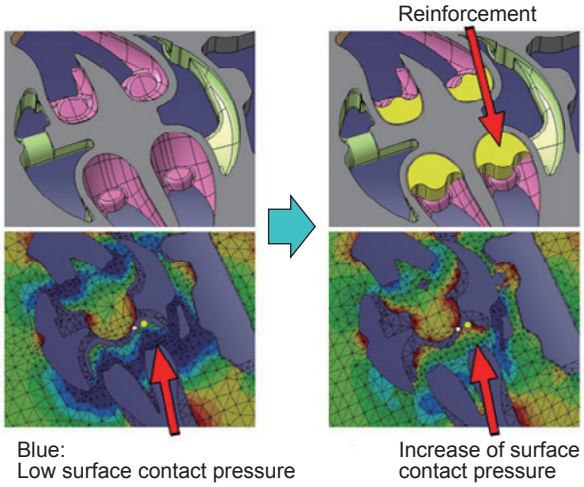


Fig. 3 Equalizing of surface contact pressure

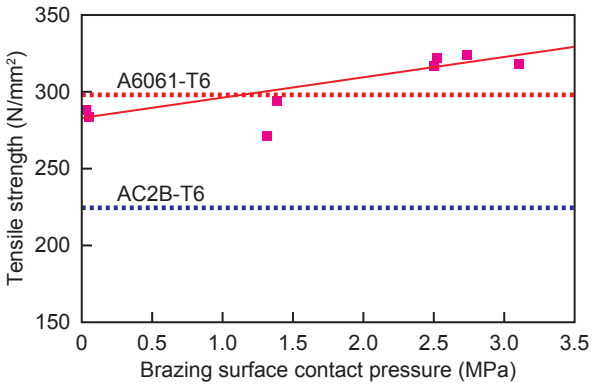


Fig. 4 Comparison of calculation of surface contact pressure and measurement of brazing tensile strength

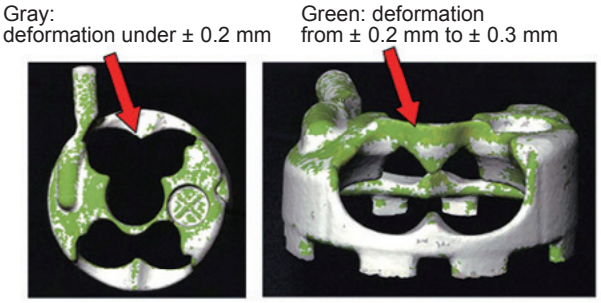


Fig. 5 Measurement of hollow construction deformation by using X-ray CT

4. Rapid Dividing and High-Speed Machining Technology

Performing mechanical machining in a short period of time requires a 3D model dividing technique, a rapid programming technique for 3D machining data, and optimization of high-speed machining technique.

4.1. Optimum Dividing Technique for 3D Model

When dividing into a greater number of pieces, the undercut area (impossible machining area using 3-axis machining) diminishes accordingly. However, the decrease in individual stiffness means that deformation occurs from the press during brazing. These factors are taken into consideration as the hollow-shaped part is divided into cross-sectional slices at locations that will not result in the formation of a separated island shape. The dividing locations are further subjected to optimization (Fig. 6) for the shortest possible tooling and machining time by a combination of 3-axis machining, 5-axis machining, and other such methods.

4.2. Rapid Programming Technique for 3D Machining Data

Ordinarily, 3-axis machining equipment is called a vertical machining center. This refers to equipment that has three axes (X-axis, Y-axis, and Z-axis) and performs

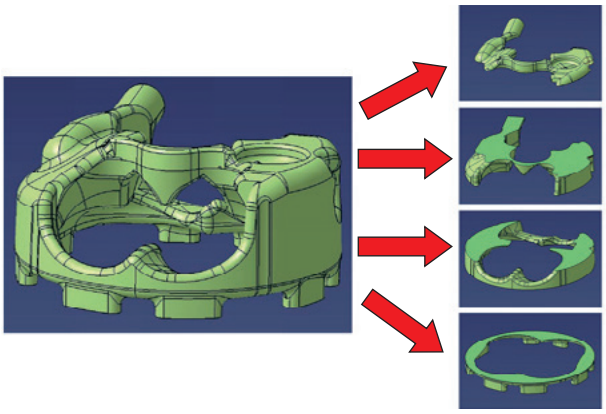


Fig. 6 Optimum dividing of hollow construction

mechanical machining by numerical control. The tool only moves vertically (Z-axis) in relation to the table and it is not capable of machining overhang parts. The 5-axis machining equipment has two further axes in addition to the three axes, and it is constructed so that the tool (Z-axis) can be tilted to any angle. This enables machining of overhang parts that 3-axis machining equipment is incapable of. When pieces divided into slices are all to be subjected to machining only by 5-axis machining equipment, a collision check is conducted of the holder and spindle for every tool angle. Since this increases the machining data programming time, the basic rule is to perform 3-axis machining from the upper and lower surfaces.

The machining conditions when 3-axis machining (tool, stepover, toolpass type, etc.) are registered as a template for each machining shape. This enables use of the template to easily configure the machining condition for each machining part, which enables high-speed programming of the machining data. With this approach, the undercut area is subject to automatic detection and 5-axis machining is kept to the necessary minimum.

4.3. 5-Axis High-Speed Machining Technique

The respective machined surface roughness is configured for the inlet and exhaust port, combustion chamber, and other such functional surfaces, as well as for other, external surfaces and the like. The configured machined surface roughness is taken as a basis for reducing the machining time by means of a machining condition that takes maximum advantage of the machine capacity. Machining utilizes two 5-axis machining machines. On the 5-axis complex machine, a special jig (Fig. 7) is used to enable continuous machining of the upper and lower surfaces with a single tooling configuration. On the 5-axis machining center, a special index jig (Fig. 8) is used to enable machining of four sides with a single tooling configuration. These measures were taken for tooling time reduction and for schedule reduction with unmanned operation.

5. Feasibility Verification

5.1. Application to Off-road Race Engine

A cylinder head for the purpose of verifying performance was created (Fig. 9) by changing the position of the exhaust manifold. Compared to conventional sand-mold casting, this product shortened the manufacturing schedule by 60% and reduced the manufacturing cost per unit by 75%. The product was also capable of application in a preliminary test without any issues related to strength.

6. Conclusion

A block-buildup brazing and high-speed machining technique was established and yielded the following results.

(1) The manufacturing schedule could be shortened by 60% relative to the sand-mold casting technique.

(2) A cost reduction of 75% per unit was achieved relative to use of the sand-mold casting technique to manufacture a preliminary test product.

(3) The machining consists entirely of processes for removal (cutting, grinding, etc.), and so enables manufacture of high-precision components.

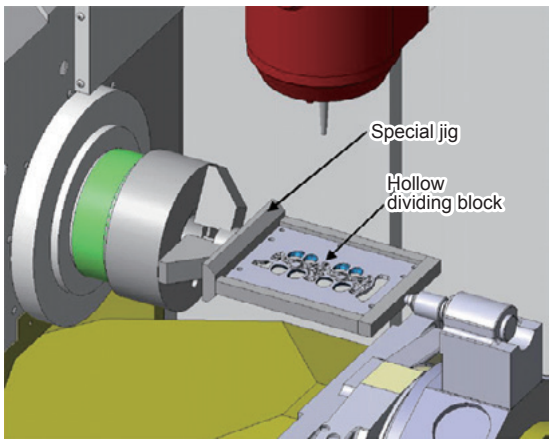


Fig. 7 Special jig for 5-axis integrated mill turn center

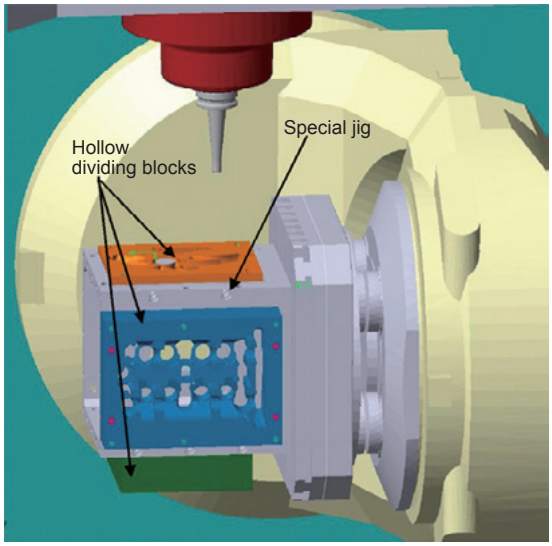


Fig. 8 Special jig for 5-axis machining center



Fig. 9 Final product

Afterword

Schedule reduction is an issue that should always be addressed in quality manufacturing. This article used the example of a water-cooled cylinder head with a hollow construction part to introduce a rapid-trial production technique that incorporates buildup-brazing technology and rapid dividing and high-speed machining technology to determine how quickly the example product could be brought to use in a preliminary test. The surface contact pressure distribution analysis utilizing CAE, in particular, yielded knowhow about the use of reinforcement for the purpose of reducing deformation due to press during brazing. This provided a deeper understanding of how brazing quality could be enhanced. The intention is eventually to apply this understanding to preliminary tests of multi-cylinder engines.

Acknowledgements

The authors would like to take this opportunity to express their profound gratitude to the members of the NDK Kakou Center Co., Ltd., who provided their generous cooperation with buildup brazing of aluminum.

References

(1) Ohashi, O.: Pulse Electric Current Bonding, Congress Proceedings of The Japan Welding Society, Vol. 71, p. 29-32 (2002)
(2) Suzuki, Y.: Seimitsukakusansetugougijyutu wo riyoushita Cyuukuubuhin no Seisakurei, Transactions of The Japan Society of Mechanical Engineers, Vol. 15, p. 387 (2007) (in Japanese)
(3) Kotani, K., Ikeuchi, K., Matsuda, F.: Interfacial Phases in Diffusion-Bonded Joints of Commercial Al Alloys, Transactions of The Japan Welding Society, Vol. 14, No. 2, p. 382-388 (1996)

■ Author ■


Takeshi WADA


Tatsuo JIKIMOTO


Hidenori OKAJIMA

Research on Expansion of Premixed Charge Compression Ignition (PCCI) Diesel Combustion Operation Range

Junichi HATANO* Takeya HARADA* Kazuhiro MATSUI*
Hiroki KOBAYASHI* Ryuta MATSUI*

ABSTRACT

In the area of diesel engines, the reduction of soot and NOx emissions is demanded through the achievement of increased combustion performance. High expectations are placed on premixed charge compression ignition (PCCI) combustion as a combustion method that will achieve breakthrough reductions in NOx and soot emissions. However, the use of this combustion method is restricted to the low-speed, low-load range because it becomes challenging to realize an ignition delay and combustion noise increases as the engine load increases.

The research discussed in this paper attempted to expand the range of application of PCCI combustion by increasing exhaust gas recirculation (EGR) cooling performance and employing a low compression ratio. The results of the research indicated that it was possible to extend the application of PCCI combustion to virtually the entire operating range employed in the European NEDC and North American FTP75 modes.

1. Introduction

Concern towards environmental issues is growing on a global scale, and demand for diesel engines, which have a considerable effect in reducing CO_2 emissions and display outstanding dynamic performance, has increased in the past several years, in particular in Europe.

However, the reduction of polluting emissions, in particular soot and NOx, represents an issue for diesel engines. It is thought that lean NOx catalysts[1), 2)] and SCR systems[3)] will be effective measures in response to the introduction of more stringent emissions regulations in the future. However, when after-treatment systems are added, manufacturing costs increase, vehicle weight increases, and a variety of economic burdens cannot be avoided, for example for the construction of infrastructure for the supply of urea. This makes it necessary to develop technologies that will reduce NOx and soot emissions by increasing the efficiency of combustion to the greatest possible extent.

Against this background, a great deal of research has been conducted by automakers and research laboratories on PCCI combustion as a combustion method capable of reducing NOx and soot emissions[4), 5)]. However, given that the application of the method is restricted to the low-load range, and it presents issues from the perspective of combustion stability during transient operation, a variety of issues remain to be resolved for its practical application.

The research discussed in this paper focused on one of the issues impeding practical application of the method, its restriction to the low-speed, low-load operating range, and attempted to reduce NOx and soot emissions across a wide range by extending the range of its application.

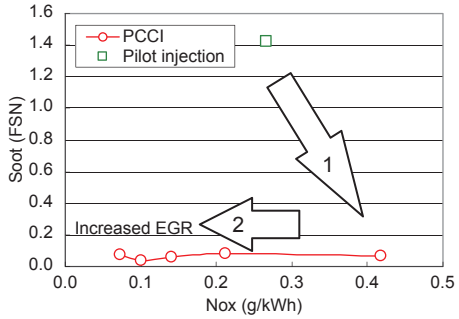
2. Range of Application of Conventional PCCI Combustion

This chapter will explain the mechanism of PCCI combustion based on combustion behavior at 1500 rpm and 25% load. Figure 1 shows a comparison of conventional diffusive combustion using pilot injection and PCCI combustion. Figure 1(a) shows the behavior of NOx and soot emissions, Fig. 1(b) shows the behavior of combustion noise ($dP/d\theta$ max), and Fig. 1(c) shows the distribution of the local equivalence ratio and the local temperature. PCCI combustion generates an ignition delay through comparatively early injection of the fuel, promoting mixture of the air and fuel and reducing soot formation in comparison to conventional combustion. However, because the air-fuel mixture with an equivalence ratio of close to 1 is higher at ignition, combustion is rapid, and NOx and

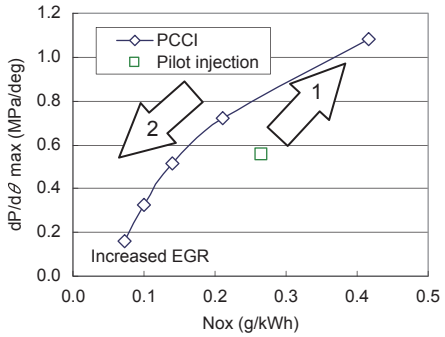
* Automobile R&D Center

dP/dθ max increase as a result (Arrow 1 in the figures). High-volume EGR is therefore introduced in order to control the rapid combustion and reduce NOx emissions and dP/dθ max[6] (Arrow 2). By this means, it is possible to simultaneously reduce NOx and soot emissions in the low-speed, low-load range without increasing dP/dθ max.

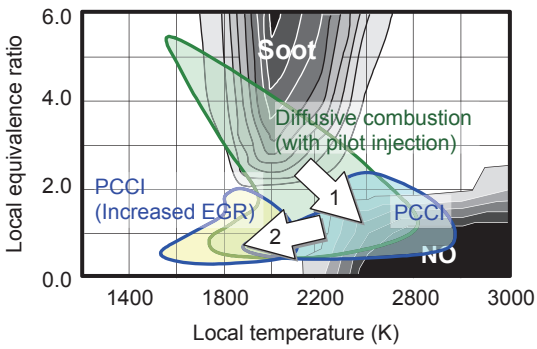
However, it becomes challenging to achieve an ignition delay as the engine load and speed increase. In addition, the air-fuel mixture with an equivalence ratio close to 1 increases with a greater volume of fuel, thus increasing the speed of combustion and raising dP/dθ max. This makes it challenging to expand the operating range in which PCCI combustion can be applied. Figure 2 shows the operating ranges of North American FTP75 mode and European NEDC mode. The curve in the upper section of the graph is the curve generated by full load at each engine speed. For the reasons discussed above, the application of PCCI combustion is limited to part of the low-speed, low-load range. Expansion of its range of application would therefore be desirable.



(a) NOx and soot emissions



(b) NOx and dP/dθ max



(c) Local temp. and local equivalence ratio

Fig. 1 Comparison between diffusive combustion and PCCI on soot, dP/dθ max and Φ-T map

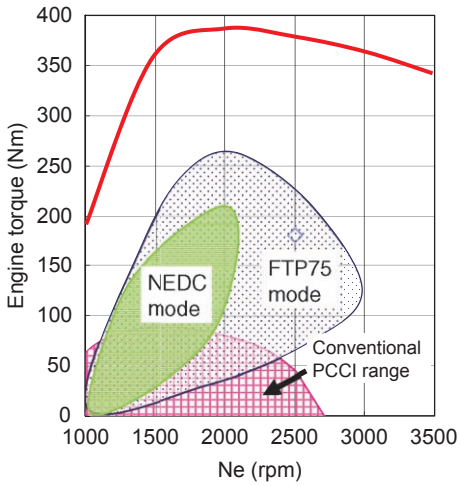


Fig. 2 Conventional PCCI combustion application range

3. Approach to Expansion of Range of PCCI Combustion

As discussed above, it is necessary to achieve an ignition delay and control the speed of combustion in order to expand the range in which PCCI combustion can be applied. Reducing the compression end temperature is an effective method of realizing an ignition delay. The project therefore attempted to increase the ignition delay by increasing the cooling performance of the EGR cooler and reducing the compression ratio, and to control the speed of combustion by increasing EGR[6), (7)].

4. Test Engine, Test Fuel, and Test Conditions

Table 1 shows the specifications of the diesel engine used in tests. A 2.2-L prototype diesel engine was used as the basic framework. 1500 rpm/140 Nm and 2500 rpm/180 Nm were selected as representative test conditions that would cover virtually the entire range of FTP75 and NEDC modes.

5. Expansion of Range of Application of PCCI to High-speed, High-load Range

5.1. Effect of EGR Cooling

Figure 3 shows the results of comparison of dP/dθ max for PCCI and diffusive combustion at differing intake gas temperatures at 2500 rpm/180 Nm. In the case of diffusive combustion, the speed of main combustion can be

Table 1 Test engine specifications

Cylinder configuration	In line 4
Bore × stroke (mm)	85 × 96.8
Displacement (cm^3)	2197
Compression ratio	17.2, 16.2
Valve train	DOHC 4 valves
Fuel injection system	180 MPa common rail
Nozzle type	7 holes 680 cm^3/sec
Intake system	Turbocharged, inter-cooled system
EGR cooling capacity	3.0 kW or 6.3 kW at 2500 rpm 180 Nm
Fuel properties	Cetane number: 44 Sulfur: 11.5 ppm

controlled by means of pilot injection, but combustion is rapid in the case of PCCI combustion. In the results shown in Fig. 3, as the cylinder intake gas temperature declines, the speed of combustion is reduced and dP/dθ max declines. Figure 4 shows the relationship between the cylinder intake gas temperature, combustion speed (with the period from a mass burn fraction of 5% to 90% as the index), and the EGR rate. Increasing the cooling performance of the EGR cooler produced a greater EGR mass flow in the cylinders, and the increase in the ignition delay (considered as the period from the completion of injection to a mass burn fraction of 5%) resulting from a reduction in the intake gas temperature reduced soot emissions. Because of this, it was possible to further increase EGR until the same level of soot emissions was reached, thus reducing the speed of combustion.

Figure 5 shows soot and NOx emissions and the relationship between break specific fuel consumption (BSFC) and dP/dθ max when EGR is cooled. Due to the effect of PCCI combustion, NOx emissions are reduced by 39% at the same level of soot emissions. However, fuel efficiency is reduced because the ignition timing must be retarded to control the increase in dP/dθ max.

The results discussed above indicate that increasing EGR cooling performance can be considered an effective method of expanding the range of application of PCCI combustion.

5.2. Low Compression Ratio

The compression end temperature can be reduced through the use of a low compression ratio, and this could be expected to increase the ignition delay. Figure 6 shows dP/dθ when the compression ratio is varied at 2500 rpm/180 Nm. The lower compression ratio produces an ignition delay, realizing slower combustion with a low dP/dθ max.

Figure 7 shows the relationship between compression ratio, ignition delay, and EGR rate at 2500 rpm/180 Nm.

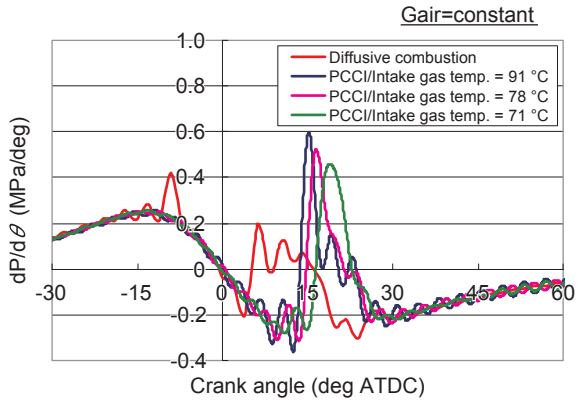


Fig. 3 Effect of intake gas temperature on dP/dθ

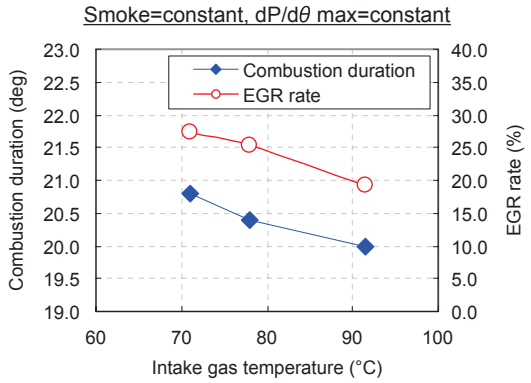
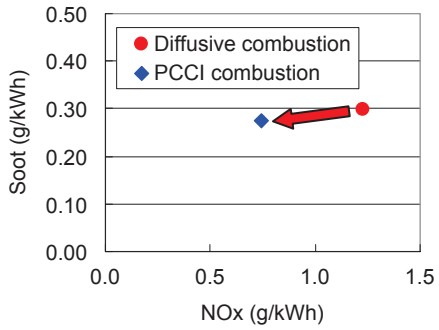
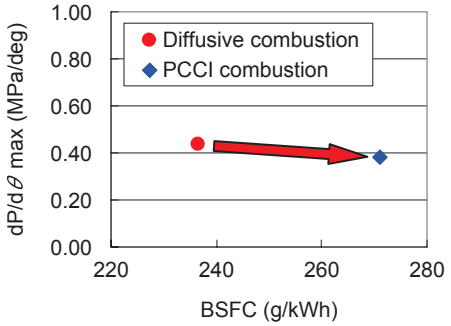


Fig. 4 Effect of intake gas temperature on combustion duration and EGR rate



(a) NOx and soot emissions



(b) BSFC and dP/dθ max

Fig. 5 Effect of combustion pattern on emissions, BSFC and dP/dθ max

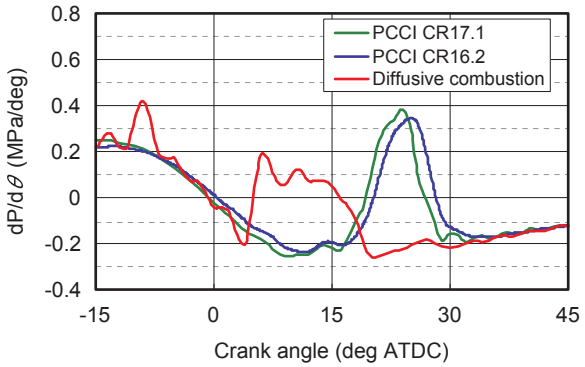


Fig. 6 Effect of compression ratio on dP/dθ

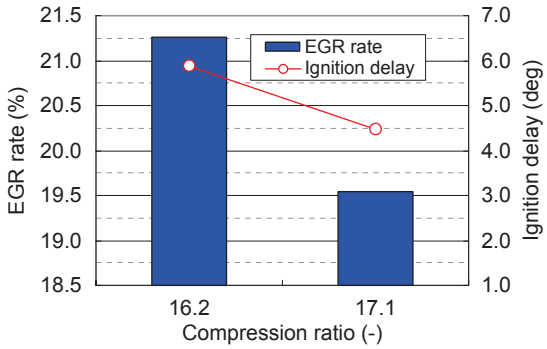
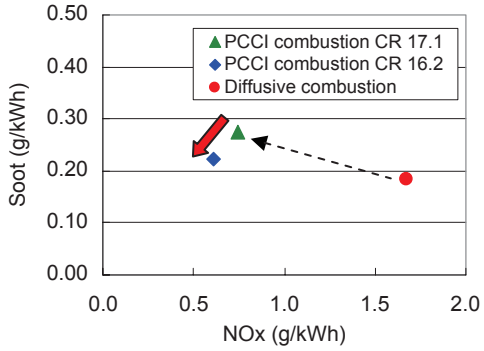
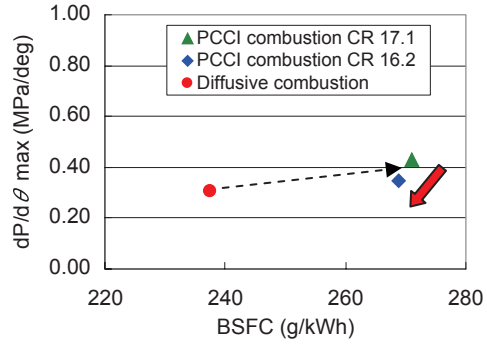


Fig. 7 Effect of compression ratio on ignition delay and EGR rate



(a) NOx and soot emissions



(b) BSFC and dP/dθ max

Fig. 8 Effect of combustion pattern and compression ratio on emissions, BSFC and dP/dθ max

Figure 8 shows the relationship between emissions, fuel efficiency, and dP/dθ max at the reduced compression ratio. Reducing the compression ratio increases the ignition delay, promoting mixture of the air and fuel and reducing soot emissions. Because EGR can be increased until the same level of soot emissions is reached, it is possible by this means to reduce NOx and dP/dθ max.

These results indicate that lowering the compression ratio can also be considered an effective method of expanding the range of application of PCCI combustion.

6. Expansion of the Range of Application of PCCI Combustion to the Low-speed, High-load Range

6.1. Issues of Application of PCCI Combustion in the Low-speed, High-load Range

The results obtained indicated that using the methods discussed above, it would be possible to expand the range of application of PCCI combustion to the high-speed, high-load range (as represented by 2500 rpm/180 Nm) without an increase in dP/dθ max, and that the soot-NOx tradeoff could be ameliorated. However, control of dP/dθ max in the low-speed, high-load range remained challenging. Figure 9 shows the relationship between cylinder intake gas temperature and EGR rate at 1500 rpm/140 Nm. Even when the cooling performance of the EGR cooler is increased, there is almost no change in dP/dθ max and only a slight increase in the EGR rate.

One reason that can be considered for this is a time factor. Because the piston speed is comparatively slow in the low-speed range, dP/dθ max necessarily increases in proportion with increasing loads at which a greater amount of fuel is injected for each unit crank angle, and the speed of combustion tends not to decline. In addition, the turbocharger employed in this project was not capable of supercharging sufficiently in the low-speed, high-load range. The air-fuel mixture therefore tended to become rich, and soot emissions increased with increased EGR. It would therefore be challenging to realize slower combustion by increasing EGR in this operating range, and it was considered that it would be necessary to employ pilot injection.

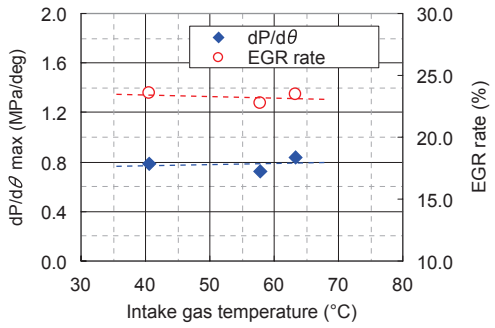


Fig. 9 Effect of intake gas temperature on dP/dθ max and EGR rate

6.2. Modification of Combustion Behavior using Pilot Injection

If the range of application of PCCI combustion is to be expanded to the low-speed, high-load range by increasing EGR cooling performance and lowering the compression ratio, it would be challenging to reduce dP/dθ max using single-stage injection. The use of pilot injection would be the most effective means of resolving this issue, but it would be unable to realize a sufficient ignition delay like PCCI combustion, and the combustion generated by pilot injection in the high-load range would produce increased soot emissions in proportion to the increase in the EGR rate. This project therefore attempted to ameliorate the NOx-soot tradeoff by employing closed pilot injection, which is able to reduce soot emissions to a level below that of conventional pilot injection.

6.2.1. Mechanism of soot reduction through use of closed pilot injection

Figure 10 shows the rate of heat release and the rate of injection when the pilot interval is varied at 1500 rpm/140 Nm, and Fig. 11 shows NOx and soot emissions. In diffusive combustion, the pilot spray is combusted prior to main combustion, and the increase in in-cylinder ambient temperature and ambient pressure promotes the ignition of main combustion. By contrast, in the case of closed pilot injection, the ignition of the pilot spray almost overlaps with main combustion. However, because the ignition timing of main combustion remains virtually the same irrespective of the pilot interval, the ignition delay of main combustion cannot be increased using closed pilot injection. Nevertheless, as Fig. 11 shows, the use of closed pilot injection does reduce soot emissions against conventional pilot injection. This suggests the existence of a soot reduction mechanism other than the increase in the ignition delay, as indicated in Chapter 2.

An analysis was conducted using 3D-CFD (KIVA-3V code) in order to determine the reason for this phenomenon. The results are shown in Figs. 12 and 13. Figure 12 shows the distribution of the local equivalence ratio in the cylinders for each crank angle. The ratio of fuel is higher the higher the figures, and the ratio of the mixture with air increases as the figures become lower, indicating that homogenization is proceeding. At a pilot interval of 1500 μs, main combustion occurs after the completion of pilot combustion. A similar pattern of combustion is observed at a pilot interval of 1000 μs, but the distribution of the local equivalence ratio is higher than in the case of 1500 μs, providing further confirmation of the increase in soot emissions shown in Fig. 11. At a pilot interval of 350 μs, main combustion is ignited prior to the completion of pilot combustion, and the local equivalence ratio is lowest.

In order to analyze the reason for the difference in the local equivalence ratio at different pilot intervals, the concentration of CO_2, which provides an index of the burned gas in the cylinders, and its distribution were

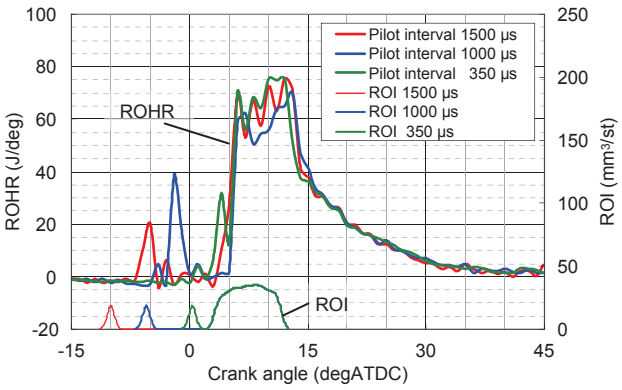


Fig. 10 Effect of pilot interval on rate of heat release and rate of injection

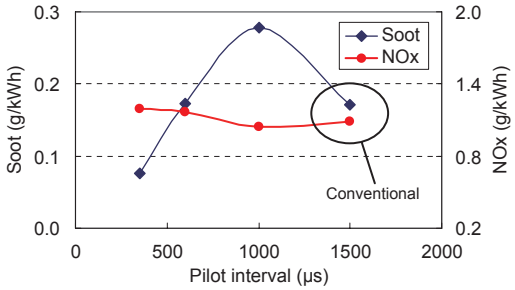


Fig. 11 Effect of pilot interval on NOx and soot emissions

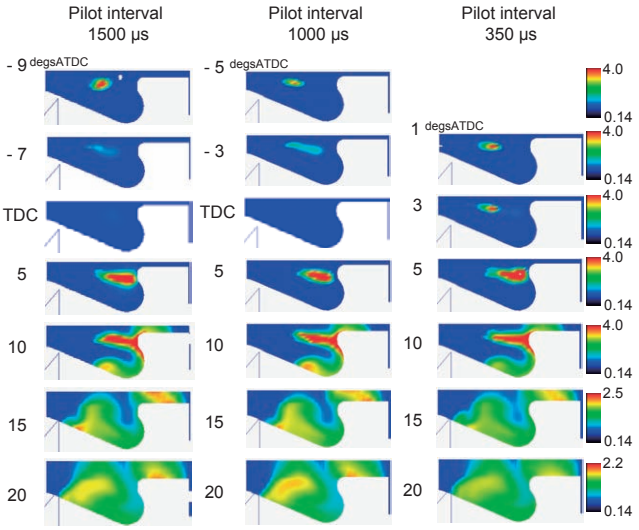


Fig. 12 Effect of pilot interval on local equivalence ratio in piston bowl

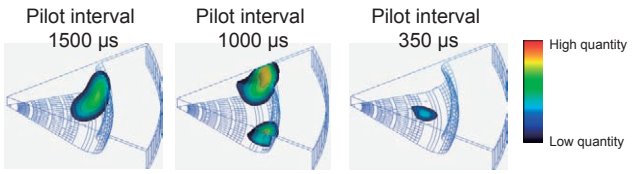


Fig. 13 Effect of pilot interval on CO_2 in piston bowl at 4 degATDC

calculated for 4 deg ATDC. The results are shown in Fig. 13. Compared to 1500 μs, at a pilot interval of 1000 μs the CO_2 concentration is higher and the distribution covers a wider range. It is thought that because the CO_2 concentration at 4 deg ATDC represents part of the composition of the gas in the cylinders close to the commencement of main combustion, if there is a large quantity of burned gas, the probability of contact between fuel and oxygen declines, and soot emissions increase. It can therefore be considered that if the pilot interval is reduced to 350 μs, soot emissions will be controlled despite the fact that pilot combustion and main combustion are continuous because little burned gas exists at the time of commencement of main combustion.

As described above, the use of closed pilot injection reduces the amount of burned pilot gas introduced to the main injection, thus controlling the local richness of the air-fuel mixture and reducing soot emissions.

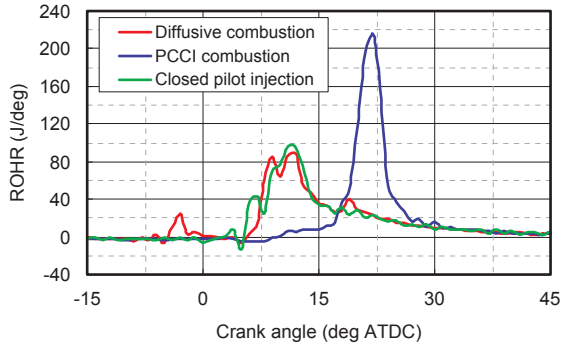


Fig. 14 Rate of heat release by each combustion pattern

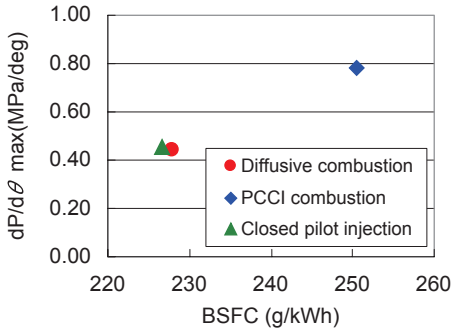


Fig. 15 Effect of combustion pattern on BSFC and dP/dθ max

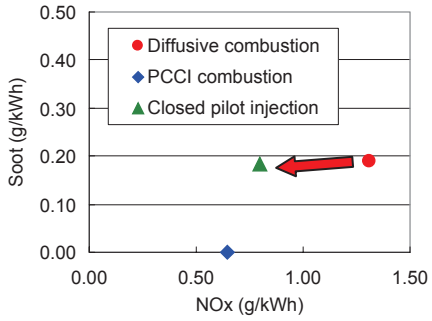


Fig. 16 Effect of combustion pattern on emissions

6.2.2. Effects of application of closed pilot injection

The following effects were obtained from the application of closed pilot injection in the low-speed, high-load range. Figure 14 compares heat release at 1500 rpm/140 Nm for each combustion pattern. Figure 15 shows fuel efficiency and dP/dθ max. In the case of PCCI combustion using single-stage injection, rapid heat release cannot be controlled even when the ignition timing is retarded, and satisfactory dP/dθ max cannot be obtained. By contrast, the heat release rate of main combustion when closed pilot injection was used was approximately half that for PCCI combustion, and dP/dθ max and combustion speed were controlled to low levels.

Figure 16 shows soot and NOx emissions. The combination of the effect of EGR cooling and the achievement of low-soot combustion through the use of closed pilot injection, while not matching PCCI combustion, did ameliorate the soot-NOx tradeoff in comparison to diffusive combustion.

7. Effect of Expansion of Range of Application of PCCI Combustion

In order to expand the range of application of PCCI combustion, it was necessary to achieve an ignition delay and to control the speed of combustion by increasing EGR. The achievement of increased EGR cooling performance and the use of a low compression ratio were tested as means of realizing these goals. It was possible to increase the range of application of PCCI combustion to the high-speed, high-load range without any increase in dP/dθ max during steady-state operation. However, because it was challenging to control dP/dθ max in the low-speed, high-load range, closed pilot injection was employed in this range in addition to the methods described above in order to ameliorate the tradeoff between soot and NOx without any increase in dP/dθ max. While not attempted in this project, it is considered that the possibility remains of extending the range of application of PCCI combustion to the low-speed, high-load range by increasing supercharging performance at low speeds.

Whatever methods may be used, the research discussed in this paper did indicate that it is possible to extend the range of application of PCCI combustion to almost entirely cover the operating ranges used in European NEDC Mode and North American FTP75 Mode (Fig. 17).

Figure 18 shows the reduction in soot and NOx emissions and the effect on fuel efficiency of extending the range of application of PCCI combustion. It is clear that the effect of reduction of soot and NOx emissions that was previously restricted to the low-speed, low-load range has been extended to the high-speed, high-load range.

Because closed pilot injection is employed in the

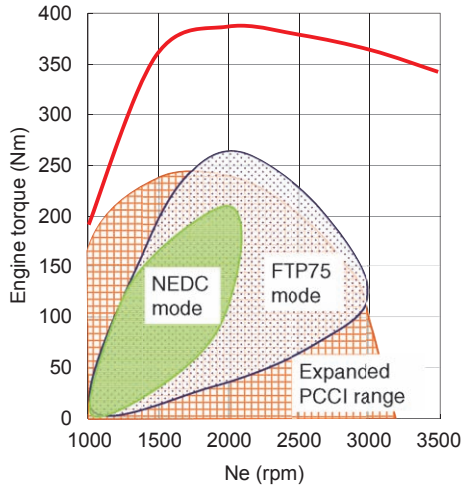
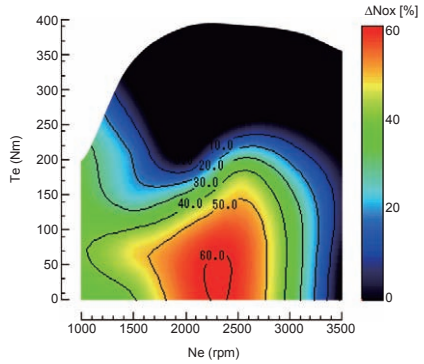
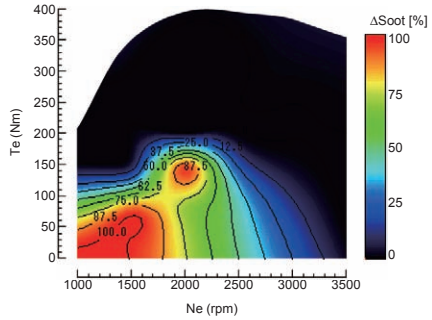


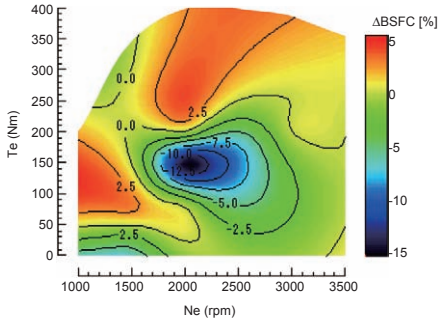
Fig. 17 PCCI combustion application range



(a) NOx reduction rate



(b) Soot reduction rate



(c) Fuel consumption enhancement rate

Fig. 18 Effect of PCCI combustion on emissions and fuel efficiency

low-speed, high-load range, the rate of reduction of soot emissions does not match that achieved in the high-speed, high-load range, but NOx emissions are reduced by approximately 30% against diffusive combustion.

In addition, while a decline in fuel efficiency can be observed in the high-speed, high-load range because the main injection timing has been retarded in order to control combustion noise, in the low-speed, low-load range, main combustion has been advanced due to the reduced speed of combustion, and this has resulted in increased fuel efficiency.

8. Conclusion

The following results were obtained in relation to the expansion of the range of application of PCCI combustion.

(1) In order to expand the range of application of PCCI combustion, it is necessary to achieve an ignition delay and control the speed of combustion; the realization of increased EGR cooling performance and the use of a low compression ratio are effective means of achieving these goals.

(2) In the low-speed, high-load range, in which it is challenging to control the speed of combustion due to restrictions on the introduction of EGR, the modification of combustion behavior through the use of closed pilot injection helped to enable the amelioration of the soot-NOx tradeoff with no increase in $dP/d\theta$ max.

(3) The research indicated that the expansion of the range of application of PCCI combustion made it possible to expand simultaneous NOx and soot reductions to almost the entire operating range employed in FTP75 and NEDC modes during steady-state operation.

In future, looking towards the practical realization of the system, it will be necessary to develop real-time combustion control technologies for transient states.

References

(1) Morita, T., Suzuki, N., Satoh, N., Wada, K., Ohno, H.: Study on low NOx emission control using newly developed lean NOx catalyst for diesel engines: SAE paper, 2007-01-0239 (2007)

(2) Wada, K., Suzuki, N., Satoh, N., Morita, T., Yamaguchi, S., Ohno, H.: Study on emission-reducing method with new lean NOx catalyst for diesel engines: SAE paper, 2007-01-1933 (2007)

(3) Murata, Y., Komiya, R., Kaneko, A., Daisho, Y., Suzuki, H., Ishii, H.: A study on the improvement of NOx reduction efficiency for a urea SCR system (Third report) -High NOx reduction efficiency mechanism at transient operation with low exhaust gas temperatures: JSAE paper, 20085846 (2008)

(4) Kimura, S., Aoki, O., Kitahara, Y. , Aiyoshizawa, E.: Ultra-Clean combustion technology combining a low-temperature and premixed combustion concept

for meeting future emission standards: SAE paper, 2001-01-0200 (2001)
(5) Akihama, K., Sasaki, S.: Mechanism of smokeless rich diesel combustion by reducing temperature: SAE paper, 2001-01-0655 (2001)
(6) Kanda, T., Hakozaki, T., Uchimoto, T., Hatano, J., Kitayama, N., Sono, H.: PCCI operation with early injection of conventional diesel fuel: SAE paper, 2005-01-0378 (2005)
(7) Kanda, T., Hakozaki, T., Uchimoto, T., Hatano, J., Kitayama, N., Sono, H.: PCCI operation with fuel injection timing set close to TDC: SAE paper, 2006-01-0920 (2006)

■ Author ■


Junichi HATANO


Takeya HARADA


Kazuhiro MATSUI


Hiroki KOBAYASHI


Ryuta MATSUI

Enhancement of Low-temperature Combustion in Flexible Fuel Vehicle (FFV) Engine

Susumu NAKAJIMA*

ABSTRACT

A variety of vegetable oil-based alternative fuels have been suggested in recent years with a view to preventing global warming due to the CO_2 emitted by internal combustion engines. One of those fuels is bio-ethanol. Flexible fuel vehicles (FFV) that are able to run on varieties ranging from 100% aqueous ethanol (E100) to a 22% mixture of ethanol with gasoline (E22) are in use in Brazil. Ethanol is a single-component fuel that does not contain any low-boiling-point components, and there are issues with combustion at low temperatures. The optimum compression ratio was selected to enhance the combustion of ethanol at low temperatures. The flow was also raised and low-temperature combustion was enhanced by operating with one intake valve. In order to raise the commercial product appeal when using E100 at low temperatures, a new engine control was built exclusively for the FFV. Through the use of these technologies, a dedicated FFV engine was developed that achieves a balance of commercial product appeal and power output when using E100.

1. Introduction

Bio-ethanol has been the object of attention in recent years as an alternative fuel with potential for limiting global warming. Bio-ethanol is manufactured from plants that have grown by photosynthesis using the sun's energy. Consequently, extracting that energy by combustion will not increase the total amount of CO_2 in the atmosphere, which is why this is treated as a carbon neutral fuel.

On the other hand, there are issues with the use of ethanol in automobile engines. These are its high latent heat of evaporation and its low vaporizability at low temperatures because it does not include any low-boiling-point components.

In Brazil, bio-ethanol is produced from sugar cane, and fuel that is 100% ethanol is sold side-by-side with fuels containing mixtures of 20-25% ethanol with gasoline. In other words, an FFV engine[(1)] intended for Brazil will be required to provide adequate performance at any concentration of ethanol ranging from 20-100%.

2. Properties of Ethanol as an FFV Fuel

Table 1 shows the characteristics of ethanol and gasoline.

1. High octane number
2. No low-boiling-point components
3. High latent heat of evaporation
4. Rather high heating value per mass of air
5. Low heating value per volume

These fuel properties would suggest that the issue with ethanol as used for automobile engines would be combustion at low temperatures.

3. Characteristics of Ethanol Combustion at Low Temperatures

3.1. Confirmation of Combustion at Low Temperatures

Table 2 shows the specifications of the test engine. Figure 1 shows a comparison of E100 and gasoline at different excess air ratios in terms of total hydrocarbon (THC) and CO_2 at low temperature. The comparison was made at a low load (-60 kPa) corresponding to a fast idle and at a high load (-13 kPa) corresponding to a standing start. With E100, THC is higher at high load. The reason is probably that, since E100 has no low-boiling-point components, the latent heat of evaporation is higher, so that a large amount of fuel is not completely vaporized under high load. This explanation is supported by the phenomenon of CO_2 emissions characteristics tending to be displaced toward the rich side.

3.2. Demanding Driving Conditions for FFV

The FFV does not start easily at low temperatures with E100. Therefore, it is equipped with an E22 fuel tank and

* Automobile R&D Center

Table 1 Fuel characteristics

		Gasoline	Ethanol
Octane number RON/MON		93/81	110/92
Boiling point (°C)		25-200	78
Latent heat of evaporation (kJ/Air kg)		30.2	101
Low calorific value	(MJ/Air kg)	2.95	2.99
	(MJ/kg)	43.4	26.9
	(MJ/L)	32	21.2
Theoretical air fuel ratio	(Weight)	14.7	8.9
	(Volume after carburetion)	43.1	14.3
Ratio of the number of moles of combustion before and after		1.07	1.14
Specific gravity (kg/L)		0.737	0.789

Table 2 Engine specifications

Fuel		Gasoline
Cylinder configuration		In-line 4-cylinder
Bore × stroke (mm)		81 × 87.3
Displacement (cm^3)		1799
Compression ratio		10.5
Valve		2 intake valves
Valve diameter (mm)	In.	32
	Ex.	26

injection system dedicated to low-temperature starts. Figure 2 shows how the different fuels are used for different purposes immediately after startup. The solid line represents the low-temperature fuel injection amount, and the broken line represents the high-temperature fuel injection amount. When the temperature is low, E22 is used for starting, and then the system switches over to E100. It is desirable to keep the time spent operating with E22 to a minimum, and in that case, the conditions that make FFV operation challenging are:

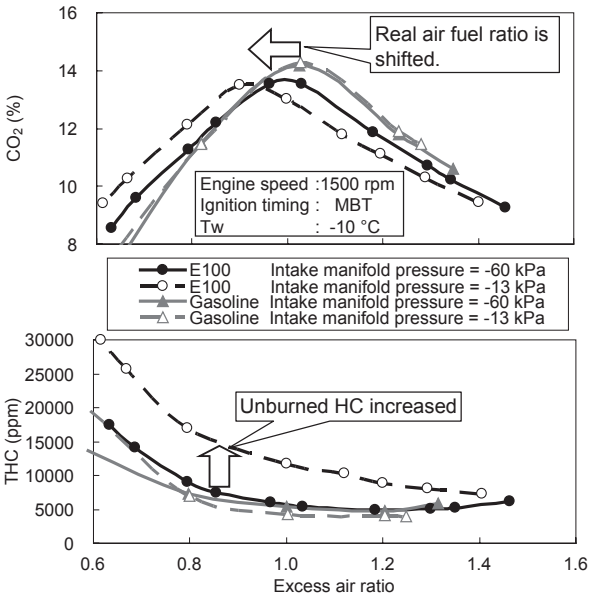


Fig. 1 Characteristics of excess air ratio at low temperature

1. Startability at the lower temperature limit when using E100 (part A of Fig. 2)
2. Shift to high-load driving when ambient temperature is low (part B of Fig. 2)

3.3. Starting Test with E100

Startability with E100 at low ambient temperature was confirmed. Figure 3 shows the relationship between

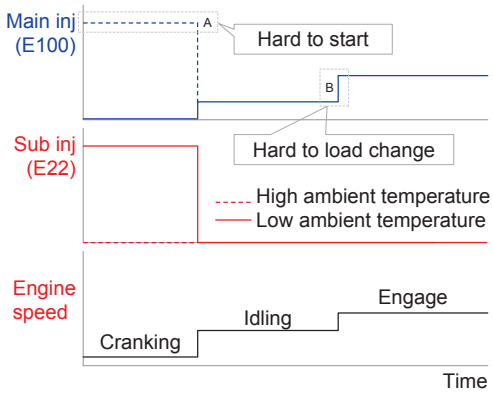


Fig. 2 Fuel used at starting and after start

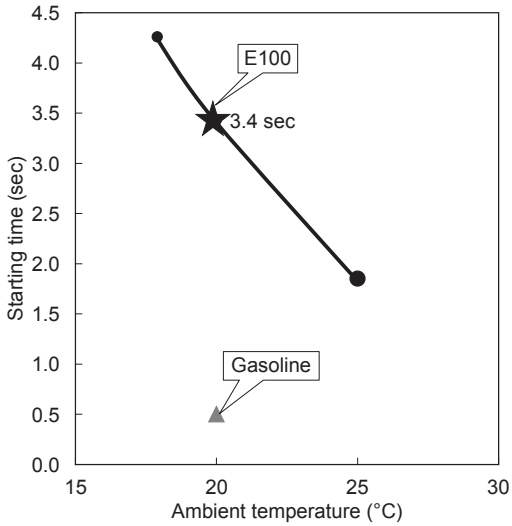


Fig. 3 Relationship between ambient temperature and starting time

ambient temperature and starting time, with lower ambient temperatures bringing longer starting times. The reason is probably the reduced vaporizability of ethanol during a cold start. Considering that E100 is used for starting at temperatures down to 20°C, it is necessary to shorten the starting time of 3.4 sec.

3.4. Load-increasing Test at Low Temperature

The FFV starts up with E22 when the temperature is low, then runs with E100. Figure 4 shows a conceptual diagram of the transient torque characteristics when the engine idles for two seconds immediately after startup and then is suddenly placed under a high load equivalent to a standing start in a manual transmission car. When the temperature of the water (Tw) is high, torque is generated in proportion to the throttle opening. When the water temperature is low, however, the engine misfires. Figure 5 shows the water temperature and torque characteristics when

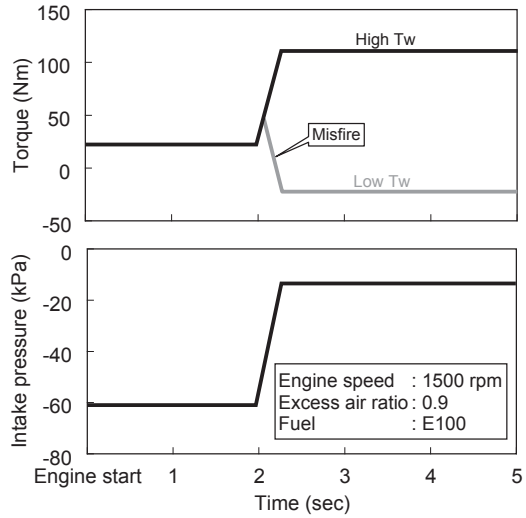


Fig. 4 Transient torque characteristics under high loads immediately after starting

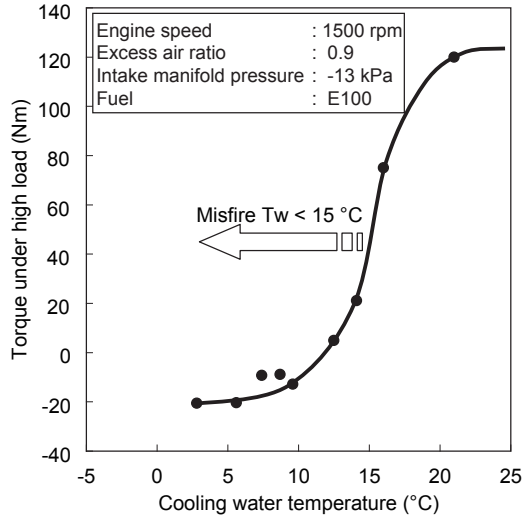


Fig. 5 Relationship between cooling water temperature and torque immediately after shifting to high load

Table 3 Comparison of engine performance when using gasoline and E100

Engine type		Gasoline	
Fuel		Gasoline	E100
Bore × stroke (mm)		81 × 87.3	
Displacement (cm^3)		1799	
Compression ratio		10.5	
Valve		2 intake valves	
Power		97.8	102
Torque (Nm)	Max	165	173
	At 2000 rpm	147	151
Starting time (sec; Ta = 20 °C)		0.5	3.4
Ambient temperature limit (°C)		-25 °C	15 °C

under high load. It is apparent that at water temperatures of 15°C or lower, attempting to change to high-load driving immediately after startup would cause misfires when E100 is being used. The cause, as discussed earlier, is probably that when driving under high load, there is a large amount of fuel that cannot be completely vaporized.

Table 3 shows the performance of an engine configured for gasoline when it is used without modification in an FFV. This confirms that at low temperatures there are issues with increased starting time due to decreased vaporizability and with commercial product appeal due to ambient temperature limits and related matters. Optimization of the air fuel ratio (A/F), which was lean because of vaporizability at low temperatures, was considered as a means of resolving these issues.

4. Examination of Low-temperature A/F Optimization

Methods for optimization of low-temperature A/F include increasing the proportion of vaporized fuel and decreasing the amount of air. Among the methods to promote vaporization of the fuel are:

1. Raise the temperature of the air-fuel mixture
2. Minimize amount of fuel adhering to the cylinder wall
3. Lower the boiling point by reducing the pressure during compression

A method for reducing the amount of air is to optimize the air-fuel mixture volume during startup.

More specifically, these methods include:

1. Raise the compression ratio and advance the ignition timing in order to use the resultant cooling loss to raise the temperature of compression stroke ends
2. Minimize adhesion by strengthening the in-cylinder flow
3. Optimize the volume of air-fuel mixture to reduce fuel and reduce pressure during compression

The following describes confirmation of the effectiveness of these methods.

4.1. Optimization of the Compression Ratio

Raising the compression ratio causes the temperature

of compression stroke ends to rise, which increases the vaporizability of the fuel. The following shows the perspectives involved in determining the optimal compression ratio for an FFV.

1. Output characteristics are adequate at any of the ethanol concentrations
2. Enhanced fuel economy and power when using E100

Figure 6 shows the power output at different compression ratios when using E100. Since E100 has a high octane number, it enables minimum advance for best torque (MBT) operation largely across the entire range with a compression ratio of 12.5. This verified that a compression ratio of 12.5 or higher is desirable when using E100. Figure 7 shows the power output when E22 was used. It is clear that with E22, which is at the lower limit for ethanol concentration, raising the compression ratio too much would cause knocking. This necessitates retarding the ignition timing, which reduces the power output. Figure 8 shows the relationship of compression ratio, low-speed torque, and power output. A compression ratio of 11.5 was selected in order to provide torque equal to or higher than a gasoline engine even when driving with a fuel at the lower limit for ethanol concentration.

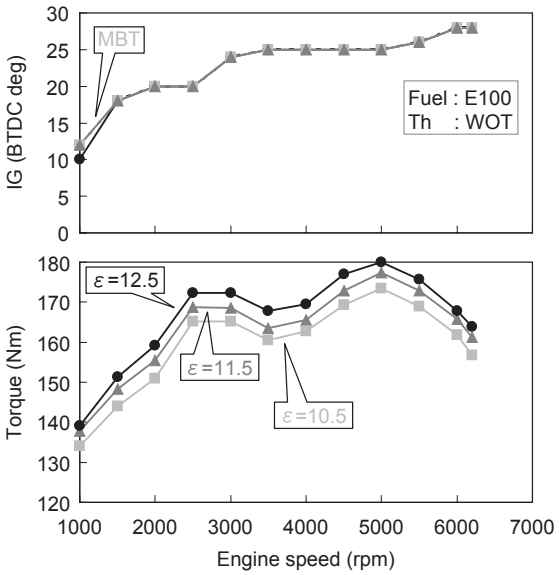


Fig. 6 Relationship between compression ratio and torque (E100)

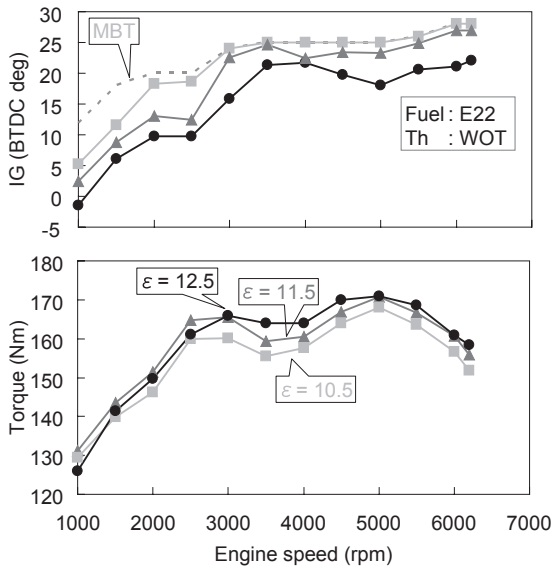


Fig. 7 Relationship between compression ratio and torque (E22)

4.2. Strengthening the In-cylinder Flow

In order to verify the effectiveness of enhancing the flow, an examination was made of operation with one intake valve, which can increase flow speed and generate swirls. The simulation and test below were conducted on the assumption of an engine idling immediately after startup.

4.2.1. Enhancing flow speed and generating swirls

When the lift of one intake valve is set to the bottom limit and the engine is operated with one intake valve, the flow speed increases and swirls are generated. Figure 9 shows the results from simulation of operation on one intake valve and operation on two intake valves with a state of turbulence at the compression stroke ends. It is apparent that turbulence remains to the compression stroke ends when operating with one intake valve. These swirls reduce the adhesion of fuel to the cylinder wall and are expected to promote flame propagation after ignition.

4.2.2. Reducing amount of fuel adhesion to cylinder wall

A simulation was conducted to show the amount of fuel adhering in the various areas of the piston, cylinder head, and sleeve in order to verify that enhancing flow speed is

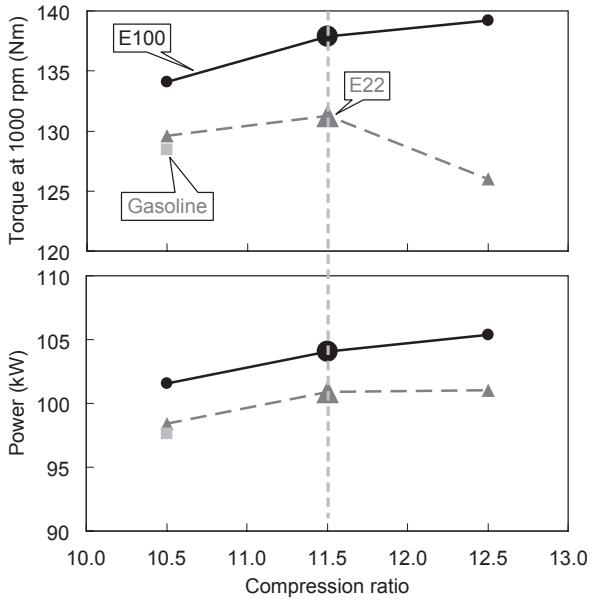


Fig. 8 Relationship between compression ratio and engine power (E22, E100)

an effective means of reducing fuel adhesion to the cylinder wall. Gasoline was used as the fuel. Figure 10 shows the simulation results. It can be seen that fuel adhesion to the sleeve primarily on the exhaust side decreases during operation with one intake valve. It can be reasoned that vaporizability will be enhanced as a result.

	1 intake valve	2 intake valves
Engine speed	1300 rpm	1300 rpm
Charging efficiency	41.7%	46.6%
Crank angle ATDC	5 deg	5 deg

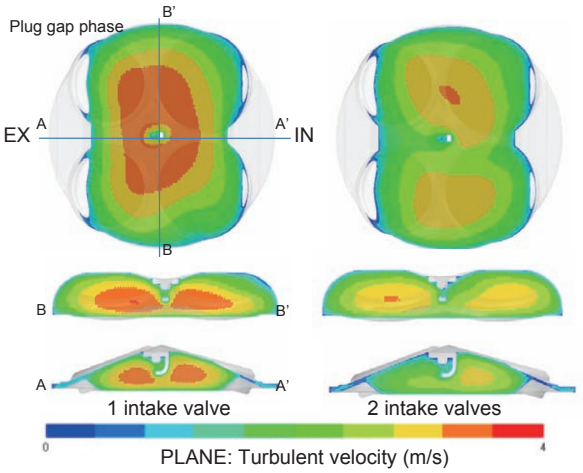


Fig. 9 Turbulent velocity simulation results (1 intake valve, 2 intake valves)

4.2.3. Promoting flame propagation

When swirls remain until compression stroke ends, fuel vaporizability increases. This is thought to promote flame propagation. In order to verify this, a high-speed flame ionization detector was used to measure the THC concentrations in the different areas of the combustion chamber. The state of consumption of the fuel was measured. In order to match with the simulation, gasoline was used as the fuel. Figure 11 shows the measurement results. The angle at which the combustion THC concentration has decreased to approximately one-half is defined as the angle at which flame is propagated in that part.

(1) Operation with two intake valves

The sequence of flame propagation has combustion go from ignition to the vicinity of the plug part (A in Fig. 11), following which, almost simultaneously, the flame propagates to the exhaust side (D and E in Fig. 11). After that, it propagates to the intake side (B and C in Fig. 11). Flame propagation is thought to proceed radially with the plug part as its center, and to advance somewhat faster in the exhaust system, where temperatures are higher.

(2) Operation with one intake valve

The sequence of advancing combustion goes from ignition to combustion of the air-fuel mixture in the vicinity of the plug part (A in Fig. 11). After that, the flame propagates in the same direction as the swirling flow (E-C-B-D in Fig. 11), and combustion advances rapidly.

It can be confirmed that the generation of a swirling flow

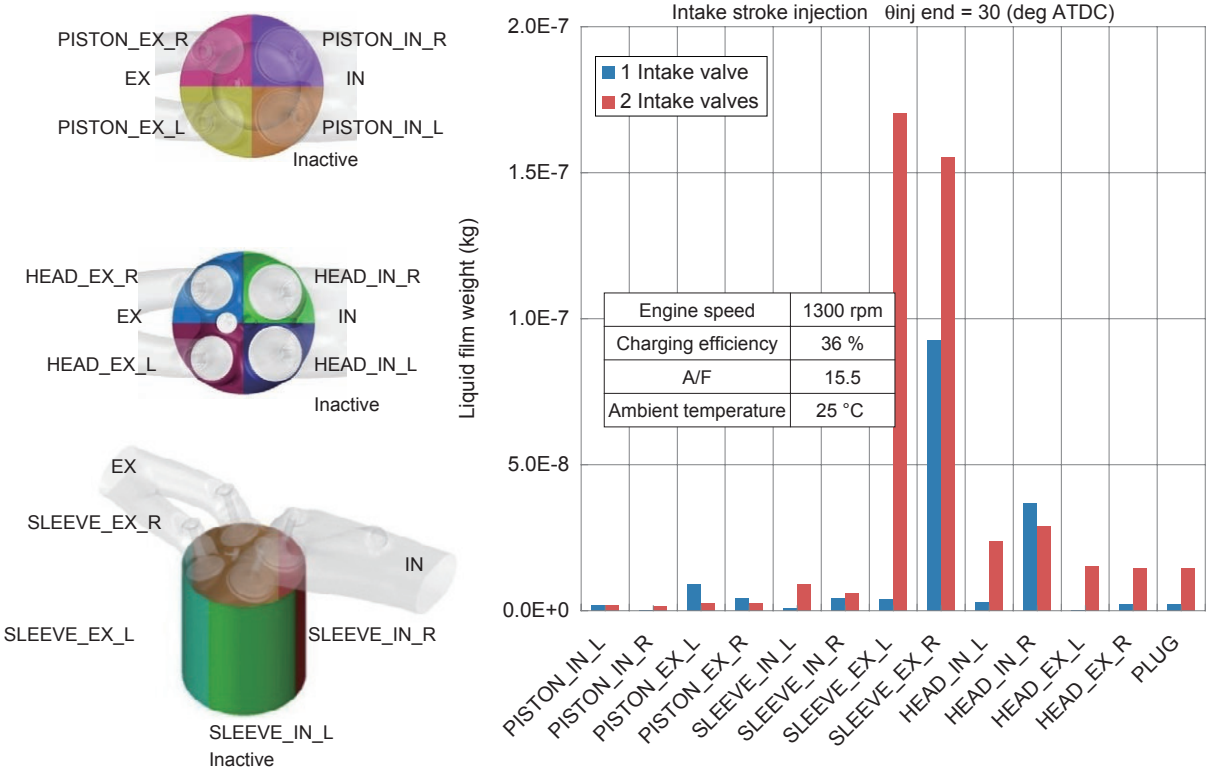


Fig. 10 Results of simulation of liquid film weight of fuel

by operation with one intake valve results in enhancement of vaporizability as well as promotion of flame propagation. Figure 12 shows a conceptual diagram of flame propagation. The above simulations and measurements confirmed that operation with one intake valve enhances vaporizability and promotes flame propagation.

4.3. Ignition Timing Angle

The temperature of the combustion chamber can be made to rise by advancing the ignition timing, which increases the cooling loss. In order to extend the advance limit, vaporization has to have advanced sufficiently even during the compression stroke.

4.3.1. Extending the advance limit during operation with one intake valve

Operation with one intake valve, which proved effective in enhancing vaporizability, is also effective in extending the advance limit. The combustion stability zone was represented by defining it in terms of excess air ratio and ignition timing. Stable combustion is defined as the zone in which the variation of the mean effective pressure is 7.5% or less. Figure 13 shows the advance limit and retard limit versus the excess air ratio. It is apparent that operation with one intake valve extends the combustion limit on the advanced side.

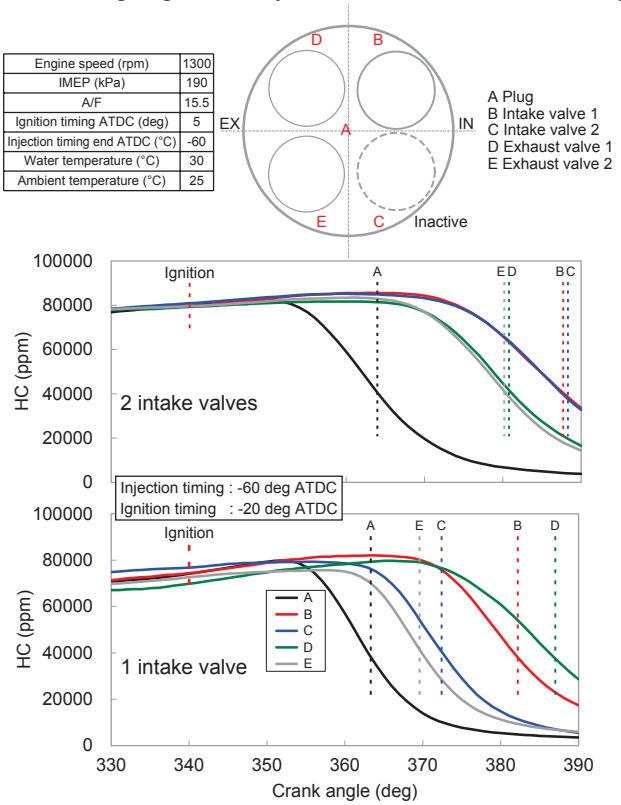


Fig. 11 Test result using high speed FID

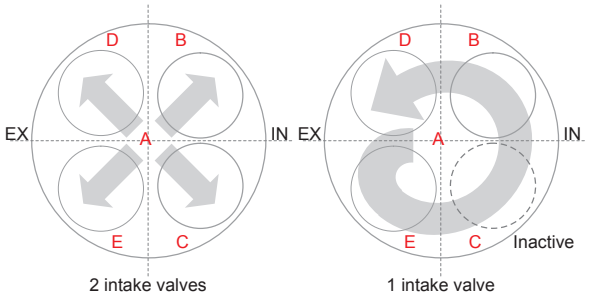


Fig. 12 Conceptual diagram of fire propagation

4.3.2. Verification by load change test

Based on the above results, the combination of operation with one intake valve and advanced ignition timing enables enhancement of the vaporizability of fuel when making the transition to high load at low temperatures (Fig. 14). Figure 15 shows the results from load change tests conducted during operation with a combination of one intake valve deactivation and advanced ignition timing. It is apparent

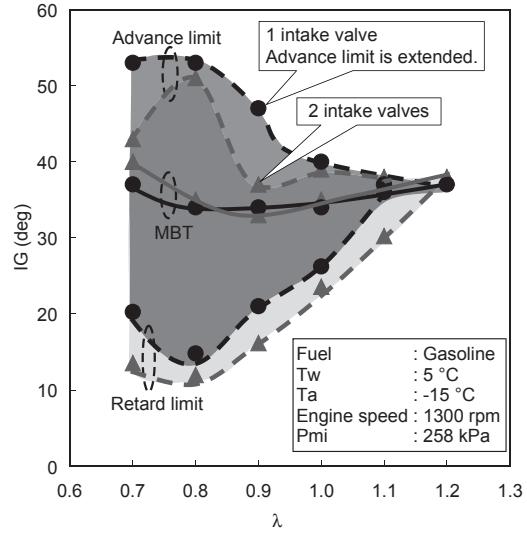


Fig. 13 Comparison of combustion stability zone with one intake valve and two intake valves

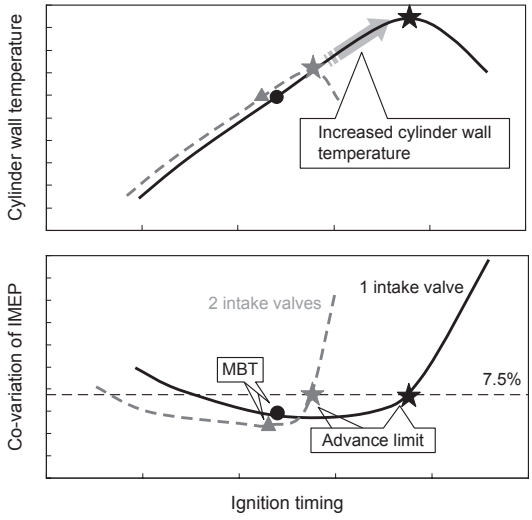


Fig. 14 Effect of ignition timing advance to increase cylinder wall temperature

Table 4 Test result at low ambient temperature

Engine type	Gasoline	FFV (optimized)
Compression ratio	10.5	11.5
Intake valve	2 intake valves	1 intake valve
Ignition timing (Fast idle at low Tw)	MBT	MBT + 5deg
Throttle opening angle (Engine start)	Normal	Close
Fuel	E100	E100
Starting time (sec; Ta = 20 °C)	3.4	2.0
Ambient temperature limit (°C; at load change test)	15	-10

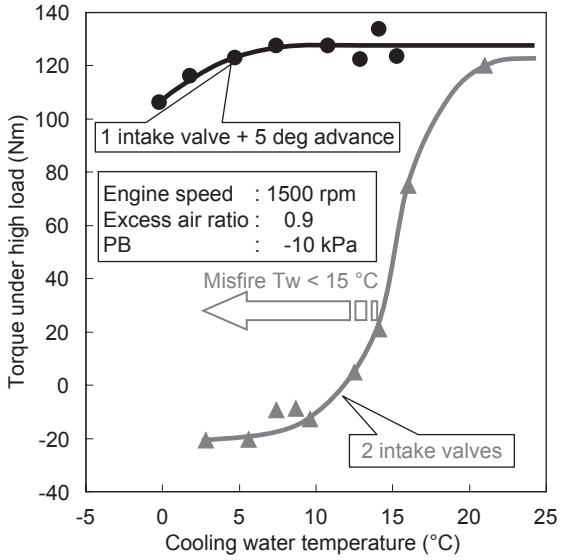


Fig. 15 Relationship between cooling water temperature and torque immediately after shifting to high load

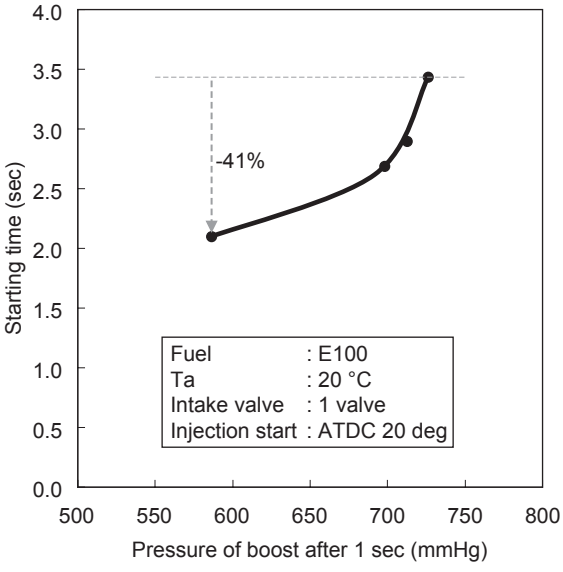


Fig. 16 Relationship between air intake pressure and starting time

that this combination enables high-load operation with E100 alone immediately after startup when the ambient temperature is low.

4.4. Optimizing the Volume of Air-fuel Mixture

As discussed above, the volume of air-fuel mixture is low and vaporizability is favorable under low load. It is conceivable that this characteristic could be used as a method for enhancing vaporizability by reducing the air-fuel mixture during startup to a volume lower than in a gasoline engine. Reducing the volume of air-fuel mixture reduces the quantity of heat required for vaporization. Furthermore, the pressure is reduced without changing the temperature at the compression stroke ends, so there is the additional effect of lowering the boiling point. Figure 16 shows the relationship between air intake pressure and starting time. It is apparent that as the air intake pressure is reduced, the starting time becomes shorter. The engine speed is raised without delay after startup by means of air volume control using drive-by-wire.

5. Effects of Optimizing Engine Specifications

5.1. Verification of Performance at Low Temperatures

Table 4 shows the results of enhanced combustion at low temperatures obtained by operation with one intake valve. Compared to the unmodified gasoline engine used for FFV, the engine with specifications optimized for FFV use has enhanced startability at low temperatures, is capable of load change operation from low water temperatures, and has enhanced commercial product appeal.

5.2. Achieving a Balance of Enhanced Combustion and Power Output

The balance of enhanced combustion at low temperatures with power output achieved through operation with one intake valve is enabled by the valve timing electronic control (VTEC) system. Table 5 shows a comparison of performance of an unmodified gasoline engine used for FFV with an engine optimized for FFV and including VTEC. It is apparent that the performance is enhanced beyond the gasoline engine for fuels from E22 to E100.

Table 5 Test result of engine performance

Engine type		Gasoline		FFV (optimized)	
Fuel		Gasoline	E100	E22	E100
Compression ratio		10.5		11.5	
Valve train system		Normal		VTEC	
	Low engine speed	2 intake valves		1 intake valve	
	High engine speed			2 intake valves	
Power (kW)		97.8	102	101	105
Torque (Nm)	Max	165	173	171	177
	2000 rpm	147	151	150	162

6. Conclusion

When a gasoline engine is applied to FFV use without modification, there will be issues with combustion at low temperatures and related matters. As the result of a search for methods to resolve such issues, the following conclusions were reached:

(1) The issue of combustion with E100 at low temperatures probably arises because the latent heat of evaporation is approximately three times greater than gasoline. Consequently, the fuel cannot be completely vaporized at low temperatures, so that it adheres to the sleeve and other such areas.
(2) Selection of an optimal compression ratio can enhance the vaporizability of E100, as well as power output and fuel economy, without degrading the performance when using E22.
(3) Operation with one intake valve increases flow speed and generates swirls. This can reduce the amount of E100 adhesion at low temperatures, which enhances vaporizability and promotes flame propagation.
(4) Operation with one intake valve extends the ignition timing advance limit.
(5) Extension of the ignition timing advance limit can advance the timing beyond MBT, raise the cylinder temperature, and prevent misfires even in load change tests that envision standing starts.
(6) Limitation of air intake volume during startup causes a reduction in the amount of fuel required, lowers the pressure at compression stroke ends, and lowers the boiling point so that both vaporizability and startability are enhanced.
(7) By the adoption of VTEC, operation with one intake valve and operation with two intake valves can be utilized differently, thus achieving a balance of maximum power output and commercial product appeal at low ambient temperatures.

Reference

(1) Saiki, R., Nakajima, S., Nakashima, H., Miki, K., Oki, H., Goryozono, Y.: Development of 1.8L Flexible Fuel Vehicle System for 2007 Model Year CIVIC for Brazil, Honda R&D Technical Review, April, 2007, p. 13-20

■ Author ■



Susumu NAKAJIMA

Verification of Equivalent Indicated Mean Effective Pressure Measurement Method

Keiichi NAGASHIMA* Keiji MIURA* Masahiko MATSUMOTO*
Naoki HANADA* Yoshito TSUKAMOTO* Kazuo TSUCHIYA**

ABSTRACT

Indicated mean effective pressure (IMEP) is generally used as a parameter directly expressing the status of combustion in an internal combustion engine. Issues of data stability, cost, and lifespan, among others, have made the use of pressure transducers in vehicle control applications challenging. The use of a method in which changes in engine vibration and bolt tightening force originating in the pressure diagram are measured and used to monitor equivalent IMEP, which has a strong correlation with IMEP, has potential for the future.

The research discussed in this paper studied a method in which signals originating in the pressure diagram were measured using a piezoelectric ignition plug washer-type force sensor and the results were used in the calculation of equivalent IMEP. When measurements were conducted in an actual engine, a correlation coefficient of 0.799 was obtained between IMEP, as determined from the pressure diagram, and equivalent IMEP, as determined using the force sensor. Alteration of the charge amplifier settings and the setting of a computation gate increased the correlation between equivalent IMEP and IMEP, raising the correlation coefficient to 0.990.

1. Introduction

Measures to reduce pollution and increase fuel efficiency in response to air pollution and climate change on a global scale have become an urgent responsibility in the automotive field[1]. In order to satisfy these demands, direct injection gasoline engines have been developed and research is being conducted on homogeneous charge compression ignition (HCCI) engines in attempts to achieve increased thermal efficiency. The variable mechanisms seen in recent valve systems are also playing an important role in increasing fuel efficiency and reducing emissions. On the negative side, the number of control parameters is increasing, and high-volume control data in the form of maps is becoming necessary. In addition, supporting the optimal control for transient operation that is being considered for introduction using conventional map and table reading and interpolation methods[2] will be challenging.

Understanding the status of combustion is an important consideration for the development of these types of engines and the use of these control systems, and the measurement of pressure diagrams has conventionally been employed as the standard method of doing so. Pressure diagrams represent important data, given that the maximum in-cylinder pressure, amount of heat release, and IMEP, which directly expresses volume of work for each cycle, can be derived from them. Moreover, measurements of transient states in actual vehicles are also important for parameter setting for the abovementioned control data and for control. In these cases, data stability in long-term measurements is prioritized even if a certain amount of distortion occurs in the pressure diagram, and the setting of the time constant of the measurement system is an important factor.

Compared to the conventional numerical integration method, the IMEP calculation method proposed by Tsuchiya et al.[3] offers a lower rate of calculation error, a higher calculation speed, and makes it possible to conduct calculations using only low-frequency data, even when less data is sampled per cycle.

* Automobile R&D Center
** Meiji University

Using this method, effective utilization of the measurement system can be expected even when there are restrictions upon it. In addition, if the frequency characteristic of the measurement system is known, correction is a simple matter[2], and the necessity of applying a frequency characteristic to the measurement system and determining the natural frequency of the sensors themselves is alleviated.

However, the high-accuracy pressure transducers used in engine development are expensive and present issues in terms of sensor life and mounting in the combustion chamber, and modifications are necessary for their use either in vehicle tests or in future engine control systems.

Rather than using pressure transducers that present issues of cost and life in addition to restrictions on layout, the project discussed in this paper used a method of measuring equivalent IMEP, which is strongly correlated with aforementioned IMEP as determined by an expression, from pressure diagram-related signals obtained from a piezoelectric ignition plug washer-type force sensor that can be positioned without any necessity for vehicle modification. This method displayed good results in actual engine tests.

2. Expression for IMEP and Concept of Equivalent IMEP

2.1. Method of Calculating IMEP using Pressure Diagrams based on Expanded Fourier Series

IMEP is generally defined using Eq. (1), based on stroke volume, Vs, in-cylinder pressure, P, and combustion chamber volume change, dV.

$$IMEP = \frac{1}{Vs} \oint PdV \tag{1}$$

If the periodicity of the in-cylinder pressure and the combustion chamber volume change is focused on and they are each expressed as the sum of periodic functions of the Fourier series type, expanded, and organized, Eq. (2) is obtained.

In this paper, the method of calculating IMEP shown as Eq. (2) will be termed "this equation." Here, the frequency component identical to the angular speed of the engine is treated as the fundamental harmonic.

$$\{IMEP\}_f = \frac{\pi}{2h}\{C_1 \cos\phi_1 + KC_2 \cos\phi_2\} \tag{2}$$

However, $K = (1+1/4\lambda^2)/2\lambda$

$\{IMEP\}_f$: IMEP as determined using this equation

C_1, C_2 : Amplitude of 1st- and 2nd-order frequency components

ϕ_1, ϕ_2 : Phase of 1st- and 2nd-order frequency components

λ : Conrod length / Crank radius

h : Constant (2 cycle: 1; 4 cycle: 1/2)

Equation (2) indicates that IMEP is determined exclusively by the 1st- and 2nd-order frequency components in the pressure diagram.

2.2. Concept of Measurement of Equivalent IMEP

Because the pressure transducers used in the measurement of in-cylinder pressure are directly positioned in the combustion chamber, their diaphragms are exposed to high-temperature gases, generating issues of durability and output voltage drift. A method of employing sensors outside the combustion chamber to measure signals expressing changes in the bolt tightening force and acceleration originating in combustion in the cylinders, and using Eq. (2) to determine the equivalent IMEP, which is strongly correlated with IMEP, would therefore be an effective measure[4, 5]. There is no negative effect if the high-frequency components of the signals being detected are damped while they are being transmitted in the combustion chamber, and a sensor optimized for low frequencies can be employed. The research discussed in this paper employed a piezoelectric ignition plug washer-type force sensor ("test sensor" below), positioned directly above the combustion chamber. This layout necessitated no modification of the engine.

3. Calibration of Test Sensor

3.1. Calibration Device

Hydraulic dead weight calibration systems are generally employed in the calibration of pressure sensors, but because the DC component cannot be detected in the case of piezoelectric sensors, a drift occurs in relation to gradual pressure changes, and calibration at a steady pressure therefore represents a challenge. A dynamic calibration system[6] was therefore used in the present research. Figure 1 shows the overall configuration of this system, and Fig. 2 shows the pressure transfer device. This device moves the pistons, and alternately impresses and releases a calibration pressure from a pressure tank. The maximum impressed pressure is 980 kPa, and the maximum

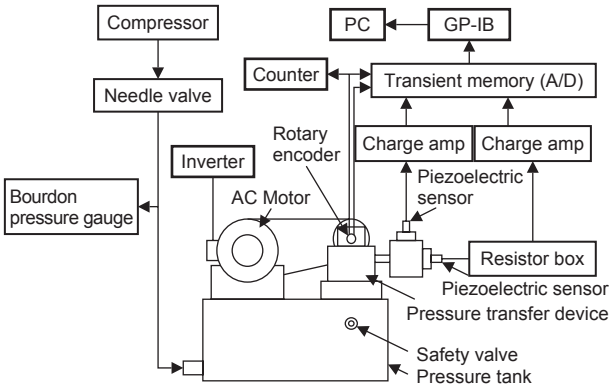


Fig. 1 Dynamic calibration system

impressed pressure frequency is 50 Hz. A combination of the 7061B piezoelectric pressure transducer and 5010 charge amplifier manufactured by Kistler was used as the reference transducer. LONG mode was employed for the time constant.

3.2. Measurement System employing Test Sensor

Figure 3 shows the measurement system, comprising the test sensor, charge amplifier, and cables. This system incorporates a feedback capacity C_f necessary for the conversion of the electric charge Q into output voltage and a feedback resistance R_f necessary for control of the output voltage drift.

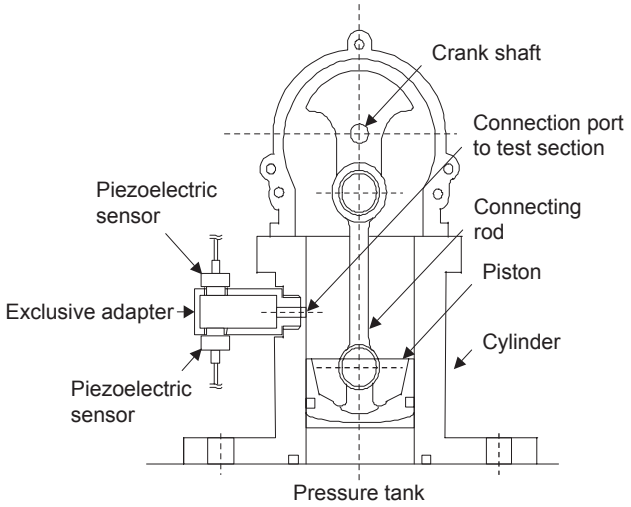


Fig. 2 Pressure transfer device

C_0 : Capacitance of piezoelectric element C_c : Capacitance of cable

R_{OC} : Sum of piezoelectric element insulation resistance and cable insulation resistance

C_f : Feedback capacitance R_f : Feedback resistance

E_i : Input voltage E_0 : Output voltage

Z_i : Input impedance of operational amplifier I_i : Total current

I_0, I_1, I_2 : Branch current Q : Generated electric charge

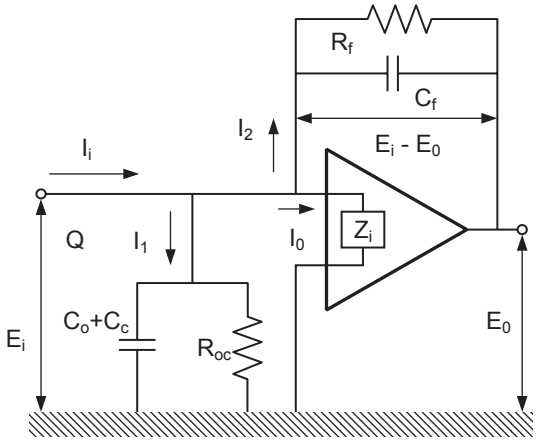


Fig. 3 Measurement system

3.3. Method of Calculation of Sensitivity

The sensor was calibrated with charge amplifier settings of C_f=1000 pF and R_f=10^9 Ω (time constant τ = 1 sec), at a calibration pressure of 400 kPa and an impressed frequency of 10 Hz from the dynamic calibration system. Figure 4 shows the results of measurement of the output waveform for crank angle increments of 0.5 deg and the application of averaging processing to 50 cycles. This graph shows that a voltage drop known as sag occurs in the output waveform, and the output voltage declines with the elapse of time.

If sag occurs in the output waveform, it becomes unclear which output voltage corresponds to the calibration pressure at a given crank angle, making it challenging to employ the conventional method of determining sensitivity from the amplitude of the output waveform in relation to the calibration pressure. In the present project, sensitivity was therefore determined from Fig. 5, showing the output voltage of the reference transducer on the horizontal axis, and the output voltage of the test sensor on the vertical axis. The gradient of the line shows the sensitivity of the test sensor, and y_1 corresponds to the drop in output voltage due to sag. Below, this method will be termed the slope method.

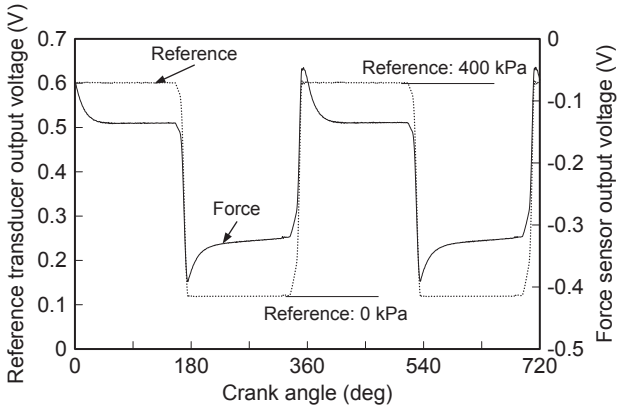


Fig. 4 Results of calibration

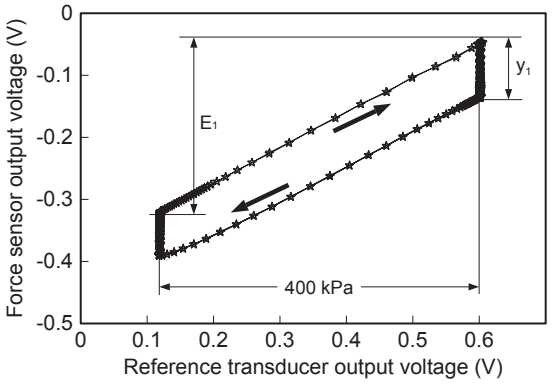


Fig. 5 Calculation of sensor sensitivity using slope method

Table 1 Sensor sensitivity

Calibration pressure (kPa)	Sensitivity (kPa/V)
100	1721
200	1751
300	1864
400	1842
500	1849

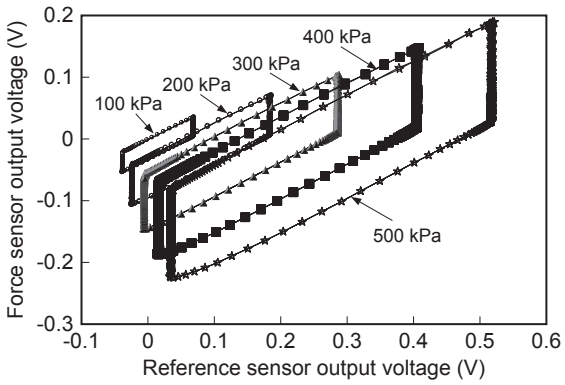


Fig. 6 Result of calibration using slope method

3.4. Calibration using the Slope Method

Figure 6 shows the results of calibration for each 100 kPa increment of impressed pressure from 100 kPa to 500 kPa, at charge amplifier settings of C_f=1000 pF and R_f=10^8 Ω (time constant τ = 100 msec) and an impressed frequency of 10 Hz. Table 1 shows the sensitivity for each increment of impressed pressure, giving an average sensitivity of 1805 kPa/V.

4. Natural Frequency of Test Sensor

In order to accurately determine equivalent IMEP, it is important that the sensor employed should not possess a natural frequency close to the 1st- and 2nd-order frequency components of engine speed. The maximum engine speed of a mass production vehicle is approximately 8000 rpm, while that of a racing vehicle is approximately 20000 rpm. The respective 2nd-order frequency components of these engine speeds is 266.7 and 666.7 Hz. The natural frequency of the sensor should therefore be below this frequency band.

In order to measure the natural frequency of the test sensor when attached in its measurement position, a test sensor and an acceleration sensor were attached to a cylinder head, and a steel ball impact test was conducted. Figure 7 shows the test device. Steel balls of 0.48 mm in diameter and 0.48 g in mass were rolled down a guide secured on a stand and dropped to impact close to the central electrode of the spark plug to which the test sensor was attached. The vibration resulting from the impact was measured by the test sensor and the acceleration sensor, and a frequency analysis was conducted using an FFT analyzer. The acceleration sensor was attached at the point shown as A in Fig. 8.

Figures 9 and 10 respectively show the output waveform and power spectrum for the acceleration sensor. The results show that the test sensor attached in the measurement position does not possess any natural frequencies within the frequency band that would affect IMEP measurements.

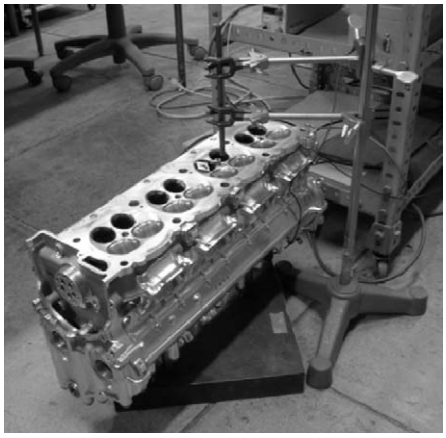


Fig. 7 Steel ball impact test

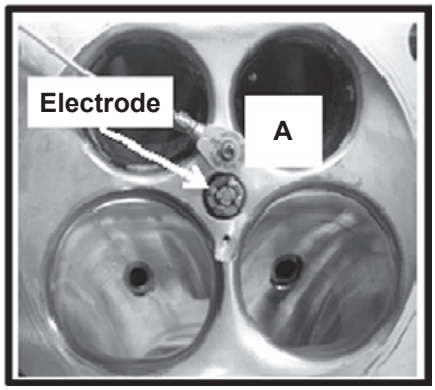


Fig. 8 Location of sensors

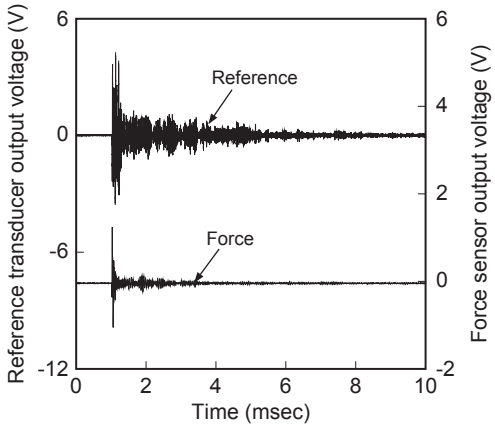


Fig. 9 Sensor output voltage

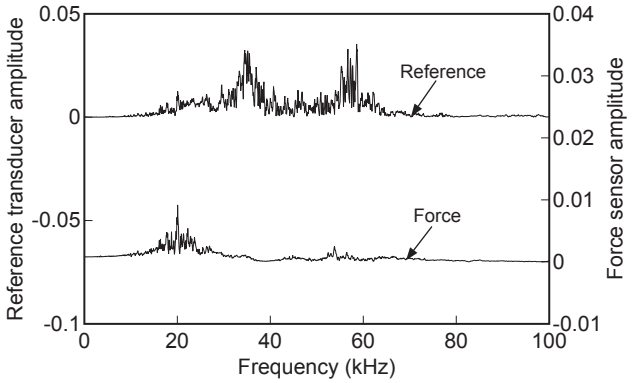


Fig. 10 Power spectrum

5. Measurement of Equivalent IMEP in an Actual Engine

5.1. Test Equipment and Test Engine

Figure 11 shows the test equipments. A test sensor and a pressure transducer to provide data for comparison were positioned as shown in the figure. The output waveforms of the sensors were sent to a Fourier series type combustion analyzer[7], and sensor outputs in the same cycles were compared. A Kistler 7061B pressure transducer was employed. The transducer was connected to a 5011B charge amplifier, and the time constant was MEDIUM. (This pressure transducer will be termed the "reference transducer" below.) The test engine spark plugs rather than the test sensor were used to provide the spark. Table 2 shows the specifications of the engine used in the tests and the test conditions.

5.2. Results of Measurement of Equivalent IMEP

The system shown in Fig. 3 was used in these tests as the measurement system incorporating the test sensor. C_f was 1000 pF and R_f was 10^9 Ω, corresponding to the SHORT mode of pressure diagram measurements. At this time, the time constant τ was 1 sec and the low-range cutoff frequency, fc, was 0.159 Hz.

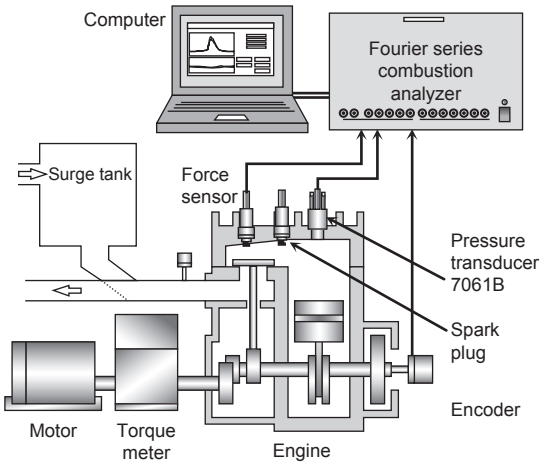


Fig. 11 Test equipments

Table 2 Engine specifications and test conditions

Engine type	Shibaura GEF30RE
Bore × Stroke	78 × 62 (mm)
Displacement	296 (cm^3)
Compression ratio	7.4
Engine speed	1,800 (rpm)
Throttle	1/4 - 3/4
Ignition timing	BTDC 22 (deg)
A/F	12.7, 15.3

The output waveforms of the test sensor and the reference transducer were recorded for 300 cycles under the conditions shown in Table 2 (A/F=12.7), and then averaged. The results are shown in Fig. 12. These results indicate that except for the high harmonic noise component of the output waveform of the pressure transducer, its form is close to that of the pressure diagram. Figure 13 shows the changes in IMEP and equivalent IMEP over a continuous 300 cycles. The equivalent IMEP almost exactly traces IMEP.

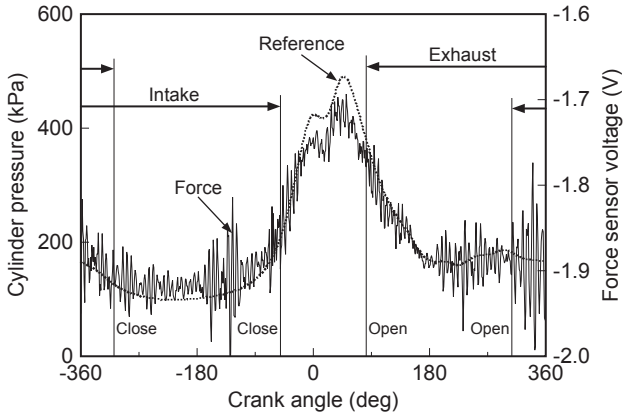


Fig. 12 Cylinder pressure and force sensor output voltage waveforms

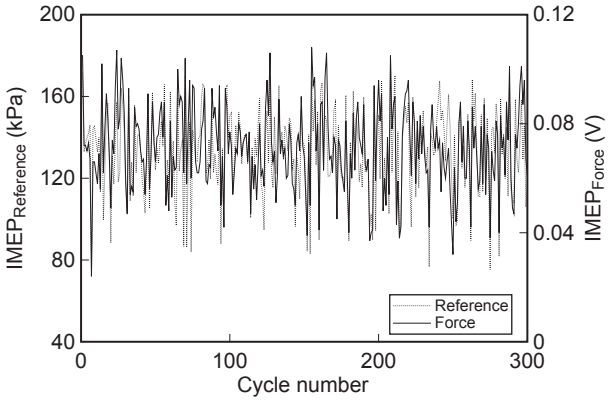


Fig. 13 IMEP and equivalent IMEP in continuous cycles

Figure 14 shows the correlation between the equivalent IMEP and IMEP. The correlation coefficient was 0.799.

The results discussed above indicate that rough monitoring of IMEP is possible under the test and measurement conditions employed in this research. However, more precise tracing and an increased level of correlation would be necessary for the achievement of more accurate measurements of equivalent IMEP and their application in engine control.

5.3. Achievement of Increased Equivalent IMEP Measurement Accuracy

When measurements are conducted using the combination of a piezoelectric sensor and a charge amplifier, if the insulation electric resistance (R_{oc} in Fig. 3) declines, baseline drift occurs in the output waveform. If this drift continues for an extended period, it eventually exceeds the measurement range, and measurements can no longer be conducted. Decline in the insulation electric resistance results from factors such as infiltration of fluid droplets into the connectors and increases in the temperature of the elements, and to control it, it is necessary to use a low setting for the feedback resistance, R_f. The stability of the baseline was therefore verified at an R_f setting of 10^9 Ω, the setting used in the previous sections. The engine described in Table 2 was used as the test engine. 2/4 throttle and an A/F of 12.7 were selected as the test conditions. A pressure diagram was measured using the reference transducer for the purposes of comparison. The results are shown in Fig. 15. As the figure shows, baseline drift occurs in the test sensor output as the engine is operating, and it tends to exceed the measurement range. It was therefore necessary to set R_f at a lower figure. It was possible, however, that employing a lower setting for R_f might reduce the ability to detect low-frequency components, and thus affect measurements of equivalent IMEP. If the frequency characteristic of the measurement system was determined in advance, correction could be applied[4] as a measure in response to this phenomenon. It was therefore practical to prioritize the achievement of stability by setting R_f at a lower figure.

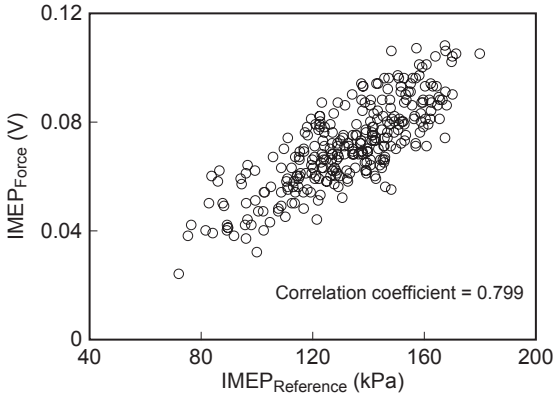


Fig. 14 Relation between IMEP and equivalent IMEP

In addition, electric noise and vibration is superimposed on the test sensor output waveform, as shown in Fig. 12. In this case, the SN ratio declines in the range in which in-cylinder pressure is low, such as the intake and exhaust strokes, and the SN ratio becomes comparatively good when the in-cylinder pressure is high, close to compression top dead center. A computation gate was therefore positioned close to compression top dead of center, where the SN ratio was favorable, and equivalent IMEP was calculated using only the data inside the computation gate.

Figures 16 and 17 show the results obtained when R_f was changed to 10^8 Ω and a computation gate was set at compression top dead of center ±120 deg in order to test the accuracy of measurements of equivalent IMEP. Figure 16 indicates that equivalent IMEP traces changes in IMEP, while Fig. 17 shows an increase in the correlation coefficient from the figure of 0.799 shown in Fig. 14 to 0.990.

5.4. Application in High-speed Engine

This section will discuss the application of the method to a high-speed engine using the results obtained up to the previous section. A V8 racing engine with a bore of 97 mm, a stroke of 40.25 mm, and a compression ratio of 13.0 was employed. The engine was operated at 14000 rpm at

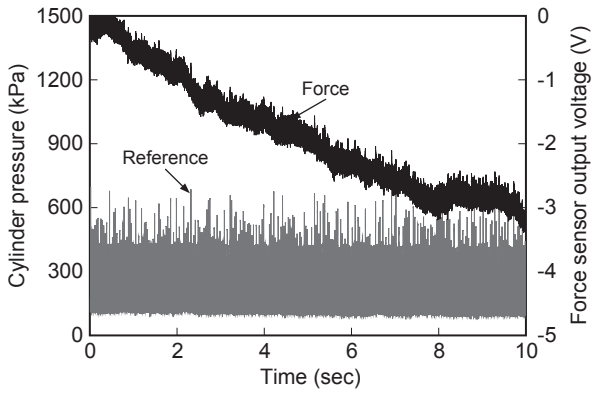


Fig. 15 Baseline drift of sensors

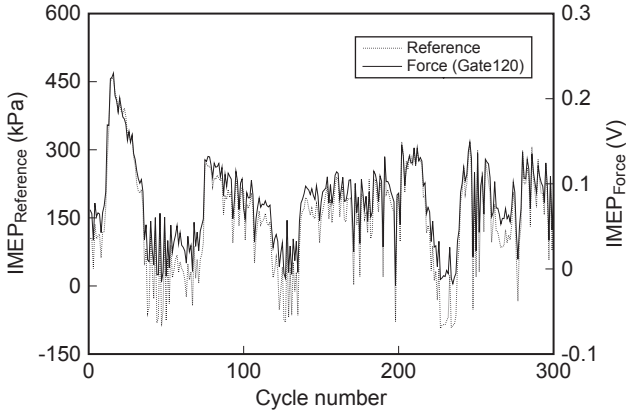


Fig. 16 IMEP and equivalent IMEP in continuous cycles (R_f modified)

wide-open throttle, an A/F of 13.1, and an ignition timing corresponding to MBT. In the case of the measurement system used for detection of equivalent IMEP, a test sensor was positioned in the 7th cylinder, and the feedback resistance of the charge amplifier was set at $R_f=10^8$ Ω. For purposes of comparison, a pressure diagram was measured simultaneously using a Kistler 6081AQ05 transducer and 5011 charge amplifier (MEDIUM mode was used for the time constant). No gate was set for the data processing.

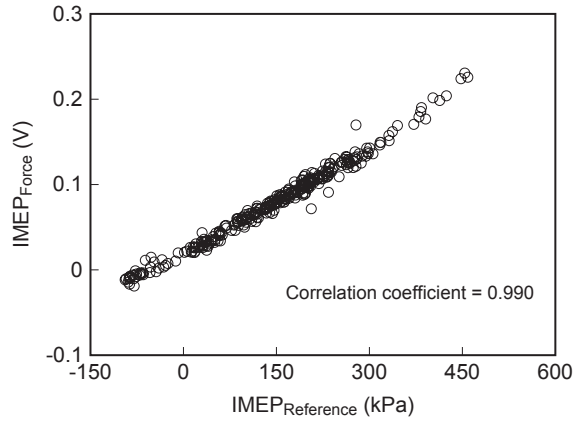


Fig. 17 Relation between IMEP and equivalent IMEP (R_f modified)

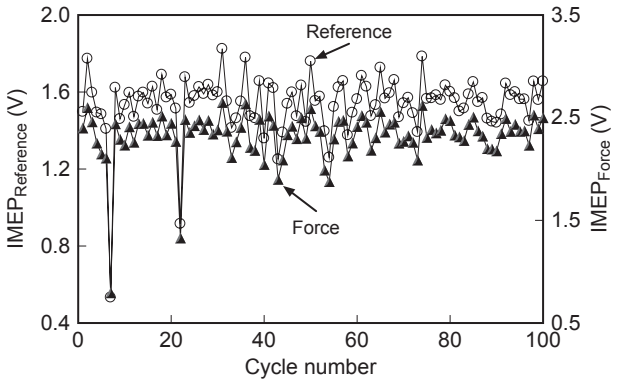


Fig. 18 IMEP and equivalent IMEP in continuous cycles (in high-speed engine)

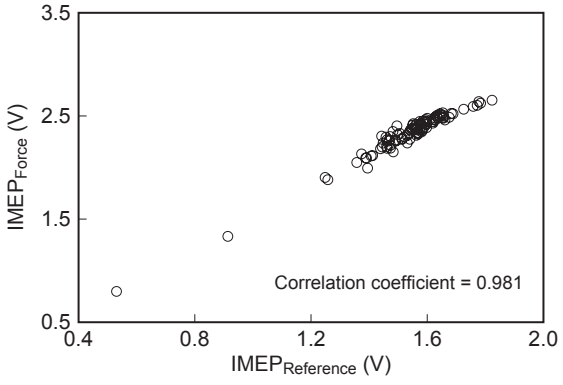


Fig. 19 Relation between IMEP and equivalent IMEP (in high-speed engine)

Figure 18 shows changes in IMEP and equivalent IMEP over 100 cycles, indicating that equivalent IMEP is able to trace changes in IMEP even in a racing engine. Figure 19 shows the correlation between equivalent IMEP and IMEP. A high level of correlation is achieved, with a correlation coefficient of 0.981.

The results above demonstrate that equivalent IMEP can be accurately measured even in a high-speed engine such as a racing engine if the charge amplifier settings are optimized.

6. Conclusions

The use of an ignition plug washer-type force sensor that could be positioned without modification of the engine helped to enable the measurement of equivalent IMEP, a parameter with a strong correlation with IMEP. The results obtained are as follows:

(1) When measurements of equivalent IMEP were conducted using the ignition plug washer-type force sensor using a setting corresponding to the SHORT mode of the time constant for pressure diagram measurements ($R_f=10^9$ Ω), a correlation coefficient of 0.799 was obtained between equivalent IMEP and IMEP. This correlation was adequate for rough monitoring, but the achievement of increased ability to trace IMEP and a higher level of correlation were necessary for use of the method in applications such as engine control.

(2) The use of an R_f setting of 10^8 Ω and the setting of a computation gate at ±120 deg in order to use only data close to compression top dead center in the calculation of equivalent IMEP increased the ability of equivalent IMEP to trace IMEP and increased correlation to 0.990.

(3) The correlation between equivalent IMEP and IMEP could be increased even in a racing engine operated at high engine speeds by optimization of the charge amplifier settings.

References

(1) Daisho, Y.: A Prospect on Automobiles for the 21st Century -Resolving Problems Associated with Environment and Energy-, Journal of JSAE, Vol. 56, No. 1, p. 18-24 (2002)

(2) Tsuchiya, K.: Applications of Indicated Mean Effective Pressure to Engine Control, Journal of JSAE, Vol. 58, No. 4, p. 25-30 (2004)

(3) Tsuchiya, K., Nagashima, K.: A Calculation Method for Indicated Mean Effective Pressure Based on Harmonic Analysis of Pressure Waveform, International Journal of Engine Research (JER03702), Vol. 4, No. 2, June (2003)

(4) Tsuchiya, K., Kouchi, Y., Miyamoto, T.: Monitoring Method of Indicated Mean Effective Pressure by Use of Acceleration, Force and Gap Sensors, JSAE Annual Congress Proceedings, 28-06, p. 5-8 (2006)

(5) Nishio, S., Tsukahara, S., Tsuchiya, K., Sakai, M.: Development of Marine Diesel Engine Management System (2nd Report), 76th, JIME Annual Congress Proceedings, A109 (2007)
(6) Kawa, T., Miura, K., Hatano, Y., Minagawa, T., Kawa, H., Yanagihara, S.: Development of Dynamic Calibration Systems for Cylinder Pressure Sensors, JSAE Annual Congress Proceedings, 14-07, p. 1-4 (2007)
(7) Nagashima, K., Tsuchiya, K., Kamimoto, T.: Development of Fourier Series Type Combustion Analyzing System, JSAE Transactions, Vol. 33, No. 2, p. 31-36 (2002)

■ Author ■


Keiichi NAGASHIMA


Keiji MIURA


Masahiko MATSUMOTO


Naoki HANADA


Yoshito TSUKAMOTO


Kazuo TSUCHIYA

Prediction Method of Low-cycle Fatigue Breakdown in HSDI Diesel Cylinder Head

Shohei MIKAMI* Koichi OGINO* Mitsumasa SORAZAWA*

ABSTRACT

This paper introduces a method of predicting low-cycle fatigue breakdown that takes as its focus the area around the glow plug hole of the diesel engine cylinder head, where cracks frequently occur during operating modes in which hot and cold cycles are repeated. Because an understanding of the strain amplitude and temperature of the areas in which cracks originate is necessary in predicting fatigue breakdown, strain analyses were conducted using CAE, and at the same time a method of calculating temperature from hardness measurements was used to determine local temperatures. This made it possible to study the local conditions of the cylinder head combustion chamber, which had previously represented a challenge. In addition, a hot-and-cold cycle endurance test using a prototype engine demonstrated the validity of predictions of low-cycle fatigue breakdown using the new method. The project also proposes the incorporation of the method in the design process in order to employ it as a tool for the review of specifications in new engine development.

1. Introduction

The occurrence of cracks between the valve seats of the cylinder head combustion chamber (Fig. 1) due to hot-and-cold cycles has been a major issue in diesel engine development up to the present. This type of cracking is considered to be a thermal fatigue phenomenon[1]. When cyclic loads are applied to the combustion chamber during the hot-and-cold cycle, plastic deformation occurs repeatedly, becoming the origin of the cracks.

In this type of cracking due to low-cycle repetition, a method of predicting fatigue life using the strain amplitude as an index is available, as shown by the Manson-Coffin equation[2]. Because the strength characteristic of materials varies with temperature, it is necessary to measure the temperature of the area under analysis in addition to its strain amplitude in order to predict the fatigue life of the cylinder head combustion chamber.

However, the measurement of the strain amplitude while the engine is in operation is highly technologically challenging. Up to the present, methods such as the estimation of the strain amplitude from the comparatively more easily measured temperature, based on the relationship between strain amplitude and temperature in a limited operating area, have been attempted (Fig. 2). Such estimates are, however, not always sufficiently accurate, and it has not been possible to accurately predict fatigue life. Because of this, there has been no option but to use endurance tests involving actual engines as the main means when attempting to verify the durability and reliability of engines, resulting in an increase in the number of engine prototypes constructed.

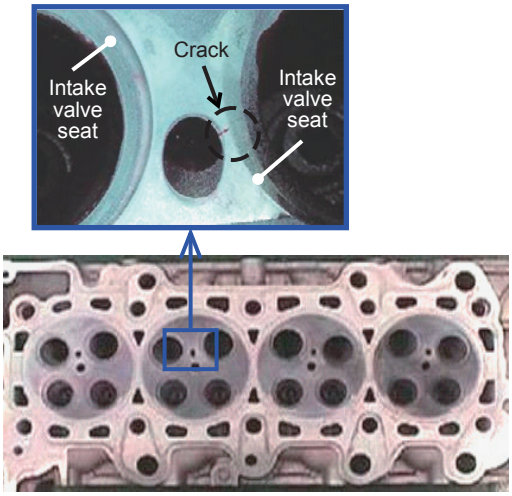


Fig. 1 Crack found beside glow plug hole

* Automobile R&D Center

The research discussed in this paper, therefore, attempted to formulate a method of accurately measuring and analyzing the temperature and strain amplitude of the areas in which cracks originate, in addition to attempting to predict the occurrence of cracks during the hot-and-cold cycle by studying the conditions of strain amplitude and temperature in each part of the combustion chamber and comparing this with the fatigue limit diagram of the heat cycle for the cylinder head material.

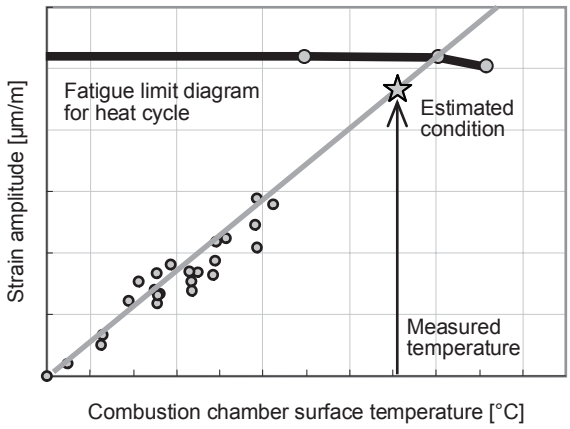


Fig. 2 Estimation of combustion chamber surface condition based on measured temperature

2. Method of Prediction of Low-cycle Fatigue Breakdown

2.1. Subject of Analysis

Hot-and-cold cycle endurance tests were conducted using prototype engine A in order to develop and verify a method of prediction of low-cycle fatigue breakdown in the cylinder head combustion chamber. Figure 3 shows an overview of hot-and-cold cycle test mode 1, which was used in the present research. This endurance test mode was selected because past experience of the development of diesel engines has indicated that of several test modes available, it is severe and thus appropriate for evaluation of cracking in the cylinder head combustion chamber. For the present research, this test mode was repeated approximately 104 times. The status of cracking in each part of the combustion chamber was varied by varying the temperature of the surface of the combustion chamber, giving four separate endurance test cases in which the cooling conditions and the combustion conditions were changed. Table 1 shows the endurance test conditions and the state of the cylinder head combustion chambers following completion of the tests. The temperatures beside the glow plug holes and the temperatures between the exhaust valves as shown in Table 1 are the highest surface temperatures reached during the endurance test modes, and were measured on flat areas of the surface using thermocouples.

In Case 1, cracks occurred between the intake valve seats (beside the glow plug hole) (“a” in Table 1), between the exhaust valve seats (“b” in Table 1), and between the intake and exhaust valve seats (“c” in Table 1) on the surface of the cylinder head combustion chamber. In Case 2, cracks occurred beside the glow plug hole and between the intake and exhaust valve seats, and in Case 3, cracks occurred beside the glow plug hole. No cracks occurred in Case 4.

Figure 4 shows the results of observation of the fracture face of a crack beside the glow plug hole. Generally, the glow plug hole is a hole drilled in the surface of the cylinder head combustion chamber by machining; the surface of the cylinder head combustion chamber is also formed by machining. Because of this, the glow plug hole has a right-angled or obtuse-angled edge. Observation of fracture faces showed that cracks originated on the edge of the glow plug hole rather than on the flat sections of the surface of the combustion chamber. The project therefore worked towards prediction of low-cycle fatigue breakdown with this area as the subject of analysis.

2.2. Method of Analysis of Strain Amplitude

When a strain gauge is used to measure strain, because it is not possible to directly attach the gauge to the edge of the glow plug hole, local measurements of strain cannot be taken. In addition, the limits of the heat resistance of the strain gauge prevent measurements from being taken

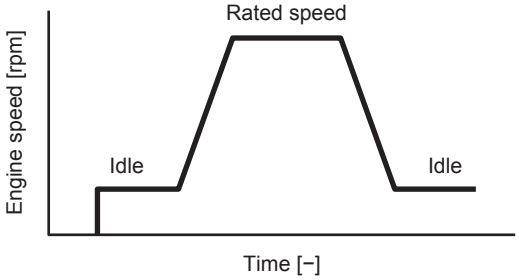


Fig. 3 Hot and cold cycle test mode 1

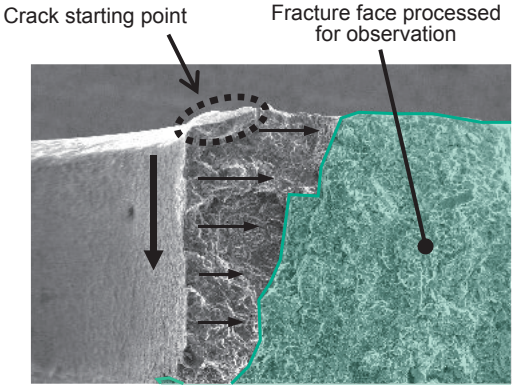
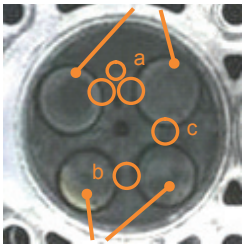
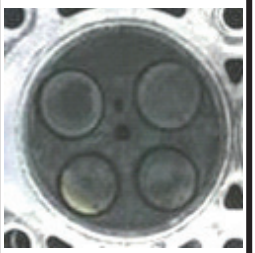


Fig. 4 SEM image of broken-out section of crack beside glow plug hole

Table 1 Hot and cold cycle endurance test conditions and resulting cracks

	Prototype engine A			Indicates location of crack observed after test
Case No.	1	2	3	4
Occurrence of cracks	Intake valve  Exhaust valve			
Engine load	Full load	Full load	Full load	Full load
Coolant temperature [°C]	96	97	80	82
Coolant flow rate	Base	Base +75%	Base +26%	Base +39%
Nozzle cone angle	Base	Base	Base	Base -3 deg
Temperature beside glow plug hole [°C]	282	253	226	225
Temperature between exhaust valve seats [°C]	298	256	236	230

in high-temperature environments at high engine output. A strain analysis was therefore conducted using computer-aided engineering (CAE).

The generation of strain due to inhomogeneous temperature distribution in the combustion chamber and the concentration of that strain is thought to be the origin of cracking in the cylinder head combustion chamber during hot-and-cold cycle endurance tests. Figure 5 shows the average temperature distribution in the combustion chamber during the cycle. The temperature is high at the center of the combustion chamber, in particular at the injector hole. The high temperature at the center of the combustion chamber results in thermal expansion towards the external circumference of the chamber. By contrast, the rate of thermal expansion of the external circumference of the combustion chamber is lower than that of the center, because its temperature is comparatively low. This difference in the rate of thermal expansion due to inhomogeneous distribution of temperature results in compressive strain in the radial direction in the combustion chamber. It is thought that this compressive strain concentrates in areas with a low cross-sectional area, such as beside the glow plug hole and between the valve seats, and that these areas of concentrated strain become the origin points of cracks with repeated hot-and-cold cycles.

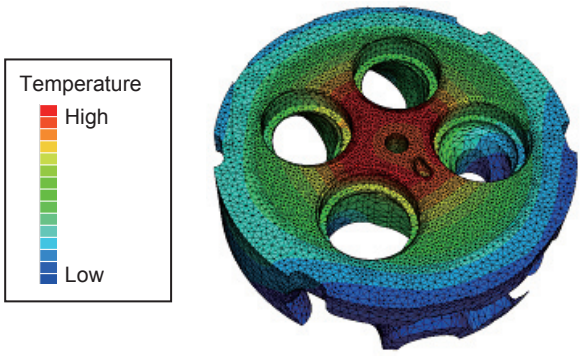


Fig. 5 Temperature distribution of combustion chamber surface

The flow of the analysis was therefore established as follows: first the temperature distribution was determined by means of a thermal analysis, then a strain analysis was conducted on the basis of the temperature distribution. The analysis followed the order (1) to (5) described below (Fig. 6):

(1) A finite element method (FEM) model of the cylinder head was formulated (Fig. 7).
(2) Heat transfer coefficients determined using computational fluid dynamics (CFD) analysis were mapped onto the surfaces of the water jacket in the FEM model, and thermal boundary conditions were imparted. VECTIS (a three-dimensional fluid dynamics program) was used as the analytic solver.
(3) Thermal boundary conditions were imparted to the combustion chamber and other cylinder head surfaces. The area was segmented and figures for gas temperature and heat transfer coefficient were set in such a way

that the analysis results would agree with the results of thermocouple measurements of the combustion chamber surface temperature under the same operating conditions as an actual endurance test. The thermal boundary conditions were set in response to the higher and lower temperatures occurring during the endurance test mode, occurring at rated output and during idling, respectively. Here, measurements should be taken at multiple points in order to determine the temperature distribution of the combustion chamber using thermocouples.

(4) A thermal analysis was conducted using ABAQUS (a general purpose nonlinear finite element analysis program).

(5) The strain amplitude during hot-and-cold cycles was analyzed based on the determined temperature distribution. ABAQUS was used as the analytic solver, as in the case of the temperature analysis.

There are also examples in which a combustion analysis using CFD has been conducted as the stage of imparting thermal boundary conditions to the surface of the combustion chamber[3), 4)]. Figure 8 shows the flow of the analysis in this case. However, accurately modeling the actual state of combustion using CFD necessitates numerous processes – an in-port pulsation analysis, an in-cylinder flow analysis, a spray analysis, and a combustion analysis – and a high level of analytic accuracy is necessary for each of these processes. Spray and combustion analyses in particular involve a large expenditure of time for the coordination and verification of multiple parameters. In addition, it is necessary to compare the results of a combustion analysis with the results of temperature measurements taken in an actual engine as one means of verification of the accuracy of the analysis. Taking into consideration the main purpose of the analysis in predicting low-cycle fatigue breakdown and the reduction of computation time, the method shown as (3) above was devised in the case of the present project. Figure 9 shows an example of the setting of thermal boundary conditions for the combustion chamber for the high-temperature state of the endurance test mode using this method. Figure 10 compares the temperature of the surface of the combustion chamber at this state as measured using thermocouples and as determined by a CAE thermal analysis.

The relationship between temperature and strain amplitude determined in Step (5) using CAE was compared with actual measurements taken using thermocouples and strain gauges. The area compared was the flat section beside the glow plug hole, as shown in Fig. 11. Figure 12 shows the results of the comparison.

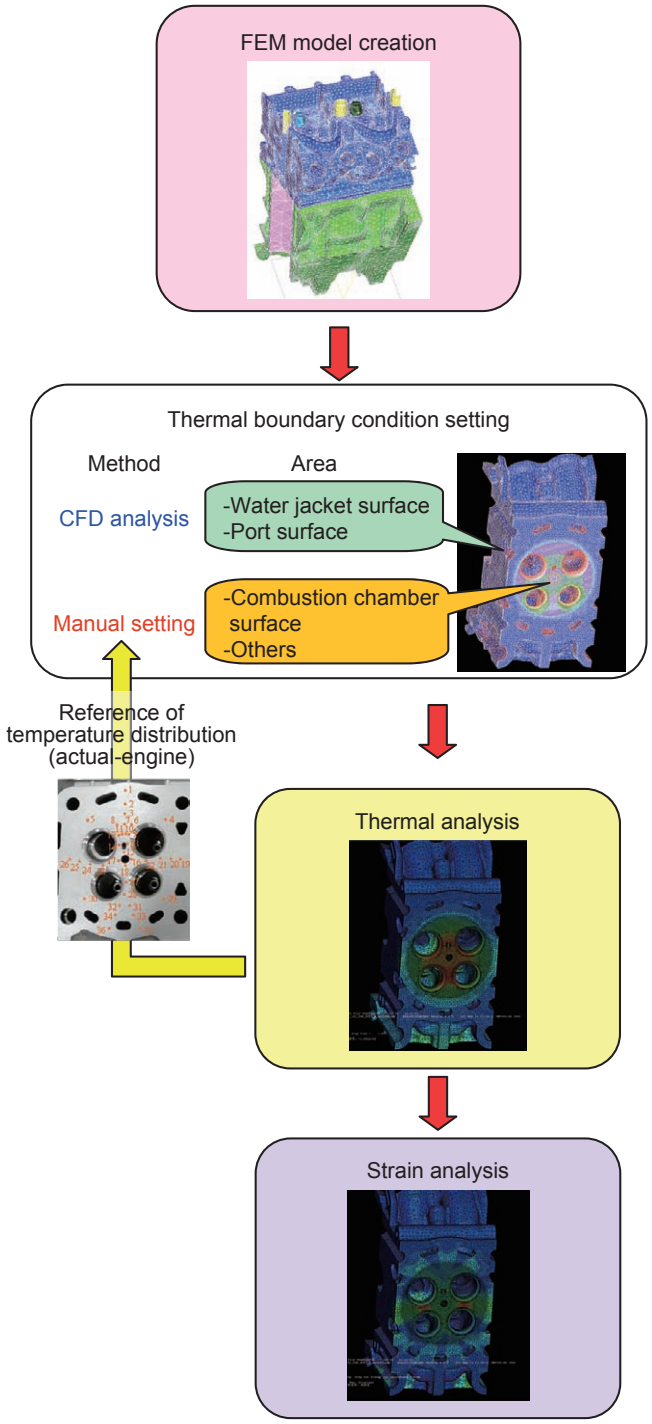


Fig. 6 Flow diagram of strain analysis

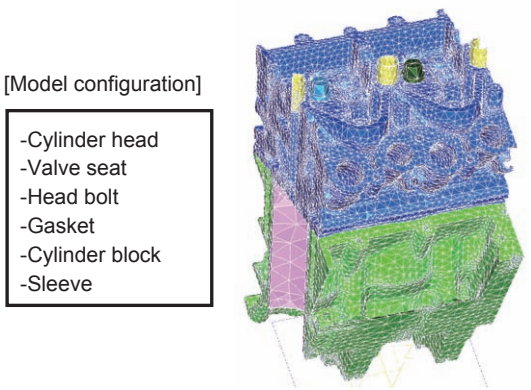


Fig. 7 FEM model configuration

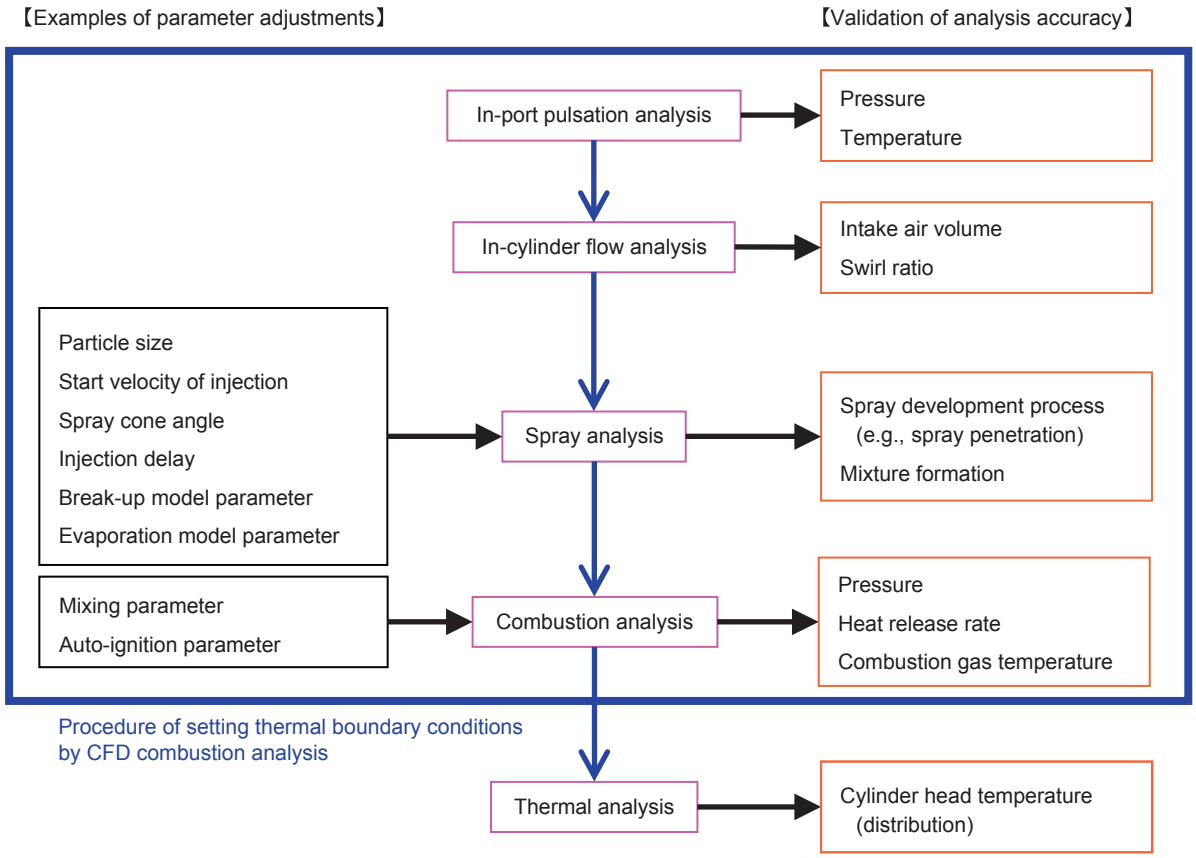


Fig. 8 Procedure of CFD combustion analysis and examples of parameters and validation at each step

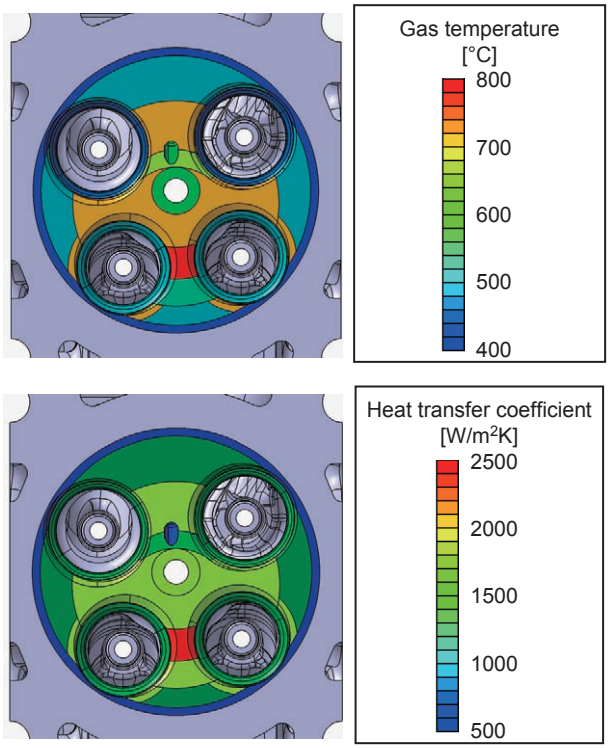


Fig. 9 Combustion chamber thermal boundary conditions (high-temperature state of endurance test)

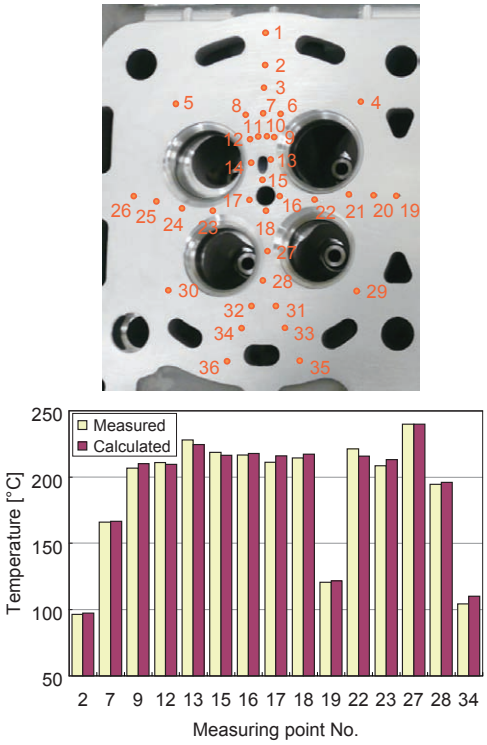


Fig. 10 Measured and calculated values of combustion chamber surface temperature (high-temperature state of endurance test)

The temperatures shown on the horizontal axis are the highest temperatures reached in the flat area during the endurance tests. The CAE results correspond well with the approximation curve for the strain amplitude against temperature as determined from actual measurements. In addition, study of the points at which the maximum strain amplitude was generated in the CAE results showed that they corresponded to the specific points at which cracks originated during actual endurance tests (Fig. 13).

2.3. Method of Analysis of Local Temperature

Next, a detailed analysis of the surface temperature beside the glow plug hole was attempted. Thermocouples are generally employed as the method of measuring the surface temperature of combustion chambers. However, as in the case of strain gauges, it is not possible to directly embed thermocouples in the edge of the glow plug hole. The conventionally used method has therefore been to take temperature measurements using thermocouples on the adjacent flat area to the edge, and to use these temperatures as representative of the temperature of a given area which includes the edge.

In the present project, in addition to temperature measurements using thermocouples, the local temperature of peripheral areas including the glow plug hole edge was determined by means of a method of converting to temperature from measurements of the hardness of the surface of the combustion chamber, using the overaging characteristic of the material (termed "the hardness method" below). The order of the analysis is described in (1) to (4) below.

(1) Temperature measurements of the surface of the combustion chamber were taken under the same conditions as the endurance test, using thermocouples.
(2) The hardness of the surface at the same points at which temperature measurements were taken was measured using the Vicker's method[5].
(3) The correlation function between the temperature measurements taken using the thermocouples and the hardness measurements was determined. The temperatures employed were the highest temperatures reached during the endurance test modes.
(4) The hardness of arbitrary points was measured, and the local temperature was calculated using the correlation function determined in Step (3).

Figures 14(a), (b), and (c) respectively show examples of temperature measurements, hardness measurements, and the correlation function obtained from them. The relationship between surface hardness and the temperature reached following hot-and-cold cycle endurance tests can be approximated as a line. By this means, the temperature of the edge can be found from the hardness of the edge.

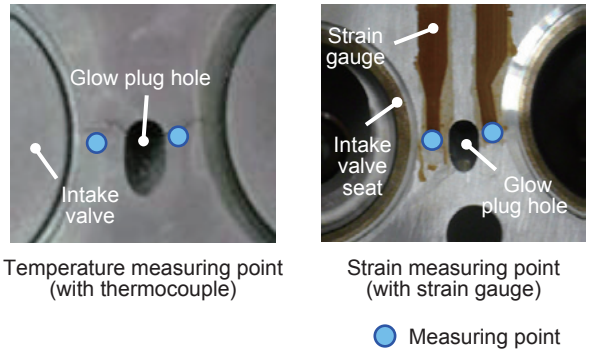


Fig. 11 Temperature and strain measuring points beside glow plug hole

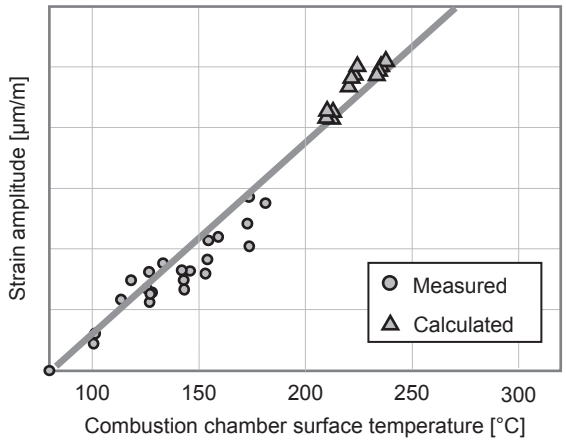


Fig. 12 Measured and calculated strain amplitudes and temperature beside glow plug hole

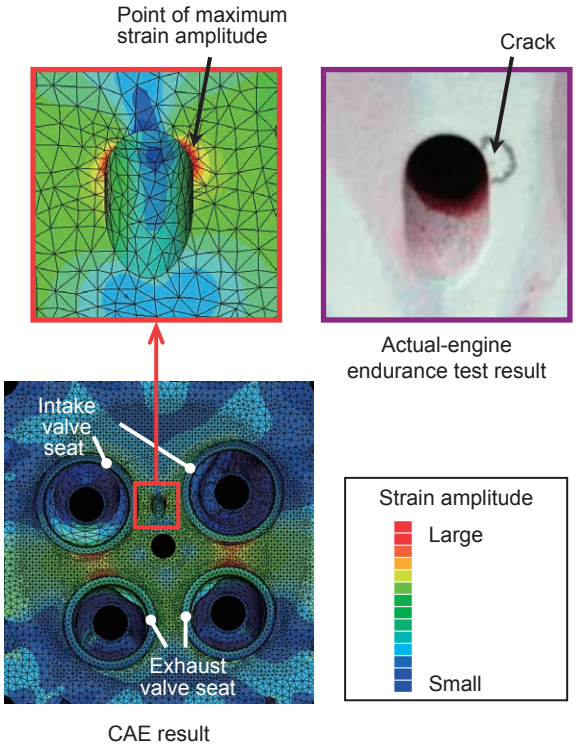


Fig. 13 Strain amplitudes in hot and cold cycle endurance test

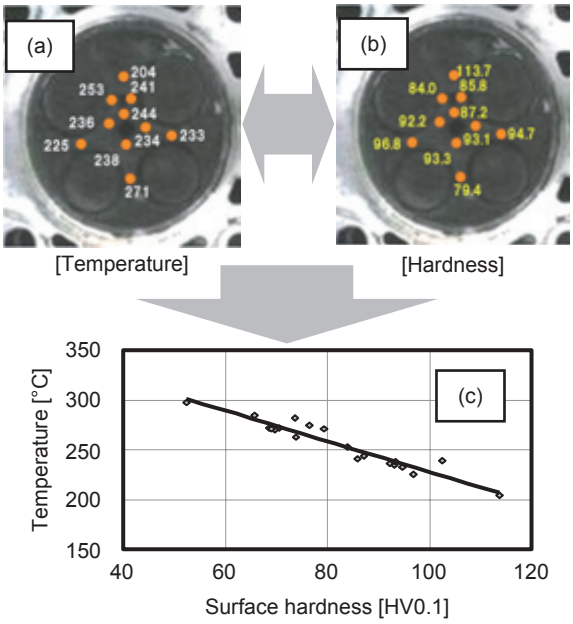
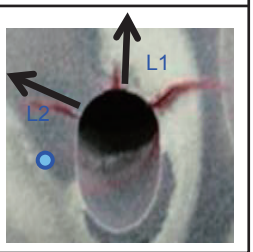


Fig. 14 Relationship between temperature and hardness of combustion chamber surface

Figure 15 shows temperatures beside the glow plug hole for the hot-and-cold cycle endurance test in Case 2, determined using this method. The edge temperature determined using the hardness method was 278˚C, 25 ˚C higher than the temperature measured in the flat area using a thermocouple. The new method showed that a large temperature gradient (following lines L1 or L2 in the figure) existed within even a mere 1.5-mm range, and local high temperatures occurred in the edge, the origin point of cracks.

Figure 16 shows a comparison of temperatures beside the glow plug hole for Cases 3 and 4. While there was virtually no difference between the cases in terms of the temperatures of the flat areas as measured using thermocouples (226˚C and 225˚C), there was a difference from the perspective of occurrence of cracks. In Case 4, the temperature distribution of the combustion chamber was deliberately varied locally by varying the state of combustion through changes in the injector nozzle cone angle. Accordingly, when the temperature of the edge of the glow plug hole was determined using the hardness method, it was found that a 20˚C temperature difference

Case No.	2
Crack occurrence	Yes
Flat area temperature	253 °C
Edge temperature	278 °C
Flat area temperature measuring point (with thermocouple)	

[Hardness measuring position]
Hardness was measured along lines L1 and L2 from the edge as the origin.
(crack starting point to propagation area)

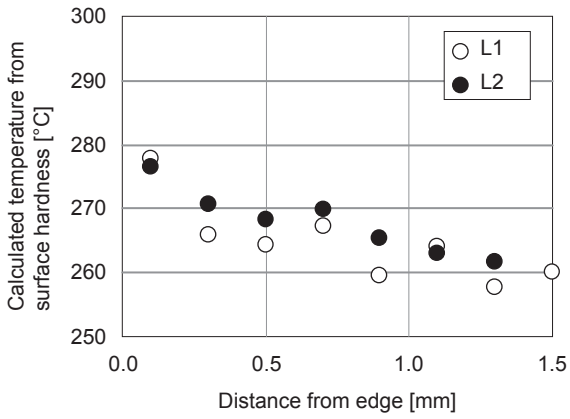
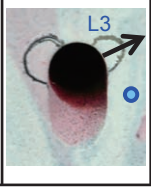


Fig. 15 Edge temperature calculation from measured hardness

Case No.	3	4
Crack occurrence	Yes	No
Nozzle cone angle	Base	Base -3 deg
Flat area temperature	226 °C	225 °C
Edge temperature	255 °C	235 °C
Flat area temperature measuring point (with thermocouple)		

[Hardness measuring position]
Hardness was measured along lines L3 and L4 from the edge as the origin.
(crack starting point to propagation area)

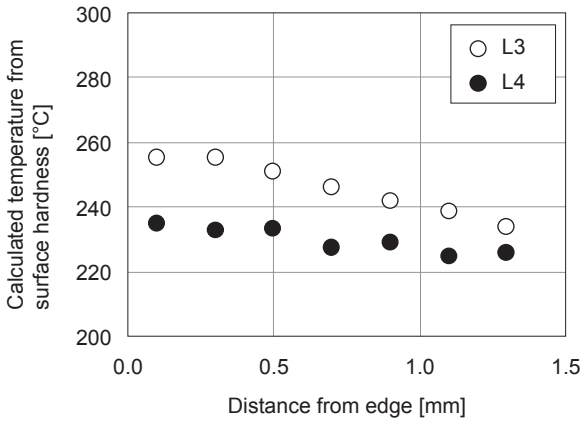


Fig. 16 Influence of nozzle cone angle on edge temperature

existed, with the edge reaching 255˚C in Case 3, in which cracking occurred, but only 235˚C in Case 4, in which no cracking occurred. It is conjectured that this localized difference in temperature was related to the significant difference between the cases in the occurrence of cracking. As this indicates, determining the temperature of the edge, where cracks originate, is an important factor in predicting fatigue breakdown. It was also shown that the calculation of temperature based on hardness measurements was an effective method of doing so.

2.4. Fatigue Limit for Heat Cycle of Cylinder Head Materials

In order to predict fatigue breakdown based on the strain amplitudes and temperatures determined as described in Sections 2.2 and 2.3, a criterion based on the strength characteristic of the cylinder head material was necessary. Unit tests were therefore conducted on the material used for the cylinder head, and an attempt was made to use the obtained limit strain amplitude as a criterion of fatigue breakdown.

The limit strain amplitude was determined in steps (1) to (5) below (Fig. 17):

(1) AC2B-T6[6), (7)] was used as the material for the test pieces. Table 2 shows the chemical composition of the material. With regard to heat treatment conditions, following heating at 500˚C for four hours, the material was quenched in water, after which it was subjected to aging treatment at 200˚C for four hours. The test piece was a round bar with an external diameter of 7 mm, and a distance of 12 mm was used between reference points.

Table 2 Chemical compositions of AC2B alloy [wt%]

Si	Cu	Mg	Zn	Fe	Mn	Ni	Al
6.3	3.2	0.17	0.01	0.13	<0.01	<0.01	Balance

(2) With the local conditions in which cracks would occur in mind, endurance tests were conducted, imparting a temperature and strain cycle in which compressive strain occurred repeatedly at high temperatures and tensile strain occurred repeatedly at low temperatures (out-of-phase heat fatigue cycle) to the test piece. For strain control, an extensometer was used to set conditions such that the total amplitude of mechanical strain was a range from 0.6 to 1.6%. An induction heater was used for heating, and natural convection for cooling. The temperature cycles were 50 to 200˚C, 50 to 250˚C, and 50 to 280˚C.

(3) Cycle to fatigue failure was plotted against the strain amplitudes determined from the tests, and the limit

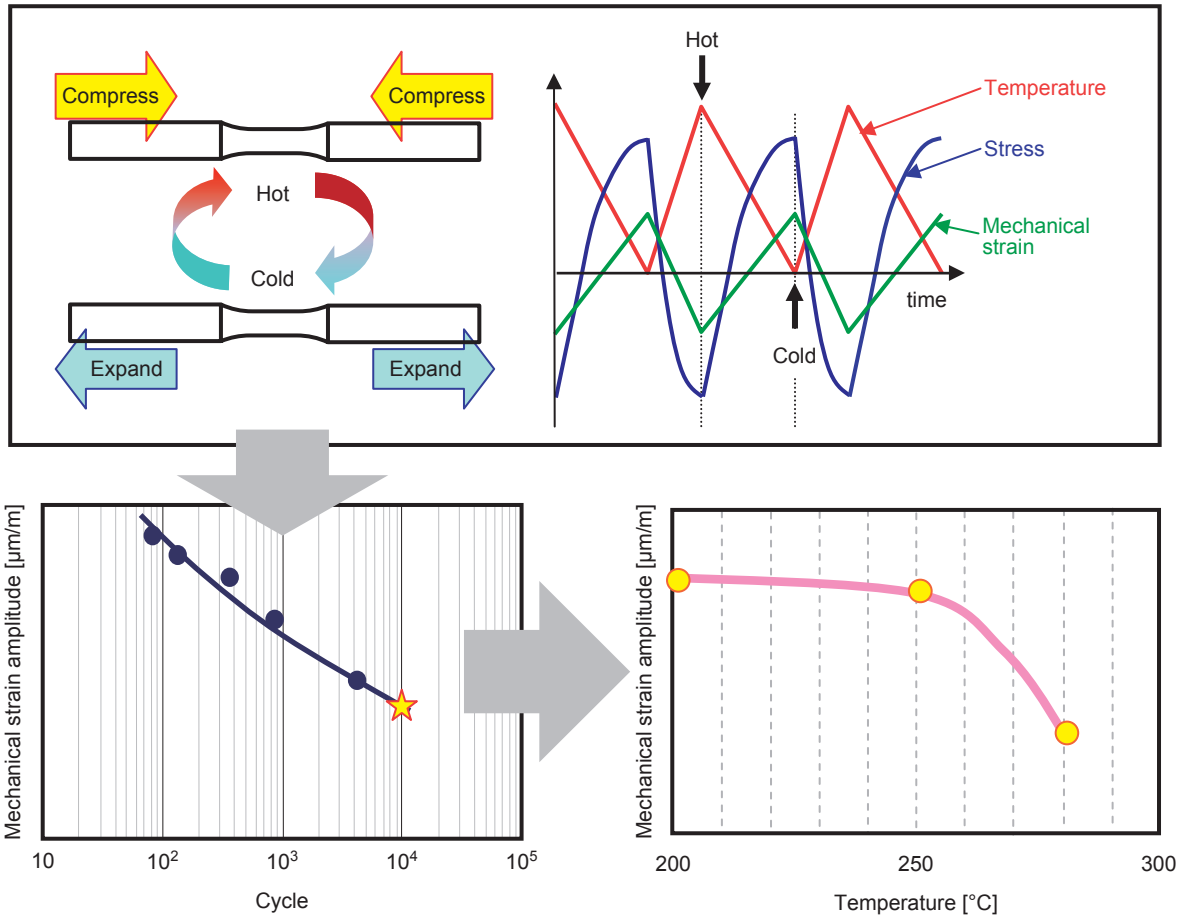


Fig. 17 Steps taken to obtain material fatigue limit diagram for heat cycle

strain amplitude (failure probability: 50% (B50)) for 104 cycles was obtained.

(4) The limit strain amplitude discussed above was found for each temperature cycle.

(5) The limit strain amplitude for the highest temperature reached during each temperature cycle was plotted on a strain amplitude-temperature graph, and the fatigue limit diagram for the heat cycle was determined for the cylinder head material.

3. Results of Combustion Chamber Analysis and Verification of Effectiveness of Technology for Prediction of Low-cycle Fatigue Breakdown

The strain amplitude and temperature of the surface of the combustion chamber during a hot-and-cold cycle endurance test were determined using the method described above, and compared with a fatigue limit diagram for the heat cycle. The results are shown in Fig. 18. The graph shows only results for edges where the possibility of cracking is high. Circles mark areas in which cracks did not occur, while crosses mark areas in which cracks occurred. As evidenced from the graph, the occurrence of cracking during a hot-and-cold cycle endurance test can be studied on the basis of the relationship between strain amplitude and temperature and the fatigue limit diagram for the heat cycle obtained using this method.

Focusing on the margin of each section of the combustion chamber in relation to the fatigue limit diagram, it is greatest in the case of the edge between the exhaust valve seats, followed by the edge between the intake and exhaust valve seats, and the edge of the glow plug hole.

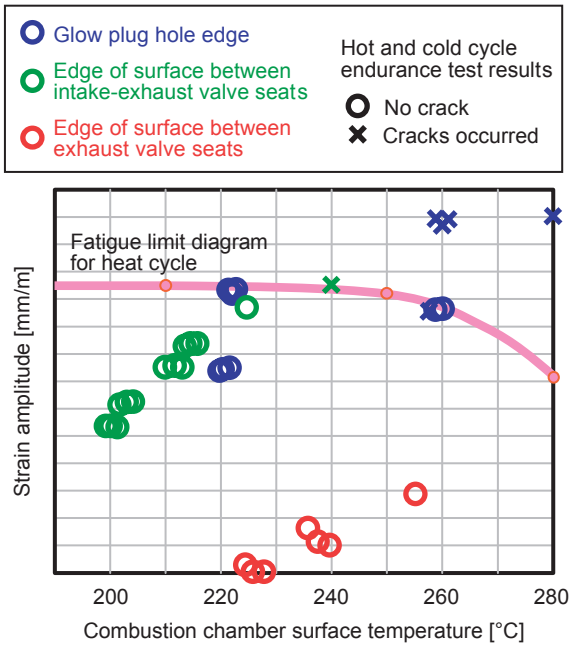


Fig. 18 Strain amplitudes and temperature of prototype engine A

Table 3 Prototype engines A and B - changes in specifications

	Prototype engine A	Prototype engine B
Engine output	Base	Base +10%
Fuel injection timing	Base	Base +2 deg advance
Valve skew angle	Provided	None
Coolant flow direction in cylinder head	Longitudinal flow	Cross flow
Coolant flow rate	Base	Base +17%

This accords with the tendency displayed when the number of points of occurrence of cracking was gradually reduced in a series of hot-and-cold cycle endurance tests (Table 1).

In order to verify the effectiveness of the new method of predicting low-cycle fatigue breakdown, it was incorporated in the cylinder head design process, and new engine specifications and geometries were designed to maintain the conditions of the surface of the combustion chamber during hot-and-cold cycle endurance tests within the range determined by the fatigue limit diagram. Prototype engine B was constructed on this basis. Table 3 shows the main points of difference between engine A and engine B. As was the case previously, an endurance test was conducted using hot-and-cold cycle test mode 1 and the occurrence of cracking was studied. Figure 19 shows the conditions of strain amplitude and temperature and the occurrence of cracking, focusing only on the edges for which the potential for cracking is high.

As in the case of prototype engine A, the area in which

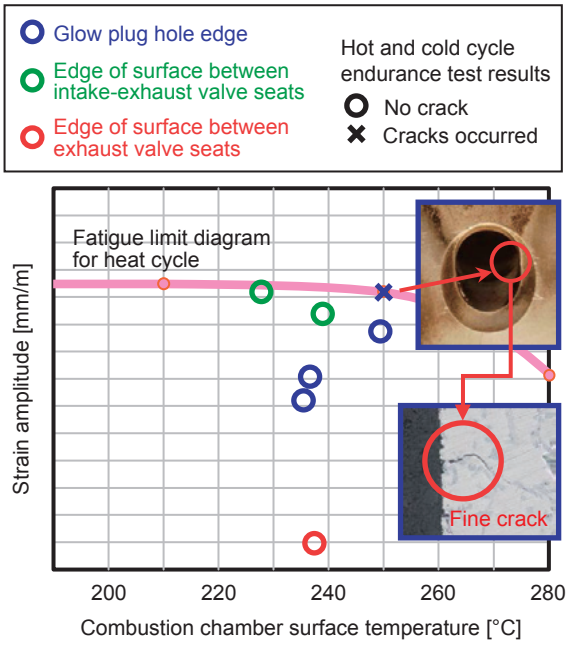


Fig. 19 Strain amplitudes and temperature of prototype engine B

the potential for cracking was highest in prototype engine B was the edge of the glow plug hole. This area was almost entirely on the curve of the fatigue limit diagram. When the area was studied in detail using an optical microscope following the completion of the hot-and-cold cycle endurance test, a microscopic crack of approximately 50 μm was discovered.

The results discussed above show that the new method is effective in the prediction of low-cycle fatigue breakdown during hot-and-cold cycle endurance tests, even for engines of differing specifications.

4. Proposal for Cylinder Head Design Process using New Method

A method of incorporating the new method in the new engine design process is proposed (Fig. 20). The magnitude of the strain amplitude in the cylinder head combustion chamber and the inhomogeneous combustion chamber temperature distribution that produces it originate in the shape of the combustion chamber, in particular the valve layout, the combustion conditions, and the cooling conditions of the cylinder head. Because these factors not only affect the durability of the cylinder head, but impact on a wide range of areas including engine power, it would be desirable to establish appropriate parameters at the initial stage of engine development. It would therefore be effective to front-load the prediction of low-cycle fatigue breakdown at the stage of formulation of engine specifications by incorporating the new method in the development process.

The rapid prototyping engine in Fig. 20 is designed to test estimations of the temperature increase of the edges, and estimations of gas temperature and heat transfer coefficient. Because of this, the engine need only be constructed with the minimum shape and specifications to fulfill this purpose. It would be desirable if such an engine could be designed and developed in a short period of time.

The future goal of the authors is to introduce the CFD combustion analysis shown in Fig. 8 into the CAE strain analysis flow shown in Fig. 6, and to incorporate this in the design process. However, taking into consideration the level of analytic accuracy of CFD and the time necessary for the calculation of full combustion models, the process proposed in this paper can, at present, be deemed the more feasible.

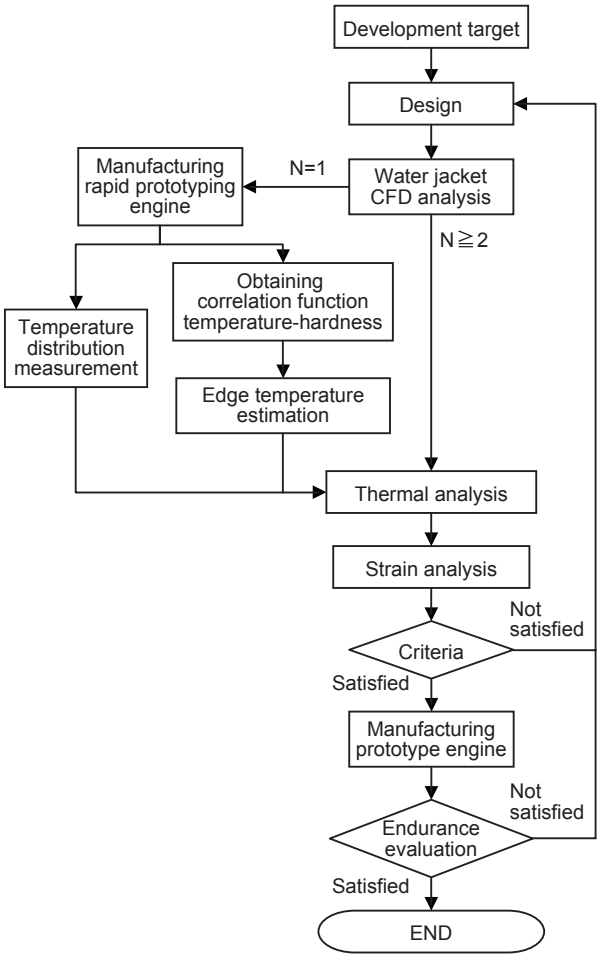


Fig. 20 Proposal of low-cycle fatigue evaluation in design process

5. Conclusion

An attempt was made to develop a method of prediction of low-cycle fatigue breakdown in cylinder head combustion chambers. The following results were obtained:

(1) Cracks originate in edges; because both the strain amplitude and the temperature of the edges differ from those of adjacent flat areas, understanding the local conditions of these parameters is necessary for the prediction of cracking.

(2) Taking the area around the glow plug hole as the subject of analysis, it was shown that valid figures for strain amplitude and temperature could be obtained, respectively, by CAE strain analyses and the hardness method.

(3) Fatigue limit diagrams for heat cycles, plotted using limit strain amplitudes that were obtained from unit heat fatigue tests on materials, were compared with the conditions of strain amplitude and temperature obtained from CAE and the hardness method. By this means, it was made possible to accurately predict low-cycle fatigue breakdown in cylinder head combustion chambers during hot-and-cold cycle endurance tests.

(4) It would be desirable to front-load a method of prediction of low-cycle fatigue breakdown in the new engine development process, and it was possible to incorporate the new method in the design process within the time constraints demanded in engine development.

References

(1) Ikuno, H., Iwanaga, S., Awano, Y.: Evaluation of Thermal Fatigue Property for Aluminum Alloy Castings,

Toyota Central R&D Labs R&D Review, Vol. 31, No. 2, p. 73-84 (1996)
(2) Koibuchi, K., Kokubo, K.: Seihin Kaihatsu no tameno Zairyou Rikigaku to Kyodo Sekkei Know-how, The Nikkan Kogyo Shimbun, p. 86-93 (2002) (in Japanese)
(3) Miyazaki, T., Kagaya, H., Nishino T., Murakami, N., Torigoe, Y., Ikeda, M.: Prediction of Cylinder Head Thermal Fatigue Life, 2005 JSAE Annual Congress Proceedings, No. 111-05, p. 23-26 (2005)
(4) Kubo, M., Imai, K., Tsubouchi, M., Nomura, Y., Ishiguro, T., Kaneko, H., Kondo, M.: Durability Evaluation Technique Using Thermal Analysis on Diesel Engine Cylinder Head, 2008 JSAE Annual Congress Proceedings, No. 90-08, p. 19-22 (2008)
(5) International Standard ISO/DIS 6507-1: 1995, Metallic materials-Vickers hardness test-Part 1: Test method
(6) Japanese Industrial Standards JIS H 2211: 1960, Aluminum alloy ingots for castings
(7) Japanese Industrial Standards JIS H 0001: 1972, Aluminum, magnesium and their alloys-Temper designation

Author


Shohei MIKAMI


Koichi OGINO


Mitsumasa SORAZAWA

Effects of Low-viscosity Engine Oil on Fuel Economy and Wear

Yosuke OKUYAMA* Daichi SHIMOKOJI* Syouji KAWAUCHI*
Takeshi HATTA* Masashi MARUYAMA*

ABSTRACT

The effects of lower engine oil viscosity on fuel economy and engine reliability were investigated, unhampered by the SAE viscosity standard, with the aim of enhancing fuel economy. The fuel economy effects were predicted by using low-viscosity engine oil and measuring the friction torque. The results showed that lowering the engine oil viscosity provides favorable prospects for enhancing fuel economy.

Engine reliability was investigated by confirming the effects on sliding wear at high temperature, which is the greatest issue for low-viscosity engine oil. These effects were confirmed through CAE analysis and engine endurance tests. The results provided prospects for wear resistance of sliding parts at high temperature, even when using engine oil with a lower viscosity than specified in the SAE viscosity standard in the tested mass-production engine.

In addition, a number of prototype engine oils with a lower viscosity than specified in the SAE viscosity standard were created, and the property values and positioning of these prototype engine oils relative to the SAE viscosity standard were confirmed.

Engine oil with a lower viscosity than specified in the current SAE viscosity standard can be expected to further enhance fuel economy, so the establishment of further low-viscosity standards is desired.

1. Introduction

Suppression of global warming and other recent issues are increasing demands for enhanced automobile fuel economy to reduce CO_2 emissions. Lowering the engine oil viscosity is known to be an effective method of enhancing fuel economy[(1), (2)]. However, lowering the viscosity by too much has the opposite effect of reducing fuel economy for some engine mechanisms[(3), (4)]. In addition, there are concerns that simply lowering the engine oil viscosity may result in increased wear at high temperature, lower operating performance of hydraulic devices, and increased oil consumption[(5)].

Engine oil is a general-purpose part with the highest replacement frequency and market availability, so a number of standards have been established, as typified by the Society of Automotive Engineers (SAE) viscosity standard (SAE-J300), which guarantees fuel economy and sliding wear at high temperature. For this reason, many papers concerning the impact of engine oil on fuel economy and sliding wear report with the premise of compliance with the current SAE viscosity standard[(2)-(5)].

Therefore, this study first predicted the fuel-saving effects of using low-viscosity engine oil, unhampered by the current SAE viscosity standard. Next, the wear resistance of sliding parts at high temperature was verified, which is the greatest issue for low-viscosity engine oil. A number of prototype low-viscosity engine oils were then created based on these results, and their position relative to the SAE viscosity standard was confirmed.

2. Course of This Study

Engine oil has characteristics such that the viscosity falls at high temperature, and rises at low temperature. When the viscosity is high at normal temperature, there are concerns that viscosity resistance may lower fuel economy. On the other hand, when the viscosity falls by too much at high temperature, sliding wear becomes a concern. Recently, there have been demands to develop fuel-economy engine

* Automobile R&D Center

Table 1 SAE viscosity standard

	Viscosity grade	CCS viscosity		MRV viscosity		Kinematic viscosity (100 °C) (mm²/s)		HTHS viscosity (150 °C) (mPa·s)
		mPa·s	°C	mPa·s	°C	Min.	Max.	
Winter grade	0 W	6200	-35	60000	-40	3.8		
	5 W	6600	-30	60000	-35	3.8		
	10 W	7000	-25	60000	-30	4.1		
	15 W	7000	-20	60000	-25	5.6		
	20 W	9500	-15	60000	-20	5.6		
	25 W	10000	-10	60000	-15	9.3		
	20					5.6	9.3	2.6
	30					9.3	12.5	2.9
	40 (0 W, 5 W, 10 W)					12.5	16.3	2.9
	40 (15 W, 20 W, 25 W)					12.5	16.3	3.7
	50					16.3	21.9	3.7
	60					21.9	26.1	3.7

oil with further reduced viscosity at normal temperature, and that maintains viscosity at high temperature[6].

To meet these needs, polymer components called viscosity index improvers are often added to engine oil. Engine oil with viscosity index improvers added is known to become a non-Newtonian fluid[7].

The viscosity of engine oil that has become a non-Newtonian fluid drops temporarily under shear conditions such as engine operation. This temporary drop in viscosity is produced by the polymer orientation[8]. In particular, the ratio of this drop in viscosity is known to increase under high-speed shear conditions. On the other hand, Newtonian fluids do not have polymer components added, so there is no temporary drop in viscosity due to shear.

Engine tests using Newtonian fluids that do not experience changes in viscosity due to shear are better from the standpoint of more accurately understanding the correlations between viscosity and fuel economy, and between viscosity and sliding wear. Therefore, it was thought that engine tests can be performed using Newtonian fluids, by dividing normal temperature (approximately 80°C) and high temperature (approximately 130°C) into separate cases, and adjusting the viscosity using separate oils.

That is to say, one case adjusted the Newtonian fluid oil focusing on only the viscosity at normal temperature, to understand the relationship between fuel economy and viscosity. Verification used friction torque measurement (motoring friction torque on an engine bench tester), and estimated the correlation between fuel economy and viscosity.

The other case adjusted the Newtonian fluid oil focusing on only the viscosity at high temperature, to understand the relationship between sliding wear at high temperature and viscosity. Verification used bearing oil film analysis by CAE and engine endurance tests (firing endurance on an engine bench tester), and confirmed the feasibility of application of low-viscosity oil. Note that the viscosity of the Newtonian fluid was calculated by multiplying the kinematic viscosity with the density[9].

The test results using Newtonian fluid oils were used to create a number of prototype low-viscosity engine oils with an emphasis on fuel economy. Viscosity index improver polymer components were added, so the finally created prototype fuel-economy engine oils were non-Newtonian fluids. As previously mentioned, Newtonian fluids and non-Newtonian fluids exhibit different viscous behavior under shear conditions. To minimize this difference in effects, the viscosity of the prototype fuel-economy engine oils was evaluated by measuring the high-temperature high-shear (HTHS, ASTM D4624) viscosity, which lowers the viscosity of non-Newtonian fluids more than that of Newtonian fluids.

3. SAE Viscosity Standard and Positioning of Commercially Available Oils

Table 1 gives an overview of the current SAE viscosity standard. As shown in Table 1, the SAE viscosity specifies the viscosity at high temperature, but there is no specification for viscosity at normal temperature. However, if the aim is to enhance the fuel economy of engine oil, it is important to understand the viscosity at normal temperature.

Therefore, the viscosity at normal temperature of commercial oils that comply with the SAE viscosity standard was investigated, and this information was used to help set the viscosity of the test oils used in this study. As described in the previous chapter, recent multi-grade engine oils are non-Newtonian fluids, so the viscosity was

organized according to the HTHS viscosity. Figure 1 shows the HTHS viscosity of commercial oils at each temperature. The HTHS viscosity is measured at 100°C and 150°C, and values calculated based on those measured values are used for the HTHS viscosity at other temperatures[9].

The results of investigating commercial oils confirmed that of the oils complying with the SAE viscosity standard, Honda 0W-20 oil occupies the position with the lowest HTHS viscosity, in any temperature range.

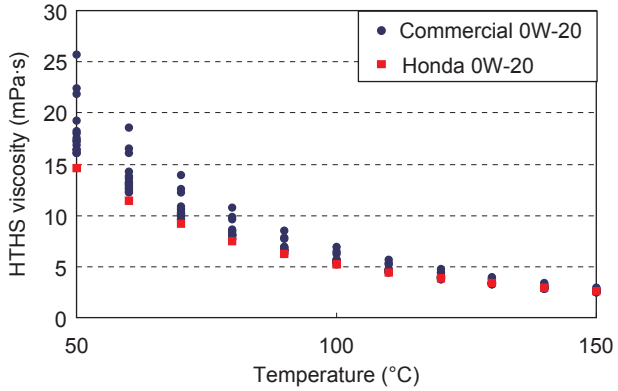


Fig. 1 Market data for commercial oil (HTHS viscosity)

4. Fuel-saving Effects of Low-viscosity Engine Oil

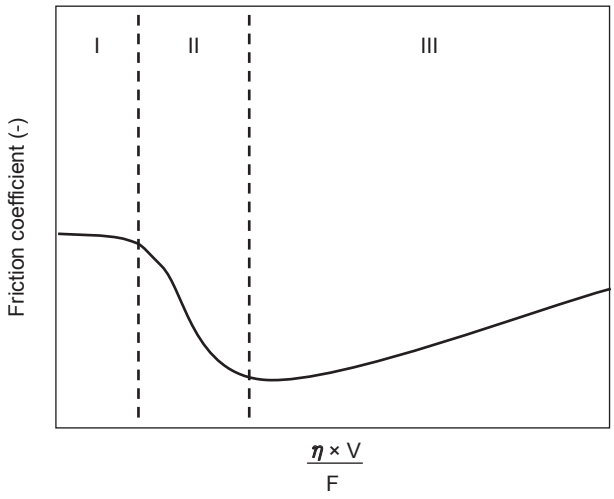
4.1. Determination of Friction Loss Reduction Effects of Low-viscosity Engine Oil

The Stribeck curve is well known as a friction theory[8]. Figure 2 shows a Stribeck curve. Assuming constant load and velocity conditions, the friction coefficient decreases together with the engine oil viscosity under hydrodynamic lubrication (III in Fig. 2). Therefore, when considering the contribution to fuel economy of engine oil under hydrodynamic lubrication, a lower viscosity is effective. However, it is said that when the engine oil viscosity is lowered by too much, mixed lubrication and boundary lubrication that result in metal contact eventually occur, and the friction coefficient increases[3), (4)].

Therefore, it is important to determine the limit of the effects of lowering engine oil viscosity on reducing friction loss.

4.2. Friction Torque Measurement Conditions

The friction torque was measured, which is a typical method of confirming the friction loss reduction effects of engine oil[1]. Figure 3 shows the test apparatus used to measure friction torque, and Fig. 4 shows the viscous properties of the test oils used to measure friction torque. The viscosity of the test oils was set based on the results of investigating commercial oils complaint with the SAE viscosity standard. To understand the fuel-saving effects of simply lowering the viscosity, the friction torque was measured using Newtonian fluid oil (only the base oil) without any additives. Table 2 lists the engine specifications and test conditions used. In consideration of 10·15 mode, which represents typical driving conditions,



η : Viscosity
V : Velocity
F : Load
I : Boundary lubrication
II : Mixed lubrication
III : Hydrodynamic lubrication

Fig. 2 Stribeck curve

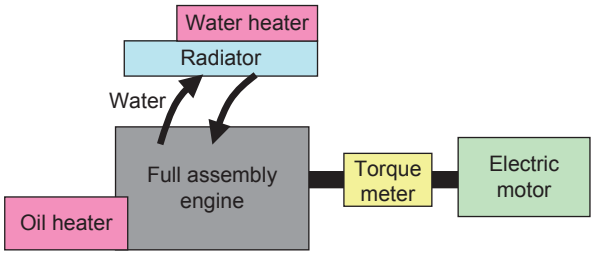


Fig. 3 Schematic diagram of engine motoring tester

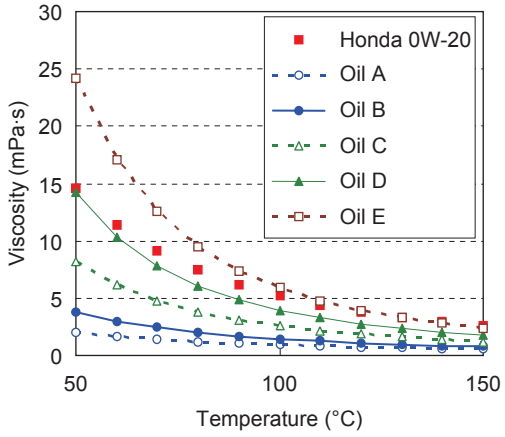


Fig. 4 Viscosity of test oils with engine motoring tester

Table 2 Engine specifications (friction torque tests)

Engine	L13
Number of cylinders and configuration	Inline 4
Valve train	SOHC 4-valve, Roller follower
Displacement (cm^3)	1,339
Bore × Stroke (mm)	73.0 × 80.0
Compression ratio	10.5

the test conditions were an oil temperature of 80°C and engine speeds between 700 and 3500 rpm[2), 6)].

4.3. Friction Torque Measurement Results and Analysis

Figure 5 shows the correlation between viscosity (80°C) and friction torque at each engine speed. The friction torque decreases together with the viscosity at almost all engine speeds, and enhancement of friction torque was confirmed even for engine oil with a viscosity lower than that reported in 1995 by Nagashima et al.[4] This is thought to be because advances in engine technology such as roller-follower valve trains and reduced surface roughness of each sliding part resulted in lower overall engine friction.

On the other hand, a slight increase in friction torque was confirmed under low engine speed, low-viscosity conditions. This is thought to be because, according to the Stribeck curve theory, the circumferential velocity and viscosity dropped excessively, and the mixed lubrication and boundary lubrication ranges were reached.

4.4. Prediction of Fuel-saving Effects

The results of friction torque measurement were used to predict the fuel economy enhancement effects of the test oils A to E. Equation (1) shows the base formula of the arithmetic algorithm used to predict fuel economy[10].

$$\Sigma\, Gfuel = \Sigma\{BSFC \times Pse \times Hr\} \quad (1)$$

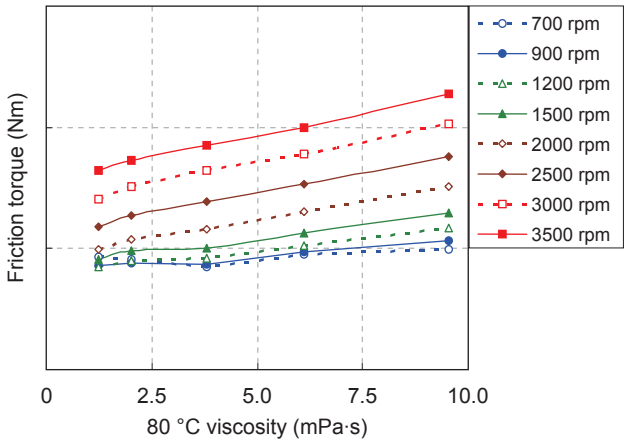


Fig. 5 Friction measured in fully assembled engine

Gfuel: Fuel consumption amount
BSFC: Net fuel consumption rate
Pse: Net output power
Hr: Time

Equation (2) shows the formula used to calculate Gfuel when the test oil is changed, relative to Eq. (1).

$$\Sigma\, Gfuel' = \Sigma\{BSFC' \times Pse \times Hr\} \quad (2)$$

$$BSFC' = \{(Pse + Psf'') \times BSFC\}/(Pse + Psf) \quad (3)$$

Gfuel': Fuel consumption amount after changing the test oil
BSFC': Net fuel consumption rate after changing the test oil
Psf: Engine (friction) loss
Psf'': Engine (friction) loss after changing the test oil

Figure 6 shows a concept drawing of the method used to predict the fuel-saving effects. As shown in Eq. (1) to Eq. (3) and Fig. 6, when vehicle characteristics and mode data are present and the net fuel consumption rate, net output power and engine loss (friction torque) have been measured using a standard oil, the fuel-saving effects can be predicted simply by measuring the friction torque of the test oil to be evaluated.

Therefore, Honda 0W-20 oil was used as the standard oil, and the net fuel consumption rate, net output power and friction torque in a Honda L13 engine were measured.

The fuel economy enhancement effects were predicted using these measurement data and the friction torque measurement results shown in Fig. 7. The fuel consumption mode used to predict the fuel economy enhancement effects was the typical 10·15 mode. Figure 7 shows the results of predicting the fuel-saving effects. Figure 7 shows that when the typical actual cruising mode is taken into account, fuel economy enhancement effects are seen even with low-viscosity oil that was confirmed to increase the friction torque slightly under lower engine speed conditions. That

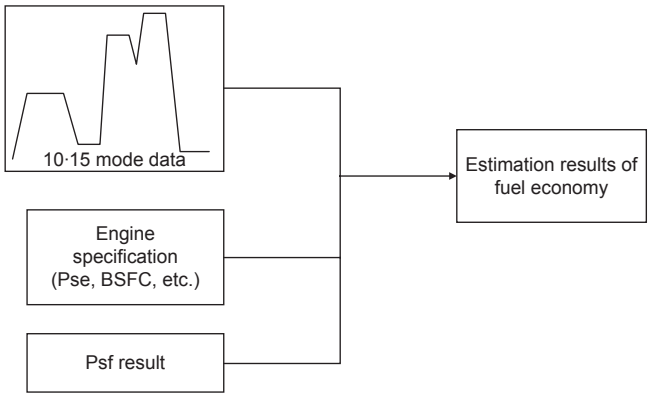


Fig. 6 Simulation model structure

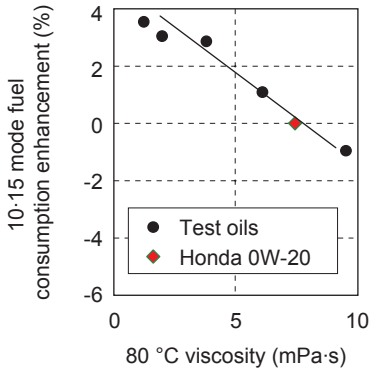


Fig. 7 Relationship between 80 °C viscosity and estimated fuel economy enhancement

is to say, in consideration of fuel economy during actual cruising, the fuel economy performance increases as the viscosity at normal temperature decreases.

5. Effect on Sliding Part Wear

5.1. Concerns of Sliding Wear at High Temperature due to Lower Viscosity

Under high-speed high-load conditions, the engine oil temperature increases and the viscosity decreases, making wear resistance for sliding parts an issue. In particular, the connecting rod big end bearing is given as one of the engine sliding parts most affected by wear due to explosive load and inertia load[11]. Therefore, the effects of lower viscosity on bearing wear were confirmed using the following two approaches.

(1) Oil film calculations by CAE
(2) Engine endurance tests

5.2. Test Oils Used

Table 3 lists the test oils used for the CAE and engine endurance tests. The test oil viscosity was set based on the investigation results of commercial oils compliant with the SAE viscosity standard. In addition, the oil I in the position with the highest viscosity was adjusted so that the viscosity at high temperature is approximately equal to that of Honda 0W-20 oil. Figure 8 shows the viscosity data for the test oils. To understand the effects on sliding wear of simply lowering the viscosity, engine endurance tests were performed using Newtonian fluid oil (only the base oil) without any additives. In addition, oil film analysis using CAE also treated the oil as a Newtonian fluid.

5.3. Oil Film Calculation Method and Conditions

Oil film calculations were performed by elastohydrodynamic (EHD) calculations to take into account the elastic deformation of the connecting rod big end. The oil film characteristics were calculated by calculating the oil film thickness and oil film pressure based on the report by Sato et al.[12]

Table 3 CAE and engine bench test oils

Oil name	CAE	Engine bench
F	✓	
G	✓	
H	✓	✓
I	✓	✓

The connecting rod model and various data used in the calculations were the engine data used in the engine endurance tests described hereafter. The calculation conditions used the same high-speed high-load operation mode as the endurance conditions.

5.4. Results of Oil Film Calculation Using CAE, and Observations

Reducing the minimum oil film thickness raises concerns about metal contact in locations with coarse surface roughness, and increasing the maximum oil film pressure raises concerns about fatigue delamination of sliding parts and other issues. Figure 9 shows the minimum oil film thickness and maximum oil film pressure for each

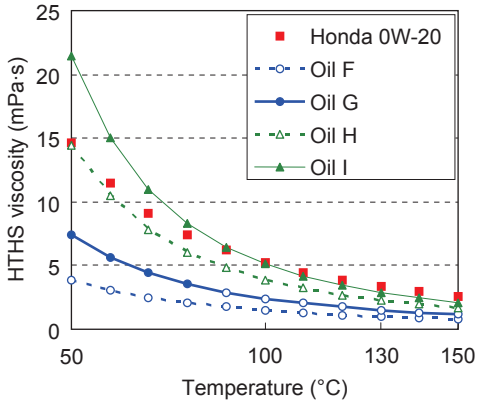


Fig. 8 HTHS viscosity of CAE and engine bench test oils

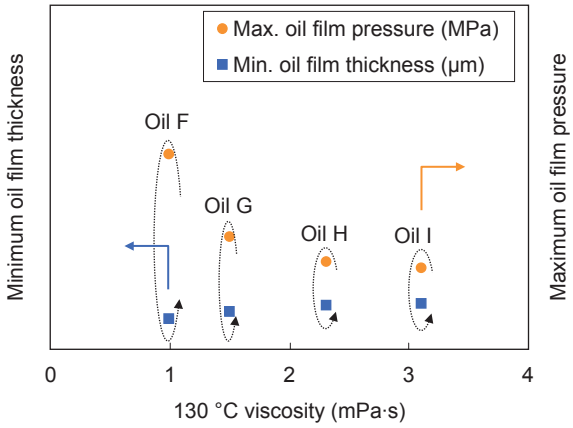


Fig. 9 CAE results of oil film on conrod bearing

Table 4 Engine bench test conditions

Engine	L13
Engine speed	High
Throttle	Wide open
Engine oil temperature	About 130 °C

viscosity, as the result of oil film calculations. Figure 9 confirms that as the engine oil viscosity decreases, the minimum oil film thickness tends to decrease slightly, and the maximum oil film pressure tends to increase noticeably.

The reason for this is thought to be that when the oil film thickness is thin enough, even a slight additional decrease in the thickness produces a considerable reaction effect to try and maintain the oil film. Therefore, when applying low-viscosity engine oil, wear originating in fatigue delamination as the oil film pressure increases is thought to be a greater issue than wear due to metal contact.

When performing engine bench tests using an actual engine, attention was given to this point, and the test oil viscosity was adjusted so that the oil film pressure was almost equal to that of current SAE viscosity standard compliant oil.

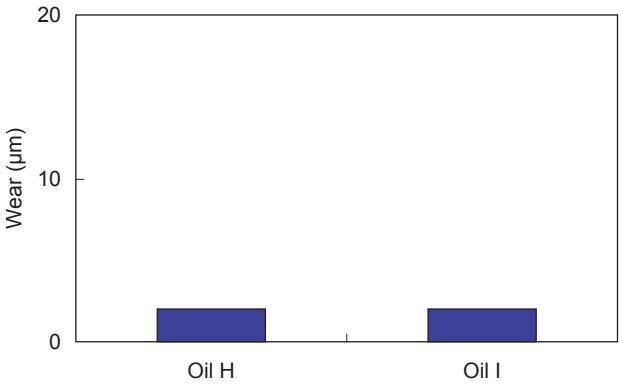


Fig. 10 Average bearing wear results

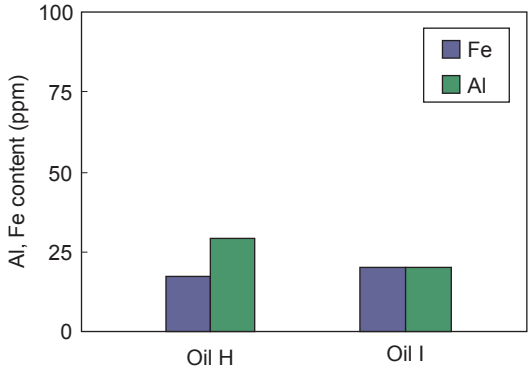


Fig. 11 Metal contents in engine oil after endurance tests

5.5. Engine Durability Test Conditions

Table 4 lists the engine endurance test conditions. To coordinate with CAE, an L13 engine was used, and the test was conducted in the high-speed high-load operation endurance mode. In addition, based on results of calculating the oil film pressure using CAE, the test oils H and I were used in the engine endurance tests.

5.6. Engine Durability Test Results

Figure 10 shows the amount of wear to the connecting rod big end bearing after the engine endurance tests. Figure 11 shows the Fe and Al contents obtained by ICP analysis (ASTM D5185) of the engine oils before and after the engine endurance tests.

The oil I viscosity at high temperature is approximately the same as that of Honda 0W-20 oil, so it is thought that lowering the viscosity would not tend to result in much noticeable wear (Fig. 10). In addition, no noticeable wear due to lower viscosity was confirmed in sliding parts other than the connecting rod big end bearing. As corroborating data, no noticeable increase was confirmed in the Fe and Al contents in the engine oil at lower viscosities (Fig. 11).

These results are thought to indicate that even when the high-temperature viscosity is lower than current SAE viscosity, as long as the generated oil film pressure can be kept to the same approximate level as that of current SAE viscosity standard compliant oil, sliding wear is not an issue.

6. Approach toward Oil Formulation

6.1. Approach toward Oil Formulation of Low-viscosity Oils

Verification was performed using Newtonian fluid oil to understand the relationship between fuel economy and viscosity, and between sliding wear and viscosity. This is because the tests performed as parameter studies were divided into normal-temperature viscosity and high-temperature viscosity. However, in the course of the development, both lower viscosity at normal temperature and maintenance of viscosity at high temperature are demanded, so viscosity index improvers are required. Based on the test results thus far, prototype low-viscosity engine oil was created with the aim of optimizing the viscosity index from the following two standpoints.

- Fuel economy is enhanced as the viscosity at normal temperature decreases.
- To secure resistance to sliding wear at high temperatures, the viscosity should be set so that the oil film pressure does not increase.

Table 5 gives an overview of the prototype oil formulation. A blend of Gr. III, IV and V were used as the base oils to aim for better temperature-viscosity characteristics. Polymethacrylate (PMA), which is highly effective at enhancing the viscosity index, was used as the viscosity index improver to transform the oil into a non-

Table 5 Prototype engine oil formulation

Base oil	Viscosity index improver	Other additives
Gr. III Gr. IV Gr. V	PMA-1 PMA-2	Commercial additive pack (GF-4)

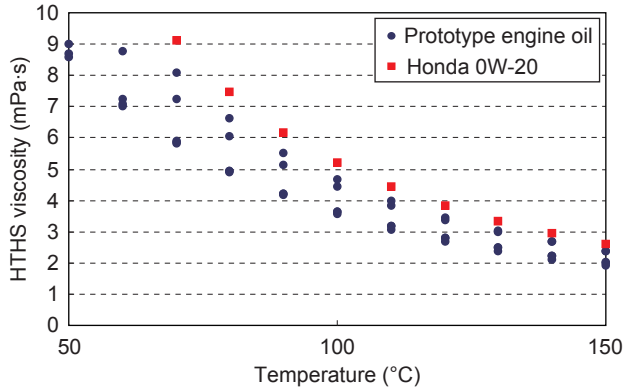


Fig. 12 HTHS viscosity of prototype engine oil

Newtonian fluid[8]. Other additives consisted of an additive package equivalent to ILSAC GF-4, which was used to formulate a number of low-viscosity engine oils.

6.2. Prototype Oil Viscosity and Position relative to the SAE Viscosity Standard

Figure 1 shows that of the various 0W-20 oils, Honda 0W-20 oil is positioned with the lowest HTHS viscosity at normal temperature. Therefore, when an attempt is made to further lower the HTHS viscosity at normal temperature, it is a challenge for the high-temperature viscosity to comply with the current SAE viscosity standard, as seen with the prototype oils in Fig. 12.

7. Conclusions

Fuel-saving effects and sliding wear at high temperature were investigated using low-viscosity engine oil in the tested mass-production engine. The results yielded the following information.

(1) Even when the viscosity at normal temperature is reduced, almost no effect to increase friction due to boundary lubrication or mixed lubrication was confirmed, indicating that reducing viscosity is an effective means of creating fuel-economy engine oil.

(2) The effects on sliding wear at high temperature were verified, and the results provided prospects for wear resistance even at viscosities lower than specified in the current SAE viscosity standard.

(3) When viscosity at normal temperature is reduced to a certain level or less, it is a challenge to comply with the high-temperature viscosity prescribed by the SAE viscosity standard.

These results indicate that to pursue further fuel economy by lowering the engine oil viscosity, additional low-viscosity standards should be established in the SAE viscosity standard.

8. Future Prospects

This study presented the effects of low-viscosity engine oil, and prospects for wear resistance of sliding parts at high temperature, which is one of the greatest issues. However, it is thought that attention should be given to the following points in order to actually apply engine oils with a lower viscosity than specified in the current SAE viscosity standard to mass production.

- Consideration for hydraulic mechanisms due to a predicted drop in oil pressure.
- Consideration for engine oil evaporation and other items in standards such as those prescribed by the International Lubricant Standardization and Approval Committee (ILSAC).
- Consideration for engine reliability related to phenomena thought to be the boundary lubrication and mixed lubrication at low engine speeds confirmed as a result of friction torque measurements.

References

(1) Tanaka, H., Nagashima, T., Sato, T., Kawauchi, S.: Effect of 0W-20 Low Viscosity Engine Oil on Fuel Economy, HONDA R&D Technical Review, Vol. 11, No. 2, p. 143-148

(2) Sagawa, T.: Development 0W-20 ILSAC GF-3 Gasoline Engine Oil, SAE Paper, 2002-01-1636

(3) Tamoto, Y., Namigishi, T.: Gasorinenjinyu no Syounenpi heno Torikumi, IDEMITSU TRIBO REVIEW, No. 29, p. 1-4 (2006) (in Japanese)

(4) Nagashima, T.: Research on Low-Friction Properties of High Viscosity Index Petroleum Base Stock and Development of Upgraded Engine Oil, HONDA R&D Technical Review, Vol. 7, p. 131-139

(5) Sato, T., Kawauchi, S.: Development of ILSAC GF-4 0W-20 Gasoline Engine Oil, Honda R&D Technical Review, Vol. 16, No. 2, p. 171-176

(6) Kobayashi, N., Suzuki, T., Kamioka, R., Murakami, M., Yamashita, M., Ogawa, T., Komiya, K., Moritani, H.: Study of Future Engine Oil (First Report): Future Engine Oil Scenario, SAE Paper, 2007-01-1977

(7) Nishida, M.: Nenndoshisuukoujyouzai no Kinou to Youto, Jyunkatsukeizai, Vol. 3, p. 14-18 (2003) (in Japanese)

(8) Konishi, S., Ueda, R.: Junkatsuyu no Kiso to Ouyou, Corona Publishing (1992) (in Japanese)

(9) Tamoto, Y.: Possibility of Ultra Low Viscosity Fuel Saving Gasoline Engine Oil, SAE Paper, 2004-01-1936

(10) Yamamoto, K., Aoki, T.: Analysis of the Influence on Fuel Economy about CVT and Automated MT, and the Estimation of Fuel Economy Improvement, HONDA

R&D Technical Review, Vol. 12, No. 1 p. 63-72 (2000)
(11) Nagashima, T.: Tribology wo Kataru, Tribologist, Vol. 53, No. 2, p. 1 (2008) (in Japanese)
(12) Sato, K., Machida, K., Makino, K.: Effect of connecting rod big end stiffness to oil film pressure, HONDA R&D Technical Review, Vol. 12, No. 1, p. 33-38

■ Author ■


Yosuke OKUYAMA


Daichi SHIMOKOJI


Syouji KAWAUCHI


Takeshi HATTA


Masashi MARUYAMA

Prediction Technology of Output Power and Intake-Exhaust Noise Using 1D-Simulation for Small-Displacement Motorcycles

Hiroshi HORIKAWA* Hideki KIDO*
Satoshi IIJIMA* Yasuo MURAKAMI*

ABSTRACT

Using a 1D simulation that transforms the 3D shape of intake-exhaust systems into one dimension and calculates the thermodynamics and fluid gas dynamics of internal combustion engines, a prediction technology of the output power and intake-exhaust noise for small-displacement single-cylinder motorcycles was established. Output power can be calculated accurately for various engines with different displacements and cooling systems by adjusting the boundary conditions in the calculation model. The intake-exhaust noise can be calculated accurately by clarifying some important points for accuracy when transforming the 3D shapes of the intake-exhaust system into the 1D model and by reflecting them in the calculation model. As for mufflers that have complicated internal structures, the calculation of exhaust noise cannot be made with sufficient accuracy because 1D simulation does not calculate spatial flow behavior. But, enhancement of accuracy is expected using a 1D-3D coupled simulation.

1. Introduction

Nowadays, reduction of noise from motorcycles is becoming increasingly important in Southeast Asian countries, the main market for small-displacement motorcycles. It takes a lot of time to decide the specifications of their engines and intake-exhaust systems in mass production development, because the shapes of the intake-exhaust systems are complex due to limited space in the layout. Usually, in the development of a new model, the specifications of the engine and intake-exhaust system are designed using various methods[(1), (2)]. These methods specialize in either output power calculation or intake-exhaust noise calculation, and it is a challenge to evaluate the influence on output power and intake-exhaust noise coincidentally when specifications are changed. As a result, specifications are often decided by repeating experiments using a prototype vehicle. Therefore, there has been a demand for the development of a prediction technology that can calculate both output power and intake-exhaust noise coincidentally in initial stages of development.

1D simulation is one solution to this issue. A higher level modeling approach is required for 1D simulation to calculate the output power and intake-exhaust noise accurately at the same time. While studies of 1D simulation for automobiles and large-displacement multi-cylinder motorcycles have been reported in the past[(3)-(5)], there are no systematic studies found on the intake-exhaust system and single-cylinder engines for small-displacement motorcycles. A prediction technology that allows the calculation of both output power and intake-exhaust noise coincidentally for motorcycles with small-displacement single-cylinder engines using 1D simulation has been developed.

2. Simulation Method

2.1. 1D Simulation

In this study, WAVE®, a 1D simulation analysis software manufactured by RICARDO plc, was used[(6)]. This 1D simulation calculates the dynamic behaviors of a working fluid by discretizing and solving basic equations such as the mass conservation law, Navier-Stokes equation, energy conservation law, and gas state equation after transforming the 3D shapes of the intake-exhaust system into a 1D shape.

1D simulation enables the calculation of output power

* Motorcycle R&D Center

and pressures in the intake-exhaust system. Moreover, sound waves that propagate to the surrounding space (i.e., intake-exhaust noise) can be calculated using flow velocity at the open end of intake-exhaust system.

2.2. Calculation Model

There are some factors that affect calculation accuracy in a 1D simulation. Representative factors are as follows:

(1) The accuracy of numerical values given as input conditions, such as port discharge coefficients and mechanical friction losses.
(2) The accuracy of boundary conditions related to heat transfer such as the inner surface temperatures of pipes and cylinders.
(3) Modeling techniques that transform three-dimensional shapes such as duct length, duct diameter, and volume into the 1D shape.

Since the influence of these factors changes depending on engine type and load conditions, sufficient consideration is needed to consistently obtain a higher calculation accuracy under various conditions. Figure 1 shows an example of a calculation model. The range of the calculation model is all pipes and volumes from the opening of the intake duct in the air cleaner to the tail pipe end in the muffler, and the engine cylinder.

The main input conditions and boundary conditions used for calculation are as follows:

- The discharge coefficients of the intake-exhaust port are based on data that are measured with the test rig on steady flow.
- As mechanical friction losses, the data that subtract pumping losses calculated by a 1D simulation from the total friction losses measured by the motoring friction method are used.
- As a heat release by combustion, the Wiebe function with adjusted parameters to correspond to the measured heat release rate is used
- The inner wall temperature of the intake pipe is based on measured data, and the wall temperatures of the cylinder and exhaust pipe are based on appropriate values referring to past measured values.

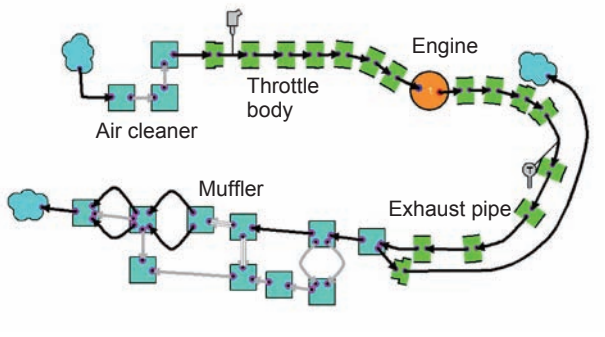


Fig. 1 Calculation model

3. Verification of Calculation Accuracy

3.1. Test Motorcycles

Table 1 shows the major specifications of the engine and intake-exhaust system of the test motorcycles used for verification. Each engine has a two-valve layout, and electronically-controlled fuel injection systems. The only major differences of engine specifications are the engine displacement and the cooling system. On the other hand, the intake-exhaust systems are different in each test motorcycle. For example, Test Motorcycle (C) has a complex curved intake duct as shown in Fig. 2, and Test Motorcycle (B) has a U-shaped, curved pipe in the muffler as show in Fig. 3. These are typical examples of arranging components efficiently in the limited space with small-displacement motorcycles.

3.2. Output power

The output power of the test motorcycles was measured using a dynamometer under full load conditions. Figure 4 shows a comparison of the measured and calculated output power and torque. The calculated result corresponds most closely with the measured result in the case of Test Motorcycle (A), which has an air-cooled engine. The calculation error is only around 2%, and the characteristics of the output power curve also correspond closely to the measured result. In the case of Test Motorcycle (B), which has a water-cooled engine, the calculated result is lower than the measured result when using the same boundary conditions as Test Motorcycle (A). The calculated volumetric efficiency is also lower than

Table 1 Specification of motorcycles used for verification

Test motorcycles	A	B	C
Engine type	4-stroke single cylinder	4-stroke single cylinder	4-stroke single cylinder
Cooling system	Air-cooled	Water-cooled	Air-cooled
Displacement (cm^3)	150	125	110
Valve layout	IN: 1 / EX: 1	IN: 1 / EX: 1	IN: 1 / EX: 1
Ignition type	Spark ignition	Spark ignition	Spark ignition
Air cleaner volume (L)	2.6	3.7	2.3
Muffler volume (L)	4.7	3.6	2.2
Muffler structure	3-pass	3-pass	3-pass

the measured result, so the boundary conditions were adjusted for Test Motorcycle (B). As a result, sufficient accuracy of calculation is obtained. Thus, it was found that it is necessary to set differing boundary conditions for water-cooled and air-cooled engines. In the case of Test Motorcycle (C), there is a slight error between the measured and calculated result at lower engine speeds. However, the measured and calculated characteristics of the output power curve correspond almost exactly, so it can be said that there is sufficient accuracy for practical use.

In order to confirm the validity of the input conditions and boundary conditions, accuracy validation was carried out adding another four test motorcycles with different engine displacements and cooling systems. Like the results of Test Motorcycles A, B, and C, there are very few calculation errors.

Figure 5 shows the correlation between measured and calculated results for maximum output power for all test motorcycles. The gradient of the approximation curve and the coefficients of correlation are each approximately 1, and this indicate that a higher calculation accuracy is obtained. From these results, it was found that a 1D simulation can calculate the output power with sufficient accuracy for most small-displacement single-cylinder motorcycles.

Next, the calculation accuracy of the indicated work was verified. Test Motorcycle (A) and (B) were verified, with a measurement engine speed of 6000 r/min which generated maximum torque under full load conditions. Figure 6 shows a comparison of P-V diagrams for measurement and calculation. As the diagrams show, the pumping loss in the charging strokes and the exhaust strokes correspond closely. In addition, the transition of in-cylinder pressure at the

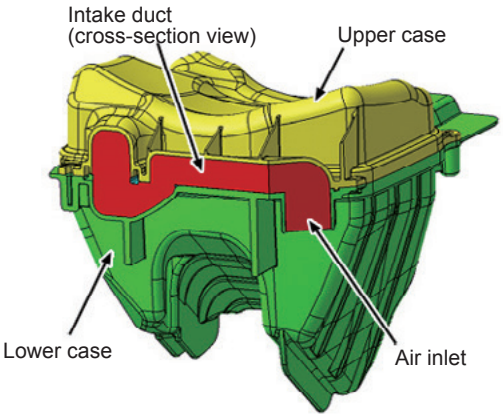


Fig. 2 Intake duct of test motorcycle (C)

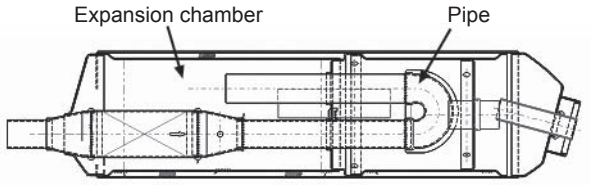


Fig. 3 Structure of muffler of test motorcycle (B)

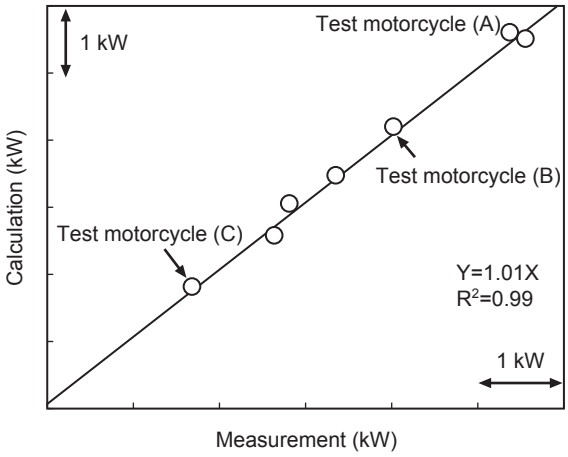


Fig. 5 Comparison of measured and calculated maximum output power

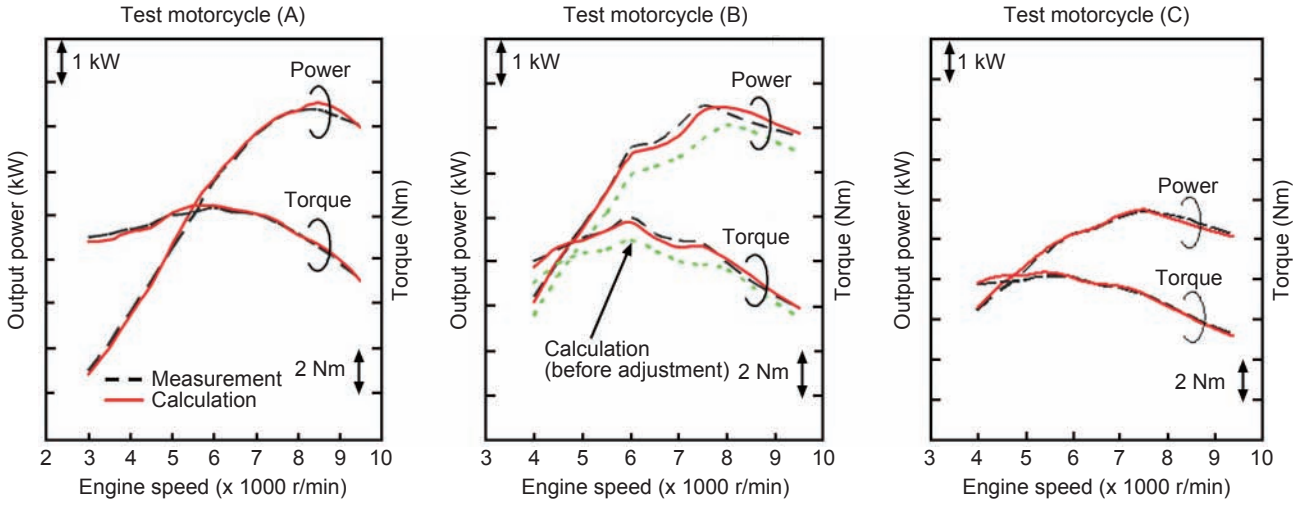


Fig. 4 Comparison of measured and calculated output power and torque

compression strokes and the expansion strokes, maximum pressure, and the timing of maximum pressure also correspond almost closely. This proves that the volumetric efficiency, heat release by combustion, and cooling losses for the cylinder wall are calculated accurately.

Next, it was verified whether these models can calculate changes of output power when the specifications of the exhaust systems were modified. The modifying point of specification was exhaust pipe length upstream of the catalyst.

Figure 7 shows the measured and calculated output power characteristics. Figure 8 shows the rate of output power change. The measured results indicate that output power increases at lower engine speeds and decreases at higher engine speeds when the exhaust pipe length upstream of the catalyst becomes longer, and the opposite when the exhaust pipe length upstream of the catalyst becomes shorter. The calculated results show the same tendencies, and the results for the rate of output power change are similar to the measured results. Thus, it was confirmed that these calculation models could also calculate output power accurately even when the exhaust system specifications are modified.

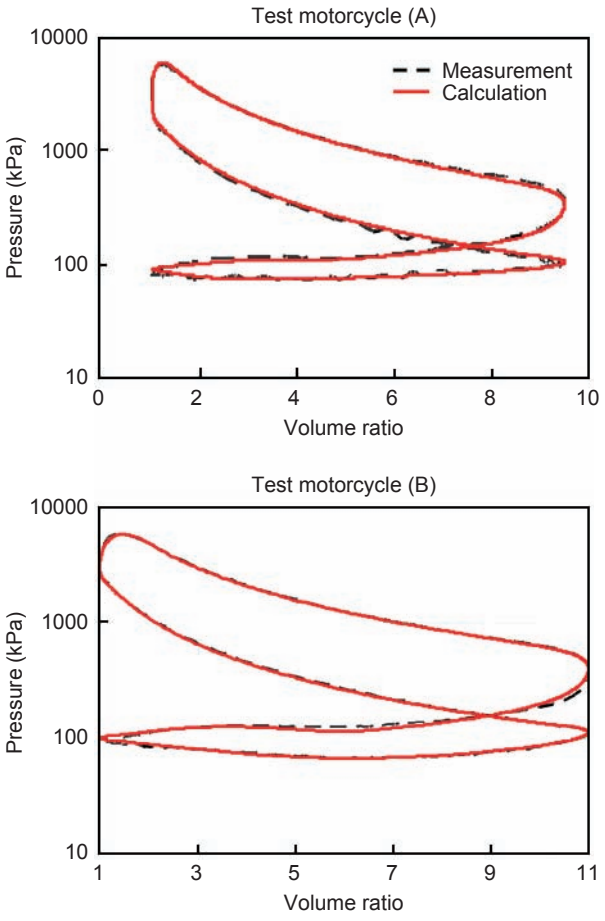


Fig. 6 Comparison of measured and calculated P-V diagram

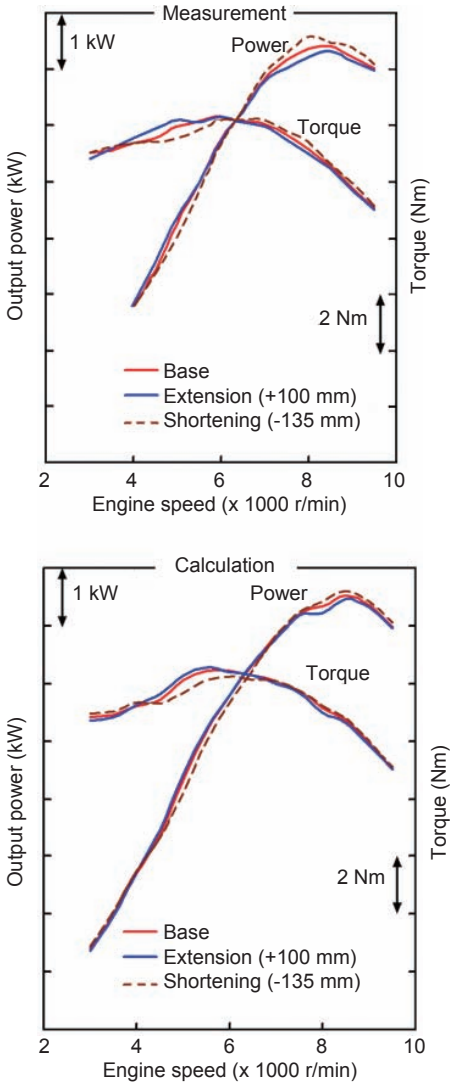


Fig. 7 Comparison of measured and calculated output power and torque when changing exhaust pipe length

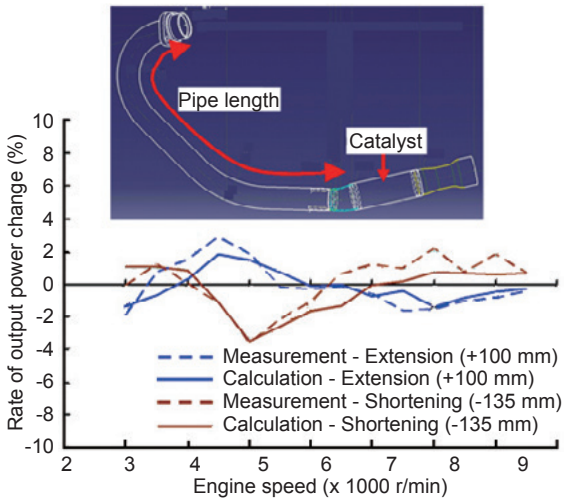


Fig. 8 Rate of output power change when changing exhaust pipe length

3.3. Intake-exhaust Noise

The calculation accuracy of intake-exhaust noise was verified using Test Motorcycle (A), (B), and (C). Table 2 shows measurement and calculation conditions. The intake-exhaust noise was measured at the engine speed where the sound pressure level indicates maximum value in pass-by noise measurements. Intake noise was measured inside the intake duct by a pressure sensor, and exhaust noise was measured near the tail pipe by a microphone. By measuring at such places, noises other than the intake-exhaust pulsation noise, (e.g., the shell noise of the air cleaner box, the mechanical noise inside the engine), were reduced as much as possible. The verified frequency domain was up to 500 Hz for both intake noise and exhaust noise, because the sound pressure level in this domain contributed greatly to the overall sound pressure level. In the criteria for accurate calculation of the intake-exhaust noise, it was assumed that the measured and calculated results were in the same tendency concerning the sound pressure level of each order components in the frequency analysis. In addition, the pressure of time domain near the intake and exhaust valves was measured at the same time as measuring the intake-exhaust noise. By evaluating them in those positions, the calculation accuracy of the pressure waves that are regarded as the source of intake-exhaust noise were verified indirectly.

3.3.1. Intake noise

Figure 9 shows a comparison of the measured and calculated frequency analysis result and overall sound pressure level of intake noise. For the intake noise, Test Motorcycle (A) and (B) show favorable correlations between measurement and calculation. But, for Test Motorcycle (C), the calculated sound pressure level was higher than the measured one, especially below the 100 Hz frequency domains. Figure 10 shows the pressure near the intake valve. The measured and calculated results correspond well for Test Motorcycle (A), (B) and (C). Therefore, it was thought that the sound transfer function could not be calculated accurately for Test Motorcycle (C) because the 1D modeling of the intake system had been inadequate.

Then, the element that was thought to have a large influence on sound transfer function was clarified, and the input shape and size were reviewed in the calculation model. Figure 11 shows a comparison of the measured intake noise and that calculated with the modified model of Test Motorcycle (C). The calculated sound pressure level lower than 100 Hz in the frequency analysis is enhanced, so a favorable correlation can be confirmed.

3.3.2. Exhaust noise

Figure 12 shows a comparison of the measured and calculated frequency analysis result and overall sound pressure level of exhaust noise. Test Motorcycle (A) and (B) show a favorable correlation between measurement and calculation. However, in case of Test Motorcycle (C), the calculated sound pressure level is much lower

Table 2 Measurement and calculation conditions of intake-exhaust noise

Load condition	Full load
Operation condition	Steady state
Throttle condition	Wide-open throttle
Measured engine speed	At Max. sound pressure level in pass-by noise measurement
Measurement position	Inside intake duct (Intake noise)
	Near tail pipe opening (Exhaust noise)
Analysis method	Frequency analysis
Frequency range	0 - 500 Hz
Frequency resolution	4 Hz
Window function	Hanning

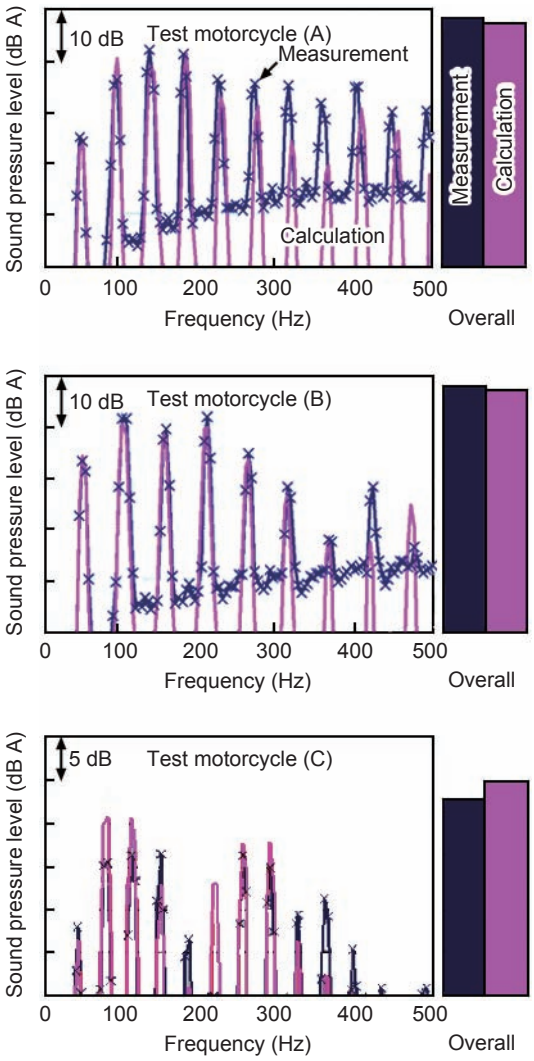


Fig. 9 Comparison of measured and calculated intake noise inside intake duct

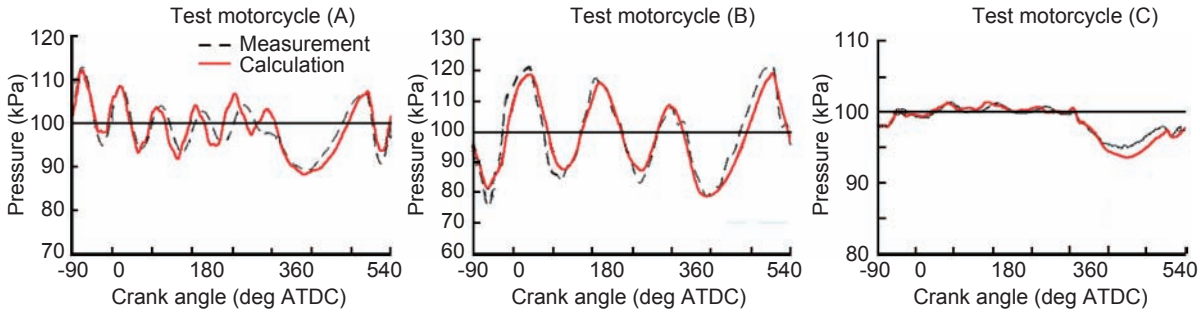


Fig. 10 Comparison of measured and calculated pressure wave near intake valve

than the measured one at frequencies over 200 Hz, so the correlation between measurement and calculation is not sufficient.

Figure 13 shows the pressure near the exhaust valve. As in the case of the pressure near the intake valve, measured and calculated results correspond well for all test motorcycles. Therefore, it was considered that the 1D modeling of the area downstream from the exhaust pipe was inadequate for Test Motorcycle (C).

Figure 14 shows the internal structure of the muffler of Test Motorcycle (C). Comparing the differences of internal structure between the mufflers of Test Motorcycle (A) and (B), which have higher calculation accuracy, and that of Test Motorcycle (C), it was found that the distance between the exhaust pipe and inner pipe is closer and the central axes of both pipes are almost coaxial in Test Motorcycle (C). It was assumed that these characteristics are the main reason for the decreased calculation accuracy of exhaust noise for Test Motorcycle (C). In order to verify this assumption, the single-chamber mufflers shown in Fig. 15 were made. These mufflers have the same chamber volume, pipe length and diameter, while the relative dimensions of the central axes between the exhaust pipe and inner pipe are different from each other. Figure 16 shows a comparison of the measured and calculated exhaust noise for both mufflers.

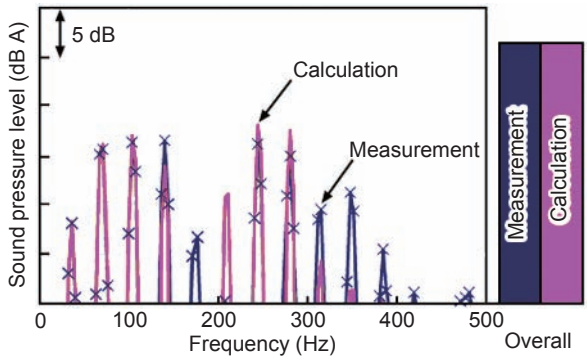


Fig. 11 Comparison of measured intake-noise inside intake duct and that calculated with modified model of test motorcycle (C)

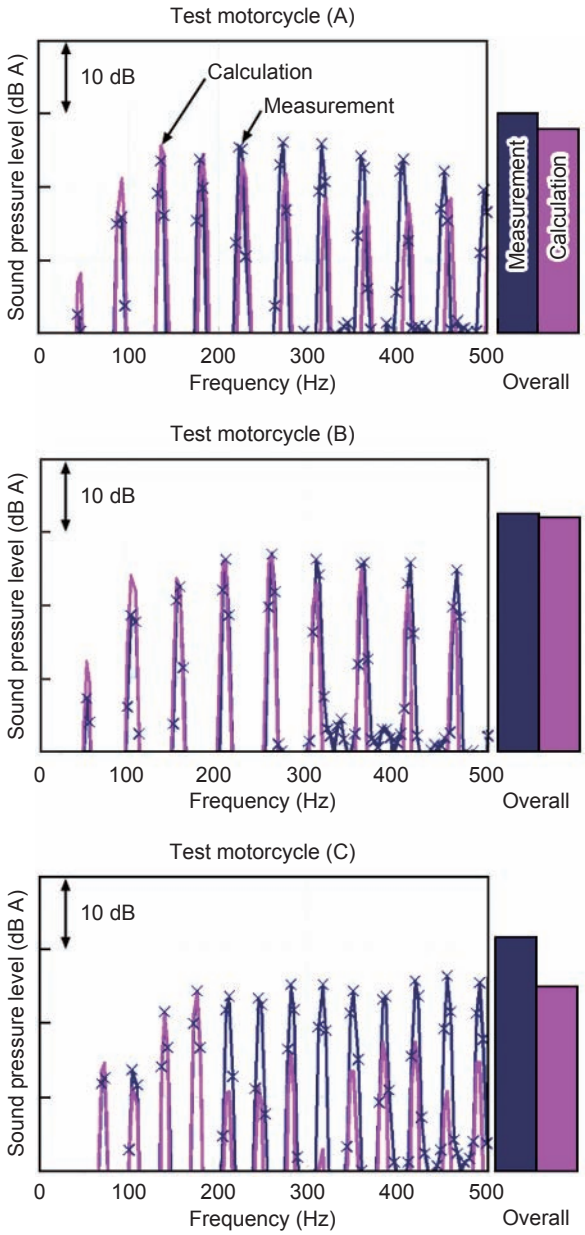


Fig. 12 Comparison of measured and calculated exhaust noise

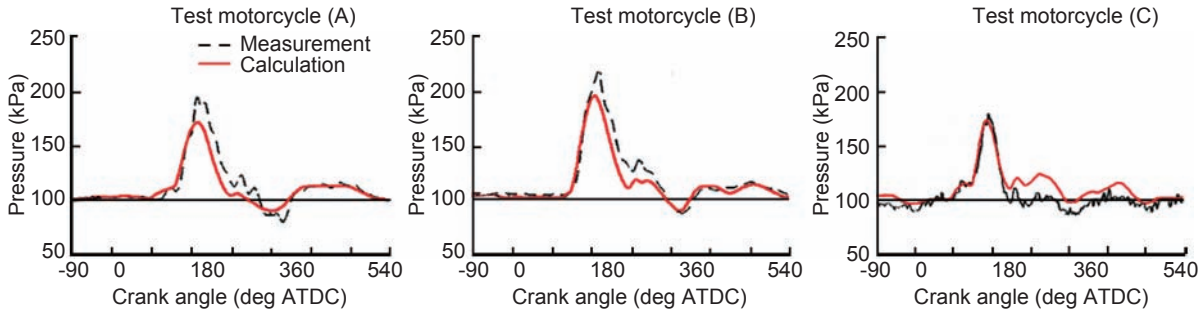


Fig. 13 Comparison of measured and calculated pressure wave near exhaust valve

When the central axes of the exhaust pipe and the inner pipe in the muffler are coaxial ("coaxial configuration" below), the calculated results are lower than the measured result for all frequency domains. At higher frequencies in particular, the differences are more than 20 dB. On the other hand, a favorable correlation can be confirmed when each pipe is not in a coaxial configuration. Considering these results, it was found that a 1D simulation could calculate exhaust noise as long as each pipe is not in a coaxial configuration, and that sufficient calculation accuracy is not obtained using a 1D simulation alone if each pipe is coaxial configuration.

It is known that calculation accuracy in a 1D simulation can be enhanced by discretizing the volume section of the muffler in detail. But, the calculation accuracy had not been enhanced in this verification though detail discretization was done.

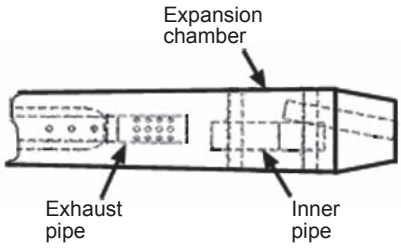


Fig. 14 Structure of muffler of test motorcycle (C)

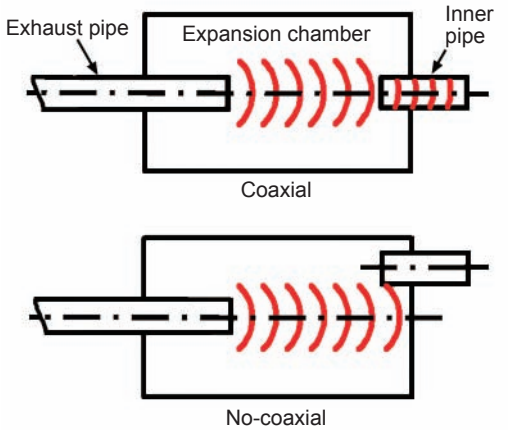


Fig. 15 Structure of single-chamber mufflers

3.4. Approach for Enhancing Calculation Accuracy of Exhaust Noise by Applying a 1D-3D Coupled Simulation

For the mufflers that the exhaust pipe and the inner pipe are in a coaxial configuration, it was estimated that the reason that the measured result was higher than the calculated result is that the emission gas actually run through the next pipe without sufficient expansion in the expansion chamber. In order to re-create this phenomenon using a 1D simulation, verification was executed with single-chamber mufflers. However, the calculation accuracy could not be adequately enhanced. Then it was verified whether the calculation accuracy could be enhanced by

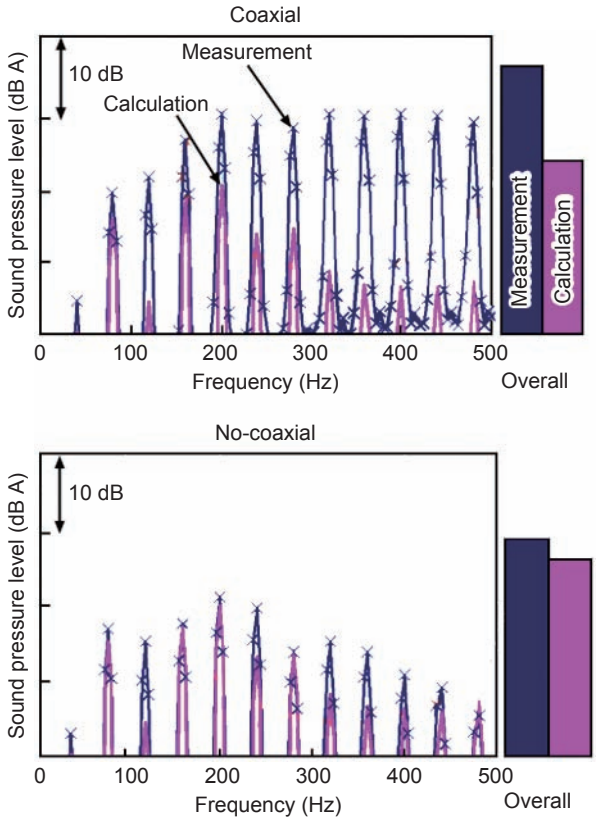


Fig. 16 Comparison of measured and calculated exhaust noise for different pipe positions

coupling a 1D simulation with a 3D simulation ("1D-3D Coupled Simulation" below). 1D-3D coupled simulation is executed by alternately transferring data on pressure, flow velocity, gas temperature and so on, at the connecting point. The software used for the 3D simulation was VECTIS, a commercial 3D thermo and fluid dynamics analysis software made by Ricardo Plc[7].

Figure 17 shows multi-chamber mufflers. Three different mufflers were made. In the first one, the exhaust pipe and inner pipe are in a coaxial configuration (Type 1); in the second, they are partly in a coaxial configuration (Type 2); and in the third, they are not in a coaxial configuration (Type 3). For all mufflers, the measured and calculated exhaust noise was compared. Figure 18 shows the 3D simulation model. The scope of the 3D simulation is from the exhaust pipe to the tail pipe.

To start with, Fig. 19 shows the measurement results. The exhaust noise tended to increase as the pipes in the mufflers approached a coaxial configuration, and that the tendency is clearly shown in the high-frequency range, the same result as the single-chamber muffler. Next, Fig. 20 shows calculation results for a 1D simulation and for a 1D-3D coupled simulation. This figure should be treated as a qualitative comparison because the calculation process for each simulation is different because of functional restrictions of the WAVE® software. In a 1D simulation, the calculation results are not affected by pipe position, as with a single chamber muffler, so a 1D simulation cannot re-create the tendency of the measured results. On the other hand, in a 1D-3D coupled simulation, the exhaust noise shows the tendency that the closer each pipe is in a coaxial configuration, the higher the sound pressure level is. Therefore, a 1D-3D coupled simulation can re-create the tendency of the measured results.

Figure 21 shows a comparison of the calculated emission gas flows using 3D simulations. In the case of the Type 3 muffler, in which the pipe is not in a coaxial configuration, the jet flow from the exhaust pipe goes into

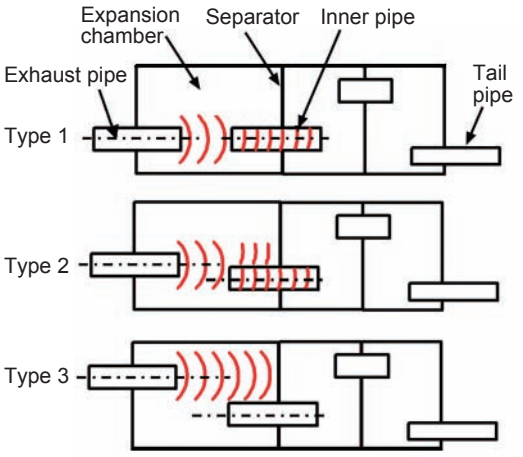


Fig. 17 Structure of multi-chamber mufflers

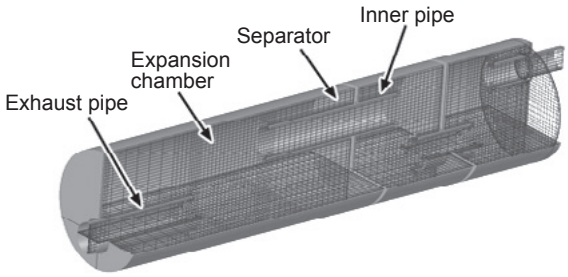


Fig. 18 3D-simulation model

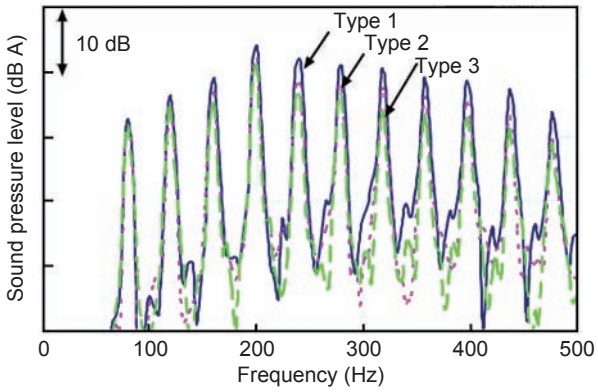


Fig. 19 Measured exhaust noise for different pipe positions

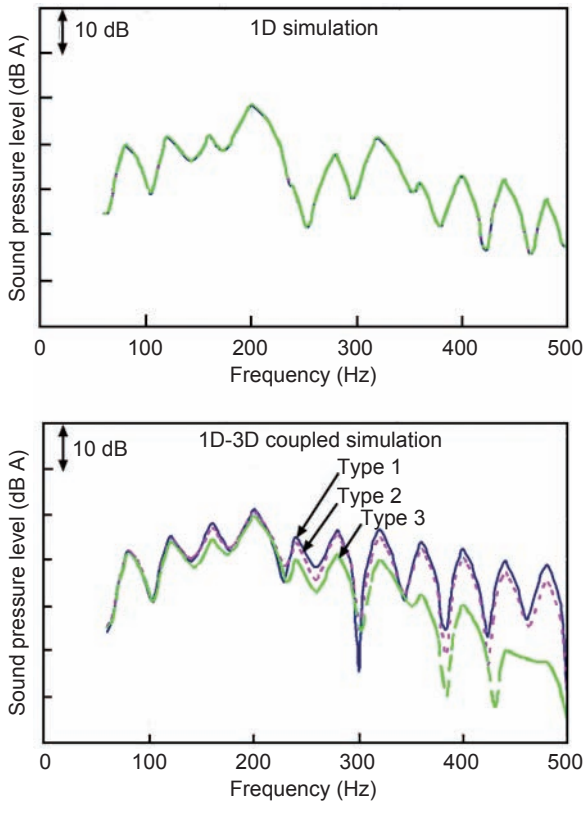


Fig. 20 Calculated exhaust noise for different pipe positions

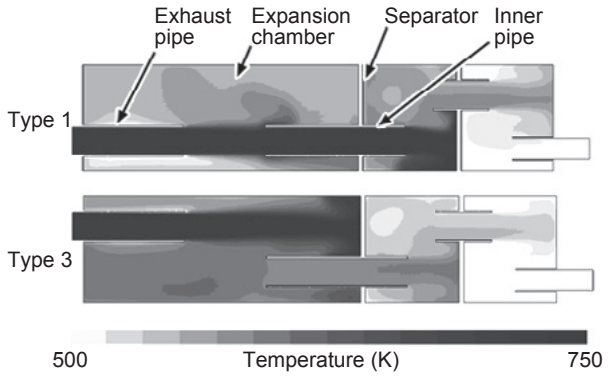


Fig. 21 Exhaust gas flow in muffler for different pipe positions (at ATDC 270 deg)

the inner pipe after running up against the separator. On the other hand, in the case of the Type 1 muffler, in which the pipe is in a coaxial configuration, the jet flow goes directly into the inner pipe without sufficiently expanding in the expansion chamber. For these results, it was found that there is a possibility to enhance the calculation accuracy of exhaust-noise by using a 1D-3D coupled simulation even in the case of muffler structure for which sufficient calculation accuracy cannot be obtained by using a 1D simulation.

4. Approach for Enhancement of Prediction Accuracy at the Initial Stages of Development

In the present accuracy verification, output power and intake-exhaust noise could be calculated with a higher accuracy by using the measured data of test motorcycles for part of the input conditions. However, at the initial stages of development, accurate calculations must be performed even when the measured data are not available as input conditions. So, a predicting method of input conditions to enable accurate calculations was developed.

- Intake-exhaust port flow coefficients: 3D computational fluid dynamics (CFD) calculations are performed for intake-exhaust port, and the obtained flow coefficients are used.
- Mechanical friction loss: Based on the friction loss of a similar engine, the value that calculates the amount of change from the dimensional difference of the part that becomes a friction factor and adds or subtracts it is used.
- Combustion conditions: In most cases, ignition timings for small-displacement single-cylinder motorcycles are set to the minimum advanced timing for best torque (MBT). Therefore, combustion conditions derived from ignition timings under full load in multiple mass production engines are used.

Figure 22 shows the results of calculated maximum output power and overall intake-exhaust noise for test motorcycles (A), (B), and (C) using the predicted input conditions. The maximum differences with the case that the measurement value is used for the input conditions are about 0.3 kW in output power and about 0.5 dB in the intake-exhaust noise, therefore it can be said that there is sufficient accuracy for practical use. From these results, it was verified that output power and intake-exhaust noise can be calculated with a sufficient accuracy even when using the predicted input conditions.

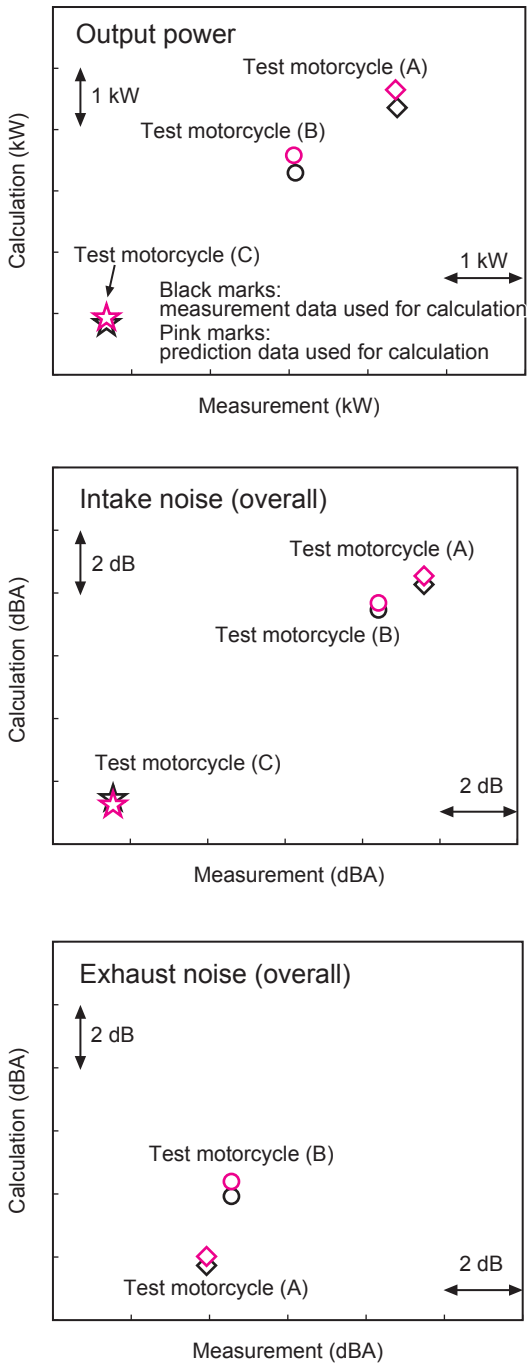


Fig. 22 Change in output power and intake-exhaust noise when using prediction data

5. Conclusion

A prediction technology that can concurrently calculate both the output power and intake-exhaust noise for small-displacement single cylinder motorcycles using a 1D simulation was constructed, and the following conclusions were obtained.

(1) Output power can be calculated accurately.
(2) Intake noise can be calculated accurately.
(3) Exhaust noise can be calculated accurately provided that the pipes in the muffler are not in a coaxial configuration.
(4) Sufficient calculation accuracy of the exhaust noise is not obtained by using a 1D simulation when the pipes in the muffler are in a coaxial configuration, and there is a possibility to enhance the calculation accuracy by using a 1D-3D coupled simulation.
(5) Output power and intake-exhaust noise can be calculated with sufficient accuracy by using the predicted input conditions even when the measured data are not available as an input condition.

References

(1) Kido, H., Kuwahara, H., Brechlin, E., Boonen, R.: Modeling the Sound Source of an Intake and Predicting the Intake Sound Pressure Level for a Motorcycle, SAE paper, 2003-32-0058 (2003)
(2) Yagi, S., Fujii, I., Sono, H., Ishibashi, Y., Fijiwara, K.: Total Engine Loss and Engine Output Characteristics in Four Stroke S.I. Engines, HONDA R&D Technical Review, Vol. 3, p. 99-114
(3) Ciocci, F., Noceti, D., Bradamante, E.: Intake System Analysis of the 550 Maranello using the WAVE code, http://www.ricardo.com/Documents/Downloads/pdf/wave_intake_system_analysis_ferrari.pdf
(4) Wirtz, R., Mazzoni, D.: Application of WAVE in Motorcycle Prototyping, http://www.ricardo.com/Documents/Downloads/pdf/wave_motorcycle_prototyping_ducati.PDF
(5) Mochkaai, Y.: GT-POWER as a Tool for Acoustic and Dynamic Optimization of Exhaust Systems, http://www.gtisoft.com/confarch/EMCON2009.pdf
(6) http://www.ricardo.com/en-gb/Software/Products/WAVE/
(7) http://www.ricardo.com/en-gb/Software/Products/VECTIS/

■ Author ■


Hiroshi HORIKAWA


Hideki KIDO


Satoshi IIJIMA


Yasuo MURAKAMI

Study of Upshift Control Method by Estimation of Acceleration Waveform

Shintaro KAMEDA* Yasushi INAGAWA*

ABSTRACT

Control that corrects the torque output deviation of shift clutches is required to suppress the shift-shock produced when automatic transmissions up-shift, and enhance product quality. Control technology was developed that serves this purpose by estimating and evaluating the vehicle acceleration waveform generated when shifting, from the variation in output shaft rotations, and then detecting the output deviation of clutch torque and performing learning correction based on that acceleration waveform.

1. Introduction

Recently, the number of automatic transmission gear stages is increasing, and enhancement of shift-shock during up-shifting is becoming an important issue. As the number of gear stages increases, the number of shift times while accelerating to a certain vehicle speed also increases, and shift-shock gives drivers an unpleasant feeling. Conversely, acceleration that does not give a feeling of shift-shock is exhilarating for drivers, and can help to further enhance product quality. Based on case studies of shift-shock using actual vehicles, the aim was to realize a vehicle acceleration waveform (hereafter, "acceleration waveform") that does not produce the swaying feeling accompanied with the absorption of inertia torque (hereafter, "inertia shock") during the period when the input shaft rotations change (inertia phase). However, due to the output deviation of clutch torque originating in dispersion, it is a challenge to maintain stable product quality by using only feed-forward control.

This study developed an up-shift control method that corrects the output deviation of clutch torque without adding new sensors, in order to realize a stable acceleration waveform without inertia shock and enhance product quality during shifting.

2. Study Goals

The torque transmission formulas during up-shift in a parallel axis automatic transmission[1] are shown below.

Equations (1) and (2) show the torque transmission formulas during the period when the torque transmission path switches from the opening-side clutch to the conclusion-side clutch (torque phase).

$$T_{in} = T_{of} + Tc_{on} \tag{1}$$

$$T_{out} = (T_{of} \cdot i_{of} + Tc_{on} \cdot i_{on}) \cdot i_f \tag{2}$$

Nomenclature
T_{in} : Input torque [Nm]
T_{of} : Opening side clutch torque capacity [Nm]
Tc_{on} : Conclusion side clutch torque [Nm]
T_{out} : Output shaft torque [Nm]
i_{of} : Opening side gear ratio [-]
i_{on} : Conclusion side gear ratio [-]
i_f : Final reduction gear ratio [-]

When the torque of the conclusion-side clutch is increased and the torque of the opening-side clutch is reduced to establish the relationship shown in Eq. (3), the inertia phase starts.

$$Tc_{on} > (T_{of} + T_{in}) \tag{3}$$

Equations (4) and (5) show the torque transmission formulas in the inertia phase.

$$T_{in} = Tc_{on} - Tc_{of} + J_{in} \cdot \dot{\omega}_{in} \tag{4}$$

Nomenclature
Tc_{of} : Opening side clutch torque [Nm]
J_{in} : Input shaft inertia [kg·m^2]
$\dot{\omega}_{in}$: Input shaft angular acceleration [rad/s^2]

* Automobile R&D Center

$$T_{out} = (Tc_{on} \cdot i_{on} - Tc_{of} \cdot i_{of}) \cdot i_f \quad (5)$$

Assuming the torque of the opening side clutch after the start of the inertia phase to be "0" yields the following Eq. (6).

$$T_{out} = Tc_{on} \cdot i_{on} \cdot i_f \quad (6)$$

Thus, the output shaft torque during the inertia phase is determined by the torque of the conclusion side clutch.

Control methods based on cooperation between the shift clutch torque and the engine torque, that is to say, the clutch input torque[2), (3)], are generally applied to create an acceleration waveform without inertia shock. Figure 1 shows this concept drawing. In the torque phase (time t_0 to t_1), the torque of the conclusion side clutch is increased so that it becomes the same value as the clutch input torque when the torque phase finishes (time t_1), and the torque of the opening side clutch is reduced correspondingly. Then, the input shaft rotations begin to change in a manner that satisfies the conditions in Eq. (3), by reducing the clutch input torque after clutch torque switching is completed.

In addition, in the inertia phase (time t_1 to t_2), an acceleration waveform without inertia shock is achieved by performing smooth output relative to the clutch input torque after the torque of the conclusion side clutch finishes shifting.

However, the actual clutch torque has output deviation originating in the initial tolerance and other dispersion. Therefore, even when feed-forward control of clutch torque based on the clutch input torque is used to create an acceleration waveform without inertia shock, inertia shock is still generated due to this output deviation of clutch torque. That is to say, dispersion also occurs in the shift-shock, making it a challenge to secure stable product quality. For example, when the clutch torque is lower than the command value, insufficient clutch torque in the torque phase results in phenomena such as high-rpm idling. Likewise, when the clutch torque is higher than the command value, inertia shock is generated.

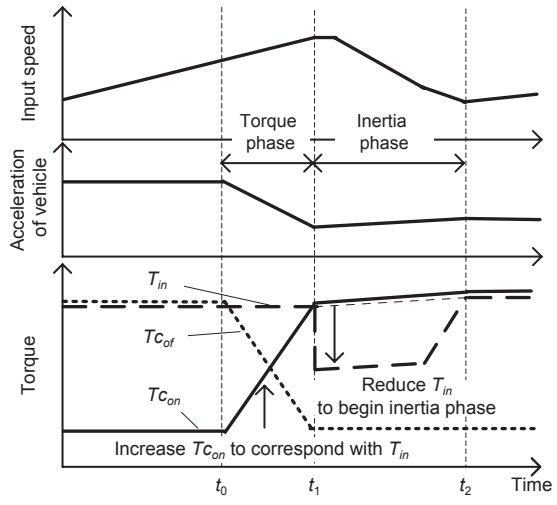


Fig. 1 Concept of reducing fluctuation of longitudinal acceleration during inertia phase

In addition, it is thought that this output deviation of clutch torque can be detected by adding a hydraulic sensor or a torque sensor, but this leads to increased cost and weight. Methods have been devised that use torque converter characteristics formulas to estimate the output shaft torque during the inertia phase from the rate of change in the input shaft rotations, and then use that estimated torque to perform shift control[4), (5)]. However, when beginning to change the rotations by reducing the clutch input torque, the transient reduction in the clutch input torque needs to be accurately estimated to detect the output deviation of clutch torque. Therefore, it is desirable to estimate only the clutch torque from the output shaft torque, according to the relationship in Eq. (6).

For these reasons, this study aimed to correct the output deviation of clutch torque without adding new sensors, and realize a stable acceleration waveform without inertia shock by:

(1) Estimating the acceleration waveform while shifting from the existing rotation sensor signal; and
(2) Performing clutch torque learning correction so that the acceleration waveform approaches the target waveform, based on evaluation of the inertia shock resulting from the estimated waveform.

3. Clutch Torque Learning Control

3.1. Overview of Control

Equation (7) shows the relationship between the clutch torque and running resistance.

$$T_{out} = T_{rl} + J_v \cdot \dot{\omega}_v \quad (7)$$

Using this output shaft torque as the target value yields the following.

$$\hat{T}_{out} = T_{rl} + J_v \cdot \hat{\dot{\omega}}_v \quad (8)$$

$$T_{out} - \hat{T}_{out} = J_v \cdot (\dot{\omega}_v - \hat{\dot{\omega}}_v) \quad (9)$$

$$Tc_{on} - \hat{T}c_{on} = J'_v \cdot (\dot{\omega}_v - \hat{\dot{\omega}}_v) \quad (10)$$

$$J'_v = J_v / (i_{on} \cdot i_f) \quad (11)$$

$$\Delta Tc_{on} = J'_v \cdot \Delta\dot{\omega}_v \quad (12)$$

Nomenclature
T_{rl} : Road load torque [Nm]
J_v : Vehicle inertia [kg·m^2]
$\dot{\omega}_v$: Output shaft angular acceleration [rad/s^2]
$\hat{T}_{out}$: Target output torque [Nm]
$\hat{\dot{\omega}}_v$: Target output angular acceleration [rad/s^2]
$\hat{T}c_{on}$: Target clutch output torque [Nm]
ΔTc_{on} : Output deviation of clutch torque [Nm]

$\Delta\dot{\omega}_v$: Deviation of output angular acceleration [rad/s^2]

Therefore, as shown in Fig. 2, the output deviation of clutch torque can be obtained without the effects of running resistance, from the inertia mass of the vehicle and the angular acceleration of the output shaft; that is to say, the deviation between the target acceleration waveform and the actual acceleration waveform.

The clutch torque learning correction in this study uses this relationship to detect the output deviation of clutch torque from the acceleration waveform output as a result of feed-forward control based in the clutch input torque, as shown in Fig. 3 (a). The feed-forward control output value is then corrected the next time shifting is performed so that the acceleration waveform approaches the target waveform, as shown in Fig. 3 (b).

3.2. Configuration of Clutch Torque Learning Control System

Figure 4 shows the configuration of the clutch torque learning control system.

The control system comprises a feed-forward control unit based on estimation of the clutch input torque, an acceleration waveform evaluation unit, and a learning correction clutch torque calculation unit.

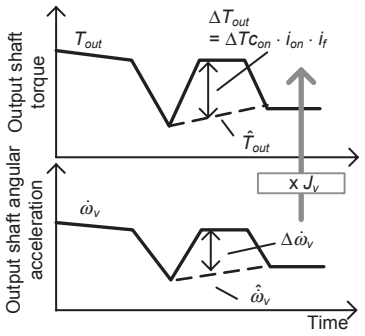


Fig. 2 Relation between output shaft torque and output angular acceleration deviation

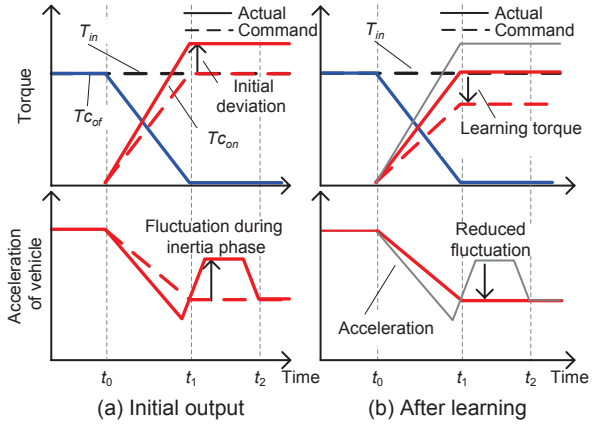


Fig. 3 Concept of learning control for reducing fluctuation of longitudinal acceleration during inertia phase

3.2.1. Feed-forward control unit

The feed-forward control unit uses the control concept shown in Fig. 1 to calculate the clutch torques required for both the opening and conclusion sides in order to realize the target acceleration waveforms for the torque and inertia phases, based on the estimated clutch input torque values.

3.2.2. Acceleration waveform evaluation unit

The acceleration waveform evaluation unit estimates the acceleration waveform and calculates the evaluation value of the output deviation of clutch torque based on the estimated waveform.

The acceleration waveform is estimated based on the pulse signal from the existing counter-shaft rotation pickup. The rotations are calculated from the cycle of the pulse signal from the rotation pickup, and differential processing is performed to calculate the angular acceleration. However, due to noise generated by the vibration of the transmission gear used for pulse detection and other factors, simply performing differential processing is insufficient for evaluating the fluctuation in the output shaft torque. This study set a low-pass filter that is suitable for detecting the torque fluctuation during shifting, based on the output shaft torque waveform during shifting measured using an actual vehicle, and the frequency characteristics of the acceleration waveform. The estimated acceleration waveform value is then obtained by passing the angular acceleration obtained

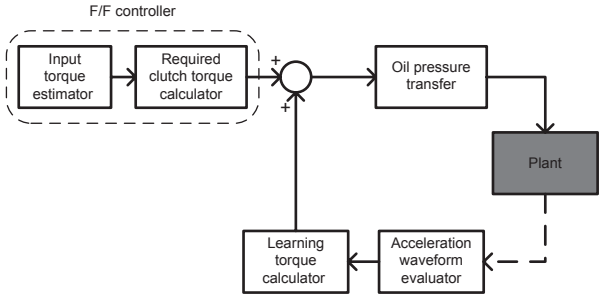


Fig. 4 System diagram of clutch torque learning control for experiment

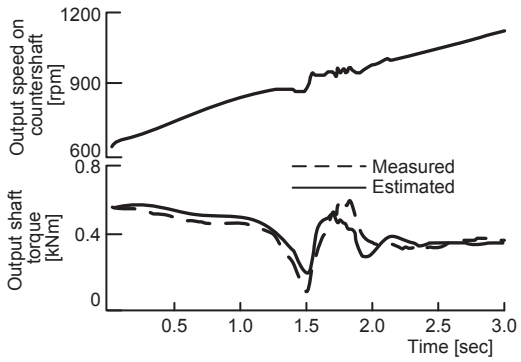


Fig. 5 Comparison of measured and estimated output shaft torque

by differential processing through the set low-pass filter.

Figure 5 compares the results of converting the estimated acceleration waveform value into the output shaft torque based on the relationship in Eq. (7), with the measured output shaft torque waveform. The estimated waveform exhibits the same tendencies as the measured torque waveform, so it is thought that inertia shock can be adequately evaluated using the estimated waveform.

In addition, to realize an acceleration waveform without inertia shock, it is important to match the torque of the conclusion side clutch with the clutch input torque at the end of the torque phase, i.e., in the early stage of the inertia phase. When the torque of the conclusion side clutch exceeds the clutch input torque in the early stage of the inertia phase, the pull-in torque in the torque phase increases due to the relationship shown in Eq. (2) and Eq. (3). In addition, inertia absorption torque is generated due to the relationship shown in Eq. (4). This increase in the pull-in torque and the generation of inertia absorption torque lead to increased inertia shock. Therefore, the subject of learning control is the output deviation of clutch torque in the early stage of the inertia phase, and the control system evaluates the variation in the estimated acceleration waveform value that occurs as a result of this output deviation.

Figure 6 shows the method of calculating the evaluation value in the early stage of the inertia phase. The waveform that linearly connects the minimum estimated acceleration waveform value in the torque phase with the estimated acceleration waveform value after shifting ends is set as the target waveform. The period until the rate of change in the gear ratio reaches a certain level is set as the initial inertia phase interval, and the average value of the deviation between the estimated acceleration waveform value and the target waveform during this initial interval is used as the evaluation value in the early stage of the inertia phase.

3.2.3. Learning correction clutch torque calculation unit

The learning correction clutch torque is calculated as an integral amount by comparing the relative sizes of the evaluation value in the early stage of the inertia phase and the convergence target value, and adding to or subtracting from the previous learning correction clutch torque. The addition/subtraction amount per learning time is fixed, and the set value is obtained by dividing the maximum value of the output deviation of clutch torque by the target convergence times.

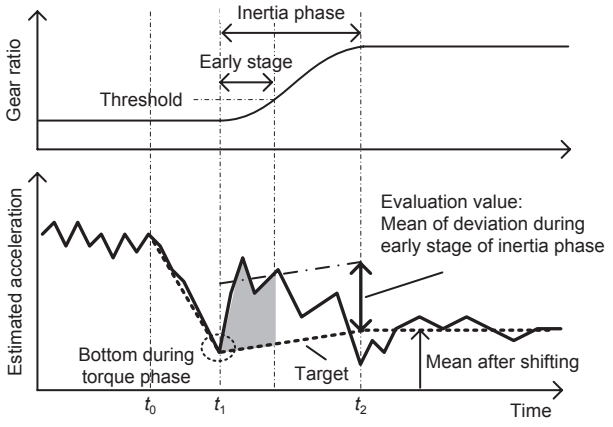


Fig. 6 Evaluation of deviation during early stage of inertia phase

4. Confirmation in an Actual Vehicle

4.1. Test Conditions

Running tests were performed using an actual vehicle, and the test conditions were set as follows:

(a) The shift mode was 1-2 up-shift, which has a large difference in driving power before and after the shift, making shift-shock quality an issue.

(b) A constant accelerator pedal opening value was used to limit the clutch input torque conditions, and learning was repeated at the same shift point according to a preset shift map.

4.2. Validity of Evaluation by Estimation of Acceleration Waveform

Figure 7 shows the results of calculating the waveform evaluation values in the early stage of the inertia phase from the vehicle acceleration measured using an acceleration sensor and the above-mentioned estimated acceleration waveform values.

The respective waveform evaluation values in the early stage of the inertia phase exhibit a correlation, which confirmed that the estimated acceleration waveform values can adequately function as a substitute for the acceleration sensor.

4.3. Progression of Clutch Torque Learning and Convergence

Figure 8 shows the learning results when initial output deviation of clutch torque of +40 Nm is applied relative to the feed-forward control value.

The addition/subtraction amount per learning time was

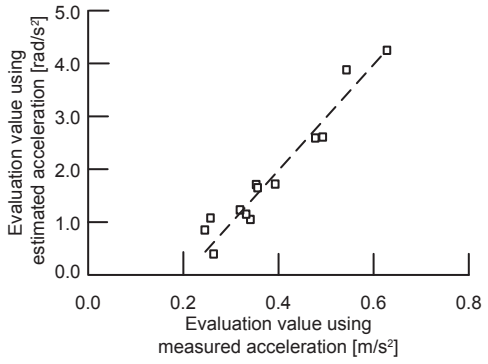


Fig. 7 Comparison of evaluation value using measured and estimated acceleration

set using a number of convergence target learning times of 20 times. In addition, the value corresponding to an output deviation of clutch torque of +10 Nm was set as the convergence target value.

At the learning initial point A (Fig. 9), the rotations began to change and inertia shock was generated when the inertia torque was absorbed by the clutch torque due to output deviation of clutch torque. At the learning transient point B (Fig. 10), clutch torque learning was performed relative to point A, and a decrease in the inertia shock was confirmed. At point C after learning had converged (Fig. 11), inertia was not absorbed by the clutch torque, inertia shock was not generated, and the acceleration waveform was confirmed to have converged to the target waveform. These results show that output deviation of clutch torque could be converged to a range of approximately 10 Nm, which indicates that clutch torque learning control using estimation of the acceleration waveform can realize a stable shift-shock waveform without inertia shock.

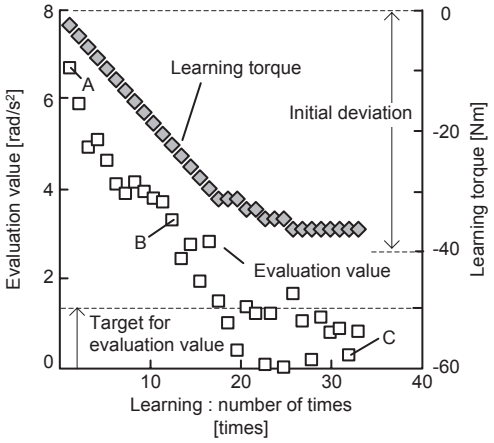


Fig. 8 Results of clutch torque learning control

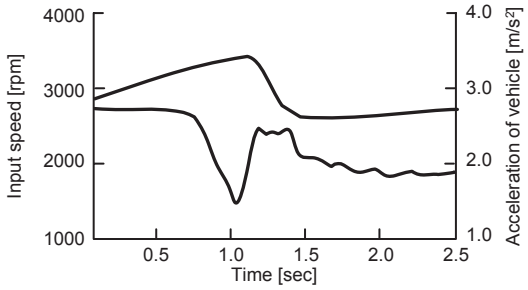


Fig. 9 Input speed and acceleration at A

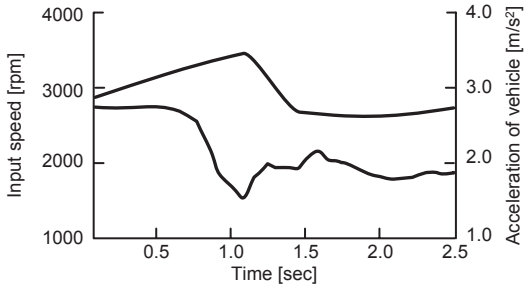


Fig. 10 Input speed and acceleration at B

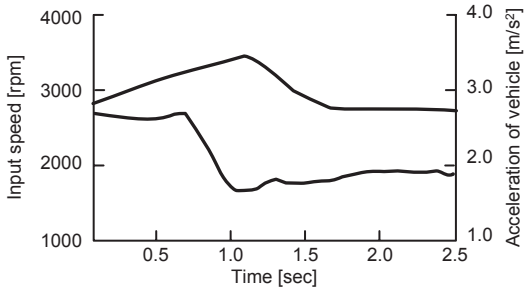


Fig. 11 Input speed and acceleration at C

In addition, the input shaft rotations in Figs. 9 through 11 show that the inertia phase time lengthened by 0.2 sec as learning converged. This is because only clutch torque learning was performed, so the amount of decrease in the clutch input torque remained at the initial setting, and the input shaft rotations changed more slowly due to the relationship in Eq. (4). There are concerns that a longer inertia phase time may produce a slow feeling that lowers product quality, or that heat generation may affect clutch durability. In response, convergence of the inertia phase time to a target time is also thought to be possible by having the control system simultaneously learn the amount of decrease in the clutch input torque corresponding to the clutch torque learning correction.

5. Conclusion

The following developments were performed to enhance product quality during up-shift without adding new sensors.

(1) Estimated acceleration waveform values during shifting were obtained by performing differential processing and appropriate filter processing on the counter-shaft rotation sensor signal.
(2) A method was established for evaluating the output deviation of clutch torque during the initial inertia phase interval based on the estimated waveform.
(3) A learning control method was developed that corrects output deviation of clutch torque based on the evaluation results, and realizes a stable acceleration waveform without inertia shock.

References

(1) JSAE: Jidoushagijutu Handbook, Vol. 3, Sekkei (powertrain)-hen, p. 246-248 (2005) (in Japanese)
(2) Tokura, T., Asami, T., Hasegawa, Y., Sugimura, T., Kono, K., Aoki, K.: Development of Smooth Up-Shift Control Technology for Automatic Transmissions with Integrated Control of Engine and Automatic Transmission, SAE Paper, 2007-01-1310 (2007)
(3) Najork, R., Steinberg, I.: The GETRAG PowerShift® Transmission 6DCT470 (TC-SST) of Mitsubishi Lancer

Evolution and Ralliart, JSAE No. 05-08 Symposium, p. 38-43 (2008)
(4) Minowa, T., Ochi, T., Kuroiwa, H., Liu, K.: Smooth Gear Shift Control Technology for Clutch-to-Clutch Shifting, SAE Paper, 1999-01-1054 (1999)
(5) Ibamoto, M., Uchida, M., Kuroiwa, H., Minowa, T., Sato, K.: Transient control of gear shift by means of estimated torque feedback without turbine speed sensor, 1995 JSAE Annual Congress Proceedings, No. 954, p. 57-60

■ Author ■


Shintaro KAMEDA


Yasushi INAGAWA

Fuel-Efficient and Low-Noise Steering Systems in Large and Heavy Vehicles using Variable Displacement Pump Technology

Jinghong YU* Jon HASKELL*

ABSTRACT

A variable displacement pump (VDP) is a fuel-efficient and cost-effective technology that has been applied to steering systems in small- and medium-sized vehicles. However, it is a challenge to apply this technology to large and heavy vehicles due to marketability concerns. This study tested VDP technology in a large light truck and strived to achieve a well-balanced and high-performance steering system with regard to noise, fuel economy, and dynamic performance. Steering noise was analyzed in terms of both the source noise characteristics of the VDP and the noise attenuation characteristics of the steering system. Significant noise reduction was achieved by redesigning the VDP in its number of vanes, structure stiffness, internal component clearances, and rotor position with improved flow ripple characteristics; and by optimizing the steering system's attenuation characteristics using a design of hose-tuning cable devices with optimal pulsation transmission loss characteristics. To ensure gains in fuel economy, a new design specification was developed to control the pump's power consumption by limiting the input torque at various pump speeds. Steering dynamic performance and feel were improved by enhancing the pump's design to provide an adequate flow rate under high pressures while maintaining flow rate and torque characteristics under low pressures. As a result of the study, VDP technology was successfully applied to 2011 model year Odyssey.

1. Introduction

The automotive industry continues to face a number of business environment challenges, including a weakened global economy and severe energy crises. For automotive manufacturers and their customers, the demand for cost-effective technologies to improve fuel economy continues to increase. Electric power steering (EPS) technology is a fuel efficient steering technology that is increasingly used in small- and medium-sized vehicles; however, its high cost and capacity limitations are barriers for use in heavy vehicles. In contrast, using VDP technology in small and medium-sized vehicles has proven gains in fuel economy, with a higher benefit-to-cost ratio versus EPS. Until EPS technology becomes economically feasible to use in large and heavy vehicles, there is an opportunity to use VDP technology.

The technical challenges in applying VDP technology to heavy and large vehicles stem from the difficulties in achieving marketability, fuel economy, and vehicle performance. Due to the increased steering load, heavier vehicles demand larger displacement and higher relief pressures from power steering pumps than do smaller vehicles. The increase of displacement and pressure potentially cause a higher level of system noise, which can negatively affect marketability. Additionally, due to the unbalanced mechanism of its unique design (see Fig. 1), a VDP inherently produces a higher level of

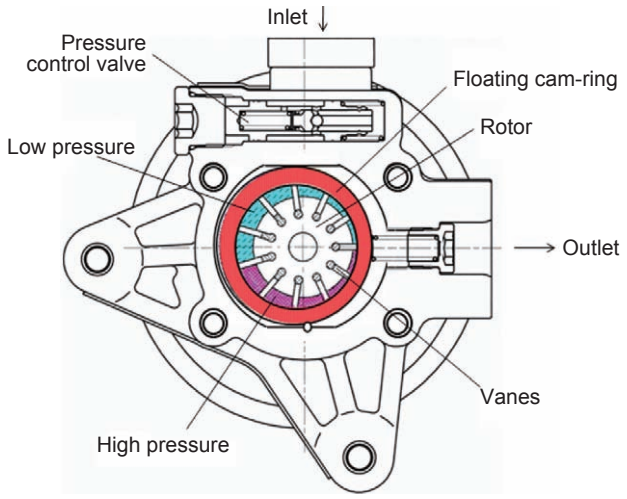


Fig. 1 Structure of variable displacement pump

* HONDA R&D AMERICAS, INC.

noise than a conventional constant displacement pump (CDP)[1), 2)]. The VDP's output flow rate and relief pressure must be sufficient to achieve good vehicle dynamic performance; however, its displacement must be minimized to limit energy consumption and improve fuel economy.

Extensive investigation was conducted to achieve a balance between steering noise performance, fuel consumption reduction, and vehicle steering performance when VDP technology is integrated into a large light truck. First, the source noise characteristics of the VDP and the noise attenuation characteristics of the steering system were analyzed by using the concepts of source flow ripple and pulsation transmission loss, and design measures were proposed to improve the noise source and attenuation characteristics. Second, to ensure benefits in fuel economy, a new design specification was proposed to control the VDP's power consumption by limiting the input torque at critical pump speeds. Finally, achieving good vehicle dynamic performance requires a high flow rate in the VDP, but this directly conflicts with noise and fuel economy requirements; therefore, appropriate flow rate characteristics were determined. This paper summarizes the achievements in steering noise reduction, fuel economy benefits, and vehicle steering performance.

2. Marketability Improvement

2.1. Problem Identification

A vehicle operational study was conducted to identify possible noise concern areas in a large light truck equipped with a VDP. An initial prototype of a variable displacement pump, VDP1, was used to compare with a constant displacement pump, CDP0, currently used in mass production. Both pumps are similar in displacement and relief pressure, but the vane pump design for CDP0 has 10 vanes while VDP1 has 9. Noise performance is mainly evaluated under four vehicle conditions: (1) idle engine speed and no steering input, (2) idle engine speed and continuous steering input, (3) engine speed sweep and with/without steering input, and (4) idle engine speed and steering held at rack end. Figure 2 shows a sample comparison of the cabin sound pressure spectra when the vehicle is equipped with CDP0 and VDP1 separately, and includes a basic requirement line (maximum allowable level) for the noise contributed by the steering pump.

The operational study revealed the following four major noise concern areas:

(1) Without steering input, VDP1 induces higher levels at the 1st and 2nd harmonic frequencies than CDP0.
(2) With steering input, VDP1 causes a much higher 2nd harmonic order than CDP0.

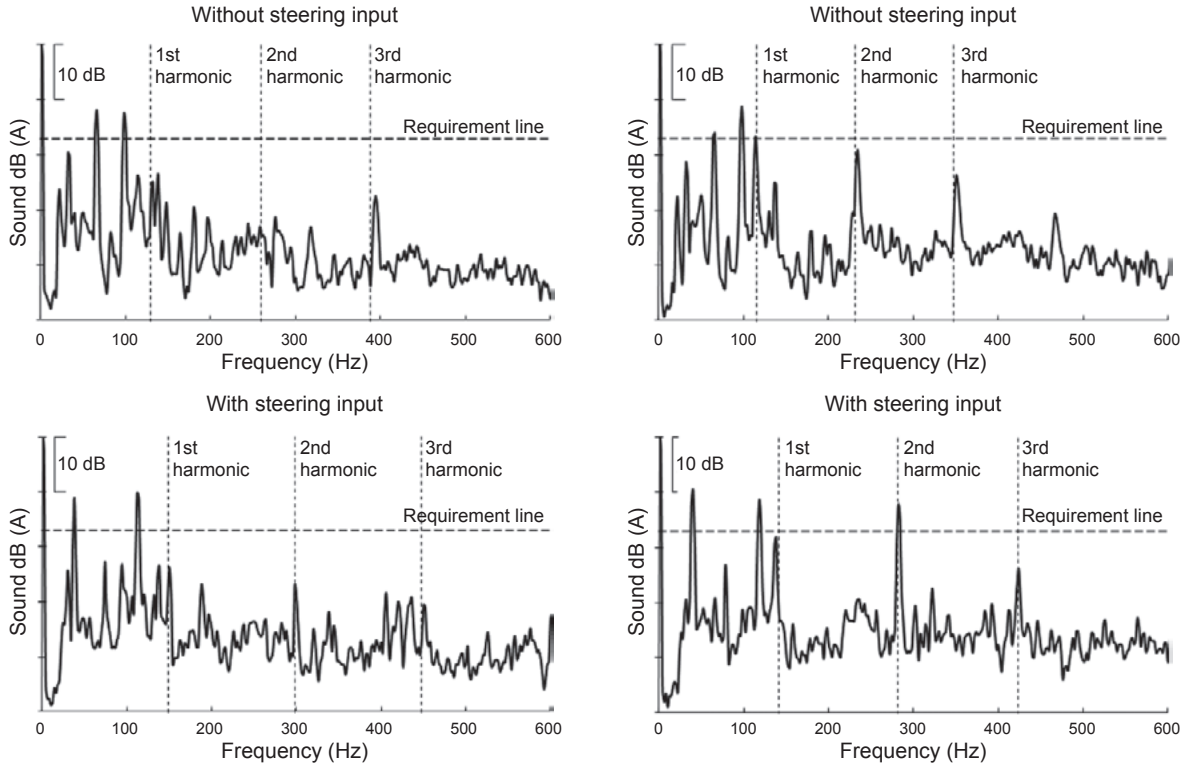


Fig. 2 Comparison of cabin noise spectra of test vehicle equipped with different pumps at engine idle speed

(3) The 1st harmonic frequency of VDP1 is coincidently in line with one of the engine accessory frequencies.
(4) During engine speed sweep mode, VDP1 generates much higher noise at the 2nd harmonic frequency than CDP0.

2.2. Source Noise Characteristics

In a hydraulic power steering system, the source flow ripple generated by the steering pump interacts with the connected hose, pipes, and steering gearbox to generate pressure pulsations and excite airborne noise and mechanical vibrations. For a given pump structure and type of fluid, the source flow ripple is the key parameter representing the source noise potential of the pump. The source flow ripple characteristics are evaluated through established measurement methods and systems[3), (4)].

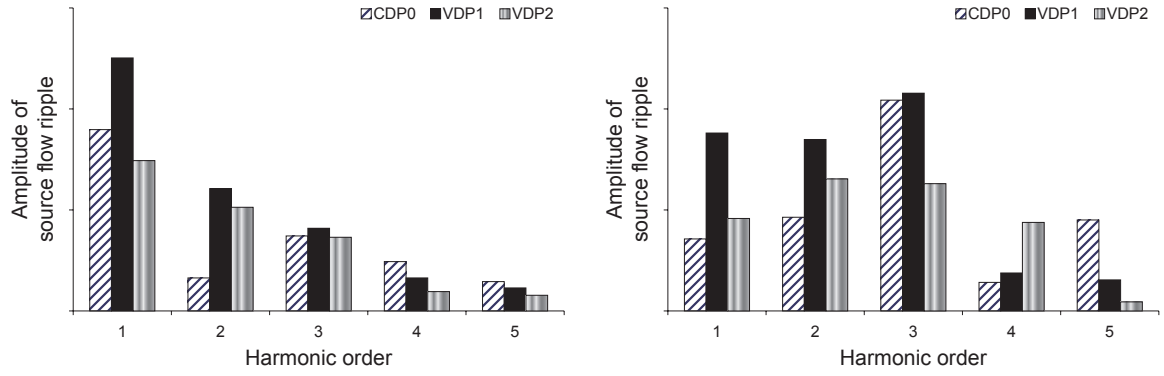
Figure 3 shows a comparison of harmonic spectra of measured source flow ripple of different pumps under two test conditions, where the first condition represents a vehicle condition at idle engine speed and without steering input, and the second represents a vehicle condition at low engine speed and with steering input. It is shown that compared with CDP0, VDP1 generates much higher levels of source flow ripple for the 1st and 2nd harmonic orders under both test conditions. This corresponds to the vehicle noise problems identified during the vehicle operational study.

To improve the source flow ripple characteristics, a proposed design (VDP2) was made that changed the following areas: the number of vanes (9 to 11), structure stiffness, the clearance among the internal components, and the position of the rotor. As shown in Fig. 3, compared to VDP1, VDP2 generates a significantly lower level of the 1st harmonic flow ripple and yields considerable reductions at the 2nd and 3rd harmonics under the 930 rpm and 5 MPa test conditions. Increasing the number of vanes from 9 to 11 also helps separate the pump's harmonic frequencies from the engine accessory frequencies.

2.3. System Pulsation Attenuation Characteristics

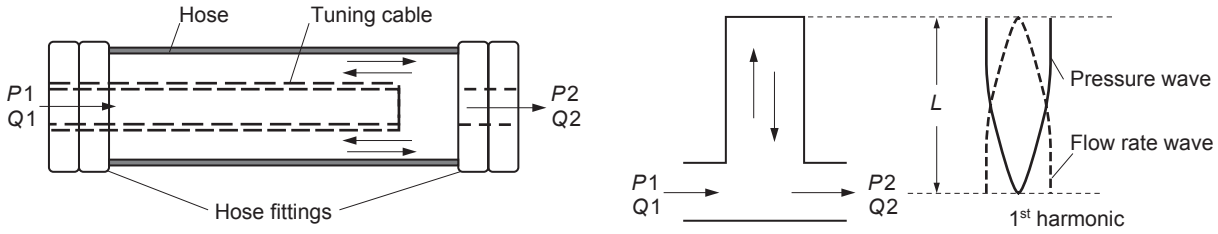
Noise reduction was further achieved by optimizing steering system attenuation characteristics. Typically, hose-tuning cable devices are used to attenuate the pressure pulsations and minimize the resultant audible noise in steering systems. Figure 4 illustrates the mechanism and the corresponding quarter-wavelength side-branch resonator model of such a device. Within the side-branch resonator, standing waves of pressure and flow pulsations are excited at the fundamental resonant frequency of the quarter-wavelength and at its odd number harmonic frequencies. For such standing waves, since the pressure pulsation becomes zero at the outlet of the side-branch, the pressure pulsation is attenuated at those frequencies.

The pulsation attenuation characteristics of a hose-tuning cable can be evaluated through a pulsation transmission loss (PTL) value. It can be determined either through experimental methods[5), (6)] or through theoretical



(a) 780 rpm and 1 MPa (b) 930 rpm and 5 MPa

Fig. 3 Comparison of measured source flow ripple spectra of different pumps



(a) Hose - tuning cable mechanism (b) Conceptual quarter-wavelength side-branch

Fig. 4 Pulsation attenuation mechanism used in hydraulic power steering system

prediction based on analytical models of flexible hoses[7), 8)]. Figure 5 shows examples of PTL measurement results and how it can be tuned to target different frequencies.

In this study, two hose-tuning cable devices were combined. The design was optimized to provide a maximum PTL value targeting primarily at the 2nd harmonic order and secondly at the 1st and 3rd harmonic orders of the pump at engine idle speed.

2.4. Noise Performance

Steering noise performance of the vehicle equipped with VDP2 and optimal hose design was confirmed under various driving conditions. Figure 6 shows the measured cabin noise harmonic spectra at engine idle speed with and without steering input conditions. The final setting has achieved overall levels similar to or slightly better than CDP0, and the noise levels are within the requirement line (i.e., the maximum allowable line) within substantial margins.

Using a 10-point rating system, with 1 representing extremely poor performance and 10 being excellent performance, the noise was subjectively evaluated under both normal and extreme steering usage modes, such as the steering wheel held at rack end during engine sweeping.

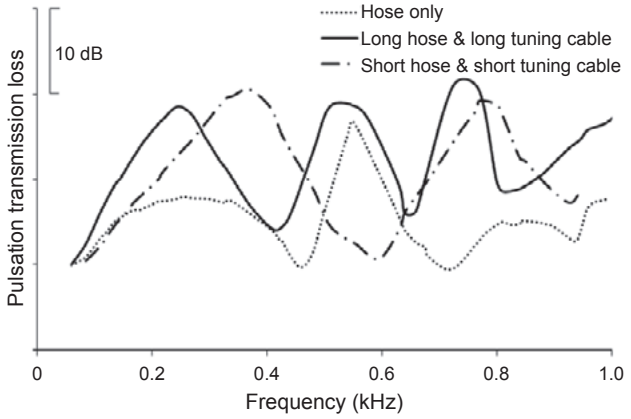


Fig. 5 Examples of measured pulsation transmission losses of different hose-tuning cable systems

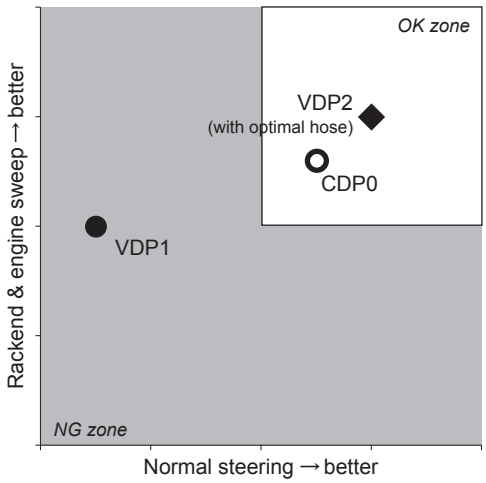


Fig. 7 Subjective evaluation results for vehicle equipped with different pumps

Figure 7 illustrates that VDP2 with optimal hose design has achieved the noise performance slightly better than CDP0 for both normal steering and extreme steering conditions.

3. Gains in Fuel Economy

3.1. Mechanism of Lower Fuel Consumption

The VDP's unique flow-speed characteristics yield improvements in fuel economy. A typical constant displacement pump (CDP) has a fixed displacement that produces a flow rate almost linear to pump speed. Conversely, the VDP has a floating cam-ring mechanism (Fig. 1) so that the cam-ring's position can be regulated with pump speed. When the pump speed reaches a preset rpm, the cam-ring is repositioned toward the rotational center of the pump shaft, thereby reducing the flow rate.

As shown in Fig. 8, the pumped flow rate of a CDP is usually much higher than what is needed for the flow rate tuned for vehicle performance, while the pumped flow rate of a VDP can be much closer to the flow rate curve needed. Consequently, the VDP has less internal bypass flow and less energy loss than a CDP.

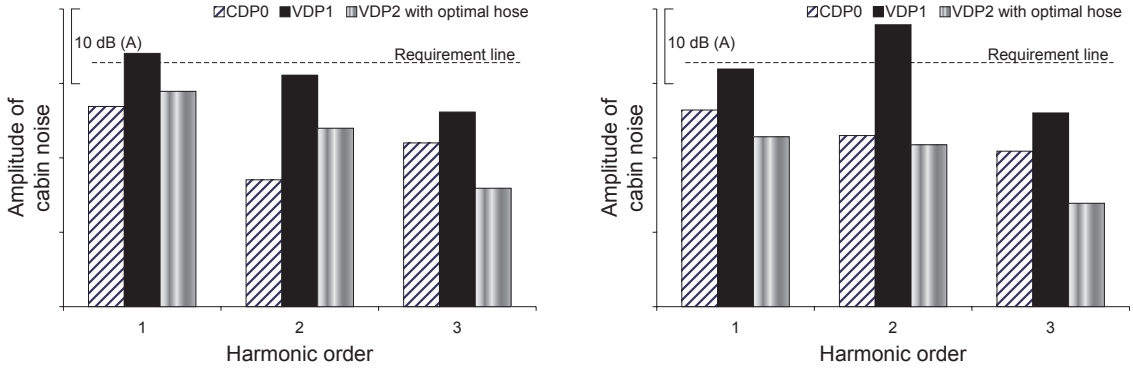
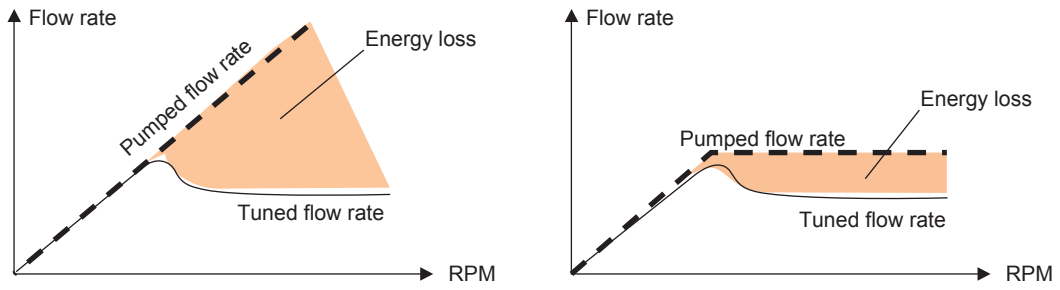


Fig. 6 Comparison of cabin steering noise harmonic spectra when different pumps are used



(a) Constant displacement pump (b) Variable displacement pump

Fig. 8 Conceptual flow rate-speed characteristics of CDP and VDP

3.2. Specification for Controlling Power Consumption

Since the operating torque of a VDP in relation to operating speed (pulley RPM) is directly related to power consumption, an operating torque specification must be established to guarantee gains in fuel economy.

Figure 9 illustrates how the maximum operating torque is related to the fuel economy gain under different driving modes. The gain is quantified as the mileage difference between the test vehicle equipped with VDP versus CDP0.

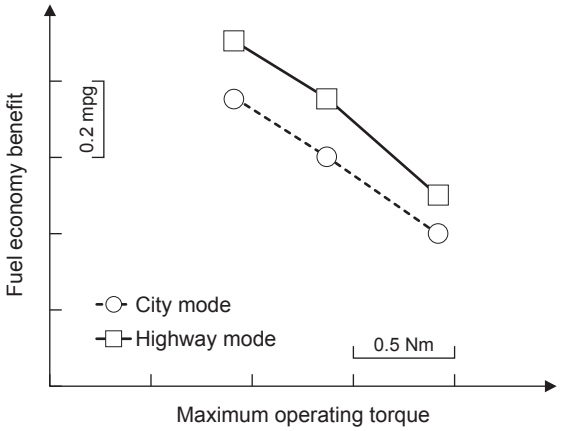


Fig. 9 Fuel economy benefits in relationship to pump's maximum operating torque

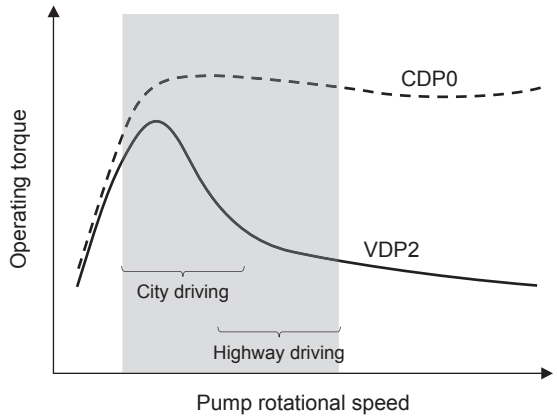


Fig. 10 Comparison of operating torque curves between VDP2 and CDP0

It is clearly shown that the fuel economy gain has a linear relationship to the operating torque. Figure 10 shows a comparison of the operating torque curves between CDP0 and VDP2. In a VDP, the maximum operating torque occurs around the engine idle speed and reduces as speed increases. In a CDP, the maximum operating torque occurs at the same engine idle speed, but remains roughly constant as speed increases. As shown in Fig. 8, this corresponds to the different flow rate characteristics between variable and constant displacement pumps.

A new specification to control the VDP's operating torques was established so that the operating torque curve is constrained by a boundary curve (Fig. 11) for maximum allowable torque. During typical customer usage, operating the vehicle with steering inputs is a small portion of total usage; therefore, the operating torque specification focuses on the lower operation pressure condition of the VDP.

In this specification, three different pump speeds are used to define the boundary curve. The first point is set at the engine idle speed at which the VDP is near its maximum flow output and thus its maximum operating torque. This point is very important to control since it reflects the engine speed conditions in a typical city driving mode. The second point is set at the average engine speed for highway cruising. The last point is set at a high pump speed to capture driving conditions during accelerated engine speeds. It was confirmed that VDP2 meets the requirements of this new specification.

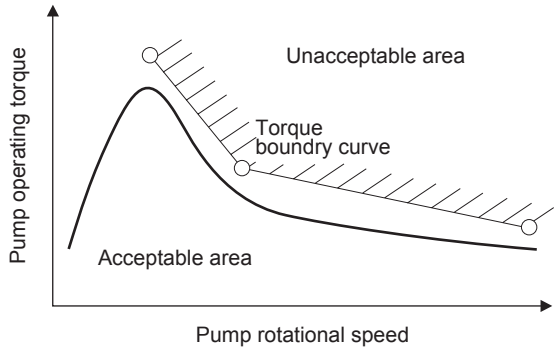


Fig. 11 VDP torque control specification

4. Vehicle Steering Performance

4.1. High Steering Rate Catch-up Performance

Many areas of vehicle dynamic performance are affected by the characteristics of the power steering pump, such as flow rate and pressure characteristics. The design of VDP2 was confirmed to yield satisfying results in these performance areas. As two examples, high steering rate catch-up performance and steering feeling performance are described herein.

High steering rate catch-up performance (also referred to as "catch-up") is described as the effort in turning a steering wheel at a high steering angular rate. The steering angular rate can reach a critical point, called the "maximum assisted steering rate," at which the fluid entering the rack cylinder is not supplied fast enough to provide full power steering assist. As shown in Fig. 12, beyond the maximum assisted steering rate, the steering effort increases at a significantly greater ratio, called the "catch-up effort ratio," compared to the steering angular rate. Therefore, better catch-up performance requires a higher maximum assisted steering rate and a lower catch-up effort ratio.

To achieve satisfying vehicle catch-up performance, the design of VDP2 was enhanced to provide an adequate flow rate under high pressures while maintaining the flow rate and torque characteristics under low pressures. Various tolerances of the internal components of the pump were carefully designed to reduce internal fluid leakage under high pressures. Additionally, the design of the steering gearbox was also refined to minimize the fluid leakage inside the gearbox. As shown in Fig. 12, the final enhanced system with VDP2 provides much better catch-up performance.

4.2. Steering Feel

Steering feel is another important vehicle performance area for VDP use in large and heavy vehicles. At lower speeds, the steering effort should feel light and easy to operate, while at higher speeds, the steering effort should feel solid and secure.

To achieve these steering feel characteristics, VDP2 is designed with a drooping flow rate, that is, the flow rate decreases as the pump speed increases. Consequently, sufficient power assisting force is provided for parking and low-speed maneuvers and less force at high speeds or highway cruising. In addition, the drooping flow rate also has a fuel economy benefit because as less fluid is being pumped with increasing pulley speeds, the power consumption is less.

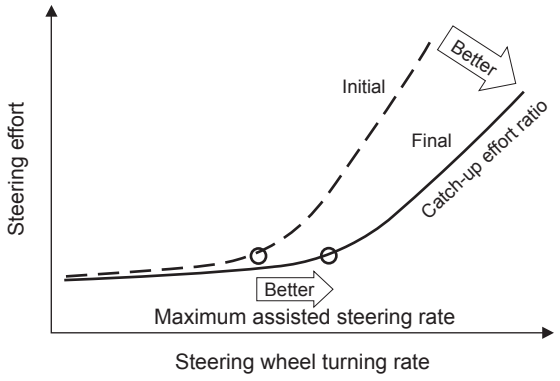


Fig. 12 High steering rate catch-up performance

This study confirmed that the vehicle steering effort characteristics with VDP2 and CDP0 are very similar. With VDP2, the test vehicle achieved a nimble steering feel at low speeds and a secure and natural steering feel at high speeds.

5. Conclusion

A systematic investigation has been conducted to integrate VDP technology in a large light truck and achieve a well-balanced system with regard to steering noise, fuel economy, and steering performance. The steering noise has been analyzed in terms of both the source noise characteristics of the VDP and the noise attenuation characteristics of the steering system. Design measures were proposed and significant noise reduction was achieved. To ensure sufficient fuel economy gains with the VDP, a new specification to control the input torque characteristics of the pump has been developed. Finally, high steering dynamic performance has been achieved by the appropriate setting of the pump's flow rate characteristics.

This research proves that VDP technology can be applied to large and heavy vehicles to obtain both good fuel economy and a high level of steering performance. As a result of the study, VDP technology has been successfully applied to 2011 model year Odyssey.

References

(1) Yu, J., E. Hosni, J. Haskell.: Application of Fuel and Cost Efficient Steering Technology – Variable Displacement Pump – to SUV/SUTs, FISITA 2010 World Automotive Congress, International Federation of Automotive Engineering Societies(2010)

(2) Kojima, E.: Development of a Quieter Variable-Displacement Vane Pump for Automotive Hydraulic Power Steering System, International Journal of Fluid Power 4 (2)(2003)

(3) Yu, J., D. Ritchie.: Method for Objectively Evaluating Power Steering Pump Noise and its Correlation with Subjective Vehicle Feeling Judgment, Honda R&D Technical Review Vol.20, No.1, p.148-154(2008)

(4) Yu, J.: Determining Source Fluidborne Noise Characteristics of Automotive Fluid Power Pumps, SAE International, April, no. 2001-01-1612(2001)

(5) Kojima, E., J. Yu, T. Ichiyanagi.: Experimental Determining and Theoretical Predicting of Source Flow Ripple Generated by Fluid Power Piston Pumps, SAE International, September, No. 2000-01-2617(2000)

(6) Yu, J., F. Johnson, F. Iwami, N. Verrecchia.: Experimental Evaluation for Fluidborne Noise Attenuation in Tuning Cables and Hoses of Automotive Power Steering Hydraulic Systems, SAE International, May, No. 1999-01-1777(1999)
(7) Yu, J., E. Kojima.: Wave Propagation in Fluids Contained in Finite-Length Anisotropic Viscoelastic Pipes, Journal of Acoustical Society of America, Vol. 104, p.3227(1998)
(8) Kojima, E., T. Ogawa, J. Yu.: Design Optimization of Resonator Hoses for Automotive Hydraulic Power Steering System, Transactions of the Japan Fluid Power System Society(2002)

■ Author ■



Jinghong YU



Jon HASKELL

Study of Low-temperature CO Oxidation Cycle on Precious Metal-supported CeO_2

Yoshiyuki NAKANISHI* Hiroki TAKEORI*
Masanori HASHIMOTO* Takayuki WATANABE*

ABSTRACT

Low-temperature active catalysts that oxidate CO at low temperatures and use the reaction heat produced to convert HC and NOx are available as technologies to respond to the reduction of exhaust gas temperatures as a result of the achievement of increased fuel efficiency. Pd/CeO_2 catalysts, in which a palladium catalyst is supported on a cerium oxide carrier, represent one of these technologies. The mechanism of supply and resupply of active oxygen by the cerium oxide carrier was focused on and an analysis was conducted in order to increase the low-temperature activity of these catalysts. This study resulted in the determination of a mechanism of low-temperature CO oxidation able to accelerate the CO oxidation reaction from low temperatures by means of the achievement of supply of active oxygen from low temperatures through the use of highly dispersed palladium particles, and the achievement of rapid and high-volume resupply of active oxygen through the coexistence of H_2O and O_2.

1. Introduction

Demands for the reduction of emissions of CO_2, a factor in global warming, are today increasing. The achievement of increased fuel efficiency is critical to reducing CO_2 emissions, and a variety of technologies are available to respond to this need, including increase of combustion efficiency and hybridization of powerplants. It can be assumed that these technologies will result in increased automotive emissions by reducing the temperature of exhaust gases and expanding the range that is not converted by the catalyst at engine start. The development of a catalyst able to convert target emissions (carbon monoxide (CO), hydrocarbons (HC), and nitrogen oxide (NOx)) from lower temperatures than existing catalysts (a low-temperature active catalyst) can therefore be considered necessary.

Gold (Au) catalysts[1),2)] and palladium-supported cerium oxide catalysts (Pd/CeO_2)[3)] that oxidize CO at low temperatures and use the reaction heat to convert HC and NOx are available as low-temperature active catalysts. However, the use of Au catalysts in automotive applications is challenging, given their low heat resistance. The temperature range at which Pd/CeO_2 catalysts oxidate CO is higher than that of Au catalysts, necessitating performance enhancements, but the catalysts are heat-resistant and can be employed as automotive catalysts. Pd/CeO_2 catalysts were therefore focused on, and research was conducted on enhancing their low-temperature activity.

Research has recently been progressing on the characteristics of active oxygen desorbed by oxygen storage/release materials, as exemplified by cerium oxide (CeO_2)[4)-6)]. This research has shown that when palladium (Pd) is supported on cerium oxide (CeO_2), the substances exert a mutual interaction at the Pd/CeO_2 interface[7)]. In addition, steam (H_2O) in exhaust gas is adsorbed at areas in which the Pd is activated, inhibiting the CO oxidation reaction[8)].

Oxidation reactions can be initiated from low temperatures using the active oxygen desorbed by CeO_2. In order to enhance the low-temperature activity of Pd/CeO_2, it was necessary to achieve supply of the active oxygen desorbed by the surface of the CeO_2 to the Pd at a lower temperature, and to resupply the surface of the CeO_2 with active oxygen more rapidly. In addition, it was also necessary to study the effect of H_2O, which normally reduces CO oxidation performance.

Study of the mechanism of supply and resupply of active oxygen in Pd/CeO_2 catalysts in this research showed that rather than simply being adsorbed at points of Pd activation, when it impedes the CO oxidation reaction, H_2O more generally promotes the resupply of active oxygen, and therefore accelerates the CO oxidation reaction from lower temperatures. The modification of the catalyst based

* Automobile R&D Center

on this result reduced the temperature at which 50% of HC, CO, and NOx is converted (the light-off temperature) by approximately 20˚C.

This report will discuss the determination of the mechanism of low-temperature oxidation of CO by means of the study of supply and resupply of active oxygen, which represented an important orienting factor in the modification of the catalyst.

2. Study of Promotion of Supply of Active Oxygen

Figure 1 shows a hypothetical mechanism scheme of low-temperature oxidation of CO by desorption of active oxygen.

As (1) in Fig. 1 shows, it is theorized that CO oxidation reactions tend not to occur at low temperatures in the palladium-supported alumina catalysts (Pd/Al_2O_3) that are widely used as automotive catalysts because they do not release active oxygen at low temperatures.

As (2) and (3) in Fig. 1 show, in the case of a Pd/CeO_2 catalyst, the Pd donates electrons to the CeO_2, promoting the desorption of active oxygen by the CeO_2 contiguous to the Pd. The Pd can therefore be supplied with active oxygen from low temperatures. It is conjectured that the supplied active oxygen and the CO adsorbed by the Pd react, promoting the oxidation of CO at low temperatures. However, when the diameter of the Pd particles is large, as shown in (2), little active oxygen is desorbed from low temperatures, and there is a minimal effect of promotion of the CO oxidation reaction at low temperatures. When the Pd particles are small in diameter (when the particles have been refined), as in the case of (3), it is theorized that because there is a significant amount of electron donation from the Pd to the CeO_2, and the amount of active oxygen that can be supplied from low temperatures also increases, there is a significant effect of promotion of the CO oxidation reaction at low temperatures.

In order to demonstrate the validity of the hypothetical mechanism scheme shown in Fig. 1, the amount of active oxygen supplied was measured using Pd/Al_2O_3 and two types of Pd/CeO_2 with particles of different sizes (Fig. 2). The diameter of the Pd particles was measured

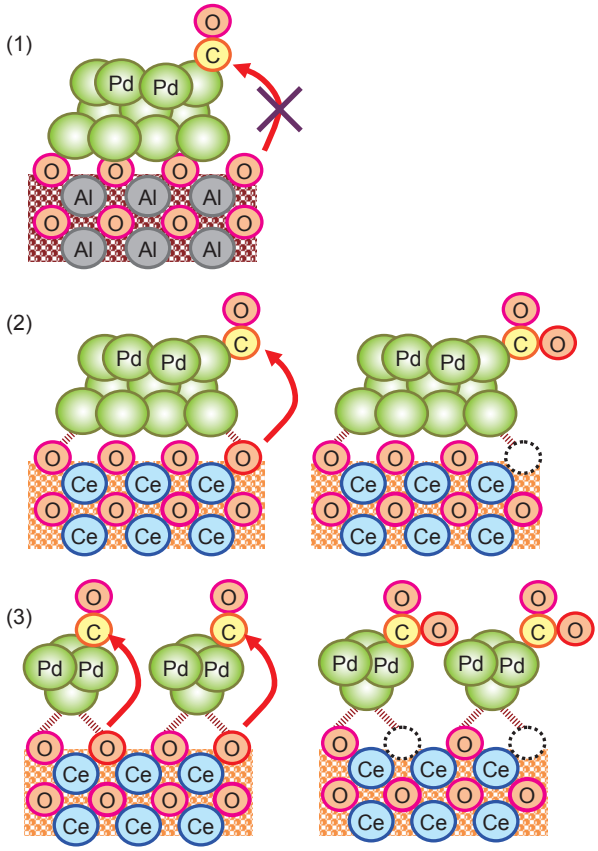
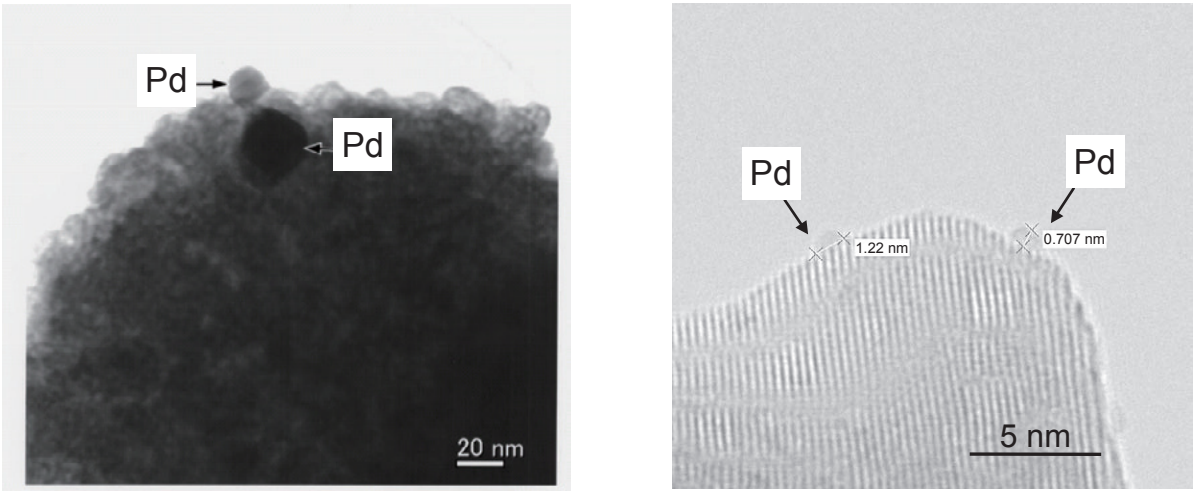


Fig. 1 Mechanism scheme of CO oxidation on (1) Pd-supported Al_2O_3, (2) Pd (large particle size) -supported CeO_2 and (3) Pd (small particle size) -supported CeO_2



(a) Pd/CeO_2 (Pd particle size: 20 nm) (b) Pd/CeO_2 (Pd particle size: 1 nm)

Fig. 2 TEM image of Pd (1 wt%)/CeO_2

using transmission electron microscopy (TEM). The amount of active oxygen supplied was calculated from the concentration of reacted CO_2 when a CO-N_2 mixed gas was heated from room temperature to 400˚C at 20˚C / min using a Simulated Gas Generator & Catalyst Test System manufactured by HORIBA, Ltd. The results are shown in Fig. 3.

While the Pd/Al_2O_3 desorbed almost no active oxygen at temperatures of 200˚C and below, the tests showed that the Pd/CeO_2 released active oxygen at these temperatures. In addition, the results indicated that while the Pd with a particle size of approximately 20 nm desorbed active oxygen from approximately 200˚C, the Pd with a particle size of approximately 1 nm desorbed it from approximately 100˚C. The CO conversion of the Pd/Al_2O_3 and the two forms of Pd/CeO_2 with differing Pd particle sizes was also studied. The results are shown in Fig. 4. In the conversion tests, a mixed gas of CO, O_2, H_2O, and N_2 was heated from room temperature to 450˚C at 20˚C / min using the Simulated Gas Generator & Catalyst Test System. The gas was measured following reaction, and the CO conversion at each temperature interval was measured. The results shown in Fig. 4 indicate that the Pd/CeO_2 is able to oxidate CO from a lower temperature than the Pd/Al_2O_3. In addition, the results show that the CO light-off temperature of the CeO_2 supported on Pd particles of approximately 1 nm in diameter was approximately 64˚C lower than that of the CeO_2 supported on Pd particles of approximately 20 nm in diameter.

The results discussed above indicate that active oxygen supplied from the surface of the carrier is an important factor in the oxidation of CO at low temperatures. In addition, the highly dispersed Pd particles enhance the mutual interaction of the Pd and Ce, and this boosts CO oxidation performance by promoting the supply of active oxygen from low temperatures.

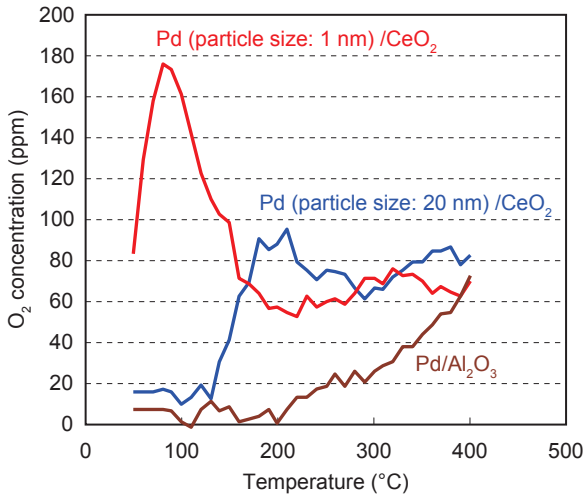


Fig. 3 O_2 release temperature of different Pd particle size-supported CeO_2 and Pd/Al_2O_3

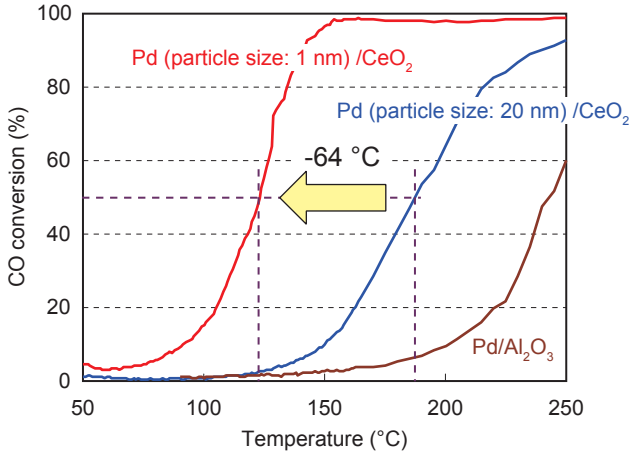


Fig. 4 Conversion for CO oxidation over different Pd particle size-supported CeO_2 and Pd/Al_2O_3

3. Study of Resupply of Active Oxygen

When active oxygen is supplied, oxygen disappears from the surface of the CeO_2 (oxygen defects), and if oxygen is not resupplied, the active oxygen necessary for the CO oxidation reaction cannot be supplied. Resupply by oxygen within the CeO_2 (bulk oxygen) and resupply from the components of the gas formed during the reaction can be considered as mechanisms of resupply of oxygen-to-oxygen defects.

First, resupply of oxygen defects by means of bulk oxygen was examined. Figure 5 compares results for the CO conversion of the Pd/CeO_2 catalyst and temperatures for bulk oxygen desorption by CeO_2. In the CO conversion

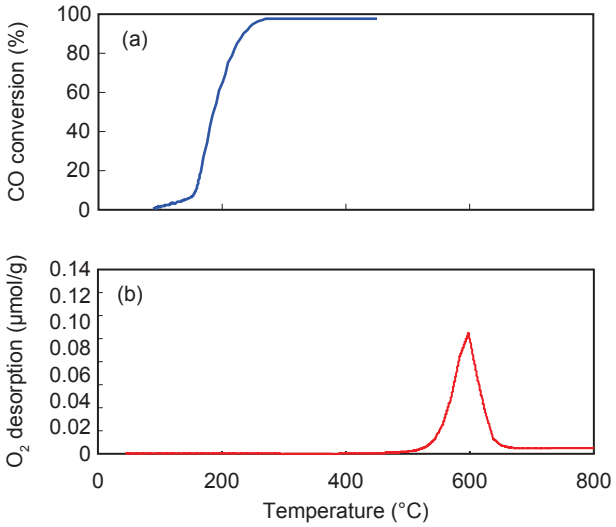


Fig. 5 Concern of O_2 desorption from CeO_2 and CO light-off temperature
(a) CO light-off (catalyst: 1 wt% Pd/CeO_2 fresh)
(b) O_2-TPD (catalyst: CeO_2)

tests, a mixed gas of CO, O_2, H_2O, and N_2 was heated from 50˚C to 450˚C at 20˚C / min using the Horiba Simulated Gas Generator & Catalyst Test System. The gas was measured following reaction, and the CO conversion at each temperature interval was measured. The amount of bulk oxygen desorbed at each temperature was measured using O_2 temperature programmed desorption (O_2-TPD). The results showed a significant difference in temperature, with a CO light-off temperature of approximately 200˚C and a temperature for desorption of bulk oxygen of approximately 600˚C. Given this, it was unlikely that CeO_2 bulk oxygen was contributing to the resupply of active oxygen, and it was therefore conjectured that resupply from the components of the gas formed during the reaction was the mechanism of resupply.

The gas formed in the CO conversion test contained carbon monoxide (CO), oxygen (O_2), water (H_2O), and nitrogen (N_2). Of these, O_2 and H_2O are the components able to resupply oxygen.

Figure 6 shows the results of tests conducted to determine the effect of CO and O_2, CO and H_2O, and CO, O_2, and H_2O mixed gases (N_2 balance) on CO conversion. Oxidation of CO occurs in the presence of both O_2 and H_2O, but the catalyst light-off temperature in the case of O_2 is approximately 190˚C lower than that of H_2O. In addition, the results show that H_2O has an effect in promoting the CO conversion, with the light-off temperature being approximately 30˚C lower when O_2 and H_2O are present together than when O_2 is present in isolation.

Given this, it was conjectured that active oxygen would be resupplied by the coexistence of O_2 and H_2O.

Figure 7 shows the theoretical mechanism scheme of this resupply. First, in the case of resupply by H_2O ((a) in

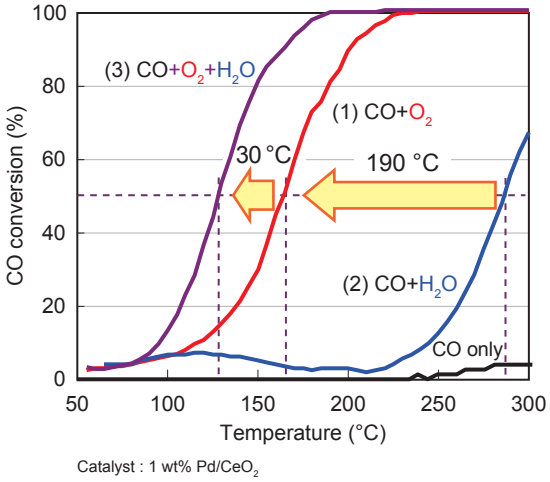


Fig. 6 Effect of CO conversion with (1) O_2, (2) H_2O and (3) H_2O+O_2 addition

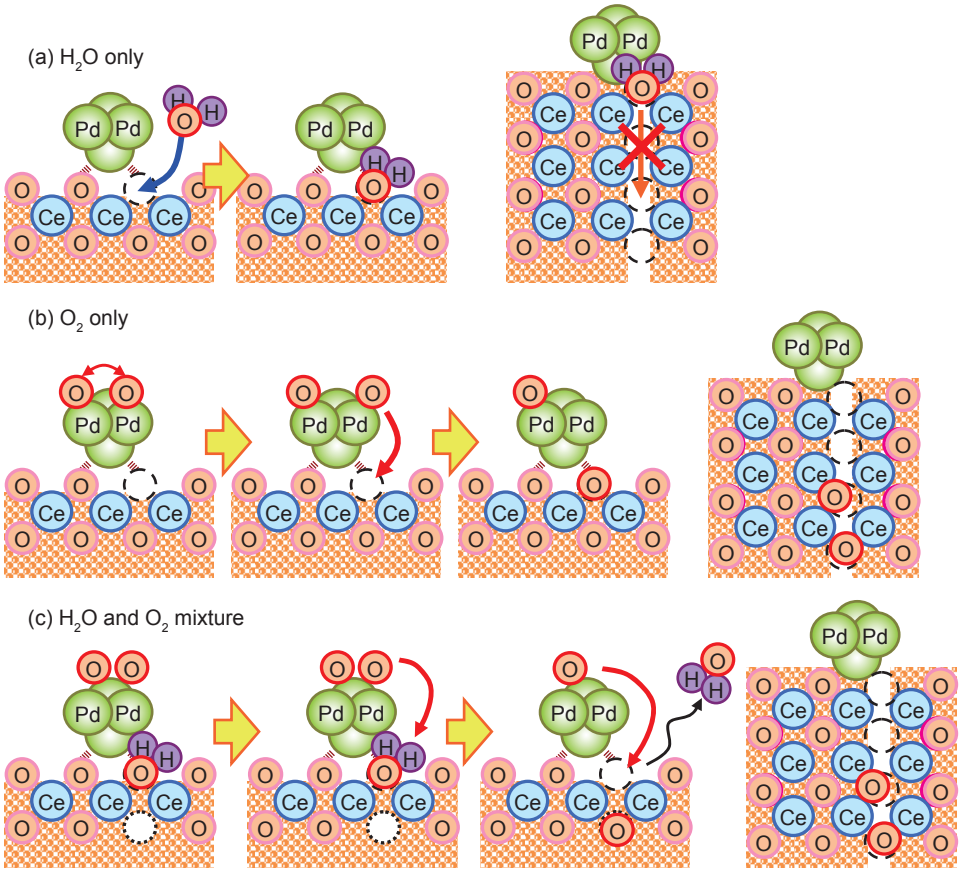


Fig. 7 Mechanism scheme of O_2 supply on CeO_2 with addition of (a) H_2O only, (b) O_2 only and (c) H_2O and O_2 mixture

the figure), resupply is rapid because H_2O is able to directly resupply oxygen defects in the surface. However, because the H_2O molecules are larger in size than the oxygen defects (steric hindrance), the molecules are unable to penetrate to the interior, and only resupply the surface. In the case of resupply by O_2 ((b) in the figure), because resupply commences after adsorption and disaggregation of the O_2 by the Pd, the speed of resupply is slow. However, oxygen atoms are small, and they are able to penetrate into the interior.

Considering the combined effect of H_2O and O_2 in terms of these mechanisms, it can be conjectured that the H_2 formed during resupply of oxygen defects by H_2O ((c) in the figure) rapidly react with O_2, and oxygen atoms are resupplied in the interior. In addition, the oxygen atoms not used in the reaction are resupplied. It is theorized that in this way, the H_2 produced as a result of the coexistence of H_2O and O_2 promotes the resupply of oxygen-to-oxygen defects.

In order to demonstrate the validity of this hypothetical mechanism, different gases (O_2, H_2O, and H_2O+O_2) were released with CeO_2 in a reduced state, and the performance of each gas in resupplying oxygen was measured. The amount of UV-visible light absorbed at 150˚C was measured using ultraviolet-visible spectroscopy[(9)-(11)] to measure oxygen resupply performance. The results are shown in Fig. 8. The upper section of the vertical axis shows the reduced state, with the substance becoming more oxidated (increasing resupply of oxygen) with increasing distance down the axis.

The measurement results indicated the following:

(1) H_2O displays a higher speed of resupply of oxygen defects than O_2.
(2) H_2O produces a lower amount of resupply of oxygen defects than O_2 in isolation.
(3) The coexistence of H_2O and O_2 results in more rapid resupply of oxygen defects than O_2 in isolation, and an equivalent amount of resupply as O_2 in isolation.

Given that, based on items (1) to (3), the effect of the coexistence of H_2O and O_2 promotes resupply of oxygen defects, it was clear that CeO_2 was taking in active oxygen from H_2O and O_2, components of the gas formed during the reaction.

Next, the contribution of the promotion of resupply of oxygen defects by the coexistence of H_2O and O_2 to the CO oxidation cycle was studied. In these tests, H_2 was added separately to H_2O, and the effect on CO conversion was examined. The results are shown in Fig. 9. The CO light-off temperature is lower in the cases of $CO+O_2+H_2$ and $CO+O_2+H_2O$ than in the case of $CO+O_2$. H_2 promotes the oxidation of CO from low temperatures by reacting with the O_2 on the Pd, and promoting resupply of the excess O. The amount of resupply of oxygen defects is low when H_2 exists in isolation, but when H_2O forms H_2, the oxygen in the H_2O resupplies oxygen defects, and the H_2 dissociates the oxygen on the Pd, promoting oxidation of CO. Because of this, the CO light-off temperature is approximately 8% lower in the case of $CO+O_2+H_2O$ than $CO+O_2+H_2$.

Figure 10 shows the mechanism scheme of low-temperature oxidation of CO, reflecting the effects of promotion of supply of active oxygen and of resupply of active oxygen, as determined in the present project.

The highly dispersed Pd particles on the CeO_2 helped results in active oxygen being supplied from approximately 100˚C, and this highly dispersed Pd particles therefore promotes the commencement of the CO oxidation cycle shown as (1), (2), (3a), and (4a) in the figure (the CO cycle due to O_2 in isolation) from low temperatures.

Next, the fact that the speed of resupply of active oxygen is greatest and a high amount of resupply can be achieved in the case of coexistence of H_2O and O_2 was verified, and the CO oxidation cycle shown as (1), (2), (3b), (4b), (5b), and (6b) in the figure (the CO oxidation cycle

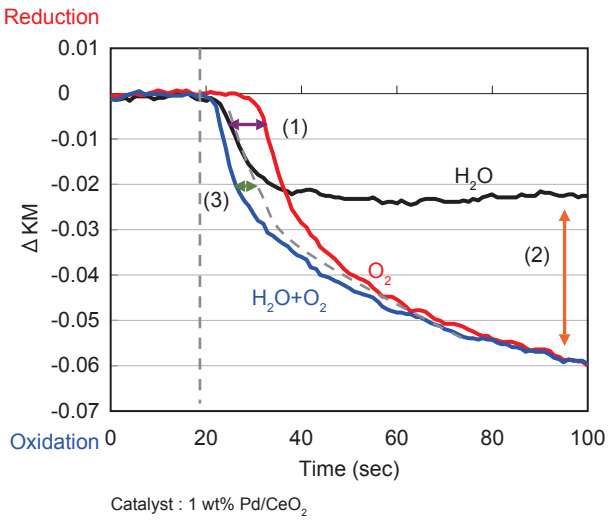


Fig. 8 UV-visible spectra of added (1) H_2O, (2) O_2 and (3) H_2O+O_2 at 423 K

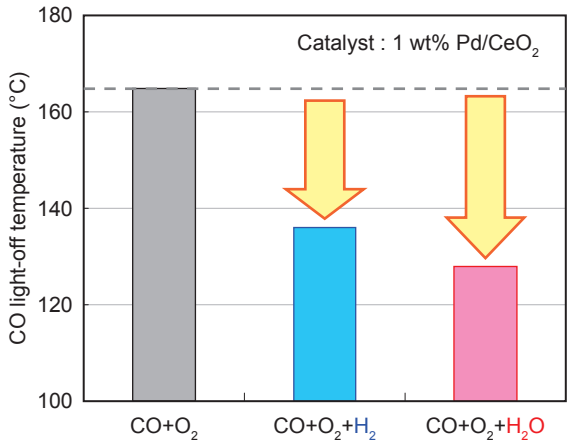


Fig. 9 Effect of added H_2 and H_2O on CO light-off temperature

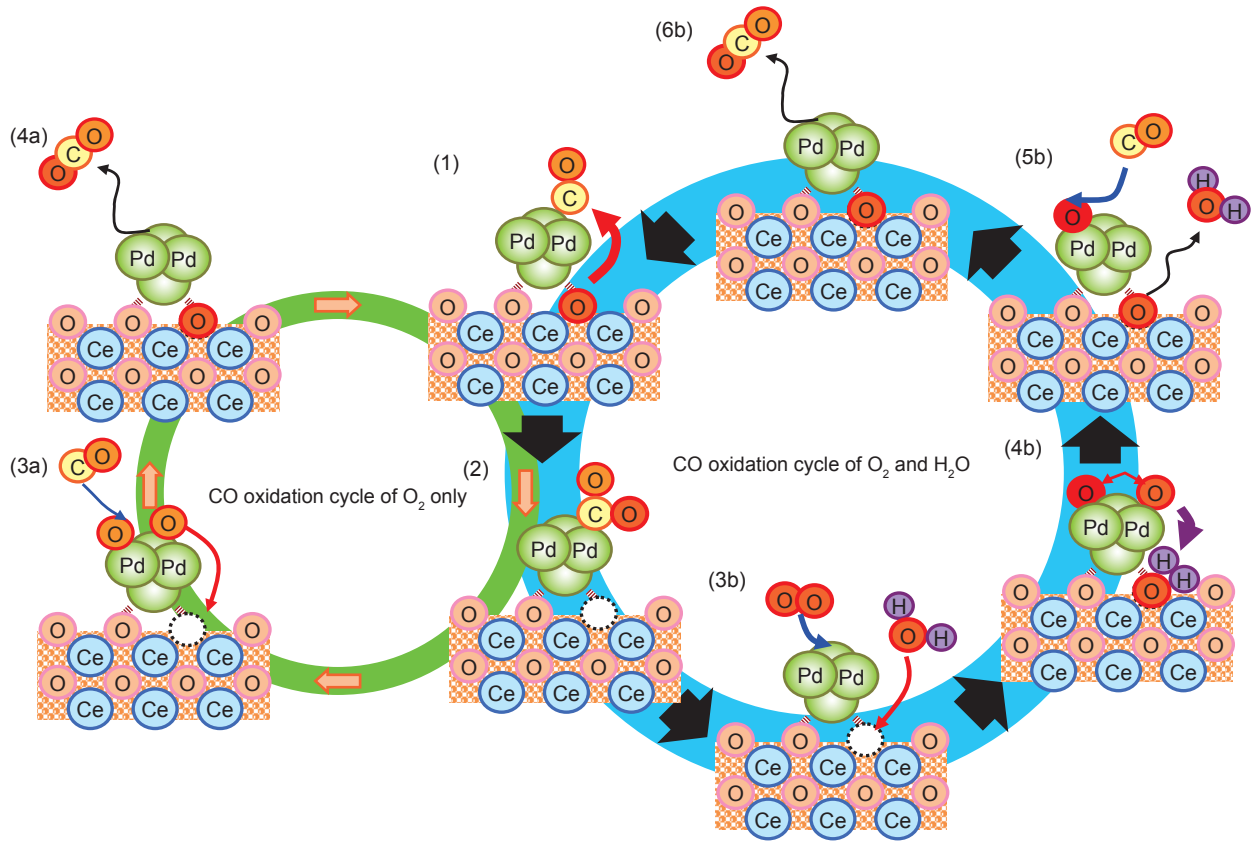


Fig. 10 Mechanism scheme of low temperature CO oxidation

due to H_2O and O_2) was identified. The results indicated that the CO oxidation cycle resulting from the presence of O_2 is supplemented by the CO oxidation cycle resulting from the presence of H_2O and O_2, accelerating the CO oxidation reaction at low temperatures.

4. Conclusions

The project discussed here indicated that combining a CO oxidation cycle in which the resupply of active oxygen is promoted and resupply occurs in high quantities due to the coexistence of H_2O and O_2, and a CO oxidation cycle in which the supply of active oxygen is promoted by the highly dispersed Pd particles, accelerated the CO oxidation reaction at low temperatures. Focusing on the promotion of resupply of active oxygen through the coexistence of H_2O and O_2, knowledge obtained in the present project, it was possible to identify methods of reformation of low-temperature CO oxidation catalysts through consideration of additive elements to CeO_2 and other factors.

References

(1) Haruta, M.: Low-temperature Combustion Catalysts -Mainly for CO Oxidation-, Journal of the Japan Petroleum Institute, Vol. 37, No. 5, p. 480-491 (1994)
(2) Date, M., Haruta, M.: Support Effects on the Catalysis of Gold Nanoparticles and Their Applications, Catalysts & Catalysis, Vol. 47, No. 1, p. 8-13 (2005)
(3) P 05-285387
(4) Takami, A., Takita, Y.: Syokubaiseinou ni Oyobosu Kinzokuhukugousankabutsu no Tantaikouka ni kansuru Kenkyu III, Annual Report of Research and Development Center Oita University, No. 13, p. 55-56 (2008) (in Japanese)
(5) Fan, J., Weng, D., Wu, X., Wu, X., Ran, R.: Modification of CeO_2-ZrO_2 mixed oxides by coprecipitated/impregnated Sr: Effect on the microstructure and oxygen storage capacity, J. Catal., Vol. 258, No. 1, p. 177-186 (2008)
(6) Fujita, T., Osumi, K., Nakamura, K., Tashiro, Y.: Pt/CeO_2 kei Sankasyokubai no Sanso Kyuuhousyutsukinou, 100th CATSJ Meeting Abstracts, p. 268 (2007) (in Japanese)
(7) Hinokuma, S., Fujii, M., Okamoto, M., Ikegami, K., Machida, M.: Pd/CeO_2 no Netsusyori niyoru CO Sankasyokubaikassei no Koujou, 105th CATSJ Meeting Abstracts, p. 31 (2010) (in Japanese)
(8) P3952314
(9) Binet, C., Badri, A., Lavalley, J.: A Spectroscopic Characterization of the Reduction of Ceria from Electronic Transitions of Intrinsic Point Defects, J.

Phys. Chem., Vol. 98 (25), p. 6392-9398 (1994)
(10) Oda, T., Shimizu, K., Satsuma, A.: Ag/CeO_2 Syokubai niyoru CO Sankahannou ni okeru Kasseiseigyoinshi, 102nd CATSJ Meeting Abstracts, p. 181 (2008) (in Japanese)
(11) Oda, T., Shimizu, K., Satsuma, A.: CO Sankayou Koutainetsusei Rh/CeO_2 Syokubai, 104th CATSJ Meeting Abstracts, p. 455 (2009) (in Japanese)

Author


Yoshiyuki NAKANISHI


Hiroki TAKEORI


Masanori HASHIMOTO


Takayuki WATANABE

Microstructure and Mechanical Properties of Heat-resistant Mg-Zn-Y Cast Alloys with Addition of Fourth Elements

Yuichi IENAGA* Kenshi INOUE* Mitsumoto KAWAI*

ABSTRACT

Extruded Mg-Zn-Y alloys with long-period stacking ordered (LPSO) structures are known to display increased strength at high temperatures, and are therefore useful in achieving weight savings in automotive components. Seeking to realize these attractive properties in cast components, the project discussed in this paper focused on controlling the microstructure of $Mg_{96}Zn_2Y_2$ (at.%) cast alloy by the addition of a fourth element. First, the effects of refining the crystal grains through the addition of zirconium and modification of the cooling rate on microstructure and mechanical properties were investigated. With the addition of Zr and the achievement of a high rate of cooling, the resulting $Mg_{95.8}Zn_2Y_2Zr_{0.2}$ cast alloy displayed fine equiaxed grains (approx.10 μm in diameter) and excellent tensile and fatigue properties, equivalent to or greater than those of commercial aluminum alloys at high temperatures above 200˚C. At 250˚C, this alloy exhibited a tensile strength of 223 MPa, approximately twice that of the A4032-T6 alloy used for automotive pistons. The project also focused on strengthening LPSO structures by means of stacking fault energy (SFE), and used a first principle calculation to select a further element for addition to the alloy. The addition of Ag increased yield strength by 60 percent.

1. Introduction

Magnesium alloys are the lightest of the metal materials in practical use, and are therefore expected to contribute to the resolution of environmental issues, for example by reducing automotive fuel consumption. Among these alloys, it is known that the strength characteristic of Mg-Zn-Y alloys, which possess long-period stacking ordered (LPSO) structures, can be increased even in high temperature ranges by extrusion processing and refinement of the microstructure[1), 2)]. Processing including forging and machining is necessary following extrusion in order to form parts; in the case of parts for automotive and other engines, it would be desirable to achieve increased strength in cast materials, helping to enable cost reductions through near-net shape formation. However, standard cast magnesium alloys are lower in strength than heat-resistant aluminum alloys. The project discussed here, therefore, set out to develop a cast heat-resistant magnesium alloy displaying a higher level of strength than heat-resistant aluminum alloys. The project sought to control the solidified microstructure of the alloy, refining the microstructure through the addition of crystal grain refining elements and increasing the rate of cooling, in addition to increasing the strength of the LPSO strengthening phase through the addition of a fourth element. This paper will discuss the achieved structural morphology, mechanical properties, and physical properties of the alloy.

2. Method of Development of New Cast Alloy

A strength characteristic exceeding the strength characteristics of heat-resistant aluminum alloys can be achieved in Mg-Zn-Y magnesium alloys by subjecting them to extrusion and other plastic working processes[2)]. In addition to compound dispersion strengthening during casting, this is due to strengthening due to work hardening during extrusion, texturing, and refinement of the crystal grains. However, casting in isolation coarsens the LPSO phase (the strengthening phase) and the other compound phases, and only a level of strength equivalent to that of conventional magnesium alloys can be obtained.

* Fundamental Technology Research Center

Experimentation therefore proceeded with a focus, from among the abovementioned factors producing increased strength, on refinement of the crystal grains and the compound phase morphology, which could be expected to result in increased strength even simply by casting. The effect of refining the crystal grains in increasing strength is much higher in the case of magnesium than in other metals such as iron and aluminum. The present project sought to refine the crystal grains through the addition of Zr, which has a high melting point and was expected to act as the point of origin of crystal nucleation. It was considered that by this means it would also be possible to refine the LPSO phase and other compound phases crystallizing at the grain boundary. It was also considered that the achievement of a higher rate of cooling would promote refinement of the crystal grains, and would also control the coarsening of the compound phases formed by diffusion of the constituent elements. These effects were demonstrated in the study.

Next, in order to achieve a further strength increase by increasing the strength of the LPSO phase, the main strengthening phase in the alloy, first principle calculations were employed in LPSO phase strength design. Stacking faults identified during localization of the structure of the LPSO phase were the focus in materials modeling. If the LPSO phase is considered as the strengthening phase, then increasing this stacking fault energy could be expected to increase the yield strength of the alloy. This consideration was based on the concept that because the LPSO phase is coherent with the α-Mg phase (the matrix), the difference in stacking fault energy with the matrix would represent a migration barrier to dislocation. The Vienna Ab-initio Simulation Package (VASP), a first principle calculation software package based on a density-functional calculation method, was used to determine the elements that would increase the stacking fault energy (strengthen the LPSO phase) by substitution for other elements in the materials model. Based on the results of these calculations, it was judged that Ag would be an effective candidate for addition, and tests were conducted with Ag as an additive element.

3. Test Method

Tests employed $Mg_{96}Zn_2Y_2$, $Mg_{95.8}Zn_2Y_2Zr_{0.2}$ and $Mg_{93}Zn_2Y_2Ag_3$ alloys as test materials. The alloys were melted in a graphite crucible in an Ar gas environment using a high-frequency induction melting system, and the melted alloys were cast in copper ship-shaped molds with an average width of 18 mm, height of 25 mm, and length of 160 mm, and similar transverse cross-sections to those specified for casting molds by JIS H 5203. Table 1 shows the chemical composition of the alloys employed. In order to study the effect of the rate of cooling, the $Mg_{95.8}Zn_2Y_2Zr_{0.2}$ alloy was cast in 50 mm-wide step-shaped molds of 2 mm, 4 mm, and 8 mm in thickness, as shown in Fig. 1. Following casting, the phases formed were identified using powder X-ray diffraction (XRD), and the microstructures were examined by means of scanning electron microscopy (SEM). An analysis was also conducted using electron back-scatter diffraction (EBSD) to evaluate the diameter of the crystal grains.

Table 1 Chemical composition of Mg alloys used in this study (at. %)

Alloy	Zn	Y	Zr	Ag	Mg
$Mg_{96}Zn_2Y_2$	2.11	2.06	–	–	Bal.
$Mg_{95.8}Zn_2Y_2Zr_{0.2}$	1.86	1.81	0.21	–	Bal.
$Mg_{93}Zn_2Y_2Ag_3$	2.31	2.02	–	2.96	Bal.

The mechanical properties of the alloys were evaluated in tensile tests, tension-compression fatigue tests, creep tests, Rockwell hardness tests, and Charpy impact tests. For the tensile tests, the ship-shaped castings were formed into ASTM E8 standard test piece forms, with a diameter of 6.35 mm in the parallel portions and a gauge length of 25.4 mm, and the step-shaped castings were formed into mini test pieces with a thickness of 2 mm, a width of 4 mm, in the parallel portions, and a gauge length of 4 mm. The tests were conducted using a strain rate of $5x10^{-4}$ /s, at temperatures ranging from 25 to 300˚C. The fatigue tests were conducted on the mini test pieces described above, using a stress ratio of R = -1, sine wave frequencies of 20-40 Hz, a maximum number of repetitions of 10^7 times, and a temperature of 200˚C. The creep tests were conducted at 200˚C x 90 MPa, and the hardness tests, based on JIS Z 2245, used the Rockwell B scale and a total test force of 980 N. The Charpy impact tests were based on JIS Z 2242, and used V-notch test pieces at room temperature. Thermal conductivity was measured using the laser flash method specified in JIS R 1611, coefficient of thermal expansion was measured using the thermo-mechanical analysis method specified in JIS R 1618, Young's modulus was measured using ultrasonic method, as specified in JIS Z 2280, and density was measured using the Archimedes method, as specified in JIS Z 8807. Results were compared with results for existing materials.

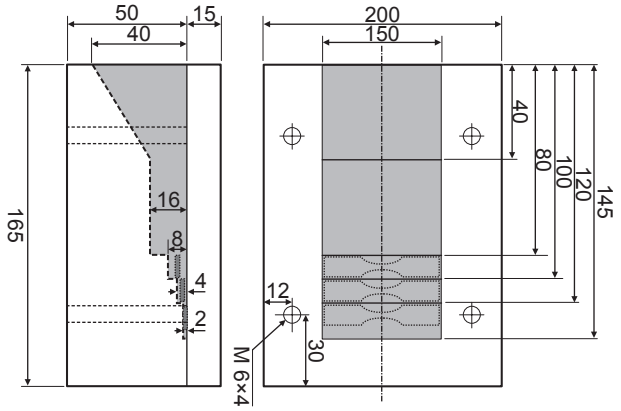


Fig. 1 Step-shaped copper mold and sampling points

4. Test Results and Discussions

4.1. Strength Increase due to Refinement of Crystal Grains

4.1.1. Effect of addition of Zr on microstructure

The refining effect of the addition of Zr on the microstructures of Mg-Zn-RE (rare earth) alloys is well known[3]. $Mg_{96}Zn_2Y_2$ and $Mg_{95.8}Zn_2Y_2Zr_{0.2}$ alloys were cast in ship-shaped molds in order to study the effect of the addition of Zr in refining the microstructure of $Mg_{96}Zn_2Y_2$ alloy. Figure 2 shows XRD patterns for both the alloys. The addition of Zr produces no change in the structural phases, with both alloys being made up of α-Mg, $Mg_{12}ZnY$ (LPSO), and $Mg_3Zn_3Y_2$ phases. Figure 3 shows back-scattered electron (BSE) SEM images for the alloys. Based on the results of energy-dispersive X-ray spectrometry (EDS) and previously published reports[4], the black areas can be assumed to represent the α-Mg phase, and the gray and white areas the LPSO and $Mg_3Zn_3Y_2$ phases, respectively. As Fig. 3(a) shows, the α-Mg phase in the $Mg_{96}Zn_2Y_2$ alloy frequently forms dendritic structures. Figure 3(b) shows that the $Mg_3Zn_3Y_2$ phase displays a coarse morphology that disrupts the LPSO phase that crystallizes in a network around the α-Mg phase. By contrast, in the $Mg_{95.8}Zn_2Y_2Zr_{0.2}$ alloy, the α-Mg phase forms cell shapes, as shown in Fig. 3(c), and the $Mg_3Zn_3Y_2$ phase is refined, as indicated in Fig. 3(d). Because, however, no significant difference in the diameter of the α-Mg grains was observed with the addition of the Zr, EBSD analysis was used to study the crystal grains. The results are shown in Fig. 4. The figure shows that the grain diameters of the $Mg_{96}Zn_2Y_2$ and the $Mg_{95.8}Zn_2Y_2Zr_{0.2}$ alloys are approximately 200 μm and 20 μm, respectively, indicating a significant refining effect with the addition of the Zr. In addition, as indicated by the arrow in Fig. 3(d), large numbers of fine particles can be observed among the α-Mg grains. Figures 5(a) and 5(b) respectively show a transmission electron microscope (TEM) image and the results of EDS analysis of these fine particles. The results show that the fine particles are angular, block-shaped, Zr-rich particles of approximately 0.5 μm. It is

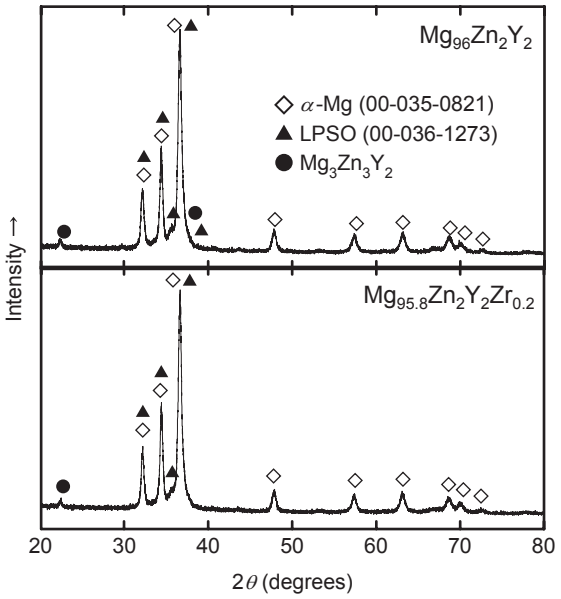


Fig. 2 XRD patterns of $Mg_{96}Zn_2Y_2$ and $Mg_{95.8}Zn_2Y_2Zr_{0.2}$ alloys

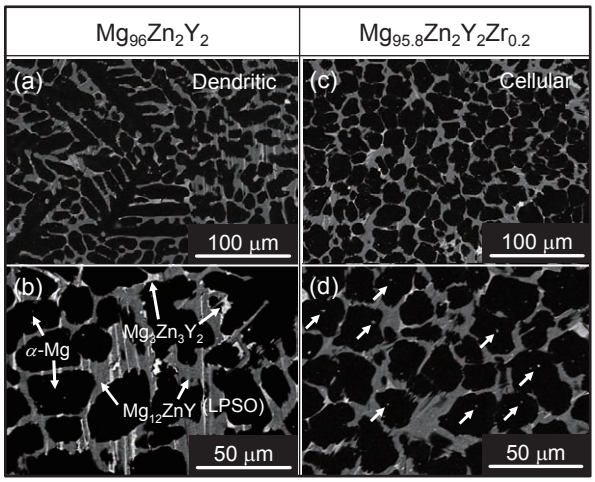


Fig. 3 BSE (Back scattered electron)-SEM images of $Mg_{96}Zn_2Y_2$ and $Mg_{95.8}Zn_2Y_2Zr_{0.2}$ alloys

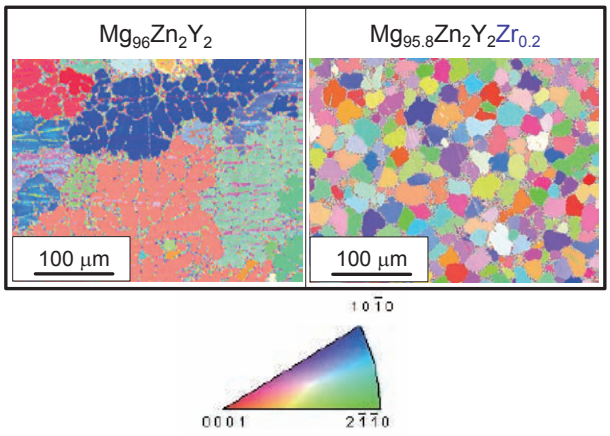


Fig. 4 Crystal orientation imaging maps of $Mg_{96}Zn_2Y_2$ and $Mg_{95.8}Zn_2Y_2Zr_{0.2}$ alloys

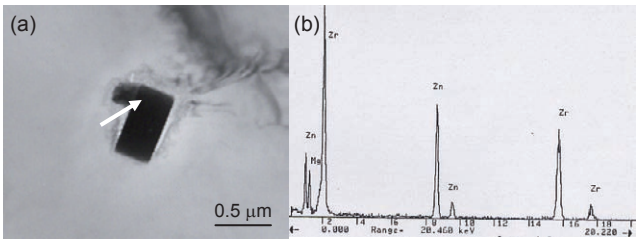


Fig. 5 (a)TEM image of Mg grains in $Mg_{95.8}Zn_2Y_2Zr_{0.2}$ alloy (b) TEM-EDS analysis obtained from particle indicated by white arrow in Fig. 5 (a)

thought that because the solid solubility limit of Zr in Mg (0.12 at.%[5]) is lower than the additive amount of Zr (0.2 at.%), Zr that is not in solid solution exists in the alloy, and this forms the point of origin for nucleation of the α-Mg phase, resulting in the refinement of the microstructure of the $Mg_{95.8}Zn_2Y_2Zr_{0.2}$ alloy.

4.1.2. Effect of cooling rate on microstructure

In order to study the effect of the cooling rate on the microstructure of the $Mg_{95.8}Zn_2Y_2Zr_{0.2}$ alloy, $Mg_{95.8}Zn_2Y_2Zr_{0.2}$ alloy castings of 2 mm, 4 mm, and 8 mm in thickness were produced using step-shaped molds. XRD results showed that differences in the cooling rate did not produce any changes in the structural phases, with the thick areas of each casting being composed of α-Mg, LPSO, and $Mg_3Zn_3Y_2$ phases. Figure 6 shows BSE-SEM images, and Fig. 7 shows EBSD crystal orientation maps for the 2 mm-, 4 mm-, and 8 mm-thick $Mg_{95.8}Zn_2Y_2Zr_{0.2}$ alloy castings. Figure 6 indicates that the microstructure tends to become more refined as the cooling rate increases. Figure 7 shows that the average crystal grain diameters for the three thicknesses of casting are 8 μm, 11 μm, and 16 μm. By contrast, the crystal grains were coarse (50-100 μm) in the 2 mm-thick casting using the alloy to which Zr was not added. Therefore, in the range of thicknesses from 2-20 mm, the addition of Zr, which reduced the crystal grain diameter from 200 μm to 20 μm, can be considered to have a greater effect than the cooling rate. Refinement of the alloy microstructure through the addition of Zr can therefore be indicated as being more effective in the case of engine parts, the majority of which are no greater than 20 mm in thickness.

4.1.3. Mechanical properties

Figure 8 shows the test-temperature dependence of the tensile strength of the $Mg_{95.8}Zn_2Y_2Zr_{0.2}$ alloy castings (2 mm, 4 mm, and 8 mm in thickness). Results for the tensile strength of A4032-T6 aluminum alloy are shown for

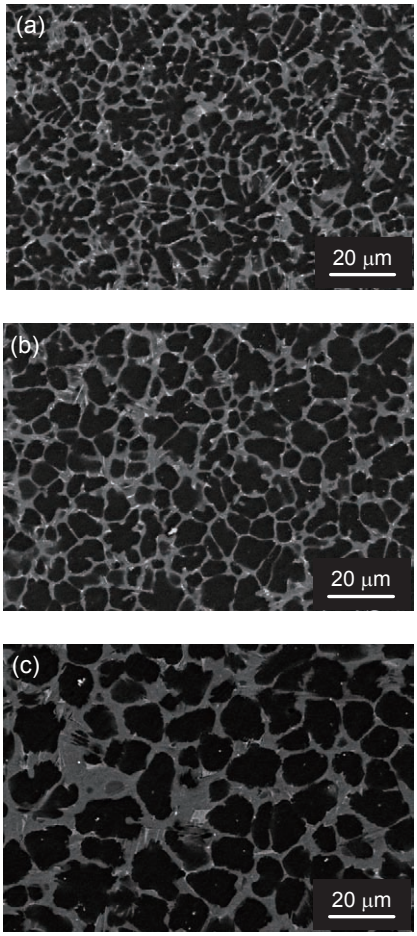


Fig. 6 BSE-SEM images of $Mg_{95.8}Zn_2Y_2Zr_{0.2}$ alloy in thickness of (a) t = 2 mm, (b) t = 4 mm and (c) t = 8 mm

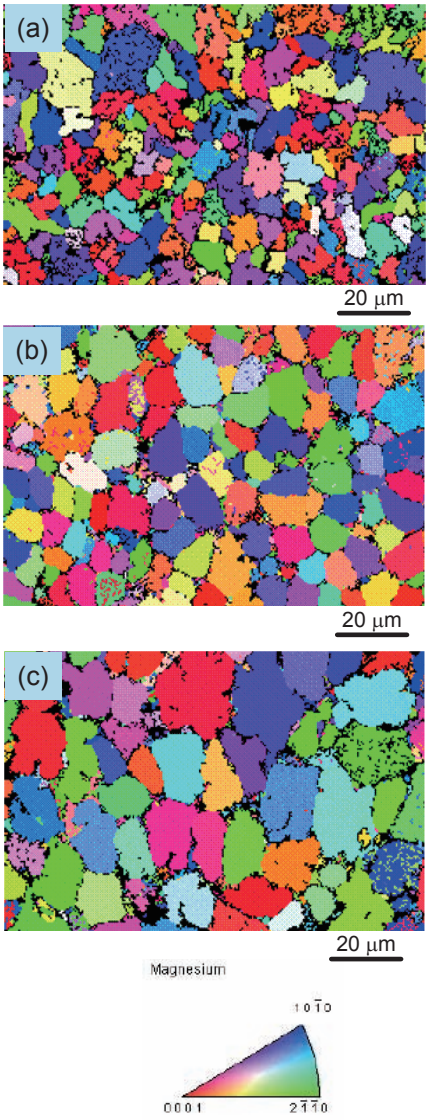


Fig. 7 Crystal orientation imaging maps of $Mg_{95.8}Zn_2Y_2Zr_{0.2}$ alloy with (a) t = 2 mm, (b) t = 4 mm and (c) t = 8 mm

comparison. By contrast with A4032-T6, which displays a decline in strength at 200˚C and above, no rapid decline in strength is observed in the case of the $Mg_{95.8}Zn_2Y_2Zr_{0.2}$ alloy. In addition, the strength of the alloy increases with greater refinement of the crystal grains, and it is particularly noteworthy that the alloy displaying a fine microstructure with a crystal grain diameter of 10 μm or below achieves a high-temperature strength exceeding that of the A4032-T6 alloy, displaying a tensile strength (223 MPa) approximately twice that of the latter at 250˚C, and close to three times in magnitude at 300˚C. Even at a thickness of 8 mm, the $Mg_{95.8}Zn_2Y_2Zr_{0.2}$ alloy displays approximately 1.5-times greater tensile strength than the A4032-T6 alloy.

Figure 9 shows the relationship between the crystal grain diameter and yield strength at room temperature, plotted to help enable study of the relationship between crystal grain diameter and yield strength. The 0.2% proof strength was employed as yield strength. The $Mg_{96}Zn_2Y_2$ alloy with no added Zr displays a dendritic microstructure, and because it is thought that this contributes to strength at the dendritic interface in addition to the grain boundary, calculations were performed for four points in the case of the $Mg_{95.8}Zn_2Y_2Zr_{0.2}$ alloy. The results derived from a least squares analysis can be arrayed along the straight line obtained using Hall-Petch equation in the figure, indicating that strength increases with the greater refinement of the grains, in accordance with the aim of the project. Figure 10 compares the fatigue strength characteristics (S-N curves) of the $Mg_{95.8}Zn_2Y_2Zr_{0.2}$ alloy and A4032-T6 aluminum alloy at 200˚C. The arrows show test pieces that have not yet failed. Despite having been cast, the $Mg_{95.8}Zn_2Y_2Zr_{0.2}$ alloy displays almost identical fatigue strength (10^7 cycle) to the A4032-T6 alloy at 200˚C. In addition, while the strength of the aluminum alloy continues to decline as the number of repetitions increases, it can be conjectured that the fatigue strength of the $Mg_{95.8}Zn_2Y_2Zr_{0.2}$ alloy will remain stably higher than that of the A4032-T6 alloy at 10^7 cycles and above, making the material preferable from the perspective of design. It is reported that the LPSO phase increases fatigue strength in Mg-Zn-Y alloys[6], and the existence of the LPSO phase can similarly be considered to increase fatigue strength in the $Mg_{95.8}Zn_2Y_2Zr_{0.2}$ alloy. Figure 11 shows alloy creep properties at 200˚C and 90 MPa. The $Mg_{95.8}Zn_2Y_2Zr_{0.2}$ alloy displays greater creep properties than the heat-resistant ACM522[7] magnesium alloy employed in hybrid vehicle oil pans, and an identical level of creep strain to the ADC12 aluminum alloy used in transmission cases, for which a higher level of heat resistance is demanded. In addition, the $Mg_{95.8}Zn_2Y_2Zr_{0.2}$ alloy displays a failure life approximately twice that of ADC12 under high stress (110 MPa), and approximately four times greater at the higher temperature of 300˚C at 50 MPa. It is reported that control of grain boundary sliding by the compound phases that

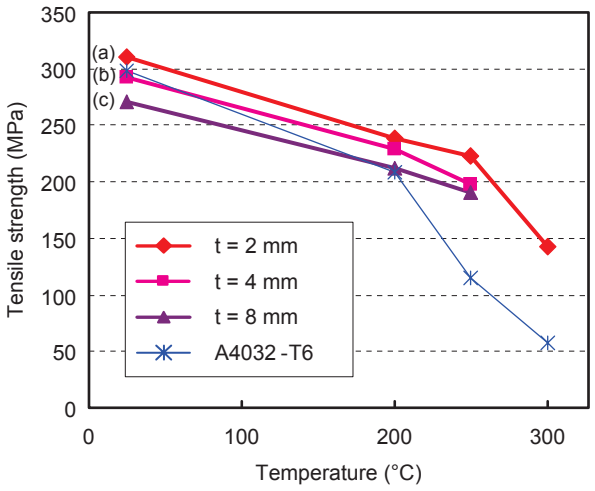


Fig. 8 Tensile properties of $Mg_{95.8}Zn_2Y_2Zr_{0.2}$ alloy with (a) t = 2 mm (b) t = 4 mm and (c) t = 8 mm at 25 °C, 200 °C, 250 °C and 300 °C

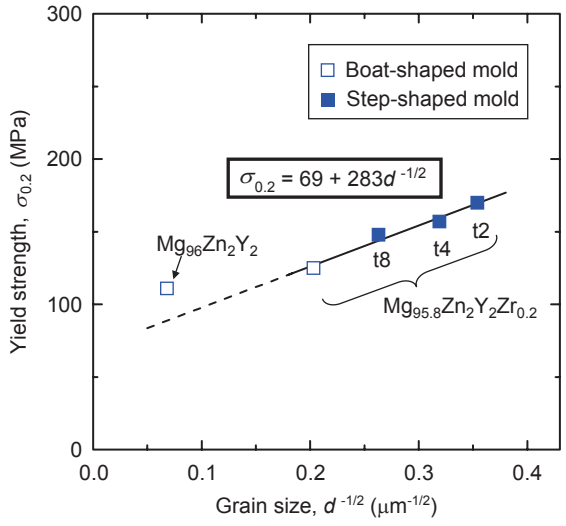


Fig. 9 Relationship between yield strength and grain size for Mg-Zn-Y alloys

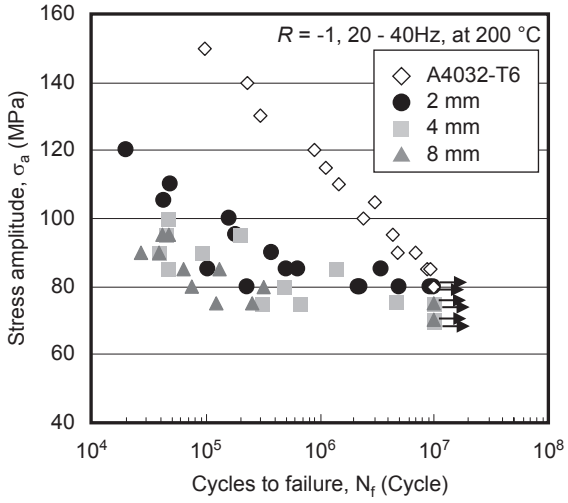


Fig. 10 S-N curves of $Mg_{95.8}Zn_2Y_2Zr_{0.2}$ and A4032-T6 alloys

crystallize at the grain boundary and strengthening of the matrix by stacking faults enhances creep properties at high temperatures[8]. As indicated above, the $Mg_{95.8}Zn_2Y_2Zr_{0.2}$ alloy demonstrated strength characteristics equivalent to or greater than those of high heat-resistance aluminum alloys in the high-temperature range of 200˚C and above.

Next, the $Mg_{95.8}Zn_2Y_2Zr_{0.2}$ alloy was subjected to a high-temperature dimensional stability test (at 230˚C) and a softening test (at 250˚C), in order to study factors producing the alloy's superior high-temperature strength. The change in dimension of the $Mg_{95.8}Zn_2Y_2Zr_{0.2}$ alloy following 100 h of the high-temperature dimensional stability test, at $4x10^{-3}$%, was lower than that of the A4032-T6 alloy at $33x10^{-3}$%. Figure 12 shows changes in the hardness of the alloys when soaked for 100 h at 250˚C.

In the time range of 100 h, while the A4032-T6 alloy undergoes a rapid decline in hardness (from HRB60 to HRB10), the $Mg_{95.8}Zn_2Y_2Zr_{0.2}$ alloy displays almost no decline in hardness. It was conjectured that the rapid decline in hardness in the A4032-T6 alloy was due to the coarsening of the compound phases. Figure 13 shows the microstructures of the $Mg_{95.8}Zn_2Y_2Zr_{0.2}$ and A4032-T6 alloys before and after the test. The microstructure of the A4032-T6 alloy has actually coarsened, but no change can be observed in the $Mg_{95.8}Zn_2Y_2Zr_{0.2}$ alloy microstructure. It can therefore be considered that the $Mg_{95.8}Zn_2Y_2Zr_{0.2}$ alloy displays better high-temperature characteristics than age-hardening aluminum alloys such as A4032-T6 due to the greater stability of its microstructure at high temperatures.

Despite being cast, the $Mg_{95.8}Zn_2Y_2Zr_{0.2}$ alloy displayed better characteristics than the forged A4032-T6 alloy in the Charpy impact test, with a result of $3.6x10^4$ J/m^2 against the latter's $2.0x10^4$ J/m^2. These results were for V-notch shapes, and the $Mg_{95.8}Zn_2Y_2Zr_{0.2}$ alloy displayed similarly superior characteristics when tested as plane-type specimens. Next, to study ductility, the $Mg_{96}Zn_2Y_2$ and $Mg_{95.8}Zn_2Y_2Zr_{0.2}$ alloys were cast in ship-shaped molds, in order to help ensure a sufficient gauge length. Table 2 shows the tensile properties of the alloys at room temperatures. In addition to increasing the strength of the alloy, the refinement of the material's microstructure through the addition of Zr also increased its elongation. The elongation of age-hardened heat-resistant magnesium alloys to which Zr has been added in order to

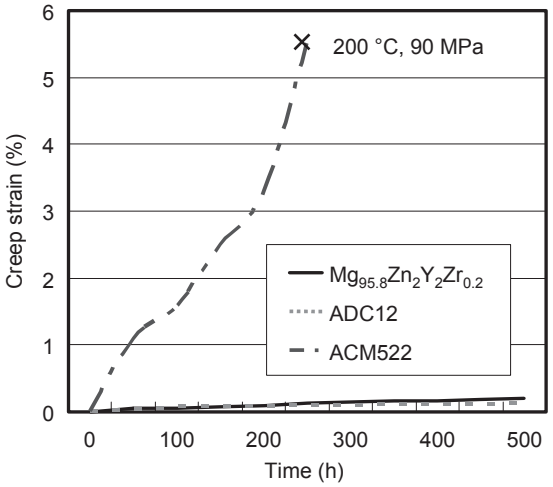


Fig. 11 Creep properties of $Mg_{95.8}Zn_2Y_2Zr_{0.2}$ (t = 8 mm), ADC12 and ACM522 alloys

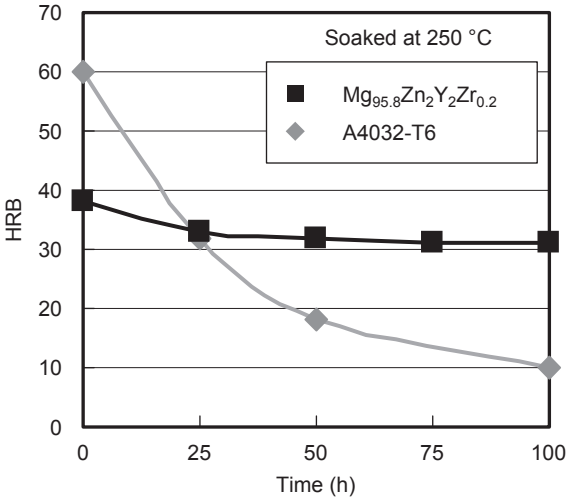


Fig. 12 Relationship between hardness and soak time for $Mg_{95.8}Zn_2Y_2Zr_{0.2}$ (t = 8 mm) and A4032-T6 alloys

Table 2 Mechanical properties of $Mg_{96}Zn_2Y_2$ and $Mg_{95.8}Zn_2Y_2Zr_{0.2}$ alloys

Alloy	Tensile strength (MPa)	Yield strength (MPa)	Elongation (%)
$Mg_{96}Zn_2Y_2$	216	116	4.3
$Mg_{95.8}Zn_2Y_2Zr_{0.2}$	249	125	10.5

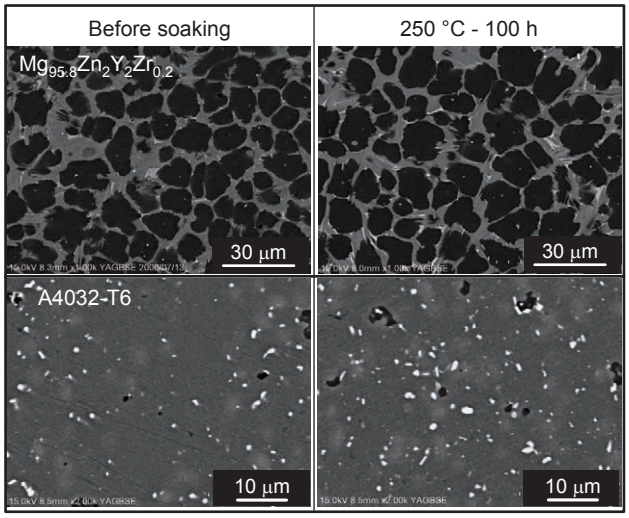


Fig. 13 BSE-SEM images of $Mg_{95.8}Zn_2Y_2Zr_{0.2}$ and A4032-T6 alloys before and after soaking

Table 3 Characteristics of $Mg_{95.8}Zn_2Y_2Zr_{0.2}$ alloy compared to commercial aluminum and magnesium alloys

Alloy	Thermal conductivity (W/m·°C) at 200 °C (25 °C)	Thermal expansion coefficient (1/°C) at 25 - 300 °C	Young's modulus (GPa)	Density (kg/m^3)
$Mg_{95.8}Zn_2Y_2Zr_{0.2}$	102 (92.5)	26.6×10^{-6}	45.8	1890
A4032-T6	141	21.5×10^{-6}	73	2690
AC8A-T6	128	21.4×10^{-6}	78	2720
AZ91D-T6	(51)	27.2×10^{-6}	45	1830
WE54-T6	(52)	24.6×10^{-6}	44	1850

refine the microstructure (EZ33A, QE22A, EQ21A, ZE41A, WE54A, and others) is generally around 4%, despite of their refined microstructures[9]. By contrast, the $Mg_{95.8}Zn_2Y_2Zr_{0.2}$ alloy displays superior elongation, recording a figure of more than 10%. While the test conditions do not necessarily match exactly, for reference Fig. 14 shows the relationship between tensile strength at 250˚C and elongation at room temperature for $Mg_{95.8}Zn_2Y_2Zr_{0.2}$ and a variety of light alloys. The $Mg_{95.8}Zn_2Y_2Zr_{0.2}$ alloy not only displays good high-temperature strength, but also exhibits a high ductility at room temperatures, and can therefore be indicated as possessing a good strength-ductility balance.

4.1.4. Physical properties

Table 3 shows various properties of the $Mg_{95.8}Zn_2Y_2Zr_{0.2}$ alloy. Results for commercial aluminum alloys (A4032, AC8A) and commercial magnesium alloys (AZ91, WE54) are also shown for comparison. Thermal conductivity represents an issue from the perspective of cooling performance when a material is considered for use in an automotive part that will experience high temperatures (for example, pistons). The $Mg_{95.8}Zn_2Y_2Zr_{0.2}$ displays superior results in terms of this property, with a level of thermal conductivity higher than that of the commercial magnesium alloys, and close to that of the commercial aluminum alloys.

The $Mg_{95.8}Zn_2Y_2Zr_{0.2}$ alloy displays a similar thermal expansion coefficient and Young's modulus to the commercial magnesium alloys, with figures lower than those for the commercial aluminum alloys in both cases. However, the material displays a low density like the commercial magnesium alloys, recording a figure of around 70% of the figures for the commercial aluminum alloys, and can therefore be expected to be effective in reducing the weight of engine parts in automotive and other applications.

4.2. Increasing Strength by Increasing LPSO Phase Strength

The tests conducted to this point had indicated that the $Mg_{95.8}Zn_2Y_2Zr_{0.2}$ alloy displayed good high-temperature characteristics, but the result for yield strength at room temperatures, as shown in Fig. 9, could not necessarily be considered a high figure. Further strengthening of the material was therefore attempted through the addition of Ag, which had been selected based on calculation results. Figure 15 shows XRD patterns for $Mg_{93}Zn_2Y_2Ag_3$ and $Mg_{96}Zn_2Y_2$ alloys. The results show that in addition to the three phases that form in the $Mg_{96}Zn_2Y_2$ alloy, it was possible that the $Mg_{93}Zn_2Y_2Ag_3$ alloy had formed the new

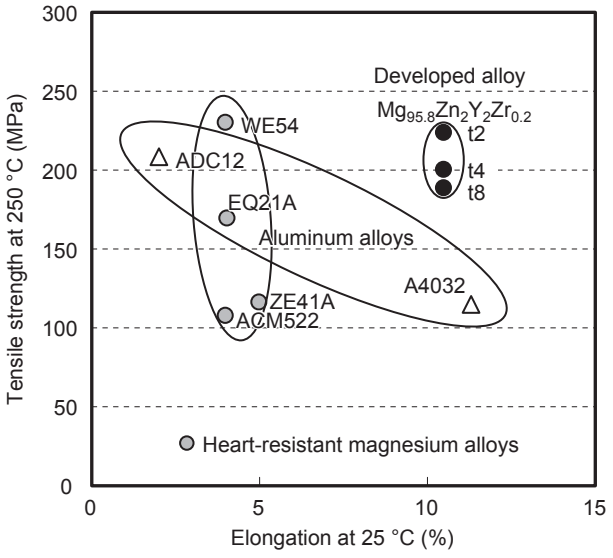


Fig. 14 Relationship between tensile strength at 250 °C and elongation at 25 °C

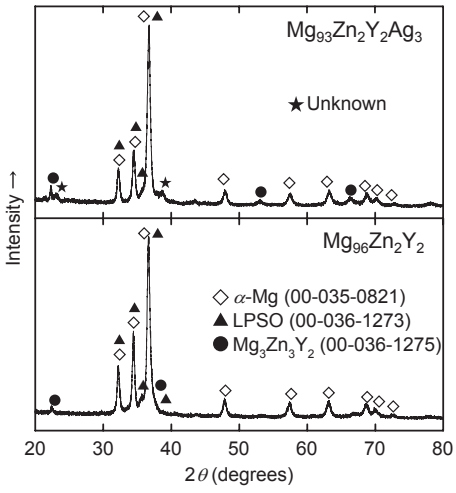
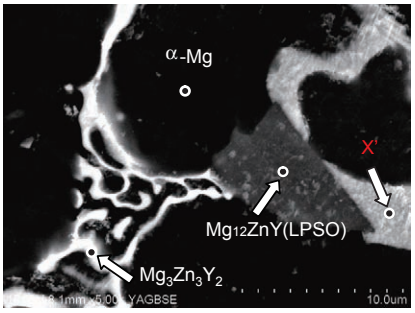


Fig. 15 XRD patterns of $Mg_{93}Zn_2Y_2Ag_3$ and $Mg_{96}Zn_2Y_2$ alloys

phase marked in the figure by the star. Figure 16 shows a BSE-SEM image of the $Mg_{93}Zn_2Y_2Ag_3$ alloy and the results of an EDS analysis of the phases making it up. As in the XRD results, the $Mg_{93}Zn_2Y_2Ag_3$ alloy is made up of four phases, the α-Mg matrix, an LPSO phase, an $Mg_3Zn_3Y_2$ phase, and an unknown X' phase. The results of EDS analysis indicated that Ag was present in the matrix in solid solution, and was present in the X' phase in a quantity that exceeded the solid solubility limit of Mg (approximately 4 at.%). This indicated that it was possible that the Ag did not simply exist in solid solution, but had formed a new phase. High-angle annular dark-field scanning transmission electron microscopy (HAADF-STEM) was applied to this phase. Figure 17 compares HAADF-STEM images of the LPSO and X' phases. In HAADF-STEM images, contrasts are produced by differences in atomic number; the higher the atomic number, the whiter the appearance in the image. The base LPSO phase displays a cyclic alternation of 2 monolayers (ML) which appear white, indicating a high concentration of Zn or Y, which have higher atomic numbers than Mg[10]. The alloy with added Ag displays further white areas in addition to the concentrated 2 ML, and with consideration of the results of the EDS analysis, it can be conjectured that Ag has been substituted for Mg here. It can therefore be considered that an LPSO phase in which Ag has been substituted has been formed in accordance with the desired atomic model.



	Mg	Zn	Y	Ag
α-Mg	96.90	1.00	0.80	1.29
X'	75.99	3.56	4.91	15.54
LPSO	87.21	4.75	5.39	2.65
$Mg_3Zn_3Y_2$	51.79	25.57	18.14	4.49

Fig. 16 BSE-SEM image and point EDS analysis of $Mg_{93}Zn_2Y_2Ag_3$ alloy (at. %)

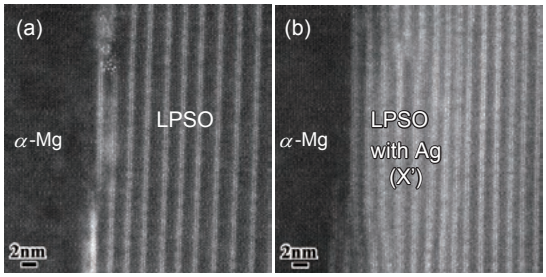


Fig. 17 HAADF-STEM images of (a) $Mg_{95.8}Zn_2Y_2Zr_{0.2}$ alloy and (b) $Mg_{93}Zn_2Y_2Ag_3$ alloy

Next, ship-shaped specimens were processed and subjected to tensile tests in order to study the increase in the yield strength of the $Mg_{93}Zn_2Y_2Ag_3$ alloy. Figure 18 shows the relationship between grain size and yield strength at room temperature, compared with data obtained up to this point. The results show a clear increase in strength against the strength increase expressed by the Hall-Petch equation, which was achieved by refining the crystal grains through the addition of Zr and the modification of the cooling rate. An increase of approximately 60% in strength has been achieved when converted for the same grain size. This can be considered to be a strength increase brought about by the LPSO phase that contains Ag. The $Mg_{93}Zn_2Y_2Ag_3$ alloy fulfilled the design aims established for it by forming an LPSO phase containing Ag, and this contributed to an increase in yield strength.

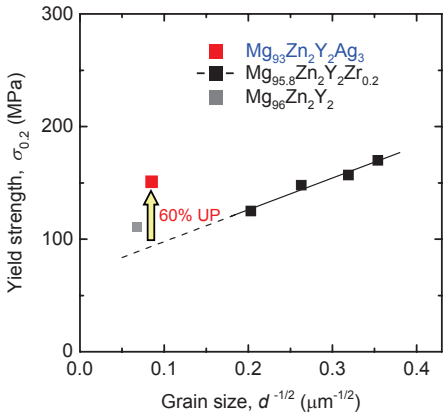


Fig. 18 Relationship between yield strength and grain size of Mg-Zn-Y-X alloys

5. Conclusions

The microstructure and various properties of Mg-Zn-Y alloys in which the solidified microstructure had been controlled were studied in an attempt to achieve weight savings in structural and other parts through the application of a high-strength, cast, heat-resistant magnesium alloy. The following results were obtained:

(1) The addition of Zr to an $Mg_{96}Zn_2Y_2$ alloy transformed the α-Mg phase from dendritic to cell-shaped structures, and refined the microstructure of the cast alloy. In addition, increasing the rate of cooling when the alloy was cast tended to further refine the microstructure.

(2) The alloy displayed high heat stability at high temperatures of 200˚C and above, exhibiting a tensile strength (223 MPa) approximately twice that of A4032-T6 at 250˚C, and close to three times its strength at 300˚C. The alloy displayed equivalent or

better tensile, fatigue, and creep characteristics to heat-resistant aluminum alloys when cast, with no further treatment. In terms of physical properties, the material is low-density, with a density approximately 70% that of an aluminum alloy. In addition, its thermal conductivity, an issue when a material is used in parts, was higher than that of commercial magnesium alloys, and close to that of commercial aluminum alloys.

(3) The addition of Ag, as selected based on the results of a first principle calculation, in order to produce a microstructure with a stronger LPSO phase, resulted in a 60% increase in yield strength at room temperatures.

As these results indicate, the new alloy can be considered as an effective cast alloy when seeking to achieve weight savings in heat-resistant components.

References

(1) Yoshimoto, S., Yamasaki, M., Kawamura, Y.: Microstructure and Mechanical Properties of Extruded Mg-Zn-Y Alloys with 14H Long Period Ordered Structure, Mater. Trans., Vol.47, p.959-965 (2006)

(2) Ienaga, Y., Inoue, K., Kawamura, Y.: Mechanical properties of large-scale extruded Mg-Zn-Y alloys, Proceedings of the 110th Conference of Japan Institute of Light Metals, p. 145-146 (2006)

(3) Emley, E. F.: Principles of magnesium technology, Oxford, Pergamon press, p.126-156 (1966)

(4) Yamaguchi, T., Saito, K., Kawamura, Y.: Mechanical properties of continuously consolidated $Mg_{96}Zn_2Y_2$ magnesium alloy chips, JILM, Vol. 57, No. 7, p. 286-292 (2007)

(5) Okamoto, H.: Phase diagrams of dilute binary alloys, ASM International, p. 170 (2002)

(6) Ando, S., Toda, K., Tsushida, M., Kitahara, H., Tonda, H., Kawamura, Y.: Fatigue Properties of Mg-Zn-Y Alloys with Long Period Ordered Structure, J. Japan Inst. Metals, Vol. 71, No. 9, p. 699-703 (2007)

(7) Koike, S., Washizu, K., Tanaka, T., Baba, T., Kikawa, K.: Development of Lightweight Oil Pans Made of a Heat-Resistant Magnesium Alloy, HONDA R&D Technical Review, Vol. 12, No. 1, p. 167-174

(8) Shibata, A., Suzuki, M., Maruyama, K.: Effects of Eutectic Compounds Formed along Grain Boundaries in Thixomolded Alloy $Mg_{96}Zn_2Y_2$ on Creep Deformation, Mater. Trans., Vol.50, p.1426-1432 (2009)

(9) Busk, R. S.: Magnesium Products Design translated by the association of light metals, The association of light metals, p. 146 (1988)

(10) Abe, E.: Jisedaino koukyoudo/koutainetsusei magunesiumugoukinno tokusyubisaikouzou-HAADF niyorukaiseki, Proceedings of the 10th Conference of the Association of Magnesium Alloy Development and Processing, p. 61-62 (2006) (in Japanese)

The first half of this paper is modified from the earlier paper published in the Journal of Japan Institute of Light Metals, Vol. 60, No. 6 (2010).

Author


Yuichi IENAGA


Kenshi INOUE


Mitsumoto KAWAI

Galvanic Corrosion Prediction Technology for Aluminum Parts of Chassis

Takahiro MIZUKAMI*

ABSTRACT

The time for evaluations can be reduced because it is now possible to predict corrosion by simulation of the depth of galvanic corrosion in aluminum chassis parts. Based on input of polarization curves conforming to the specific corrosion environment, this simulation technology is able to calculate the reduction in aluminum volume due to galvanic corrosion from the corrosion current, and to output the depth of corrosion. It can replace corrosion tests previously requiring 5000 hours with a simulation of approximately 20 minutes, making it possible to predict the depth of galvanic corrosion occurring in the market in a short period.

1. Introduction

The use of aluminum rather than steel materials is one method of achieving weight savings in automotive chassis, but because galvanic corrosion (corrosion occurring due to the difference in electrolytic potential between different materials) can be expected in areas such as the suspension parts that are used in corrosion-promoting environments, methods of evaluation of corrosion resistance are becoming an issue. During the development of suspension parts, corrosion resistance is evaluated by studies using accelerated corrosion testers employing corrosion conditions corresponding to those found in the market, and of the status of corrosion during driving on test courses. However, these tests require a period of several months, necessitating their replacement by a method enabling an equivalent evaluation in a shorter period. For this purpose, the project discussed here selected the existing galvanic corrosion simulation software (3D-Cafe[(1)], manufactured by Mizuho Information and Research Institute, Inc.) from among methods using computer-aided engineering (CAE), but because this software simulated immersive environments such as seawater, it was unable to reproduce the galvanic corrosion occurring in the different environments to which automobiles are exposed.

A peripheral program using 3D-Cafe was therefore developed in order to reproduce automotive environments. This program added a new function to the commercially available simulation software, making it possible to respond to changing corrosion environments such as automotive environments. In addition, the project focused on the fact that the automotive corrosion environment involved a state of coverage with thin water films rather than being an immersive environment, and measured the parameters to be input into the simulation under conditions approximating those of a water film environment. This made it possible to reproduce the depth and the profile of corrosion in actual test specimens in simulations. The program discussed in this paper is a simulation technology that can be used in place of accelerated corrosion tests, and its ability to reproduce the results of these tests has been verified.

2. Mechanism of Galvanic Corrosion

Galvanic corrosion is a phenomenon in which the metal with the lower electric potential is preferentially corroded when metals of differing electric potential are in contact in a corrosion environment. It is also called bimetallic corrosion. Figure 1 shows the galvanic series for various metals in seawater[(2)].

As Fig. 1 shows, the electric potential of aluminum is lower than that of steel. In this case, the aluminum is termed base, and the steel is termed noble. When aluminum and steel are in contact in a corrosion environment such as a saltwater solution, electrons are transferred from the aluminum to the steel in the reactions represented by Eqs.

* Automobile R&D Center

(1) and (2), and galvanic corrosion occurs, in which the aluminum is preferentially corroded.

$$2H_2O+O_2+4e^-\rightarrow 4OH^- \quad (1)$$

$$Al\rightarrow Al^{3+}+3e^- \quad (2)$$

Equation (1) shows the reaction occurring on the surface of the steel, termed the cathode reaction, and Eq. (2) shows the reaction occurring on the surface of the aluminum, termed the anode reaction. The current occurring due to electron transfer is called the corrosion current. The corrosion current flows through a circuit formed from the steel, aluminum, saltwater solution, and steel, in that order. The corrosion current divided by the area of the cathode is termed the cathode current density, and the corrosion current divided by the area of the anode is termed the anode current density.

Because galvanic corrosion between steel and aluminum is cathode-dominant, the reaction shown in Eq. (1) governs the corrosion reaction. The current density at this time can be read from the polarization curves of the steel and aluminum.

Figure 2 shows the polarization characteristics of steel and aluminum. The polarization curves are divided into anode polarization curves and cathode polarization curves. The signs of the two types of curve are opposite, and to aid visualization they are generally expressed as absolute values. At the point at which the corrosion current is 0, the steel and aluminum are at their equilibrium potentials, E_{eq} (Fe) and E_{eq} (Al), respectively. The potential at which the cathode curve of the steel and the anode curve of the aluminum intersect is the potential at which galvanic corrosion occurs, E_{corr}, and the current density at this time is I_{corr}, the current density at which galvanic corrosion occurs.

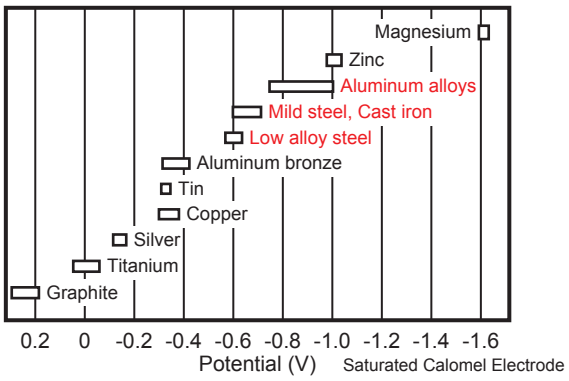


Fig. 1 Corrosion potential in sea water

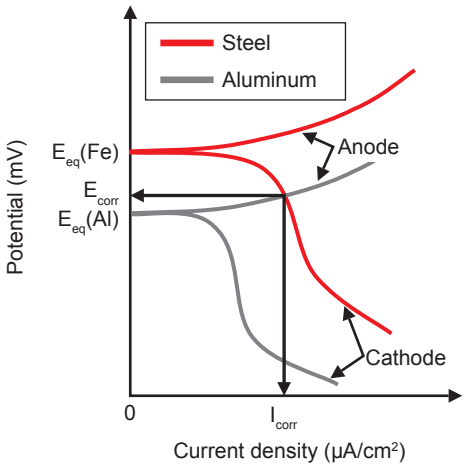


Fig. 2 Polarization curve

3. Theory of Simulation of Galvanic Corrosion

Galvanic corrosion occurs due to the corrosion current generated when different metals are in contact. It is therefore necessary to calculate the corrosion current in order to simulate galvanic corrosion. The commercial software employed in the research discussed here (3D-Cafe) calculates corrosion current for each mesh using a boundary element method (BEM). This section will discuss the basic theory of this simulation software[3].

First, a system consisting of a steel bolt and an aluminum material covered by a solution (saltwater) will be considered. Figure 3 shows a diagram of this system.

The area bounded by the solution in the diagram will be termed Area Ω. The current density, i, the electrical conductivity of the solution, κ, and the internal electric potential, ϕ, satisfy the following relationships:

$$\mathrm{div}\, i=0 \quad (3)$$

$$i\equiv-\kappa\,\mathrm{grad}\,\phi \quad (4)$$

$$\nabla^2\phi=0 \quad (5)$$

The relationship between the internal electric potential, ϕ, and the external electric potential when polarization measurements were taken, E, is shown by Eq. (6).

$$\phi=-E \quad (6)$$

Next, the boundary conditions of Area Ω will be considered. As Fig. 3 shows, the boundary between the solution and air is termed Γ_n, the boundary between the

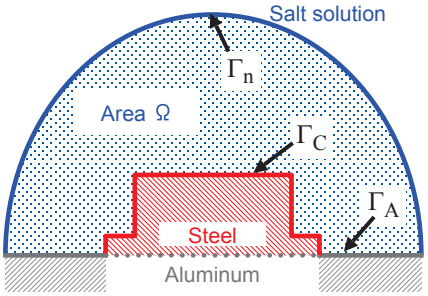


Fig. 3 Model of galvanic corrosion

Table 1 CCT conditions

Order	State	Salt concentration	Temperature	Humidity	Duration time
1	Salt spray	5 wt%	35 °C	98%	1 hr
2	Drying		50 °C	30%	2 hr
3	Wetting		35 °C	95%	3 hr

Table 2 Measurement conditions

Order	State	Salt concentration	Temperature
1	Salt spray	5 wt%	35 °C
2	Drying	26 wt%	50 °C
3	Wetting	26 wt%	35 °C

solution and the steel bolt is termed Γ_C, and the boundary between the solution and the aluminum is termed Γ_A.

Because there is no exchange of current across the boundary between the solution and the air, Γ_n, the current density here is 0. At Γ_C and Γ_A, current densities are generated in response to specific electric potentials, ϕ. Based on the preceding discussion, the following boundary conditions can be assumed:

$$\text{At } \Gamma_n, \quad i=0 \tag{7}$$

$$\text{At } \Gamma_A, \quad \phi=f_A(i) \tag{8}$$

$$\text{At } \Gamma_C, \quad \phi=f_C(i) \tag{9}$$

$f_A(i)$ and $f_C(i)$ are nonlinear functions measured by means of polarization measurements.

Governing equation (5) will be solved on the basis of these boundary conditions. Terming the N x N matrices $[H]$ and $[G]$, the following boundary integral equation can be obtained.

$$\kappa[H]\{\phi\}-[G]\{i\}=\{0\} \tag{10}$$

If calculations are conducted using a corrected Newton-Raphson method until the solutions to Eq. (10) converge, because the electric potential, ϕ, and the current density, i, of each element are known, the level of corrosion for each element can be obtained from Faraday's Law.

The commercial simulation software employed is based on the theory outlined above, but because it is configured to output a single solution for a single corrosion-promoting environment, when it is applied to changing corrosion environments like those faced by automobiles, a new function must be added.

In addition, because the software simulates the depth of corrosion from the corrosion current, it is unable to simulate corrosion weight loss that is unrelated to the corrosion current, for example corrosion weight loss due to the phenomenon of crystal grain dropouts due to grain boundary corrosion. In these cases, it is necessary to conduct the calculations while applying a correction factor to the obtained figures for corrosion weight loss. In order to simulate changing corrosion environments, the research discussed in this paper formulated a routine program that integrates individual results and outputs the ultimate depth of corrosion.

4. Input Model and Parameter Setting

4.1. Corrosion Environments for Simulation

It was essential to set the input models and parameters in accordance with the corrosion environments that would be simulated. This paper presents a case examination of a method of setting models and parameters for input based on cyclic corrosion tester (CCT) data obtained under conditions close to those of a rust environment in an actual vehicle.

Table 1 shows the CCT test conditions used when comparing models and parameters.

The saltwater was supplied in a spraying process, and adhered to the test piece whether in dry or wet states. It can be assumed that in the drying process, the evaporation of the water increased the concentration of the salt, resulting in saturation, and that in the wetting process, the deliquescence of the salt resulted in absorption of moisture, producing a saturated salt concentration.

The salt concentration at saturation was therefore set at 26 wt%. Table 2 shows the environment in which the input parameters were measured.

The data output by the simulation are corrosion current density (mA/cm^2), electric potential (mV), and speed of corrosion (mm/year). The depth and the profile of the corrosion can be obtained from the product of the speed of corrosion and the period of the CCT tests. The models and parameters for input were therefore verified by comparison with the actually measured corrosion current density and depth and profile of corrosion.

4.2. Setting Model for Input

In order to conduct a simulation, it is first necessary to set a model. Because galvanic corrosion between steel and aluminum was to be simulated, Γ_n was the surface of the

saltwater solution, Γ_C was the surface of the steel, and Γ_A was the surface of the aluminum. The analysis described below was conducted assuming an M10 bolt fastened in an aluminum sheet. Figure 4 shows the analytic model. The model is a one-dimensional simulation model in which the centerline of the bolt in the test piece is regarded as the axisymmetric axis of symmetry, and the distance in the radial direction is a variable. The saltwater solution covers the steel bolt and the aluminum sheet, and the point of contact between the steel boundary line and the aluminum boundary line is the area of contact of the steel bolt. The thickness of the saltwater solution, d (termed "water film thickness" below), was set through comparison with the results of profile measurements taken following CCT tests.

4.3. Setting Input Parameters

4.3.1. Polarization characteristics

Polarization measurement tests were conducted in order to obtain the polarization characteristics of steel and aluminum. 50 x 15 x 2 mm test pieces were obtained from corrosion test materials. The test pieces were abraded with #600 emery paper, leaving a 1 cm^2 test surface, and were coated with silicon gum. Ag/AgCl was used for the reference electrode. Polarization was measured in sweeps at a voltage of 0.02 V/min. Measurements were conducted in a solution under the conditions shown in Table 2. The simulation results obtained using the measured polarization curve were verified through comparison with the corrosion current densities measured in CCT tests.

4.3.2. Electrical conductivity of solutions

Table 3 shows the results of electrical conductivity measurements for each of the corrosion environment solutions shown in Table 2.

4.3.3. P hysical values of materials

Table 4 shows the ionic valence, specific gravity, and mass per 1 mol of the materials.

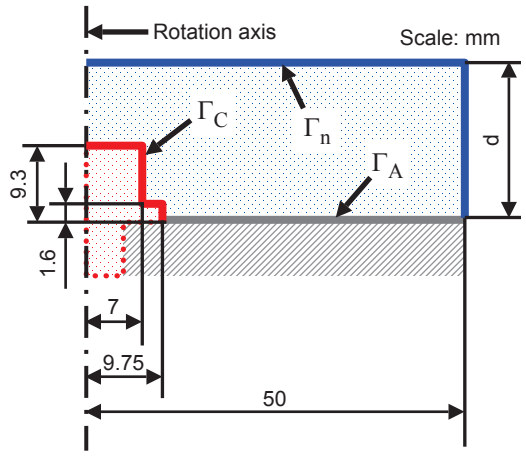


Fig. 4 Simulation model

Table 3 Electrical conductivity

Salt concentration	Temperature	Electrical conductivity
5 wt%	35 °C	9.56 S/m
26 wt%	50 °C	49.47 S/m
26 wt%	35 °C	40.03 S/m

Table 4 Physical values for materials

Material	Ionic valence	Specific gravity (g/m^3)	Mass (g/1 mol)
Aluminum	3	2.69×10^{-3}	26.982
Steel	2	7.86×10^{-3}	55.845

5. Accelerated Corrosion Tests

5.1. Test Materials

A356[4] was used as the aluminum material, and SCM435[5] was used for the steel bolts.

5.2. Accelerated Corrosion Test Method

A CCT manufactured by Suga Test Instruments Co., Ltd. was used in the accelerated corrosion tests. The tests used conditions 1 to 3 as shown in Table 1, repeated in that order. The test pieces were fitted in the tester at a 75° incline.

5.3. Corrosion Current Measurements during CCT Tests

Figure 5 shows a cross-section of a test piece used for measurements of corrosion current. To create the test piece, a steel bolt and an aluminum sheet with an electric wire attached were coupled, with a Teflon sheet insulating the

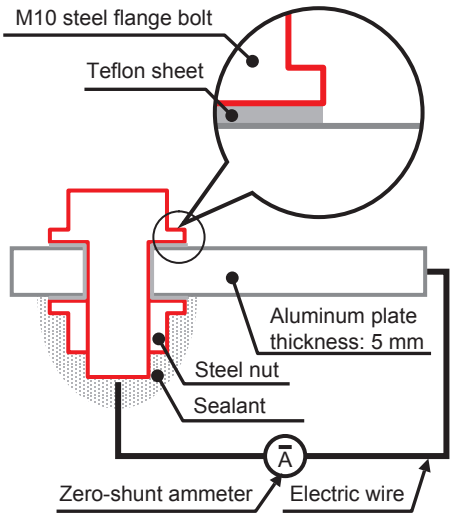


Fig. 5 Cross-section of test piece for corrosion current measurement

contacting surfaces. Using this test piece, corrosion currents were measured during the CCT tests using a zero-shunt ammeter.

5.4. Measurement of Oxygen Concentration in Corroded Area during CCT Tests

In order to obtain the electric potential of the aluminum during CCT tests, oxygen concentration was measured in the area undergoing galvanic corrosion and the general area (i.e., not undergoing galvanic corrosion). The measurements were conducted using a test piece that had undergone 1728 hours of CCT testing (Fig. 6). The measurement device was a Microx TX3 oxygen meter fitted with a needle, manufactured by PreSens Precision Sensing GmbH. ϕ0.5 mm holes were drilled 1.5 mm and 5 mm from the area of contact with the steel bolt, and the needle of the oxygen meter was inserted from the underside. Using this setup, the oxygen concentration was then measured after the state of corrosion had been stabilized in one day of CCT tests.

5.5. Measurement of Corrosion Profile following CCT Tests

Following the corrosion tests, the steel bolts were taken out and the corrosion product ($Al(OH)_3$) was removed from the surfaces of the aluminum sheets. The solution used to remove the corrosion product was formulated by adding 1 L 85 wt% H_3PO_4 and 340 g CrO_3 to 10 L distilled water. The aluminum sheets were immersed in the solution, heated to 60˚C and ultrasonically cleaned. The status of removal of the corrosion product was checked every hour, and when completely removed the aluminum sheet was washed in tap water. After the aluminum test piece was dried following washing, the corrosion profile on the sheet was measured using a Conoscan 3000 non-contact, three-dimensional measurement system manufactured by Optical Metrology Ltd. The relationship between the average depth of corrosion in concentric circles with the same radii and the distance of each circle from the bolt contact area was compared with simulation results.

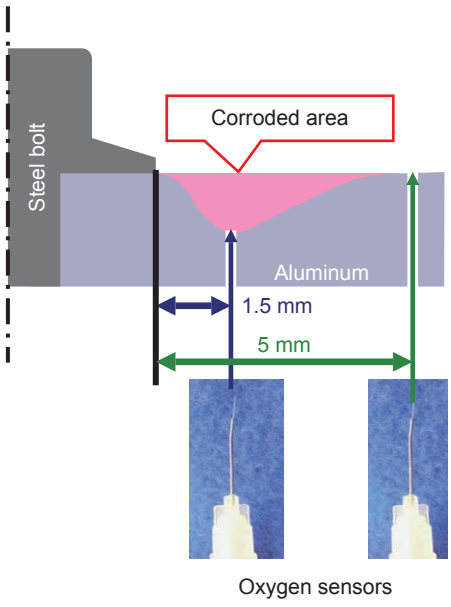


Fig. 6 Measurement of oxygen concentration

6. Setting Models and Parameters through Comparison with Actual Measurements

6.1. Setting Water Film Thickness Model

Figure 7 shows the effect on the simulation when the water film thickness was varied, using the analytic model shown in Fig. 4. The vertical axis shows the ratio of the depth of corrosion to the maximum depth of corrosion considered as 1, and the horizontal axis shows the distance from the area of contact with the steel bolt. When the water film is thin, galvanic corrosion tends to be concentrated in the area of contact with the steel bolt. Just as electrical resistance increases as an electrical wire becomes finer, electrical resistance increases when the water film becomes thinner, and it is considered that this results in the flow of the corrosion current being concentrated close to the area of contact with the steel bolt. Because of this, the area of corrosion becomes narrower as the water film decreases in thickness. Here, the corroded area is defined as the area extending from the area of contact with the steel bolt in which the depth of corrosion is at least 5% of the maximum depth of corrosion, as shown in Fig. 8. Figure 9 shows the results of profile measurements of the corroded area on a

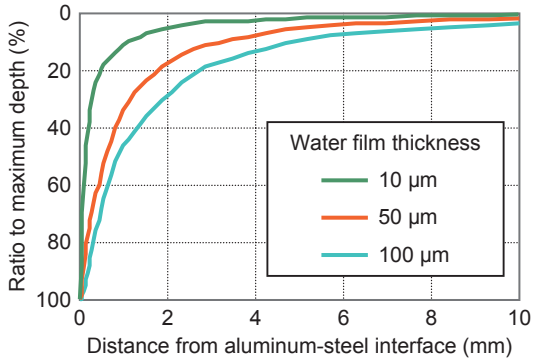


Fig. 7 Influence of water film thickness on simulation

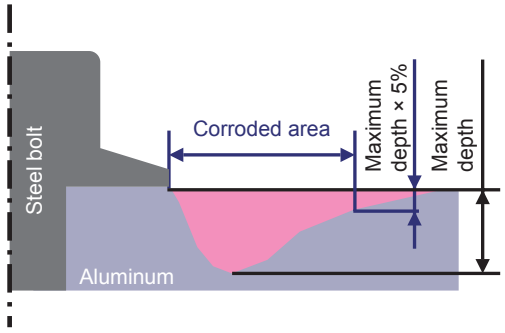


Fig. 8 Definition of corroded area

test piece following 816 hours of CCT testing. The area of corrosion on this test piece was 3.1 mm. Figure 10 shows the results in Fig. 7 organized for water film thickness and area of corrosion. For a 3.1 mm area of corrosion, Fig. 10 shows a corresponding water film thickness of 30 μm. The thickness of the water film in the simulation model was therefore set at 30 μm.

6.2. Parameter Setting

6.2.1. Polarization curve of steel

Table 5 shows a comparison of values for corrosion current density obtained from the simulation using the polarization curves measured under the conditions shown in Table 2, and measurements of corrosion current density taken during CCT tests.

The figures for corrosion current density obtained from the simulation are clearly low. Figure 11 shows the polarization curve during the saltwater spray, as used in the simulation. The figure shows that the corrosion current was 20 μA/cm^2 when the corrosion electric potential during the saltwater spray was -670 mV. For the steel polarization curve, there is almost no change in current density in response to changes in electric potential in the area close to the point of intersection of the steel cathode curve and the aluminum anode curve. The current in this area is called an oxygen diffusion current, and the amount of oxygen consumed by reduction on the surface of the steel is in equilibrium with the amount of supplied oxygen that diffuses through the solution. A higher supply of oxygen would therefore activate the cathode reaction, while a lower supply would inhibit it.

Because test materials must be immersed in saltwater for measurement of polarization curves, as shown in Fig. 12, measurements were conducted using a bulk solution. A bulk solution is a solution that fills the test vessel.

By contrast, the saltwater adhering to the test materials

Table 5 Comparison of corrosion current density

Condition	Simulation	Measured value
Salt spray	20 μA/cm^2	120 μA/cm^2
Drying	10 μA/cm^2	100 μA/cm^2
Wetting	10 μA/cm^2	100 μA/cm^2

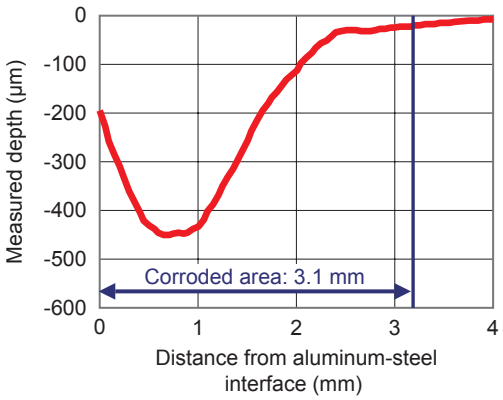


Fig. 9 Corrosion profile after 816-hour CCT test

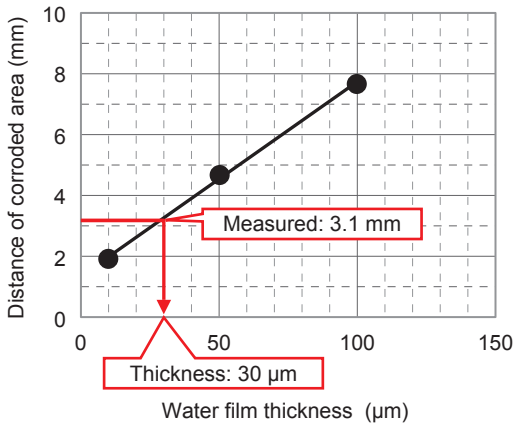


Fig. 10 Water film thickness versus distance of corroded area

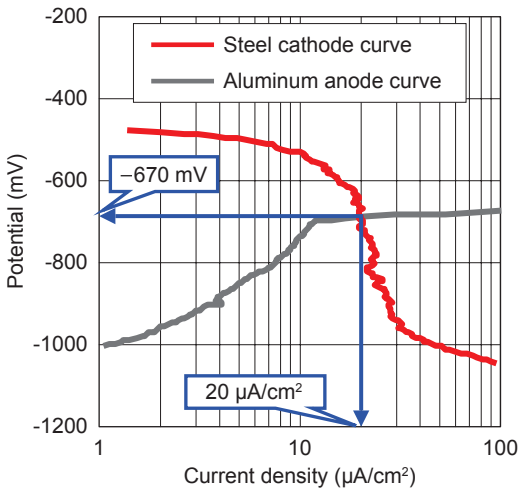


Fig. 11 Potential versus current density in galvanic corrosion

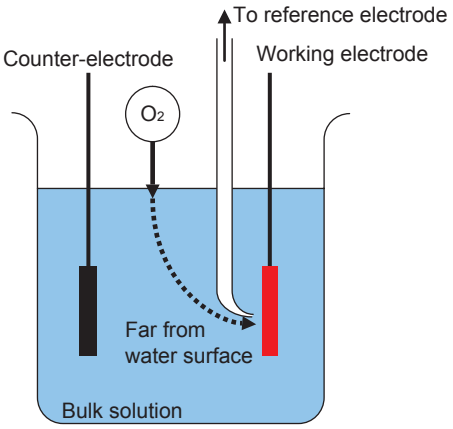


Fig. 12 State of salt solution for polarization measurement

in the CCT tests forms a thin water film on the surface of the test materials, as shown in Fig. 13. This state is called a water film environment.

Because the necessary distance for oxygen diffusion from the boundary between the water and air to the cathode reaction boundary is shorter in a water film environment than a bulk solution environment, the amount of oxygen diffusion supplementing the oxygen consumed by the cathode reaction is greater[6]. It can therefore be considered that the cathode reaction is active, and the oxygen diffusion current becomes higher.

Because the cathode reaction is taking place on the surface of the steel when galvanic corrosion occurs, it is the polarization curve of the steel that is affected by this phenomenon. By contrast, because the dissolution reaction of aluminum during galvanic corrosion is an anode reaction, it is almost entirely unaffected.

It is necessary to input the polarization curve in a water film environment in order to simulate such an environment, but because there is no method of directly measuring the polarization characteristic in this type of environment, hydrogen peroxide was added to the bulk solution. By this means, an artificial water film environment with an equivalent amount of oxygen supply was created, and measurement of the polarization curve in this environment made it possible to estimate the polarization curve in an actual water film environment.

Hydrogen peroxide breaks down as shown in Eq. (11), and promotes the cathode reaction by supplementing the oxygen consumed on the surface of the steel or being directly reduced on the surface of the steel as shown in Eq. (12).

$$2H_2O_2 \rightarrow 2H_2O + O_2 \quad (11)$$

$$H_2O_2 + 2e^- \rightarrow 2OH^- \quad (12)$$

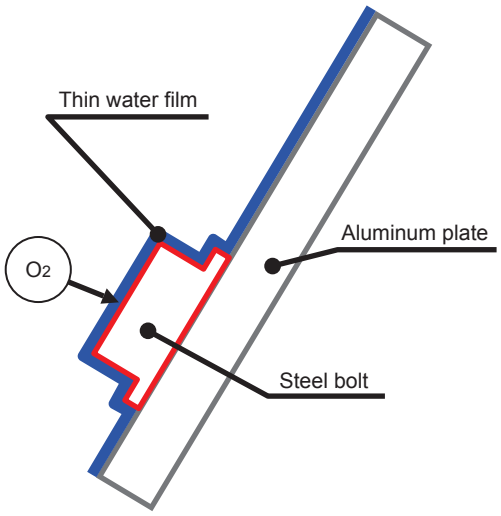


Fig. 13 State of salt solution for CCT

Hydrogen peroxide was added to the solution under the conditions shown in Table 2, and the polarization characteristic of the steel was measured. As Fig. 14 shows, the oxygen diffusion current density increased as the amount of hydrogen peroxide added was increased.

Figure 15 shows the dependence of the corrosion current density on the concentration of hydrogen peroxide when the corrosion electric potential is -670 mV for the polarization curves obtained when the hydrogen peroxide concentration was varied. The relationship between the concentration of hydrogen peroxide and current density is described by a linear expression. Figure 15 shows that the current densities of 120 μA/cm^2 and 100 μA/cm^2 measured under the conditions in Table 5 correspond to concentrations of hydrogen peroxide of 0.0075% and 0.015%, respectively.

Table 6 shows the simulation results for corrosion current density when the polarization curves measured at these concentrations of hydrogen peroxide were input. It was possible to bring simulation values for corrosion current

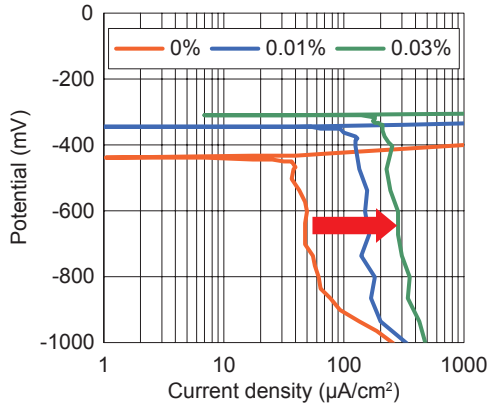


Fig. 14 Polarization characteristic when hydrogen peroxide is added

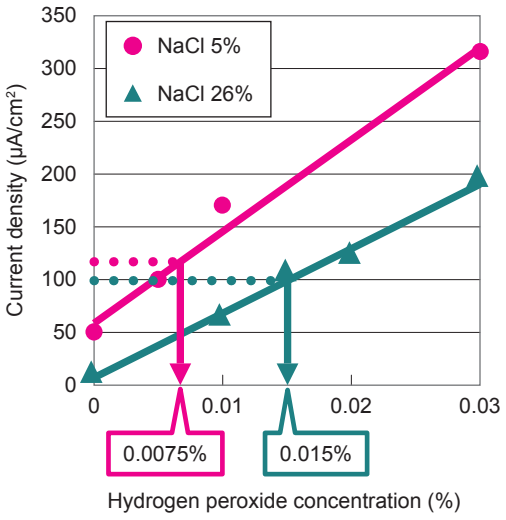


Fig. 15 Hydrogen peroxide concentration versus current density

Table 6 Simulation results for current density using polarization curves measured at different hydrogen peroxide concentrations

Condition	Salt concentration	Measured value	Hydrogen peroxide concentration	Simulated value
Salt spray	5 wt%	120 μA/cm²	0.0075%	123 μA/cm²
Drying	26 wt%	100 μA/cm²	0.015%	96 μA/cm²
Wetting	26 wt%	100 μA/cm²	0.015%	103 μA/cm²

density closer to measured values by using polarization curves measured in solutions to which an appropriate amount of hydrogen peroxide had been added.

6.2.2. Polarization curve of aluminum

Figure 16 shows results for measurements of the corrosion profile from the simulation and CCT tests for test pieces after 816 and 1728 hours of CCT testing. The horizontal axis shows the distance from the area of contact with the steel bolt, and the vertical axis shows the depth of galvanic corrosion. The area of maximum corrosion in the simulation was the area of contact with the steel bolt, while the area of maximum corrosion was distant from this in the actual measurements.

Figure 17 shows the relationship between the distance from the aluminum-steel interface to the maximum depth of corrosion and the depth of corrosion at that time for aluminum materials used in actual tests. The relationship between the maximum depth of corrosion, x (mm), and the distance from the aluminum-steel interface, y (mm), is given by Eq. (13). The area of maximum galvanic corrosion moves further from the aluminum-steel interface with the increase in the depth of corrosion. This shows that points more distant from the aluminum-steel interface are more prone to corrosion than the aluminum-steel interface itself.

$$y = 0.77x + 0.06 \quad (13)$$

Here, if it is hypothesized that the state of the areas of deep galvanic corrosion on the aluminum is similar to those of differential aeration corrosion and pitting corrosion, it can be conjectured that oxygen is consumed in the cathode reactions occurring on the surface of the steel and in the areas of shallow galvanic corrosion on the aluminum, and that the oxygen concentration and the electric potential are low in the areas of deep galvanic corrosion on the aluminum. Figure 18 shows the results of measurements of the oxygen concentration in actual areas of galvanic corrosion using the method described in Section 5.4. Oxygen concentration was as low as 0% in the area of

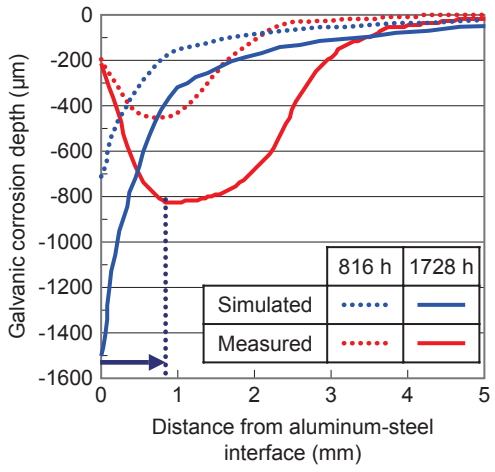


Fig. 16 Comparison of corrosion profiles

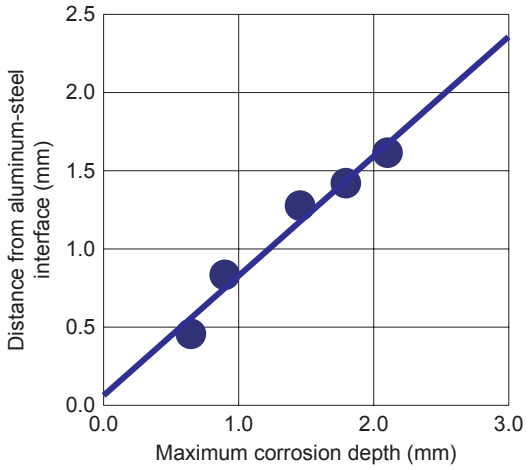


Fig. 17 Maximum corrosion depth versus distance from aluminum-steel interface

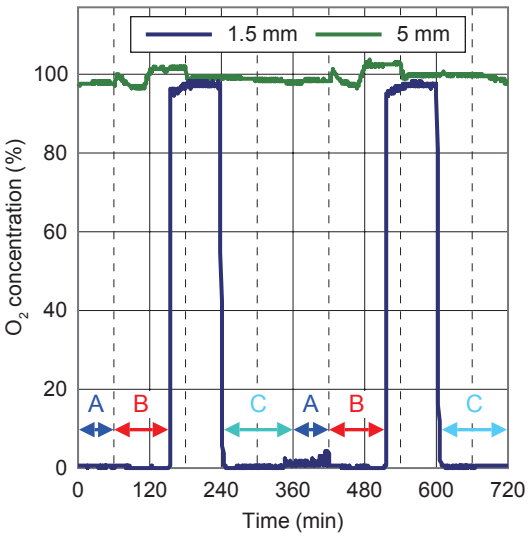


Fig. 18 O_2 concentration

deep galvanic corrosion (1.5 mm from the aluminum-steel interface) when galvanic corrosion was occurring (during saltwater spray: A; until saltwater dries: B; when test piece was wet and salt had deliquesced: C). The polarization characteristic when the oxygen concentration was 0% was obtained by conducting measurements after sufficient substitution of N_2 gas (deaeration) had occurred in the solution used in the measurements.

A program that uses empirical Eq. (13), derived from the relationship shown in Fig. 17, and with the polarization curve when the oxygen concentration is 0% in the areas of deep galvanic corrosion in the aluminum newly set, was therefore added to the previously formulated routine program. However, because the relationship shown in Fig. 17 is described by an empirical formula, it will be necessary to conduct actual measurements for each material.

6.2.3. Setting correction factor

Figure 19 shows the microstructure of an area with galvanic corrosion. Because galvanic corrosion tends to proceed following the grain boundary, and some crystals detach from the parent phase, the detached crystals are removed together with the corrosion product. As discussed above, the simulation software was unable to simulate corrosion weight loss that did not depend on corrosion current, and because of this it was necessary to set a correction factor. Figure 20 shows the weight loss calculated from theoretical galvanic corrosion and weight loss measured after removal of the corrosion product. The theoretical galvanic corrosion weight loss was calculated using Faraday's Law, with 0.25 mA as the average corrosion current for the various conditions used in CCT tests. The weight loss following removal of the corrosion product was calculated from the volume of corrosion of the areas in which corrosion profiles were measured. Figure 20 shows that the measured weight loss in the test pieces following CCT tests is 2.0 X the theoretical value converted from the corrosion current. The correction factor for the corrosion weight loss in simulation results was therefore set at 2.0.

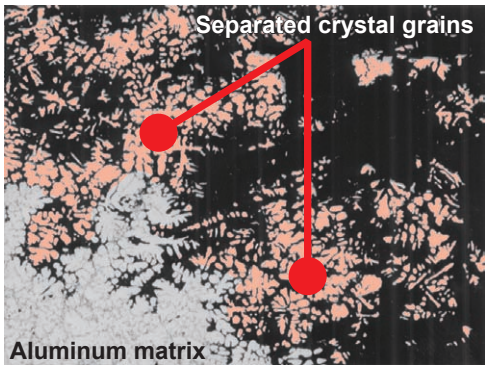


Fig. 19 Microstructure of area with galvanic corrosion

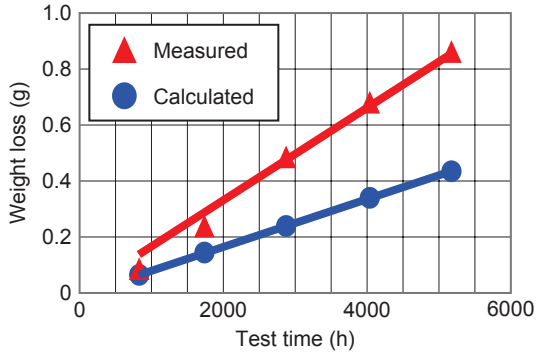


Fig. 20 Measured and calculated weight loss versus CCT testing time

6.2.4. Simulation results

A simulation program was created based on the results obtained up to this point. Figure 21 compares corrosion profiles for test pieces following 2880 and 5084 hours of CCT testing and for the simulation.

The profiles obtained from the simulation correspond well with the actually measured profiles. The developed routine program could calculate results for 5084 hours of CCT testing in approximately 20 minutes, and was able to reproduce the profile and depth of galvanic corrosion.

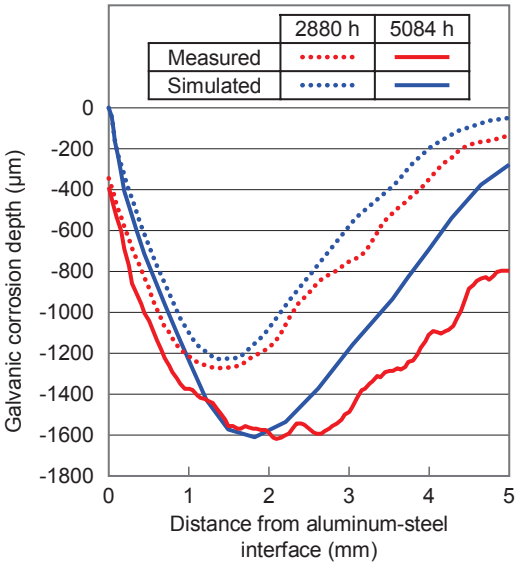


Fig. 21 Simulated and measured profiles

7. Conclusions

A technology for the simulation of CCT tests was developed in order to predict the galvanic corrosion of aluminum parts in the market. The following results were obtained:

(1) Modeling of water film environment

Because the area of corrosion was typically wide in the simulation model if the water film was thick, the water film thickness was set at 30 μm. Consequently, the model corresponded with the actual area of corrosion.

(2) Polarization curve of steel

In order to activate the cathode reaction, hydrogen peroxide was added to the bulk solution when polarization was measured. Consequently, the model corresponded with the corrosion current density in a water film environment.

(3) Polarization curve of aluminum

A corrosion-promoting environment was reproduced by setting the polarization curve for an oxygen concentration of 0% (N_2 deaeration) in the areas of deep galvanic corrosion. Consequently, the model corresponded with the actually measured profile of galvanic corrosion.

(4) Effect of grain boundary corrosion

A correction factor was set by comparing the amount of galvanic corrosion calculated from the corrosion profiles of test pieces following galvanic corrosion and the amount of corrosion converted from actually measured corrosion current. Consequently, the model corresponded with the actually measured depth of galvanic corrosion.

The developed routine program can calculate results for 5084 hours of CCT testing in approximately 20 minutes, and is able to reproduce the profile and depth of galvanic corrosion.

The developed simulation software can be made to respond to a variety of environments by conforming the input polarization characteristics and electrical conductivity to the corrosion environment. This method is not limited to 3D-Cafe, but can be applied to all solvers that use polarization curves to simulate corrosion current.

References

(1) http://www.mizuho-ir.co.jp/solution /research/digital/manufacture/fushoku/index.html, 2010/6/25
(2) Miyasaka, M.: Lecture on Corrosion and Corrosion Protection of Seawater Pumps - Part 1 Basics of Corrosion and Seawater Corrosion Characteristics -, EBARA ENGINEERING REVIEW, No. 220, P. 32 (2008)
(3) Aoki, S., Amaya, K., Miyasaka, M.: Boundary element analysis on corrosion problems, Shokabo, P. 17-39 (1998)
(4) JIS H2211: 1960, Aluminum alloy ingots for casting
(5) JIS G 4053: 2003, Low-alloyed steels for machine structural use
(6) Bousei-bousyokusouranhensyuuiinkai, Bousei-bousyokusouran, Sangyougijutsu service center, P. 99 (2000) (in Japanese)

Author



Takahiro MIZUKAMI

Establishment of Prediction Technology of Fatigue Strength in Roots of Internal Thread for Crankcase Assembly and Application in Product Development

Hiroshi KURIBARA* Junya SAITO*
Hideki SAITO* Daisuke SEKIYA*

ABSTRACT

Aluminum alloy crankcases are generally used in motorcycle engines. Fatigue fractures sometimes occur in the roots of the internal threads of the cylinder head fastening bolts and the crankshaft main bearing fastening bolts in durability tests in the prototype stage. Conventionally, theoretical evaluation of absolute values of fatigue strength in the roots of the internal threads was a challenge, so evaluation of fatigue strength had to rely on durability tests using actual engines.

This study developed technology that uses FEM analysis to theoretically evaluate the fatigue strength of the entire crankcase, including the internal thread portions of the main bolts. This technology performs parallel calculation processing on a large-scale FEM model that takes into account the forms and contact characteristics of the external and internal threads, and was found to be practical in terms of both calculation accuracy and calculation time. Examples of applying this new method to product design showed that fatigue strength in the roots of the internal threads for crankcase assembly can be enhanced without increasing the weight, by modifying the form around the bolt fastening area and the form of the bolt tip.

1. Introduction

Aluminum alloy crankcases are used in motorcycles mainly from the viewpoint of weight reduction. However, a characteristic issue for these engines is fatigue fracture starting from the roots of the internal threads of the fastening areas of bolts subject to high axial force, such as the cylinder head stud bolts and the crankshaft main bearing fastening bolts. When both the external and internal threads are made of steel, fastening area fractures generally occur starting from the underhead fillet of the bolt flange or the roots of the external thread that is not engaged with the internal thread. However, when fastening a steel external thread to an internal thread made of aluminum, which has lower material strength than steel, fractures may originate on the internal thread side. Figure 1 shows the location of a fracture starting from the roots of the internal thread that occurs in durability tests in the prototype stage. The starting point is in the roots of the internal thread where the engaging with the external thread ends, and the fracture surface occurs as a fatigue fracture surface.

Demands to reduce the environmental load and product development costs by reducing durability tests are increasing the importance of technology that can evaluate performance in the product development process. Crankcases have complex shapes, and design requires a high degree of balance between weight reduction and durability. Therefore, evaluation of fatigue strength using FEM analysis in the initial design stages is a useful and important method.

However, in conventional evaluation of the fatigue strength of bolt fastening areas, the roots of the internal threads for crankcase assembly had to be excluded from the evaluation subject due to their detailed form and complex contact modes. Therefore, the strength of these areas was evaluated by durability tests using actual engines. Many studies have analyzed the stress in the bolt fastening

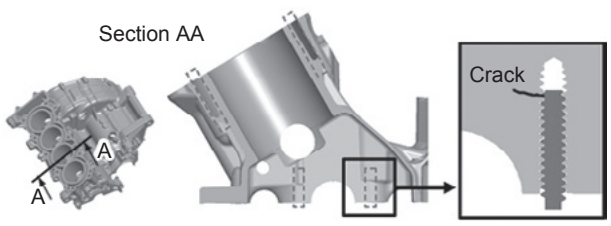


Fig. 1 Location of starting point of fatigue fracture at internal thread

* Motorcycle R&D Center

areas[(1)-(3)], but practical studies that aim to evaluate the fatigue strength of the overall product form are rare. This study developed technology for evaluating the fatigue strength of the entire crankcase, including around and inside the bolt fastening areas.

2. Development of Technology for Evaluating Fatigue Strength of the Crankcase including Bolt Fastening Areas, and Verification of Validity

Three processes were used to develop the technology as follows.

Step 1: Construction of an FEM model for stress analysis of the bolt fastening area

Test pieces focusing on the bolt fastening area were used to measure the strain at the roots of the internal thread and the external surface of the bolt fastening area, and the stress was analyzed using a FEM model that simulates strain tests using test pieces. The correlation between the strain and stress was then investigated to construct an accurate modeling method for stress analysis of the bolt fastening area.

Step 2: Construction of an FEM model for stress analysis of the entire crankcase

A stress analysis model for the entire crankcase was constructed that incorporates the bolt fastening area analysis model constructed in Step 1. The strain was measured using an actual engine, and the validity of the model to reproduce the stress distribution of the entire crankcase was verified.

Step 3: Construction of a method for calculating the fatigue safety factor

A method was constructed for calculating the fatigue safety factor of the entire crankcase, including the bolt fastening areas, based on the material strengths and the history of stress generated in the engine assembly process and during operation.

2.1. Construction of a Model for Stress Analysis around the Bolt Fastening Area

2.1.1. Construction of a model for stress analysis at the roots of the internal thread

Following construction of an FEM model that takes into account the detailed characteristics of the bolt fastening area, equivalent measurements were performed using an actual test piece, and the validity of the model proposed by this study was evaluated by comparing the respective results. Figure 2 shows an overview of the FEM model. M6 to M12 bolts are often used as the main bolts in motorcycle engines, but it is a challenge to accurately measure the strain, so the nominal bolt diameter was set at ø64. In addition, actual bolts have a spiral thread form, but with regards to fractures occurring at the roots of the internal thread, it was assumed that the effects of the load in the lead direction generated by contact at the bolt lead angle are small enough to be ignored. Therefore, this study used a model with an axisymmetric form for the thread form. The bolts are made of steel and have a single external thread, the internal thread side forms seven valleys inside an aluminum block, and the external thread is inserted and places an axial force load on the fourth valley from the top. A limit-sliding model was used for the location where the parts contact each other to reproduce the load and slipping behavior between the external and internal thread contact surfaces. Measurement values obtained from actual test pieces were used for the forms and material characteristics of each part.

Figure 3 shows the test piece form and the strain measurement sequence used to measure the strain at the roots of the internal thread. First, strain gauges were attached to the roots of the internal thread with the test piece in the divided condition. Next, the two base bodies were bolted together with the external thread bolt inserted to the internal thread portion. Finally, a nut was fastened to the thread cut in the upper portion of the external thread bolt, and the axial force and strain at the roots of the internal thread were measured. Figure 4 shows the positions for evaluating the strain at the roots of the internal thread. Stress evaluation points were set in three locations at different angles in the circumferential direction, in each of three roots consisting of the root that holds the bolt external

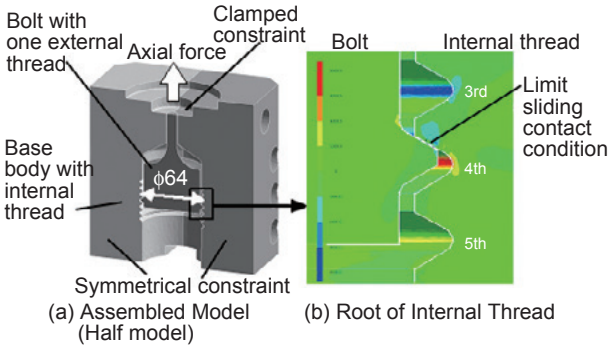


Fig. 2 FEM model for strain analysis at root of internal thread

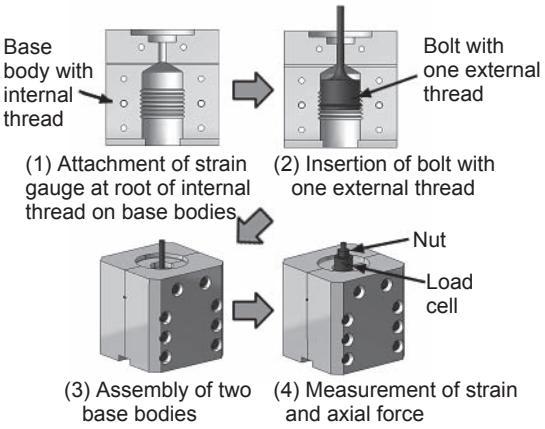


Fig. 3 Measurement sequence for strain at root of internal thread

thread and the roots immediately above and below in the axial direction. Both the measurements and FEM analysis obtained the strain in the direction of the bolt axis along the root fillet.

Figure 5 compares the strain values at the roots of the internal thread obtained by FEM model analysis and actual measurements. The measurement results show that both the stress distribution and quantitative values match closely for the internal thread root that engages with the bolt external thread and for the internal thread roots immediately above and below the meshed root, thus confirming the validity of the model proposed by this study.

2.1.2. Verification of stress analysis accuracy at the external surface of the bolt fastening area

When evaluating the fatigue strength of the crankcase, it is necessary to accurately reproduce the stress conditions not only at the roots of the internal threads of bolts subject to high axial force, but also in surrounding areas. Therefore, the correlation between measurements and simulations was verified for the strain at the external surface of the bolt fastening area. Figure 6 shows the test piece used to measure the strain at the external surface of the bolt fastening area. The test piece has three columns, with an internal thread formed on the center cylindrical column. Strain gauges are attached to the surface of the center column at intervals matching the thread pitch in the axial direction. The strain at the external surface of the bolt fastening area is measured by inserting a spacer to this test

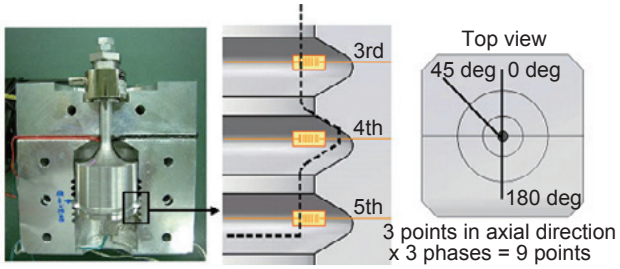


Fig. 4 Measurement point for strain at root of internal thread

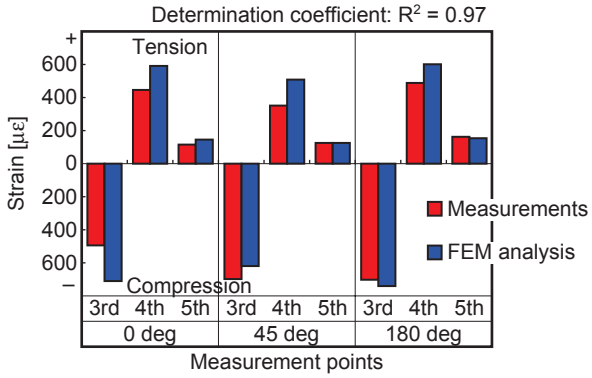


Fig. 5 Strain at root of internal thread: Measurements vs. FEM analysis

piece and applying axial force. Figure 7 shows an overview of the FEM model used to simulate experiments using this test piece. The modeling method was the same as that used to create the stress analysis model for the roots of the internal thread.

Figure 8 compares the strain values at the external surface of the bolt fastening area obtained by measurements

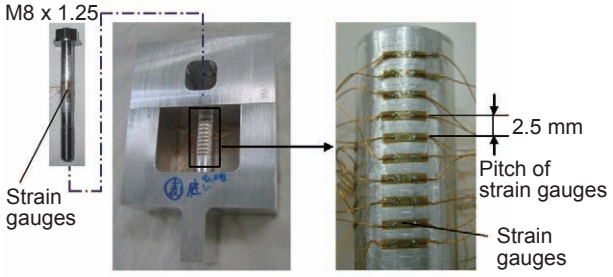


Fig. 6 Test piece for measurement of strain at external surface of bolt fastening area

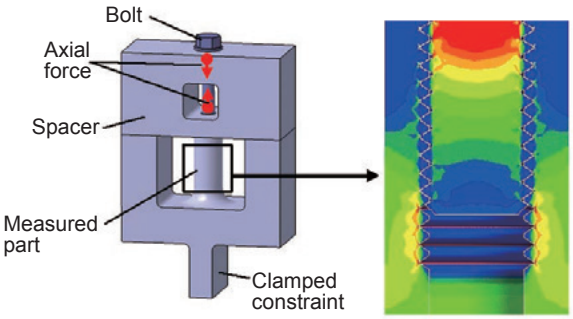


Fig. 7 FEM model for strain analysis at external surface of bolt fastening area

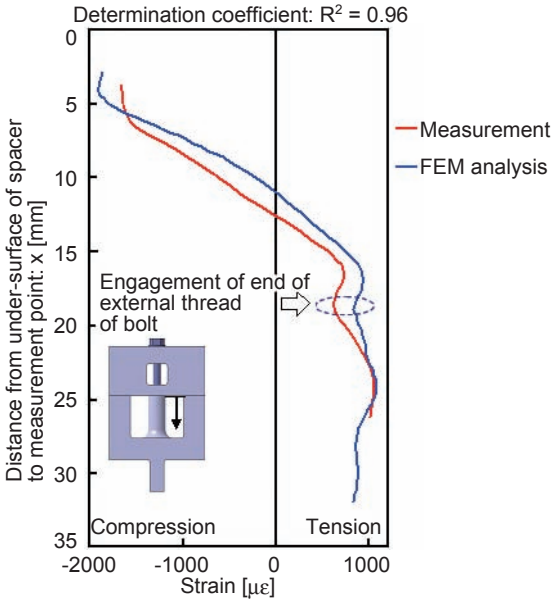


Fig. 8 Strain at external surface of bolt fastening area: Measurements & FEM analysis results

and by FEM model analysis. The measurement and simulation results match closely for both the strain at the roots of the internal thread and the strain distribution at the external surface of the bolt fastening area, thus confirming the validity of the model proposed by this study.

2.2. Construction of a Stress Analysis Model for the Entire Crankcase

A stress analysis model of the entire crankcase was constructed that incorporates the bolt fastening area model described in section 2.1. into the internal thread portions of the crankcase stud bolt fastening areas. Figure 9 shows an overview of the model and the flow of analysis using a single-cylinder engine as an example.

The main types of strain generated in the crankcase during engine operation are: (1) residual strain generated by the casting, heat treatment, and machining processes; (2) strain generated in the engine assembly process; (3) strain generated by the cylinder pressure load and the bearing reaction forces of the crankshaft, transmission and other parts; (4) strain generated around the engine mounts from supporting the inertial motion of the engine; and (5) strain rooted in non-uniformity of the temperature distribution and differences in the coefficients of thermal expansion of different components. This study focused on strains (2) and (3), which have a particularly large effect on the stress mode at the roots of the internal thread. The loads taken into account were the stud bolt axial force, cylinder pressure, piston thrust force, the crankshaft main bearing and transmission bearing loads, and the uniaxial primary balancer bearing load.

In addition to the crankcase that is the evaluation subject, the parts needed to transfer and receive the loads (2) and (3) above were also selected and assembled into the FEM model. In addition, the stress-strain curve calculated from tensile tests using test pieces cut from actual parts was used for the crankcase material characteristics.

As shown in Fig. 9, the measurement values for the cylinder head fastening bolt axial force and the cylinder pressure were used for the quantitative load condition values. Calculation values obtained by flexible multibody dynamics[4] were used for the crankshaft, transmission shaft and balancer shaft bearing loads.

FEM models of engine assemblies that include detailed thread forms have large numbers of elements, and require calculations that take into account the nonlinearity of contact and materials, so the calculation scale becomes quite large. Therefore, a parallel calculation solver was used as the solver to enable calculations to be performed in a short time for even these types of large-scale models. Table 1 gives an overview of the analysis scale for the engine assembly model. Even though the calculation scale is large, analysis can be performed in a time period that enables repeated investigation of specifications in the design stage.

The strain values generated on the crankcase during engine assembly and operation were measured to evaluate the validity of the analysis model. Figure 10 shows a photograph of the engine used for measurement. Six locations were selected as the strain measurement points, in reference to the strain distribution map obtained by FEM analysis. Figure 11 shows the locations where the strain

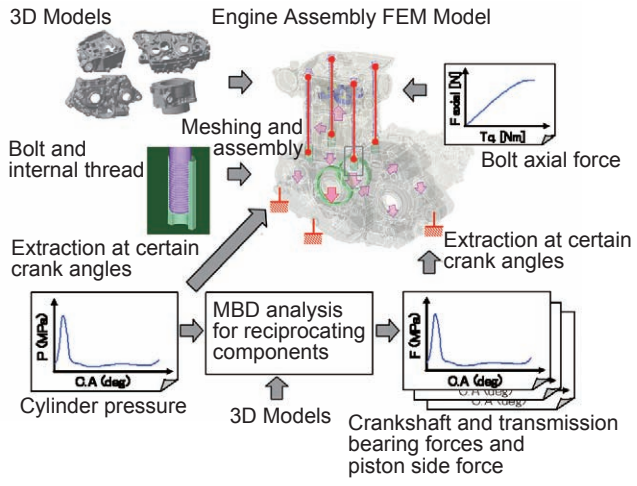


Fig. 9 Stress analysis model for entire crankcase

Table 1 Scale of FEM stress analysis model for entire crankcase

Number of elements	10 million elements
Number of contact elements	1 million elements
Minimum mesh size	25 μm
Number of CPUs used in calculation	50 CPUs
Calculation time/One boundary condition	5 hours

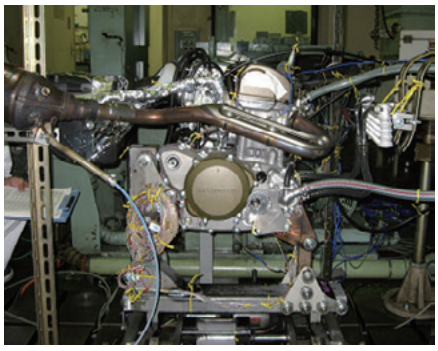


Fig. 10 Engine used to measure strain when assembled and under operating conditions

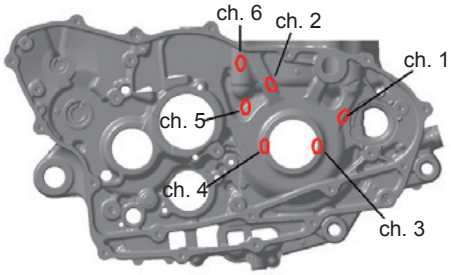


Fig. 11 Locations for attachment of strain gauges

gauges were attached. The strain gauges were attached in the directions in which the maximum principal strain and minimum principal strain are generated.

Figure 12 shows the correlation between the strain calculation results and strain measurement results at each point, at a crank angle of 16 degrees which results in the maximum cylinder pressure, during steady-state operation at wide open throttle and an engine speed of 6000 rpm. The strain values shown in this figure are the sum of the strain generated by the effects of axial force and the strain generated during engine operation due to the effects of the cylinder pressure load and each bearing load. The mean of the strain measurement results for ten cycles was used for the measured strain data, to minimize the effects of cycle fluctuation in the cylinder pressure.

Comparison of the FEM model analysis results and the measurement results showed that the location with the greatest stress for both results was ch.5, which is subject to a large tensile load during both engine assembly and operation. The strain gauge for ch.6 was attached to the head side of the stud bolt meshing position, so the stress value results indicated a high compression stress. The results for the other ch.1 to ch.4 were all within the range of the tensile internal force of the cylinder pressure and the crankshaft main bearing load, indicating that tensile strain was generated in sync with the combustion timing.

Comparison of measurements and the simulation results confirmed a high qualitative and quantitative correlation, and verified the validity of the engine assembly FEM model.

2.3. Calculation of Fatigue Safety Factor and Evaluation of Fatigue Strength

To evaluate the fatigue strength of the crankcase, fatigue should be evaluated not using the stress values for a single load state, but rather in consideration of stress fluctuations during engine operation and the fatigue strength characteristics of the materials.

The method used by this study to evaluate fatigue strength first calculates the mean stress and stress amplitude based on the results of static stress analysis at multiple crank angles, and then calculates the fatigue safety factor using a modified Goodman fatigue limit diagram as the strength judgment index. Figure 13 shows the flow through calculation of the fatigue safety factor.

Using the hypothetical case of durability tests performed at a constant speed as an example, stress analysis is performed for three conditions that are characteristic stress states that affect the crankcase fatigue strength. These are (1) the load state at the peak cylinder pressure, (2) the load state with the piston at the top dead center (TDC) before intake and the TDC side inertia force of the reciprocating system at a maximum, and (3) the state with the piston near the midpoint between the TDC and bottom dead center (BDC) and the crankshaft main bearing load at a minimum. The fatigue safety factor can be calculated at all nodes of the crankcase FEM model by performing the series of fatigue calculation processes on these analysis results.

This processing renders visible the fatigue safety factor and stress distribution at each crankcase location as shown in Fig. 13. This makes it easier to judge the strength, and can also be used as a reference for investigating forms, such as when the strength is insufficient or when reducing the weight.

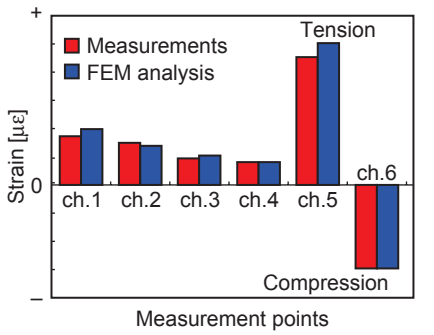


Fig. 12 Strain at points of attachment of gauges on crankcase: Measurements and FEM analysis results

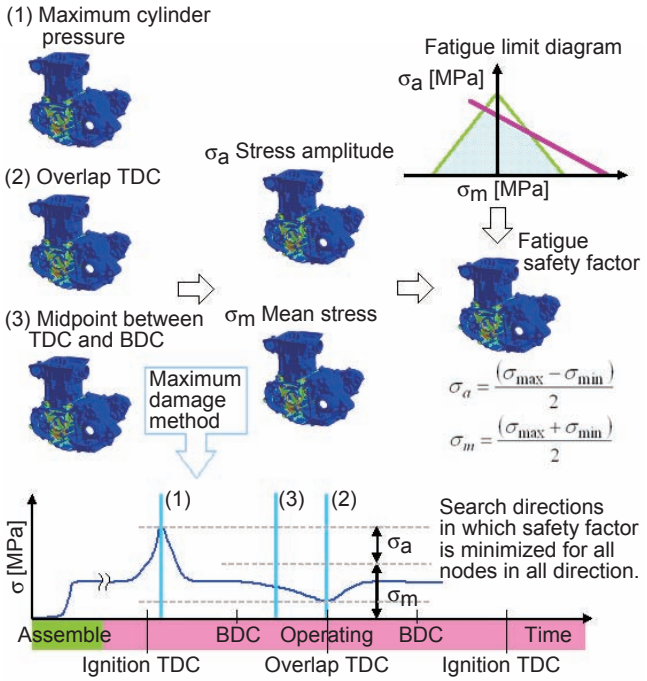


Fig. 13 Method of calculation of safety factor

3. Examples of Applying this Technology to Product Development

Two examples of using this analysis method to investigate the strength of the roots of internal threads are introduced below.

3.1. Study on Preventing Fractures at the Roots of Internal Threads by Using Stud Bolts with a Hollow Tip

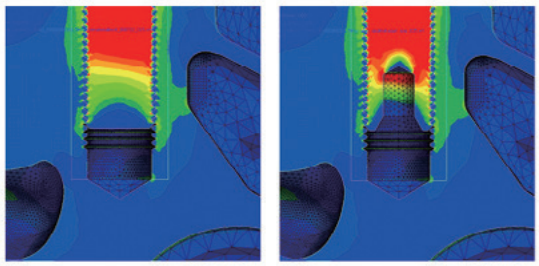
One means of increasing the fatigue strength of the roots of internal threads is to use a hollow bolt tip as shown in Fig. 14, and this has been confirmed by durability tests to actually increase the crankcase fatigue strength. Analysis was performed to investigate the effects of a hollow form, with all conditions the same except for the presence or lack of a hollow form at the tip of the bolt. Figure 15 focuses on a cylinder head fastening bolt in a single-cylinder engine, and shows the mean stress and stress amplitude at the roots of the internal thread over a single circuit of the roots of the internal thread, plotted on a fatigue limit diagram. This shows that using a hollow-tip bolt reduced both the mean stress and stress amplitude at the roots of the internal thread. Previously only the experimental effects of hollow-tip bolts had been confirmed, but the developed technology enabled quantitative evaluation of the effects.

3.2. Study on Preventing Fractures at the Roots of the Internal Thread by Changing the Crankcase Form

This example increased the fatigue strength at the roots of the internal thread by modifying the crankcase form around the stud bolts. Stress analysis was performed and the fatigue strength at the roots of the internal thread was compared for crankcases A and B, which have different forms around the stud bolts. The durability test results clearly showed that crankcase B has a higher fatigue strength than crankcase A.

Stress calculation and fatigue evaluation processing was performed on engine assembly models incorporating crankcases A and B, using the same axial force and bearing load conditions. Figure 16 shows a graph that plots the mean stress and stress amplitude over a single circuit of the roots of the internal thread. Crankcase B exhibits a lower mean stress and stress amplitude at the roots of the internal thread than crankcase A, and these effects are greater than when using hollow-tip bolts. Modifying the form around the stud bolt fastening area in the design stage involves a high degree of design freedom and does not increase the cost or weight, so it can be said to be an efficient method.

The above examples show that the establishment of this technology enables efficient design of crankcases that are both lightweight and have the necessary fatigue strength.



(a) Standard bolt (b) Bolt with hollow tip

Fig. 14 Form of hollow cylinder at tip of bolt

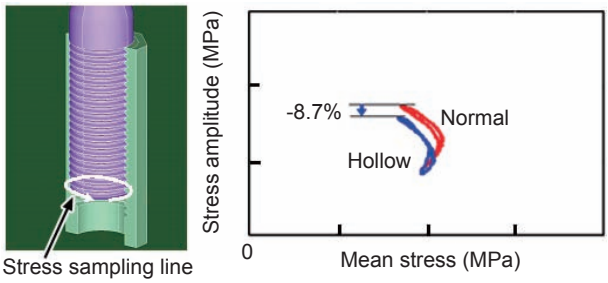


Fig. 15 Reduction of stress at root of internal thread using bolt with hollow cylinder at tip

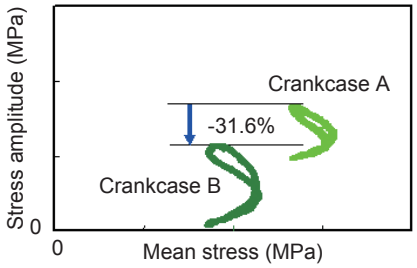


Fig. 16 Reduction of stress at root of internal thread by changing form around bolt fastening area

4. Conclusions

(1) Technology for evaluating the fatigue strength of the entire crankcase was developed. This technology can evaluate the fatigue strength of the roots of the internal threads of the cylinder head fastening bolts and the crankshaft bearing fastening bolts.

(2) The strength of the crankcase, including the roots of the internal threads, can be evaluated quantitatively in the design stage. This enabled efficient crankcase design that minimizes increases in weight and cost, by modifying the structure and form.

References

(1) Fukuoka, T., Yamasaki, N., Kitagawa, H., Hamada, M.: Stress Concentration at the Root of a Screw Thread (Efficient of Root Radius and Friction Coefficient), Transactions of the Japan Society of Mechanical Engineers, A, 52 (481), p. 2201-2208 (1986)

(2) Fukuoka, T., Nomura, M., Morimoto, Y.: Proposition of Helical Thread Modeling with Accurate Geometry and Finite Element Analysis, Transactions of the Japan Society of Mechanical Engineers, A, 72 (723), p. 1639-1645 (2006)

(3) Momii, H., Ikeda, S., Tanoue, M., Ushijima, K., Takahashi, N.: Stress Analysis Method for Bolt Thread

under Operating Condition of Automotive Engine, 2009 JSAE Annual Congress Proceedings, No. 99-09, p. 13-16 (2009)
(4) Niino, T., Iwamoto, T., Ueda, S.: Development of simulation technology for dynamic behavior of crankshaft systems in motorcycle engines, JSAE Review, Vol. 23, p. 127-131 (2002)

■ Author ■


Hiroshi KURIBARA


Junya SAITO


Hideki SAITO


Daisuke SEKIYA

Study of Mechanism of Silencer Drainage Noise

Osamu MATSUDA* Michihiro TOKUNAGA*

ABSTRACT

Noise occurring at the exhaust outlet during idling and originating in condensate water accumulating in the silencer reduces the commercial appeal of vehicles. Visualization tests reproducing a silencer and predictive calculations based on a one-dimensional model were conducted in order to elucidate the mechanism of occurrence of this noise and study measures to prevent it. The results showed that pulsative pressure from the engine and the internal resonance of the exhaust pipes were factors in drainage noise, and the noise occurred when water films that had been generated and blocked the outlet pipe in areas in which the particle velocity was highest migrated downstream and broke up.

In addition, in order to prevent drainage noise, increasing the pressure differential before and after the formation of the water film, ΔP, is an effective measure in increasing drainage performance during idling.

1. Introduction

Automotive exhaust systems reach high temperatures due to combusted gases in the engine, and are subjected to conditions of severe thermal shock as a result of the cooling of the exhaust gas by the external air as it proceeds towards discharge. These temperature changes are a factor in the generation of a variety of noises. These noises reduce the commercial appeal of the vehicle, and their amelioration is therefore necessary.

Silencer drainage noise is one of the noises that occur in the exhaust system. The hydrogen component contained in gasoline forms water vapor by bonding with oxygen in the air; cooling of this vapor in the silencer results in the formation of condensate water (termed “water” below) and drainage noise originates from the flow of this water and exhaust gas.

This type of flow field in which gas and liquid are mixed is termed a gas-liquid two-phase flow, and has been the subject of a great deal of research in relation to industrial equipment and facilities such as boilers[(1)]. Shimizu et al.[(2)] explicated the mechanism of the breaking wave phenomenon which occurs when water and air mix in siphon pipes used in water and drainage systems. This research elucidates the phenomenon mainly in the case of transport of liquids. In the case of automotive exhaust pipes, idling over long periods and other use conditions result in considerable water accumulation in the silencer, producing gas-liquid two-phase flows. However, because heat, gas flows, and pulsative pressure from the engine affect the phenomenon in complex ways, its theoretical analysis is challenging, and troubleshooting is therefore generally based on experience. Today’s use of low exhaust pressures, however, promotes the accumulation of water in the silencer, and drainage noise is becoming increasingly severe.

The research discussed in this paper analyzed the mechanism of drainage noise by attempting to understand the behavior of water through experiments. In addition, the project conducted predictive calculations based on one-dimensional models in order to study means of preventing drainage noise, and the details will be discussed in this paper.

2. Mechanism of Drainage Noise

2.1. Phenomenon of Drainage Noise

Drainage noise does not occur constantly, but is a phenomenon that occurs under specific conditions. First, the behavior of water was rendered visible to help enable the characteristics of drainage noise to be understood.

2.1.1. Characteristics of drainage noise

The greater the amount of water that accumulates in the silencer, the greater its weight becomes, and this situation is undesirable from the perspectives of the occurrence of rust and the maintenance of the strength of the exhaust system components. Because of this, silencer layouts that actively encourage drainage are employed in order to reduce the amount of water accumulating. However,

* Automobile R&D Center

when the vehicle is idling, exhaust pressure declines and water tends to accumulate in the silencer. The frequency of drainage noise from the exhaust pipe exit is particularly high when the vehicle has been idling for long periods and water has continued to accumulate in the silencer. Figure 1 shows the process leading to the occurrence of drainage noise. As diagramed in Figs. 1(A) and (B), when water that has continued to accumulate infiltrates the outlet pipe, drainage noise will tend not to occur if the water is drained immediately from the tailpipe exit. However, if the water does not drain from the tailpipe exit, the possibility that drainage noise will occur increases. Drainage noise is an intermittent croaking sound that affects the commercial appeal of the vehicle. Figure 2 shows the results of frequency analyses conducted when drainage noise occurred and when the noise did not occur. The results show that drainage noise represents an excitation of the frequency components from low frequencies up to 1.5 kHz.

2.1.2. Behavior of water when drainage noise occurs

In order to study the behavior of water when drainage noise occurs under the conditions shown in Fig. 1(A), a transparent acrylic plate was fitted in a silencer in which drainage noise had occurred, to help enable visualization (Fig. 3).

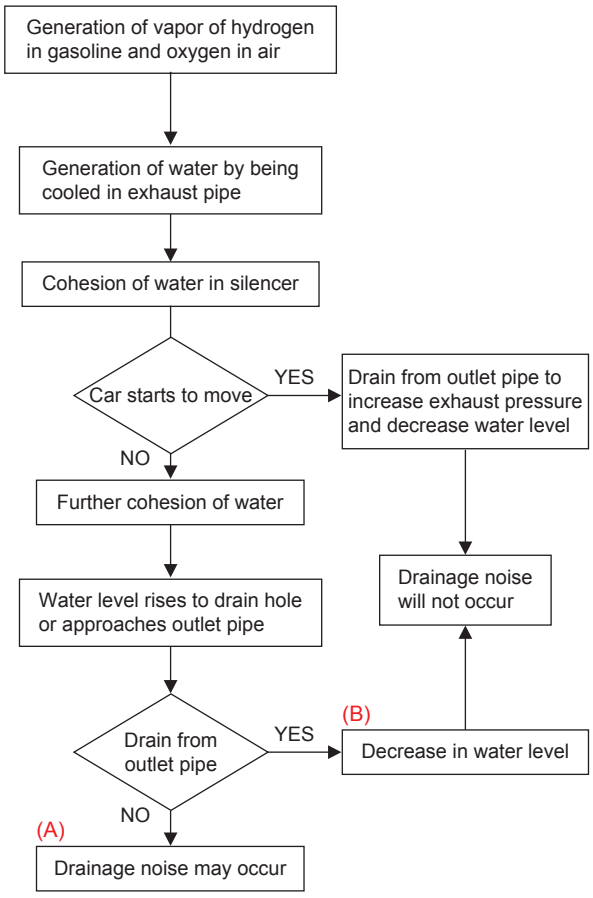


Fig. 1 Occurrence conditions of drainage noise

The results are shown in Fig. 4. When drainage noise occurs, water films are generated by fountains occurring close to the inlet of the outlet pipe, and these water films repeatedly break up and flow downstream. The results also showed that the noise occurs when these water films break up.

2.2. Analysis of Behavior of Water producing Drainage Noise

2.2.1. Specification of input factors

The input when drainage noise occurs is exhaust pressure, but exhaust pressure is composed of a fluctuating and a

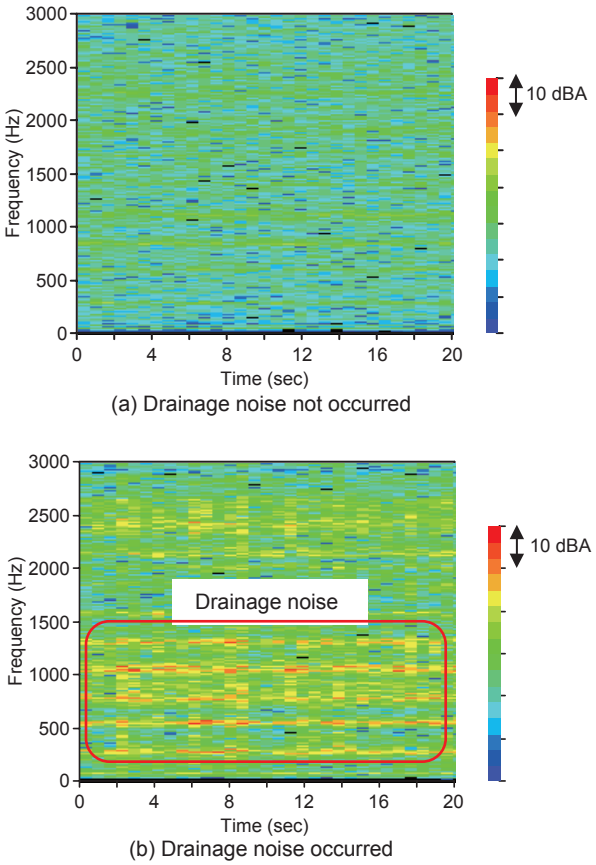


Fig. 2 Exhaust sound when drainage noise not occurred and occurred

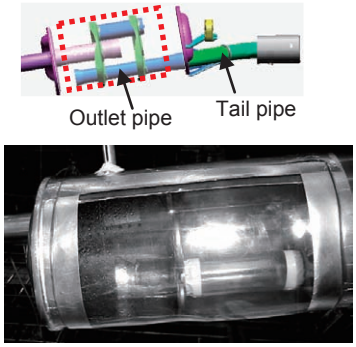


Fig. 3 Visualized silencer model

steady-state component. In order to determine which of these components was the main factor in the occurrence of drainage noise, input from a blower was used as the steady-state component and pressure fluctuations from a speaker were used as the fluctuating component (Fig. 5), and the behavior of the water and the occurrence or non-occurrence of drainage noise were studied.

As Fig. 6 shows, during the steady-state component input waves were generated but no drainage noise occurred, while when the fluctuating component was input a fountain occurred close to the outlet pipe inlet at 22 Hz, blocking the pipe and producing drainage noise.

2.2.2. Water behavior inside straight pipe model

The fact that drainage noise occurred during fluctuating component input at a specific frequency (22 Hz) in a test in which the pressure components were separated indicated that the occurrence of drainage noise was frequency-dependent. An apparatus for testing resonance in a gas column contained in a tube, known as a Kundt's tube, has existed for more than a century. Tatsuno[3] demonstrated in tests that fountains occur in the tubes in areas where the sound pressure is low. This means that the water that enters the tube is formed into fountains in areas where the particle velocity is high. In order to confirm these findings, using an acoustic particle velocity probe in the ϕ41 x 5000 mm transparent acrylic pipe shown in Fig. 7, the present project measured sound pressure and particle velocity in the tube at the first-order resonance, 33 Hz, and the second-order resonance, 66 Hz, when a speaker was used to provide

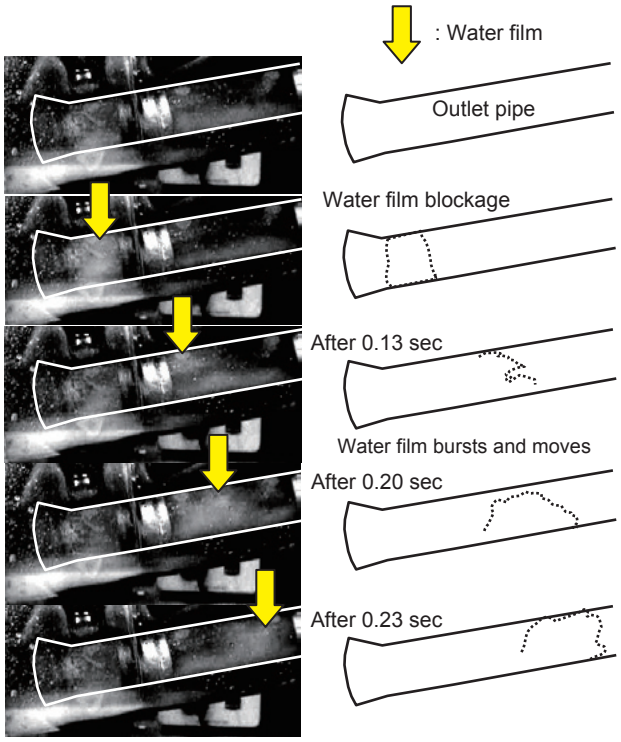


Fig. 4 Visualization of water behavior when drainage noise occurred

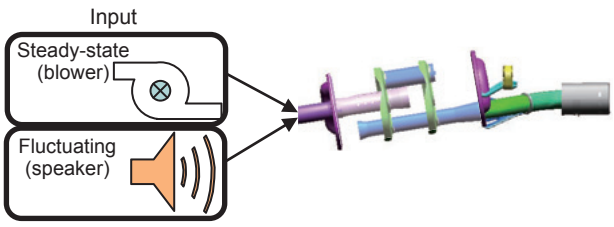


Fig. 5 Separation of influence of input components on drainage noise

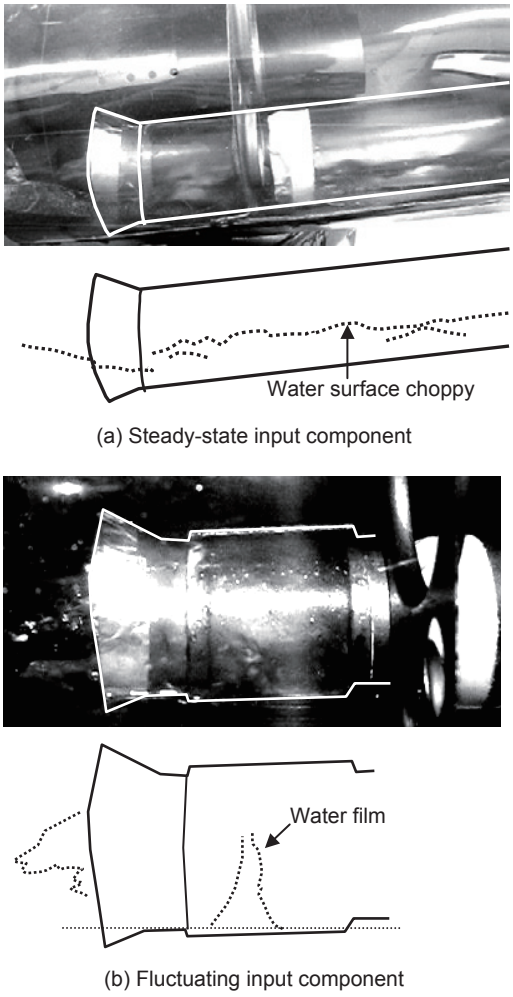


Fig. 6 Results of separation of input components

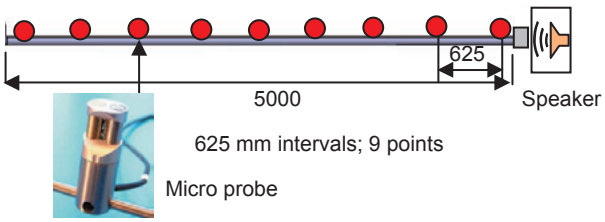


Fig. 7 Simple straight pipe model

input. In addition, water was introduced to the tube, and its behavior was observed at 28 Hz and 56 Hz. The resonance frequencies here were lower than during measurements of particle velocity because tubes with upward bends had been attached to the ends of the tube to help ensure that the water did not leak.

Figure 8 shows the results of measurements of sound pressure and particle velocity in the tube, and Fig. 9 shows results for the behavior of the water. At 28 Hz, fountains would form at both ends of the tube, where the particle velocity was high; the fountains would begin to migrate while undulating in the axial direction of the tube and would be extinguished. This process was repeated. At 56 Hz also, fountains would form close to the center of the tube where the particle velocity was high and undulate in the axial direction of the tube.

These test results indicate that water is raised into fountains in areas of the tube in which the particle velocity is high, and this results in a blockage of the tube.

2.2.3. Verification in actual system model

Tests showed that water fountains were generated and blockages occurred in areas of a straight pipe model where the particle velocity was high. In order to test whether water would cause blockages in areas in which the particle velocity was high in a silencer with a complex configuration, an actual silencer was excited using a speaker. Figure 10 shows the points for measurement of particle velocity. Points A, B, and C were inside the outlet pipe, and points D and E were inside the silencer.

Figure 11 shows the results of measurements of the particle velocity at the silencer resonance frequency of 30 Hz, at an input of 90 dB. The results show that in an actual silencer, the area in which the blockage occurs (Point A

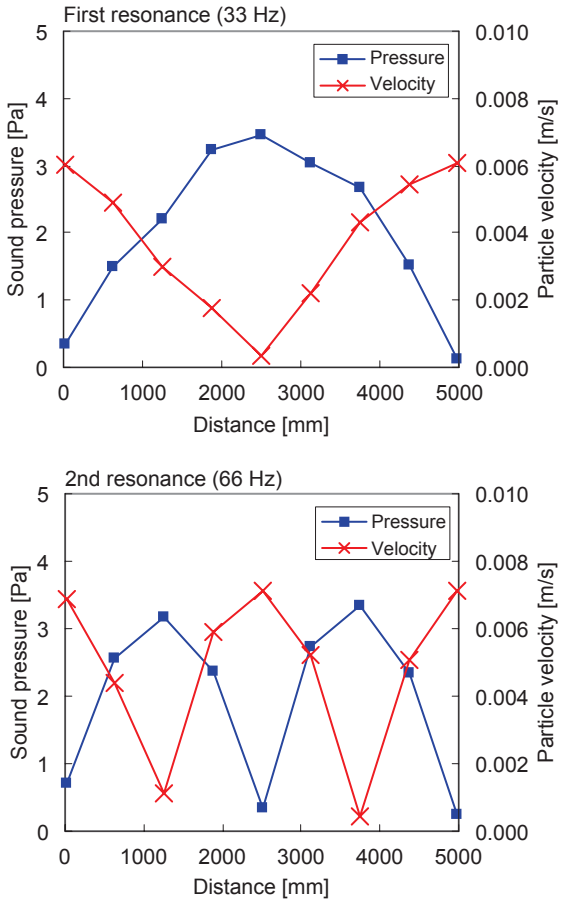


Fig. 8 Measurements of pressure and particle velocity in straight pipe

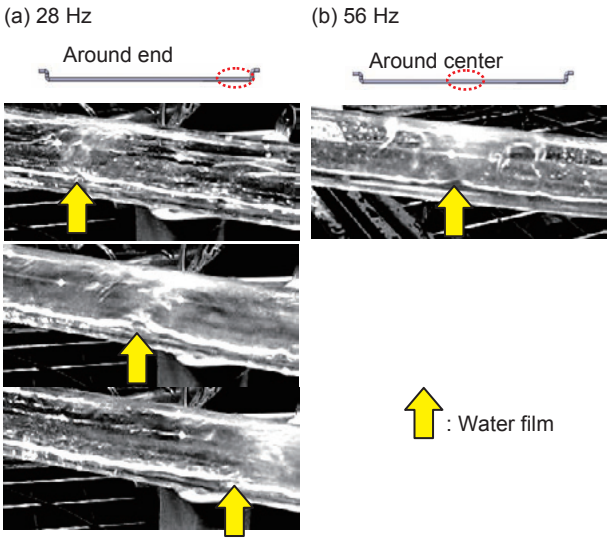


Fig. 9 Water behavior in straight pipe

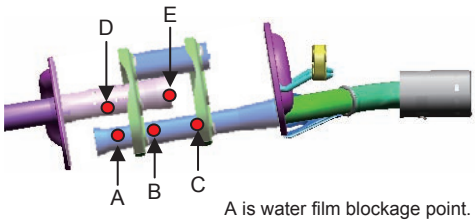


Fig. 10 Measurement points in silencer

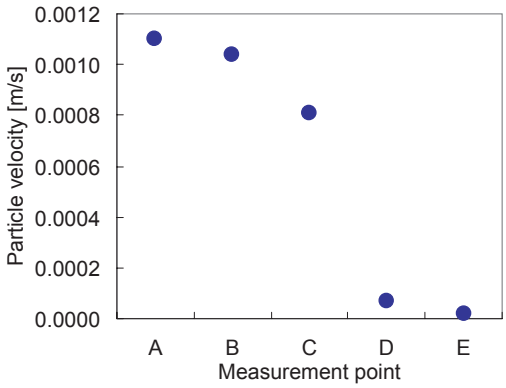


Fig. 11 Measurements results for particle velocity in silencer

in Fig. 10) coincides with the area in which the particle velocity is at its maximum. In conditions in which drainage noise occurs in an actual silencer, water forms fountains in areas in which the particle velocity is highest, and the pipe becomes blocked. These results indicate the following mechanism for the generation of drainage noise.

If water exists in the area in which the particle velocity is at its maximum at the resonance frequency of the silencer, fountains will be formed, and noise will be generated following the blockage of the pipe by those water films.

3. Study of Prevention of Drainage Noise

Based on the mechanism of drainage noise discussed in Chapter 2, the following three measures for prevention of the noise could be considered:

(1) Modification of the resonance frequencies of the silencer to prevent them falling within the idling range of the engine
(2) Reduction of the particle velocity
(3) Reduction of the amount of water accumulating in the silencer (Drainage noise does not occur in the absence of water)

Modification of the low-frequency resonance frequency, as suggested in (1), would necessitate extensive modification of the length of the exhaust system and of the volume of the silencer, and would therefore be challenging in practice. The concrete method of realizing (2), positioning holes close to the areas of the outlet pipe inside the silencer where the particle velocity is highest in order to reduce the velocity, is already in use. If the amount of water accumulating in the silencer could be reduced, as indicated in (3), it would present advantages from the perspectives of rust prevention and maintenance of strength in addition to preventing drainage noise. Given this, this chapter will discuss evidence obtained from tests concerning the mechanism of drainage of water that accumulated in the silencer from the tailpipe, as shown in Fig. 1(B), and a method for its prediction.

3.1. Prediction of Drainage Performance

In order to study factors affecting drainage performance, the behavior of water was visualized using the test model shown in Fig. 12, and pressure measurements were conducted in the area indicated in the diagram. An inline 4-cylinder engine was employed, operated in the idling range. The test results showed that when there is extensive migration of the water films and they are drained, the positive pressure peak of the outlet pipe pressure differential (ΔP: P_1-P_2) instantaneously increases (the circled area in Fig. 13). A bypass pipe was positioned on the upstream side of the silencer; the pressure differential ΔP in the silencer outlet pipe was varied by varying the diameter of this pipe, and the amount of water accumulating in the silencer was measured. Figure 14 shows the average values of the positive pressure peaks of the pressure differential ΔP and the amount of accumulated water in the silencer. These results show that the amount of accumulated water in the silencer declines in proportion with the increase in the peak value of ΔP.

Based on this, it is conjectured that the water films migrate downstream and are discharged from the tailpipe because the pressure differential ΔP increases with the addition of an instantaneous irregular component to the fluctuating component of pulsative pressure in the outlet pipe.

Given that drainage noise would not occur if the amount of water accumulating in the silencer were reduced, a physical model for the prediction of the amount of water accumulating in the silencer when the vehicle was idling was formularized and studied in tests in order to study orientations for measures to increase drainage performance.

3.1.1. Construction and formularization of drainage model

The behavior of the gas-liquid interface in a gas-liquid two-phase flow in which gases and liquids are mixed involves rather complex phenomena, and accurate prediction based on theoretical analyses represents a challenge. Recently, reports have appeared concerning the elucidation of the phenomena employing the MAC, VOF,

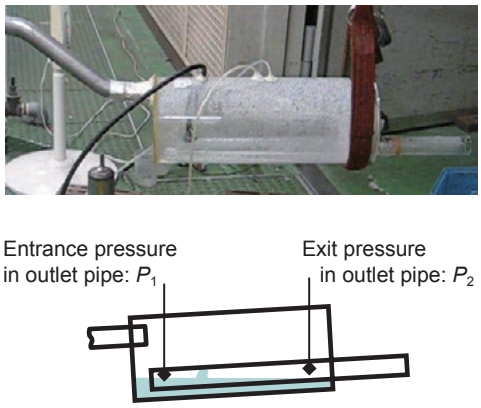


Fig. 12 Test model for study of drainage noise and drain performance

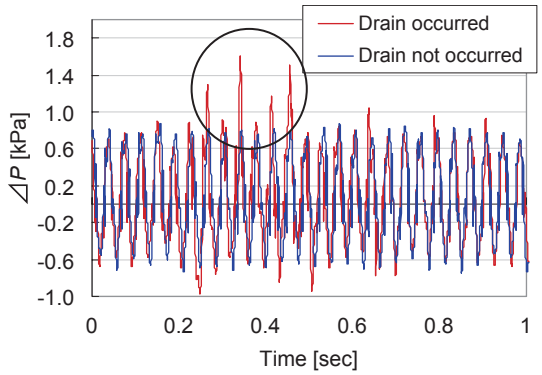


Fig. 13 Difference in pressure in outlet pipe

CIP, and other methods of Navier-Stokes numerical analysis and visualization experiments using high-speed cameras[2].

In order to predict drainage noise, it is necessary to calculate the behavior of the gas-liquid interface, but it was possible to employ a simpler model if the phenomenon was restricted to the degree of migration of the water films. Focusing on the fact that ΔP necessarily increased when the water films migrated, based on the test results discussed above, the authors conjectured that the phenomenon could be explained using two models (of the water films that blocked the interior of the pipe and of the flow of exhaust gas), and attempted to formularize these.

First, as a model of the drainage of water, a dynamics model will be considered in which the water films that block the pipe are pushed from the pipe by the pressure differential ΔP before and after the blockage occurs. As shown in Fig. 15, the internal diameter and mass of the water film are termed d and m, respectively; the velocity of migration of the film when acted upon by force F is termed V_f, the distance it migrates within the pipe is termed L, and its height at that time is termed H. The force acting on the film, F, is equivalent to the pressure differential ΔP before and after the formation of the film multiplied by the surface area of the pipe, S.

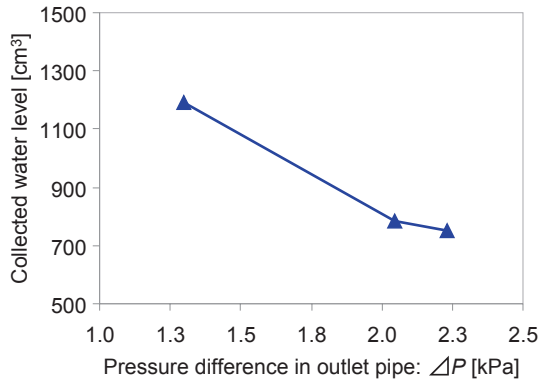


Fig. 14 Relation between ΔP and collected water level

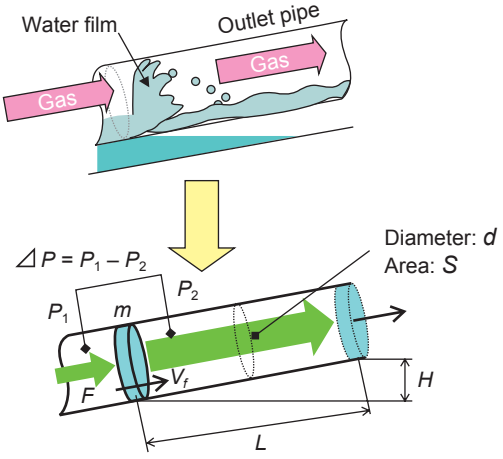


Fig. 15 Model of water film

Based on motion equations, the velocity of migration of the water film, V_f, is

$$\begin{aligned} m \cdot \frac{dV_f}{dt} &= F \\ &= (P_1 - P_2) \cdot S \\ V_f &= \frac{1}{m} \cdot \Delta P \cdot S \cdot \Delta t \end{aligned} \tag{1}$$

ΔP is the pressure differential before and after the formation of the film. If gravitational acceleration is termed g, friction loss in the pipe ΔH, and the drag coefficient of the pipe λ, then based on the principle of conservation of energy, the velocity determined in Eq. (1) gives

$$\begin{aligned} \frac{1}{2} \cdot m \cdot V_f^2 &= m \cdot g \cdot H + m \cdot g \cdot \Delta H \\ H &= \left(\frac{1}{2g}\right) \cdot V_f^2 - \Delta H \\ &= \left(\frac{1}{2g}\right) \cdot V_f^2 - \lambda \cdot \frac{L}{d} \cdot \frac{V_f^2}{2g} \end{aligned} \tag{2}$$

and the height, H, which the water film blocking the outlet pipe is able to reach can be determined. Here, the equation below, known as the Darcy-Weisbach equation, is used for ΔH. The equation indicates that friction loss has a great effect on flow velocity.

$$\Delta H = \lambda \cdot \frac{L}{d} \cdot \frac{V_f^2}{2g} \tag{3}$$

Next, the fluid model shown in Fig. 16, in which minute pressure waves are propagated in a static fluid, was employed for the gas flow.

Looking at the propagation of pressure waves in the

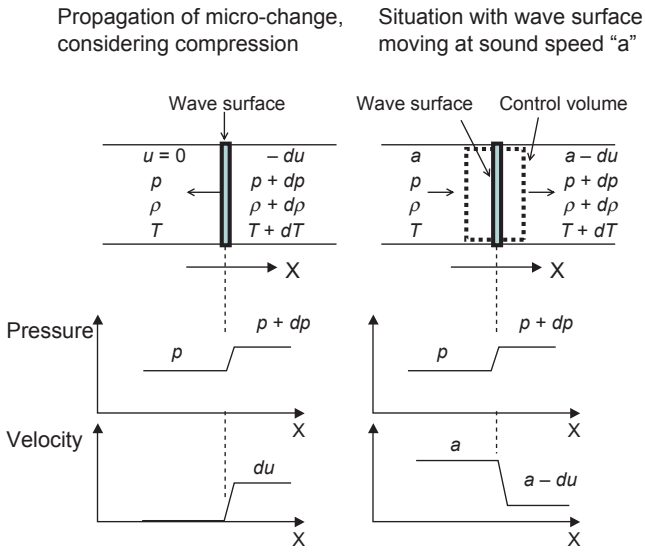


Fig. 16 Model of gas flow

negative direction of the X axis in the static fluid, pressure changes by dP and density changes by $d\rho$ due to the passage of the wave surface. It is challenging to observe and analyze a moving compression wave from outside the system. If an observer riding the compression wave and moving at speed a is therefore imagined, the speed of the flow passing the wave surface is reduced from a to a-du, while the pressure increases from P to P+dP and the density increases from ρ to ρ+$d\rho$. Because the principle of conservation of motion is applied here, if the control volume surrounding the wave surface is considered and the force acting on the control volume is made the left-hand term and the degree of motion is made the right-hand term, then the degree of change in pressure is given by

$$S \cdot [P - (P + dP)] = \rho \cdot a \cdot S \cdot [(a - du) - a]$$
$$dP = \rho \cdot a \cdot du \quad (4)$$

If it is hypothesized here that the outlet pipe is blocked by the water film and the gas flowing at velocity u is instantaneously blocked and becomes static, the change in velocity, du, is given by

$$du = u - 0 = u \quad (5)$$

From Eqs. (4) and (5), the pressure differential before and after the blockage of the pipe by the water film, ΔP, is determined by the following equation:

$$\Delta P = \rho \cdot a \cdot u \quad (6)$$

This is known to be a pressure increase due to the water hammer phenomenon[4].

In addition, the gas velocity, u, is found using the following equation:

$$u = \frac{Q}{S} \quad (7)$$

Q is volumetric flow, and is determined mainly using the engine displacement.

3.1.2. Validation of drainage model

The pressure differential before and after the blockage of the interior of the outlet pipe by the water film, ΔP, and the gas flow velocity are found using Eqs. (6) and (7), respectively. Figure 17 shows a comparison of calculated and test figures. A pitot tube was employed for the measurement of the gas flow velocity. Using the pressure differential, ΔP, the height to which the water film is able to rise in the outlet pipe can be found from Eqs. (1) and (2). Figure 18 shows a comparison of calculation and test results. The tests employed the model shown in Fig. 12, using outlet pipes of three different diameters, and varying the silencer angle in 6° increments. In addition, the heights reached by the water films were determined from test images. The calculation conditions were density ρ=1.164 kg/m^3, sound speed a=348.9 m/s, water film mass m=0.005 kg (mass as measured in tests), friction coefficient λ=0.027, Δt=0.038 s (at an idling speed of 800 rpm, the 2nd-order harmonic of the explosion is 26.6 Hz; Δt at one explosion). Because the internal walls of the pipe were smooth and the Reynolds number was less than 10^5, the Blasius equation[5] was used to find the friction coefficient.

3.2. Discussion

The two test plots for the gas velocity and the pressure differential ΔP as shown in Fig. 17 correspond well with calculated figures.

Figure 18 indicates that the pressure differential ΔP increases in proportion to the reduction in the diameter of the outlet pipe, and the height reached by the water film, H, also increases in proportion to this parameter. It is considered that differences occurring in ΔP at the same pipe diameter can be explained by the fact that variations occur in the thickness of the water films because the formation of the films is based on unstable gas-liquid interface phenomena. However, test results for the relationship between ΔP and H display a good correlation with calculation results.

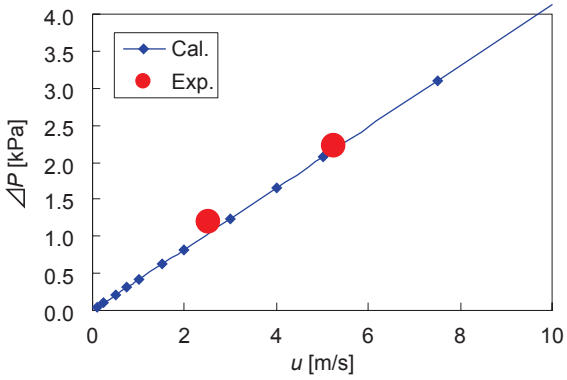


Fig. 17 Relation between u (gas velocity) and ΔP (pressure difference in outlet pipe)

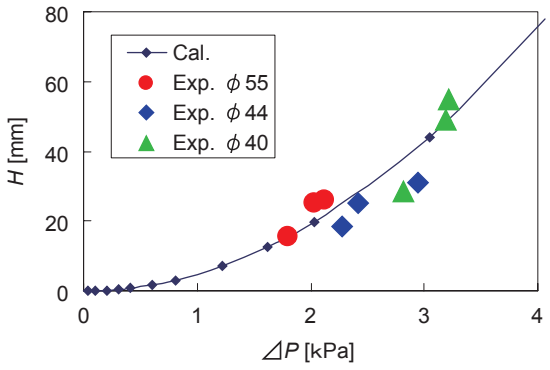


Fig. 18 Relation between ΔP (Pressure difference) and H (height reached by water film)

The results of the calculations based on the simple models formulated in the previous chapter demonstrated that the height of the water film, in other words drainage ability, could be reproduced with serviceable accuracy.

Because the gas velocity is determined by the engine displacement and the outlet pipe diameter, as a means of increasing drainage performance, an appropriate figure for the pipe diameter should first be decided on based on considerations of exhaust outlet noise and pressure loss due to exhaust gas flow. Following this, it would be effective to set the height between the inlet and outlet of the outlet pipe lower than the height that can be reached by the water film, taking into consideration the amount of water that will accumulate in the silencer.

4. Conclusion

The interior of a silencer was visualized, measurements of pressure in exhaust pipes were taken, and predictive calculations were conducted using a one-dimensional model in order to elucidate the mechanism of occurrence of drainage noise and to predict its occurrence. The following results were obtained:

(1) Pulsative pressure during engine operation and exhaust resonance is a factor in drainage noise, and it mainly occurs in the idling range.
(2) Blockage of the exhaust pipe by water occurs in areas in which the particle velocity is highest.
(3) The water films that block the exhaust pipe repeatedly flow downstream while breaking up, and drainage noise occurs when the film breaks up.
(4) The movement of the water film downstream is promoted and drainage performance increases in proportion to the magnitude of the pressure differential before and after the occurrence of the blockage due to the water film, ΔP. Increasing ΔP was shown to be an effective measure against drainage noise.

References

(1) Japan Society of Mechanical Engineers ed.,: Handbook of Gas-Liquid Two-Phase Flow Technology, Second Edition, Corona Publishing, p. 604 (2006)
(2) Shimizu, F.: Analysis of Gas/Liquid Two-Phase Flow in a Siphon Tube, 18th Symposium on Computational Fluid Dynamics, C7-4 (2004)
(3) Tatsuno, M.: Formation of Liquid Fountains in a Kundt's Tube, Reports of Research Institute for Applied Mechanics Kyushu University, Vol. 128, p. 31-36 (2005)
(4) Matsuo, K.: Compressible Fluid Dynamics, Rikogakusha Publishing, p. 29-31
(5) Nisikawa, N., Hiraoka, K.: Ryutai Rikigaku, Baihukan Publishing, p. 105 (1998) (in Japanese)

■ Author ■



Osamu MATSUDA



Michihiro TOKUNAGA

Honda R&D Co., Ltd.
Honda R&D Technical Paper Committee

Motorcycle R&D Center
Automobile R&D Center
Power Products R&D Center
Aircraft Engine R&D Center
Fundamental Technology Research Center
Honda R&D Americas

Editorial Afterword

I would like to take a brief look back on the history of the Honda R&D Technical Review. Understanding the necessity of a technical review in Honda, our predecessors, Mr. Ichiro Terui and Mr. Shin Narasaka, worked mightily to publish the first Honda R&D Technical Review in 1989. Under the situation that many companies in Japan were publishing technical reviews on their research and development results, they strongly believed that Honda's young engineers and future research centers would find value in releasing technical papers in this form and using them to create a culture at Honda. The review was intended to be "an opportunity providing 'top-level proof' of truly international creative engineers," and as such the review was based on the idea of bringing together the best of technologies in a way distinct from other companies' technical reviews. The Honda R&D Technical Review has greatly evolved in the more than 20 years since then, increasing to two issues per year, expanding in size, adding color and publishing an English edition. In the future, I hope to always be mindful of the ideals that formed its founding.

(Mikio Kato)

In July 2010, Honda R&D has reached the 50th anniversary of its founding. During this history, the Honda R&D Technical Review has been first published in 1989, and has recorded the progress of Honda's technology for 22 years. In this period, the review has become to be issued semiannually from Vol. 11 as No.1 and No.2, in order to post papers on advanced technology in a timely fashion. I have engaged as a member of editors from Vol. 8 (1996) to Vol. 22, No. 2 (2010). In some cases, I suggested to modify a manuscript in consideration of "readability, understandability and without misunderstanding." Everyone! Polish your manuscript a few days after you finish writing it, please. At that time, you can check whether it is written in natural Japanese (or English) by reading aloud it. There are basic rules for writing sentences. I recommend to read through the "Rikakei no Sakubun Gijutsu" ("Writing Techniques for Scientist") by Koreo Kinoshita (published by Chuko Shinsho) for future authors.

(Shinichi Koizumi)

©2010 Honda Motor Co., Ltd. (All rights reserved)

ISSN 1881-6223

Published by:
Honda Motor Co., Ltd.
2-1-1, Minami-Aoyama, Minato-ku,
Tokyo 107-8556, Japan

Edited by:
Honda R&D Co., Ltd.
Honda R&D Technical Paper Committee

Printed:
Sep. 1, 2010

(F1, FORMULA ONE, FORMULA 1, FIA FORMULA ONE WORLD CHAMPIONSHIP, GRAND PRIX and related logos are trademarks of Formula One Licensing BV, a Formula One group company. All rights reserved.)

